# FS/RV SONNE

# FAHRTBERICHT SO161-1&4
# CRUISE REPORT SO161-1&4
# SPOC

## SUBDUCTION PROCESSES OFF CHILE
## SUBDUKTIONSPROZESSE VOR CHILE

ANTOFAGASTA - VALPARAISO
OCTOBER 9 - OCTOBER 15, 2001
VALPARAISO - VALPARAISO
NOVEMBER 30 - DECEMBER 23, 2001

Edited by
**Ernst R. Flüh, Heidrun Kopp, and Bernd Schreckenberger**
with contributions of cruise participants

KIEL 2002
GEOMAR REPORT 102

**GEOMAR**
Forschungszentrum
für marine Geowissenschaften
der Christian-Albrechts-Universität
zu Kiel

**GEOMAR**
Research Center
for Marine Geosciences
Christian Albrechts University
in Kiel

Redaktion dieses Reports:
Ernst R. Flüh, Heidrun Kopp
und Bernd Schreckenberger

Editors of this issue:
Ernst R. Flüh, Heidrun Kopp,
and Bernd Schreckenberger

GEOMAR REPORT
ISSN 0936 - 5788

GEOMAR REPORT
ISSN 0936 - 5788

**GEOMAR**
Forschungszentrum
für marine Geowissenschaften
Wischhofstr. 1-3
D - 24148 Kiel
Tel. (0431) 600-2555, 600-2505

**GEOMAR**
Research Center
for Marine Geosciences
Wischhofstr. 1-3
D - 24148 Kiel
Tel. (49) 431 / 600-2555, 600-2505

# Table of Contents

Abstract 1
Zusammenfassung 2
Resumen 4
1. Tectonic and geological framework 6
1.1 The Chilean subduction system: tectonic setting and seismicity 6
1.2 Volcanic ridge collision 9
1.3 Subduction accretion vs. subduction erosion 11
1.4 Subduction of the Juan Fernández ridge 18
1.5 Margin Structure 21
1.6 Preliminary results of SO161 Leg 2 and 3 24
2. Participants 31
2.1 Scientists 31
2.11 Scientists – Leg SO161-1 31
2.1.2 Scientists – Leg SO161-4 31
2.2 Crew 32
2.2.1 Crew – Leg SO161-1 32
2.2.2 Crew – Leg SO161-4 33
2.3 Adresses of Participating Institutions 33
3. Agenda of the cruises So161-1 &4 38
4. Scientific Equipment 42
4.1 Shipboard equipment 42
4.1.1.1 Simrad 42
4.1.1.2 PARASOUND 42
4.1.1.3 Navigation 43
4.1.1.4 CTD 44
4.2 Computer facilities 50
4.2.1 Computer systems for navigation, gravity, and magnetics 50
4.2.2 Computer facilities for ocean bottom instrument programming and analysis 52
4.3 The GEOMAR Ocean Bottom Hydrophon/Seismometer (OBH/OBS) 53
4.4 Seismic sources 61
4.5 Gravimeter and magnetometer 64
4.5.1 The Bodenseewerke seagravimeter KSS31 64
4.5.2 The gradient magnetometer 65
4.5.3 The magnetic base station 66
4.6 Data processing 67
4.6.1 OBH/S wide angle seismics & MCS processing 67
4.6.2 Magnetics 74
4.6.3 Gravity 81
5. Experiments completed and preliminary results 95
5.1 Magnetics 95
5.2 Gravity 106
5.3 Seismology 118
5.3.1 Network Description 118
5.3.2 Processing 119
5.3.3 Data Quality and Noise Characteristics 121
5.3.4 Data Examples 124
5.3.5 Preliminary relocations of selected events 144
5.3.6 Future Work 148
5.4 Wide angle seismics 149
5.4.1 Profile SO 161-01 149
5.4.2 Profile SO 161-02 192

5.4.3 Profile SO 161-03 241
5.4.4 Profile SO 161-04 282
5.4.5 Profile SO 161-05 309
5.5 A Possible Slump Structure on the southern margin of the Punta Salinas Ridge 352
Acknowledgements 356
References 356

Appendices (Profile Tables) 359
I Captains Report 360
II Airgun Protocols 374
III OBH/S Deployments 375
VI Magnetic Profiles 381

## Summary

The main goal of the RV SONNE cruise SO161 SPOC (**S**ubduction **P**rocesses **O**ff **C**hile), Leg 1 and 4, is to investigate the effects of subducting aseismic ridges and fracture zones on seismicity and structure of the Chile Margin. In order to address this goal a multidisciplinary approach was taken including wide-angle seismic profiling, passive seismology, gravimetry, magnetics and high resolution bathymetry. Scientists from GEOMAR (Kiel), BGR (Hannover), FU Berlin (SFB 267), Universidad de Chile (Santiago), and Instituto Costaricense de Electricidad participated in the data acquisition and analysis. The legs 1 and 4 focus on two main geographic areas: the northern area covers the eastern part of the aseismic Juan Fernandez Ridge and the continental slope (31-34° S), in the southern area the Mocha and Valdivia Fracture Zones are subducting (36-41° S). This area is near to one of the target areas of the Collaborative Research Center 267 which conducts investigations on land.
From October 13-15, 2001 (Leg 1) an array of 23 ocean bottom hydrophones and seismometers (OBH/OBS) were deployed in the northern area. Two locations are on oceanic crust, the other units were used to create two sub-arrays covering Papudo Ridge and San Antonio Canyon. Between Leg 1 and 4, the BGR carried out a multi-channel reflection (MCS) seismic survey in the northern and southern areas. At the beginning of Leg 4 the OBH/OBS array was recovered, followed by wide angle profiles: Profile 01 extends a land profile laid out by the GeoForschungsZentrum Potsdam. 26 OBH/OBS were deployed in a linear array located at 38° S and oriented in W-E direction. Profile 02 was located at latitude 32° 05' S, oriented W-E and consisted of 25 OBH/OBS. Profile 03 and 04 cross the Juan Fernandez Ridge at the O'Higgins Seamount (32° 50' S/73° 38' W). Profile 03 (27 OBH/OBS) runs perpendicular to the ridge, while Profile 04 (23 OBH/OBS) is parallel to the ridge and covers also the O'Higgins Guyot. Profile 05 (26 OBH/OBS) was located at 31° S and also oriented in W-E direction. All profiles except Profile 04 were coincident with MCS profiles. For all profiles, the shot interval was 60 s; Profiles 02 and 05 were additionally shot with an interval of 40 and 30 s, respectively. During the whole cruise, gravity, magnetics, high resolution bathymetry (SIMRAD™), and sediment echo-sounding data (PARASOUND™) were recorded.
Preliminary analysis of the data has been begun on board. Many local and regional earthquakes were recorded by the passive seismological network. Preliminary locations were obtained for a number of events. All events thus far located have occurred between 15 and 30 km depth. Many events within the "Papudo Ridge Subnetwork" have been located ~10 km westwards of the previous land-based locations, which might indicate a bias in the existing catalogues.
Good record sections were obtained for all wide angle profiles, with clear seismic arrivals over offsets of more than 120 km recognisable at many stations, although, the quality of recordings varies with geologic structure, and in general better penetrations are achieved for profiles consisting predominantly of oceanic crust compared to stations located on the continental margin.Along the profiles, a total of 125 OBH/S were dropped and recorded almost 10.000 airgun shots. In Profile 01, a classic oceanic crust with a thickness of 6.5 km is observed for the stations seaward of the trench, whereas for stations on the continental margin, a layer of oceanic crust ($V_p$=6.5 km/s) could be identified beneath 20 km continental crust ($V_p$=4-6 km/s) and ~0.5 km of unconsolidated sediment. The velocity model based on the data from Profile 02 is able to resolve the lateral transition between the continental slope with accreted material ($V_p$=4.6-5.5 km/s) and the continental backstop ($V_p$=5.5-5.8 km/s) in the subsurface. Preliminary modelling of Profiles 03 and 04 show a Moho depression of some 4 km, resulting in a total depth of 13-14 km. The zone of anomalously thick crust is centred near O'Higgins Seamount and Guyot but extends beyond it, a structure typical of hotspot-related seamount chains.
Unclear magnetic anomalies are exhibited on the oceanic crust. In general the amplitudes are high. After a preliminary interpretation the magnetic anomalies do not reflect geological structures identified in multi-channel and wide angle seismic profiles. In the southern area the crustal age is determined to center

around 31 Ma, whereas in the north around 31°S the age of the Nazca Plate immediately before subduction is 41 Ma. The continental crust is characterised by the absence of long wavelength magnetic anomalies. The occurrence of low frequency anomalies hints at shallow magnetic source bodies. Offshore gravity data recorded during Leg 1 to 4 where combined with high resolution onshore data and satellite altimetry. The high resolution gravity data reflects the major structural features of the Chile margin and the Nazca Plate, particularly an increasing Bouguer gravity from south to north which is caused by an increase of its density due to the age of the plate. In curvature processing the deformation front in the trench axis is clearly imaged by the newly obtained gravity database. The Chiloé Fracture Zone extends to the east into the isthmus of Chiloé. Along the trend of the Mocha and Valdivia Fracture Zones density minimums are observed in the fore arc. Further processing, 3D-modeling and interdisciplinary interpretation will be carried out to investigate the influence and interaction of collision and subduction of the fracture zones in this transition zone.
The high resolution bathymetry data set obtained during the CONDOR and SPOC expeditions represent a complete image of the surface of the eastern part of the Juan Fernandez Ridge and the Chile Margin between 28 and 32° S. This image allows us to identify morphological features such as a giant, fault bounded slump block on the southern flank of the Punta Salina Ridge.

## Zusammenfassung

Das Ziel der FS SONNE Reise SO161 SPOC (Subduction Processes Off Chile), Abschnitt 1 und 4 war die Untersuchung der Einflüsse von subduzierenden aseismischen Rücken und Fracture Zones auf die Seismizität sowie die Struktur des Chilenischen Kontinentalhanges. Um dieses Ziel zu erreichen wurde ein multidisziplinärer Ansatz, bestehend aus seismischen Weitwinkeluntersuchungen, passiver Seismologie, Schweremessungen, Magnetik sowie hochauflösender Bathymetrie gewählt. Wissenschaftler von GEOMAR (Kiel), der BGR (Hannover), der FU Berlin (SFB 267), der Universidad de Chile (Santiago) und des Instituto Costaricense de Electridad haben bei den Messungen und Interpretationen der Daten teilgenommen. Die Arbeiten wurden in zwei Arbeitsgebieten durch geführt: das nördliche Arbeitsgebiet umfaßt den östlichen Teil des aseismischen Juan Fernandez Rückens sowie den Kontinentalhang (31-34° S), das südliche Gebiet den Bereich, in dem die Mocha und Valdivia Fracture Zone subduziert werden (36-41° S). Dieses Arbeitsgebiet liegt geographisch nahe des Schlüsselgebietes des Sonderforschungsbereiches 267, der Untersuchungen an Land durchführt. Zwischen dem 13. und 15. Oktober 2001 (Fahrtabschnitt 1) wurde ein Netz von 23 unterseeischen Hydrophonen und Seismometern (OBH/S) im nördlichen Arbeitsgebiet ausgelegt. Zwei Lokationen befinden sich auf oezeanischer Kruste, die anderen Instrumente wurden auf dem Papudo Rücken bzw. im San Antonio Canyon installiert. Zwischen dem ersten und dem vierten Fahrtabschnitt wurden von der BGR Reflexionsseismische Mehrkanaluntersuchungen (MCS Seismik) im nördlichen und südlichen Arbeitsgebiet durchgeführt. Zu Beginn des vierten Fahrtabschnittes wurden die OBH/S des bestehenden lokalen seismischen Netzes eingeholt und anschließend weitwinkelseismische Profilmessungen durchgeführt. Profil 1 verlängert ein vom GFZ Potsdam ausgelegtes Landprofil seewärts. Hierzu wurden insgesamt 26 Instrumente entlang einer Ost-West streichenden Linie bei 38°S ausgelegt. Das ebenfalls Ost-West streichende Profil 2 verläuft entlang 32° 05' S und besteht aus insgesamt 25 Geräten (OBH und OBS). Die beiden Profile 3 und 4 queren den Juan Fernandez Rückens über dem O'Higgins Seamount (32° 50' S/ 73° 38' W). Profil 3, bestehend aus 27 Instrumenten verläuft senkrecht zum Rücken, Profil 4 (24 OBH/S) streicht parallel zum Rücken und verläuft zusätzlich über dem O'Higgins Guyot. Profil 5 verläuft entlang 31° S in Ost-West-Richtung. Alle Profile mit Ausnahme des Profils 4 verlaufen entlang bestehender MCS Linien. Alle Profile wurden mit Schußintervallen von 60 Sekunden überschossen, Profil 02 und 05 zusätzlich mit 40 bzw. 30 Sekunden Schußintervall. Während der gesamten Fahrt wurden Schweremessungen, Magnetik und hochauflösende bathymetrische Vermessungen (SIMRAD$^{TM}$)

sowie Sediment Echolot (PARASOUND$^{TM}$) durchgeführt. Erste Analysen der gewonnenen Daten wurden an Bord begonnen. Zahlreiche lokale und regionale Erdbeben wurden von dem unterseeischen seismischen Netz registriert. Lokalisierungen von ausgewählten Erdbeben wurden durchgeführt. Alle bisher registrierten Erdbeben ereigneten sich in Tiefen zwischen 15 und 30 Kilometern. Bei Ereignissen, die im Bereich des Papudo Rücken lokalisiert wurden, lagen die ermittelten Positionen etwa 10 Kilometer weiter westlich als die, in lokalen Erdbebenkatalogen angegebenen Epizentren, die ausschließlich auf Daten von Landstationen basieren. Dies könnte auf eine Mißweisung der Positionen im Erdbebenkatalog hindeuten.

Von den seismischen Weitwinkelprofilen konnten sehr gute Daten gewonnen werden. Klare seismische Einsätze mit Offsets von mehr als 120 km wurden erzielt. Die Datenqualität variiert entsprechend der geologischen Strukturen; ein erhöhtes Eindringvermögen ist dort zu verzeichnen, wo überwiegend ozeanische Kruste vorherrscht. Entlang aller seismischen Linien wurden insgesamt 125 OBH/S ausgelegt, von denen insgesamt mehr als 10.000 Air Gun Schüsse registriert wurden. Auf Profil 01 konnte eine klassische ozeanische Krustenmächtigkeit von 6.5 km westlich des Tiefseegrabens vermessen werden. Ozeanische Kruste ($v_p$=6.5 km/s) konnte von Stationen östlich der Tiefseerinne mit einer Mächtigkeit von 20 km identifiziert werden. Dieser unterliegt kontinentale Kruste ($v_p$=4-6 km/s) sowie eine etwa 500 Meter mächtige, unkonsolidierte sedimentäre Deckschicht. Das auf Profil 02 basierende Geschwindigkeits-Tiefen Modell löst den lateralen Übergang zwischen dem Kontinentalhang mit akkretiertem Material ($v_p$=4,6-5,5 km/s) und dem kontinentalen Backstop ($v_p$=5,5-5,8 km/s) auf. Die Modellierungder Profile 03 und 04 ergibt, dass die Moho um etwa 4 Kilometer verlagert ist; sie befindet sich in einer Tiefe von etwa 13-14 Kilometern. Ein Bereich anomal mächtiger Kruste wurde im Bereich des O'Higgins Seamount und Guyot gemessen, was der typischen Struktur einer durch Hot-Spot Vulkanismus entstandenen Seamount Kette entspricht. Unklare magnetische Anomalien der ozeanischen Kruste wurden vermessen. Im Allgemeinen sind die gemessenen magnetischen Amplituden hoch. Nach vorläufigen Interpretationen der magnetischen Anomalien spiegeln diese nicht die auf den seismischen Profilen gewonnenen Erkenntnisse wieder. Im südlichen Arbeitsgebiet wurde das Krustenalter mit etwa 31 Ma bestimmt, im Norden hingegen, bei 31° S, beträgt das Alter der Nazca-Platte, die sich unmittelbar vor ihrer Subduktion befindet, etwa 41Ma. Die kontinentale Kruste ist dadurch gekennzeichnet, daß keine langwelligen magnetischen Anomalien zu verzeichnen sind. Die Präsenz kurzfrequenter magnetischer Anomalien deuten auf magnetische Körper in geringer Tiefe hin. Die marinen gravimetrischen Daten, die während der Fahrtabschnitte 1 bis 4 aufgezeichnet wurden, sind mit hochauflösenden Landdaten sowie altimetrischen Satelliten-Daten korreliert worden. Die hochauflösenden gravimetrischen Daten reflektieren die wichtigen und großen strukturellen Elemente der Nazca Platte und des Chilenischen Kontinentalhanges. Durch Curvature-Berechnungen konnte die Deformationsfront klar herausgearbeitet werden. Die Chiloé Fracture Zone erstreckt sich demnach bis zum Isthmus von Chiloé. Entlang der Streichrichtung der Chiloé und Valdivia Fracture Zone konnte jeweils ein Fore Arc Becken nachgewiesen werden. Weitere Datenverarbeitung, 3-D Modellierung und Interpretationen werden im Hinblick auf den Einfluß von Kollision und Subduktion solcher Fracture Zones und den beobachteten Schwereminima durchgeführt werden.

Der hochauflösende bathymetrische Datensatz, der während der CONDOR und SPOC Expeditionen gewonnen wurde repräsentiert ein komplettes Abbild der Oberflächenstruktur des östlichen Teils des Juan Fernandez Rückens und des Chilenischen Kontinentalhanges zwischen 28° und 32° S. Dieser Datensatz erlaubt uns die Identifikation morphologischer Strukturen wie etwa eines großen, durch Störungen begrenzten Rutschungsblocks auf der Südflanke des Punta Salina Rückens.

## Resumen

El objetivo principal del crucero SO 161 SPOC (Procesos de Subducción frente a Chile) del RV SONNE, tramos 1 y 4, es la investigación de los efectos que la subducción de dorsales submarinas asísmicas y zonas de fractura ejercen sobre la estructura y la sismicidad del margen continental de Chile. Para llevar a cabo este objetivo se utilizó un enfoque multidisciplinario que incluyó sísmica de refracción de gran ángulo, estudios de sismicidad, gravimetría, magnetismo y batimetría de alta resolución. Científicos de GEOMAR (Kiel), BGR (Hannover), FU Berlin (SFB 267), la Universidad de Chile y el Instituto Costaricense de Electricidad (Costa Rica) participaron en la adquisición y el análisis de los datos. La investigación se concentró en dos áreas geográficas: un área norte que cubrió la zona más oriental de la dorsal de Juan Fernández y el talud continental (31°-34° S), y un área sur donde ocurre la subducción de las zonas de fractura Mocha y Valdivia (36°-41° S); esta última área es cercana a la región del proyecto de colaboración especial 267 que lleva a cabo investigaciones en tierra.Entre el 13 y 15 de octubre de 2001, (Tramo 1) una red de 23 hidrófonos y sismómetros de fondo marino (OBH/OBS) fueron colocados en el área norte. Dos de estas unidades fueron colocadas sobre corteza oceánica y las restantes en una sub-red que cubrió la dorsal de Papudo y el cañón submarino de San Antonio. En el lapso transcurrido entre los tramos 1 y 4, BGR realizó un estudio de reflexión de sísmica multicanal (MCS) en ambas áreas. Al comenzar el Tramo 4 se recuperó la red de hidrófonos y sismómetros. Seguidamente se realizaron perfiles de refracción de gran ángulo: el primero de ellos (perfil 01) localizado en los 38° S, fue la continuación de una red de sismómetros colocada en tierra por el GeoForschungsZentrum Potsdam, que consistió de un arreglo lineal de 26 OBS/OBH con dirección este-oeste. El perfil 02, con 25 OBH/OBS, tuvo también una orientación este-oeste y se localizó en la latitud 32° 05' S. Los perfiles 03 y 04 se intersecaron sobre el monte submarino O'Higgins (32° 50'S/73° 38'W). El perfil 03 (27 OBS/OBH) fue perpendicular a la dorsal de Juan Fernández, en tanto que el perfil 04 (23 OBH/OBS) discurrió a lo largo de ella, incluyendo al guyot O'Higgins. El perfil 05 (26 OBH/OBS) estuvo orientado en dirección este-oeste, localizado en los 31°S. Todos los perfiles, a excepción del perfil 04, coincidieron con perfiles MCS realizados por BGR. En todos los perfiles el intervalo de tiempo entre disparos fue de 60 s; adicionalmente, los perfiles 02 y 05 fueron también disparados con intervalos de 40 y 60 s respectivamente. Durante todo el crucero se adquirieron datos de gravedad, magnetismo, batimetría de alta resolución (SIMRAD$^{TM}$) y datos de sonar (PARASOUND$^{TM}$). El análisis preliminar de los datos se inició abordo. Gran número de eventos sísmicos regionales y locales fueron registrados por la red sismológica pasiva. Hasta el momento todos los eventos localizados han ocurrido a una profundidad entre 15 y 30 km. Muchos eventos de la subred de Papudo han sido localizados aproximadamente a 10 km hacia el oeste de localizaciones previas hechas con base en estaciones sísmicas terrestres, lo cual puede indicar un error sistemático de los catálogos existentes .Registros de buena calidad fueron obtenidos para todos los perfiles de gran ángulo y algunos de ellos muestran arrivos de distancias superiores a los 120 km, a pesar de que la calidad varía con la estructura geológica y en general mayores penetraciones han sido obtenidas para perfiles predominantemente oceánicos. A lo largo de los 5 perfiles, fueron instalados un total de 125 OBH/OBS y se llevaron a cabo casi 10 000 disparos con cañones de aire. En el perfil 01 se encontró una estructura oceánica clásica, con un espesor 6.5 km al oeste de la fosa, mientras que para las estaciones del margen continental la corteza oceánica (Vp = 6.5 km/s) se encontró bajo 20 km de corteza continental (Vp= 4-6 km/s) y 0.5 km de sedimentos mal consolidados. El modelo de velocidad basado en el perfil 02 muestra la transición lateral entre el talud continental con material acrecionado (Vp=4.6-5.5 km/s) y el contrafuerte continental (Vp=5.5-5.8 km/s) en profundidad. El modelaje de los perfiles 3 y 4 muestra una depresión del Moho de unos 4 km, para una profundidad total de 13-14 km. El área de corteza anómalamente gruesa se centra cerca del monte submarino O'Higgins y el guyot del mismo nombre, pero se extiende lateralmente, mostrando una estructura típica relacionada con cadenas de montes submarinos. Las corteza oceánica exhibe anomalías magnéticas poco

claras. Las amplitudes son altas en general. Después de la interpretación preliminar, estas anomalías no reflejan estructuras geológicas identificadas en los perfiles MCS ni en los perfiles de refracción de gran ángulo. En el área sur, la edad de la corteza ronda los 31 Ma, mientras que hacia el norte, en los 31° S, la edad de la placa Nazca en el punto de subducción es de 41 Ma. La corteza continental se caracteriza por la ausencia de anomalías magnéticas de gran longitud de onda. La existencia de anomalías de baja longitud de onda sugiere fuentes magnéticas someras. La gravedad marina registrada durante los tramos 1 y 4 se combinó con datos de tierra de alta resolución y altimetría satelital. Los datos gravimétricos de alta resolución reflejan las características estructurales principales de la placa Nazca y del margen chileno, particularmente una incremento en la gravedad Bouguer de sur a norte, que es causado por el aumento de la densidad con la edad de la placa. En el procesamiento de curvatura, los nuevos datos de gravedad muestran claramente el frente de deformación. La zona de fractura de Chiloé se extiende hacia el este del istmo de Chiloé. En el antearco se observan mínimos de densidad alineados con el rumbo de las zonas de fractura Mocha y Valdivia. Se llevará a cabo un procesamiento posterior, junto con modelaje tridimensional e interpretación, para investigar los efectos de la colisión y subducción de estas zonas de fractura en estas áreas de baja densidad. Los datos batimétricos de alta resolución obtenidos durante los proyectos CONDOR y SPOC representan una imagen completa de la superficie oriental de la dorsal de Juan Fernández y del margen chileno entre los 28 ° y los 32 ° S. Esta imagen nos permite identificar rasgos morfológicos tales como un bloque cortical gigantesco que se ha deslizado a lo largo de fallas en el flanco sur de la dorsal submarina Punta Salinas.

# 1. Tectonic and Geological Framework

(P. O. Thierer and H. Kopp)

## 1.1 The Chilean subduction system: tectonic setting and seismicity

The western portion of the South American continent is dominated by the Andean Orogen with a total length of more than 7500 km. Its formation is linked to the compressional underthrusting of the oceanic Nazca plate of Eocene age beneath the western margin of the South American continent (Fig. 1.1.1), which occurs at a rate of approximately 8.5 cm/y (DeMets et al., 1990, DeMets et al., 1994). The Nazca plate south of the Challenger Fracture Zone, which runs obliquely offshore central Chile between 35°S-30°S, originates at the Chile Rise, whereas the northern part of the plate formed at the East Pacific Rise (Cande and Haxby, 1991). Subduction underneath South America is believed to have been continuous since Jurassic time (Bangs and Cande, 1997). The subduction process is characterized by the change in dip angle of the downgoing plate along the strike of the trench, resulting in a segmentation of the margin. Subhorizontal subduction is observed underneath central and northern Peru between 2°S and 15°S, as well as between 28°S and 33°S beneath central Chile. North and south of these 'flat' slab segments, which dip at about 10°-15°, a steep-dipping (25°-30°) slab is present (Barazangi and Isacks, 1976) as manifested in the closer depth contour spacing in Figure 1.1.2. The flat slab segments correlate with the absence of Quaternary volcanism and a central valley on the South American plate, whereas active volcanism occurs above the steeply dipping segments. The origin of the flat slab geometry is still enigmatic. Segment boundaries commonly coincide with bathymetric elevations, ridges or fracture zones on the oceanic plate (Nur and Ben Avraham, 1981; Pilger, 1981). There may exist a correlation between the buoyancy of the subducted seafloor relief and the occurrence of the shallow subduction. It has been suggested that these oceanic plate asperities form earthquake nucleating features (von Huene et al., 1997). There is considerable shallow seismic activity within the upper 50 km-75 km depth range. The 1960 Valdivia earthquake was the strongest event ever recorded (with a moment magnitude of Mw=9.5 resulting in more than 1000 casualties in Chile and additional 200 fatalities in Japan and Hawaii). Hypocenters are not evenly distributed and most of the intermediate-depth seismicity is offset into the subducting oceanic mantle, rather than lying within the subducted plate or along the subduction zone boundary (ANCORP Working Group, 1999). Seismic analyses have shown that the presence of a tear in the lithosphere (as has first been proposed to mark the transition from steep to shallow subduction (Barazangi and Isacks, 1976)) is unlikely. Cahill and Isacks (1992) used teleseismic data to resolve a sharply flexed plate at the southward transitions from steep to shallow subduction and a gradual transition from horizontal to steeply dipping slab segments.

Russo and Silver (1994) used shear-wave splitting in teleseismic data to develop a model of trench-parallel mantle flow beneath the Nazca plate. Lateral mantle flow beneath the slab is attributed to retrograde motion of the slab, the decoupling of the slab and underlying mantle and a partial barrier to flow at depth (Fig. 1.1.3). Such material transfer from the Pacific mantle reservoir to the Atlantic mantle reservoir may explain the eastward motions of the Carribean and Scotia sea plates (Russo and Silver, 1994)

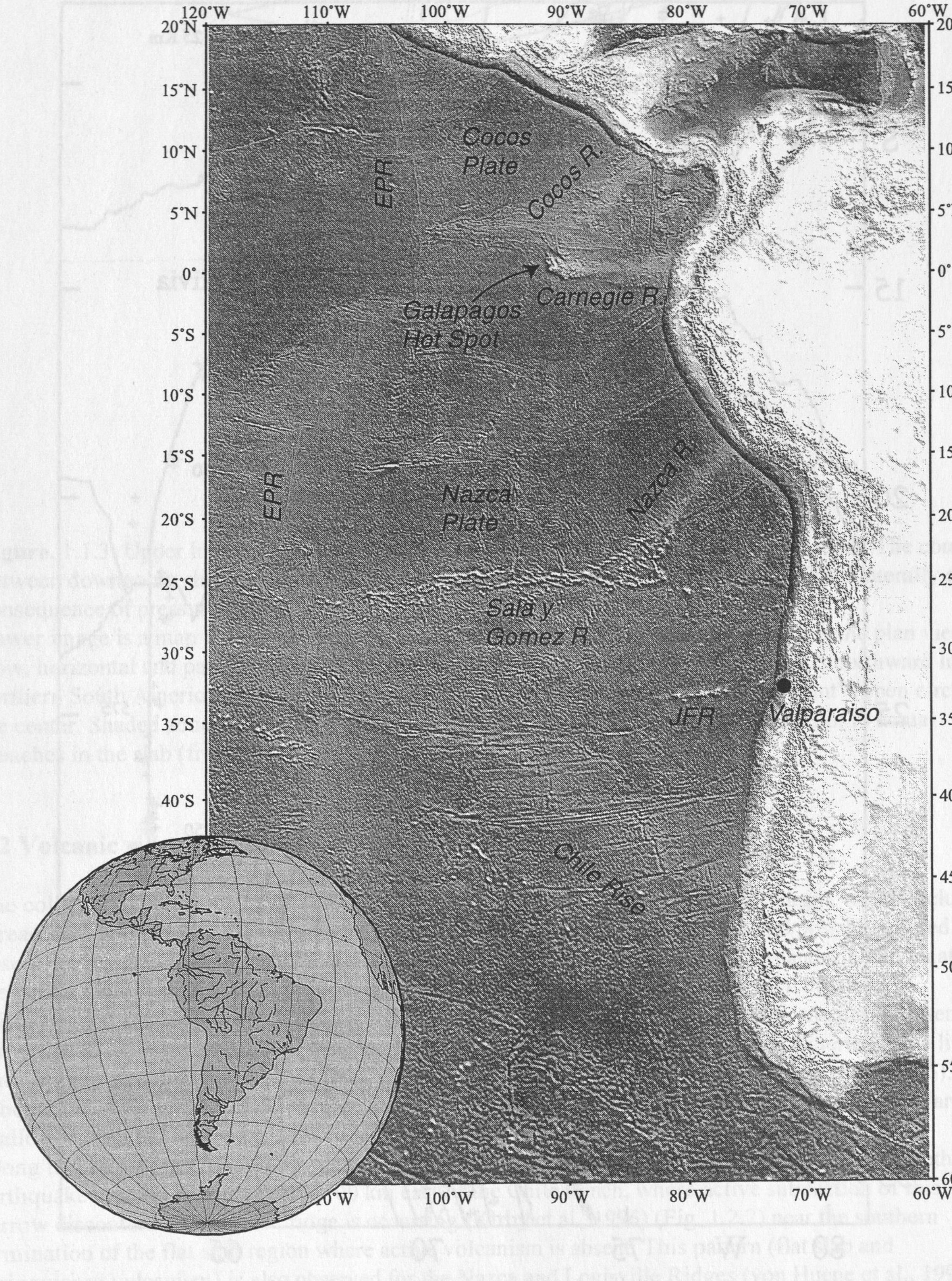

**Figure** 1.1.1: Bathymetric map of the southeast Pacific ocean where the Nazca plate is thrust beneath the South American continent along the Chile trench. EPR: East Pacific Rise, JFR: Juan Fernández Ridge.

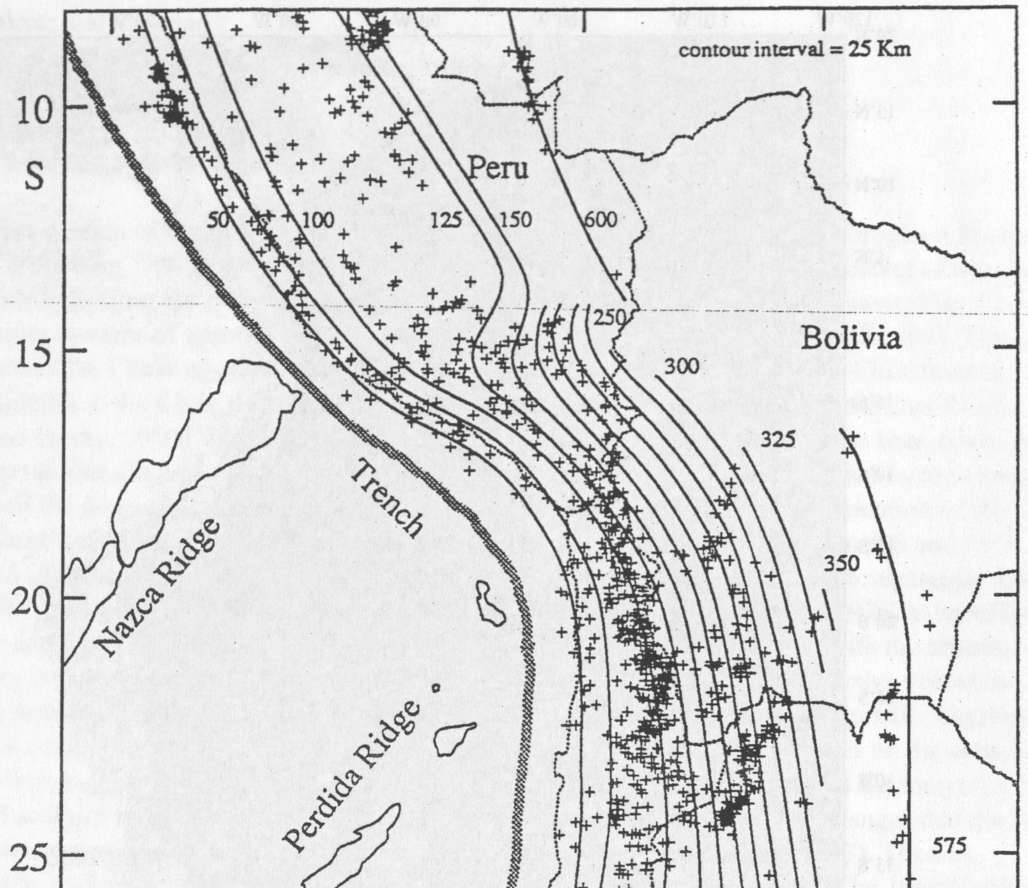

**Figure** 1.1.2: Depth contours of the Wadati-Benioff zone indicate the shape of the subducted Nazca plate

Small crosses represent epicenters of teleseismic events used to determine the contours. Shallow subduction characterized by a 'flat' slab is occurring underneath Peru and under central Chile, immediately north of the offshore Juan Fernández Ridge (from Cahill and Isacks, 1992).

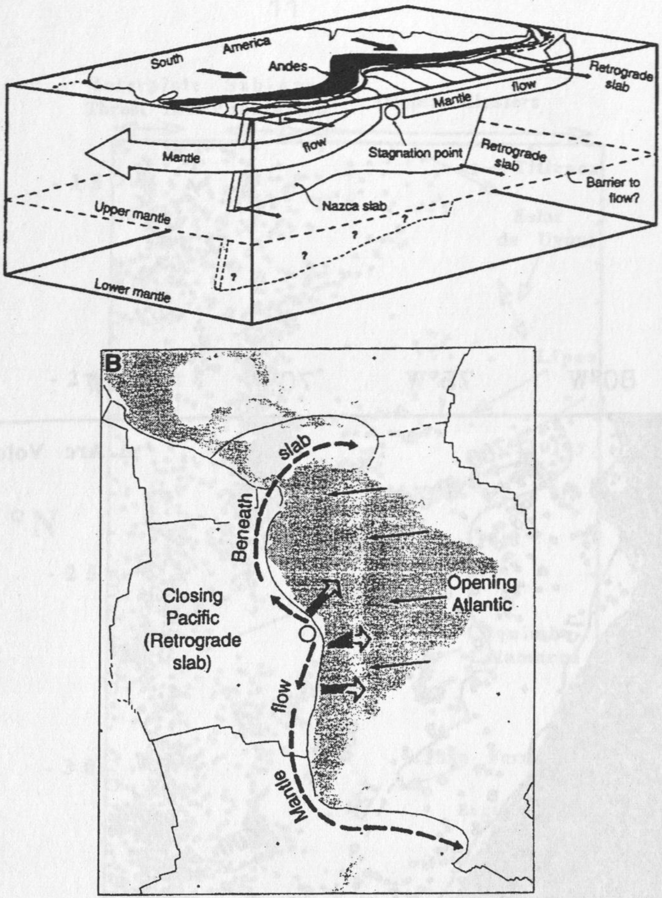

**Figure.** 1.1.3: Upper image is a schematic block view of trench parallel mantle flow model. The coupling between downgoing slab and underlying mantle is weak, and mantle just below slab flows laterally as a consequence of pressure induced by retrograde motion of slab.
Lower image is a map view of proposed retrograde flow model. The solid dashed line is the plan view of flow, horizontal and parallel to coast, passing into Caribbean and Scotia basins. Flow is northward in northern South America, southward in southern South America, with a „stagnation point“ (open circle) in the center. Shaded zones are regions of locally disrupted flow due either to contortions or to actual breaches in the slab (from Russo and Silver, 1994).

## 1.2 Volcanic ridge collision

The collision of volcanic chains and ridges will have fundamental effects on the margin, which include forearc tectonic erosion, altered slab buoyancy resulting in a decreased slab dip and possibly altered or absent arc magmatism. These effects suggest a linkage of the subducting Juan Fernandez chain located on the Nazca plate with the flat slab segment of the central Chilean margin (Fig. 1.2.1). Possible seismological expression of the subduction of aseismic volcanic ridges and volcanic chains are often fairly subtle for large, prominent features. The Nazca and Carnegie ridges in South America leave little trace in their intermediate-depth seismic events which are not unusually intense (Kirby et al., 1996). The subduction of the long-lived Louisville Ridge beneath the Tonga-Kermadec arc triggered several large shallow shocks but leaves little expression at intermediate depth (Christensen and Lay, 1988).
Along the trace of the Juan Fernández ridge at 33.5°S off Central Chile, a belt of intermediate-depth earthquake clusters extends nearly 700 km east of the Chile trench, where active subduction of this narrow discontinuous aseismic ridge is occurring (Kirby et al., 1996) (Fig. 1.2.2) near the southern termination of the flat slab region where active volcanism is absent. This pattern (flat slab and extinguished volcanism) is also observed for the Nazca and Louisville Ridges (von Huene et al., 1997, Kirby et al., 1996).

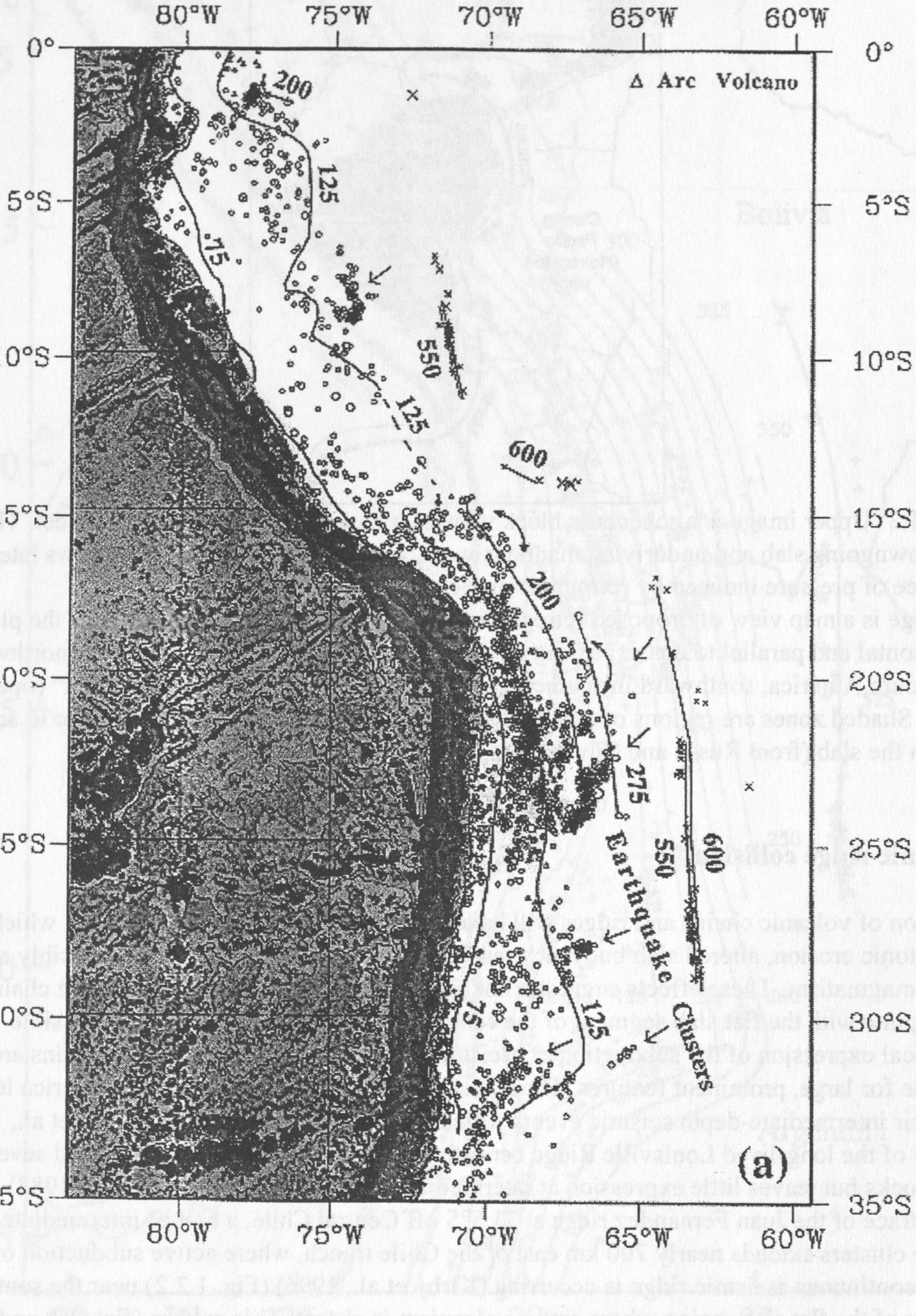

**Figure** 1.2.1: Heterogeneities in the Nazca plate and slab as revealed by earthquake locations. Contours are drawn as depth in km to the Wadati-Benioff zone. Shallow earthquakes are stripped from map east of the 75 km contour to emphasize Nazca slab seismicity. Note clustering of intermediate-depth events in roughly ENE- to NE-trending bands (arrows), especially at latitudes between 15 and 33 S. These bands are frequently aligned with offshore volcanic chains and ridges (from Kirby et al., 1996).

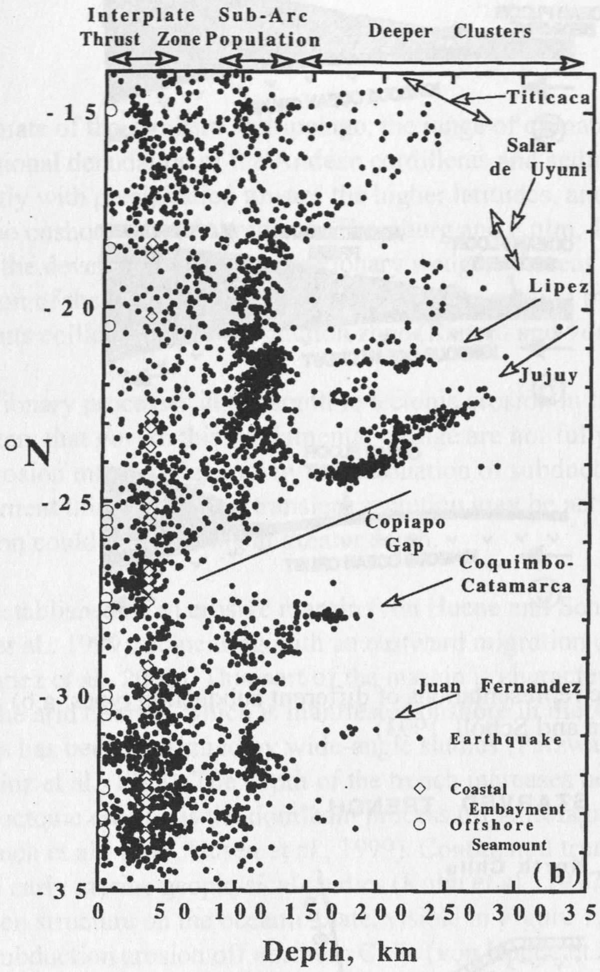

**Figure** 1.2.2: North-South cross section of Nazca intraslab seismicity. Note general tendency for earthquake clusters with labeled names to trend in the ENE to NE direction and plunge toward the north and east, corresponding to offshore trends of volcanic chains shown (from Kirby et al., 1996).

## 1.3 Subduction accretion vs. subduction erosion

Sediment accretion leads to the evolution of voluminous accretionary wedges, which contribute significantly to continental growth. This sediment accumulation has been documented for margins such as Nankai (Moore et al., 1990), Cascadia (Hyndman et al., 1990) and Sunda (Kopp et al., 2001), all of which are dominated by subduction accretion. Erosive margins then pose the other end-members of subduction zone types (Fig. 1.3.1) and have especially been found in the Pacific (Fryer, 1996, von Huene et al., 1985). These margins are typically composed of a backstop of continental rock against which a small accretionary wedge or non accretionary prism has accumulated. The Chile subduction zone is unique in that the growth and destruction of the margin may be observed in regions of subduction accretion and subduction erosion, respectively. It is a key area for investigating the interplay of processes that shape subduction zones. A number of parameters, some of which change along strike of the Chilean trench, may control the processes of sediment subduction, accretion and/or tectonic erosion. A major parameter controlling shallow subduction processes occurring near the deformation front and in the forearc domain is the amount of trench sediment fill (e.g Bangs and Cande, 1997) (Fig. 1.3.2). From the arid northern

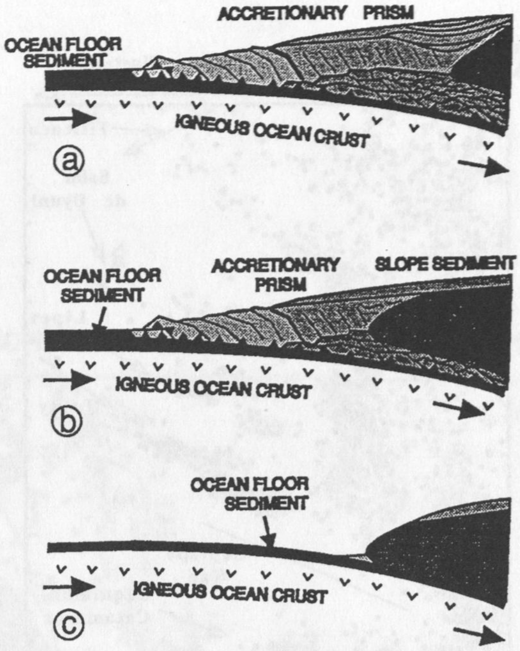

**Figure** 1.3.1: Schematic representations of different subduction types: a,b) accretionary, c) erosive (after von Huene and Scholl, 1993)

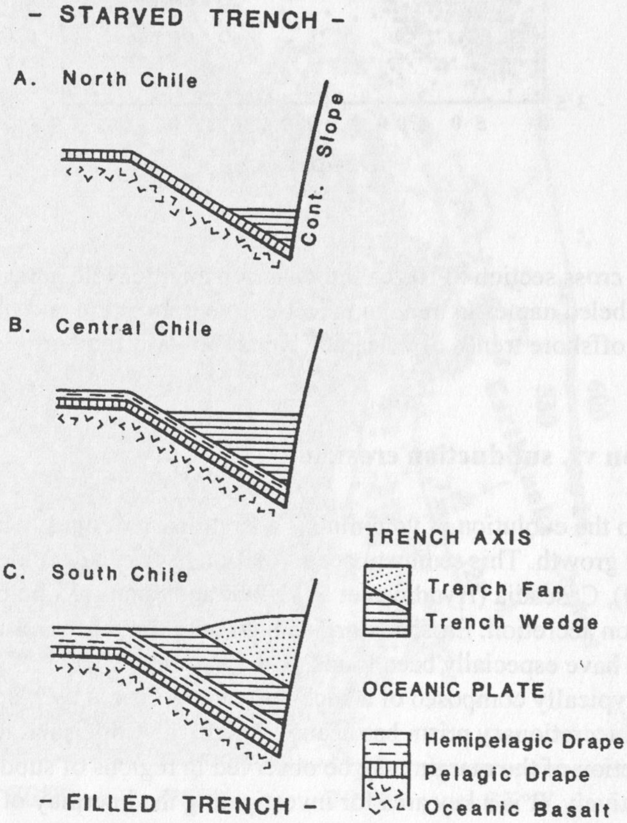

**Figure** 1.3.2: Schematic, transverse cross sections through the trench fill off Chile. Along the strike of the Chilean margin, the sediment supply varies from low (starved trench conditions) to high (filled trench), but the convergence rate remains essentially constant (from Thornburg and Kulm, 1987).

latitudes to the glacial climate of the southern archipelago, the range of climate affecting the Chilean mainland is extreme. Erosional denudation of the Andean cordilleras and sediment supply to the shelf and trench increase concurrently with precipitation toward the higher latitudes, and the volume of sediment in the trench axis parallels the onshore climatic gradient (Thornburg and Kulm, 1987). Large supplies of trench turbidites promote the development of an accretionary wedge, whereas a trench with little sediment may lead to tectonic erosion of the continental upper plate. Tectonic erosion may also occur where seafloor ridges or seamounts collide with the subduction zone (Ranero and von Huene, 2000).

The transition from accretionary processes in the south to tectonic erosion in the north is still not understood as the parameters that govern this fundamental change are not fully known. The change from accretion to upper plate erosion may be triggered by a combination of subduction slab angle, ocean plate roughness and trench sediment thickness. Also, transient accretion may be active at the front of the margin, but tectonic erosion could be occurring at greater depth.

Northern Chile has been established as an erosive margin (von Huene and Scholl, 1991, CINCA Working Group, 1997, von Huene et al., 1999), coinciding with an eastward migration of the magmatic arc since Meso-Cenozoic times (Yanez et al., 2001). This part of the margin is characterized by a starved trench, with little sediment fill. The arid climate, which is manifested onshore in the Atacama desert, prevents large sediment supplies, as has been confirmed by wide-angle studies (Patzwahl et al., 1999) and reflection seismic data (Hinz et al., 1995). The depth of the trench increases northward, reaching waterdepths of 8000 m. Tectonic erosion is the dominant process off Antofagasta and in the area studied by the CINCA project (Flueh et al., 1995, Husen et al., 1999). Continental truncation along northern Chile was already recognized in early marine geophysical studies (Kulm et al., 1977, Schweller und Kulm, 1978). The horst and graben structure on the oceanic plate, visible in Figure 1.3.3 seaward of the trench, plays a dominant role in subduction erosion off northern Chile (von Huene et al., 1999). Coastal uplift renders the upper plate slope unstable so that the crust disintegrates and forms a debris blanket creeping trenchwards. Mass wasting along the lower and middle slopes of the upper plate result in a down slope material transport which will fill the graben of the oceanic plate (von Huene et al., 1999) as presented in Figure 1.3.4. Due to the arid climatic conditions, only a modest amount of material and sediment debris is available so that the volume of graben is sufficient to accomodate subduction of all slope debris without building a significant accretionary prism. Small prisms locally act as buffers to excess material. The cause of the coastal uplift, which may be associated with underplating or duplexing, remains unresolved.

South of 33.5°S, where the Juan Fernandez aseismic ridge enters the trench, alternating erosive and accretionary phases have been documented (Bangs and Cande, 1997) and episodic flooding of the trench, fed also by the extensive canyon system (Fig. 1.3.5), favours sediment accretion. Currently the thickest trench infill along the Chilean margin occurs between the Chile triple junction at 47°S, where a shallow active spreading center is being subducted and the study area off Valparaiso (33°S) where the Juan Fernández ridge poses a topographic barrier across the trench and thus prohibits along strike sediment transportation to the north. This area is characterized by a moderate accretionary prism, however, seismic investigations have shown that a long history of accretion is not compatible with the amount of sediment accumulated here. Southern Chile has an episodic history of accretion, nonaccretion and possibly erosion (Bangs and Cande, 1997). These different subduction episodes are probably linked to temporal changes in sediment trench infill, mostly supplied by the adjacent continent. The onshore area between the Chile triple junction and the Juan Fernández ridge changes from a glacial climate to a more moderate climate, with rainfall varying from 300 cm/year to less than 100 cm/year (Bangs and Cande, 1997). Climatic conditions in this area have likely fluctuated sufficiently to cause significant variation in trench sediment supply (Rabassa and Clapperton, 1990). In addition to the trench wedge consisting of hemipelagic/pelagic

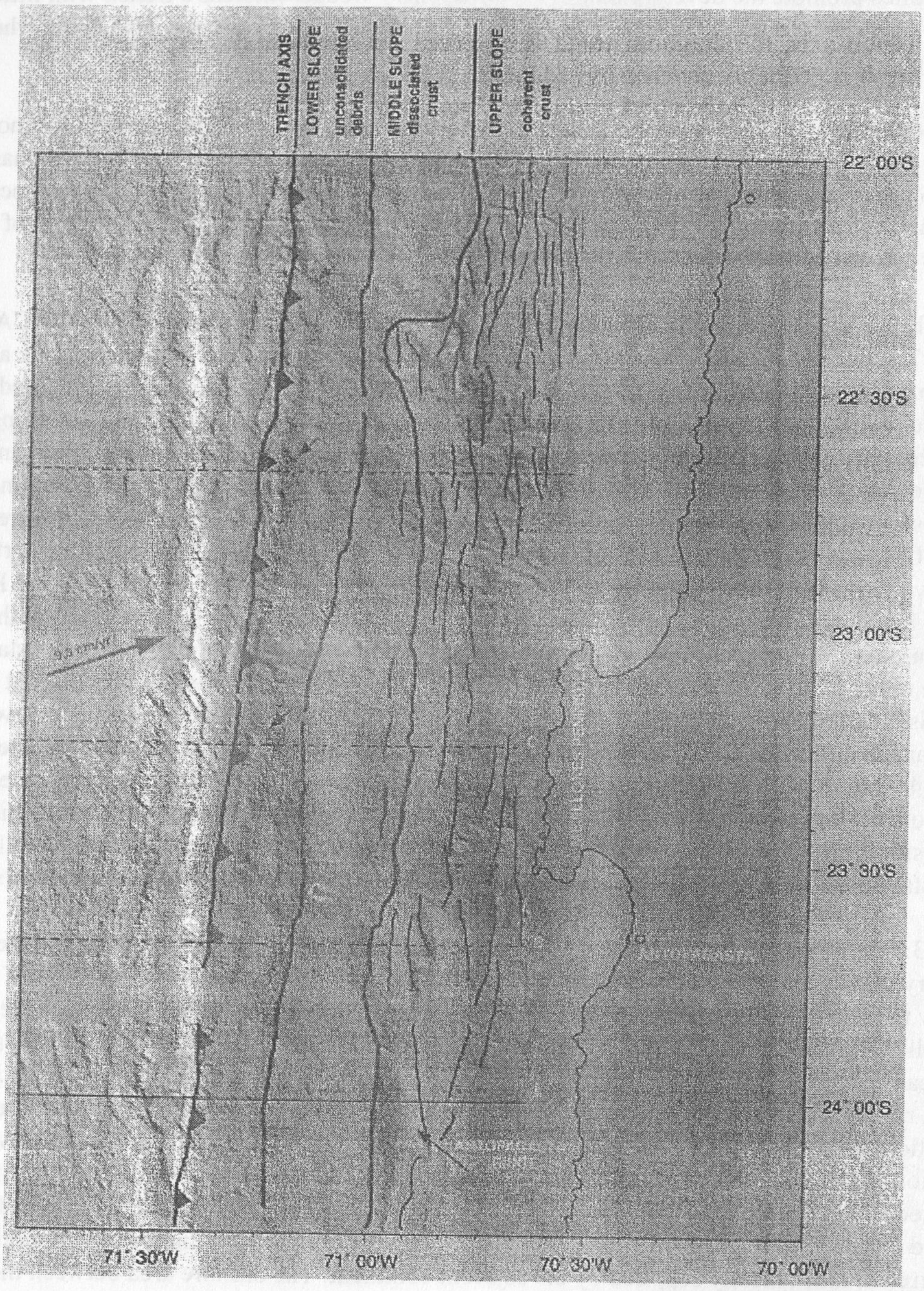

**Figure** 1.3.3: Shaded map offshore northern Chile in the CINCA study area. Note horst and graben structures seaward of the trench axis which play a crucial role in subduction erosion of the margin (from von Huene et al., 1999).

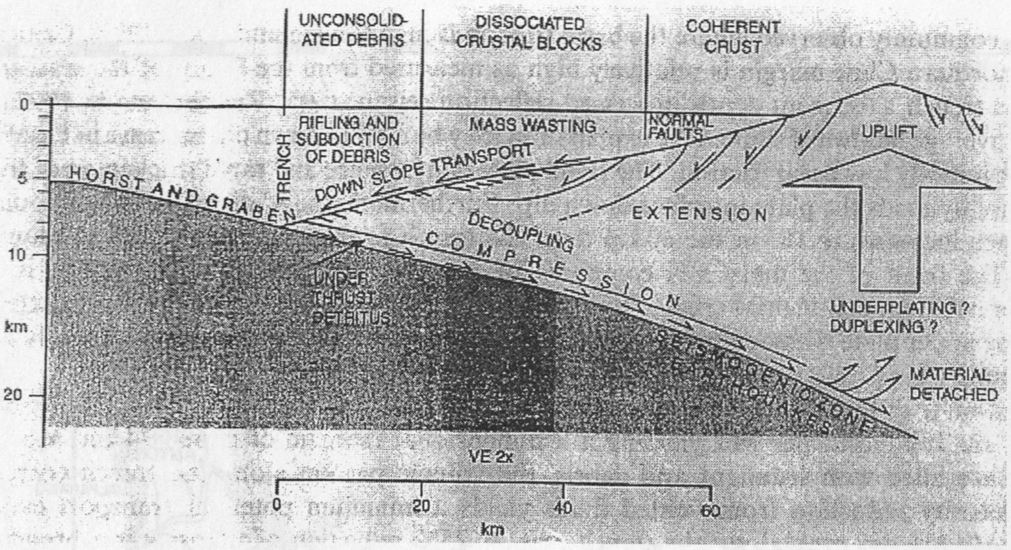

**Figure** 1.3. 4: Diagram of tectonics and mass flux off northern Chile. Material from mass wastings is underthrust and may become detached and be underplated beneath the coastal Cordillera. A net material deficit along the continental slope requires that some underthrust detritus bypass the coastal Cordillera. Alternatively, uplift may derive from duplexing isolated from the near surface extensional tectonics. Isolation of opposing tectonic regimes at the base and surface of the upper plate requires a zone of decoupling at an unknown depth. Seismogenic earthquake rupture begins beneath the coherent continental crust (from von Huene et al., 1999).

sediments and turbidites, numerous trench fans have developed off southern Chile. Here, the continental slope is extensively dissected by major submarine canyon systems, including the San Antonio Canyon off Valparaiso, the Bio Bio Fan of concepcion, the Callecalle Fan and Chacao Fan off Valdivia (Fig. 1.3.5).

The current accretionary phase follows a recent initiation of an episode of rapid accretion that has however not been sustained throughout past convergence history. From the moderate size of the accretionary prism, combined with the convergence rate, a period of 1-2 Ma of rapid accretion followed a more episodic accretion history. The spatial correlation between current accretion and thick accumulations in the Chile trench suggests that this episodicity is linked to trench accumulations. The current accretionary episode between the Chile and Juan Fernández ridges coincides with an increase in trench deposition following Pleistocene glaciation of southern Chile (Bangs and Cande, 1997). The majority of material accreted during earlier accretion phases is not preserved and has probably been tectonically eroded.

The subducting oceanic crust decreases in age and shallows southward toward the Chile Rise. During its descent into the subduction zone, the oceanic crust is flexed and subject to tensional stresses which produce step faults and grabens along the seaward trench wall. In addition, the oceanic plate off southern Chile is characterized by numerous fracture zones associated with the Chile Ridge spreading system (Fig. 1.1.1), which trend approximately 20° from perpendicular to the trench. Continental basement has been interpreted to extend from the coast to the edge of the shelf (Scholl, 1970, von Huene, 1985), where its irregular topography forms a series of forearc basins up to 3000 m thick (Bangs and Cande, 1997) (Fig. 1.3.6). A number of exploratory drillholes reached metamorphic basement here, carrying several hundred meters of Pliocene and Miocene claystones and siltstones. The oldest rocks encountered here were of upper Cretaceous age (Bangs and Cande, 1997).

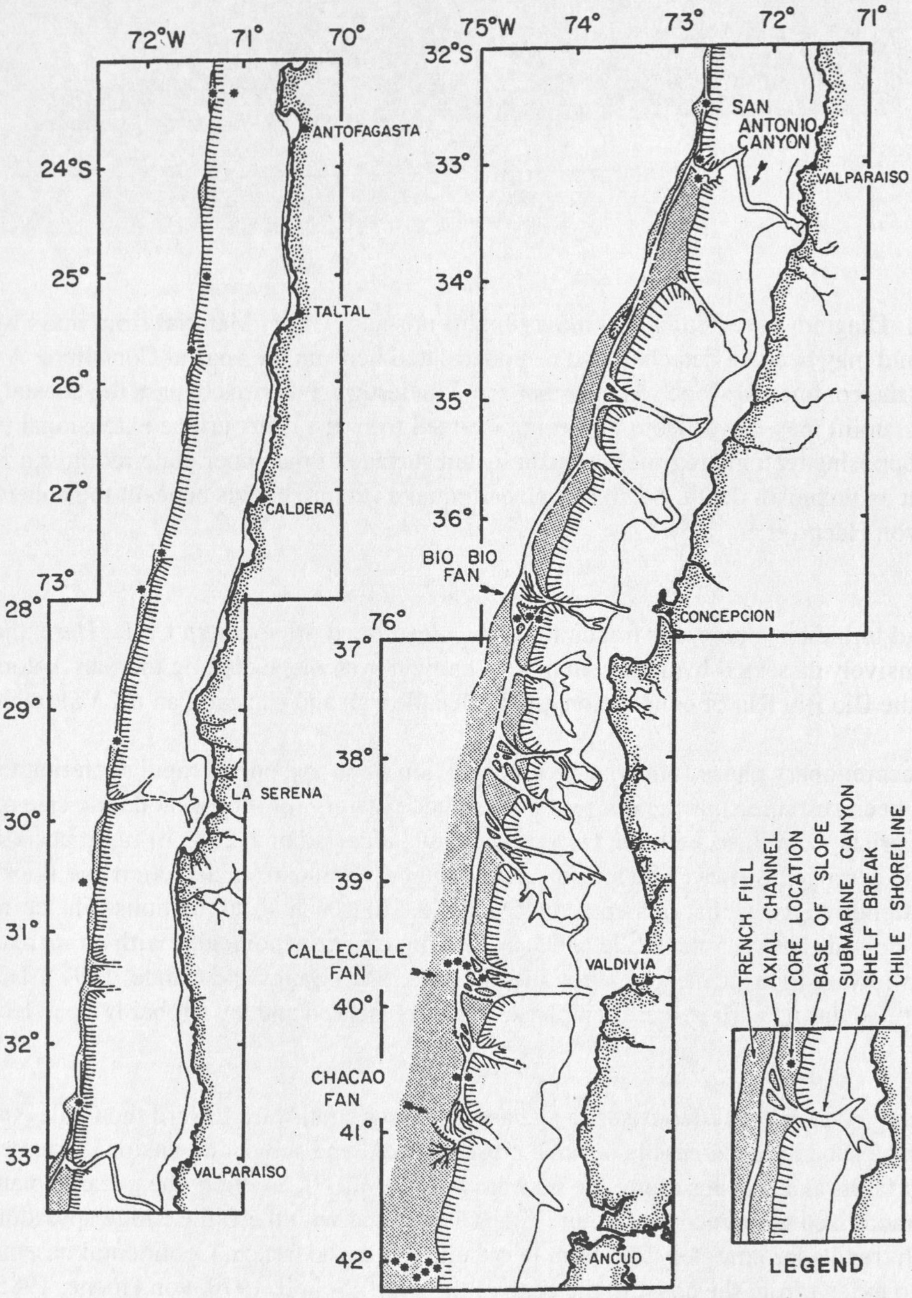

**Figure** 1.3.5: Map view of the Chile Trench sediment fill. Trench axis sediments are stippled; distributary and axial channels are unshaded. Numerous submarine canyon systems cut the Chilean forearc shelf and channel terrigenous sediment supply to the trench (from Thornburg and Kulm, 1987).

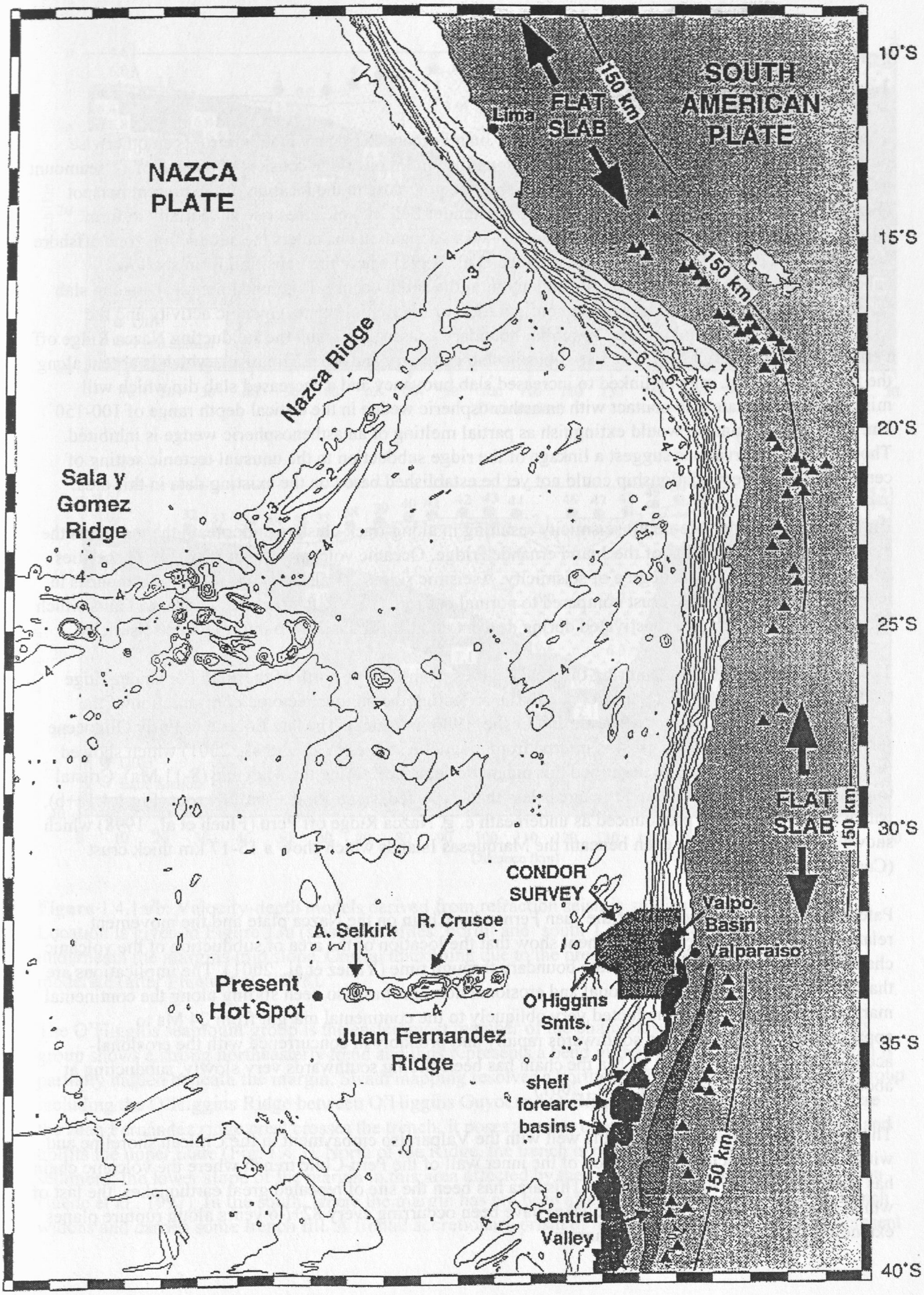

**Figure** 1.3.6: Map of central Chile displaying location of the Juan Fernández Hotspot Chain which consists of 11 seamounts originating at Alexander Selkirk Island near the current hotspot location. The oldest seamount is O'Higgins seamount off Valparaiso (from von Huene et al., 1997).

## 1.4 Subduction of the Juan Fernández ridge

The study area offshore Central Chile covers the Juan Fernández ridge, which interrupts an otherwise monotonous Pacific ocean basin. This 900 km long discontinuous ridge consists of a chain of 11 seamount groups originating at the Alexander Selkirk Island hotspot, close to the location of the present hotspot (Fig.1.3.6). Santa Clara, Robinson Crusoe and Alexander Selkirk volcanoes rise subaerially to form islands along the chain. The Ridge shows an east-west elongation and enters the subduction zone offshore Valparaiso at a typical segment boundary (Flueh et al., 1998) where the transition from shallow subduction with a flat slab to 'normal' subduction in the south occurs. This fundamental change in slab geometry coincides with changes in the configuration of the Benioff zone, volcanic activity and the structure of the continental margin. A similar boundary is associated with the subducting Nazca Ridge off Peru (von Huene et al., 1997). The variations in slab geometry and arc magmatism, which is absent along the flat slab segment, may be linked to increased slab buoyancy and a decreased slab dip which will minimize or eliminate slab contact with an asthenospheric wedge in the critical depth range of 100-150 km. Thus arc magmatism would extinguish as partial melting of an asthenospheric wedge is inhibited. Though these observations suggest a linkage of the ridge subduction to the unusual tectonic setting of central Chile, a direct relationship could not yet be established based on the existing data in this area.

An increased intermediate-depth seismicity resulting in along-track clusters underneath the margin is the evident result of subduction of the Juan Fernández ridge. Oceanic volcanic edifices represent asperities which will initiate a higher degree of seismicity. Aseismic ridges are also associated with differences in the internal structure of the crust compared to normal oceanic crust. Rift structures and large faults which survive subduction may be reactivated during descent and trigger shallow to intermediate seismicity.

The age of the oceanic crust entering the trench varies from Eocene north of the Juan Fernández ridge (32°S) to Oligocene at 34°S (Yanez et al., 2001), reflecting the oblique tectonic configuration of the margin prior to early Oligocene (Cande and Leslie, 1986 in Yanez). The late Eocene to Early Oligocene formation age of the oceanic crust is infered from magnetic studies (Yanez et al., 2001) which showed that the Juan Fernández ridge perturbed this magnetic sequence during the Miocene (8-11 Ma). Crustal thickening beneath Juan Fernández ridge is less than expected, suggesting a shallow root (Fig.1.4.1a+b), which however is not as pronounced as underneath e. g. Nazca Ridge off Peru (Flueh et al., 1998) which shows a 7 km thick root or even beneath the Marquesas Islands which show a 15-17 km thick crust (Caress et al., 1995).

Paleoreconstruction of the path of the Juan Fernandez Chain on the Nazca plate and the movement relative to the South American continent show that the location of the area of subduction of the volcanic chain has been moving along the plate boundary through time (Yanez et al., 2001). The implications are that the boundary between accretional and erosional domains has also been sliding along the continental margin. The hotspot chain subducted very obliquely to the continental margin from 24 Ma to approximately 12 Ma, moving southwards rapidly and probably in concurrence with the erosional-accretionary boundary. Since 12 Ma the chain has been sliding southwards very slowly, subducting at about the same location (Yanez et al., 2001)

The trend of the volcanic chain aligns well with the Valparaiso embayment in the Chilean shoreline and with a remarkable tectonic excavation of the inner wall of the Peru-Chile trench where the volcanic chain has collided with the shallow forearc. This area has been the site of repeated great earthquakes, the last of which occured in 1985. These earthquakes have been occurring every 82+/-6 years along rupture planes extending about 150 km along the margin.

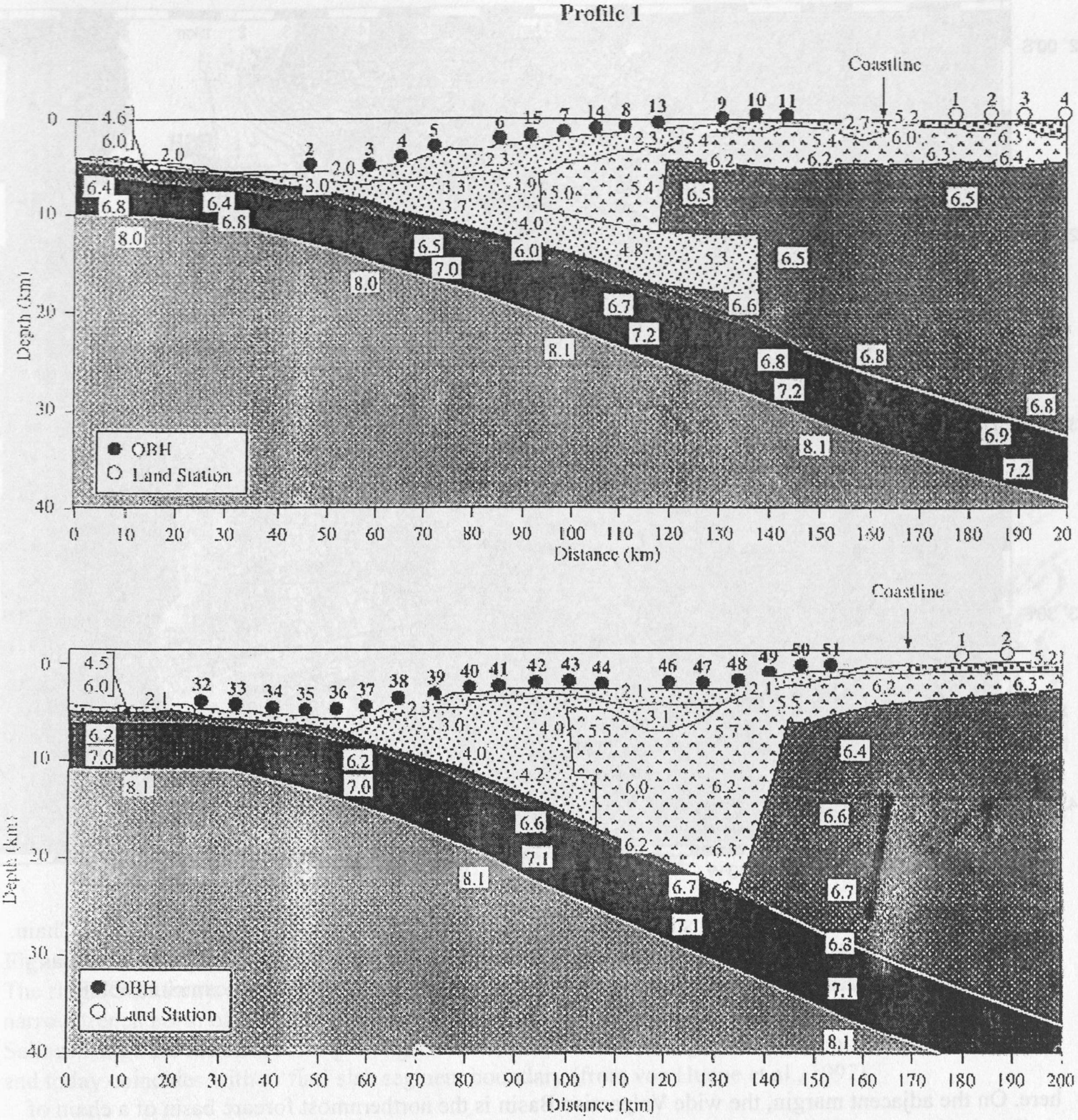

**Figure** 1.4.1a/b: Velocity-depth models derived from refraction seismic studies off central Chile. Location is given in Figure 13a (seismic profiles 'north' and 'south'). Continental crust extends to underneath the margins mid slope. Crustal thickening due to the presence of Juan Fernández Ridge is moderate (after Flueh et al., 1998).

The O'Higgins seamount group is the easternmost member of the chain close to the Chile trench. This group shows a strong northeasterly trend and thus represents a bend in the Juan Fernández ridge which is partially hidden beneath the margin. Swath mapping resolves a northeast alignment in the seamount group including the O'Higgins Ridge between O'Higgins Guyot and O'Higgins seamount (Fig. 1.4.2). Where the Juan Fernández ridge crest crosses the trench, it poses a major barrier to axial sediment transport and uplifts the upper plate (Fig. 1.4.3). North of the Ridge, the trench is narrow and has little trench-fill sediment; the lower slope of the margin in this area affected by the ridge subduction seems eroded (von Huene et al., 1997). In the south, where the margin has not been affected by ridge subduction, the trench widens and carries some trench fill. A frontal accretionary prism of approximately 25 km width is present

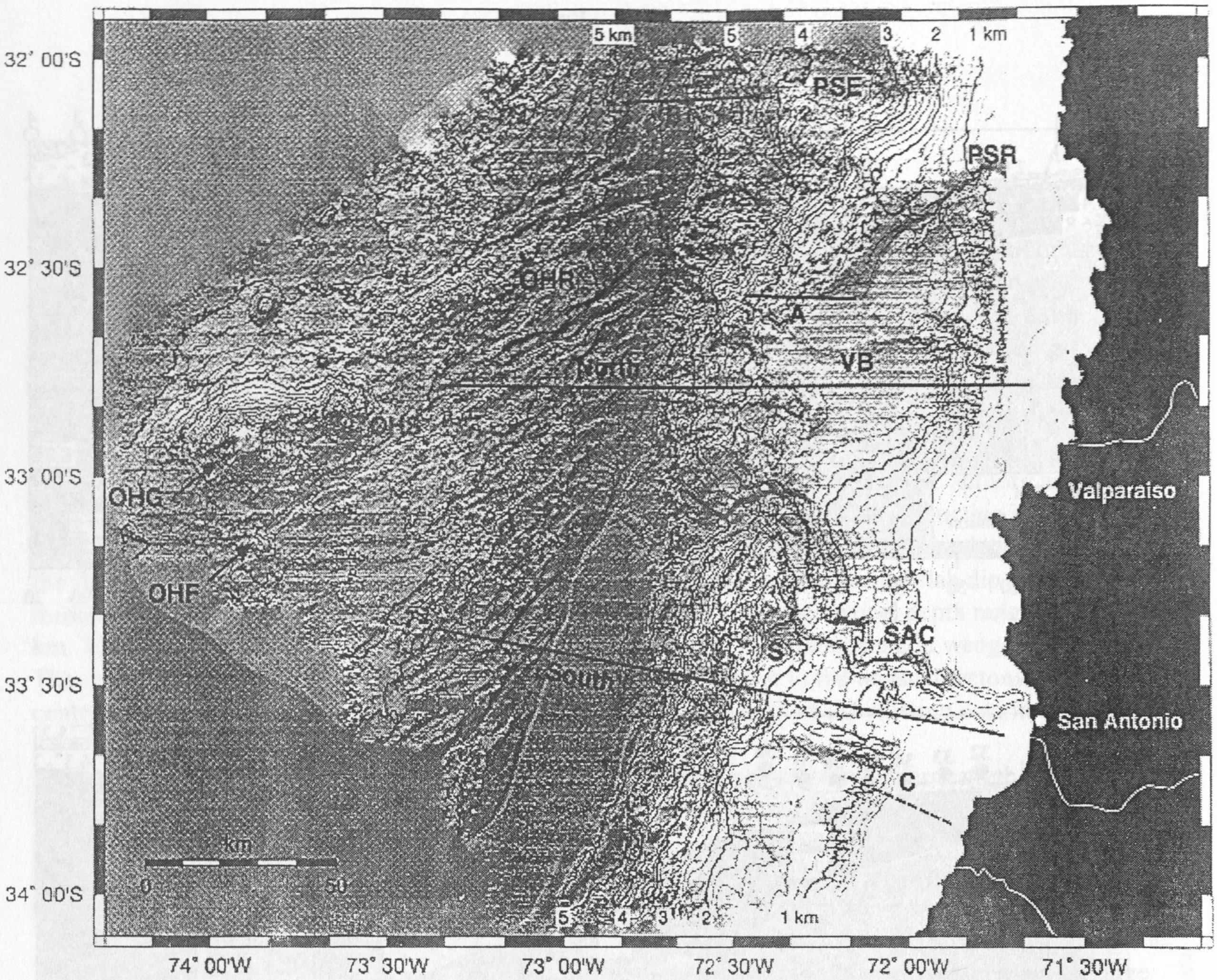

**Figure** 1.4.2: Location map of main structural tectonic features along the Juan Fernández Hotspot Chain. Abbreviations are as followed: SAC, San Antonio Canyon; VB, Valparaiso Basin; PSR, Punta Salinas Ridge; PSE, Punta Salinas Embayment; OHG, O'Higgins Guyot; OHS, O'Higgins Seamount; OHR, O'Higgins Ridge; OHF, O'Higgins Fracture.

here. On the adjacent margin, the wide Valparaiso Basin is the northernmost forearc basin of a chain of shallow basins extending far to the south (von Huene et al., 1997). Valparaiso basin however, which is the first significant forearc basin south of Peru, is the only mid-slope basin observed, whereas the southern basins are all located along the upper slope (Bangs and Cande, 1997). The unusual mid-slope position of the Valparaiso basin as well as the deformed sediment trapped in the basin are likely linked to its position adjacent to the entry of the Juan Fernández ridge (Fig. 1.4.4), which possibly reactivated preexisting structures along the margin which today form Valparaiso Basin (Flueh et al., 1998). The subducted portion of the Juan Fernández ridge is still evident in the subducted Papudo Seamount which has been detected by magnetic anomalies (Yanez et al., 2001) and produces a seafloor dome of about 400 m height (von Huene et al., 1997). Punta Salinas Ridge which forms the northern boundary of the Valparaiso basin, marks the upper plate trace of the subducted Ridge, which shows a fragmented morphology against which sediment trapped in the adjacent Valparaiso Basin is folded (von Huene et al., 1997). This tectonism is probably related to the southward migration of hte segment of the Juan Fernandey Ridge that is subducted on the northern flank of Valparaiso basin (Flueh et al., 1998).

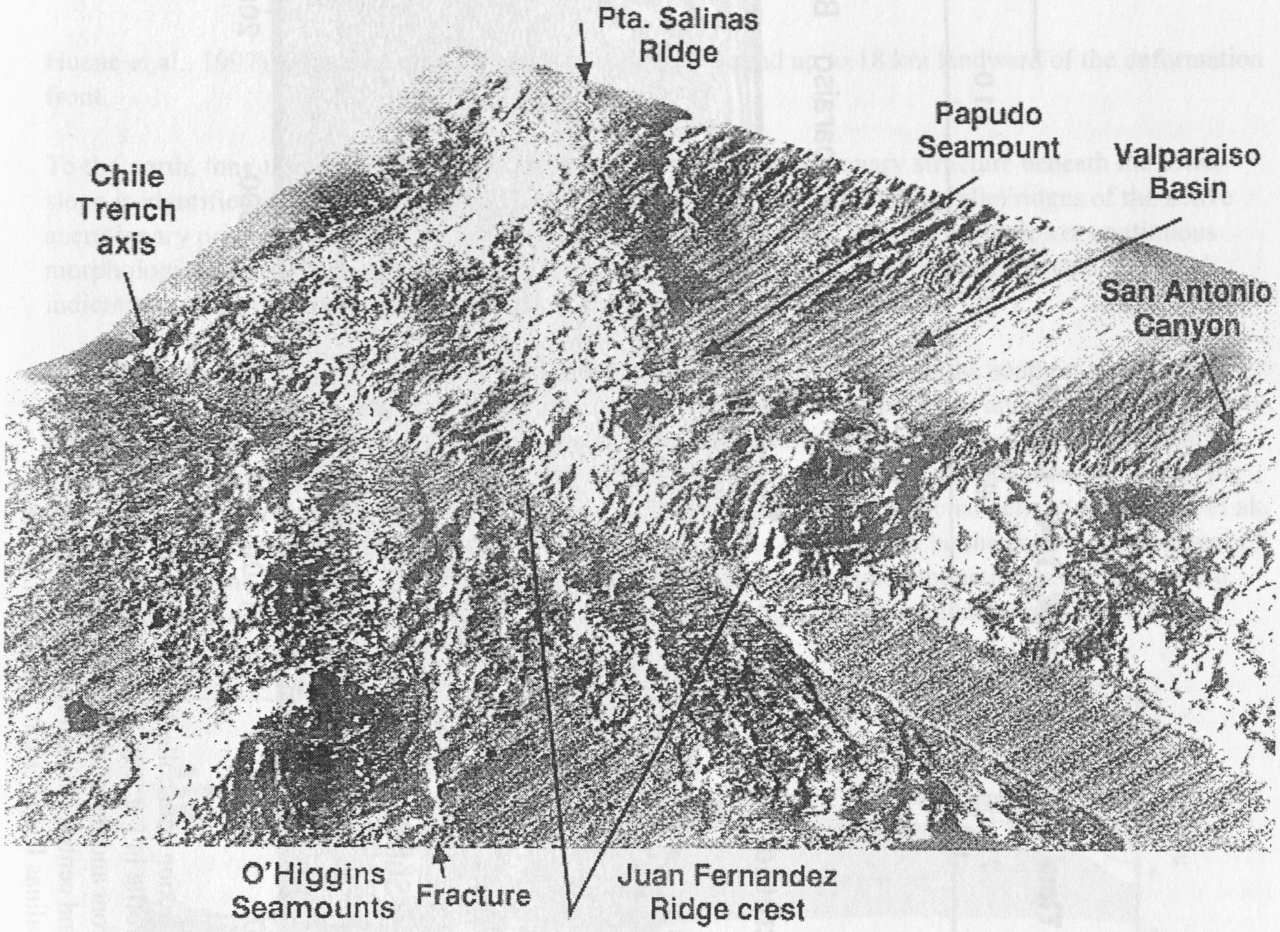

**Figure** 1.4.3: Perspective view of Juan Fernández Ridge entering the Chile trench offshore Valparaiso. The ridge crest forms a barrier to along strike sediment transport in the trench, resulting in a starved, narrow trench north of the ridge and a flooded, widening trench to the south. Papudo Seamount and Punta Salinas Ridge are the subducted prolongation of Juan Fernández Ridge, which has migrated southwards and today coincides with a 'flat' slab segment boundary (from von Huene et al., 1997).

## 1.5 Margin Structure

Seismic wide-angle and reflection data acquired during the course of the CONDOR project reveal the extent of the continental arc framework underneath the margin (von Huene et al., 1997, Flueh et al., 1998). Continental crust extends to the mid-lower slope boundary, where Mesozoic metamorphic rock is present to a depth of approximately 10 km, underneath which continental lower crust has been detected (Fig. 1.5.1). This is also reflected in morphology and magnetic data (Yanez et al., 2001). The continental basement forms a backstop for accretion. The backstop boundary is constrained to an approximately 3 km wide area in seismic sections. This transition is also observed in the bathymetry, where the rough lower slope morphology passes to a smoother surface above the unfaulted sediments.

Margin morphology at the front however is different north and south of the colliding Juan Fernández ridge. South of Juan Fernández ridge active frontal accretion is expressed in folds forming long continuous accretionary ridges where recent folds mark the deformation front. Underthrusting of substantial amounts of sediment was imaged in seismic data collected during the CONDOR study (von

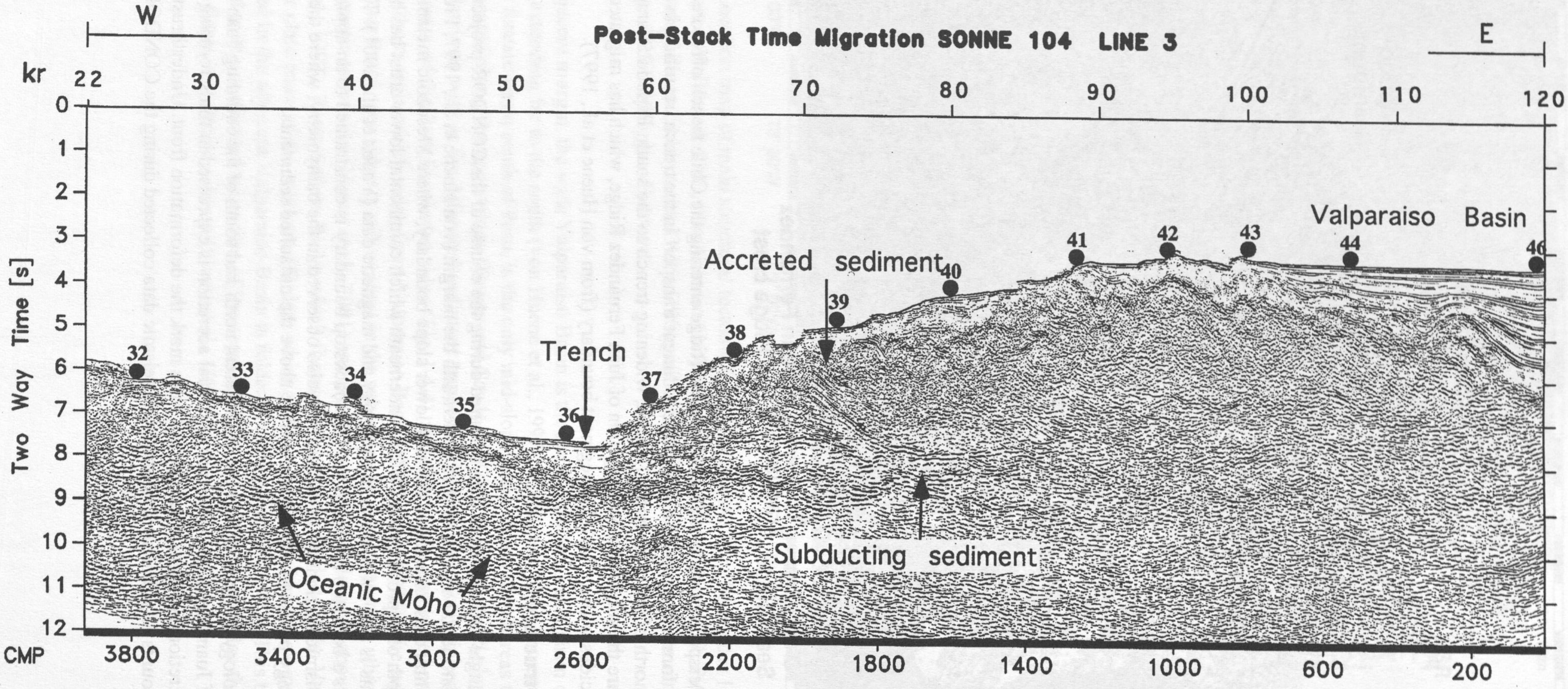

**Figure** 1.4.4: Post Stack time migration of multichannel reflection data collected during the CONDOR project. Location is along the northern seismic profile in Fig. 13a. Significant amounts of trench sediment are subducted beneath the deformation front and lower slope. Valparaiso Basin is the northernmost forearc basin along the southern and central Chilean margin. Basin sediment deformation is linked to the subduction of Punta Salinas Ridge (from Flueh et al., 1998).

Huene et al., 1997), where continuous bands of sediment extend up to 18 km landward of the deformation front.

To the north, long trench parallel ridges are absent, though an accretionary structure beneath the lower slope is identified in seismic data (von Huene et al., 1997). The long trench parallel ridges of the active accretionary prism in the south are replaced over the Juan Fernadnez Ridge crest by fewer continuous morphological trends and derangement. Transverse structures cut strike-parallel lineaments and local indications of mass wasting are manifested in morphological features.

Another striking feature in this area is the San Antonio canyon which borders the southern flank of te Valparaiso Basin. This submarine canyon heads at the mouth of the Maipo River and its path with sharply right angle bends and a zig-zag geometry appears to be tectonically controlled. The lack of a delta at the mouth of San Antonio Canyon is possibly due to the subduction of Papudo volcanoe, which blocked the trench axis for approximately 1 Ma and explains the indications of erosional channeling (von Huene et al., 1997). It has also been proposed that the mouth of San Antonio canyon may be the entry point and scar of another seamount. Unlike for newly deposited sediment, where seamount subduction leaves prominent scars (Lallemand et al., 1994, von Huene et al., 2000), the highly consolidated material of the Chile margin leaves little evidence of seamount tracks and scars.

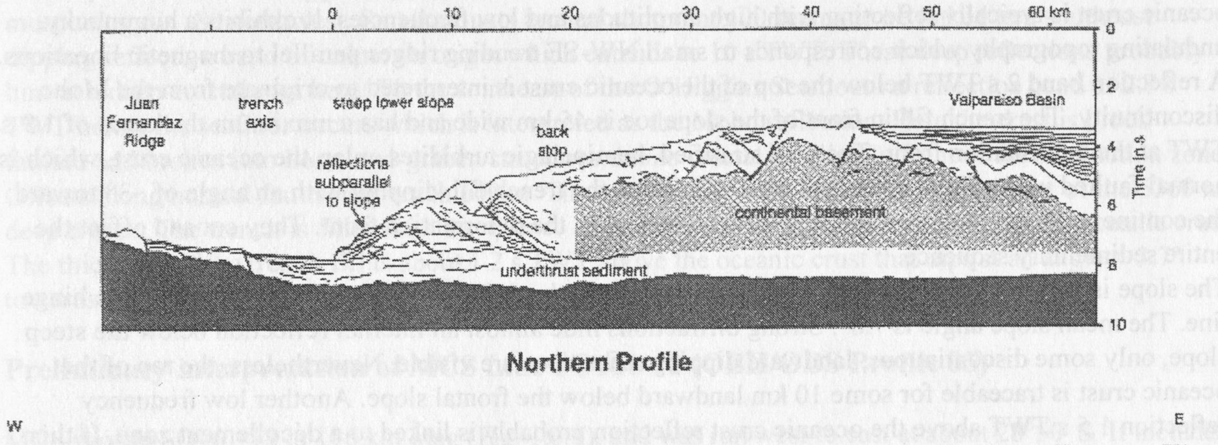

**Figure** 1.5.1: Line drawings of deep-seismic reflection profiles 'north' and 'south' in Fig. 13a. Continental basement forming backstop to the trench sediment extends to within 20 km of the deformation front (from von Huene et al., 1997).

## 1.6 Preliminary Results of SO161 Leg 2 and 3

(C. Gaedicke and B. Schreckenberger)

Altogether 35 multichannel reflection seismic (MCS) profiles with a total length of 5194 km were recorded during Leg 2 and 3 (Fig. 1.6.1). Onboard processing up to brut stacks was done for most of the profiles. We will focus our interpretation on those MCS lines where OBH/OBS wide-angle profiles were shot during Leg 4.

### Preliminary interpretation of MCS Lines SO161-38 and 42 (OBH/OBS Profile 01)

The WNW-ESE running MCS profile SO161-38 has a length of 185.5 km (Fig. 1.6.1). It crosses the deformation front at exactly 38° S. The profile extends an onshore reflection seismic profile where recording and shooting was done simultaneously under supervision of the GeoForschungsZentrum Potsdam. To avoid interference shooting with the airguns was interrupted during the landshots. In order to close the gaps of shot interruptions the line SO161-42 was run again on parts of SO161-38 (Fig. 1.6.2). In the west of the profile the Nazca Plate is being recorded for 52 km. The oceanic crust is covered by well stratified pelagic sediments of less than 120 ms two-way travel time (TWT) thickness. The top of the oceanic crust is typically reflecting with high amplitudes and low frequencies. It exhibits a hummocky, undulating topography which corresponds to small NW-SE trending ridges parallel to magnetic lineations. A reflection band 2 s TWT below the top of the oceanic crust is interpreted to originate from the Moho discontinuity. The trench fill in front of the slope toe is 45 km wide and has a maximum thickness of 1.9 s TWT at the deformation front. The well stratified, hemipelagic turbidites onlap the oceanic crust, which is normal faulted with offsets up to 400 ms TWT below the trench fill, dipping with an angle of ~3° toward the continent. Steep, landward dipping thrust faults mark the deformation front. They cut and offset the entire sedimentary sequence.

The slope is 28 km wide and has a height of 3.8 km from the deformation front to the shelf - slope hinge line. The mean slope angle is 7.8°. Strong diffractions hide almost all internal reflection below the steep slope, only some discontinuous, landward dipping reflections are visible. Nevertheless, the top of the oceanic crust is traceable for some 10 km landward below the frontal slope. Another low frequency reflection 1.5 s TWT above the oceanic crust reflection probably is linked to a décollement zone. If this interpretation is correct, then most of the sediments become subducted together with the oceanic crust. Some other internal reflections in the lower slope probably are related to duplexing and stacking of sediments. Further processing of the data is necessary to clear this question.

At the eastern part of the MCS line SO161-38 the Arauco basin is crossed. The sediments are some 1.4 s TWT thick above a band of low frequency reflections which govern the entire shelf to the slope hinge line. This strong reflection is correlated with the Paleozoic metamorphic basement drilled on Mocha Island to the south (Gonzáles, 1989). Near the shelf – slope hinge line (shotpoint 850) an angular unconformity give evidence for young uplift of the upper slope.

### Preliminary interpretation of MCS Line SO161-18 (OBH/OBS Profile 02)

The west to east running profile SO161-18 has a length of 272.8 km (Figs. 1.6.1 and 1.6.3). It covers the oceanic crust of the Nazca Plate, the narrow Chile trench and the continental slope. The oceanic crust is faulted and of hummocky appearance. Single faults have offsets of about 600 to 700 m. Narrow ridges are up to 450 m high. About 2 s TWT to 2.1 s TWT below the basement some subparallel reflection elements are observed, probably representing the crust-mantle boundary (Moho). Landward inclined intracrustal reflectors extend in places from the basement down to the mantle. They are intermingled in some cases with diffractions indicated by their convex shape (seen from the surface) and high frequencies. Further analysis and migration of the data is required to gain certainty about these features. The is trench is some 6 km wide and filled with a 0.6 s TWT thick sequence of stratified sediments which onlap the oceanic crust. The slope is subdivided into a lower slope, a 25 km wide mid slope terrace at a depth of 4.1 km, and an upper slope. The oceanic crust is clearly visible approximately up to 12 km east of the slope toe at a depth of 9 s TWT. Landward dipping reflection bands in the lower slope are preliminary interpreted as thrust faults which separate stacked sedimentary sequences. Below the mid slope terrace and the upper slope a low frequency, high amplitude reflection band with some offset is most likely explained with the acoustic basement of the continental crust. Therefore the backstop extends to the seaward end of the mid slope terrace.

## Preliminary interpretation of MCS Line SO161-19 (OBH/OBS Profile 03)

MCS Profile SO161-19 has a lenght of 218 km (Fig. 1.6.1). It crosses the inactive Juan Fernandes Ridge from the northwest to the southeast, where the western part of the Chile trench is reached (Fig. 1.6.4). In the center of the profile lies the O'Higgins Seamount which rises some 2700 m above the surrounding seafloor west of the O'Higgins Guyot. The oceanic crust of the Nazca Plate exhibits a more or less flat morphology in the northwest. Small mounts around shotpoint 400 seems to be linked to a southeast dipping reflection band of unknown origin which extends to 10 s TWT. These deep reflections probably hint at a deep crustal root here. To the southeast of the O'Higgins Seamount a reflection band at 2.7 s TWT below the seafloor occurs which is interpreted as the Moho reflection. Here the crust is block faulted and broken into horst-and-graben structures due to crustal bending in front of the subduction zone. Offsets along normal faults may reach 600 m. The profile covers 20 km of the western part of the 5360 m deep trench. The trench is filled with a sequence of well stratified turbidites which onlap the oceanic crust. The thickness of the trench fill is about 1.2 s TWT above the oceanic crust that dips at an angle > 3.7° towards the east.

## Preliminary interpretation of MCS Line SO161-12 (OBH/OBS Profile 05)

MCS profile SO161-12 is 196 km long (Fig. 1.6.1), and was run west to east at about 28°50' S. It includes 120 km of the oceanic crust of the Nazca Plate, the Chile Trench, and the continental slope (Fig. 1.6.5). The oceanic crust has a hummocky topography with a very thin pelagic sedimentary cover, through which the acoustic basement is piercing. Bending and block faulting due to the subduction process increases towards the trench, where the offset of faults reach 900 m. A reflection band some 2.5 s TWT below the top reflection of the oceanic crust is preliminary interpreted as the crust-mantle boundary. The center of the trench is 6325 m deep and 4.8 km wide. The flat lying, well stratified sedimentary fill is 0.7 s TWT thick. To the east an anticline (around shotpoint 2500) clearly indicate compression and stacking of the sediments. A landward inclined reflection band probably originate at a décollement zone. The almost constant slope angle is about 5.2°. Below the upper slope surface a high amplitude, moderate frequency reflection band is observed at a depth of 0.5 to 0.7 s TWT. Diffractions are common where offsets of the band occur, which is traceable down to the middle slope 22.5 km east of the trench. This reflection band is tentatively correlated with the block faulted continental crust. Therefore the backstop extends under major parts of the slope and only a small accretionary prism was built. The subducting oceanic crust is well imaged under the slope for a distance of 30 km east of the trench. Roughness of the oceanic crust, the small amount of trench fill, block faulting and extension of the continental crust hint at phases of tectonic erosion at this segment of the Chile Margin.

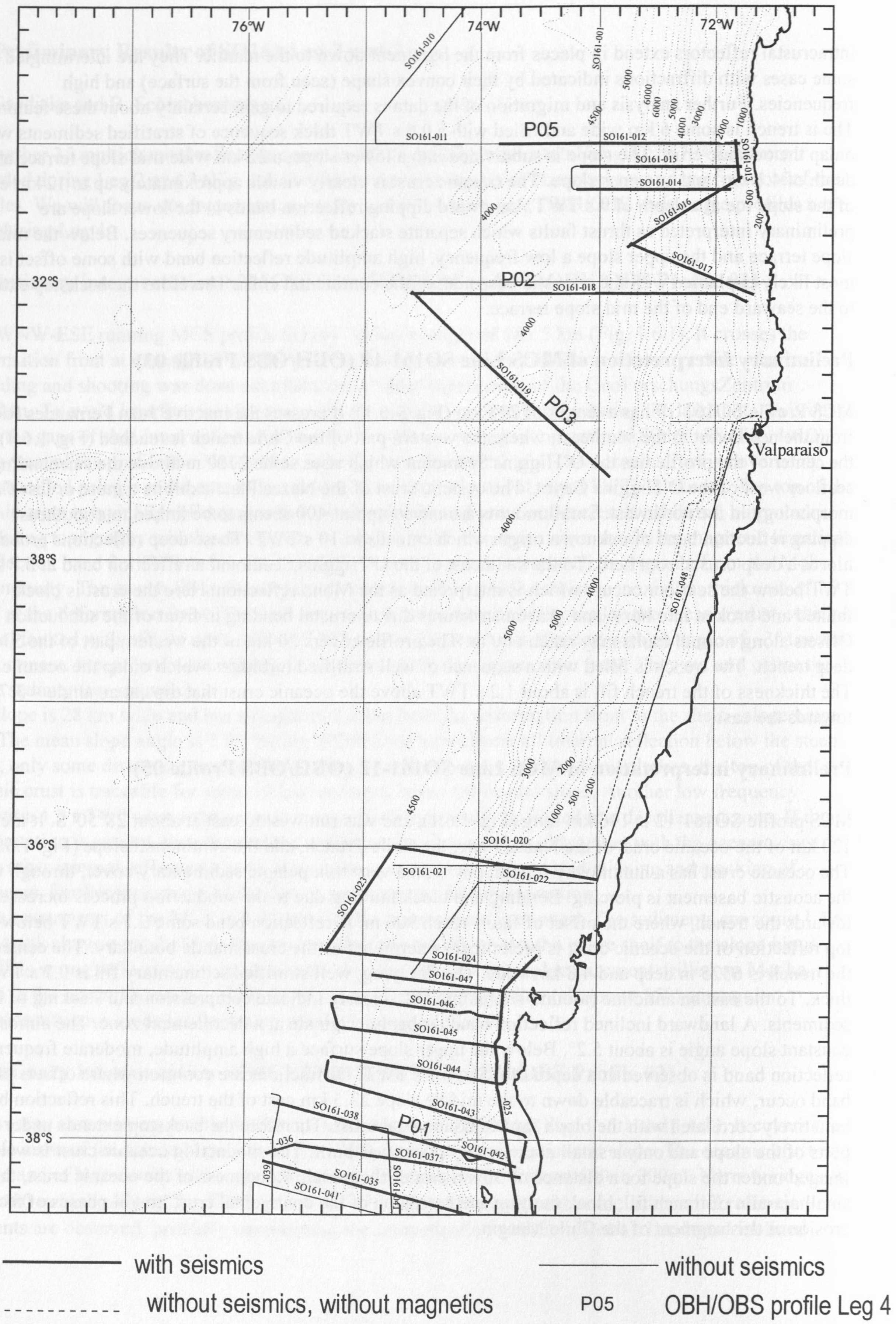

SONNE cruise 161 - SPOC Leg 2+3
Track lines

**Figure 1.6.1:** Track lines of the SONNE cruise 161 Leg 2+3. Only the northern part is shown.

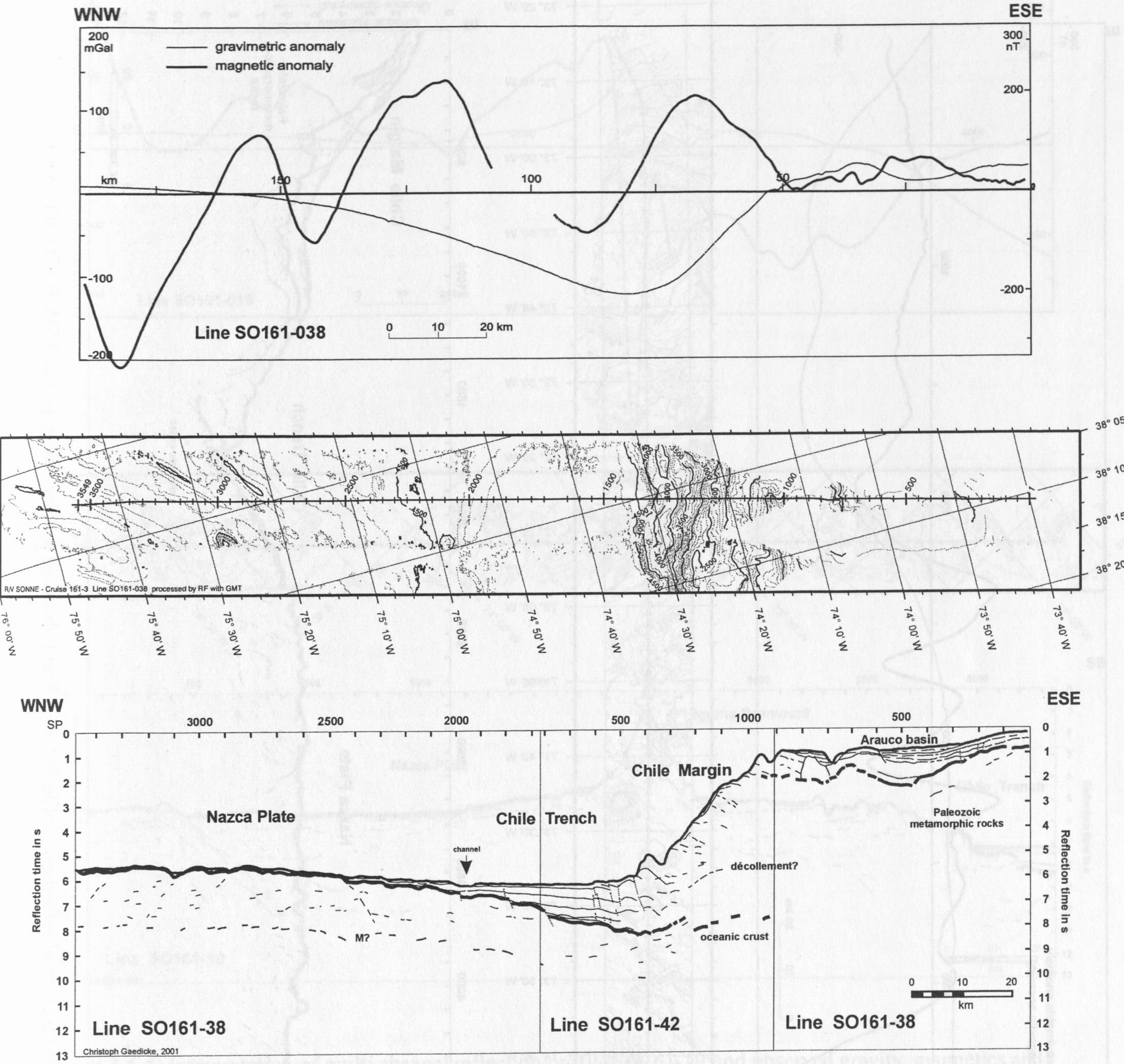

**Figure 1.6.2:** Interpretation of multi channel reflection profile SO161-38/42 and observed gravity, magnetics and SIMRAD bathymetry.

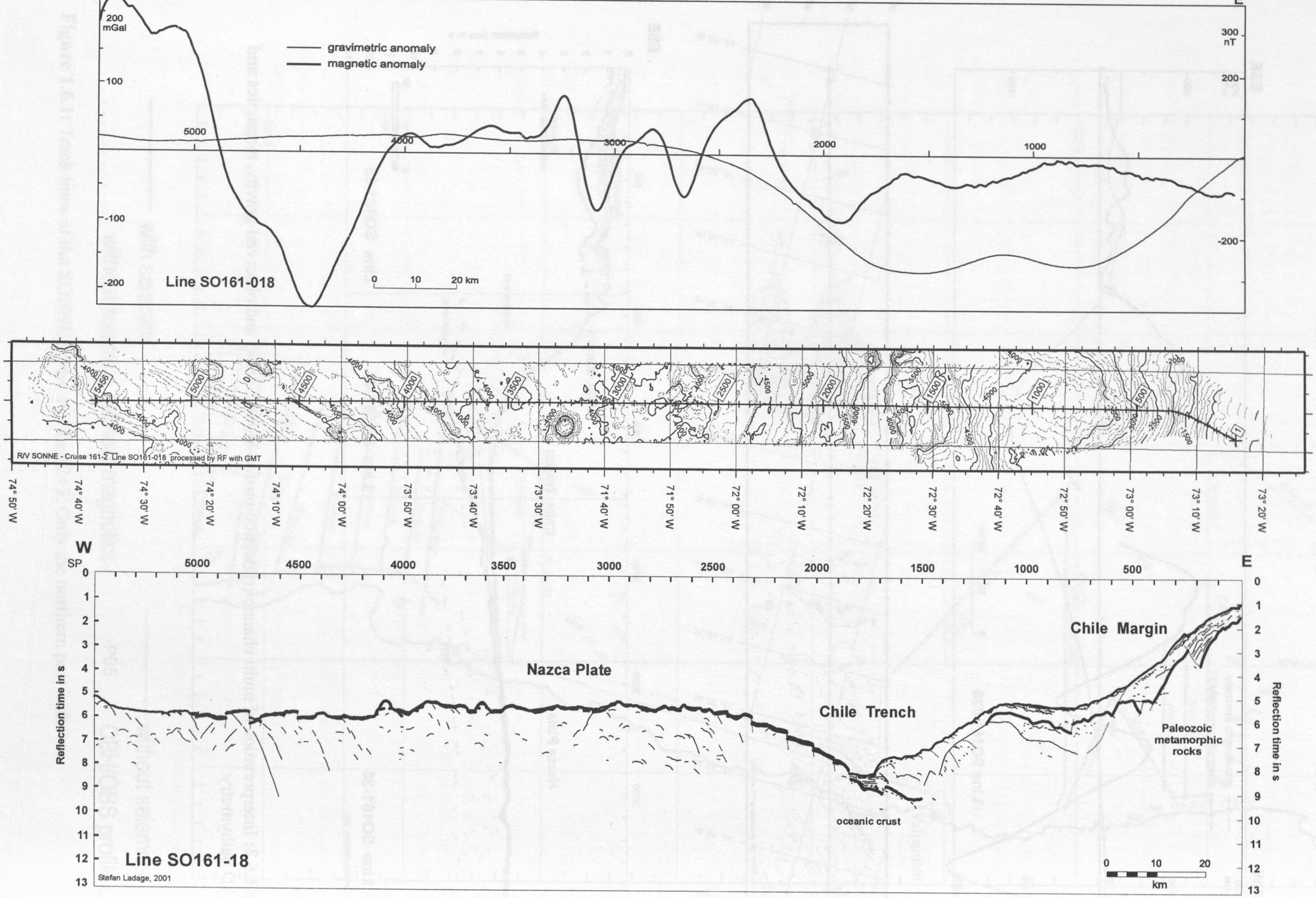

**Figure 1.6.3:** Interpretation of multi channel reflection profile SO161-18 and observed gravity, magnetics and SIMRAD bathymetry.

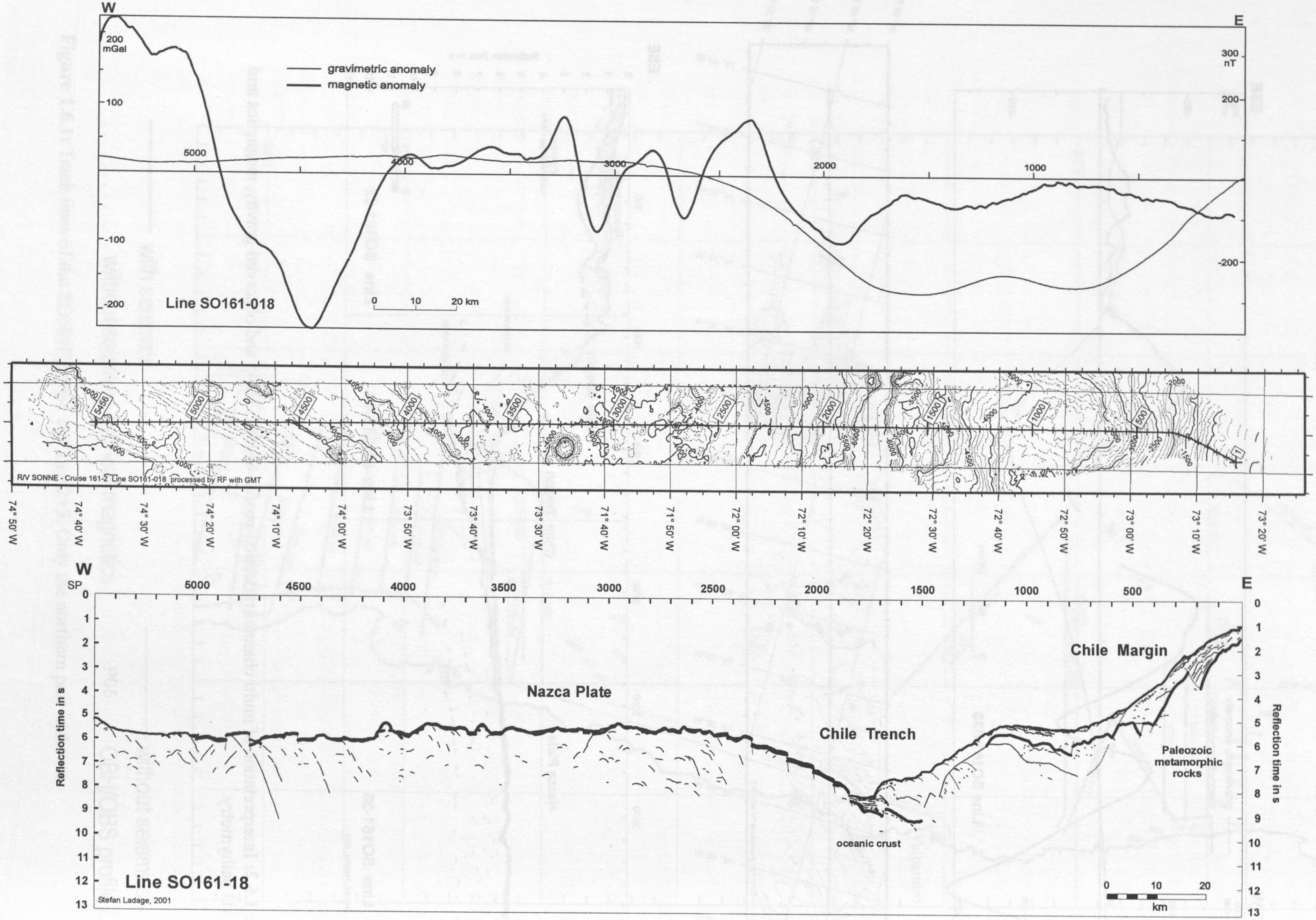

**Figure 1.6.3:** Interpretation of multi channel reflection profile SO161-18 and observed gravity, magnetics and SIMRAD bathymetry.

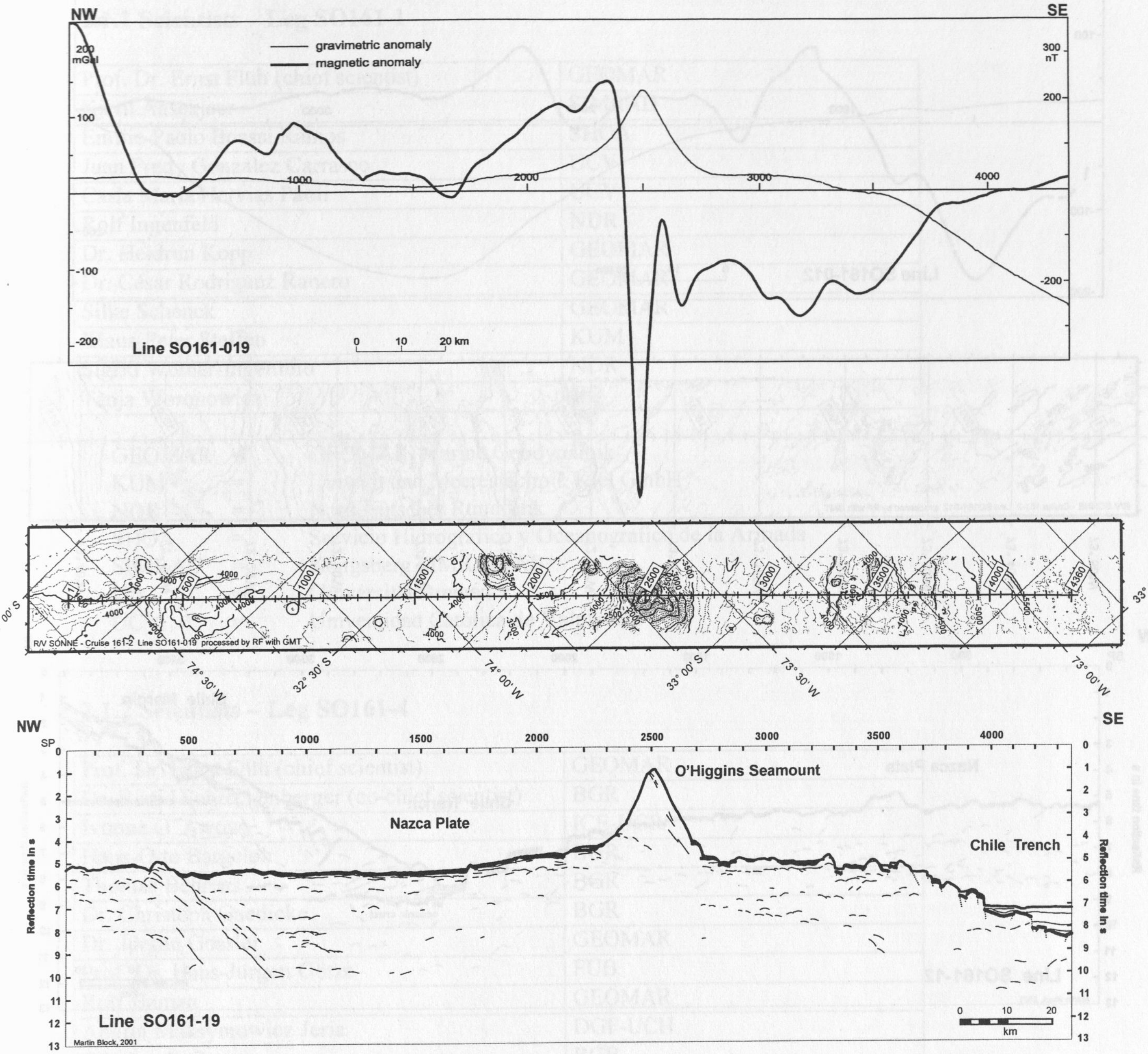

**Figure 1.6.4:** Interpretation of multi channel reflection profile SO161-19 and observed gravity, magnetics and SIMRAD bathymetry.

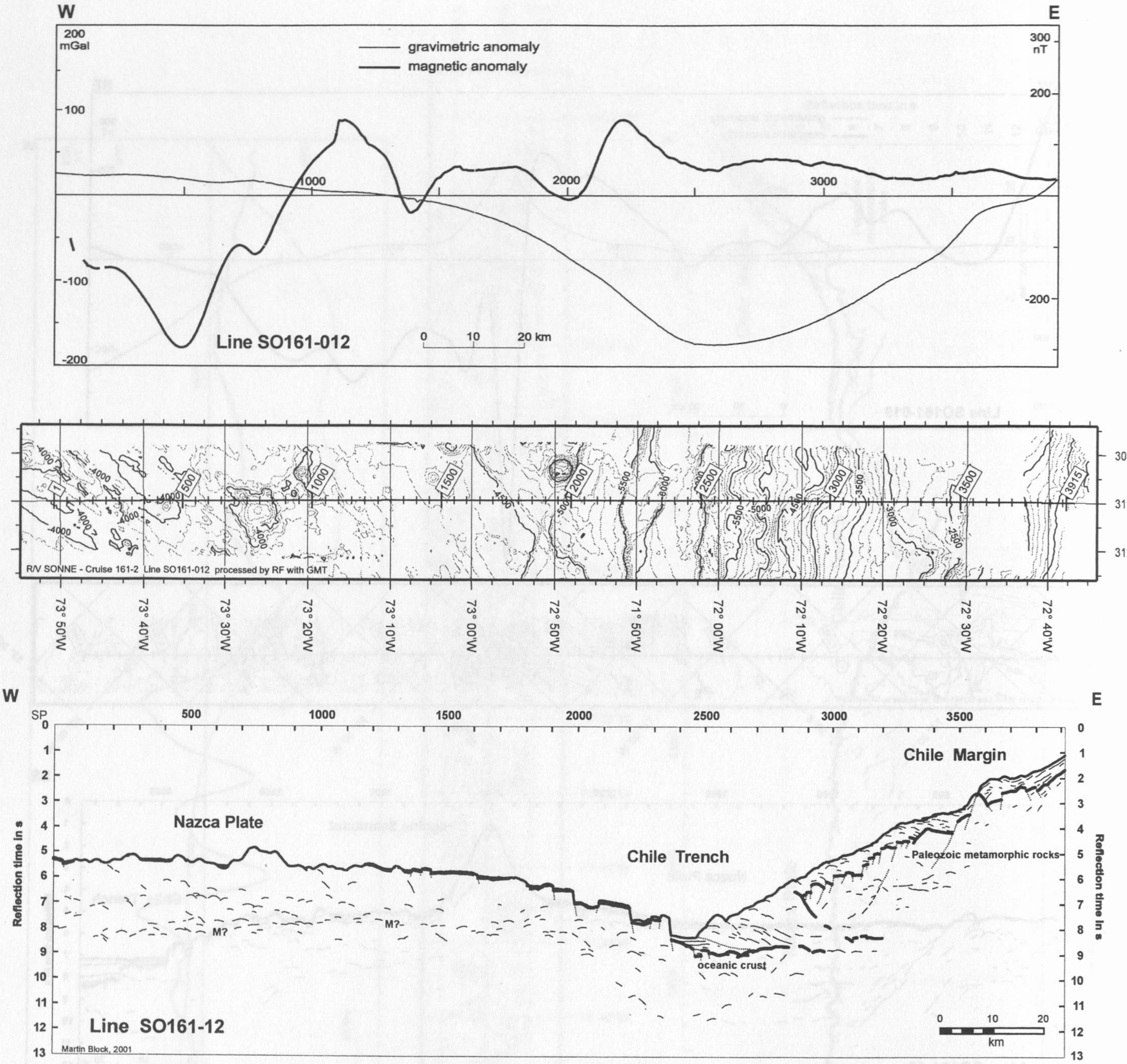

**Figure 1.6.5:** Interpretation of multi channel reflection profile SO161-12 and observed gravity, magnetics and SIMRAD bathymetry.

# 2. Participants

## 2.1 Scientists

### 2.1.1 Scientists – Leg SO161-1

| | |
|---|---|
| Prof. Dr. Ernst Flüh (chief scientist) | GEOMAR |
| Kjetil Aasekjaer | SIMRAD |
| Emilio Paolo Boassi Ramos | SHOA |
| Juan Fredy Gonzalez Carrasco | UCV |
| Carla Maria Hervias Paoli | UCV |
| Rolf Ingenfeld | NDR |
| Dr. Heidrun Kopp | GEOMAR |
| Dr. César Rodriguez Ranero | GEOMAR |
| Silke Schenck | GEOMAR |
| Klaus-Peter Steffen | KUM |
| Sigrid Werner-Ingenfeld | NDR |
| Tanja Woronowicz | UB |

GEOMAR = GEOMAR, Marine Geodynamik
KUM = Umwelt und Meerestechnik Kiel GmbH
NDR = Norddeutscher Rundfunk
SHOA = Servicio Hidrografico y Oceanografico de la Armada
SIMRAD = Kongsberg SIMRAD AS
UB = Universität Bremen
UCV = Universidad Católica de Valparaíso

### 2.1.2 Scientists – Leg SO161-4

| | |
|---|---|
| Prof. Dr. Ernst Flüh (chief scientist) | GEOMAR |
| Dr. Bernd Schreckenberger (co-chief scientist) | BGR |
| Ivonne G. Arroyo | ICE-UCR |
| Hans-Otto Bargeloh | BGR |
| Thomas Behrens | BGR |
| Dr. Christoph Gaedicke | BGR |
| Dr. Jürgen Gossler | GEOMAR |
| Prof. Dr. Hans-Jürgen Götze | FUB |
| Rolf Haman | GEOMAR |
| Andrei Maksymowicz Jeria | DGF-UCH |
| Günther Kallaus | BGR |
| Peter Kewitsch | BGR |
| Dr. Dirk Kläschen | GEOMAR |
| Dr. Heidrun Kopp | GEOMAR |
| Assoc. Prof. Dr. Juan Manuel Lorenzo | LSU-UCH |
| Cord Akram Papenberg | GEOMAR |
| Jörg Petersen | GEOMAR |
| Dr. Sabine Schmidt | FUB |
| Michael Schnabel | GEOMAR |
| Joachim Sievers | BGR |
| Klaus-Peter Steffen | KUM |
| Eike Surburg | BGR |

| | |
|---|---|
| Peter Oliver Thierer | GEOMAR |
| Dr. Frederik Tilmann | GEOMAR |
| Prof. Dr. Emilio Vera | DGF-UCH |

BGR = Bundesanstalt für Geowissenschaften und Rohstoffe
DGF-UCH = Departemento de Geofisica – Universidad de Chile
FUB = Freie Universität Berlin
GEOMAR = GEOMAR, Marine Geodynamik
ICE-UCR = Instituto Costarricense de Electricidad - Universidad de Costa Rica
KUM = Umwelt und Meerestechnik Kiel GmbH
LSU-UCH = Louisiana State University, Dept. Geology – Geophysics Universidad de Chile

## 2.2 Crew

### 2.2.1 Crew – Leg SO161-1

| | |
|---|---|
| Hartmut Andresen | Master |
| Jörn Löffler | Chief Mate |
| Frank Göldner | 1st Mate |
| Wolfgang Köthe | Radio Officer |
| Hans H. Beiersdorf | Surgeon |
| Peter Neumann | Chief Engineer |
| Andreas Rex | 2nd Engineer |
| Thorsten Damman | Electrician |
| Kurt Stammer | Chief Electronic Engineer |
| Jörg Leppin | Electronic Engineer |
| Paul Wintersteller | System Operator |
| Christian Wenz | System Operator |
| Rainer Rosemeyer | Fitter |
| Christian Kunze | Motorman |
| Gerhard Lange | Motorman |
| Lothar Fromme | Motorman |
| Johannes Arronet | Motorman |
| Klaus Hermann | Chief Cook |
| Arnold Ernst | 2nd Cook |
| Werner Slotta | Chief Steward |
| Rainer Goetze | 2nd Steward |
| Jan Hoppe | 2nd Steward |
| Norbert Bosselmann | Boatswain |
| Siegfried Becker | A. B. |
| Michael Becker | A. B. |
| Peter Rosin | A. B. |
| Helmut Krüger | A. B. |
| Dirk Schachel | A. B. |
| Stefan Tamm | A. B. |

### 2.2.2 Crew – Leg SO161-4

| | |
|---|---|
| Henning Papenhagen | Master |
| Detlef Korte | Chief Mate |
| Frank Göldner | 1st Mate |
| Rainer Hellmann | Radio Officer |
| Hans H. Beiersdorf | Surgeon |
| Peter Neumann | Chief Engineer |
| Claas Sobota | 2nd Engineer |
| Klaus Klinder | 2nd Engineer |
| Thorsten Damman | Electrician |
| Hilmar Hoffmann | Chief Electronic Engineer |
| Hans Jansch | Electronic Engineer |
| Rudolf Angermann | System Operator |
| Christian Wenz | System Operator |
| Volker Blohm | Fitter |
| Rüdiger Engel | Motorman |
| Hermann Rademacher | Motorman |
| Frank Sebastian | Motorman |
| Gerhard Lange | Motorman |
| Frank Tiemann | Chief Cook |
| Willi Bratz | 2nd Cook |
| Werner Slotta | Chief Steward |
| Gerlinde Grübe | 2nd Steward |
| Maik Steep | 2nd Steward |
| Norbert Bosselmann | Boatswain |
| Hermann Röpti | A. B. |
| Norbert Kreft | A. B. |
| Rüdiger Kuhn | A. B. |
| Karsten Bosselmann | A. B. |
| Dirk Schachel | A. B. |
| Stefan Tamm | A. B. |

### 2.3 Adresses of Participating Institutions

BGR: Bundesanstalt für Geowissenschaften und Rohstoffe
Stilleweg 2
30655 Hannover
Germany
Tel.: +49 – 511 – 643 – 0
Fax.: +49 – 511 – 643 – 3663
e-mail: Iname@bgr.de
Internet: www.bgr.de

DGF-UCH: Departemento de Geofisica – Universidad de Chile
Universidad de Chile
Santiago
Chile
Tel.: +56 – 2 – 6784565
Fax.: +56 – 2 – 6968686
e-mail: name@dgf.uchile.cl

FUB: Freie Universität Berlin
Institut für Geologische Wissenschaften
FR Geophysik
Malteserstraße 74-100, Haus N
12249 Berlin
Germany
Tel.: +49 – 30 – 83870 – 874/876
Fax.: +49 – 30 – 83870 – 763
e-mail: hajo@geophysik.fu-berlin.de
e-mail: sabine@geophysik.fu-berlin.de
Internet: http://userpage.fu-berlin.de/~wwwgravi

GEOMAR: GEOMAR
Forschungszentrum für marine Geowissenschaften der
Christian-Albrechts-Universität zu Kiel
Wischhofstraße 1-3
24148 Kiel
Germany
Tel.: +49 - 431 - 600 - 2972
Fax: +49 - 431 - 600 – 2922
e-mail: Iname@geomar.de
Internet: www.geomar.de

ICE-UCR: Instituto Costarricense de Electricidad
Apdo 10032-1000 San José
Exploración Subterránea, UEN PySA
Central America
Tel.: +506 – 220 – 6394
Fax.: +506 – 220 – 8212
e-mail: igarroyo@cariari.ucr.ac.cr

KUM: K.U.M.
Umwelt- und Meerestechnik Kiel Gmbh
Wischhofstr. 1-3, Geb. D5
24148 Kiel
Germany
Tel.: +49 – 431 – 7209 – 220
Fax: +49 – 431 – 7209 – 244
e-mail: KUM.Umweltmeerestechnik@t-online.de

LSU-UCH: Louisiana State University, Dept. Geology – Geophysics Universidad de Chile
Baton Rouge, LA 70803 – 4101
U.S.A.
Tel.: +225 – 578 – 4249
Fax: +225 – 578 – 2302
e-mail: juan@geol.lsu.edu

NDR: Norddeutscher Rundfunk
Landesfunkhaus Schleswig-Holstein
Wall 68-74
24033 Kiel
Tel.: +49-431-9876-321
Fax: +49-431-9876-790-321
e-mail: s.werner@ndr.de
Internet: www.ndr.de

SHOA: Servicio Hidrográfico y Oceanográfico de la Armada
Errazuriz 232
Playa Ancha
Valparaíso
Tel.: +56-32-266540
Fax: +56-32-266542
e-mail: prog.esp.oc.@shoa.cl

SIMRAD: Kongsberg SIMRAD AS
Strandpromenaden 50
P.O. Box 111
N-3191 Horten
NORWAY
Tel.: +47-3303-4000
Fax: +47-3304-2987
Internet: www.kongsberg-simrad.com

UB: Universität Bremen
Sektion Geowissenschaften
Klagenfurter Str.
28334 Bremen
Germany
Tel.: 0049 – 421 – 218 – 7165
Fax.: 0049 – 421 – 218 – 7163
e-mail: name@geophys2.uni-bremen.de

UCV: Universidad Católica de Valparaíso
Av. Altamirano 1480
Casilla 1020 – Valparaíso, Chile
Tel.: +56-32-274241
Fax: +56-32-274206
e-mail: name@ucv.cl

Figure: 2.1.1.1

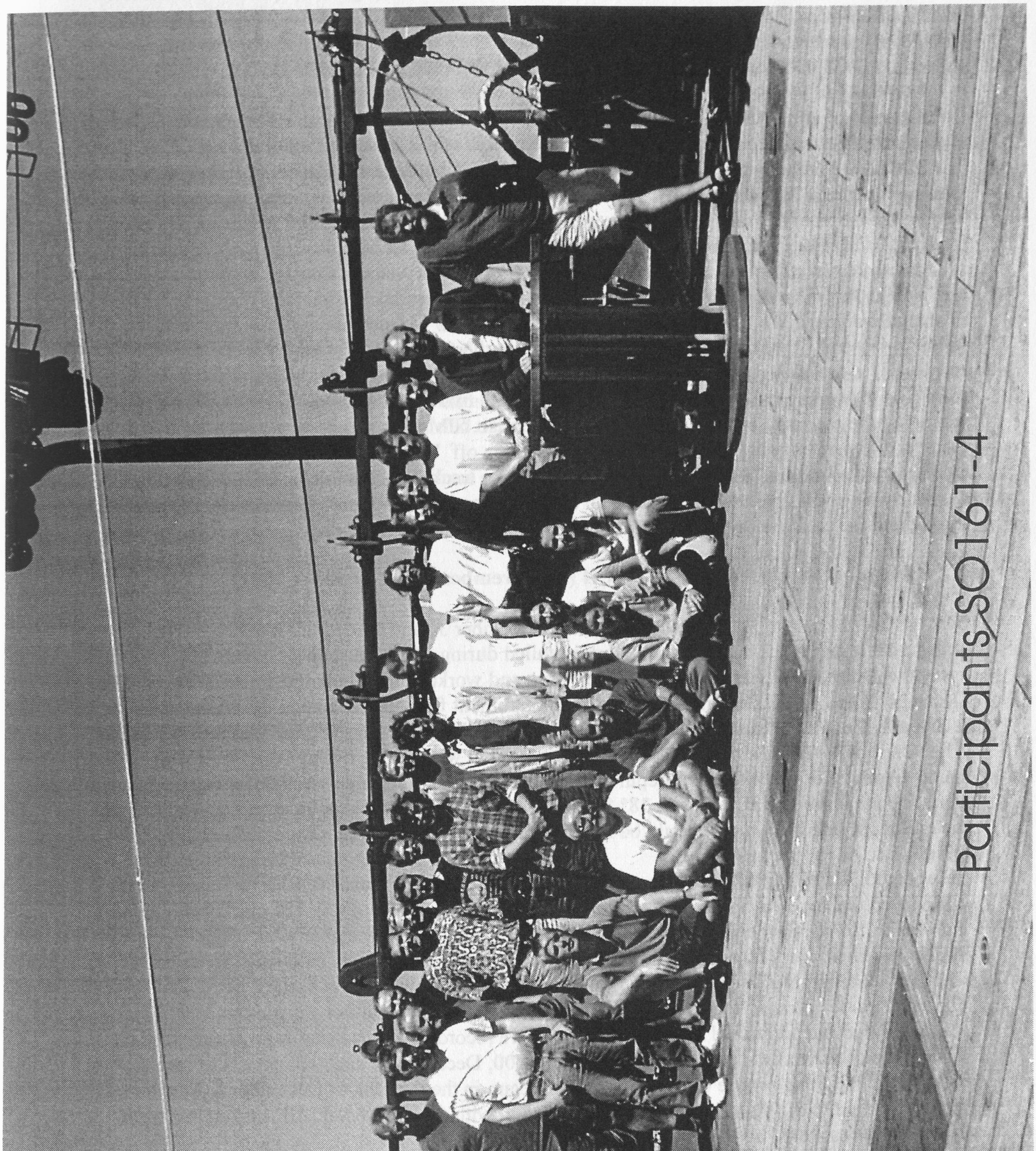

**Figure: 2.1.2.1**

## 3. Agenda

### 3.1. Agenda of the cruise SO 161 SPOC 1 (9 – 15 October 2001)

SONNE left the pier of Antofagasta at 15:00 on October 9 and headed south to the working area off Valparaiso, where a seismological network was to be installed.
In the morning of October 10, all 27 release units were tested at a water depth of 4000 m. Unfortunately, 5 units did not work. One of them could be repaired on board. The remaining four were unfit for deployment, reducing the number of stations in our seismic net from a planned 26 to 23.
The SIMRAD system was activated after passing 28°S. A bathymetric profile was mapped parallel to the trench up to 32°S.
The first location of the seismic network was reached on October 11 at 21:00. From 11-13 October, a total of 15 OBH and 8 OBS were deployed. Two locations are on oceanic crust, the other units were used to create two sub-arrays covering Papudo Ridge and San Antonio Canyon. Unfortunately, it had not been known to us that onboard testing of our new broadband seismometers is not possible because of ship movements. We finally found our way through their wiring, but only after four instruments (OBS 1, 4, 9 and 12) had already been deployed. We therefore had to go back for the instruments to be recovered, re-assembled, and re-deployed. Nevertheless, as the deployments had worked swiftly, we were able to keep up our time schedule and also to add two tracks of swath bathymetry north of 32°, extending the coverage of the CONDOR SO101 cruise. SIMRAD was de-activated at 08:00 on October 14 when entering the submarine exercise area off Valparaíso. We finally reached the port of Valparaíso on October 14 at 13:00 local time. A cruise track is shown in Fig. 3.1.1.
Considerable swell, fresh winds (4-6), cool temperatures (11-12°C) and a strong current persisted throughout the cruise, slowing the vessel down on southern courses.

### 3.2. Agenda of the cruise SO 161 SPOC 4 (30 November to 23 December 2001)

SONNE left the pier of Valparaíso at 18:40 on November 30 and headed north to the working area off Valparaiso, where a seismological network installed during Leg 1 was to be recovered. The Simrad system was turned on after leaving the 3-nm zone and worked throughout the cruise. Between 00:00 December 1 and 15:30 December 2 all but one instrument from the seismological array were recovered. The last instrument, OBS13, could not be picked up because of Navy exercises nearby. After a test of several instruments on the wire at 5000 m waterdepth, during which a profile of water sound velocities down to 2000 m depth was established using CTD measurements, the ship headed south for the first seismic profile at 38° S. The ~300 nm transit was made in such a way that gaps in the existing swath bathymetry could be filled; additionally magnetic data were collected (Profiles 101 to 107).
Between 06:30 and 16:00, December 4, 24 Ocean Bottom Hydrophones (OBH) or Seismometers (OBS) were deployed at an average spacing of about 3nm (OBH24 to 47). The start of the shooting line was ca. 20 nm further west, and shooting lasted from 21:30, December 4, to 16:20, December 5. Shots were fired every 60 s trigger at a ship velocity of 6 kn in perfectly calm seas. Instrument recovery started immediately afterwards and was finished December 6 at 10:00.
The ~400 nm long transit to the north was again chosen such that further gaps in the bathymetric map could be filled and additional magnetic profiles were recorded. The missing instrument from the seismological network (OBS13) was recovered 21:00, December 7, and deployment of instruments (OBH48 to 72) along profile 02 at 32°05´S was begun in the morning of December 8. This line was shot twice, first with 40 sec trigger interval, and then with 60 sec interval. All instruments were successfully recovered by 02:00, December 11.
During the transit towards profile 03, a the water sound profile up to a depth of 1000m was determined using CTD measurements (CTD02). Along the 120 nm long profile 03, which is coincident with the MCS line S0161-19 of leg 2 of the SPOC expeditions, a total of 27 instruments were deployed in the afternoon and evening of December 11. Shooting with 60 sec trigger pulses lasted until the early morning of December 13, the magnetometer was deployed during shooting as usual. All instruments were recovered shortly before midnight December 13.
Profile 04 is a cross profile to line 03 centred on O´Higgins seamount. Along this line 23 instruments were deployed in the morning of December 14, and shooting lasted for about 24 hours. Instrument

recovery started in the evening of December 15, and was completed by 10:00 the next day, when a considerable swell was prevailing.

During the transit to 31°S, where the last profile was to be shot, the magnetometer was deployed and the course was set such that previously unsurveyed areas were covered by swath-mapping. When the profile location was reached at 15:30, December 17, winds and swell had subsided. OBS/H 123 to 148 were deployed until 03:00 the next morning. Shooting started soon after, first with a shot interval of 30 sec sailing towards the coast (Profile 5-1), and then sailing seaward with 60 sec trigger intervals (Profile 5-2). This line was finished 15:30 on December 19, and subsequent recovery of instruments went smoothly until 14:00, December 20.

Thus, the seismic programme of the cruises comprised a total of 148 successful OBH/S deployments, into which a total of 9425 airgun shots were fired.

The remaining time at sea was used for additional swath-mapping and magnetic profiles to fill gaps in the existing coverage. The total number of magnetic profiles observed during Leg 4 was 31, in addition to the deployments of the magnetometer during shooting of the five seismic profiles. Once deployed, the instruments always worked without any technical failures.

The SIMRAD system was de-activated at 13:00 on 21 December when entering the submarine exercise area off Valparaíso. We finally reached the port of Valparaíso on 21 December at 16:30 local time, after cruising for 21 days covering a distance of nearly 3700 miles. In port, a gravity tie measurement was finally made and completed the scientific programme. A cruise track of SO161 Leg 4 is shown in Fig. 3.2.1.

The conditions at sea varied considerably from calm seas to force eight winds, and moderate temperatures persisted throughout the cruise.

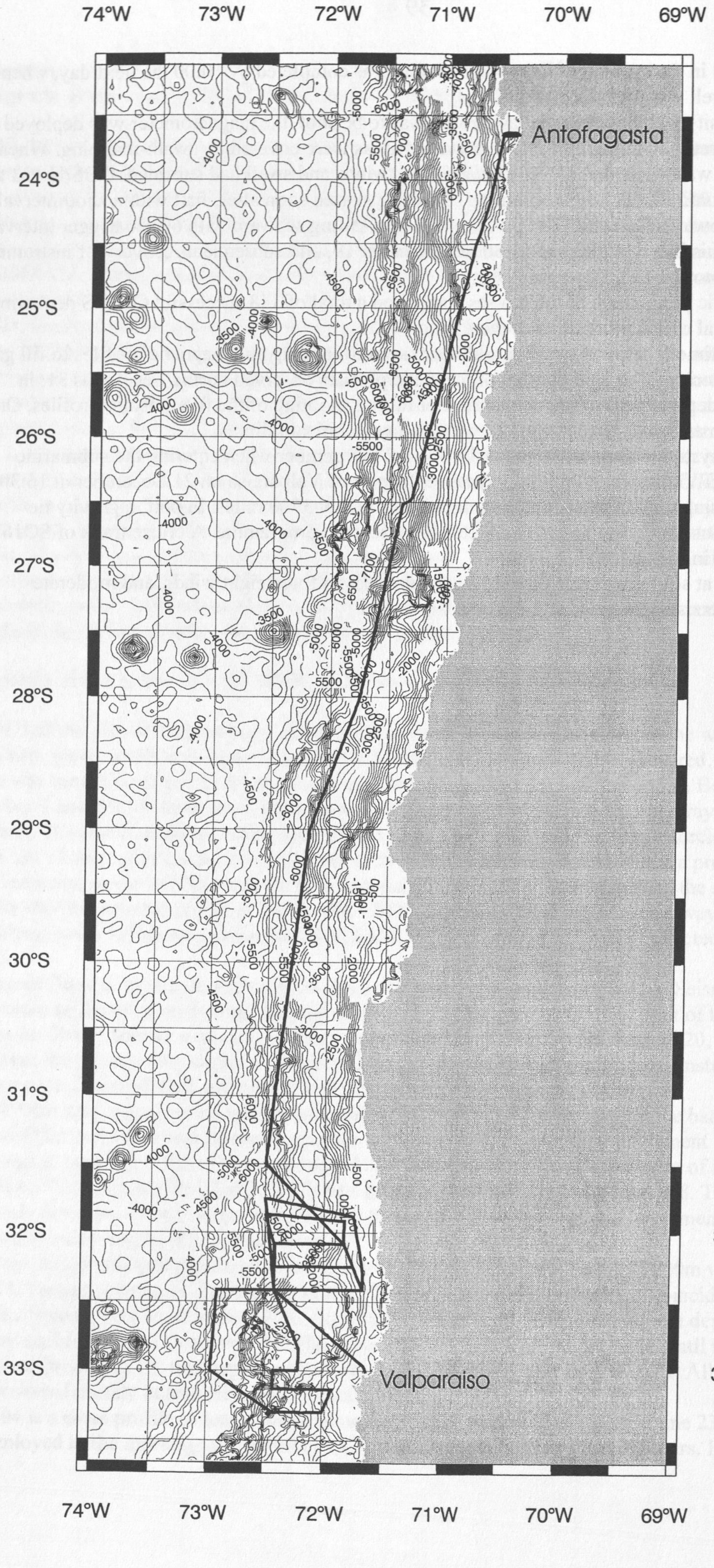

Figure 3.1.1: Track chart of cruise SO164 leg 1.

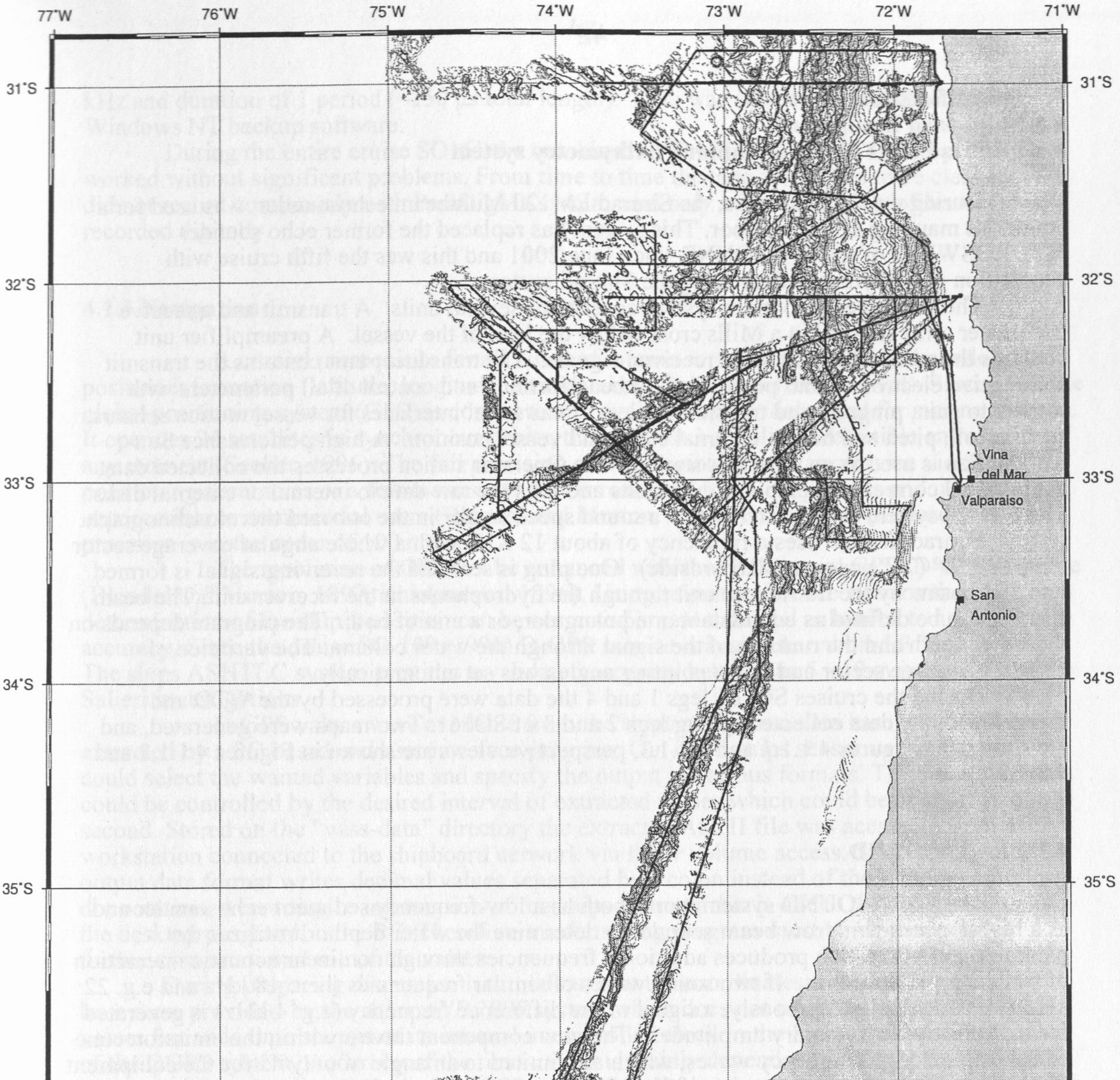

Figure 3.2.1.
**SPOC**
**GEOMAR Kiel**
R/V SONNE - Cruise 161-4
Track 30.11. 21.12.01

Map processed with GMT on Board R/V Sonne
by RF Reedereigemeinschaft Forschungsschiffahrt GmbH
DEC-2001

# 4. Scientific Equipment

## 4.1 Shipboard Equipment

### 4.1.1 Simrad EM120 swathmapping bathymetry system

During the SO161 cruise, the Simrad EM120 Multibeam echosounder was used for a continous mapping of the seafloor. This system has replaced the former echo sounder HYDROSWEEP of the R/V SONNE since June 2001 and this was the fifth cruise with acquisition of bathymetric data using the Simrad system.

The Simrad echosounder system consists of several units. A transmit and a receive transducer array is fixed in a Mills cross below the keel of the vessel. A preamplifier unit contains the preamplifiers for the received signals. The transducer unit contains the transmit and receive electronics and processors for beamforming and control of all parameters with respect to gain, pingrate and transmit angles. It has serial interfaces for vessel motion sensors, such as roll, pitch and heave, external clock and vessel position. A high performance Sun-workstation is used as an Operator station. The Operator station processes the collected data, applying all corrections, displays the results and logs the raw data to internal or external disks. The EM120 system has an interface to a sound speed sensor in the onboard thermosalinograph.

Simrad EM120 uses a frequency of about 12 KHz with a whole angular coverage sector of up to 150° (75° per port-/starbordside). One ping is sent and the receiving signal is formed into 191 beams by the transducer unit through the hydrophones in the receiver unit. The beam spacing can be defined as equidistant or equiangular, or a mix of both. The pingrate depends on the water depth and the runtime of the signal through the water column. The variation of angular coverage sector and beam pointing angles was set automatically.

During the cruises SO161 legs 1 and 4 the data were processed by the WTD and merged with the data collected during legs 2 and 3 of SO161. Two maps were generated, and are shown in nFigures 4.1.1.1 and 4.1.1.3, perspective views are shown in Figures 4.1.1.2 and 4.1.1.3.

### 4.1.2 PARASOUND

The PARASOUND system works both as a low-frequency sediment echosounder and as a high-frequency narrow beam sounder to determine the water depth. It utilizes the parametric effect, which produces additional frequencies through nonlinear acoustic interaction of finite amplitude waves. If two sound waves of similar frequencies (here 18 kHz and e.g. 22 kHz) are emitted simultaneously, a signal of the difference frequency (e.g. 4 kHz) is generated for sufficiently high primary amplitudes. The new component travels within the emission cone of the original high frequency waves, which are limited to an angle of only 4° for the equipment used. Therefore, the footprint size of 7% of the water depth is much smaller than for conventional systems and both vertical and lateral resolution are significantly improved.

The PARASOUND system is permanently installed on the ship. The hull-mounted transducer array has 128 elements within an area of $\sim 1\ m^2$. It requires up to 70 kW of electric power due to the low degree of efficiency of the parametric effect. In 2 electronic cabinets, beam formation, signal generation and the separation of the primary (18, 22 kHz) and secondary frequencies (4 kHz) is carried out. Using the third electronic cabinet located in the echosounder control room, the system is operated on a 24 hour watch schedule.

Since the two-way travel time in the deep sea is long compared to the length of the reception window of up to 266 ms, the PARASOUND System sends out a burst of pulses at 400 ms intervals, until the first echo returns. The coverage in this discontinuous mode is dependent on the water depth and also produces non-equidistant shot distances between bursts.

The main tasks of the operators are system and quality control and to adjust the start of the reception window. Because of the limited penetration of the echosounding signal into the sediment, only a short time window close to the sea floor is recorded.

In addition to the analog recording features with the b/w DESO 25 device, the PARASOUND System is equipped with the digital data acquisition system ParaDigMA, developed at the University of Bremen. The data is stored on removable hard disks using the standard, industry-compatible SEGY-format. The 486-processor based PC allows for buffering, transfer and storage of the digital seismograms at high repetition rates. Of the emitted series of pulses, usually only every second pulse can be digitized and stored, resulting in recording intervals of 800 ms for a given pulse sequence. The seismograms were sampled at a frequency of 40 kHz, with a typical registration length of 266 ms for a depth window of ~200 m. The source signal was a band limited, 2-6 kHz sinusoidal wavelet with a dominant frequency of 4 kHz and duration of 1 period (~250 µs total length). Data was stored on DAT-tapes using Windows NT backup software.

During the entire cruise SO161 the combined PARASOUND/ParaDigMa system worked without significant problems. From time to time the tape drives had to be cleaned. We did not record continously with ParaDigMa system, and only a few selected profiles were recorded digitally.

### 4.1.3 Navigation

A crucial prerequisite for all kinds of marine surveys is the precise knowledge of position information (latitude, longitude, altitude above/below a reference level). Since 1993 the global positioning system (GPS) is commercially available and widely used for marine surveys. It operates 24 satellites in synchronous orbits, thus at least 3 satellites are visible anywhere at any moment (Seeber, 1996). The full precision of this originally military service yields positioning accuracies of a few meters, yet this is restricted to military forces and usually unaccessible to commercial users (Blondel and Murton, 1997). For civilian purposes the precision is in the order of 100 meters.

The resolution of GPS can be enhanced with the Differential GPS (D-GPS) scheme (Blondel and Murton, 1997, Knickmeyer, 1996). Using several reference stations the determination of the ship's position can be corrected in real time and enhanced to a 1 m to 5 m accuracy. Since the cruise SO-109 (1996) D-GPS service is available onboard R/V SONNE. The ships ASHTEC system provides a validated accuracy better than 5 - 10 m in the area of the Salieri investigations.

D-GPS values were available from the ships navigation data base and could be extracted by a PC based end user interface program. Out of all ships sensor values the user could select the wanted variables and specify the output in various formats. The amount of data could be controlled by the desired interval of extracted values which could be as short as one second. Stored on the "wiss-data" directory the extracted ASCII file was acessable from every workstation connected to the shipboard network via ftp or volume access. Surprisingly the output data format writes decimal values separated by a colon instead of the standard american dot notation. According to information of the ships operator this is due to the chosen set up of the desktop program on the PC. Therefore a reformating program must be written prior to further computational use of the values.

During preparing discussion it turned out that the coordinates stored within the data base were provided by the *Atlas ANP 2000* system which does not copy the exact GPS time values but adds time stamps of its internal uncontrolled clock to the high precision coordinates of the DGPS system. Accuracy of the time values is mainly dependend on the operators skills by manually setting the ANP clock to GPS time. A somewhat conservative method compared to the efforts of precise positioning. To enable the most accurate GPS related time stamps within the ANP system prior to each seismic survey the system operates were informed to reset the ANP.

### 4.1.4 CTD data

To obtain accurate sound velocity profiles needed for bathymetric swathmapping we used the Simrad Sound Velocity Probe twice. The Simrad Probe was lowered down to water depth of 2000 m and 1000 m at a velocity 1 m/s measuring the sound speed in-situ continuously. These are shown in Figures 4.1.4.1 and 4.1.4.2.

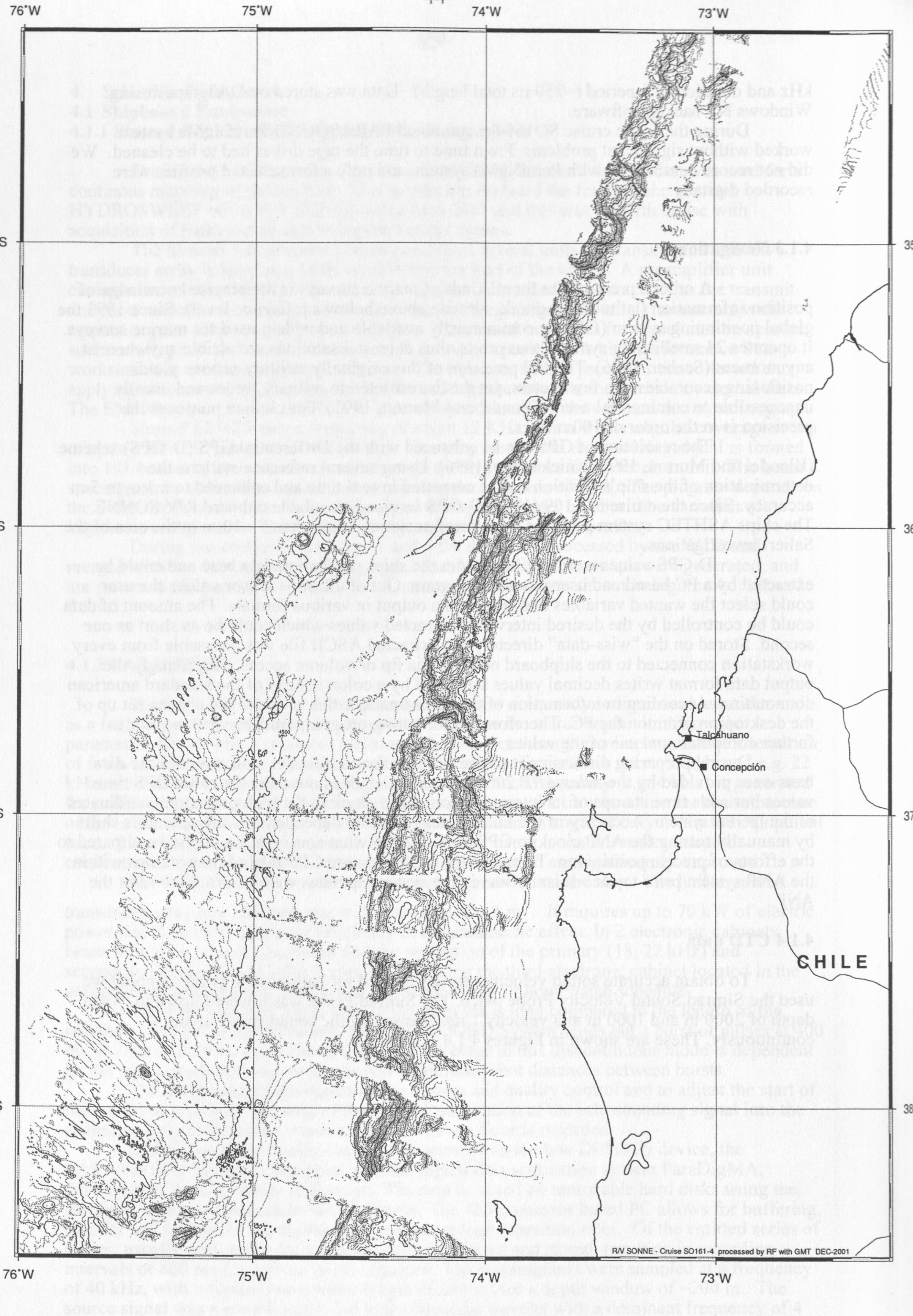

Figure 4.1.1.1.
**SPOC**
**GEOMAR Kiel**
R/V SONNE - Cruise 161-4
AREA South

Mercator Projection (WGS 84)
Scale 1:2.000.000 at 34.5°S
Grid 300 m Contour 100 m

Map processed with GMT on Board R/V Sonne
by RF Reedereigemeinschaft Forschungsschiffahrt GmbH
DEC-2001

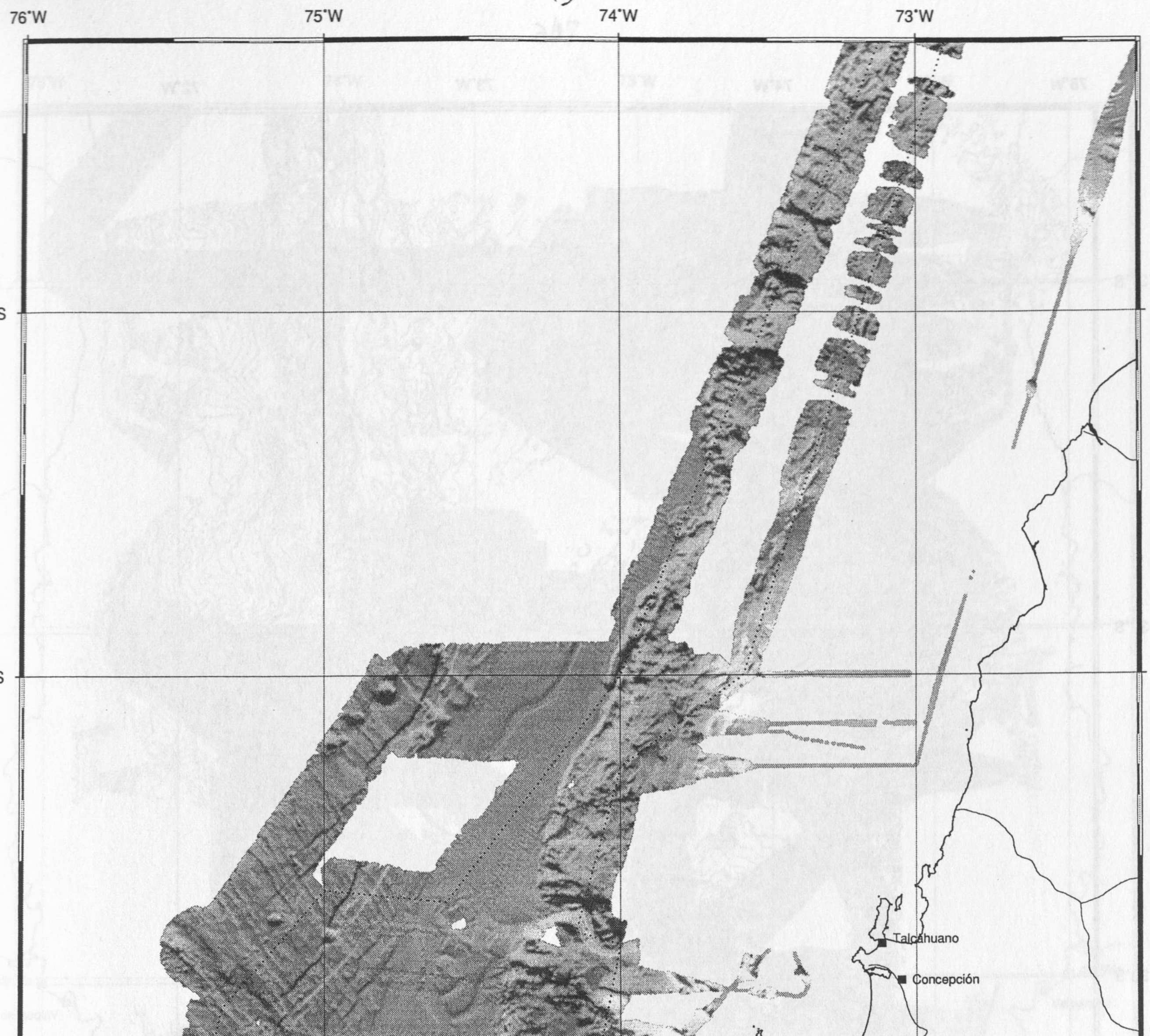

Figure 4.1.1.2.
**SPOC**
**GEOMAR Kiel**
R/V SONNE - Cruise 161-4
AREA South

Dodet lines are tracks of SO161-4
Mercator Projection (WGS 84)
Scale 1:2.000.000 at 34.5°S
Grid 300 m

Map processed with GMT on Board R/V Sonne
by RF Reedereigemeinschaft Forschungsschiffahrt GmbH
DEC-2001

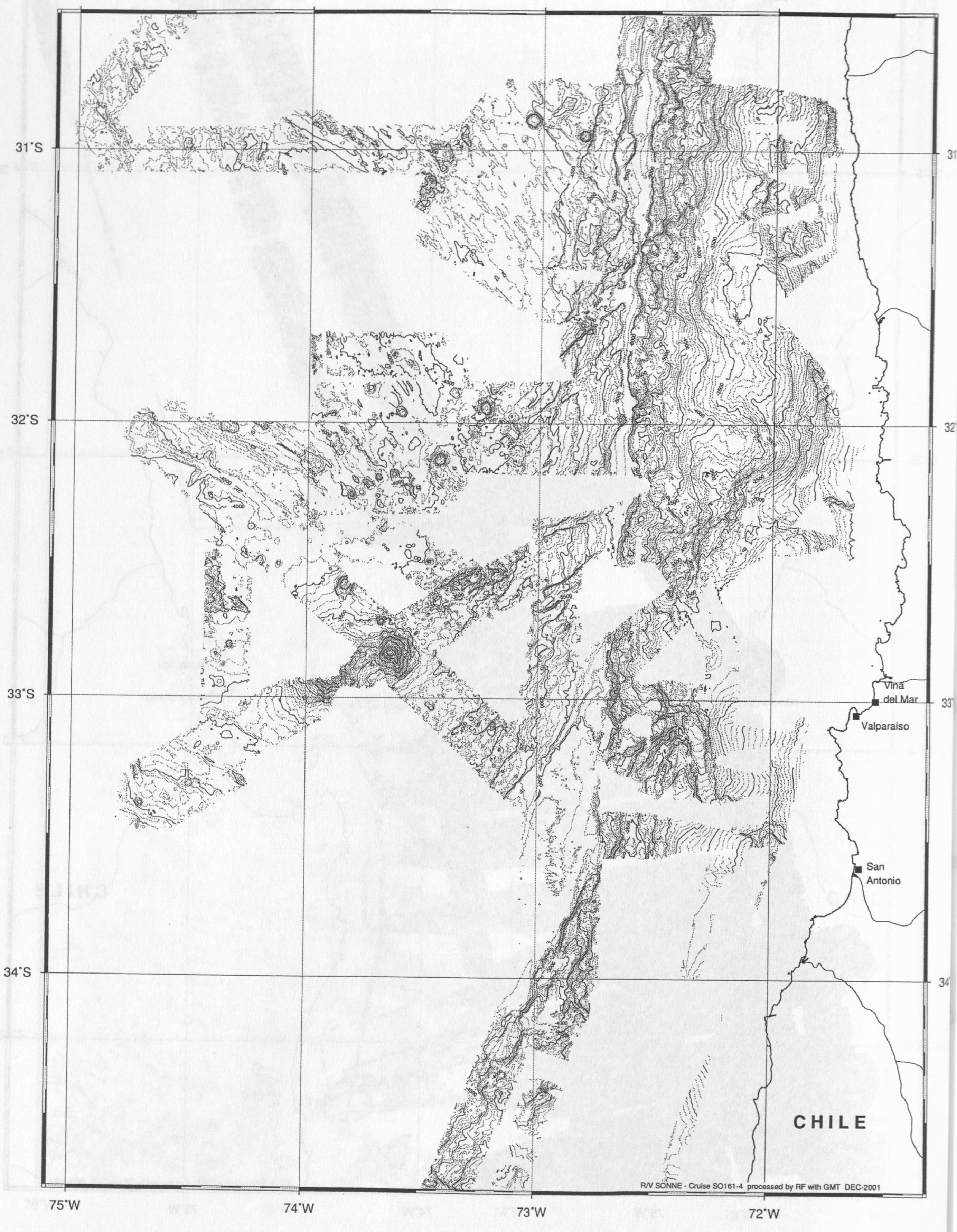

Figure 4.1.1.3.
**SPOC**
**GEOMAR Kiel**
R/V SONNE - Cruise 161-4
AREA North

Mercator Projection (WGS 84)
Scale 1:2.000.000 at 34.5°S
Grid 300 m Contour 100 m

Map processed with GMT on Board R/V Sonne
by RF Reedereigemeinschaft Forschungsschiffahrt GmbH
DEC-2001

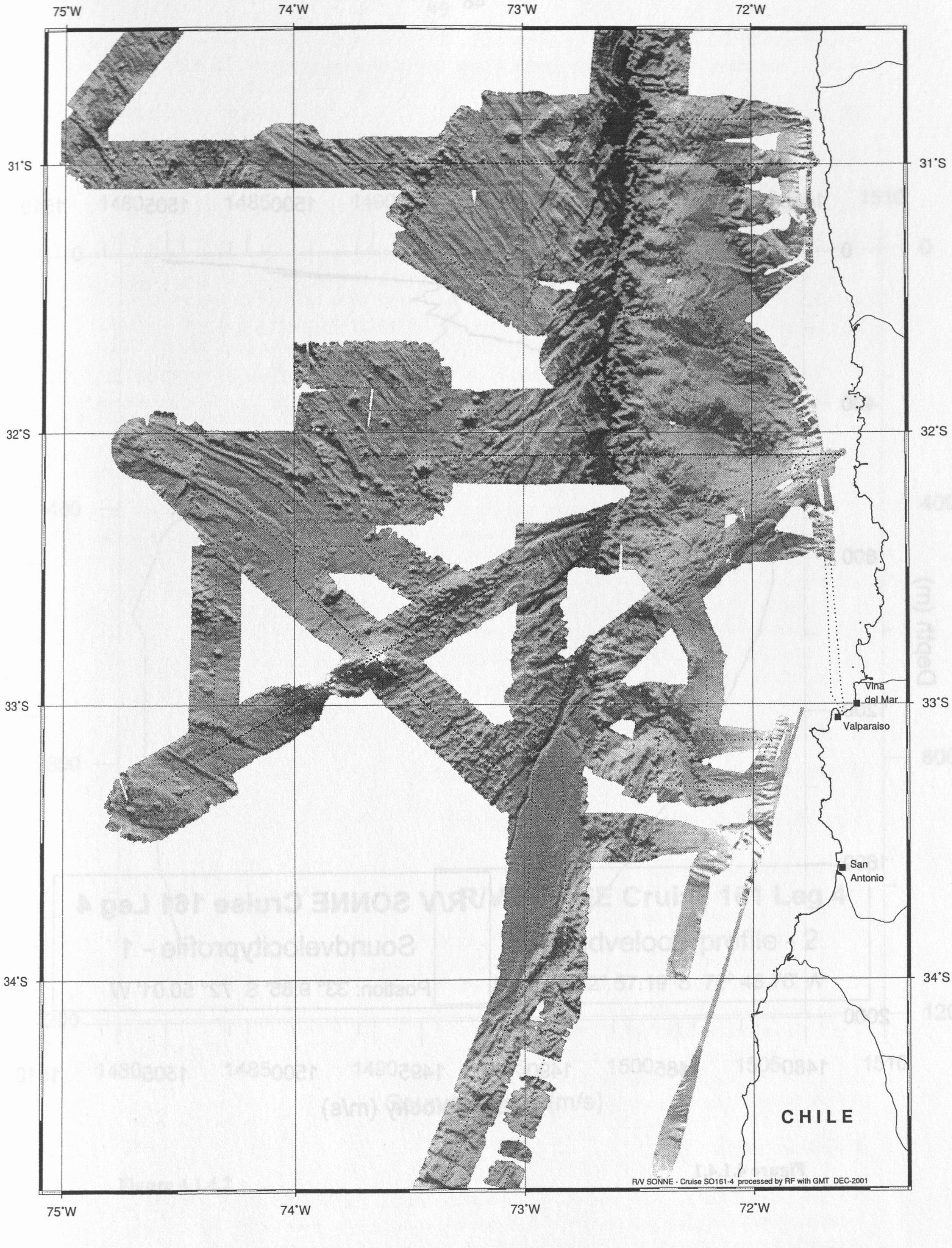

Figure 4.1.1.4.
**SPOC**
**GEOMAR Kiel**
R/V SONNE - Cruise 161-4
AREA North

Dodet lines are tracks of SO161-4
Mercator Projection (WGS 84)
Scale 1:2.000.000 at 34.5°S
Grid 300 m

Map processed with GMT on Board R/V Sonne
by RF Reedereigemeinschaft Forschungsschiffahrt GmbH
DEC-2001

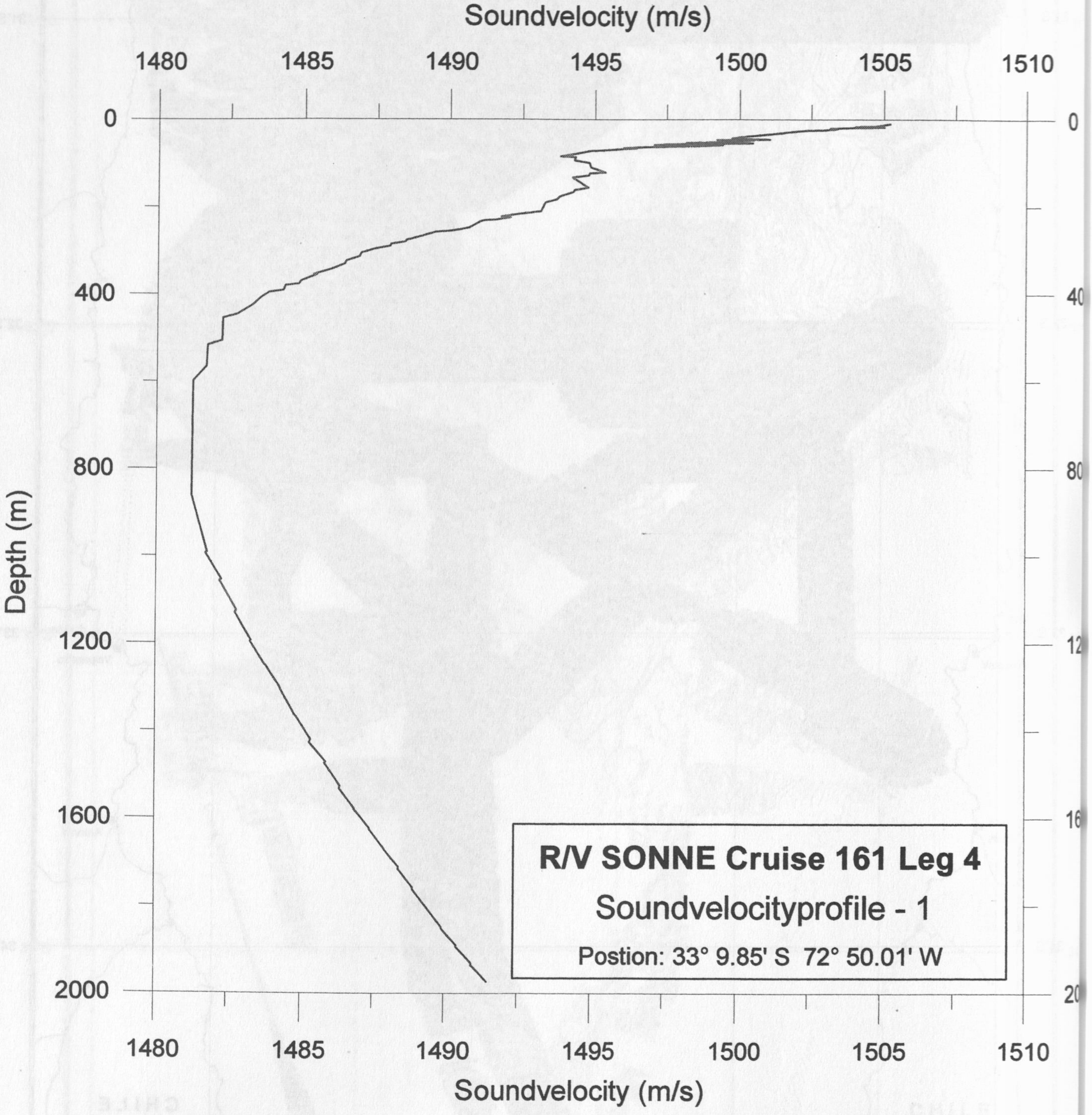
Soundvelocity (m/s)
1480
1485
1490
1495
1500
1505
1510
0
400
800
1200
1600
2000
Depth (m)
0
40
80
12
16
20
R/V SONNE Cruise 161 Leg 4
Soundvelocityprofile - 1
Postion: 33° 9.85' S 72° 50.01' W
1480
1485
1490
1495
1500
1505
1510
Soundvelocity (m/s)

**Figure 4.1.4.1**

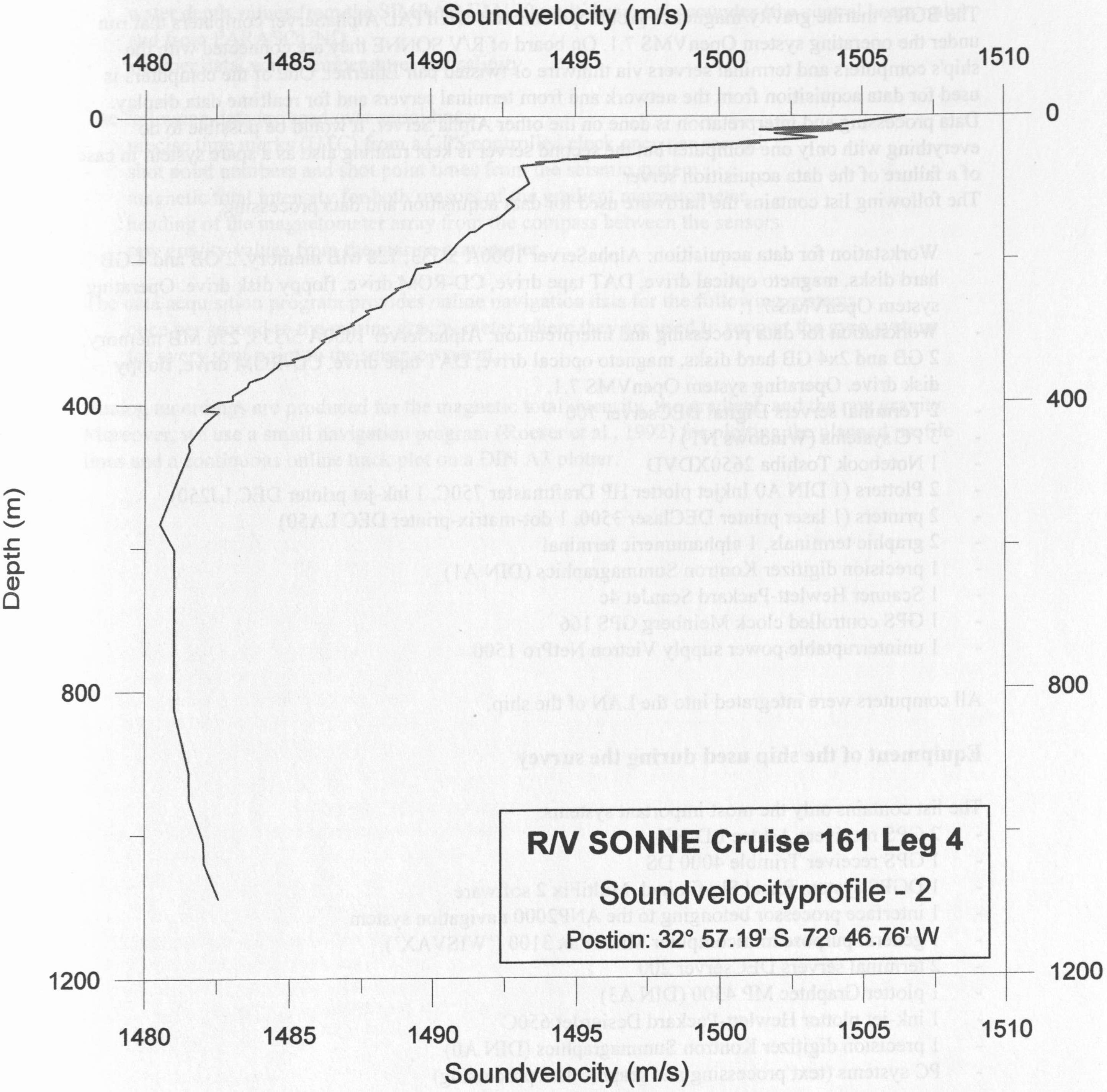
Soundvelocity (m/s)
1480
1485
1490
1495
1500
1505
1510
Depth (m)
0
400
800
1200
R/V SONNE Cruise 161 Leg 4
Soundvelocityprofile - 2
Postion: 32° 57.19' S 72° 46.76' W

**Figure 4.1.4.2**

## 4.2 Computer facilities

### 4.2.1 Computer systems for navigation, gravity, and magnetics

(B. Schreckenberger and H.-O. Bargeloh)

The BGR's marine gravity/magnetics group operates two DIGITAL AlphaServer computers that run under the operating system OpenVMS 7.1. On board of R/V SONNE they are connected with the ship's computers and terminal servers via thinwire or twisted pair Ethernet. One of the computers is used for data acquisition from the network and from terminal servers and for realtime data display. Data processing and interpretation is done on the other Alpha Server. It would be possible to do everything with only one computer but the second server is kept running also as a spare system in case of a failure of the data acquisition server.
The following list contains the hardware used for data acquisition and data processing:

- Workstation for data acquisition: AlphaServer 1000A 5/333, 128 MB memory, 2 GB and 4 GB hard disks, magneto optical drive, DAT tape drive, CD-ROM drive, floppy disk drive. Operating system OpenVMS 7.1.
- Workstation for data processing and interpretation: AlphaServer 1000A 5/333, 256 MB memory, 2 GB and 2x4 GB hard disks, magneto optical drive, DAT tape drive, CD-ROM drive, floppy disk drive. Operating system OpenVMS 7.1.
- 2 Terminal servers Digital DECserver 700
- 3 PC systems (Windows NT)
- 1 Notebook Toshiba 2650XDVD
- 2 Plotters (1 DIN A0 Inkjet plotter HP Draftmaster 750C, 1 ink-jet printer DEC LJ250)
- 2 printers (1 laser printer DEClaser 3500, 1 dot-matrix-printer DEC LA50)
- 2 graphic terminals, 1 alphanumeric terminal
- 1 precision digitizer Kontron Summagraphics (DIN A1)
- 1 Scanner Hewlett-Packard ScanJet 4c
- 1 GPS controlled clock Meinberg GPS 166
- 1 uninterruptable power supply Victron NetPro 1500

All computers were integrated into the LAN of the ship.

### Equipment of the ship used during the survey

The list contains only the most important systems:

- 2 GPS receivers Ashtec LD-XII
- 1 GPS receiver Trimble 4000 DS
- 1 DGPS system Racal Skyfix incl. MultiFix 2 software
- 1 interface processor belonging to the ANP2000 navigation system
- 1 general purpose minicomputer MicroVax 3100 ('WISVAX')
- 2 terminal servers DECserver 200
- 1 plotter Graphtec MP 4300 (DIN A3)
- 1 ink-jet plotter Hewlett-Packard DesignJet 650C
- 1 precision digitizer Kontron Summagraphics (DIN A0)
- PC systems (text processing and graphic data processing)

### Data acquisition

All data are read into the computer via serial interfaces or over the Ethernet network. There is a number of real time programs that write the data into the memory as soon as they are available. The main data acquisition program checks, reformats, and collects the data items to one data set each 20 seconds and writes it to direct access files on magnetic disk.

## 4.2 Computer facilities

### 4.2.1 Computer systems for navigation, gravity, and magnetics

(B. Schreckenberger and H.-O. Bargeloh)

The BGR's marine gravity/magnetics group operates two DIGITAL AlphaServer computers that run under the operating system OpenVMS 7.1. On board of R/V SONNE they are connected with the ship's computers and terminal servers via thinwire or twisted pair Ethernet. One of the computers is used for data acquisition from the network and from terminal servers and for realtime data display. Data processing and interpretation is done on the other Alpha Server. It would be possible to do everything with only one computer but the second server is kept running also as a spare system in case of a failure of the data acquisition server.
The following list contains the hardware used for data acquisition and data processing:

- Workstation for data acquisition: AlphaServer 1000A 5/333, 128 MB memory, 2 GB and 4 GB hard disks, magneto optical drive, DAT tape drive, CD-ROM drive, floppy disk drive. Operating system OpenVMS 7.1.
- Workstation for data processing and interpretation: AlphaServer 1000A 5/333, 256 MB memory, 2 GB and 2x4 GB hard disks, magneto optical drive, DAT tape drive, CD-ROM drive, floppy disk drive. Operating system OpenVMS 7.1.
- 2 Terminal servers Digital DECserver 700
- 3 PC systems (Windows NT)
- 1 Notebook Toshiba 2650XDVD
- 2 Plotters (1 DIN A0 Inkjet plotter HP Draftmaster 750C, 1 ink-jet printer DEC LJ250)
- 2 printers (1 laser printer DEClaser 3500, 1 dot-matrix-printer DEC LA50)
- 2 graphic terminals, 1 alphanumeric terminal
- 1 precision digitizer Kontron Summagraphics (DIN A1)
- 1 Scanner Hewlett-Packard ScanJet 4c
- 1 GPS controlled clock Meinberg GPS 166
- 1 uninterruptable power supply Victron NetPro 1500

All computers were integrated into the LAN of the ship.

### Equipment of the ship used during the survey

The list contains only the most important systems:

- 2 GPS receivers Ashtec LD-XII
- 1 GPS receiver Trimble 4000 DS
- 1 DGPS system Racal Skyfix incl. MultiFix 2 software
- 1 interface processor belonging to the ANP2000 navigation system
- 1 general purpose minicomputer MicroVax 3100 (‘WISVAX’)
- 2 terminal servers DECserver 200
- 1 plotter Graphtec MP 4300 (DIN A3)
- 1 ink-jet plotter Hewlett-Packard DesignJet 650C
- 1 precision digitizer Kontron Summagraphics (DIN A0)
- PC systems (text processing and graphic data processing)

### Data acquisition

All data are read into the computer via serial interfaces or over the Ethernet network. There is a number of real time programs that write the data into the memory as soon as they are available. The main data acquisition program checks, reformats, and collects the data items to one data set each 20 seconds and writes it to direct access files on magnetic disk.

The navigation data come via the ship's WISVAX computer over an Ethernet link once per second. On this cruise the following data were received from the ship's navigation system:

- position, speed and course from GPS
- heading from the gyro
- speed from the doppler-sonar (DO-Log)
- water depth values from the SIMRAD EM120 multi beam echosounder (the central beam only) and from PARASOUND
- weather data, water temperature, and salinity.

The following data are read over serial lines:

- precise time marks (UTC) from a GPS controlled clock once per second
- shot point numbers and shot point times from the seismic system
- magnetic total intensity for both sensors of the gradient magnetometer
- heading of the magnetometer array from the compass between the sensors
- raw gravity values from the marine gravimeter

The data acquisition program provides online navigation data for the following systems:

- once per second to the marine gravity meter where they are used to support the gyro system
- for every shot point to the seismic system.

Analog recordings are produced for the magnetic total intensity, the gradient, and the raw gravity. Moreover, we use a small navigation program (Roeser et al., 1992) for plotting the planned profile lines and a continuous online track plot on a DIN A3 plotter.

### 4.2.2 Computer facilities for ocean bottom instrument programming and analysis

The experiments and investigations during SO161 required special computing facilities in addition to the existing shipboard systems. For programming of ocean bottom stations, processing and interpretation of seismic data and analysis of magnetics and gravimetry several workstations and a dedicated PC-laptop were installed by the wide angle and seismology groups of GEOMAR.
Due to the large amount of data transfer GEOMAR installed a workstation cluster onboard comprising the following systems:

| | | | | | |
|---|---|---|---|---|---|
| 1 | ”moho” | SUN<br>Sparc 20 | 2 CPU,<br>192 MB<br>memory | 20 GB disks,<br>DAT, DLT, CD | Sun<br>Solaris 2.8 |
| 2 | ”devonia” | SUN<br>Ultra 60 | 2 CPU<br>1 GB memory | 150 GB disks,<br>1x DLT,<br>2x DAT,<br>1x Exabyte | Sun<br>Solaris 2.6 |
| 3 | ”hotblack” | SUN<br>Ultra 1 | 1 CPU,<br>128 MB<br>memory | 4 GB disks,<br>CD | Sun<br>Solaris 2.8 |
| 4 | ”galicia” | SUN<br>Sparc 10 | 1 CPU, 96 MB<br>memory | 12 GB disks,<br>DAT | SunOS 4.1.4 |
| 5 | ”crimea” | AMD<br>Duron<br>700 MHz | 1 CPU,<br>128 MB<br>memory | 68 GB disks,<br>6x PCMCIA | Windows2000 |

For seismic modelling two Macintosh computers were installed:

1 PowerMacintosh G3/300 MHz
2 PowerBook G4

In addition to these computers, a X-Windows-Terminal NCD-15r and several laptops were used. For plotting and printing two HP Postscript Laserprinters (papersize A3 and A4) as well as the shipboard color plotters were available.
The workstation cluster was placed in the Reinlabor where it was set up according to a ”client-server” model, with ”moho” being the server. One Macintosh computer was located in the Hydrosweep-Labor, the other in the Reinlabor, both being connected to the ships network. All important file systems from the main server at GEOMAR were duplicated onto the ”moho”-disks. Using NFS-, NIS-, and automounter services the computing environment was identical to that at GEOMAR, so every user found his/her familiar user interface. The convenience of network mounted file systems has to be paid for with a heavy network load, particularly during playback of OBH-data from tape to disk (c.f. SO123 cruise report, Flueh et al., 1997). This required a high-performance network, which was accomplished by a switched twisted-pair ethernet. A 12-port ethernet switching-hub (3COM-SuperstackII 1000) with an uplink connection of 100 Mbps to the server ”moho” and dedicated 10 Mbps ports for the client workstations maintained the necessary network performance. In order to keep the shipboard network undisturbed by the workstation cluster, but to allow for communication between them, the server ”moho” was equipped with two network interfaces and served as a router. This provided the additional benefit of a simplified network configuration. Considerable setup work was dedicated to ”moho”, while the other workstations used the same IP-addresses and network configuration as at GEOMAR.
This network setup showed a reliable and stable performance, and no breakdowns were observed. The Macintosh computers could not access the ships printers but with an additional network connection between ships hub and GEOMAR´s switch “moho” could be bypassed and access was possible to the GEOMAR network printers.

## 4.3 The GEOMAR Ocean Bottom Hydrophone / Seismometer (OBH/S)

### The Ocean Bottom Hydrophone

The first GEOMAR Ocean Bottom Hydrophone was built in 1991 and tested at sea in January 1992. This type of instrument has proved to have a high reliability; in fact more than 1700 successful deployment were carried out since. A total of 20 OBH and 9 OBS instruments were available for SO161. Altogether 148 sites were occupied during the SO161 cruise.

The principle design of the instrument is shown in Figure 4.3.1, and a photograph showing the instrument upon deployment can be seen in Figure 4.3.2. The design is described in detail by Flueh and Bialas (1996).

The system components are mounted on a steel pipe which holds the buoyancy body on its top. The buoyancy is made of syntactic foam and is rated, as are all other components of the system, for a water depth of 6000 m, except for the pressure cylinders holding the recording electronics. Here, various models are available for variable depths (2500 m, 3000 m, and 6000 m). Attached to the buoyant body are a radio beacon, a flash light, a flag and a swimming line for retrieving from aboard the vessel. The hydrophone for the acoustic release is also mounted here. The release transponder is a model *RT661CE* made by *MORS Technology*. Communication with the instrument is possible through the ship's transducer system, and even at maximum speed and ranges of 4 to 5 miles release and range commands are successful. For anchors, we use pieces of railway tracks weighing about 40 kg each. The anchors are suspended 2 to 3 m below the instrument. The sensor is an *E-2PD* hydrophone from *OAS Inc.*, and the recording device is a *MBS recorder of SEND GmbH,* which is contained in its own pressure tube and mounted below the buoyant body opposite the release transponder (see Figures 4.3.1 and 4.3.2).

### The Ocean Bottom Seismometer

The Ocean Bottom Seismometer (OBS) construction (Bialas and Flueh, 1999; Fig. 4.3.3) is based on the experiences with the GEOMAR OBH. For system compatibility the acoustic release, pressure tubes, and the hydrophone are identical to those used for the OBH. Syntactic foam was used as floatation again but of larger diameter due to the increased payload. In contrast to the OBH the OBS has three legs around a center post to which the anchor weight is attached (Fig. 4.3.4). While the OBH is floating about 1 m above the sea bottom, the OBS is positioned on the sea bottom to avoid collisions between the the seismometer cable and the anchor. The sensible seismometer is deployed about 1 m to the side of the system once the OBS lands on the sea floor. During descent to the ocean bottom, the footplate of the seismometer release lever is about one meter below the base of the anchor and therefore hits the seafloor first. At touch down the baseplate forces an upward movement of the lever which lays out the seismometer hook until the seismometer anchor is about 0.5 m above the seafloor. At about 45 degrees to the vertical the seismometer is released from its hook and falls to the sea floor from about 1 m height, ensuring coupling between the seismometer and the sea floor. At this time the only connection from the seismometer to the instrument is a cable and an attached wire which retracts the seismometer during ascent to the sea surface. An oscillation of the instrument caused by possible currents is therefore not transmitted mechanically to the seismometer. All three channels are preamplified within the seismometer housing and recorded by the standard Methusalem recorder as used in the OBH units. Parallel to these three channels the standard hydrophone is recorded on the fourth channel. A new self-levelling seismometer with 4.5 Hz geophones was successfully tested during SO161. The levelling of the three component geophone (termed A01) is done at a preset time by unlocking springs that clamp the geophone package against the titanium housing.

Beside the standard OBS type used for active seismic recording broadband seismometer were available and routinely deployed within the profiles. Two different types of sensors were attached to the instrument. The "Spahr Webb" type seismometer is based on *Mark-L4* sensors which are operated with a feedback loop to enable recordings of frequencies as low as about 60 sec. As the sensors are sensitive to horizontal or vertical adjustment the complete construction is fully gimbaled. Tilt is measured at selected intervals and two electric motors are used to adjust and fix for a proper positioning. The second sensor is a *PMD-113* which has a flat frequency responce curve from 95 sec. up to 30 Hz. This sensor type operates on the base of measuring levels within electrolytical tubes. This principle is less sensitive to ist horizontal adjustment. The sensor is fixed like a pendulum while ist lower third is surrounded by a viscose oil filling that gives freedom to very slow movements (within a circle of 18°) and could be assumed to be solid within the measured frequency range. Both systems are mounted within a 17" glas sphere with an additional weight at the bottom (20 kg weight in water) which should ensure a good coupling to the ground. The above discribed lever system was not able to handle this size of sensor and therefore a slide system was designed (Fig. 4.3.5 and 4.3.6) which allows to deploy the sensor about three meters to the side of the instrument carrier. A clock controled burning wire is used first as release of the slide. Then the sensor is pulled by an elastic rope along the slide until he falls off at the end of the boom. Secondly the clock releases the sledge itself to enable deployment of the sensor even if it does not drop off the slide for any reason. Both sensors are recorded by use of the *Marine Longtime Recorder (MLS)* which is manufactured by *SEND GmbH* and specially designed for longtime recordings of low frequency bands. Together with the broadband sensors the fourth channel record a Differential Pressure Gauge (DPG) build by Spahr Webb at SCRIPPS.

### Marine Broadband Seismic Recorder (MBS)

The so-called *Marine Broadband Seismic recorder (MBS;* Bialas and Flueh, 1999*)*, manufactured by *SEND GmbH,* was developed based upon experience with the DAT based recording unit Methusalem (Flueh and Bialas, 1996) over the last few years. This new recorder avoids a mechanically driven recording media, and the PCMCIA technology enables static flash memory cards to be used as unpowered storage media. Read/write errors due to failure in tape handling operations should not occur with this system. In addition, a data compression algorithm is implemented to increase data capacity. Redesign of the electronic layout enables a decreased power consumption (1.5 W) of about 25% compared to the *Methusalem* system. Depending on the sampling rate, data output could be in 16 to 18 bit signed data. Based on digital decimation filtering, the system was developed to serve a variety of seismic recording requirements. Therefore, the bandwidth reaches from 0.1 Hz for seismological observations to the 50 Hz range for refraction seismic experiments and up to 10 kHz for high resolution seismic surveys. The basic system is adapted to the required frequency range by setting up the appropriate analog front module. Alternatively, 1, 2, 3 or 4 analogue input channels may be processed. Operational handling of the recording unit is similar to the *Methusalem* system or by loading a file via command or automatically after power-on. The time base is based on a DTCXO with a 0.05 ppm accuracy over temperature. Setting and synchronizing the time as well as monitoring the drift is carried out automatically by synchronization signals (DCF77 format) from a GPS-based coded time signal generator. Clock synchronization and drift are checked after recovery and compared with the original GPS units. After software preamplification the signals are low-pass filtered using a 5-pole Bessel filter with a -3 dB corner frequency of 10 kHz. Then each channel is digitised using a sigma-delta A/D converter at a resolution of 22 bits producing 32-bit signed digital data. After delta modulation and Huffman coding the samples are saved on PCMCIA storage cards together with timing information. Up to 4 storage cards may be used. Currently, up to 640 MB per card are available. Data compression allows allows to increase this capacity. Recently technical specifications of flashdisks (disk drives of PCMCIA technology) have been modified to operate below 10 °C, therefore 2 GB drives are now available for data storage. After recording the flashcards need to be copied to a PC workstation. During this transcription the data are decompressed and data files from a maximum of four flash memory are combined into one data set and formatted according to the PASSCAL data scheme used by the *Methusalem* system. This enables full compatibility with the established processing system. While the *Methusalem* system did provide 16 bit integer data, the 18 bit data resolution of the *MBS* can be fully utilized using a 32 bit data format.

### The Marine Longtime Seismograph

For the purpose of low frequent recordings such as seismological observations of earthquakes during long term deployments of about one year time a new data logger, the Marine Longtime Seismograph (MLS) was developped by *SEND GmbH* with support from GEOMAR.
The MLS is again a four channel data logger whose input channels have been optimized for 3-component seismometers and one hydrophone channel. The modular design of the analogue front end allows to adopt for different seismometers and hydrophones or pressure sensors. Currently front ends for the Spahr Webb, PMD and Guralp seismometers as well as for a differential pressure gauge (DPG) and the OAS hydrophone are available. With these sensors we are able to record events between 50 Hz and 120 s. The very low power consumption of 250 mW during recording together with a high precision internal clock (0.05 ppm drift) allows data acquisition for one year. Data storage is done on up to 12 PCMCIA type II flashcards. The instrument can be parameterized and programmed via a RS232 interface. After low pass filtering the signals of the input channels are digitized using Sigma-Delta A/D converters. A final decimating sharp digital low-pass filter is realized in software by a Digital Signal Processor. The effective signal resolution depends on the sample rate and varies between 18.5 bit at 20 ms and 22 bits at 1 s. Playback of the data is done under the same scheme as described for the MBS above. After playback and

decompression the data is provided in PASSCAL format from where it could be easily transformed into standard seismological data formats.

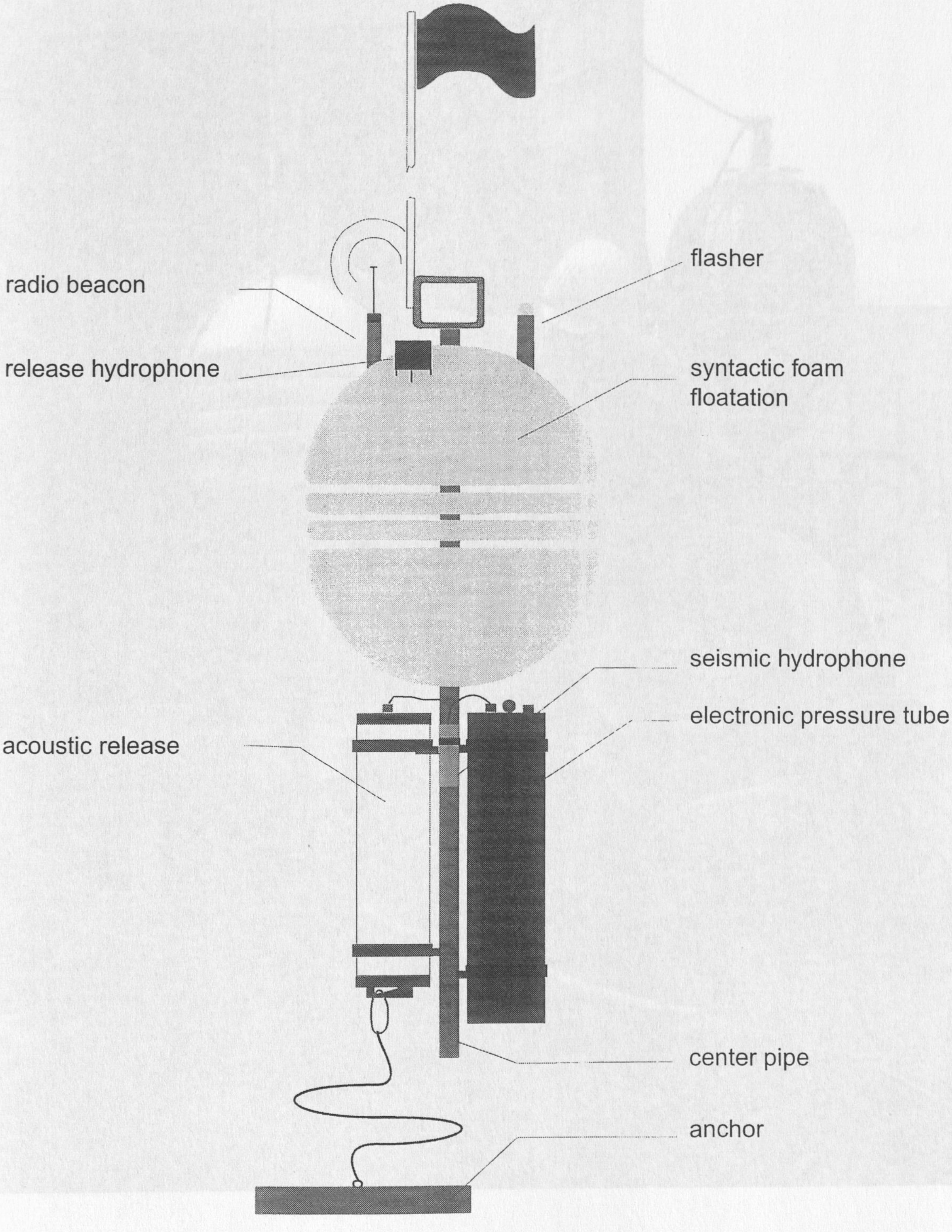

Figure 4.3.1: Principle design of the GEOMAR OBH (after Flueh and Bialas, 1996)

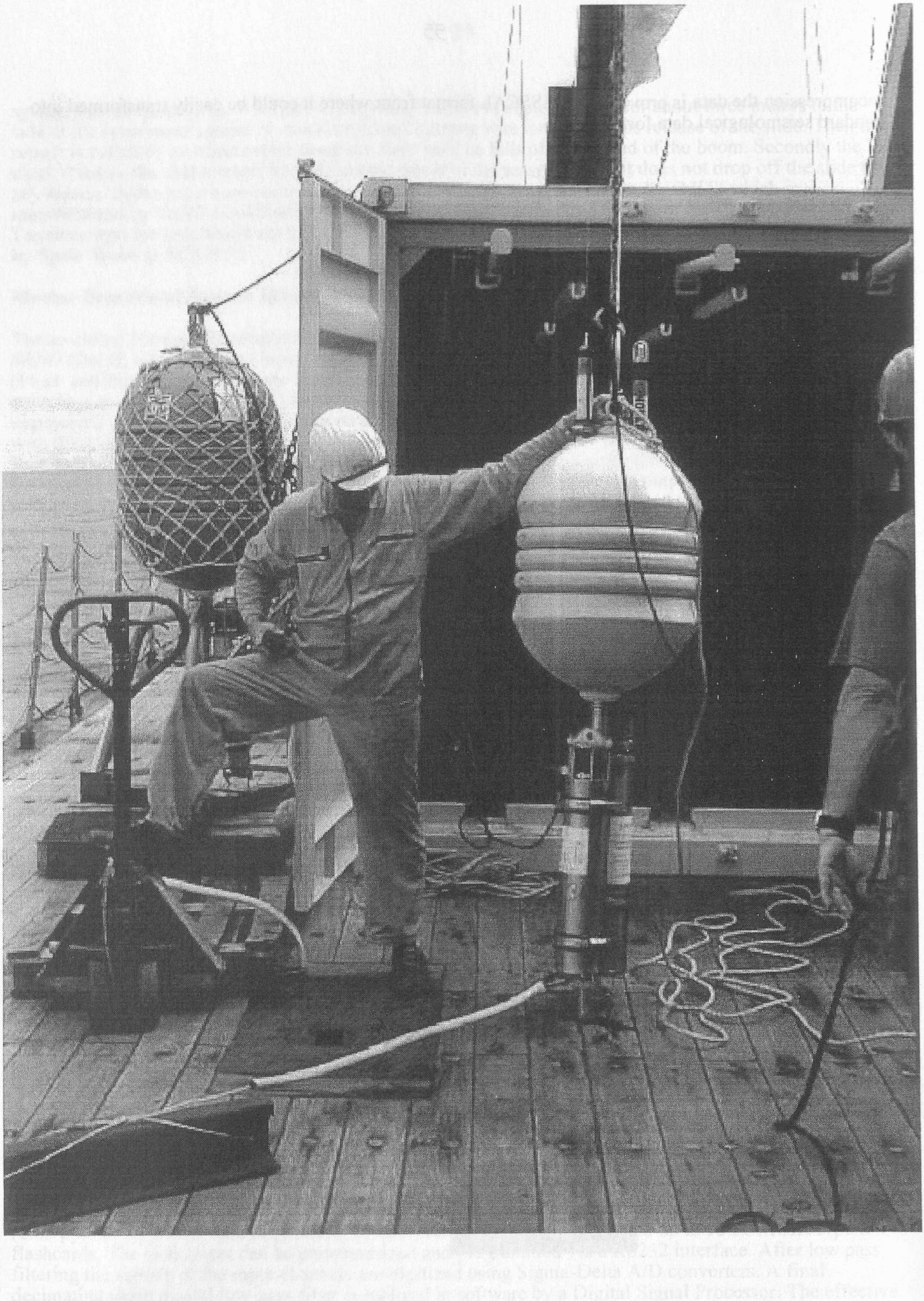

**Figure 4.3.2:** The GEOMAR OBH ready for deployment
Background left: GEOMAR OBS
Background right: OBH container

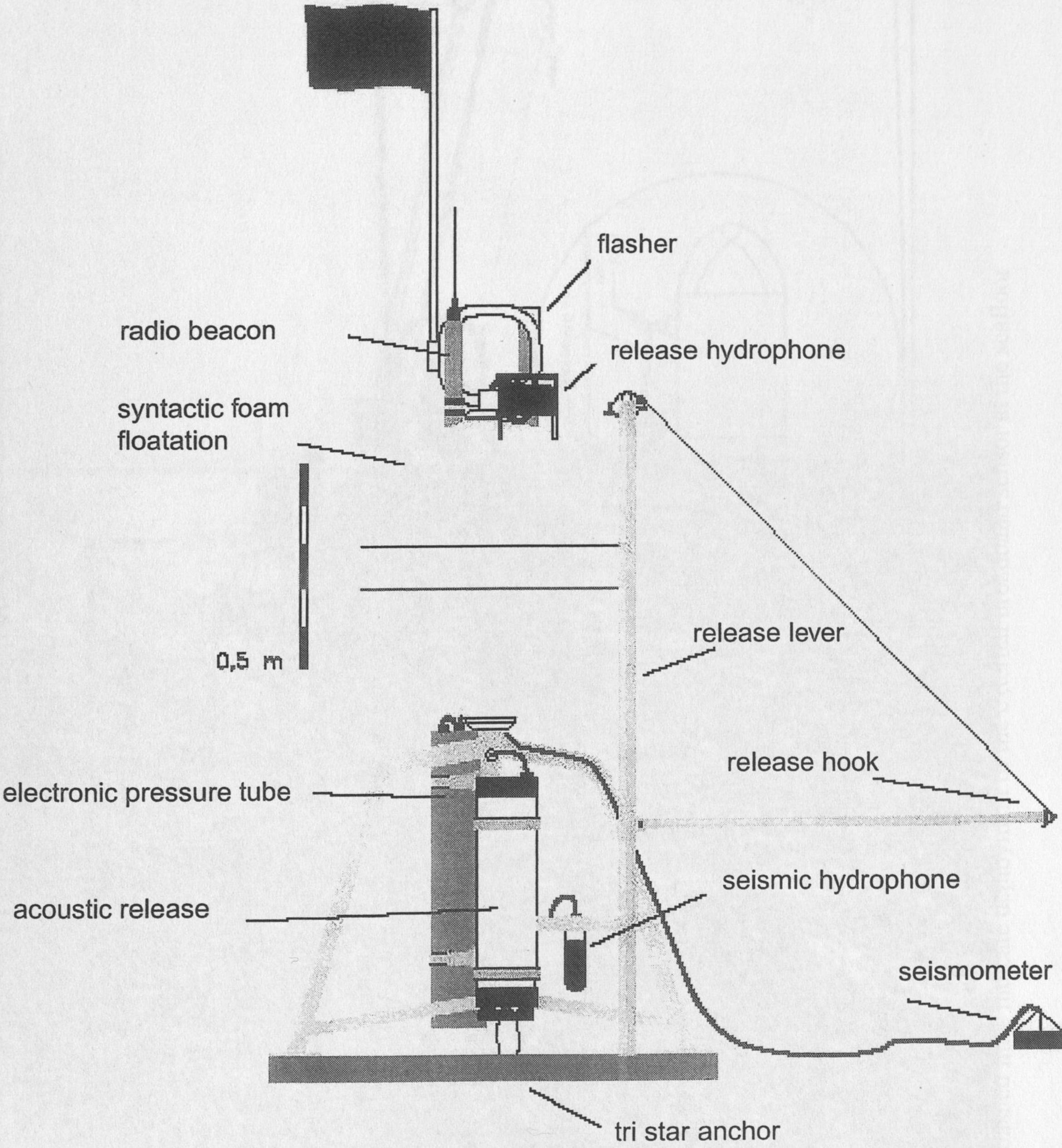

Figure 4.3.3: Priciple of the GEOMAR OBS (after Bialas and Flueh, 1999)

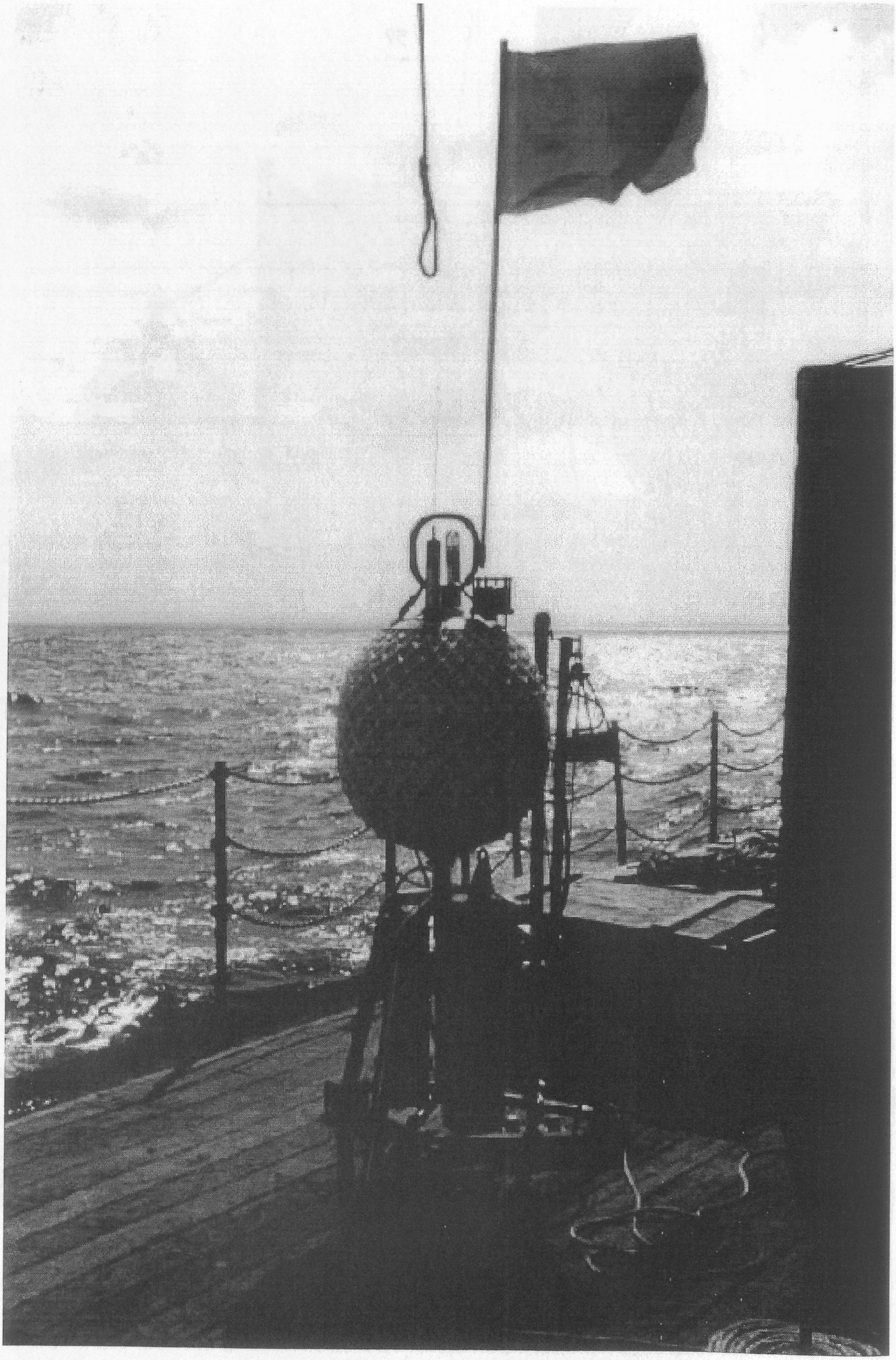

Figure 4.3.4: The GEOMAR OBS ready for deployment

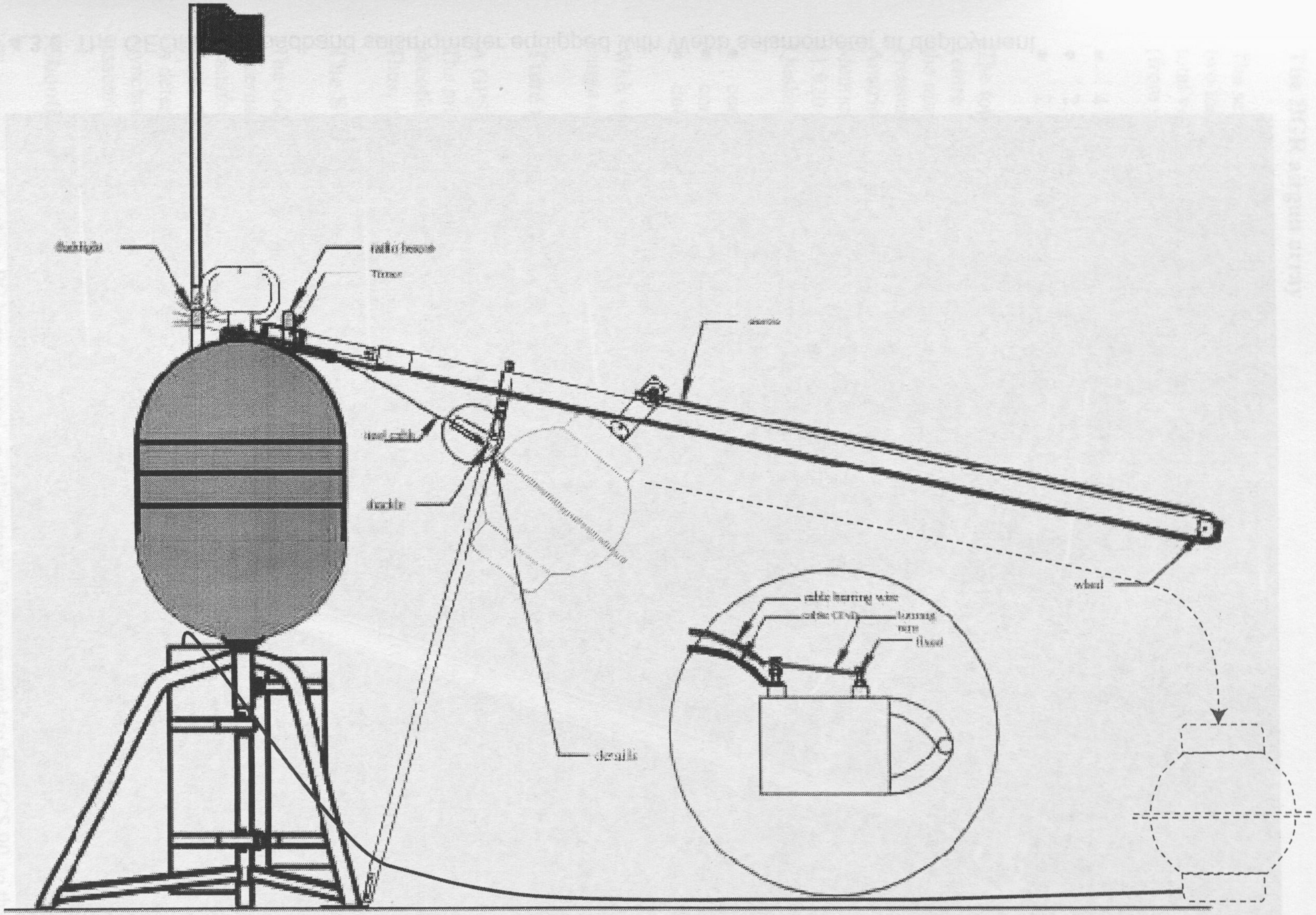

Figure 4.3.5: Scetch of GEOMAR broadband seismometer
dashed lines indicate deployment of the external broadband sensor at the seafloor

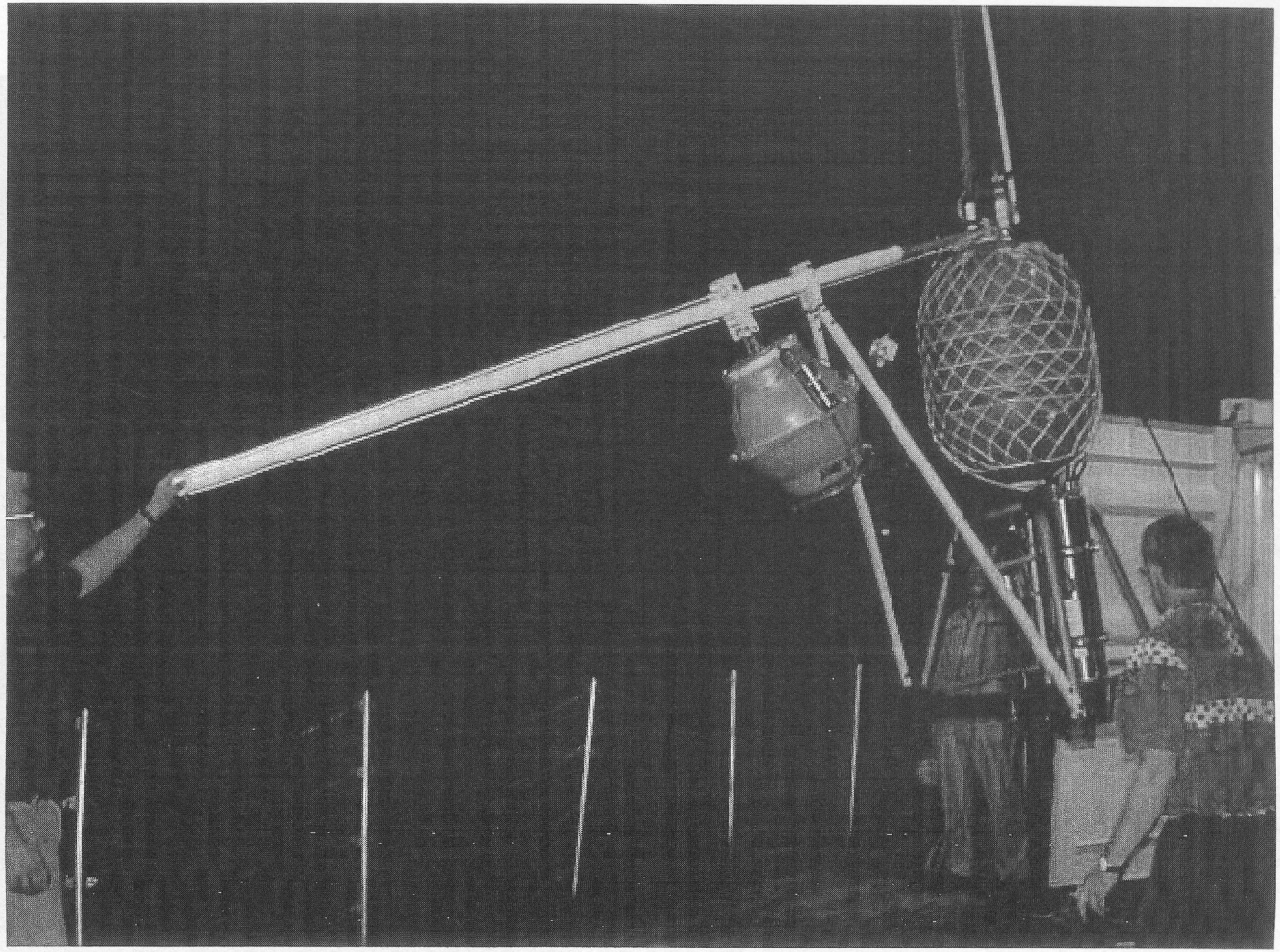

**Figure 4.3.6**: The GEOMAR broadband seismometer equipped with Webb seismometer at deployment

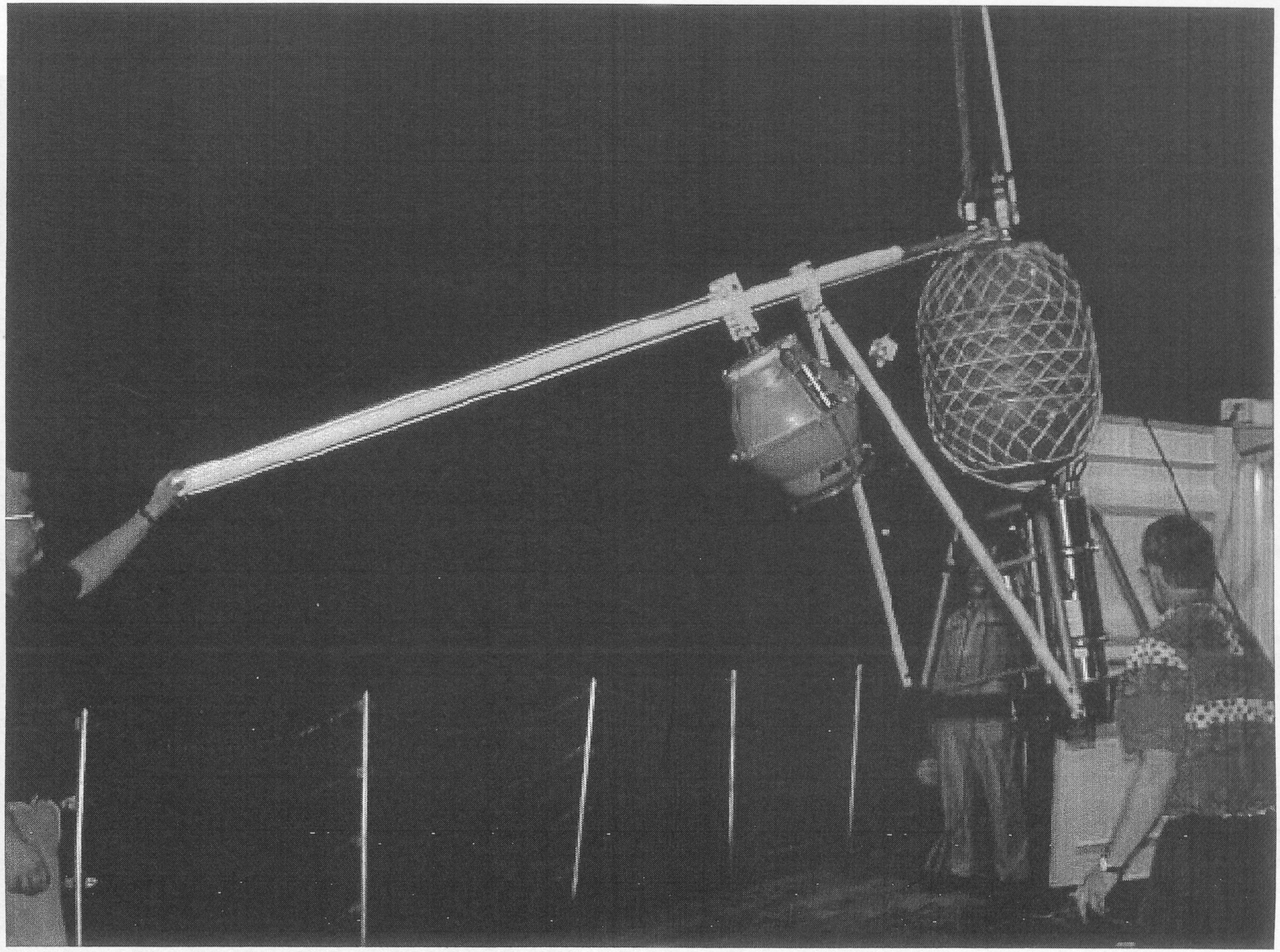

**Figure 4.3.6**: The GEOMAR broadband seismometer equipped with Webb seismometer at deployment

## 4.4 Seismic sources

(J. Sievers and B. Schreckenberger)

### The BGR airgun array

The seismic signals were generated by a tuned set of 20 airguns (VLF, Prakla-Seismos) grouped in two identical linear sub-arrays 10 m apart on starboard and port side, respectively (Fig. 4.4.1). The total volume of the BGR airgun array is 51.2 litres (3.124 cu.in.). Each sub-array consists of 3 groups (from stern to tail):

| | |
|---|---|
| 4 x 3.0 liter + 2.5 liter | (885 cu.in.) |
| 2.5 liter + 2.3 liter + 2.0 liter | (415 cu.in.) |
| 2.3 liter + 2.0 liter | (262 cu.in.) |

The total length of each sub-array is 19.6 m starting 40 m behind the stern. The geometrical airgun centre is 50 m behind the stern and 120 m behind the positioning reference point (satellite antenna on the main mast). Three buoys per sub-array keep the airguns at 7 m water depth.
Pressured air was provided by one of SONNE's LMF compressors, manufactured by Leobersdorfer, Austria. The capacity of each compressor is 25 m³/minute. In case of a malfunction the second identical LMF compressor could be used. During normal shooting operation pressured air of 135 bar (1.920 psi) is used.
Quality control during airgun operation consists of:

- continuous control of the airgun pressure
- control of the airgun operation (autopops, misfires, delays) and sensor signals
- duly maintenance of particular airgun assembly parts (e.g. gaskets, valves etc.) during off-times

With very few exceptions all 20 airguns were properly working, the air pressure was always in the range of 134-135 bar.

### Time reference

A GPS controlled clock (Meinberg GPS 166) provided the absolute universal time corrected (UTC). The minutely and secondly pulses bear an accuracy of < 1 ms. This time reference was fed into the shooting PC and sent to the seismic lab providing the time reference for the OBH/OBS measurements. Thus, an identical time base was used for shooting and seismic recording.

### The SYNTRON GCS 90 and SPS 90 units

The GCS 90 unit controls the synchronization and triggering of up to 20 airguns. According to an external trigger pulse a 20 ms TTL pulse is generated and sent to the SPS 90 unit. Here, it is transformed to 60 V and sent to the magnetic airgun valves. The valves do open and the airgun sensor sends the time break signal to the GCS 90. The offset between this response pulse and the target value is determined and used for correction of the trigger pulse sent to the airguns to provide optimum synchronization. This procedure automatically compensates for time delays produced by worn-out assembly parts of particular airguns in the course of operation.

### Shooting PC program

The so-called shooting PC keeps control on all systems. It is connected to the GCS 90, to the positioning system and - in case of multi-channel seismics - to the recording system. The program code TG2001 used to run this PC is an upgrade of the earlier version TIMER21 by J. Adam (Sievers and Adam, 1997). The program internally generates a series of suitable trigger signals for the GCS 90 with selectable intervals between 10,000 and 65,535 ms on the PC quartz clock time base. Simultaneously, a random time shift of up to ± 300 ms can be superimposed on the shot interval. In combination with multiple channel seismics and related stacking this is used to suppress seafloor multiple reflections from previous shots. This program was used to produce the trigger pulses for the profiles with 30 and 40 sec shot interval.

Alternatively, an external input (e.g. the Meinberg clock GPS 166) can be used. In this mode, TG2001 generates a series of trigger signals with selectable intervals between 10 and 65,535 seconds based on an absolute time base. The random function superposition option is inactive in this case. This mode was used during lines with 60 sec shot interval.

The trigger signals are sent to the GCS 90 that fires the airguns with a constant time delay of 170 ms due to electronic and mechanical components and returns a time break pulse to the shooting PC. The time break sent to the seismic lab also contains the 170 ms delay.

Simultaneously, different data are read via 9 serial RS232 interfaces. They are compiled in 'external header' records which are saved in a protocol file on the shooting PC. The records comprise the following information:

- shot no, status, GPS time, GPS date, PC date, PC time, actual time, nominal time, half random width
- error code, GPS latitude, GPS longitude, course, speed, shot interval
- error code, shot no, trigger mode, gun delay average interval, gun offset
- gun no, status, offset, delay, error code
- error code, sign, starboard air pressure, label
- error code, sign, port air pressure, label
- error code, latitude, longitude, altitude (corrected by BGR navigation system)
- extension
- software version

## Shot triggering during SO-161

Generally, the shots were triggered in time intervals of 60 seconds on full minutes UTC. At a speed of 5.0 knots this results in a shot point distance of 154 m. Exceptions were made on lines SO161-02 and SO161-05. This lines were shot twice with the normal 60 seconds and additionally with 30 sec (line 5-1) and 40 sec (line 2-1) interval. Details for every seismic line can be found in Appendix 9.2.

# BGR - AIRGUNARRAY

Bundesanstalt für
Geowissenschaften
und Rohstoffe

Stilleweg 2
30655 Hannover
Germany

Gesamtvolumen : 51,2l

Druck : 135bar

Arraytiefe : 7m

- FS SONNE -

AIRGUN-Typ: PRAKLA-SEISMOS -VLF-

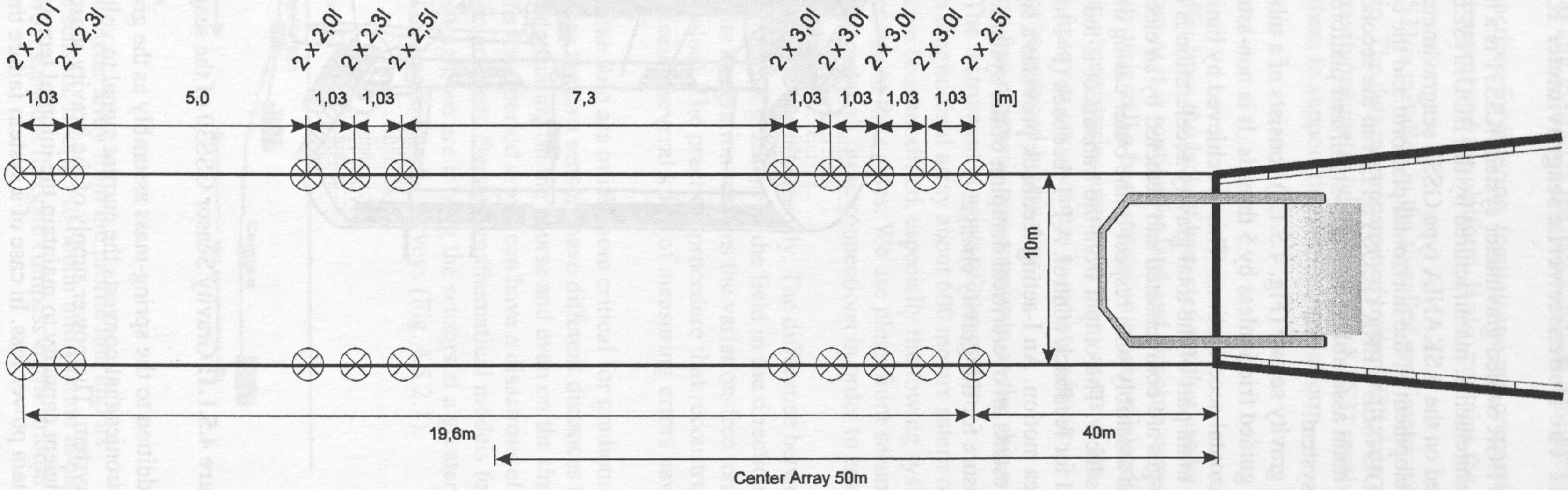

**Figure 4.4.1**: Geometry of the BGR airgun array

## 4.5 Gravimeter and Magnetometer

(B. Schreckenberger and P. Kewitsch)

### 4.5.1 The Bodenseewerke seagravimeter KSS31

The BGR owned gravimeter system KSS31 is a high performance instrument for marine gravity measurements, manufactured by the BODENSEEWERK GEOSYSTEM GmbH. While the sensor is based on the ASKANIA type GSS3 seagravimeter designed by Prof. Graf in the 60ties, the development of the horizontal platform and the corresponding electronic devices took place by the BODENSEEWERK GEOSYSTEM in the second half of the 70ties. The KSS31 system consists of two main assemblies: the gyro-stabilized platform with gravity sensor and the data handling subsystem.

The gravity sensor (Fig. 4.5.1.1) consists of a tube-shaped mass that is suspended on a metal spring and guided frictionless by 5 threads. It is non-astatized and particularly designed to be insensitive to horizontal accelerations. This is achieved by limiting the motion of the mass to the vertical direction. The main part of the total gravity acceleration is compensated by the mechanical spring, but gravity changes are compensated and detected by an electromagnetic system. A displacement of the spring-mass assembly with respect to the outer casing of the instrument is measured using a capacitance transducer. The output from the transducer is fed back into an electromagnetic moving coil system used for feedback control. A P-I feedback (P=Proportional, I=Integration) suppresses the accelerations of sea motion. An I-acting feedback provides a signal which drives the system to the zero position and represents an overcritical damping of the system. The current flowing through the moving coil is the measure for the gravity change.

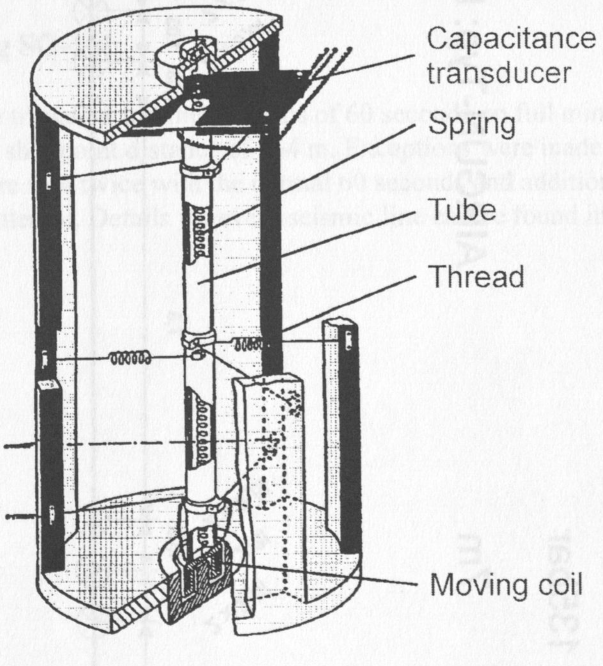

**Figure 4.5.1.1:** Gravity Sensor GSS30 of the seagravimeter-system KSS31

In addition to the spring-mass assembly as the gravity detector the sensor housing contains the control electronics that converts the current signal to voltage output and forwards it to the data handling subsystem. The power supply of the gravity sensor contains a sealed buffered battery unit with sufficient capacity to maintain the internal temperature stabilization of the sensor for 24 hours in case of main power loss. In case of a system failure the sensor electronics automatically activates a caging mechanism preventing the spring-mass assembly from damage.

The leveling subsystem consists of a platform stabilized in two axes by a vertical electrically erected gyro. The stabilization during course changes can be improved by providing online navigation data to the system. The control electronics and the power supply of the platform are located in the data handling subsystem unit. Functions like gyro run-up and run-down sequences and the automatic platform caging are performed by the system controller unit located in the data handling subsystem, too.

Additionally the data handling subsystem provides functions for filtering, logging and pre-processing of the data as well as self-testing sequences of the instrument and the platform. It also contains the power supply for the sensor and the platform.

On board R.V. SONNE the seagravimeter system KSS31 is installed in the so-called gravimeter room which is located near the geometrical centre of the ship. The data are transmitted to the BGR data acquisition and processing system (see 4.2.1) in the gravity/magnetic laboratory. The KSS31 receives the online navigation data from this system and uses them to support the stabilizing platform.

## 4.5.2 The gradient magnetometer

Generally all marine magnetometer measurements suffer from the lack of base stations that can be used in order to reduce the temporal magnetic variations as it is routine for land and airborne surveys. In the past only on a few cruises we had the opportunity to install a base station on adjacent islands or coasts. Unfortunately, permanently operating magnetic observatories are rare in many areas of the world and therefore they are nearly always too distant from our survey areas in remote oceanic regions. Particularly the short period variations can not be reduced in this way.

In order to avoid these problems and to obtain variation-free magnetic measurements on the ship we use the gradient magnetometer Geometrics G-811G. The instrument consists of two proton magnetometers which are towed 150 meters apart as a longitudinal array about 600 meters astern of the ship (Fig. 4.5.2.1). Many parts of the instrument have been modified, especially the towing system including all connections of the sensors and the splitter box to the cables. We use plugs from seismic streamer technology instead of the original fixed connectors at all these connections in order to enable fast replacement of defective cables and sensors and easy handling.

Both sensors measure the total intensity of the magnetic field simultaneously. The difference between the two measurements is an approximation for the longitudinal gradient of the field in the direction of the profile line. It is free from temporal variations and its integration restores the variation-free total intensity or magnetic anomaly (apart from a constant value). The practical procedure that reconstructs the anomaly from the gradient is by no means trivial because several kinds of measuring errors have severe effects during the integration.

The remanent, viscous, and induced magnetizations of the ship are much more critical for gradiometer than for normal marine magnetic measurements. Because the two sensors have different distances to the ship a systematic error is generated in the gradient depending on the course and even on the time due to the viscous part of the ship's magnetization. This long-period errors can have a disastrous effect during the reconstruction of the magnetic field from the gradient. Because mathematical models for the magnetic effect of the ship are by far not precise enough, we are towing the sensors at a greater distance behind the ship than it is standard for normal marine magnetic surveys (Fig. 4.5.2.1).

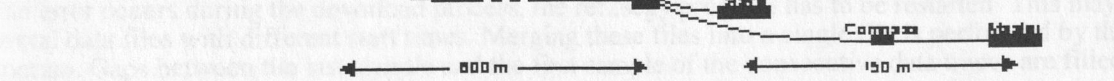

**Figure 5.4.2.1**: Gradient magnetometer configuration.

Another source of error is the deviation of the magnetometer array from the profile line and its unknown azimuth as well as the different depth of the sensors. In order to obtain information about the location and orientation of the array behind the ship we installed a fluxgate compass in the middle of the cable between the two sensors.

A more detailed discussion of errors can be found in Eilers et al. (1994). For example, magnetic fields are induced by the movement of sea water within the earth's magnetic field. This results in a distinctively raised noise level of the records during times of rough seas. However, due to the statistical character of the disturbing fields and the smoothing effect of the integration this hardly reduces the quality of the reconstructed anomaly.

### 4.5.3 The magnetic base station

Despite of the availability of gradient measurements on this cruise the BGR installed a magnetic base station in Concepcion for the duration of the SPOC Legs 2 to 4. The station was located near a private house in a remote area near Concepcion. It was operated and maintained by Klaus Bataille from the Universidad de Concepcion for the duration of the cruise (13.10.-21.12.2001). The base station consists of a proton magnetometer type Scintrex MP3. Due to the restricted storage capacity of the instrument we used the analog output channel (0 - 1000 mV, 100 nT range) and a digital recording device that also includes an A/D converter (Jumo Logoscreen 500). The last two digits of the magnetic total intensity data were digitally recorded every 10 seconds and stored on floppy disks. Once per week the data files were sent to the ship per Email.

## 4.6 Data Processing

### 4.6.1 OBH/S Wide Angle Seismic & MCS Processing

(D. Klaeschen, F. Tilmann, J. Petersen, C. Papenberg & GEOMAR wide-angle Working Group)

**Data Processing**

The OBH/S data recorded in continuous mode on the MLS and MBS units have to be converted into standard trace-based SEG-Y format for further processing. The necessary program structure was mainly taken from the existing REFTEK routines and modified for the OBH requirements and GEOMAR´s hardware platforms.

The flow chart shown in Figure 4.6.1.1 illustrates the processing scheme applied to the raw data. A detailed description of the main programs follows below:

**send2pas**

For the PC-cards used with the MBS and MLS recorders, data expansion and format conversion into REFTEK data format is performed using a DOS/Windows based PC. The program send2pas reads data from the flashcards used during recording. Decompressed data are written onto the PC's hard disk using PASSCAL data format. Either 16 or 32 bit storage is available. After ftp transmission to a SUN workstation, ref2segy and all other software can be used to handle and process the data files and store them as SEG-Y traces.

While processing the MLS recordings many time slips of one sampling interval were detected by the send2pas software, typically at a rate of one time slip every 1-2 hours. The time slips are caused by mismatch of the actual sampling rate of the MLS recorder compared to the desired sampling rate. This mismatch arises because the clock rate of the crystal oscillator in the MLS recorder is temperature dependent (Klaus Schleisiek, SEND GmbH, pers. comm.). The temperature dependence is known and corrected for in the determination of the system time, but for performance reasons the sampling pulses are directly generated from the oscillator signal without any time correction. The send2pas routine detects when the accumulated inaccuracies of the sample rate cause an effective timing error of one sample, but only reports and does not correct the "time slip".

The resulting total time error was on average 200 to 400 ms for the wide-angle profiles and up to several tens of seconds for the seismology network, showing clearly the necessity of a special time slip correction for the MLS data. After careful analysis of the problem, we concluded that the best way to address the time slip timing error in the wide-angle data is to add the time slips reported in the send2pas logfile, and regard the time slip total as an extra skew contribution which later in the processing flow is corrected within the dat2segy program (see below, note that the sign of skew and time slips are opposite, i.e., a negative sum of time slips corresponds to a positive skew). As each trace is at most a few tens of seconds long (vs. 1 hour and more between non-cancelling time slips), the corrected time is expected to be highly accurate with uncertainties well below one sample length.

**ref2segy**

The ref2segy program converts the output of send2pas to a pseudo SEG-Y trace consisting of one header and a continuous data trace containing all samples, as used by the PASSCAL suite of seismic utility programs. For each channel (normally pressure, vertical velocity, and velocity along two mutually perpendicular horizontal directions for OBS; pressure for OBH) one file is created with the name derived from the start time, the serial number of the Methusalem system, and the channel number. The file size of the pseudo-SEGY file is directly related to the recording time. For instance, a recording time of one hour sampled at 200 Hz (16 Bit) will produce a file size of 1.44 MB per channel. A record with two channels and a recording time of two days will produce a total data volume of 70 MB.

**merge**

If an error occurs during the download process, the ref2segy program has to be restarted. This may lead to several data files with different start times. Merging these files into a single file is performed by the merge program. Gaps between the last sample and the first sample of the consecutive data traces are filled with zeros. Overlapping parts are cut out.

**pql**

pql (Passcal Quick Look) is a simple display program for continuous seismic data. Its interactive zooming capability allows a rapid inspection of data quality.

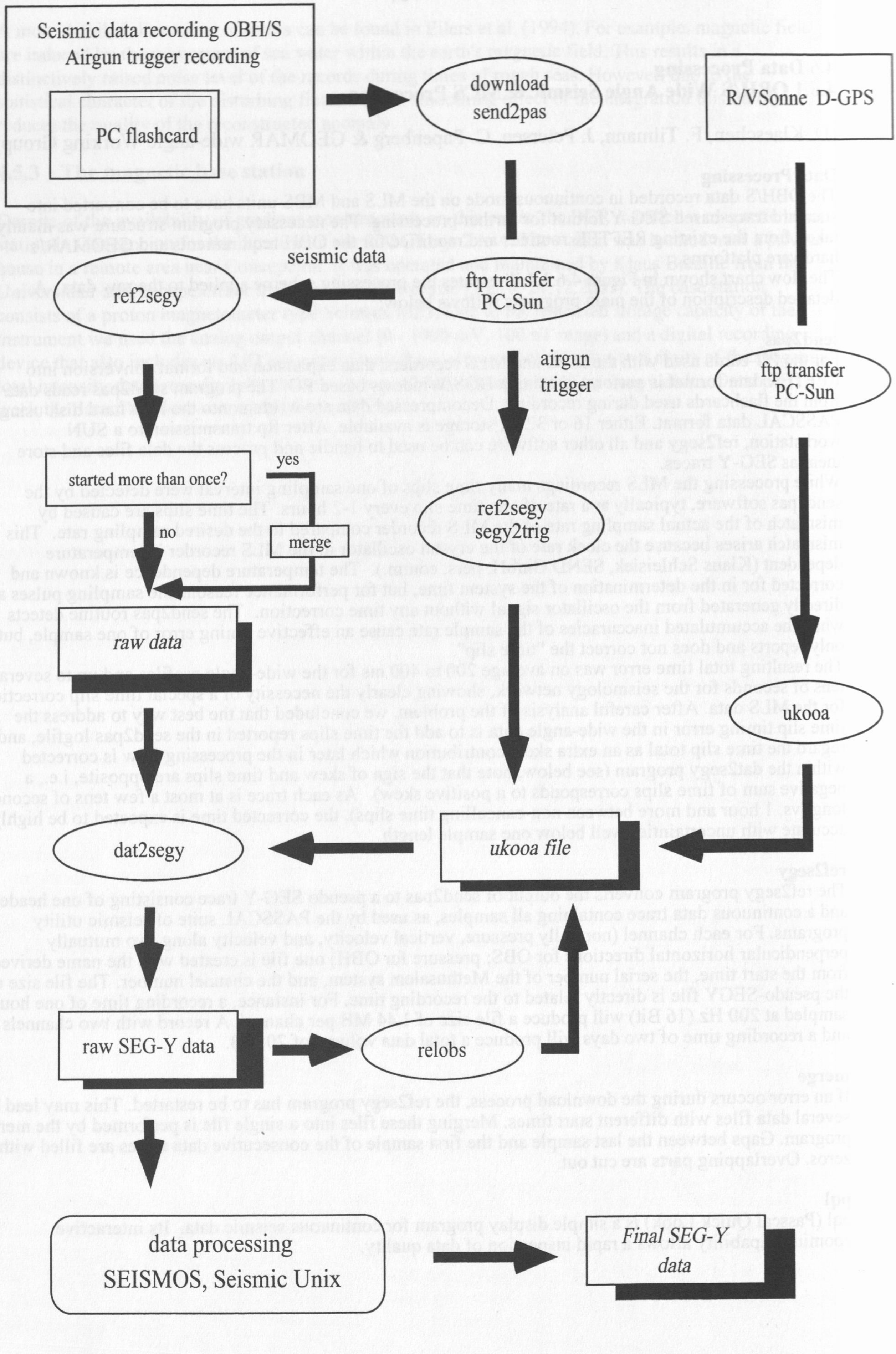

**Figure 4.6.1.1:** Processing flow of OBH/S data from raw data to SEG-Y records.

**segy2trig**
The trigger signal, provided by the airgun control system, is recorded on an additional MBS unit during the shooting period. The trigger data are treated similarly to regular seismic data and downloaded to the hard disk via the send2pas and ref2segy programs. Then, the segy2trig program detects the shot times in the data stream by identifying the trigger signal through a given slope steepness, duration and threshold of the trigger pulse. The output is an ASCII table consisting of the shot number and the shot time. Accuracy of the shot time is one of the most crucial matters in seismic wide-angle work, and must be reproduced with a precision of a few ms. Due to this demand the shot times have to be corrected with the shift of the internal recorder clock. Additionally, the trigger file contains the profile number, the start/end time of the profile and the trigger recording. The shot times are part of the ukooa file, which links them with the coordinates of the source and the hydrophones.

**ukooa**
The ukooa program is used to establish the geometric database by calculating the positions of sources at any given shot time and offset from the ship. The source is placed on the ship track using simple degree/meter conversions and then written to a file in UKOOA-P84/1 format. Corrections for offsets between antenna and airguns as well as consistency checks are included. This file will be used when creating a SEG-Y section via the dat2segy program. The program requires the trigger file to contain the shot times, the ship's navigation (see Chapter 5.5.3), and a Parameter file containing information for the UKOOA file header as basic input information.

**dat2segy**
The dat2segy program produces standard SEG-Y records either in a 16 or 32 bit integer format by cutting the single SEG-Y trace (the ref2segy output) into traces with a defined time length based on the geometry and shooting time information in the ukooa file In addition, the user can set several parameters for controlling the output. These parameters are information about the profile and the receiver station, number of shots to be used, trace length, time offset of the trace and reduction velocity (to determine the time of the first sample within a record). Also the clock drift of the recorder (skew) is taken into account and corrected for. For the MLS data the total time error resulting from the observed time slips described above was subtracted from the clock drift value. The final SEG-Y format consists of the file header followed by the traces. Each trace is built up by a trace header followed by the data samples. The output of the dat2segy program can be used as input for further processing with GEOSYS, SEISMOS or Seismic Unix (SU).

**relobs**
Because of drifting of the OBH and OBS instruments during deployment and errors in the ship's GPS navigation system, the OBH positions may be mislocated by up to several 100 m. Since this error leads to asymmetry and incorrect traveltime information in the record section, it has to be corrected. This is accomplished with the program relobs.
For input, the assumed OBH location, shot locations and the picked traveltimes of the direct wave near to its apex are needed. To simplify the picking a static correction with a hyperbolic equation was performed to flatten the direct wave. This yields a much more coherent direct arrival which would normally suffer from strong spatial aliasing in the uncorrected section making it difficult to track. By shifting the OBH position, relobs minimizes the deviation between computed and real travel times using a least mean square fitting algorithm (assuming a constant water velocity).
Fortunately, wide-angle profile 2 was shot forth and back during the cruise giving us the opportunity to adjust the source offset, i.e. the distance from the research vessel's GPS position to the center of the airgun array, which was calculated to be 80 m. Thus, an accuracy in receiver position determination of about 10 m was possible.

Beside these main programs for the regular processing sometimes additional features are needed for special handling of the raw data:

**divide**
The program divide cuts the raw data stream into traces of a given length without offset and time information, storing the output in SEG-Y format. The routine is useful for a quick scan of the raw data or if a timing error has occurred.

**segyhdr**
The routine segyhdr prints all the header values of the raw data on the screen.

**segyshift**
Segyshift modifies the time of the first sample, allowing the whole raw data trace can be shifted by a given value. This is very useful when shifting the time base from Middle European Time to Greenwich Mean Time or any local time. Because of recording problems, the data sometimes show a constant time shift, which can be corrected as well with segyshift.

**castout**
The program castout allows the user to remove out a specified time window from the raw data stream. When the shooting window is much smaller than the recording time, one can reduce the data volume by cutting out only the useful information. This will reduce the demand on disk space.

- **OBH/OBS-data analysis and processing**

**Raw data:** As an example, the OBH record section 37 for profile 01 is shown in Figure 4.6.1.2. For the analysis, offset ranges between 0-13 km and 47-60 km east are presented in detail.
**Frequency filter analysis:** To determine the frequencies of the seismic energy, filter panels with narrow frequency band passes for the offset range 0-13 km and 47-60 km, respectively, are shown in Figures 4.6.1.3 and 4.6.1.5. In the lower section of the figure the amplitude spectra of the corresponding filter panels are appended. The amplitude spectra of the used Ormsby frequency filter operators are characterized by linear slopes. The filter applied, which is minimum delay, is described by four corner frequencies: Lower stop/pass band boundary and upper pass/stop band boundary. The frequencies on the filter panels correspond to the lower and upper pass frequencies. The main energy for the reflected phases between 3.4 and 3.7 s in the offset range from 0-13 km is between 3-21 Hz and for the direct wave up to 111 Hz. The main energy of the phase between 5.6 and 6.0 s in the offset range from 47-60 km is between 3-13 Hz. As a broad frequency range is contained in the data, time and offset dependent filtering was applied (see below).

**Deconvolution analysis:** To improve the temporal resolution of the seismic data a deconvolution is applied to compress the basic seismic wavelet. The recorded wavelet has many components, including the source signature, recording filter, and hydrophone/geophone response. Ideally, deconvolution should compress the wavelet components and leaving only the earth's reflectivity in the seismic trace. We applied Wiener deconvolution in successive trace segments, based on the following assumptions:

1. The earth's reflectivity is 'white'.
2. The wavelet shows the minimum-delay phase behavior.

As in this wide-angle data the amplitude spectra of the seismic traces vary with time and offset (e.g. reflected and refracted phases), the deconvolution must be able to follow these time and offset variations. Each trace is therefore divided into 3 s data gates with 1 s overlap, in which time invariant deconvolution operators are computed from the autocorrelation function of the data segment and applied to account for the nonstationarity of the seismic signals. The overall deconvolved trace results from a weighted merging of the independently deconvolved gates.
Input for the deconvolution process is raw data. As several recordings were influenced by a DC shift, a 0-3 Hz high-pass minimum delay Kaiser frequency filter with 60 dB attenuation between the pass and reject zone was applied prior to deconvolution in order to center the amplitudes around zero. The deconvolution test panels are shown in Figures 4.6.1.4 and 4.6.1.6 for the offset range 0-13 km and 47-60 km respectively. In the lower section of the figure the autocorrelation function is appended. Constant operator lengths of 200 and 300 ms (predictive length included) and a variation of the predictive length from 4 (spike) to 160 ms is displayed.
On the undeconvolved data in Figure 4.6.1.4 and 4.6.1.6 strong energy up to 300 ms behind the zero lag is clearly visible in the autocorrelation function. The best resolution is obtained for a predictive length of 4 ms and an operator length of 300 ms but with a reduction of signal-to-noise ratio especially on the far offset traces. A predictive length of 100 ms and an operator length of 300 ms was chosen for this data set which is a compromise between temporal resolution and signal-to-noise ratio.
After deconvolution an offset- and time-variant Ormsby filter with minimum delay characteristic was applied. As the seafloor depth changes along the seismic lines, each trace was statically corrected to a fixed seafloor travel time of 11 s based on the water depth before filtering. This information is available in the trace headers. After this filter was applied, the data were shifted back to their original travel times.

**Processed data:** Comparison of the preprocessed data in Figure 4.6.1.7 to the unprocessed data in Figure 4.6.1.2 shows a clear reduction of the low and mono-frequency noise in the near and far offset traces and moderate compression of the wavelet signal. For the picking of events and model building by raytracing both sections were used to keep all available seismic information.

- **Final processing sequence**
  - Input: SEGY-data, 4 ms or 5ms sampling rate with complete geometry information.
  - Tapering the first 0.5 s to zero to reduce the response of the debias filter operator.
  - Kaiser highpass (debias).
  - Gated Wiener deconvolution: gate length 3 s, overlap 1 s, length of merge region 1 s, operator length 300 ms (prediction interval included), prediction interval 100 ms.
  - Static correction to a fixed seafloor traveltime of 11 s.
  - Time and offset-dependent Ormsby frequency filter.

On time-shifted traces with a reduced time scale of 6 km/s the following filter parameters were used:

| lower stop/pass | upper pass/stop (Hz) | offset(m) | beginfull(s) | endfull(s) |
|---|---|---|---|---|
| 3/5 | 28/48 | 0 | 0 | 12.8 |
| | | 8000 | 0 | 12.6 |
| | | 48000 | 0 | 0 |
| 3/5 | 23/38 | 0 | 13.7 | 14.3 |
| | | 8800 | 13.5 | 14.4 |
| | | 13200 | 13.0 | 13.9 |
| | | 52000 | 1.0 | 2.0 |
| | | 107000 | 0 | 0 |
| 3/5 | 18/28 | 0 | 15.3 | 16.8 |
| | | 11700 | 15.1 | 16.6 |
| | | 19200 | 14.8 | 16.3 |
| | | 61700 | 7.0 | 10.1 |
| | | 114000 | 2.0 | 3.0 |
| | | 152000 | 0 | 0 |
| 3/5 | 13/18 | 0 | 19.0 | trace length |
| | | 20000 | 18.4 | trace length |
| | | 130000 | 3.5 | trace length |

- **Data archiving**

Data recorded with the MBS/MLS recorder on flash discs were transferred via a PC to a SUN workstation. On the workstation they were transformed into a so-called PSEUDO-SEGY format. After navigation data had been merged and SEGY formatted traces with the appropriate header words had been created, the data were also archived. Finally, a third set was stored and archived after the shipboard processing, as described above, had been applied. All final processed SEGY data were archived on tapes.

- **Data exchange**

For the exchange of the OBH/OBS data, the SEGY-format on disk with a Sun tar-format was chosen. The raw segy data is in Integer2 format with trailer bytes between the record structure of SEGY. The processed data is in IBM-floating point without trailer bytes between the records.
For UTM transformation into Cartesian coordinates use: WGS84 spheroid, central meridian 73 0. 0. W, southern hemisphere.
This is the definition of the segy trace header for the GEOMAR OBS wide-angle reflection data. The extension of the standard SEGY header from 181 to 240 byte is a layout in order to process the data on the GEOSYS/SEISMOS software system. Reading bytes directly into this header will allow access to all of the fields.

| BytePos | Bytes | Information | Comments (note: not all headers available in processed data) |
|---|---|---|---|
| 1-8 | (2x4) | lineSeq, reelSeq; | /* Sequence numbers within line and reel, resp.*/<br>/* here station and shot number Def: 1, 1 */ |
| 9-12 | (4) | profNumber; | /* Original field record number */<br>/* Here profile number */ |
| 13-16 | (4) | traceNumber; | /* Trace number within the original field record.*/<br>/* Here station (receiver) Number */ |
| 17-20 | (4) | energySourcePt; | /* Energy source (shot) point numbe */<br>/* Def: 0 */ |
| 21-24 | (4) | cdpEns; | /* CDP ensemble number: shot number */<br>/* Def: 0 */ |
| 25-28 | (4) | traceInEnsemble; | /* Trace number within CDP ensemble */<br>/* Here azimuth in seconds of arc for unprocessed data*/ |
| 29-30 | (2) | traceID; | /* Trace identification code:<br>1=seismic data (Def) 4=time break 7=timing<br>2=dead 5=uphole 8=water break<br>3=dummy 6=sweep 9..., optional use */ |
| 31-34 | (2x2) | vertSum, horSum; | /* Def: 1, 1 */ |
| 35-36 | (2) | dataUse; | /* 1=production (Def), 2=test */ |
| 37-40 | (4) | sourceToRecDist; | /* Distance in (m) */ |
| 41-44 | (4) | recElevation; | /* Elevation in (m), Def: 0 */ |
| 45-48 | (4) | sourceSurfaceElevation; | /* Def: 0 (m) */ |
| 49-52 | (4) | sourceDepth; | /* Def: 0 (m) */ |
| 53-60 | (2x4) | datumElevRec, datumElemSource; | /* Def: 0, 0 (m) */ |
| 61-68 | (2x4) | sourceWaterDepth, recWaterDepth; | /* Def: 0, 0 (m) */ |
| 69-70 | (2) | elevationScale; | /* Scale elevations Def: 0 (10**0) */ |
| 71-72 | (2) | coordScale; | /* Scale coordinates<br>Def: -2, means coordinates multiplied<br>by 10**(-2) to get real value for unprocessed data.<br>NOTE: for processed data -100 means to divide by 100<br>to get the real value */ |
| 73-80 | (2x4) | sourceLongOrX, sourceLatOrY; | /* Either Cartesian or geographic */ |
| 81-88 | (2x4) | recLongOrX, recLatOrY; | |
| 89-90 | (2) | coordUnits; | /* 1= meter or feet; 2=sec of arc */ |
| 91-92 | (2) | weatheringVelocity; | /* Def: 0 (m/s) */ |
| 93-94 | (2) | subWeatheringVelocity; | /* Reduction velocity, Def: 6000 (m/s) */ |
| 95-96 | (2) | sourceUpholeTime; | /* Def: 0 (ms) */ |
| 97-98 | (2) | recUpholeTime; | /* Def: 0 (ms) */ |
| 99-102 | (2x2) | sourceStaticCor, recStaticCor; | /* Def: 0, 0 (ms ) */ |
| 103-104 | (2) | totalStatic; | /* Def: 0 (ms) */ |
| 105-106 | (2) | lagTimeA; | /* T(shottime) - T(first sample) */ |
| 107-108 | (2) | lagTimeB; | /* Def: 0 (ms) */ |
| 109-110 | (2) | delay; | /* Def: 0 (ms) */ |
| 111-114 | (2x2) | muteStart, muteEnd; | /* Def: 0, 0 (ms) */ |
| 115-116 | (2) | sampleLength; | /* Number of samples in this trace */<br>/* ( > 32767 )? = 32767<br>set long samp_rate in 185-188 byte */ |
| 117-118 | (2) | deltaSample; | /* Sampling interval in microseconds. */ |
| 119-120 | (2) | gainType; | /* 1=fixed (Def), 2=binary,<br>3=floating, 4... opt.*/ |
| 121-122 | (2) | gainConst; | /* Gain of recording channel */ |
| 123-124 | (2) | initialGain; | /* Gain of preamplifier in db */ |
| 125-126 | (2) | correlated; | /* 1=no (Def), 2=yes */ |
| 127-130 | (2x2) | sweepStart, sweepEnd; | /* min. and max. amplitude of trace */ |
| 131-132 | (2) | sweepLength; | /* Here defined as<br>fraction of second of shot time */ |

```
133-134 (29)       sweepType;                      /* Source type:
                                       1=linear,  2=parabolic,  3=exponential,  4=others
                                       5=bohrhole explosive,  6=water explosive,  7=airgun (Def)
                                       or fraction of microsecond of shot time for high resolution data */
135-138 (2x2)      sweepTaperAtStart, sweepTaperAtEnd;          /* Start and end of trace (ms)
                                                                relative to Tred(0) */
139-140 (2)        taperType;                      /* scaling factor for last two values Def: 1 (x10) */
141-144 (2x2)      aliasFreq, aliasSlope;          /* Def: 0, 0 */
145-148 (2x2)      notchFreq, notchSlope;          /* Def: 0, 0  */
149-152 (2x2)      lowCutFreq, hiCutFreq;          /* Def: 0, 0  */
153-156 (2x2)      lowCutSlope, hiCutSlope;        /* Def: 0, 0  */
157-166 (5x2)      year, day, hour,                /* Source (shot) time, the fraction of sec */
                   minute, second;                 /* is set in millisec between 131-132 byte
                                                   is set in microsec between 133-134 */
167-168 (2)        timeBasisCode;                  /* 1=local, 2=GMT, 3=MET (GMT + 1 hour) (Def) */
169-170 (2)        traceWeightingFactor;           /*  */
171-172 (2)        phoneRollPos1;                  /* Component: 1=time code, 2=radial, 3=transverse
                                                   4=vertical, 5=hydrophone (Def)  */
173-174 (2)        phoneFirstTrace;                /* Methusalem instrument number in YYNN */
175-176 (2)        phoneLastTrace;                 /* Channel number */
177-178 (2)        gapSize;                        /* Source charge in cubic inches (airgun)
                                                   or kg (explosives) */
179-180 (2)        taperOvertravel;                /* Def: 0=meaningless  1=up, 2=down     */
/* !!! Following is extension !!! */
181-182 (2)        compNo;                         /* 1=time code, 2=radial, 3=transverse
                                                   4=vertical, 5=hydrophone (Def)  */
183-184 (2)        samplingRate;                   /* samples/sec */
185-188 (4)        numberSamples;                  /* ( <= 32767) ? sampleLength | ( > 32767) */
189-190 (2)        shotPointNo;
191-192 (2)        ADCoeff;                        /* Coefficient of A/D converter in mv/digit */
193-194 (2)        receiverCoeff;                  /* Conversion coefficient of receiver,
                                                   pascal/cm2 for hydrophone,
                                                   velocity(m/s)/volt for geophone */
195-196 (2)        receiverType;                   /* 1=hydrophone (Def), 2=geophone, 3...*/
197-200 (4)        lengthData;                     /* Def: 0 (ms), not used here */
201-204 (4)        distance;                       /* Source to receiver distance in (m)  */
205-208 (4)        (float) scaleFactor;            /* Scale factor same as in <segy.h>
                                                   Here azimuth in second of arc for processed data */
209-210 (2)        azimuth;                        /* Orientation of the component in min */
211-212 (2)        eigenperiod;                    /* Eigenperiod of geo- or hydrophone in (ms) */
213-216 (4)        minAmpl;                        /* Min. peak amplitude within trace      */
217-220 (4)        maxAmpl;                        /* Max. peak amplitude within trace */
221-222 (2)        stationNo;                      /* Station number */
223-224 (2)        channelNo;                      /* Channel number (Default: 1) */
225-228 (4)        sourceCharge;                   /* Charge in kg (explosive) or cc (airgun) */
229-230 (2)        redVelocity;                    /* reduction velocity in (m/s);
                                                   Def: 0 if no reduction velocity se */
231-232 (2)        timeOffset;                     /* Time offset in (ms) of first sample
                                                   relative to reduced source time:
                                                   positive if earlier than reduced time  */
233-236 (4)        redTime;                        /* Reduced time in (ms) = distance/redVel  */
237-238 (2)        unused2;
239-240 (2)        instNo;                         /* Methusalem instrument number */
```

- **MCS processing**

Four MCS-profiles, SO161-12,18,19, and 38 collected during SO161 leg2 and leg3 which are coincident with the wide-angle profiles SO161-05,02,03, and 01 were processed up to post-stack time migration. Based on information of the streamer and shotpoint geometry from the BGR-group, velocity scans every 200cmp's were analysed. A predictive deconvolution with two gates, for the shallow sediment events and the deeper crustal events, was applied before the stack. A space and time variant frequency filter prior to a post-stack time migration completed the processing flow. The MCS profiles are displayed in the individual chapters of the wide-angle profiles.

## 4.6.2 Magnetics

(B. Schreckenberger)

The magnetic anomalies displayed in all figures of the report are the values from the master sensor of the magnetometer array although all magnetic measurements during Leg 4 were made using the gradient magnetometer. The values are displayed after subtracting the appropriate reference field IGRF2000 and an additional constant value of 50 nT which adjusts the anomalies to a level around zero. This value was determinated by calculating the mean of all anomalies in the middle of Leg 3 of this cruise. It was kept throughout the entire survey.

### Reconstruction of the magnetic anomaly from the gradient

The most simple method for the reconstruction of the magnetic field is the integration of the gradient in the space domain along the profile line. Another approach is the formulation of the problem in the frequency and in the wavenumber domain, respectively (Eilers et al., 1994). In this method the integration corresponds to a filter operation on the Fourier transform of the gradient. It provides a better insight into the problems of the reconstruction and can be combined with additional filter methods. For a first interpretation on board we usually use the simple integration/summation method in the space domain. The main source of errors, visible as crossover errors, is due to long-period variations (probably diurnal variations).

Theoretical considerations and experience with real data show that the gradient method still has limitations with respect to long-wavelength anomalies. Land-based records of the variations will be needed even in the future. For the first weeks of this cruise base station data were available. However, because the data were very noisy and because not all data were available during the cruise, we did not finally process them. Therefore, it was also not practical to process the gradient data due to poor information about the long-wavelength errors.

Anyway, the magnetic anomalies from one of the sensors, as they are drawn in all figures and maps of this report, are sufficient for many interpretations, e.g. for the identification of oceanic magnetic lineations.

### Base station data

For this cruise, support from the Universidad de Concepcion, that maintained our (BGR) magnetic base station, could be obtained. Only the last two digits of the total intensity value at the station were available to us due to the limited range of the analog output of the magnetometer. This causes jumps in the records at every crossing of full hundreds of nT which would not have been a problem if the data were clean. But due to unknown reasons, during Leg 3 the data became very noisy and we decided to process the data later.

A crossover error (COE) analysis was made using 18 of the crossing points that are displayed for the free-air gravity in 4.6.3. The standard deviation of the COEs is 27.2 nT. The largest error is 72 nT. This shows that marine magnetic measurements are strongly influenced by temporal variations of the earth's magnetic field because the absolute accuracy of the proton magnetometers is better than a few nT.

- **MCS processing**

Four MCS-profiles, SO161-12,18,19, and 38 collected during SO161 leg2 and leg3 which are coincident with the wide-angle profiles SO161-05,02,03, and 01 were processed up to post-stack time migration. Based on information of the streamer and shotpoint geometry from the BGR-group, velocity scans every 200cmp's were analysed. A predictive deconvolution with two gates, for the shallow sediment events and the deeper crustal events, was applied before the stack. A space and time variant frequency filter prior to a post-stack time migration completed the processing flow. The MCS profiles are displayed in the individual chapters of the wide-angle profiles.

## 4.6.2 Magnetics

(B. Schreckenberger)

The magnetic anomalies displayed in all figures of the report are the values from the master sensor of the magnetometer array although all magnetic measurements during Leg 4 were made using the gradient magnetometer. The values are displayed after subtracting the appropriate reference field IGRF2000 and an additional constant value of 50 nT which adjusts the anomalies to a level around zero. This value was determinated by calculating the mean of all anomalies in the middle of Leg 3 of this cruise. It was kept throughout the entire survey.

### Reconstruction of the magnetic anomaly from the gradient

The most simple method for the reconstruction of the magnetic field is the integration of the gradient in the space domain along the profile line. Another approach is the formulation of the problem in the frequency and in the wavenumber domain, respectively (Eilers et al., 1994). In this method the integration corresponds to a filter operation on the Fourier transform of the gradient. It provides a better insight into the problems of the reconstruction and can be combined with additional filter methods. For a first interpretation on board we usually use the simple integration/summation method in the space domain. The main source of errors, visible as crossover errors, is due to long-period variations (probably diurnal variations).

Theoretical considerations and experience with real data show that the gradient method still has limitations with respect to long-wavelength anomalies. Land-based records of the variations will be needed even in the future. For the first weeks of this cruise base station data were available. However, because the data were very noisy and because not all data were available during the cruise, we did not finally process them. Therefore, it was also not practical to process the gradient data due to poor information about the long-wavelength errors.

Anyway, the magnetic anomalies from one of the sensors, as they are drawn in all figures and maps of this report, are sufficient for many interpretations, e.g. for the identification of oceanic magnetic lineations.

### Base station data

For this cruise, support from the Universidad de Concepcion, that maintained our (BGR) magnetic base station, could be obtained. Only the last two digits of the total intensity value at the station were available to us due to the limited range of the analog output of the magnetometer. This causes jumps in the records at every crossing of full hundreds of nT which would not have been a problem if the data were clean. But due to unknown reasons, during Leg 3 the data became very noisy and we decided to process the data later.

A crossover error (COE) analysis was made using 18 of the crossing points that are displayed for the free-air gravity in 4.6.3. The standard deviation of the COEs is 27.2 nT. The largest error is 72 nT. This shows that marine magnetic measurements are strongly influenced by temporal variations of the earth's magnetic field because the absolute accuracy of the proton magnetometers is better than a few nT.

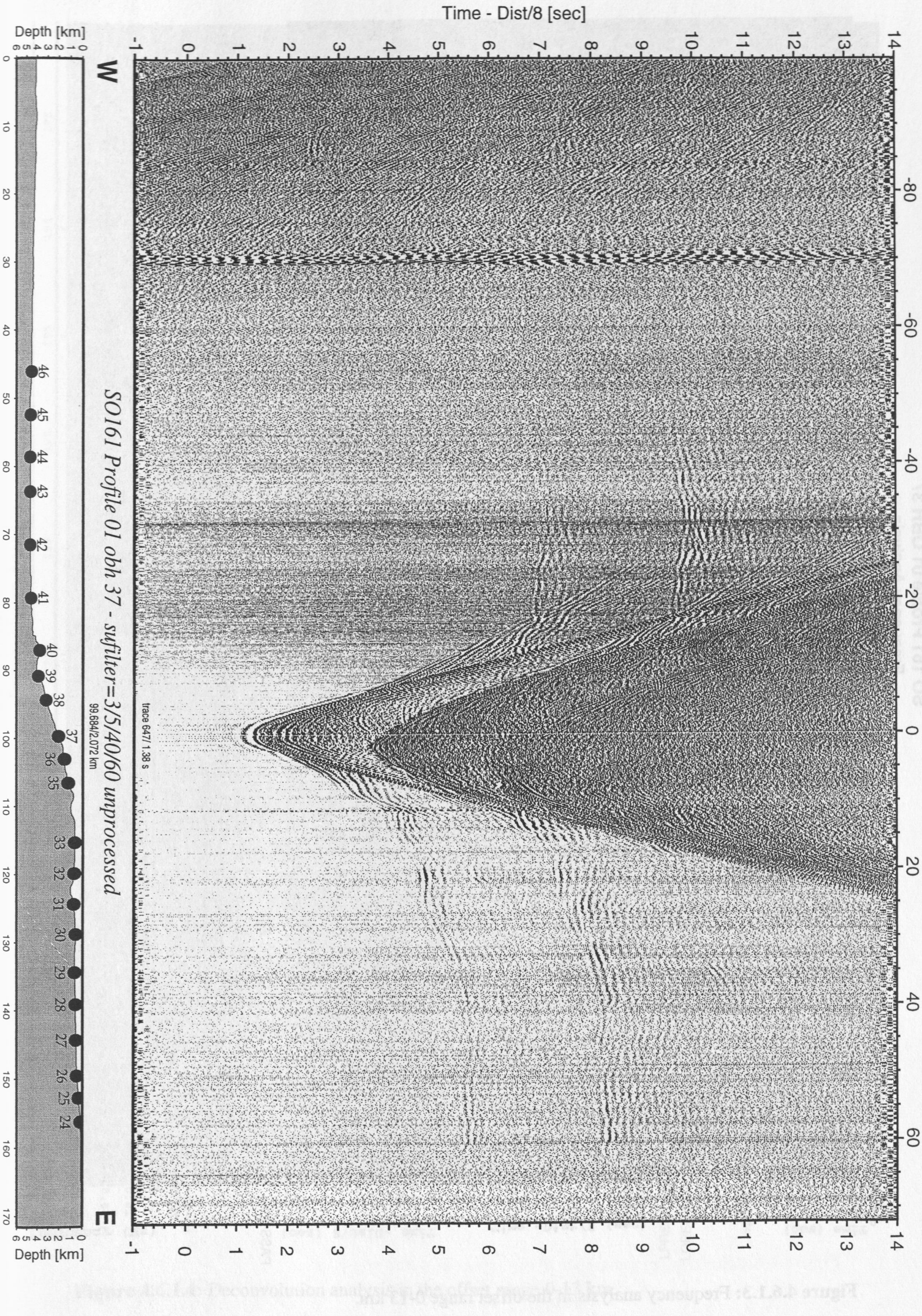

**Figure 4.6.1.2:** Record section from obh 37 unprocessed, Profile 01.

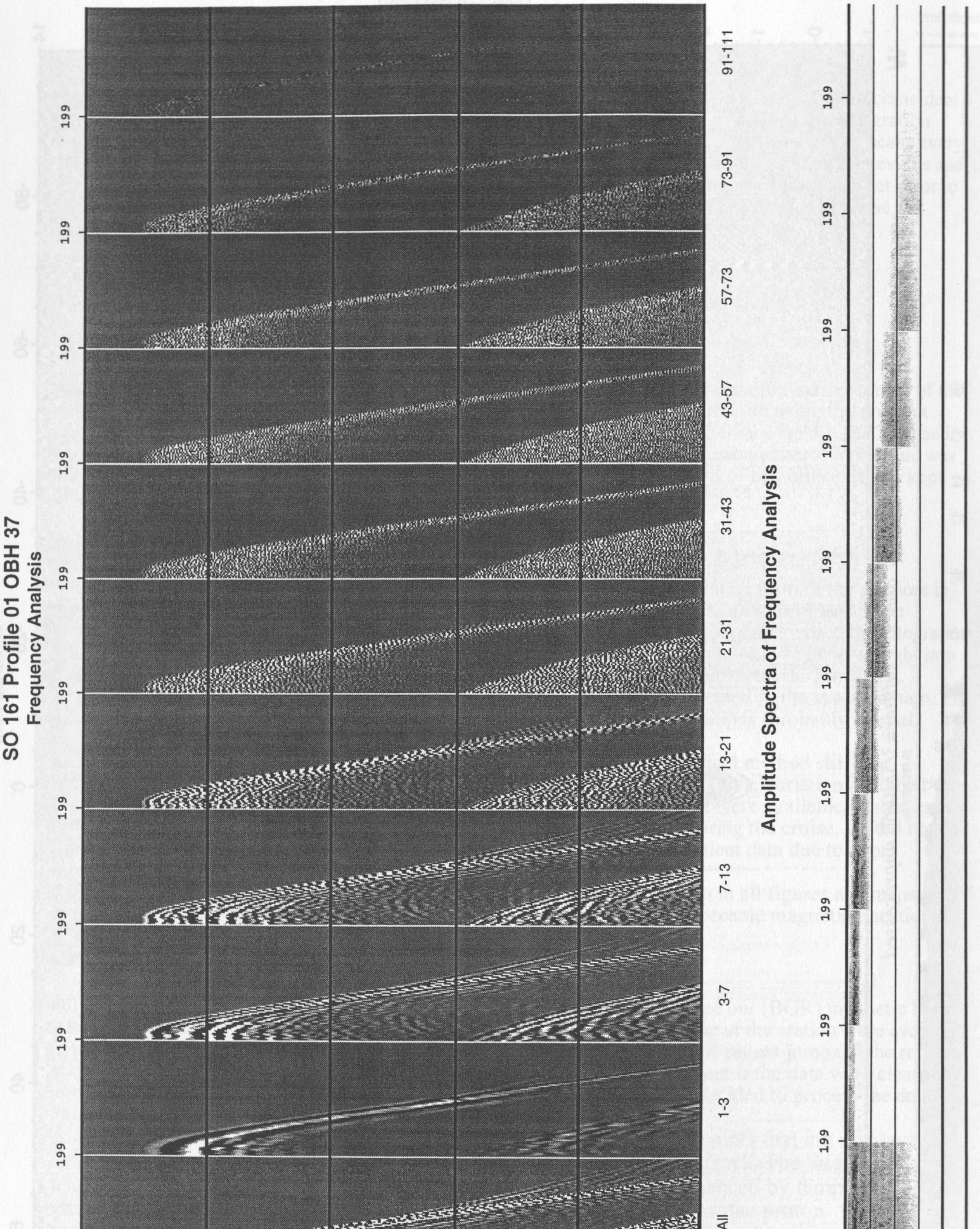

**Figure 4.6.1.3:** Frequency analysis in the offset range 0-13 km.

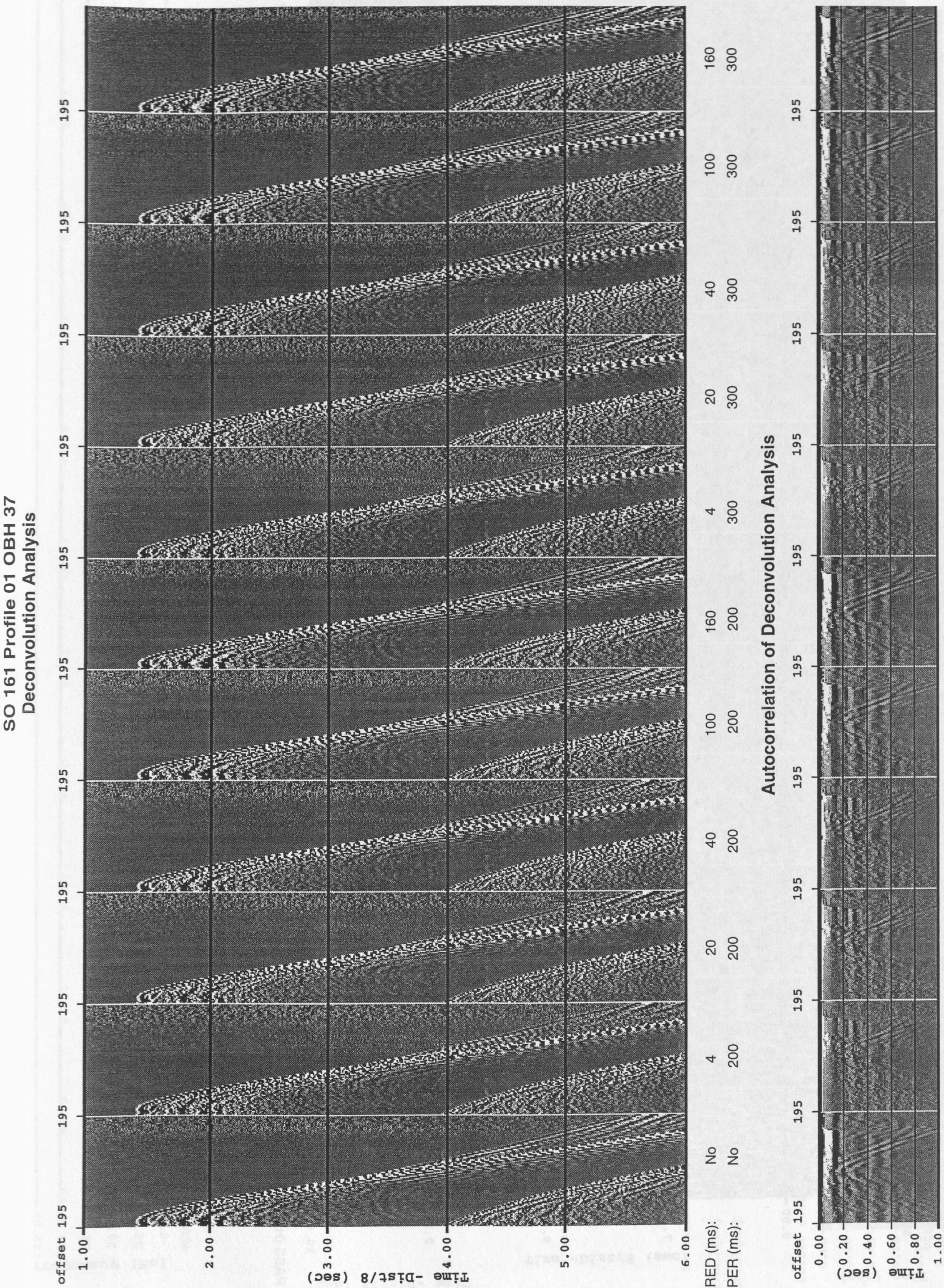

**Figure 4.6.1.4:** Deconvolution analysis in the offset range 0-13 km.

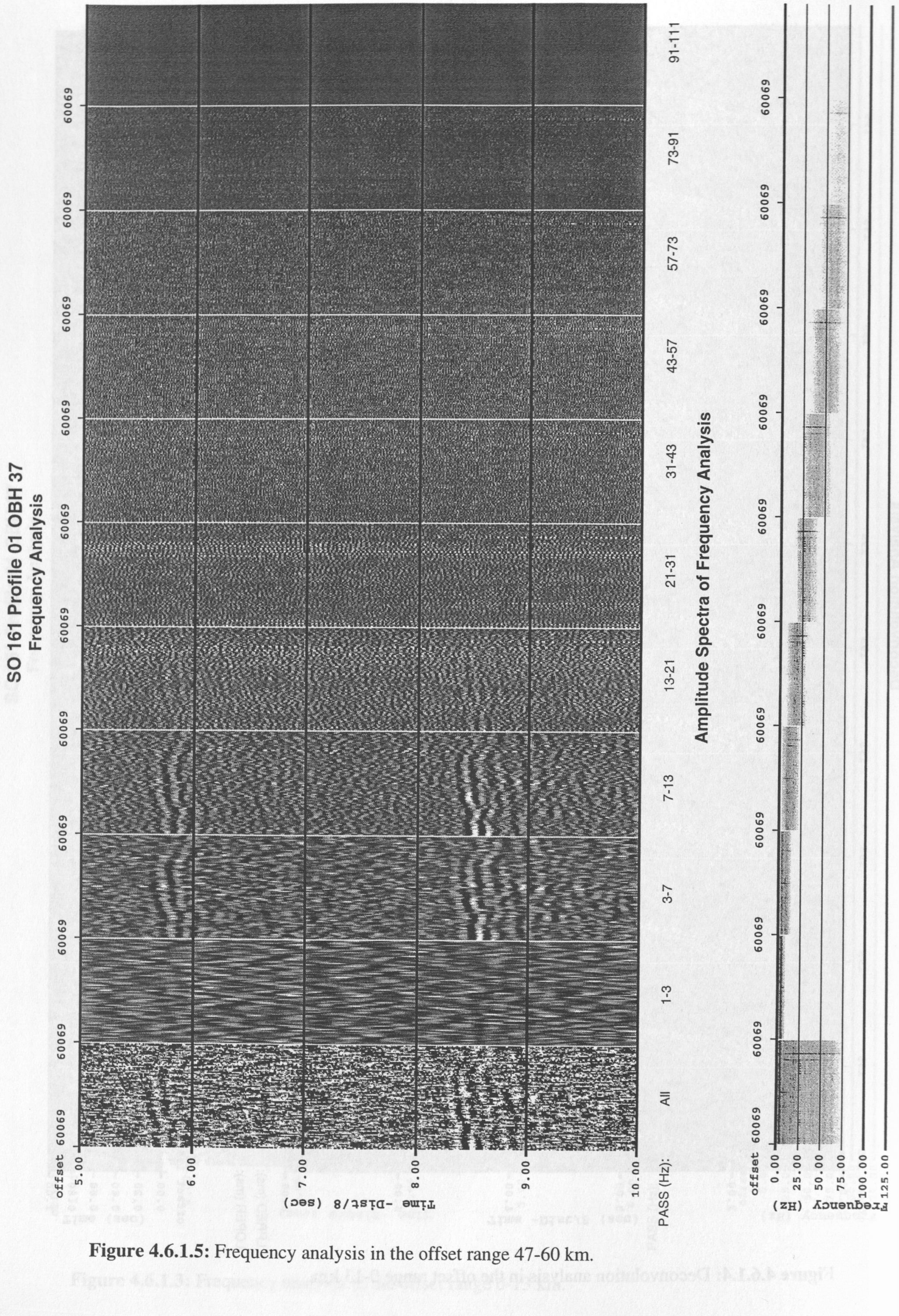

**Figure 4.6.1.5:** Frequency analysis in the offset range 47-60 km.

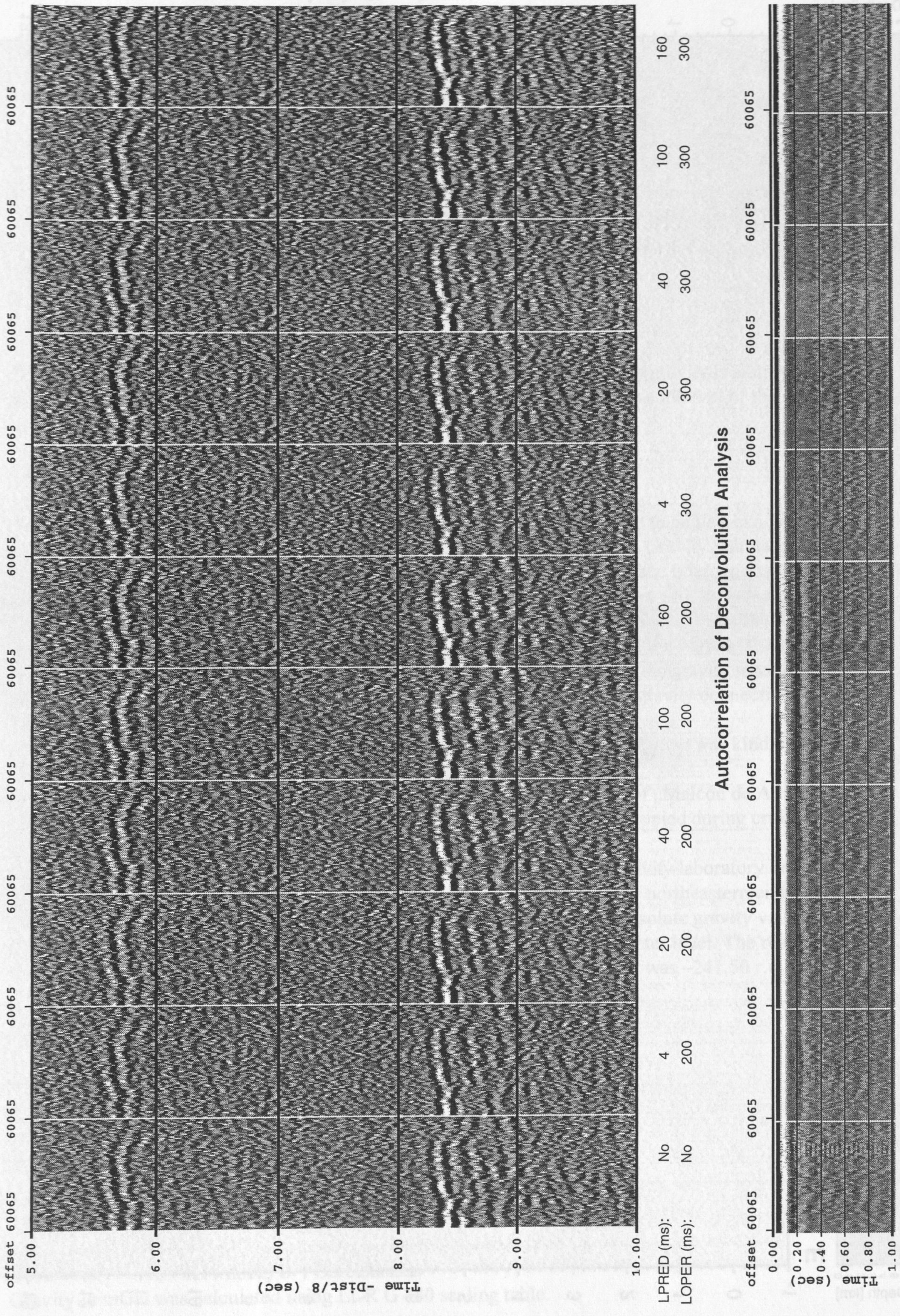

**Figure 4.6.1.6:** Deconvolution analysis in the offset range 47-60 km.

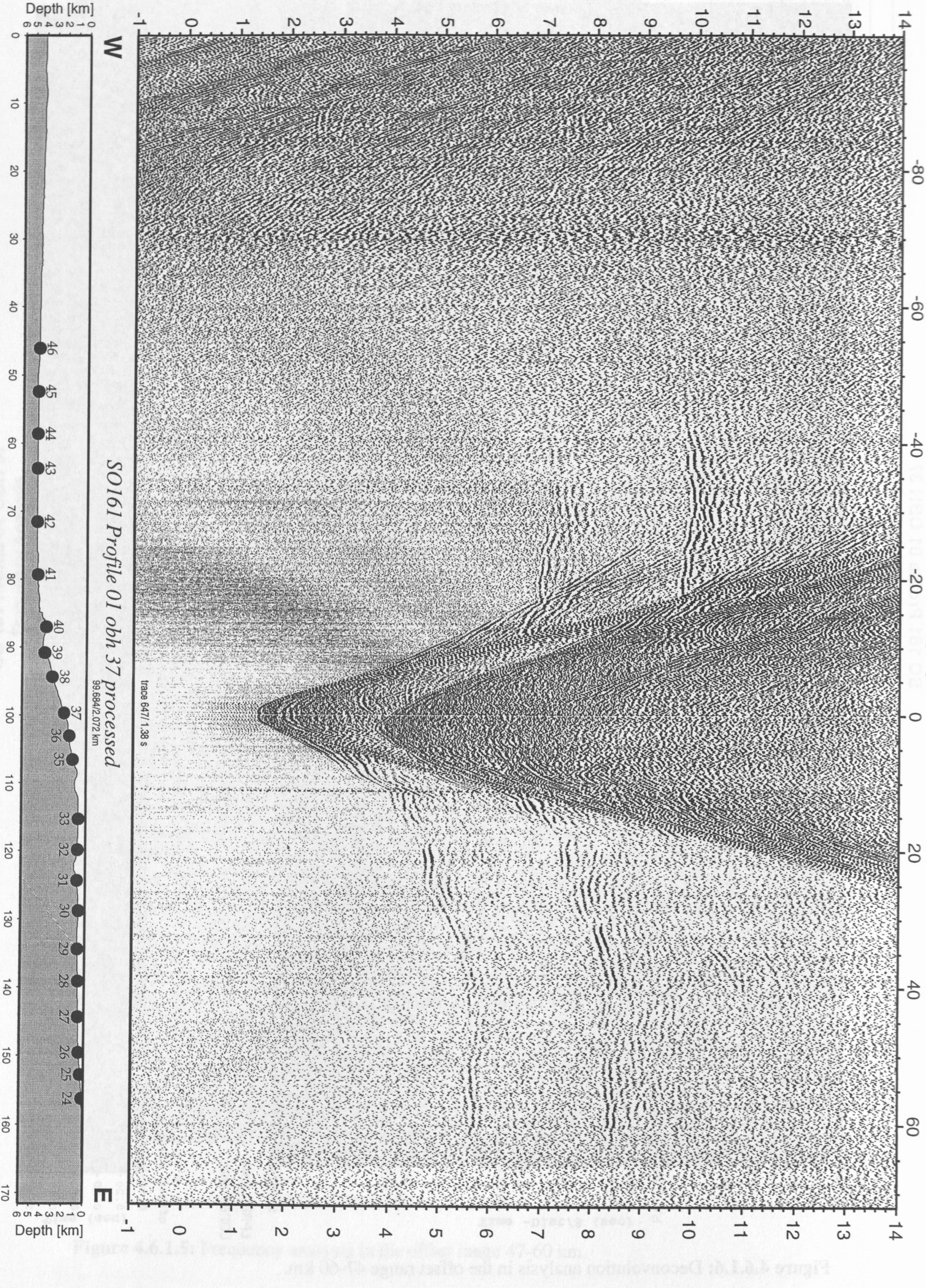

**Figure 4.6.1.7:** Record section from obh 37 processed, Profile 01.

### 4.6.3 Gravity

(B. Schreckenberger, H.-J. Götze, S. Schmidt, P. Kewitsch & U. Barckhausen)

Processing of the gravity data consists essentially of the following steps:

- a time shift of 123 seconds due to the overcritical damping of the sensor,
- conversion of the output from reading units (r.u.) to mGal by applying a conversion factor of 0.9454 mGal/r.u., on this cruise that was done in the gravimeter by hardware setting.
- connection of the harbor gravity value to the world gravity net IGSN 71,
- correction for Eötvös effect using the navigation data,
- correction for the instrumental drift,
- subtraction of the normal gravity (WGS67).

As a result, we get the free-air anomaly (FAA) which in the case of marine gravity is simply the observed gravity minus the normal gravity. According to the selectable time interval of the data acquisition system, gravity values are available every 20 seconds.

#### Gravity ties to land stations

To compare the results of different gravity surveys the measured data have to be tied in a world-wide accepted reference system. This system is represented by the International Gravity Standardization Net IGSN71 (MORELLI, 1974). The IGSN71 was established in 1971 by the International Union of Geodesy and Geophysics IUGG as a set of world-wide distributed locations with known absolute gravity values better than a few tenths of mGal. According to the recommendations of the IUGG, every gravity survey, marine or land, should be related to the datum and to the scale of the IGSN71. Therefore, gravity measurements at land have to be carried out to connect the gravity measurements at sea with the IGSN71. The marine geophysical group of BGR uses for the gravity connections a LaCoste&Romberg gravity meter, model G, no. 480.
The point description and gravity value of reference IGSN71 station in Santiago was kindly provided by the Instituto Geografico Militar (Santiago, Chile).
R/V SONNE moored at the pier of Valparaiso in the northeastern corner of „Malcón de Atraque“ (Figs. 4.6.3.1 and 4.6.3.2). The position was almost identical with that occupied during cruise SO-104 (CINCA) in 1995.
On October 18, tie measurements to point **A** as close as possible to the gravity laboratory on R/V SONNE have been made (Table 4.6.3.1). Point **A** is located 68 m from the northeastern end of the pier (see Fig. 4.6.3.2). The connection measurements resulted in an average absolute gravity value of 979621.57 mGal (with water level –4.25 m, IGSN71) for point **A** at the water level. The reading of the KSS31 at the leaving time (October 18, 2001, 21:00 UT) from the pier was –241.50 r.u.

| Station | Date | Time UT | Reading units | Measured value [mGal] |
|---|---|---|---|---|
| **BGR** / K | 10.08.01 | 06:00 | 4811.58 | 4892.53 |
| **A** / B | 17.10.01 | 12:30 | 3195.60 | 3245.78 |
| **01** / B | 17.10.01 | 18:35 | 2993.42 | 3040.00 |
| **A** / B | 18.10.01 | 12:05 | 3195.52 | 3245.70 |

Observers: K = Kewitsch, B = Barckhausen
Gravity in mGal was calculated using LCR G 480 scaling table.

**Table 4.6.3.1:** Observation report of the gravity tie measurements in Valparaiso.

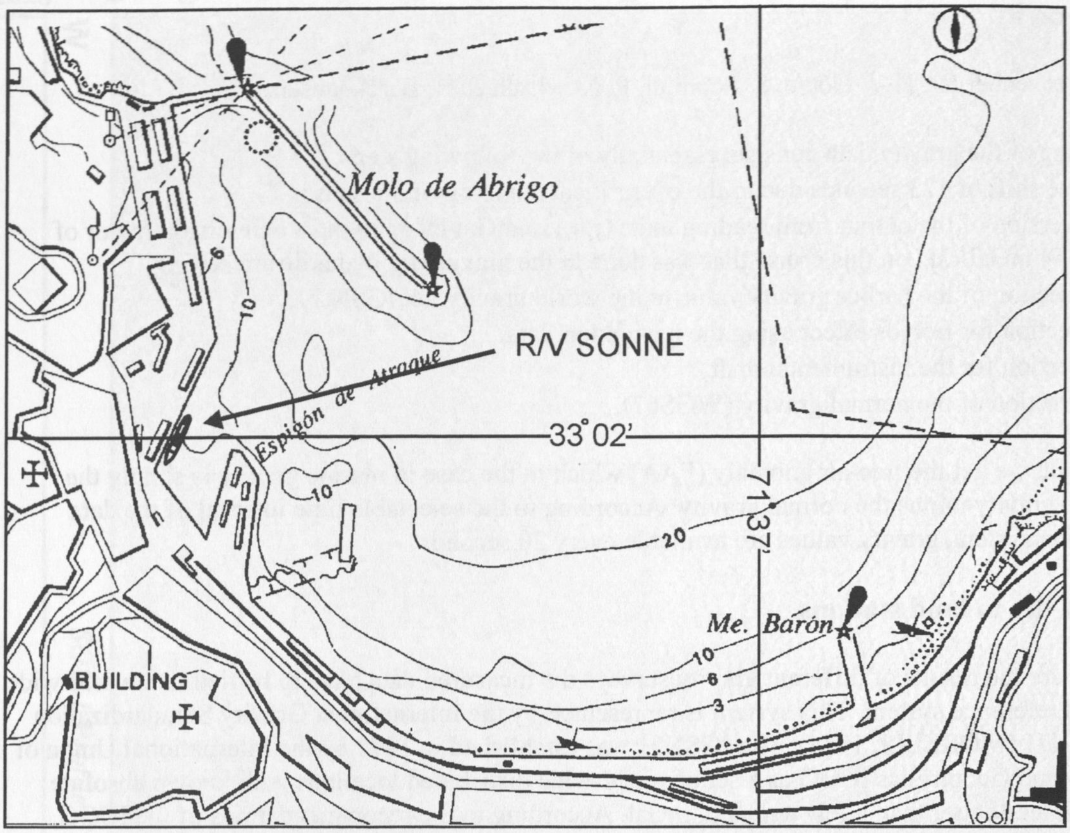

**Figure 4.6.3.1:** Location of the mooring site of R/V SONNE at the pier of Valparaiso (from the Admiralty chart 1314, Puerto de Valparaiso).

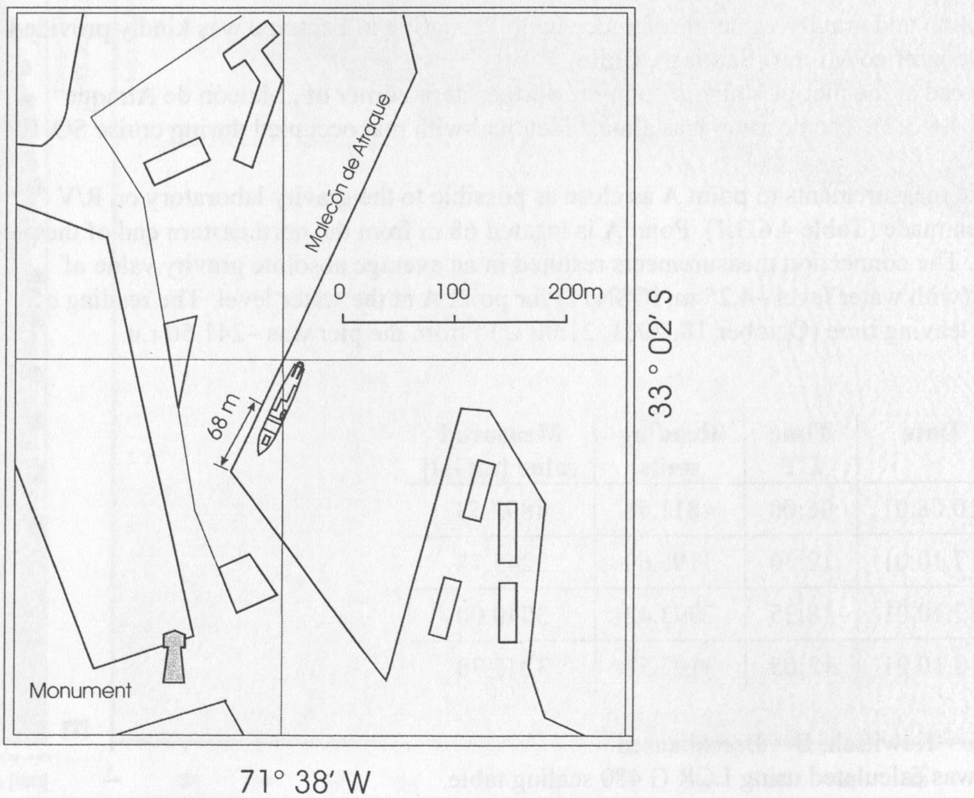

**Figure 4.6.3.2:** Close-up of the mooring site of R/V SONNE in Valparaiso during port calls on 16.-18. Oct., 31. Oct. - 02. Nov., and 28. - 30. Nov. 2001.

**Reference Stations:**

| | | |
|---|---|---|
| **BGR:** | Pillar, Room No. VB11 | 981267.730 mGal (IGSN71) |
| **01:** | Instituto Geografico Militar<br>Santiago<br>Nueva Santa Isabel 1640<br>535.77 m above main sea level | 979414.478 mGal (IGSN71) |

**Gravity station:**

**A:** Valparaiso pier, 68 m from northern end of the pier, between bollards no. 3 and 4, 9 m from bollard 4

**Differences between reference/gravity stations:**

**A – 01** = **+ 205.78** mGal

**BGR – 01** = **+ 1852.53** mGal (own measurements)
= **+ 1853.25** mGal (according to given IGSN71 values)

Absolute gravity at **A**: 979620.258 mGal

The absolute gravity for **A** (reduced to water level –4.25 m) 979621.569 mGal (IGSN71 system) was used for the gravity tie on 18.10.2001 (20:00 UT).
Reading of sea gravimeter KSS31 at that time: -241.50 r.u. = mGal (scale factor 0.9454 mGal/r.u.).
During the port call from October 31, to November 2, 2001 R/V SONNE moored at the same pier in Valparaiso again. The reading of the gravimeter during all the time was -242.0 r.u. (mgal). Compared with the value from 18.10.2001 this would imply a drift of -0.5 mgal in 18 days. This value is within the estimated accuracy of the harbor readings and no drift correction was applied for Leg 2.
During the port call from November 28, to November 30, 2001 R/V SONNE moored again at the same pier in Valparaiso. The reading of the gravimeter was highly disturbed due to strong movements of the vessel. The average reading during all the time was estimated from the analog record to be between -242.5 and -242.0 r.u. (mgal). Therefore, the KSS31 obviously showed no drift between October, 18 and November 30, 2001.
During her final port call on December 21, SONNE moored on a different pier. The reading of the gravimeter KSS31 was -243.5 r.u. (mGal). Because it was not possible to establish a new gravity connection to the new mooring site on the same day we could not verify the drift for Leg 4. Provided that the drift of the instrument during Legs 2 and 3 was nearly zero within the measuring accuracy of the harbour readings we have good reasons to assume that it also did not reach large values during Leg 4. The difference of 2 mGal in the port readings of the gravimeter between the old and the new mooring sites may also be caused by gravity differences between the two points. Therefore, the marine gravity measurements from all SPOC Legs as they are shown here in this report are preliminary but we do not expect that corrections of more than 1 or 2 mGal will be necessary in the final processing.
The necessary measurements at the new mooring site and the connetion to the former mooring site **A** will be done during the remaining time of the port call. To verify the absolute gravity value for point A in the harbour an additional connection to an absolute gravity point in Valparaiso will be also be made.

## Crossover error analysis

The accuracy of gravity measurements at sea is a crucial factor. If we assume that the tie to the absolute value of the gravity at the mooring site could be done within an accuracy of at least a few tenth of a mGal then the general inaccuracy of marine gravity measurements will be the limiting factor. Because it is only possible to check the drift of the instrument every few weeks during the port calls we have to assume that the drift of the gravimeter is linear during the survey time at sea. The analysis of crossover errors (COE) provides a valuable tool to check the internal consistency of the data in this respect.

Table 4.6.3.2 shows the crossover errors for 15 lines from Leg 3 and 4 within a selected part of the survey area. 28 crossovers could be identified by the routine x2sys of the GMT supplemental software package. The maximum COE is 1.8 mGal, only 8 values exceed 1 mGal. The mean of the absolute values of the COE is 0.70 mgal. The standard deviation of the original values is 0.85 mGal. This analysis shows that the free-air anomalies are accurate within about 1 mgal.

Figure 4.6.3.3 shows the distribution of the crossovers and the size of the COE represented by the diameter of an error circle. Visual inspection shows no indication that the errors are caused by single lines or that they have a preferred spacial distribution.

The analysis shows that our gravity measurements are far more precise than alternate methods to measure the marine gravity field e.g. the calculation of free-air anomalies from satellite altimeter measurements. Therefore, our data set can serve as a reference in the comparison of altimeter gravity models in the following paragraph.

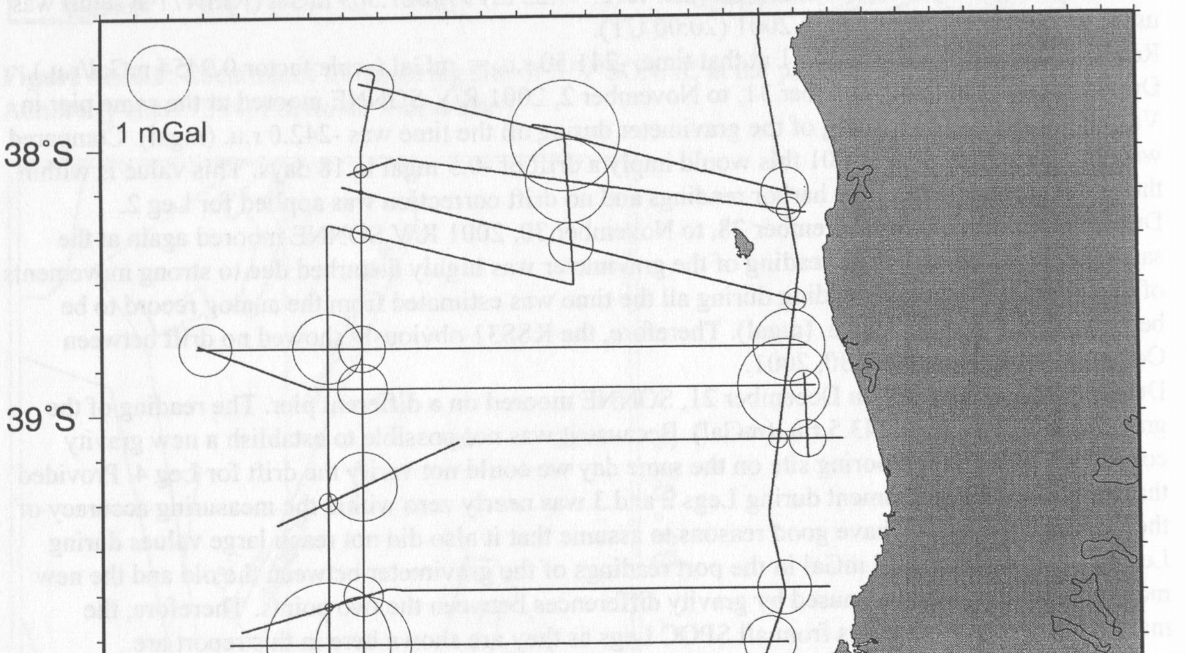

**Figure 4.6.3.3:** Crossover errors of free-air gravity between selected geophysical lines from Leg 3 and Leg 4 in the SPOC area (see also Table 4.6.3.2).

| Longitude | Latitude | COE<br>mGal | Mean<br>mGal |
|---|---|---|---|
| 284.0830 | -39.8500 | 1.808 | -4.28 |
| 286.1960 | -39.8501 | -0.748 | -24.75 |
| 284.2500 | -39.8500 | 1.401 | -12.43 |
| 284.0830 | -39.7102 | -0.116 | 15.76 |
| 284.2500 | -39.6725 | 0.576 | 7.65 |
| 286.2670 | -39.6500 | 0.787 | -36.39 |
| 284.0830 | -39.3235 | -0.275 | 1.82 |
| 284.2500 | -39.2647 | 1.007 | -3.14 |
| 286.3830 | -39.1000 | 0.546 | -36.25 |
| 286.2420 | -39.1000 | 0.279 | -14.62 |
| 284.2500 | -38.9001 | 0.729 | 5.06 |
| 286.2760 | -38.9002 | -1.348 | -2.56 |
| 284.0830 | -38.9000 | 0.020 | 5.14 |
| 286.3720 | -38.9000 | 0.431 | -19.01 |
| 284.2500 | -38.7499 | 0.672 | 3.21 |
| 286.3010 | -38.7500 | -1.058 | 7.90 |
| 284.0830 | -38.7499 | -1.018 | 2.14 |
| 283.5000 | -38.7499 | 0.769 | 16.08 |
| 286.3300 | -38.5794 | -0.328 | 19.56 |
| 285.2560 | -38.3629 | -0.647 | -97.85 |
| 284.2500 | -38.3162 | -0.259 | 4.38 |
| 286.3030 | -38.2412 | -0.360 | 28.27 |
| 286.2870 | -38.1691 | -0.697 | 28.99 |
| 284.2500 | -38.1595 | -0.064 | 14.82 |
| 285.2400 | -38.1239 | -1.222 | -97.58 |
| 284.2500 | -38.0777 | 0.199 | 12.73 |
| 285.2280 | -37.9512 | 1.610 | -86.99 |
| 284.3060 | -37.7613 | -0.647 | 7.48 |

**Table 4.6.3.2:** Crossover error (COE) analysis for gravity measurements (free-air anomaly) in a selected part of the survey area of Legs 3 and 4. Shown is the location of the crossovers and the size and the mean of the COE (see also Figure 4.6.3.3).

## Study and comparison of satellite altimeter data bases

Marine gravity data from satellite altimetry by Sandwell and Smith (1997) referred to as SDW in the following analysis are available from the Geological Data Center, Scripps Institution of Oceanography, La Jolla, CA 92093 together with another two altimetry data sets to fill in marine areas that had not been surveyed by ship borne gravity. The first is the KMS2001 "Global marine Free Air gravity field" computed from ERS-1 + GEOSAT satellite altimetry by the "Kort i Matrikel Styrelsen, Copenhagen" (Andersen and Knudsen, 2001) hitherto referred to as "KMS data set". They implemented a new technique for the interpolation of the geoid anomalies for the KMS2001 gravity field: it is called an adaptive interpolation where the parameters for the covariance function have been determined empirically from the altimetry, and subsequently interpolated to the position of interpolation. This has shown to be effective in removing track like structures in areas of high ocean variability as the variance is much better determined. The second alternative altimetry data set was published by Wang (2000) of the Goddard Space Flight Centre. In the following chapter "GSFC" refers to this data set.
The new gravity data set observed by the SO 161 cruise (SPOC) provides an excellent opportunity to test and compare the above mentioned satellite data sets with ship borne data. Here we present preliminary results because SPOC data have to be evaluated and reprocessed after the cruise.
The first series of Figures (4.6.3.4 through 4.6.3.6) shows both the altimetry gravity data sets (grey tones) and differences calculated between the gravity at SPOC stations and corresponding gravity at grid points of the three altimetry data sets. The figures contain all locations where grid points and SPOC data lie within a radius smaller than 500 metres. The Sandwell and Smith data in Fig. 4.6.3.4 provide an uneven pattern of gravity which is characterised by small "anomaly spots". Greater differences are obtained near to coastal areas. The KMS data set is more smoothed and differences are generally smaller than in the SDW data (Figure 4.6.3.5). Analysis of the data set published by Wang (GSFC in Fig. 4.6.3.6) results in rather small differences, but again shows a pattern similar to that of SDW. The histogram in Figure 4.6.3.7 provides a statistical analysis and a more differentiated insight into the results.
In a second step we were interested in the analysis of 38.915 gravity differences along the SPOC profiles. (Mapped results can be found in Figure 4.6.3.8 for SDW, KMS and GSFC data sets). In Figure 4.6.3.9 the histogram presentation of the calculations show, that the standard deviation of the KMS data set ($7.67 \cdot 10^{-5}$ m/s$^2$) is similar to the standard deviation which was calculated on base of the Wang data ($5.74 \cdot 10^{-5}$ m/s$^2$). A higher deviation was found for the SDW data set ($29.59 \cdot 10^{-5}$ m/s$^2$). These statistical results helped us to decide on the usage of the KMS data set for further gravity map compilations in areas where no SPOC ship borne data are available.

## Topographic reduction

To calculate offshore Free Air and Bouguer anomalies, a topographic reduction was performed by using a bathymetric grid of 30′′ by 30′′ (approximately 800 m by 800 m) which was compiled by the 5' x 5' ETOPO 5 grid and the bathymetry grid that was provided by R. Zapata (Universidad de Chile, Zapata, 2001). For onshore topographic reduction we got use of the USGS 1 km by 1 km topography grid. Reduction has been performed within a radius of 100 km and densities of 2.67 Mg/m$^3$ and 1.64 Mg/m$^3$ for areas above and below sea level, respectively. The biggest reduction value (which includes the reduction density already) was found in the area of the seamount "O`Higgins" with some $89 \cdot 10^{-5}$ m/s$^2$. However, for a general overview of calculated topographic reduction values refer to the histograms in Figures 4.6.3.10 and 4.6.3.11.

## Reduction procedures

The following equations describe the calculation of gravity anomalies:

SCBA $= g_{abs}\ \gamma_h + \delta\ g_{top} + \delta\ g_{bou}$ *station complete Bouguer anomaly*
FA $= g_{abs} - \gamma_h$ *Free Air anomaly*

with:

$g_{abs}$ : absolute gravity at station (measured) tied to the ISGN71 datum,
$\gamma_h$ : normal gravity at station level h; normal gravity formula of 1967,
$\delta g_{top}$ : topographic reduction,
$\delta g_{bou}$ : Bouguer slab reduction.

For topographic reduction, a true 3D-method including calculations of the Earth´s curvature developed for gravity investigations in the Alps was used, after adapting it to the special situation in the Central Andes.

To show the influence of topographic masses within a reduction radius of 100 km on the ship borne gravity data two histograms were calculated which may prove the overall dominance of bathymetry (trench and ocean bottom topography) in reduction. First, the histogram in Fig. 4.6.3.10 shows that more than 50 percent contributes to the topographic reduction of ship borne data by landmasses with amounts between 0 to $0.25 \cdot 10^{-5}$ $m/s^2$. On contrast topographic reduction values between -10 to $5 \cdot 10^{-5}$ $m/s^2$ caused by the offshore masses of oceanic crust, in particular the trench and the land near shelf were obtained at approximately 60 percent of all stations (Figure 4.6.3.11).

As an example Figure 4.6.3.12 shows bathymetry, Bouguer and Free Air anomalies along the SO 161-038 profile (in the offshore area south of Concepción). At the bottom the results of the SONNE hydrosweep (SIMRAD) observations are shown together with the Zapata data and the ETOPO 5 bathymetry grid. For test reasons we used these data sets (Fig. 4.6.3.12, BOTTOM) and calculated Bouguer- and Free Air anomaly maps and compared them with the SPOC data (Fig. 4.6.3.12, TOP). This study underlines the importance of precise bathymetry data: A less resolved ocean bottom (in particular ETOPO 5) results in large differences in the calculated anomalies (stippled and large dashed lines in Fig. 4.6.3.12, TOP) if they are compared with SPOC anomalies (black solid line in Fig. 4.6.3.12, TOP) which are reduced by the high resolution hydrosweep bathymetry.

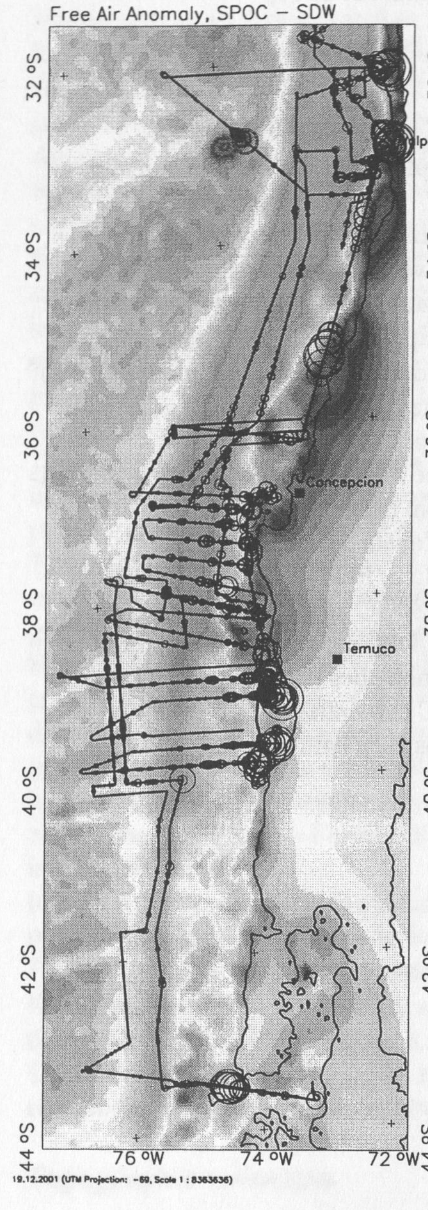

**Figure 4.6.3.4:**
Differences between SPOC and Sandwell & Smith data (SDW) at selected points. Search radius was approximately 500 m. Greater differences (big circles) appear near the coast.

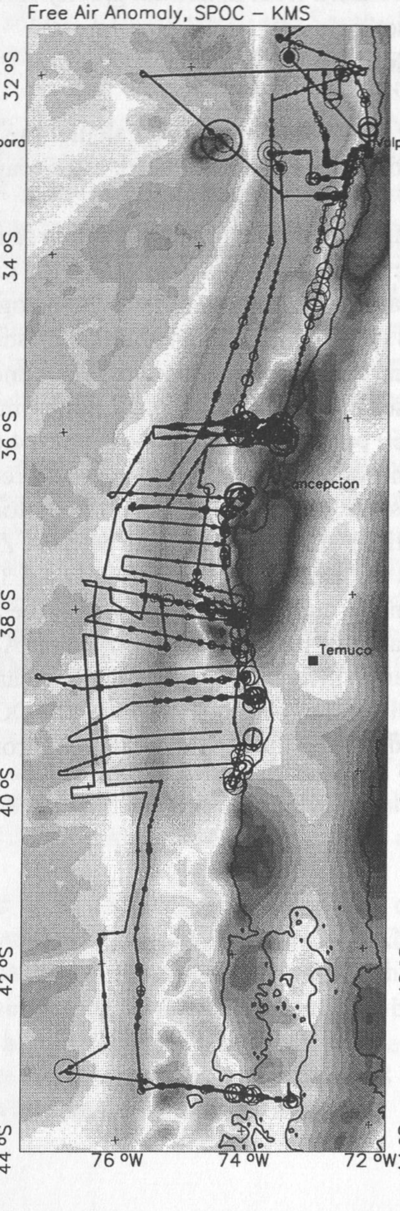

**Figure 4.6.3.5:**
Differences between SPOC and KMS - data at selected points. Search radius was approximately 500 m. Differences (big circles) are observed near the coast and above bathymetry features.

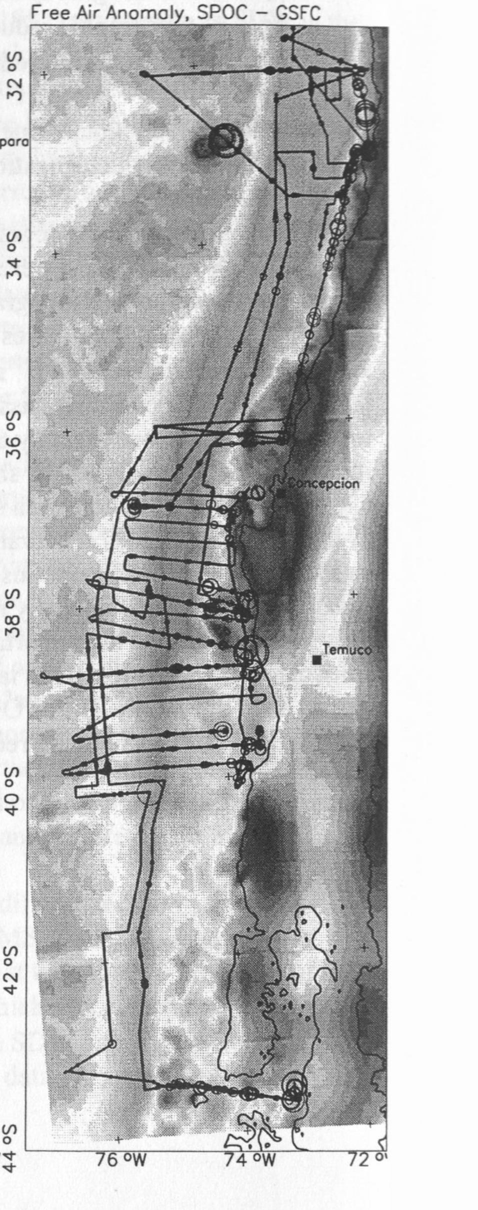

**Figure 4.6.3.6:**
Differences between SPOC and Wang data (GSFC) at selected points. Search radius was approximately 500 m. Some differences (big circles) were observed near the coast and near bathymetry features..

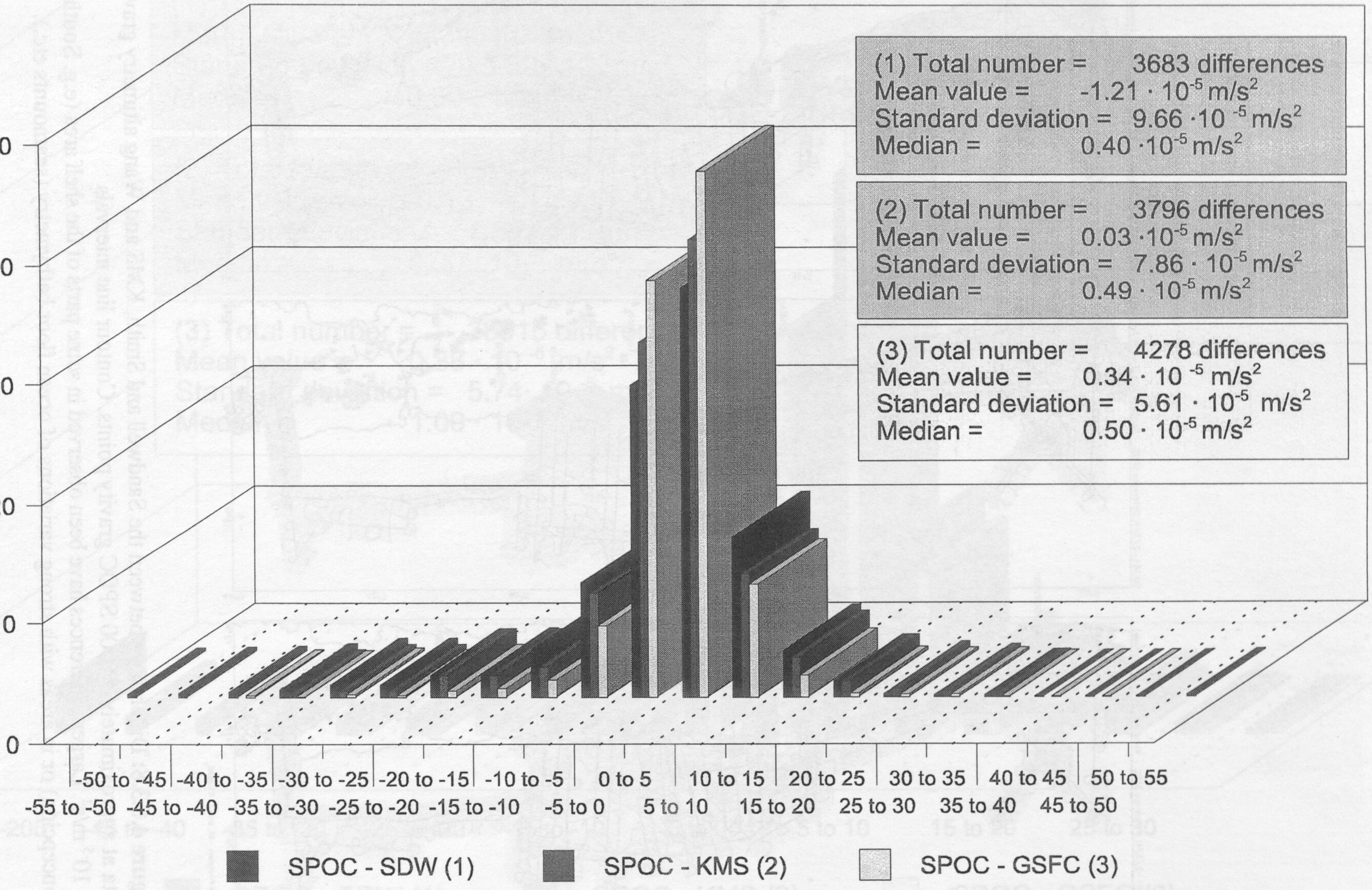

**Figure 4.6.3.7:** Histogram of selected differencenes between the SPOC database and correspondng altimeter gravity databases: values in percent. SDW = Sandwell and Smith (1997); KMS = Kort i Matrikel Styrelsen, Copenhagen; GSFC = Goddard Space Flight Center. Values of histogram clases in $10^{-5}$ m/s$^2$.

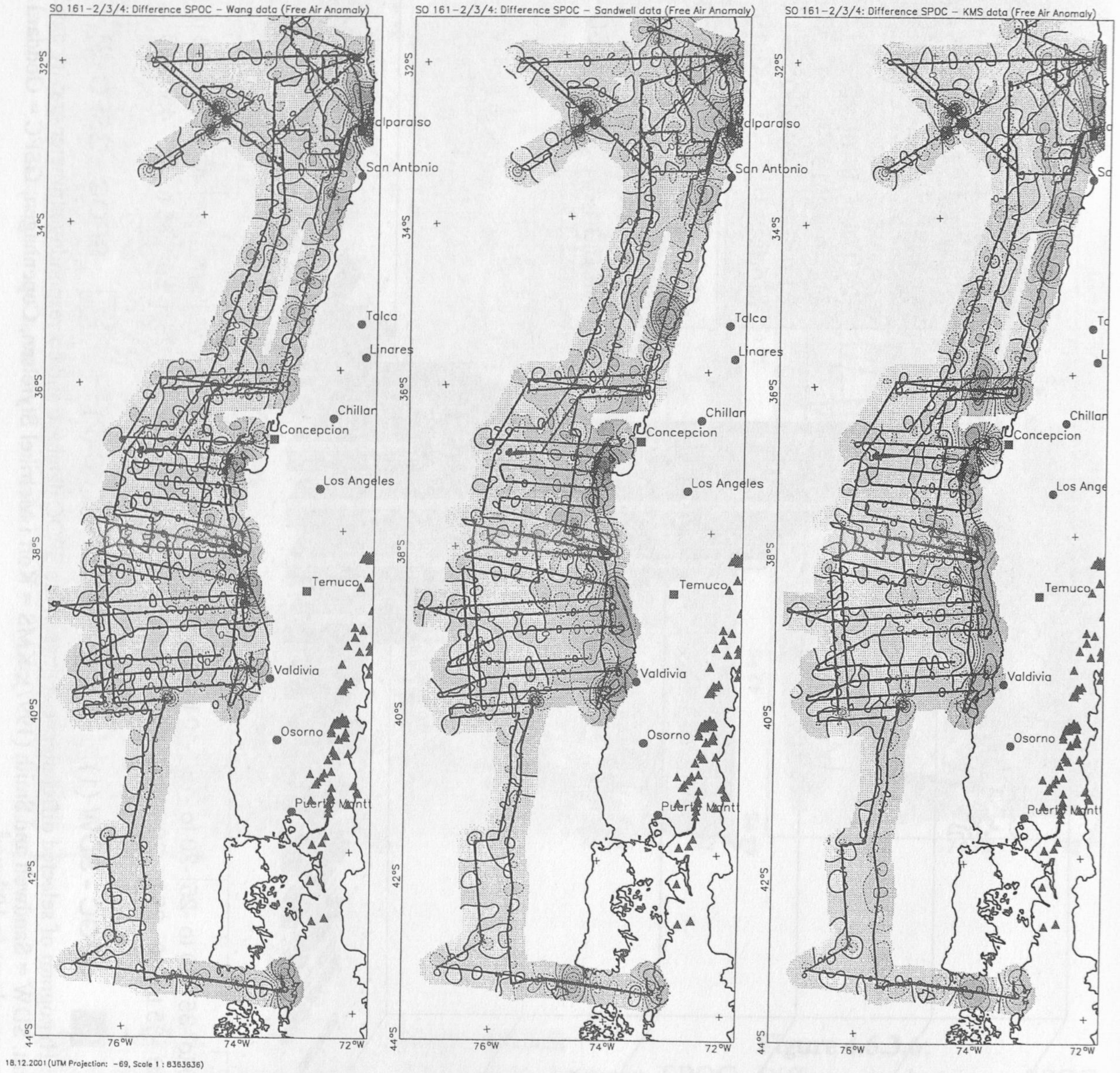

**Figure 4.6.3.8:** Differences between the Sandwell and Smith, KMS and Wang altimetry gravity data at approximately 39.000 SPOC gravity points. Contour line intervals $5 \cdot 10^{-5}$ m/s$^2$. Larger differences have been observed in some parts of the shelf area (e.g. South of Concepción) or in areas with strong variations of ocean floor bathymetry (seamounts etc.).

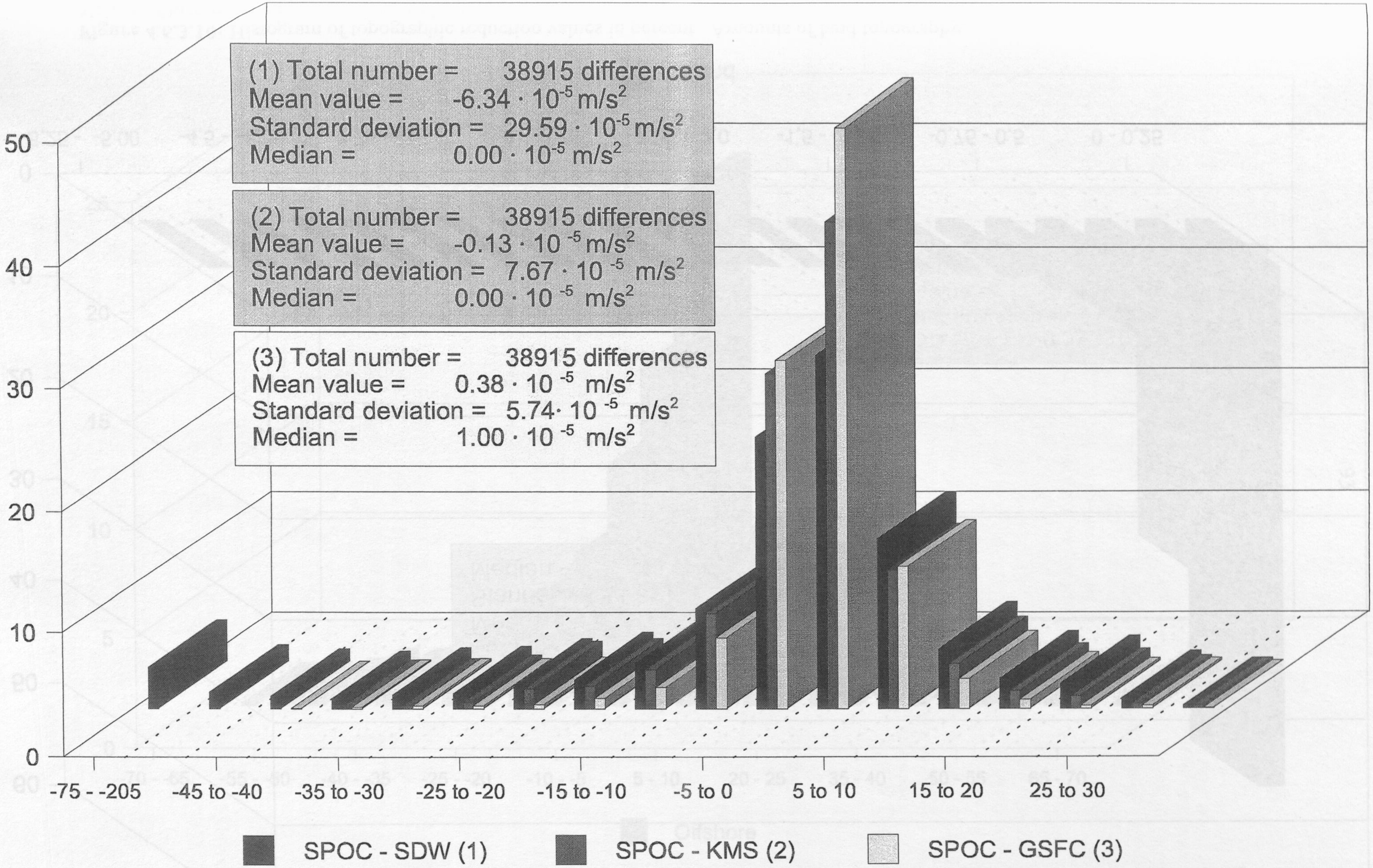

**Figure 4.6.3.9:** Histogram of differencenes between all SPOC data and corresponding altimeter gravity databases: values in percent SDW = Sandwell and Smith (1997); KMS = Kort i Matrikel Styrelsen, Copenhagen; GSFC = Goddard Space Flight Center. Values of histogram clases in $10^{-5}$ m/s$^2$.

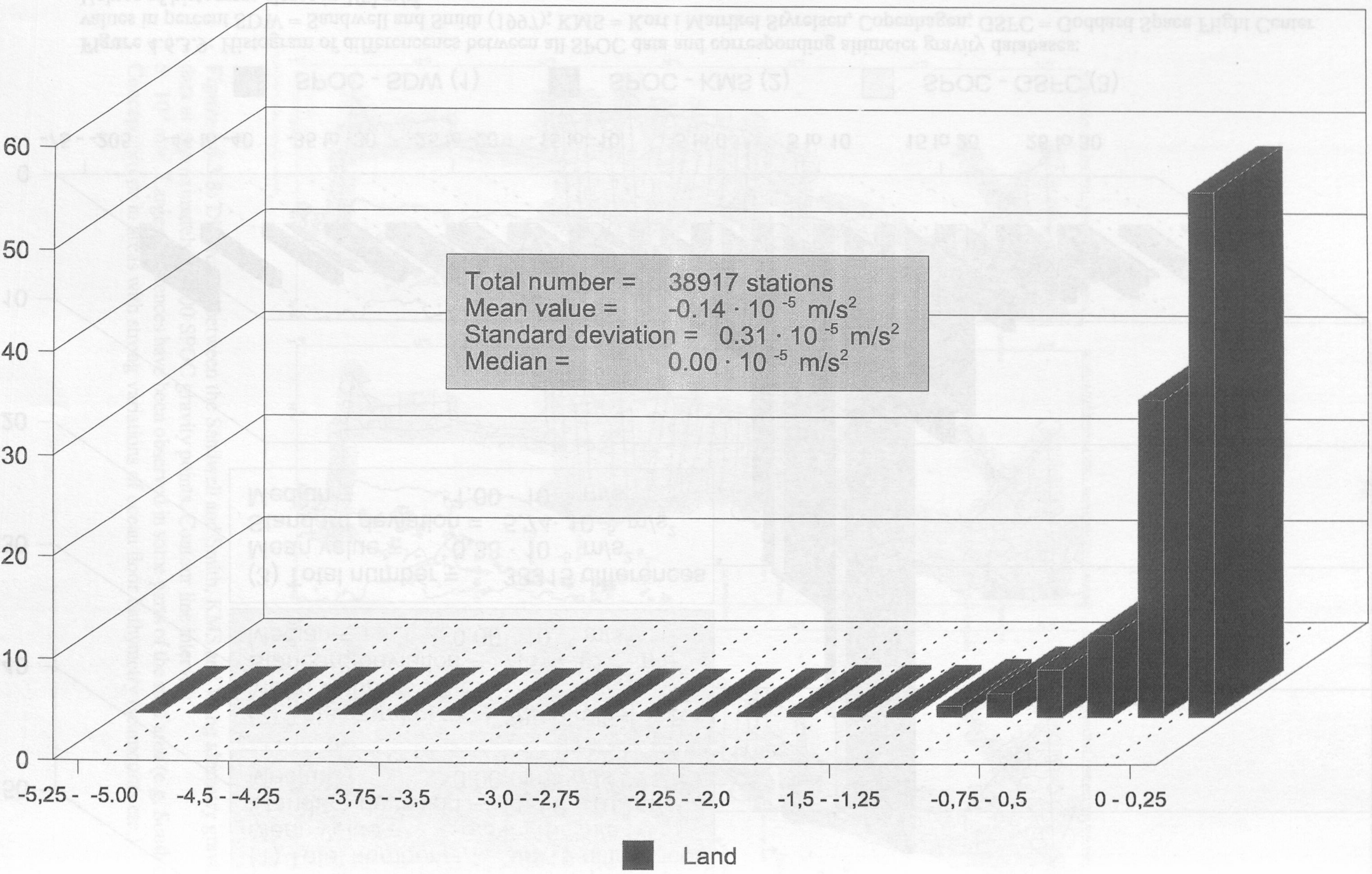

**Figure 4.6.3.10:** Histogram of topographic reduction values in percent. Amounts of land topography. Values of histogram classes given in $10^{-5}$ m/s$^2$.

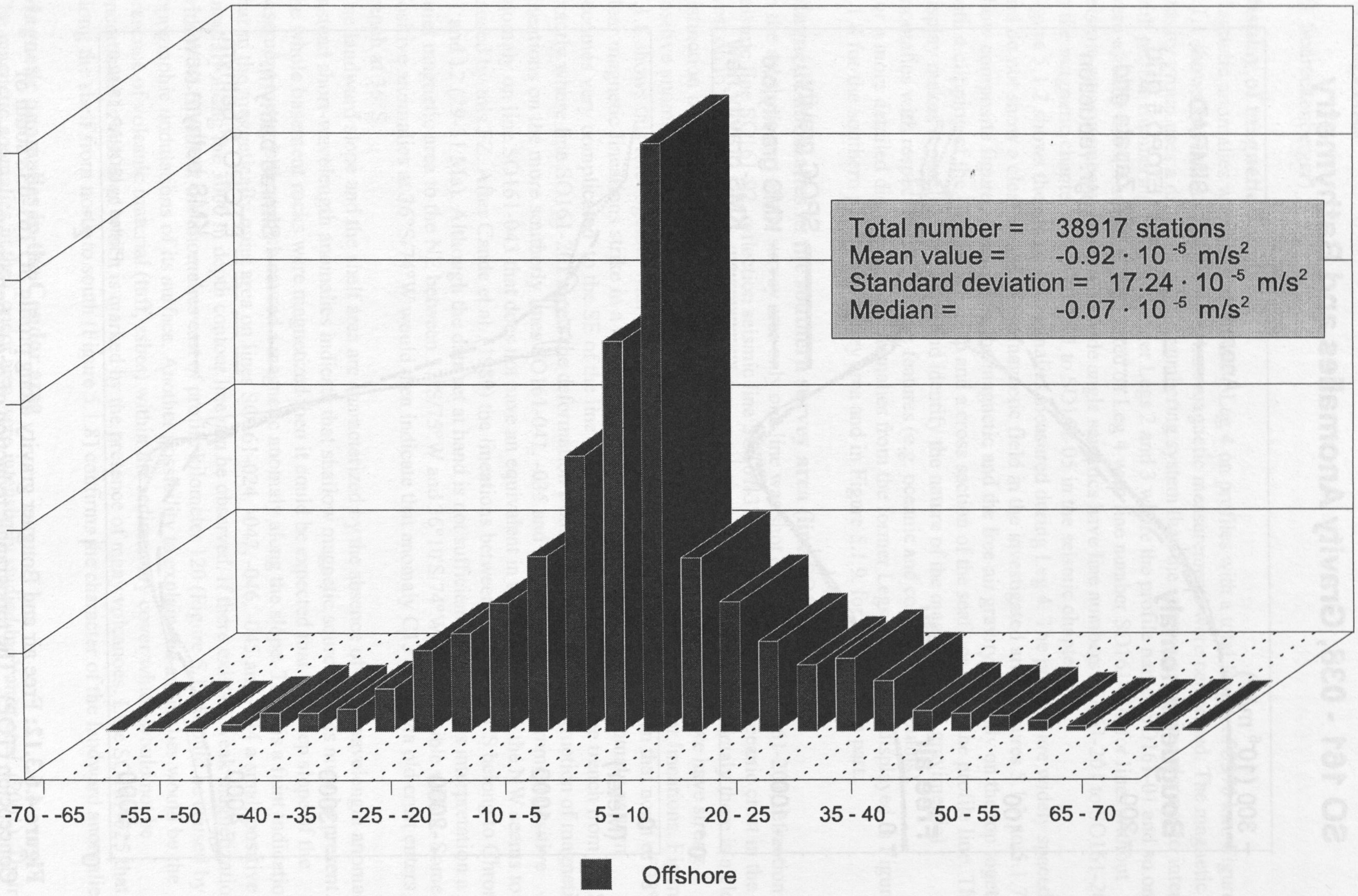

**Figure 4.6.3.11:** Histogram of topographic reduction values in percent. Amounts of offshore topography. Histogram value classes in $10^{-5}$ m/s$^2$.

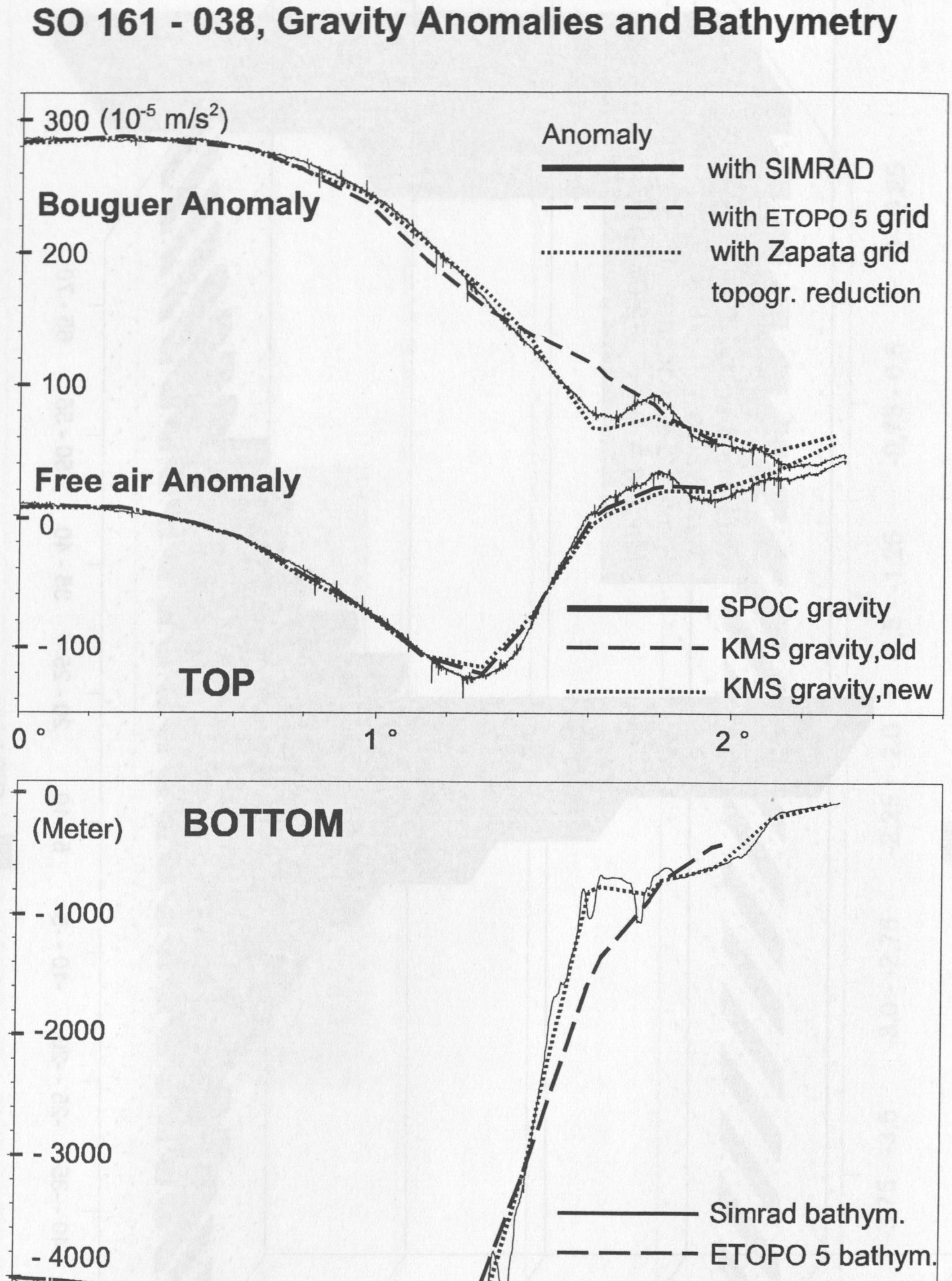

**Figure 4.6.3.12:** Free air and Bouguer gravity along profile SO 161-038 south of Concepción (TOP). The topographic reduction of ocean bottom was performed by the ETOPO 5 and Zapata batymetry grids; SPOC gravity data were reduced by the high resolution SIMRAD bathymetry (bathymetry from different sources along the profile is shown at the BOTTOM). The figure reflects the importance of precise bathymetry grids.

# 5. Experiments completed and preliminary results
## 5.1 Magnetics

(B. Schreckenberger)

### Display of magnetic anomalies

Magnetic anomalies were measured during Leg 4 on profiles with a total length of 3370 km. Figure 5.1.1 shows the location of all lines where magnetic measurements were performed. The magnetic and gravity group uses a different profile numbering system than the seismic group in order not to interfere with profile numbering from the former Legs 2 and 3 where the profile names SO161-01 and so on were already used. Therefore, we started on Leg 4 with line number SO161-100 for lines without seismic measurements. Lines with wide angle seismics have line numbers SO161-201 to SO161-205 in the magnetic chapter and SO161-01 to SO161-05 in the seismic chapters.
Figure 5.1.2 shows the magnetic anomalies measured during Leg 4. The profiles are widely spaced and do not show a clear image of the magnetic field in the investigated area. Figures 5.1.3. to 5.1.7 show composite figures that display the magnetic and the free-air gravity anomaly on the top together with a clipping of the bathymetric map and a cross section of the seafloor along the profile line. This display makes it possible to inspect and identify the nature of the magnetic (and gravimetric) anomalies with respect to bathymetric features (e.g. oceanic and continental domains).
For a more detailed discussion also anomalies from the former Legs 2 and 3 are displayed in Figure 5.1.8 for the southern part of the survey area and in Figure 5.1.9. for the northern part.

### Magnetic anomalies in the southern survey area (line SO161-202)

In the southern part of the survey area only one line was shot during Leg 4 (SO161-201, refraction seismic line SO161-02, reflection seismic line SO161-38/42). It runs from the oceanic crust in the west on to the continental shelf (Figure 5.1.3). Also in terms of the magnetic anomaly there is a clear distinction between the oceanic and the continental domain. Over oceanic crust we have strong positive anomalies of about 200 nT which obviously belong to magnetic seafloor lineations. Figure 5.1.8 shows this line together with magnetic anomalies from Leg 3. It can be seen that north of 38°S clear magnetic lineations strike in a NW-SE direction. On the other hand, the anomaly pattern becomes very complicated to the SE of the line because the Mocha FZ enters the trench from the SW exactly where line SO161-201 meets the deformation front. This causes the destruction of magnetic lineations on the more southerly lines SO161-041, -035 and -037. Also the easternmost positive anomaly on line SO161-043 that does not have an equivalent in the lineations to the NW seems to be caused by this FZ. After Cande et al. (1989) the lineations between 37°S and 38°S belong to Chrons 11 and 12 (29-31 Ma). Although the data set at hand is not sufficient to prove this interpretation a quiet magnetic area to the NE between 37°S/75°W and 36°10'S/74°W is compatible with it. Some positive anomalies at 36°S/74°W would then indicate that anomaly C13 or 33 Ma old crust enters the trench at 36°S.
The landward slope and the shelf area are characterized by the absence of long-wavelength anomalies. Instead short-wavelength anomalies indicate that shallow magnetic source bodies must be present. If the whole basement rocks were magnetized then it could be expected that the steep slope of the basement towards the trench caused a magnetic anomaly along the slope. There is a faint indication that in the magnetically quiet area on lines SO161-024, -047, -046, -045 and -044 a small positive anomaly along the 3000 m depth contour line can be observed. If there exists a weak magnetization within the basement the anomalies east of profile kilometer 120 (Figure 5.1.3) could be caused by topographic undulations of its surface. Another possibility to explain the anomalies would be the presence of volcanic material (tuff, ashes) within the sedimentary cover which would not be uncommon in this area which is marked by the presence of many volcanoes. Line SO161-025 that runs along the shelf from north to south (Figure 5.1.8) confirms the character of the landward anomalies.

### Magnetic anomalies in the Condor area

The magnetic anomalies in the Condor area were intensively studied by Yanez et al. (2001). Their dense bathymetric and magnetic survey shows many details like magnetic lineations (C17 and C18, 36.5 to 38.5 Ma) and the anomalies caused by the O'Higgins Seamounts and the buried Papudo

Seamount. The magnetic lineations become weaker where the oceanic crust bends down into the trench and they become more or less invisible under the outer trench slope.

Line SO161-202 (Figure 5.1.4) runs along the northern edge of the Condor area and shows some clear magnetic lineations that are abruptly terminated landward of the trench. They represent the magnetic lineations C17n.2 and C17n.3 (38 Ma) (Reichert et al., 2002). Also the lines SO161-125 and -123 (Figure 5.1.9) show the same character and the general NW-SW strike direction of the lineations on the Nazca Plate in this area. The quiet zone landward of profile kilometer 100 in Figure 5.1.4 is not caused by the increasing depth to the source layer due to subduction but by the wide normal polarity interval C18. Figure 5.1.9 shows the data from the longer reflection seismic line SO161-018 (see also Figure 1.6.3). At the westward end of this line outside of the Condor area a very high amplitude magnetic anomaly occurs. It is located over oceanic crust that is inconspicuous except of a dubious reflection that extends 3 s TWT below the basement. Between SP 4000 and 5000 (Figure 1.6.3) the shape of the anomaly is similar to the shape that would be expected from lineation C16n.2 but the amplitude is twice as high than that of anomaly C17. To some extend this anomaly seems to be linear with a NW-SE strike direction because SO161-121 also shows the strong minimum and because line SO161-117 seems to run entirely within the maximum. The bathymetry in Figure 5.1.9 shows a linear SW-NE striking feature that might be a fracture zone but that does not have a distinct expression in the satellite altimetry gravity maps (see below 5.2). On line SO161-012 (Figures 1.6.5 and 5.1.9) a distinct rise in the amplitude level occurs in the extension of this feature to the NE at 31°S/73.5°W. Here the crust has a considerably different age which hints to the conclusion that the reason for the enhancement of the amplitude must lie in the structure of the oceanic crust. Cande et al. (1989) and Cande and Haxby (1991) show a fracture zone (Challenger FZ) which lies about 50 km west of our anomaly in question and that also does not correspond to a feature in the satellite altimetry map. Possibly this fracture zone lies more in the east causing the unusual magnetic amplitudes.

Figure 5.1.5 (line SO161-203) and Figure 5.1.6 (line SO161-204) show two lines that cross each other over the O'Higgins Seamount. The northern end of line SO161-203 also shows the high amplitudes that were discussed in the last paragraph. The O'Higgins Seamount which comes up to about 1000 m waterdepth displays a complicated high amplitude magnetic anomaly with a sharp minimum over its crest. The larger one of the seamount group, the O'Higgins Guyot, which was crossed by line SO161-204 shows a more complicated anomaly pattern with two positive peaks separated by a narrow minimum that may indicate the presence of basalts with different magnetic polarities. Because the situation is highly three-dimensional it is difficult if not impossible to draw reasonable conclusions without detailed 3D modeling. The seamount also causes a broad long-wavelength anomaly along line SO161-203 from profile kilometers 80 to 180. In the reflection seismic section (Figure 1.6.4) the upper crust in this area does not show structures that would give an explanation for this anomaly. The modeling of the refraction seismic line on the other hand results in a crustal thickening in exactly the same area. Usually we do not see a magnetic expression from the lower parts of thick oceanic crustal roots but its presence may indicate that volcanism in general was stronger and that also the upper basaltic parts of the crust have a greater thickness. There is another location in the SW of the survey area (Figure 5.1.9) were an unusual high magnetic anomaly occurs on lines SO161-018 and SO161-204 which does not yet have an explanation.

Further in the north line SO161-205 (Figure 5.1.7 and 5.1.9) crosses the slope, the trench and the oceanic crust. Magnetic anomalies around 73°W represent lineations of C18 age (39 Ma). The trend of the lineations is also imaged on lines SO161-015 and -014. Over the landward trench slope the magnetic anomalies are very smooth. This shows that the continental basement does not have a high magnetization.

In summary the magnetic anomalies raise some questions especially at locations where unusually high amplitudes are observed and where the magnetic lineation pattern is disturbed by fracture zones. In all these situations there is the need for three-dimensional modeling and for the support from seismic and gravity interpretations.

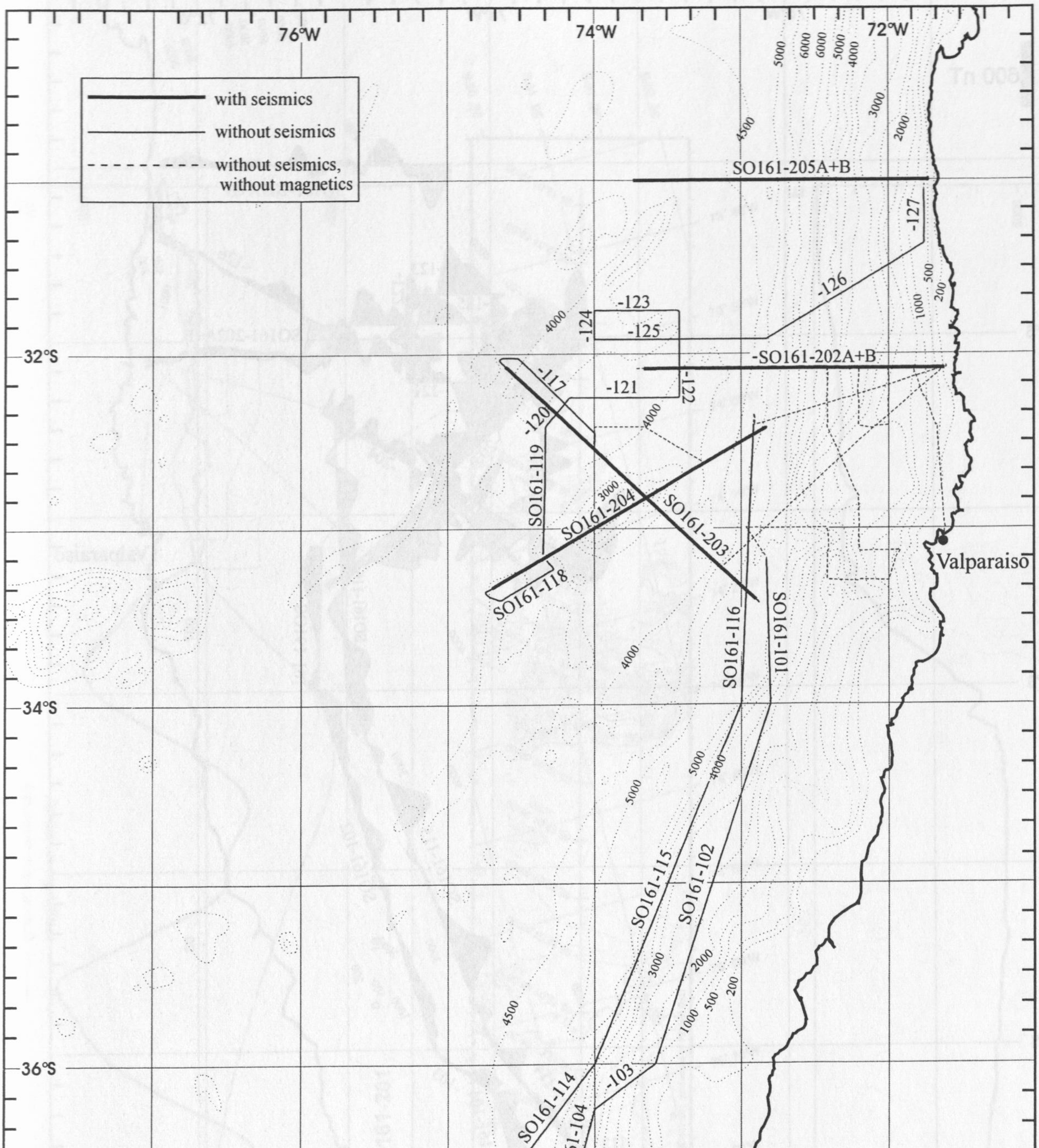

Figure 5.1.1: Location map of geophysical survey lines of cruise SO-161, Leg 4.

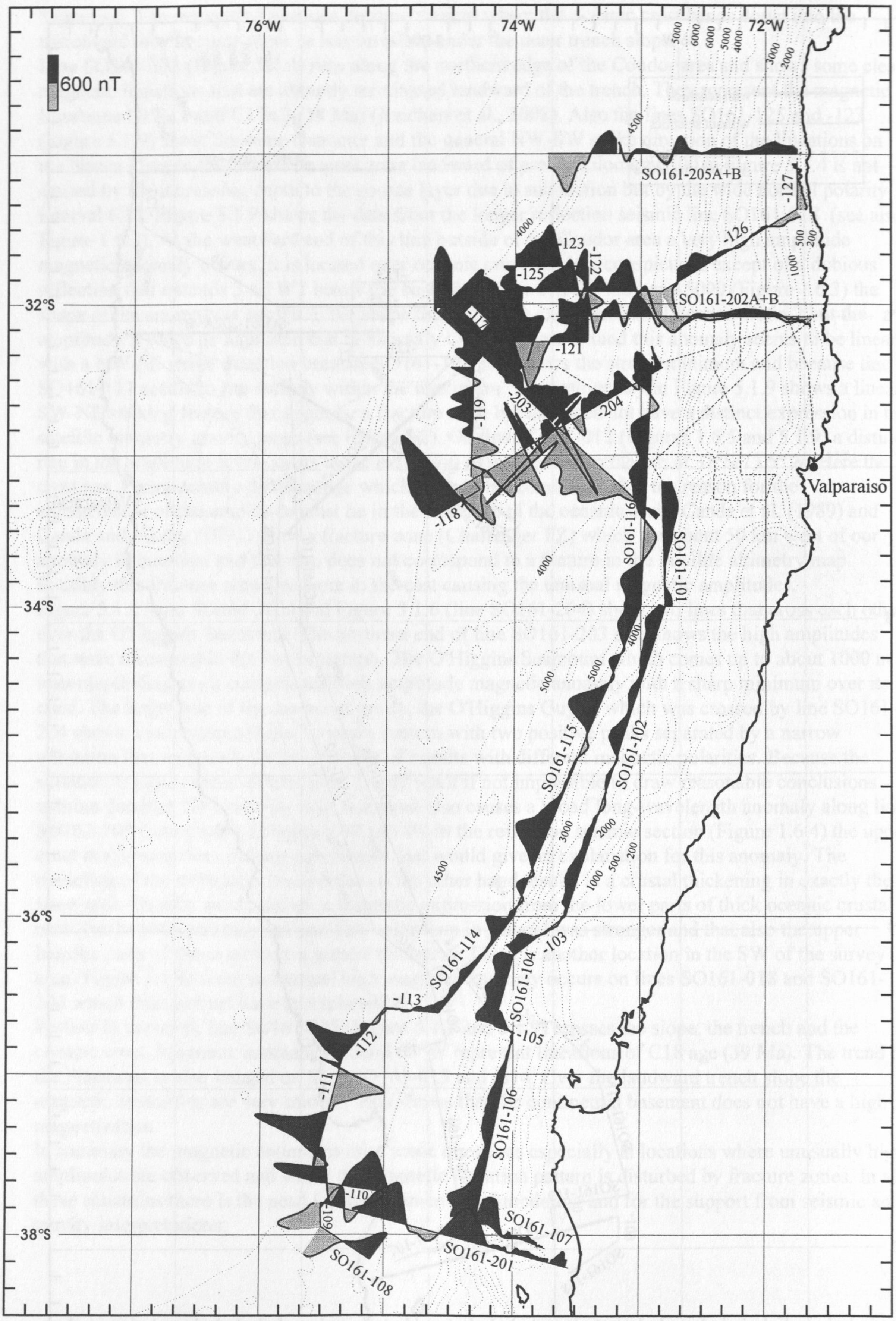

**Figure 5.1.2:** Magnetic anomalies measured during cruise SO-161, Leg 4. Dark shading denotes positive anomalies. Light shading denotes negative anomalies.

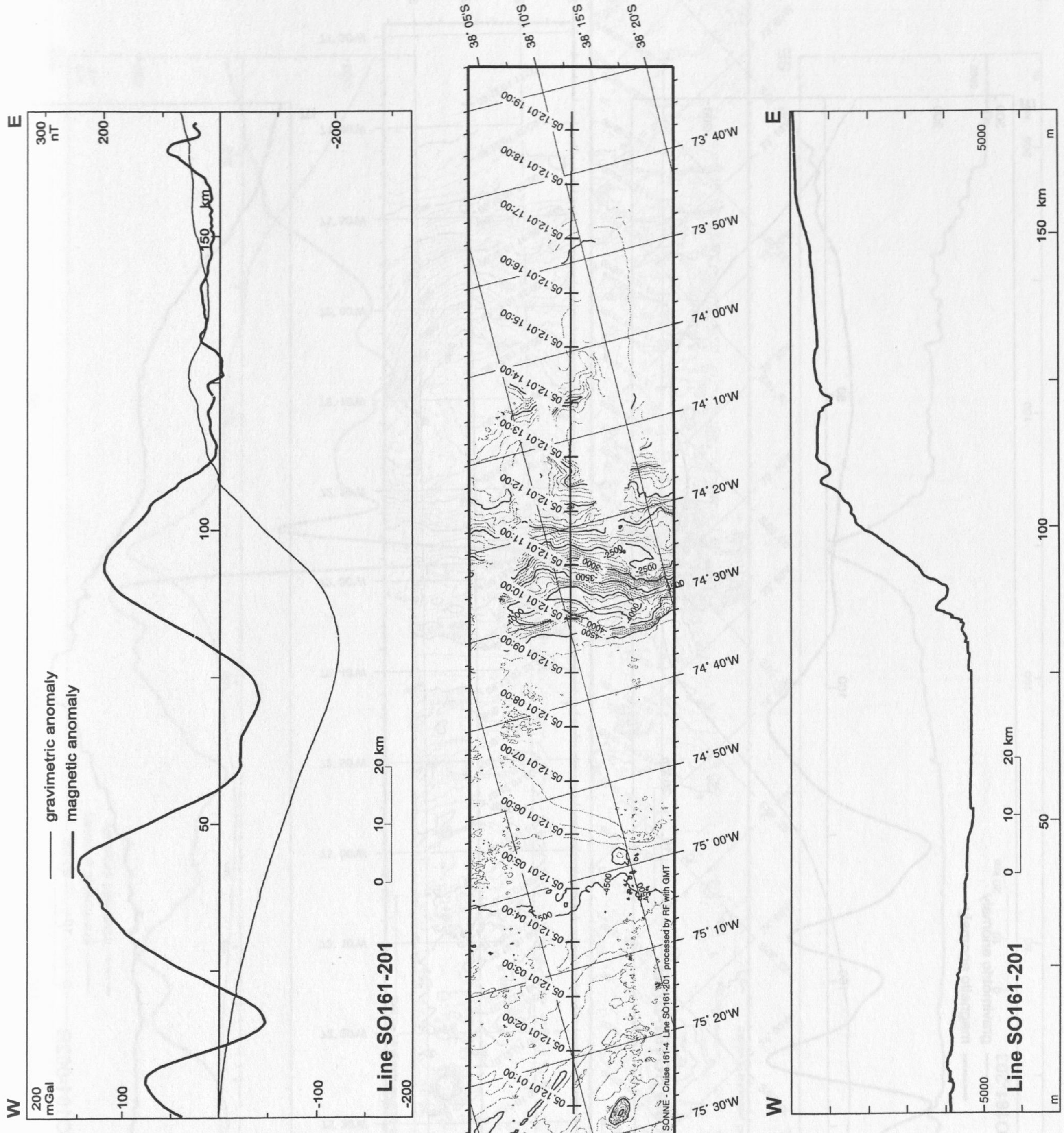

**Figure 5.1.3:** Composite display of free-air gravity and magnetic anomalies (upper panel), SIMRAD swath echosounder bathymetry (middle panel) and waterdepth displayed as a cross-section (lower panel) for line SO161-01 (seismic line numbering) or SO161-201 (magnetic line numbering), respectively.

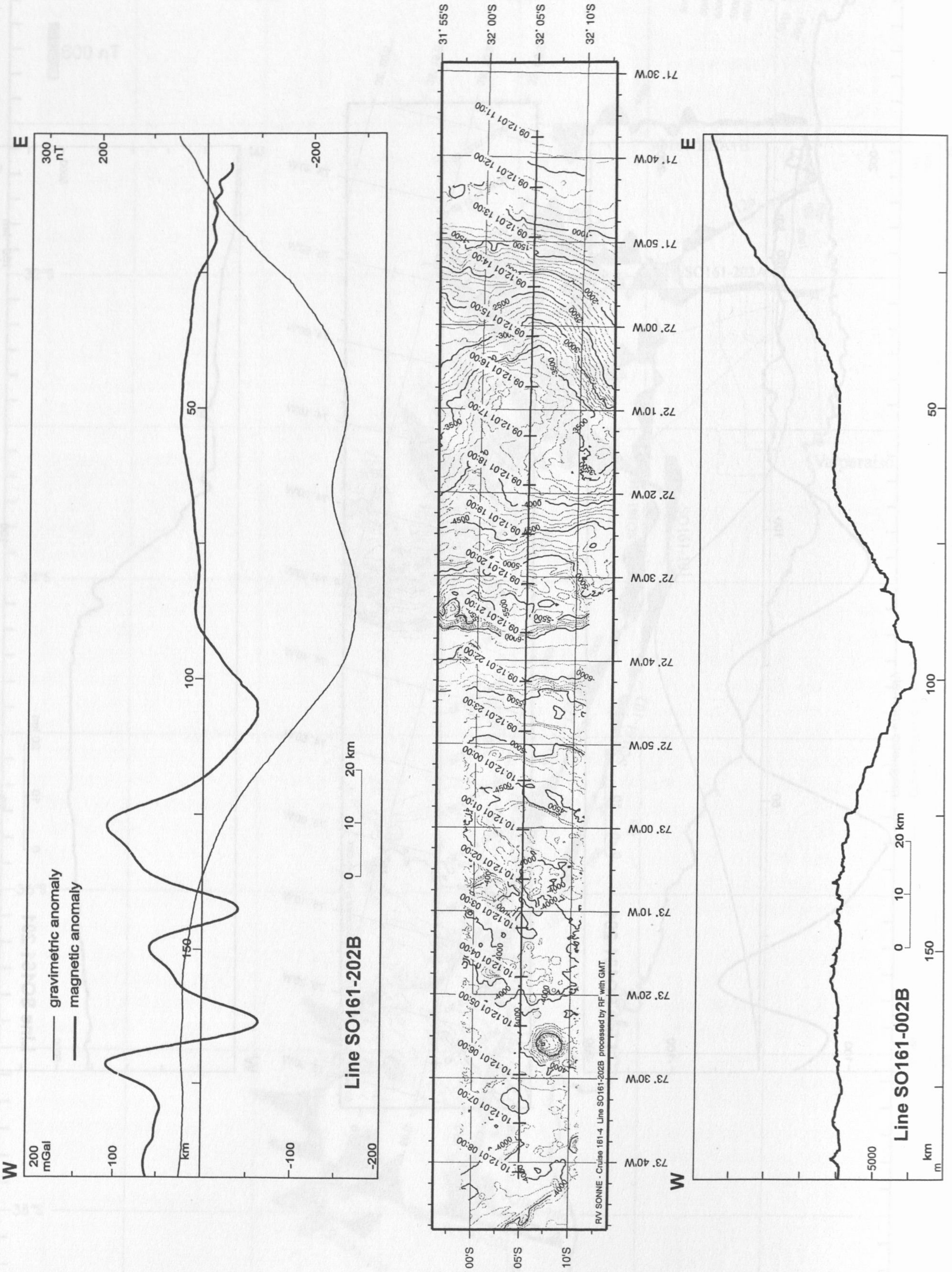

**Figure 5.1.4:** Composite display of free-air gravity and magnetic anomalies (upper panel), SIMRAD swath echosounder bathymetry (middle panel) and waterdepth displayed as a cross-section (lower panel) for line SO161-02 (seismic line numbering) or SO161-202 (magnetic line numbering), respectively.

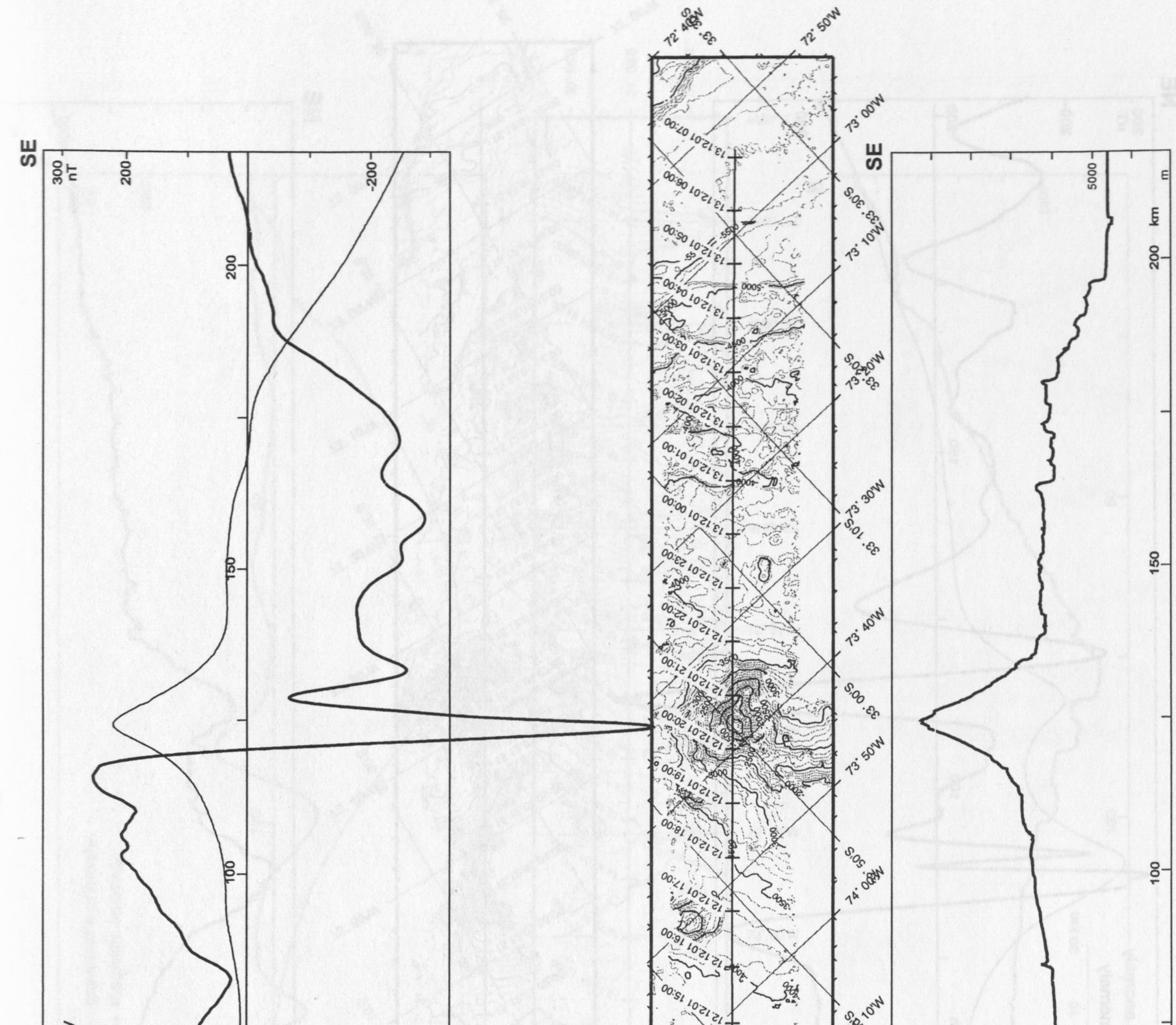

**Figure 5.1.5:** Composite display of free-air gravity and magnetic anomalies (upper panel), SIMRAD swath echosounder bathymetry (middle panel) and waterdepth displayed as a cross-section (lower panel) for line SO161-03 (seismic line numbering) or SO161-203 (magnetic line numbering), respectively.

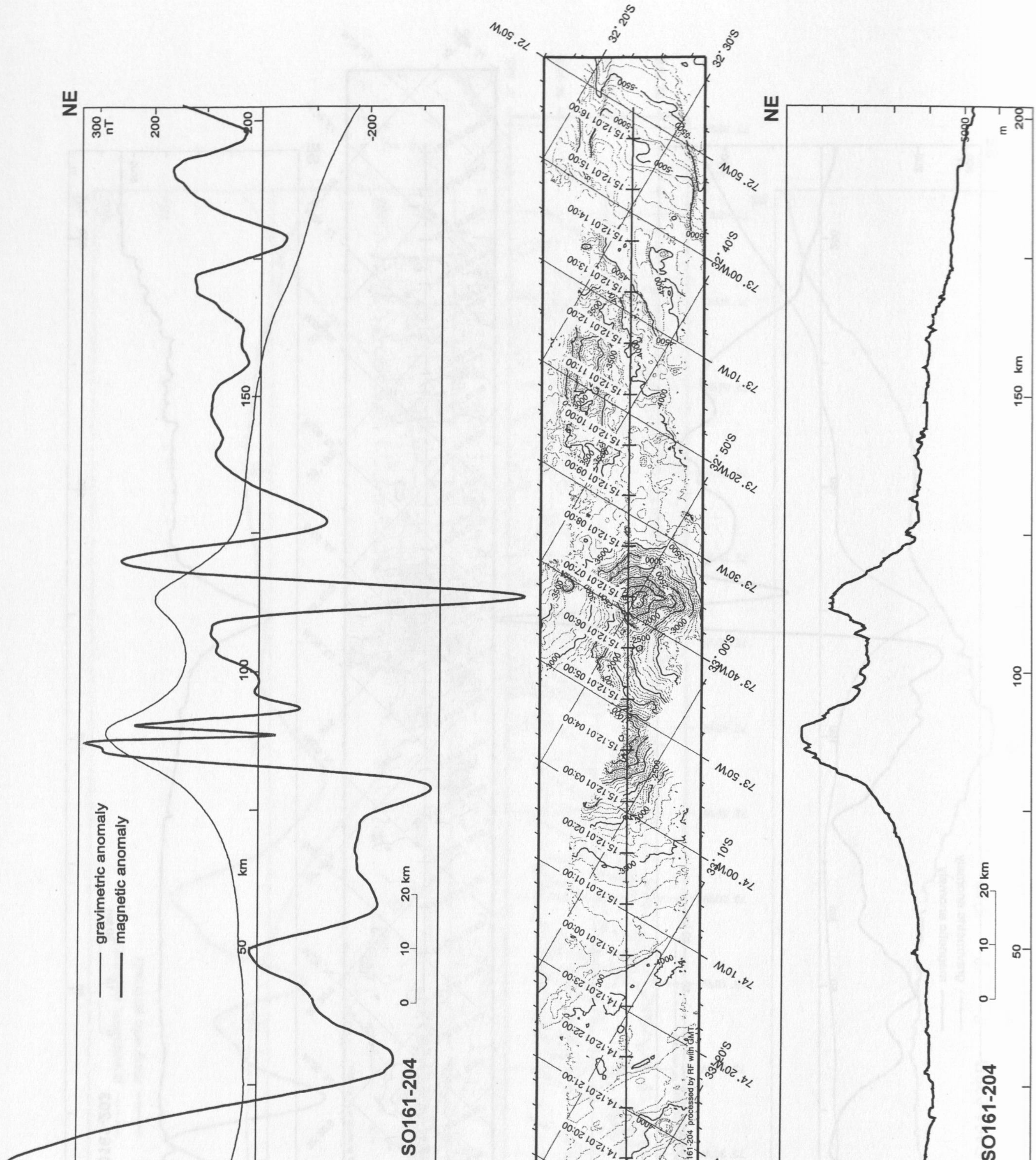

**Figure 5.1.6:** Composite display of free-air gravity and magnetic anomalies (upper panel), SIMRAD swath echosounder bathymetry (middle panel) and waterdepth displayed as a cross-section (lower panel) for line SO161-04 (seismic line numbering) or SO161-204 (magnetic line numbering), respectively.

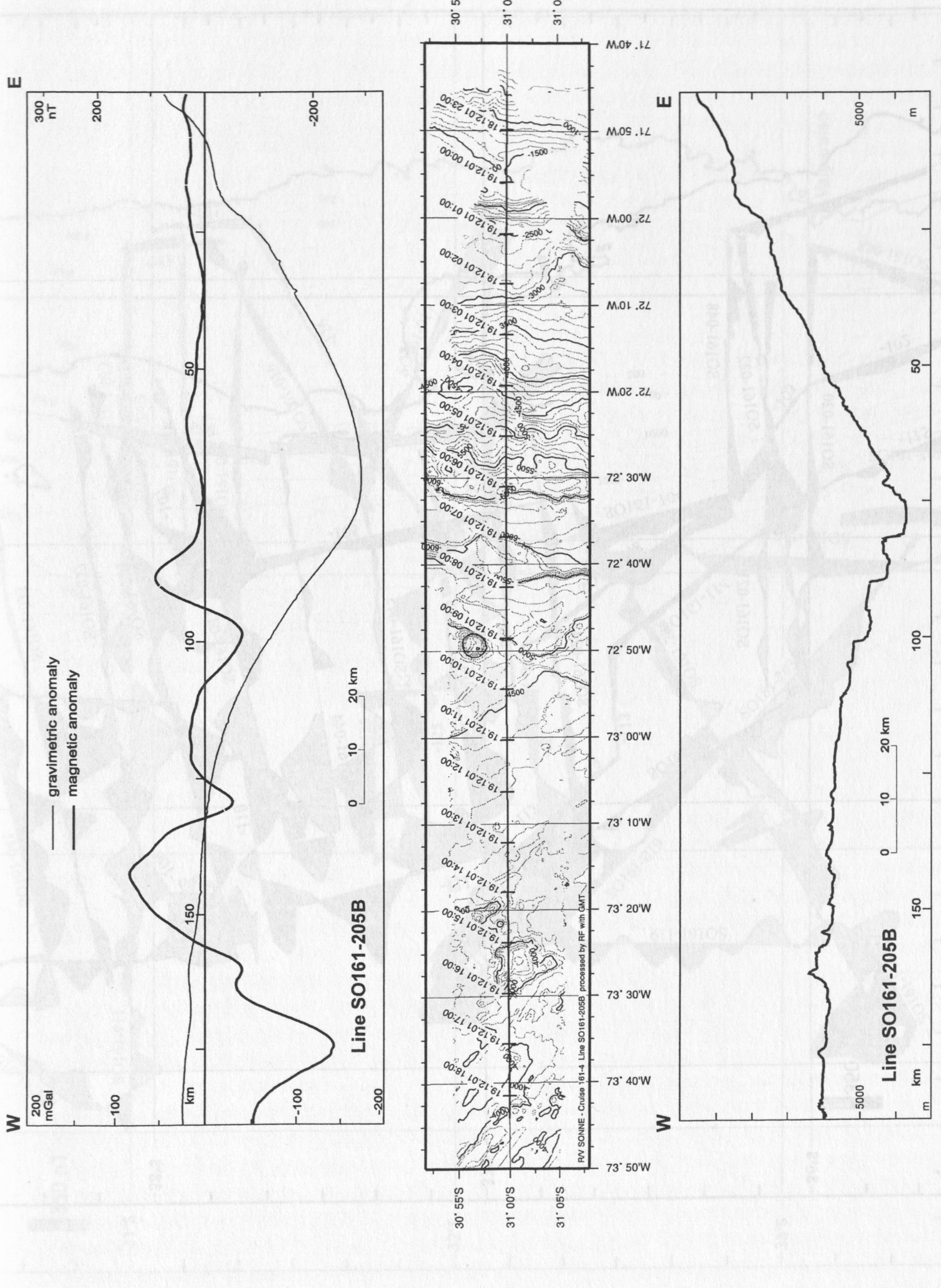

**Figure 5.1.7:** Composite display of free-air gravity and magnetic anomalies (upper panel), SIMRAD swath echosounder bathymetry (middle panel) and waterdepth displayed as a cross-section (lower panel) for line SO161-05 (seismic line numbering) or SO161-205 (magnetic line numbering), respectively.

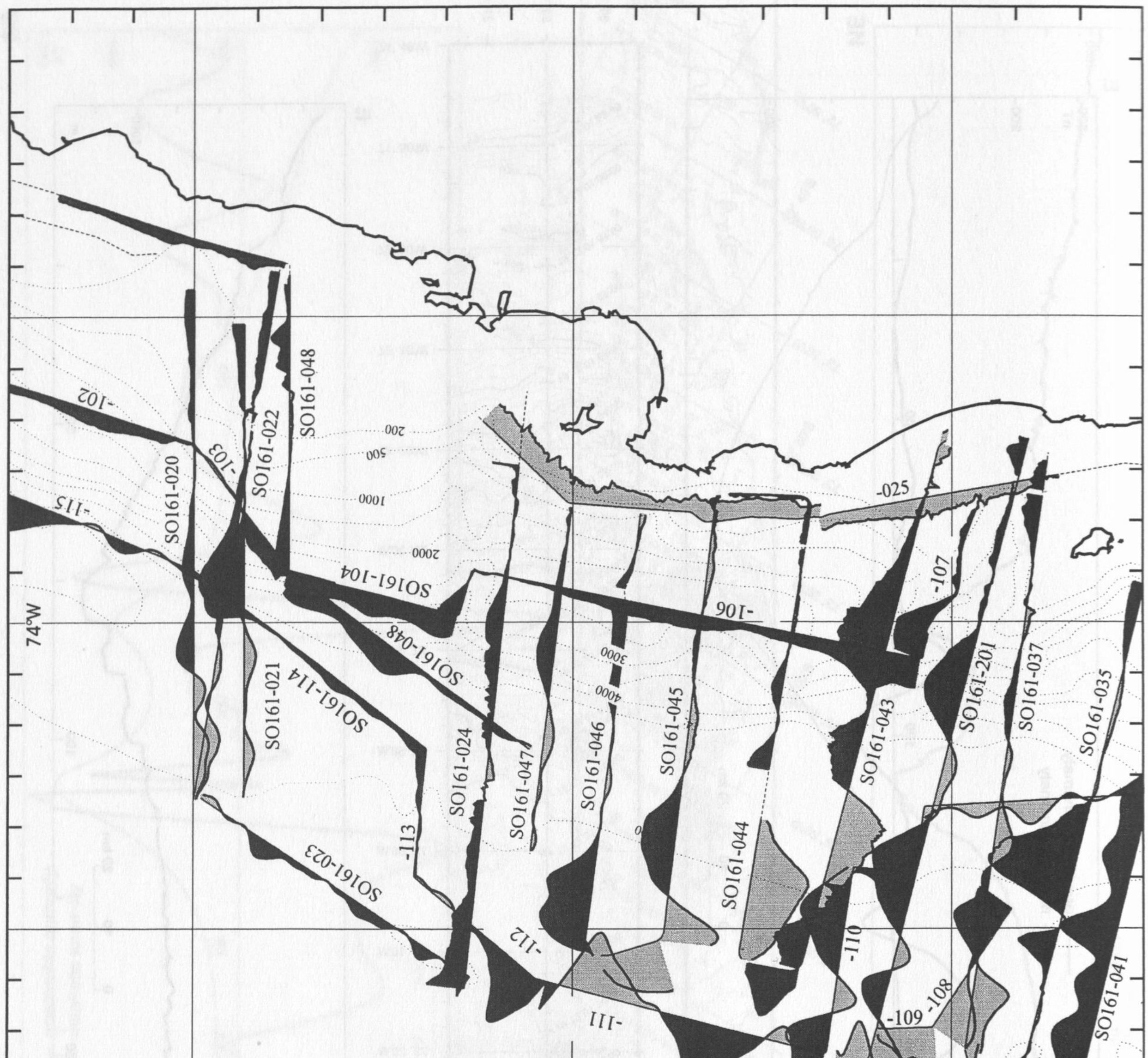

**Figure 5.1.8:** Magnetic anomalies measured during Leg 3 and 4 in the southern part of the survey area. Dark shading denotes positive anomalies. Light shading denotes negative anomalies.

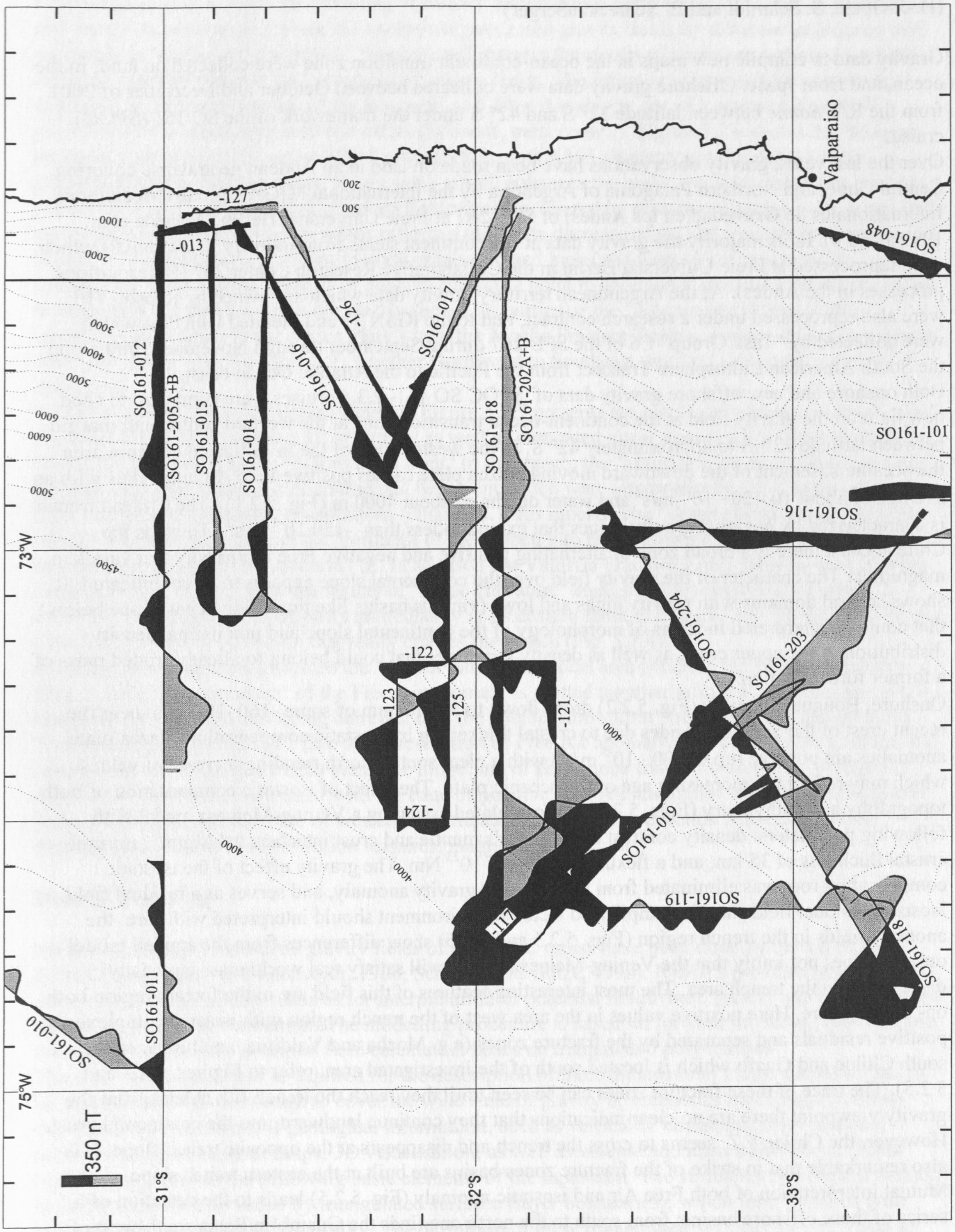

**Figure 5.1.9:** Magnetic anomalies measured during Leg 3 and 4 in the northern part of the survey area. Dark shading denotes positive anomalies. Light shading denotes negative anomalies.

## 5.2 Preliminary results: Gravity

(H.-J. Götze, S. Schmidt and B. Schreckenberger)

Gravity data to compile new maps in the ocean-continent transition zone were collected on land, in the ocean, and from space. Offshore gravity data were collected between October and December of 2001 from the R/V *Sonne* between latitude 32° S and 42° S under the framework of the SO 161 (SPOC) cruise.

Over the last years, gravity observations have been made on land in an Andean geotraverse covering Central Chile, and Northern Patagonia of Argentina by the international MIGRA group (**M**ediciones **I**nternationales de **Gr**avedad en los **A**ndes) of SFB 267 at Freie Universität Berlin (Araneda et al. 1999 a and b). In its majority the gravity data at the continent stems from industry data (ENAP) which were reprocessed at Freie Universtät Berlin in the Collaborative Research Center 267 (Deformations processes in the Andes). At the Argentinean territory gravity data which are owned by Repsol-YPF were also reprocessed under a research contract, tied to the IGSN 71 and blended with data which were collected by "Task Group" C6 of the SFB 267 during September through November 2000 along the South American Lithosphere Transect from the Pacific to the Atlantic Ocean coast.

Both onshore and new offshore gravity data of SPOC SO 161- 2,3,4 cruises were combined to shed new light on the gravity field at the continent-ocean transition zone at the western continental margin between latitude 32° S to approximately 42° S. In the western part of the investigated offshore area the oceanic basement of the downward moving Nazca plate causes positive Free Air anomalies with an average of about $10 - 20 \cdot 10^{-5}$ m/s$^2$ and water depths of about 4000 m (Fig. 5.2.1). The Chilean trench is characterized by negative gravity values that extend to less than $-150 \cdot 10^{-5}$ m/s$^2$. Towards the Chilean coast there is a broad zone of alternating positive and negative Free Air gravity that varies in magnitude. The character of the gravity field over the continental slope appears to be complicated. It shows several domains with gravity highs and lows (various basins like the Valdivia basin, see below) that could be interpreted in terms of morphology of the continental slope and non normal density distribution in the upper crust, as well as density structures that could belong to already eroded parts of a former forearc region.

Onshore, Bouguer anomaly (Fig. 5.2.2) drops down to a minimum of some $-160 \cdot 10^{-5}$ m/s$^2$ near the recent crest of the Southern Andes due to crustal thickening by isostatic compensation. Nazca plate anomalies are positive (up to $300 \cdot 10^{-5}$ m/s$^2$) with a clear south - north trending increase of values, which may reflect the increasing age of the oceanic plate. The effect of isostatic compensation of both topography and bathymetry (Figs. 5.2.3) was calculated assuming a Vening-Meinesz model with following parameters: density contrast of the Earth's mantle and crust interface 0.4 Mg/m$^3$, normal crustal thickness of 35 km, and a flexural rigidity of $10^{23}$ Nm. The gravity effect of the isostatic compensation root was eliminated from the Bouguer gravity anomaly, and serves as a residual field. Isostatic residual fields in this complicated tectonic environment should interpreted with care: the anomaly fields in the trench region (Figs. 5.2.3 and 5.2.5) show differences from the applied model only and does not imply that the Vening-Meinesz model will satisfy real world mass or density distribution in the trench area. The most interesting features of this field are in the forearc region both on- and offshore. Here positive values in the area west of the trench region with isolated complexes of positive residuals and separated by the fracture zones (e.g. Mocha and Valdivia, and further to the south Chiloe and Guafo which is located south of the investigated area, refer to Figures. 5.2.3 and 5.2.5). The trace of these fracture zones can be seen until they reach the trench fill; at least from the gravity viewpoint there are no clear indications that they continue landward into the continental crust. However, the Chiloe F.Z. seems to cross the trench and disappears at the opposite trench slope. It is also remarkable that in strike of the fracture zones basins are built at the eastern trench slope.

Mutual interpretation of both Free Air and isostatic anomaly (Fig. 5.2.5) leads to the detection of a series of these offshore basins: from south to the north one finds the Guamblin Basin south-west of Chiloe, the Chiloe and Pucatrihue Basins west and north of Chiloe, the Valdivia Basin and the Arauco Basin offshore the Peninsula of Arauco and further to the north the Chaco-Itata and the Valparaiso Basin which are marked by strong negative local gravity anomalies mainly in the isostatic residual gravity.

## Interdisciplinary interpretation

Next steps prior to 2D and 3D modeling of density distribution e.g. by forward modelling procedures and inversion techniques include the analysis of processed gravity fields by different techniques like curvature or "Euler Deconvolution". Here we will present the results of curvature techniques which enhance internal behavior and structures of gravity fields. The following figures show only three examples of curvature studies of the Bouguer- and, Free Air gravity out of a series of manifold possibilities the interactive software offers (Schmidt, pers. comm.). Figure 5.2.6 shows the Bouguer anomaly (left side) of the entire SPOC area together with KMS altimetry gravity data and the calculated field´s "dip-curvature" (right side) which enhances the highs and lows of the BA gravity. From North to South the Juan Fernandez Ridge is characterized by positive curvature in its center and surrounding negative curvature which reflects a moderate decrease of gravity towards the positive center. The Chile trench is shown in north-south oriented highs and lows of curvature. At the continental slope various patterns of positive curvature point to anomalous density distribution. More to the South the fracture zones are clearly shown. In particular the "dip curvature" proves the complicated situation at the Nazca Plate where the Mocha Fracture Zone is a rather short element and does not "touch" the Valdivia F.Z. Another Northwest to Southeast trending lineament is clearly detectable.

To shed light on this complicated situation Figure 5.2.7 presents the results of "shape curvature" which enhance convex and concave 3D structures as well as elongated linear features. For better orientation the figure contains also the "deformation front" in the trench, the "hinge line" at the continental slope and the westward extension of continental basement which were interpreted by Ch. Gaedicke from high resolution bathymetry observations (chapter 5.1 this report). The "shape curvature" shows that Mocha fracture extends from the Northeast of the graben into the Southwest, however disappears before it merges with the Valdivia F.Z. In addition the Valdivia Fracture Zones behaves as a "double Fracture Zone" if we follow the results of "shape curvature" analysis. The northern zone seems to cross the trench and but disappears immediately at its eastern flank in a basin. The same is true for the Chiloe F.Z. more to the South that really crosses the trench (Fig. 5.2.4).

A rather detailed picture provides the "dip curvature" in a local area offshore the Arauco Peninsula (Fig. 5.2.8). "Dip curvature" of the Free Air anomaly is plotted together with the interpretation of Ch. Gaedicke and shows a satisfying correlation of the "deformation front" trend, and in some parts the "western edge of trench fill". Due to the resolution of Free Air anomalies we are not able to detect the central channel inside the trench area. The hinge line of shelf-slope transition seems to correspond offshore the Aurauco Peninsular with the edge of positive Free Air anomalies. Future modelling will prove to what degree the "line of western continental basement" corresponds with geophysical findings particularly from reflection seismics, magnetics and gravity.

## Density Modelling

Model matching of measured gravity fields of the SPOC cruise have been done by the aid of the IGMAS (e.g. Götze and Lahmeyer, 1988; Schmidt and Götze, 1998). IGMAS provides interactive, computer aided graphical features for interpretation of potential fields (both gravity and magnetics) by means of numerical simulation. The modelling procedure is based on forward modelling methods and the algorithm used for potential field calculation bases on triangulated polyhedrons.

The data structure, which is required for the description of three dimensional model geometry has to be simple and flexible enough to cover the wide field of gravity or magnetics modelling: It should facilitate representations of geological information, such as vertical or horizontal cross sections, surface and depth contour maps, 3D visualisation, as well as volume and mass calculations. These requirements lead to the following basic elements of the input data: The structures (geological bodies) to be modelled are bounded by triangulated surfaces (layer boundaries), which limit domains with constant density and/or susceptibility. The definition of these triangulated surfaces may be given in two different ways: By defining polygons (lines) along vertical, parallel cross sections. The triangulation between the vertical planes is done automatically. The data input is two-dimensional, whereas the construction of the final 3D model structures is performed by IGMAS and does not require detailed knowledge about topology, data structures or triangulation techniques.

Interactive modification of model parameters, e.g. geometry, density and susceptibility, access to the numerical modelling process and direct visualisation of both, calculated and measured fields. This enables the interpreter to design the model as realistic as possible. A basic requirement for modelling is the existence of ideas and hypothesis on the investigated area, i.e. the availability of quantitative or qualitative constraints. In our case these model constraints came from 2D seismic interpretations of profiles 02 and 03, SO 161-4. The outlined procedure applied to complex interpretation tools requires a synoptic visualisation of the necessary constraining data, which have to be selected and activated by the user. Modern GeoInformationSystems (GIS) handle this task. Today these systems are based frequently on object orientated systems (OOS). The advantage of OOS is an increasing effectivity, because of direct access to data and information by the definition of 'geo-objects' (Schmidt and Götze, 1998).

The preliminary 3D density model bases on both geometry and velocity modelling of profiles SO 161 - 02, 03 and 04 (refer to chapter 5.4.3). Densities have been calculated from velocities by using standard tables. Together with model geometry (model vertices) they serve as the input files for IGMAS. The model consists of six east-west oriented vertical cross sections where profile 02 in the north coincides exactly with the location of vertical cross section 5. This cross section is shown in Fig. 5.2.9 as a screen shot: in the upper box of the Figure the modelled gravity (stippled line and asterisks) matches perfectly the measured Bouguer gravity (solid line). The lower box shows both model geometry and densities in $Mg/m^3$. Additionally, the seismic velocity model which was used as a constraint overlies the density model. In general, the fit of measured and modelled gravity field is satisfying although we have to state that this 3D interpretation has to be read with care: both the velocity and density models base on preliminary assumptions. There is one inconsistency which has be remodelled later. Between profile km 150 and 200 the velocity model consists of a steep stepwise lateral velocity gradient which can not be proved by density modelling. Secondly, the density model suggests a slightly decreased depth (1- 2 km) of the model Moho if it is compared with the velocity model. Anyway, main model features, as there are the structure of the backstop (density 2.75 $Mg/m^3$), the lower crust boundary and the distribution of sediments (1.2 Mg/m) provide a very consistent picture of the ocean - continent transition zone in seismics and gravity.

Figure 5.2.10 visualises the 3D model structure in a perspective view from Southeast to the Northwest. The double peak of the O´Higgins sea mount is seen in the centre of the image and a varying inclination of the sedimentary layer (density 2.4 $Mg/m^3$) with steeper slops in the South and a flattening to the North. The two figures prove a moderate up doming (approximately 1 km) of the oceanic crust before it enters the subductionzone (fore bulge). Future modelling has to include continental crustal structures and should be performed on base of a higher resolved density model structure by including more vertical model planes. After seismic modelling has been terminated also more model constraints will be available.

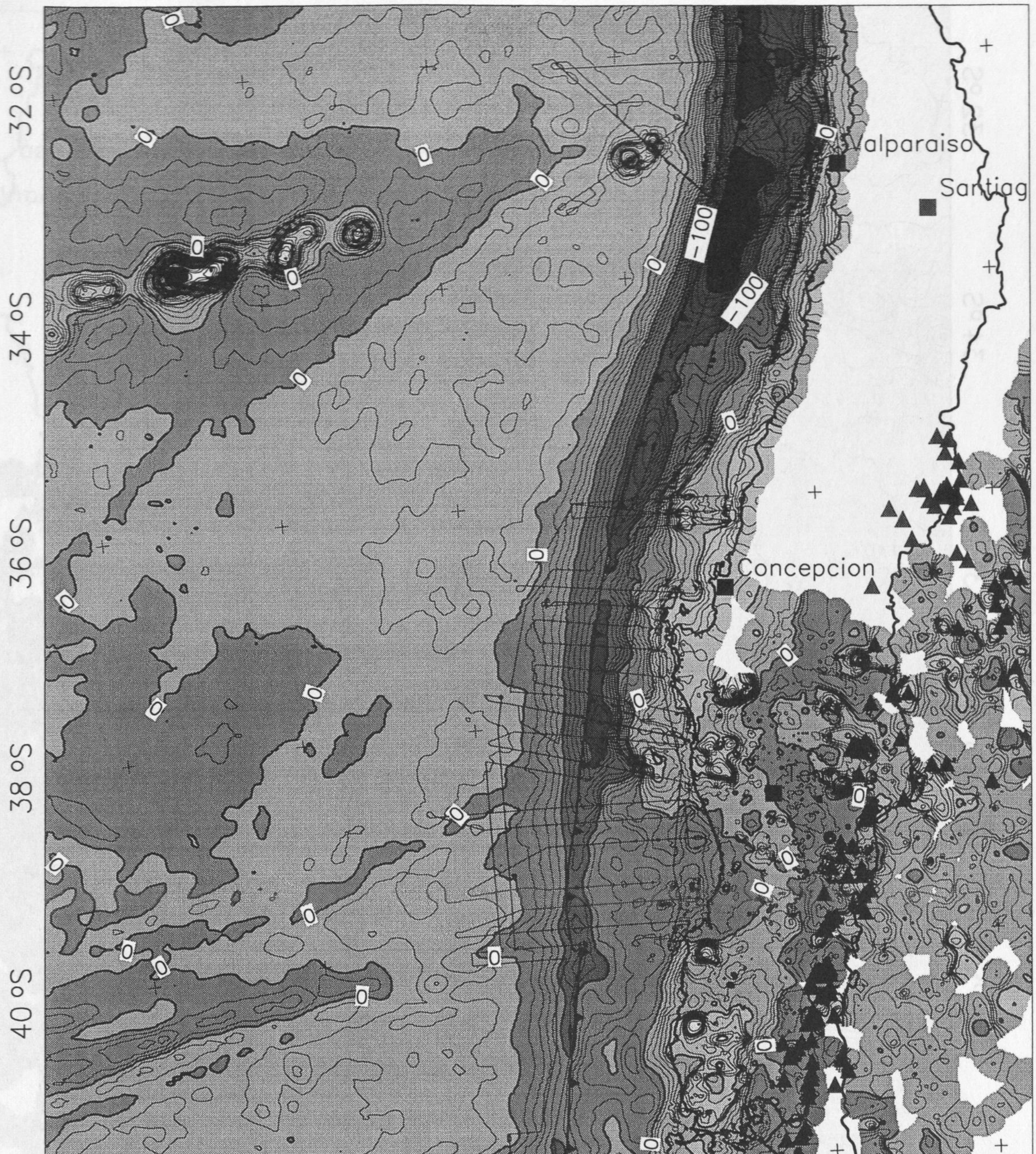

18.12.2001 (UTM Projection: −69, Scale 1 : 6666667)

**Figure 5.2.1:** Free Air Anomaly (on- and offshore). The underlying grid of gravity was compiled by merging KMS satellite altimetry data and SPOC gravity observations. On land Free Air gravity was taken from the SFB 267 data files. Dominating anomalies of the map are the anomalies caused by the O´Higgins Sea Mount (west of Valparaiso), the Juan Fernandez Ridge, the Chile Trench and the fracture zones at the Southern Nazca Plate (refer also to Figs: 5.2.6 and 5.2.7).

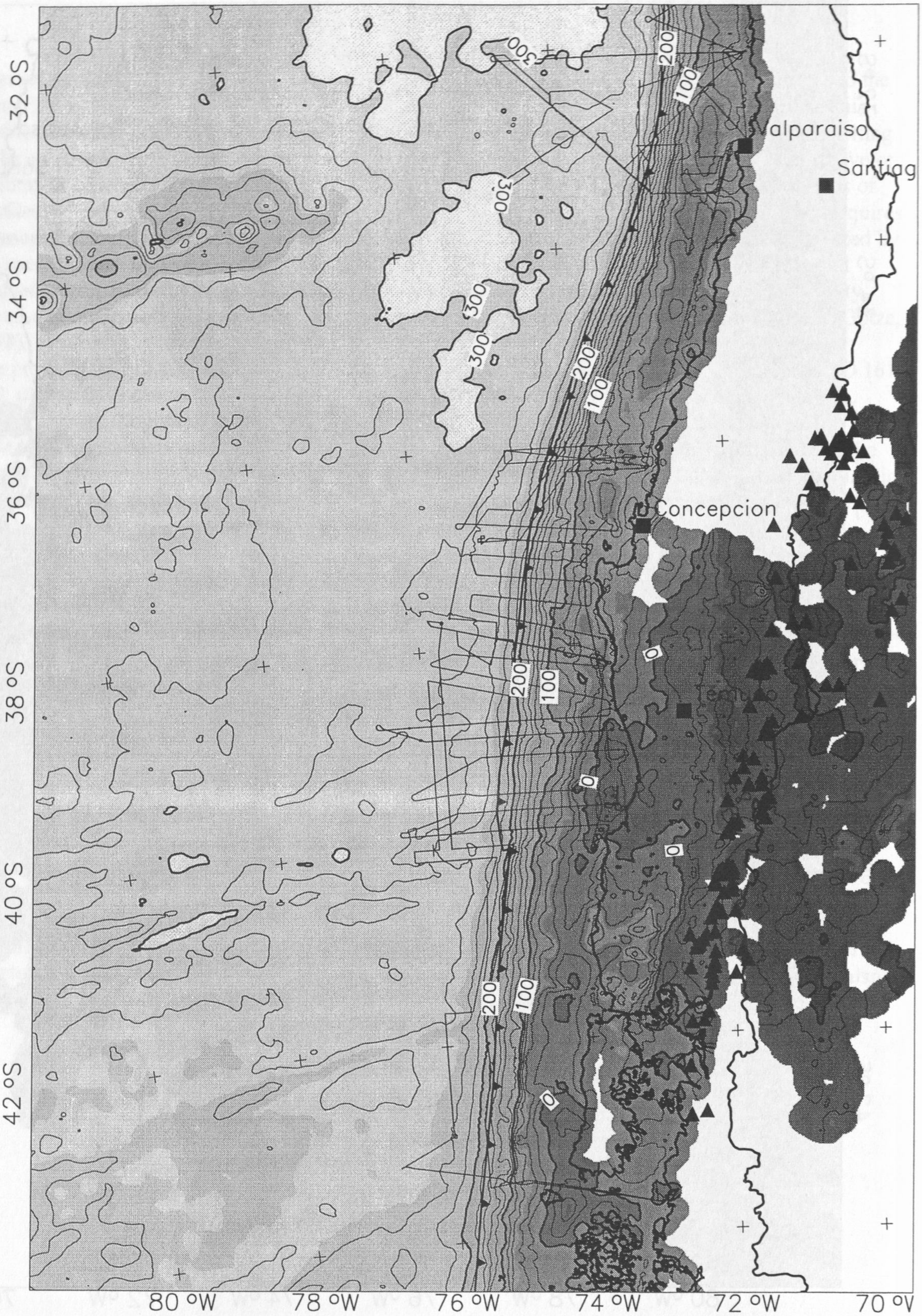

18.12.2001 (UTM Projection: −69, Scale 1 : 6666667)

**Figure 5.2.2:** Station complete Bouguer Anomaly (on- and offshore). The underlying grid of gravity was compiled by merging KMS satellite altimetry data and SPOC gravity observations. On land Bouguer gravity was taken from the SFB 267 data files. Reduction densities were 2.67 Mg/m$^3$ and 1.67 Mg/m$^3$ respectively; reduction radius was 100 Km. Ocean bottom topography was reduced by merging ETOPO 5 and the Zapata bathymetry grid. Dominating anomalies of the map are the anomalies caused by the O´Higgins Sea Mount (west of Valparaiso), the Juan Fernandez Ridge, and the fracture zones at the Southern Nazca Plate (refer also to Figs: 5.2.6 and 5.2.7). The trench area is dominated by the strong gradient of increasing anomaly.

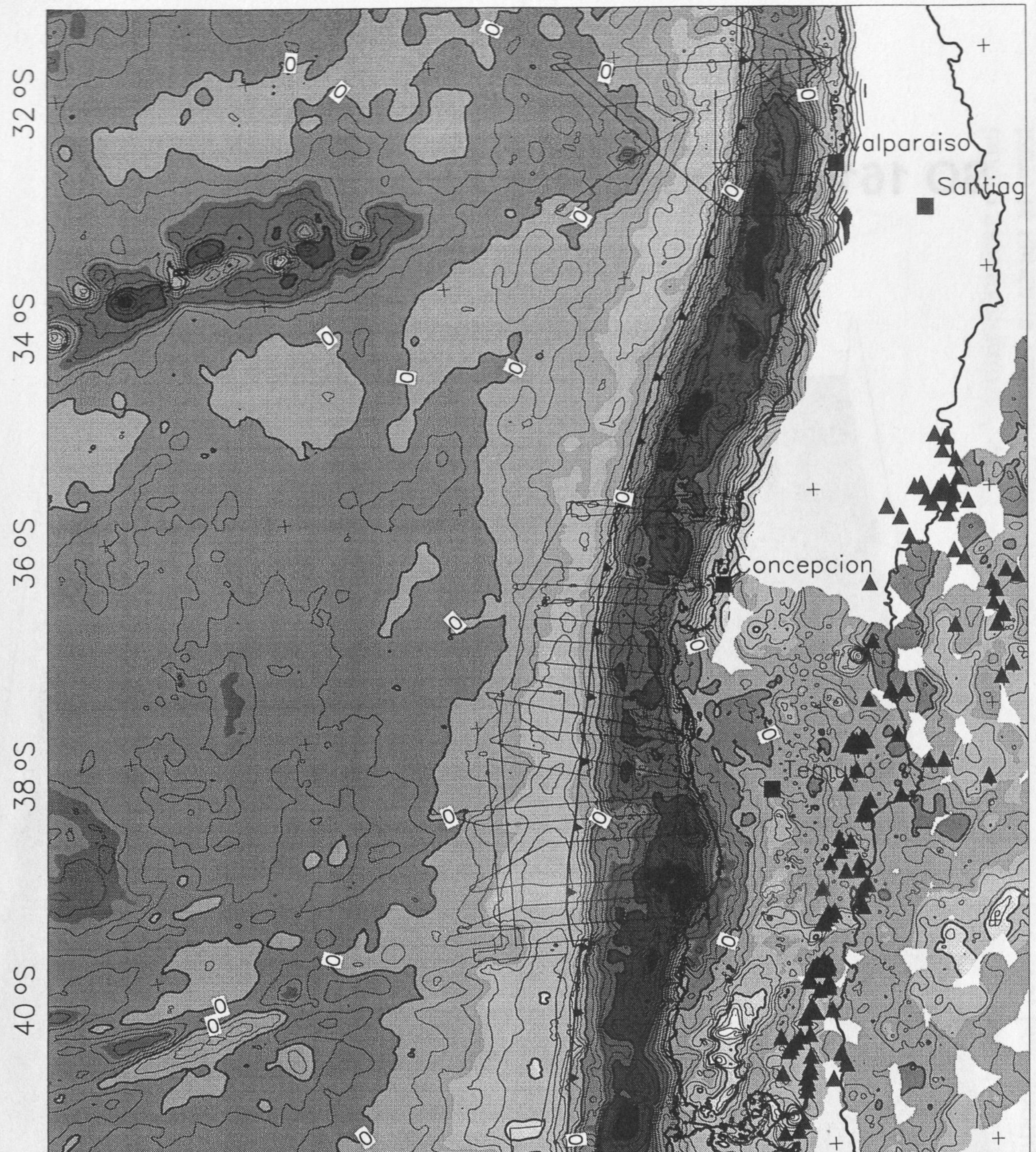

19.12.2001 (UTM Projection: −69, Scale 1 : 6666667)

**Figure 5.2.3:** Isostatic residual field (on- and offshore). Here a Vening-Meinesz isostatic anomaly was calculated by the following parameters: density contrast at the mantle-crust interface: 0.4 Mg/m$^3$ , lithospheric rigidity $10^{23}$ Nm, and normal crustal thickness: 35 km. This field was eliminated from the Bouguer anomaly (Fig. 5.2.2) and is caused by density inhomogeneities between the surface and the compensation level. For further detail refer to the text and to the interpretation e.g. in Fig. 5.2.6.

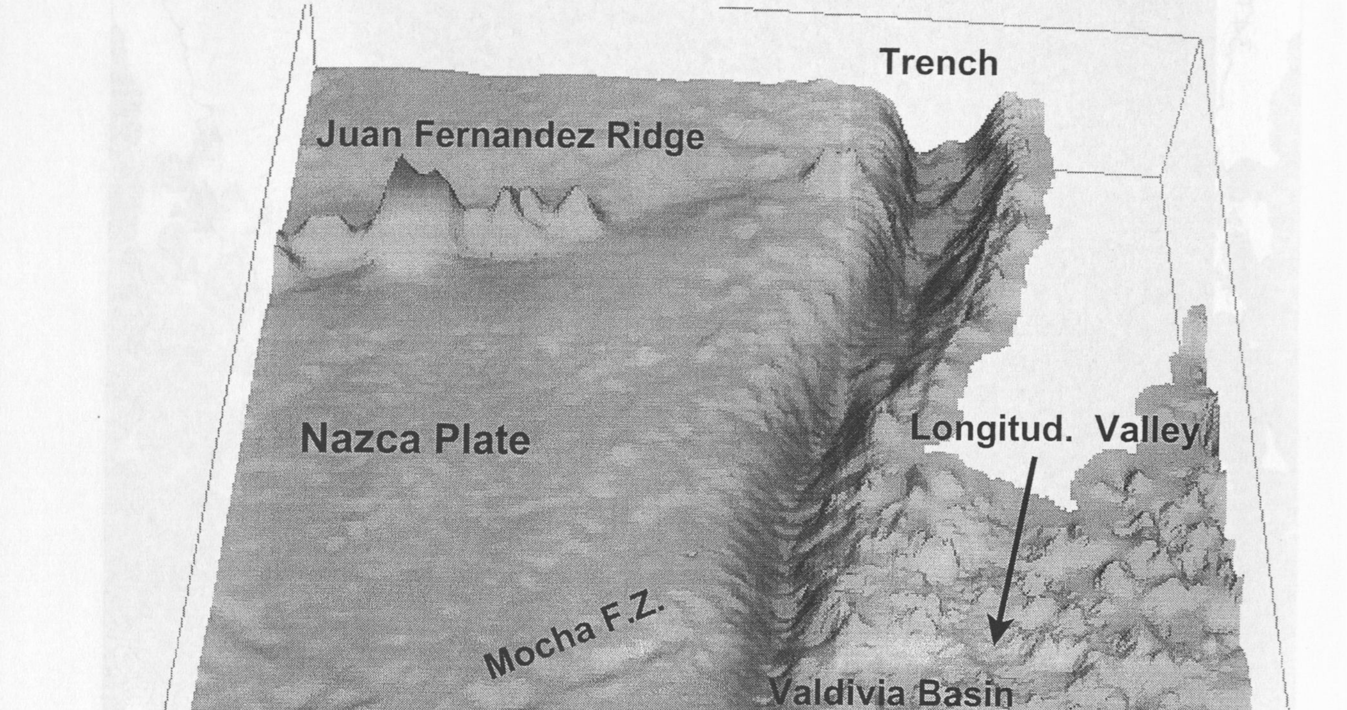

SO 161- 4, SPOC, Free Air anomaly

**Figure 5.2.4:** Perspective view of the Free Air anomaly based on SPOC and KMS databases; topographic reduction applied to on- and offshore data, reduction density is 2.67/1.67 Mg/m$^3$; all data are tied to IGSN 71. The Chiloe F.Z. seems to cross the trench and disappears at the oposite trench slope.

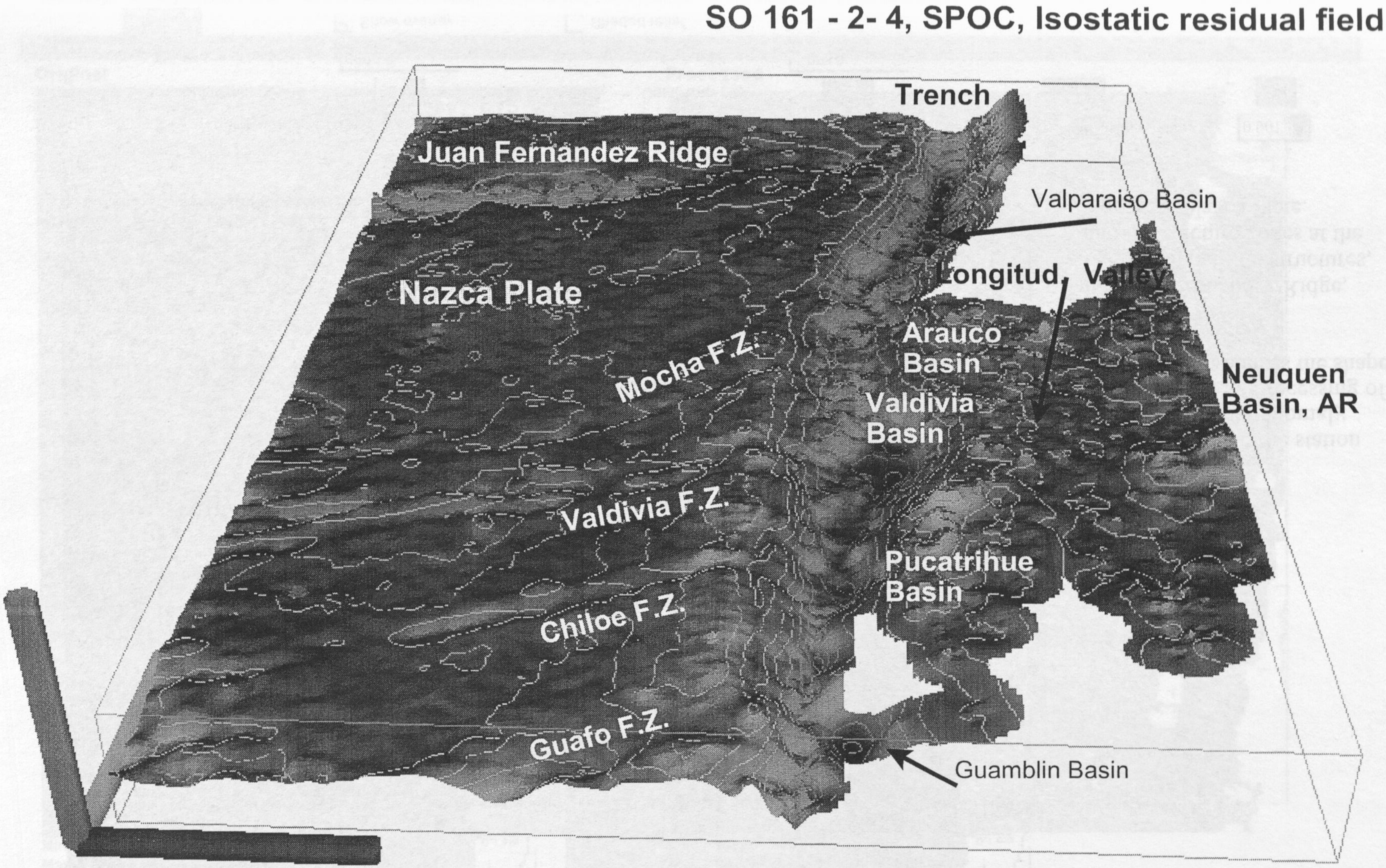

**Figure 5.2.5:** Isostatic residual anomaly based on SPOC and KMS databases (IGSN 71); a Vening-Meinesz model was calculated at on-and offshore stations, and then eliminated from the Bouguer anomaly; density contrast at crust-mantle interface is 0,4 $Mg/m^3$, rigidity $D = 10^{23}$ Nm, normal crustal thickness $T_o = 35$ km.

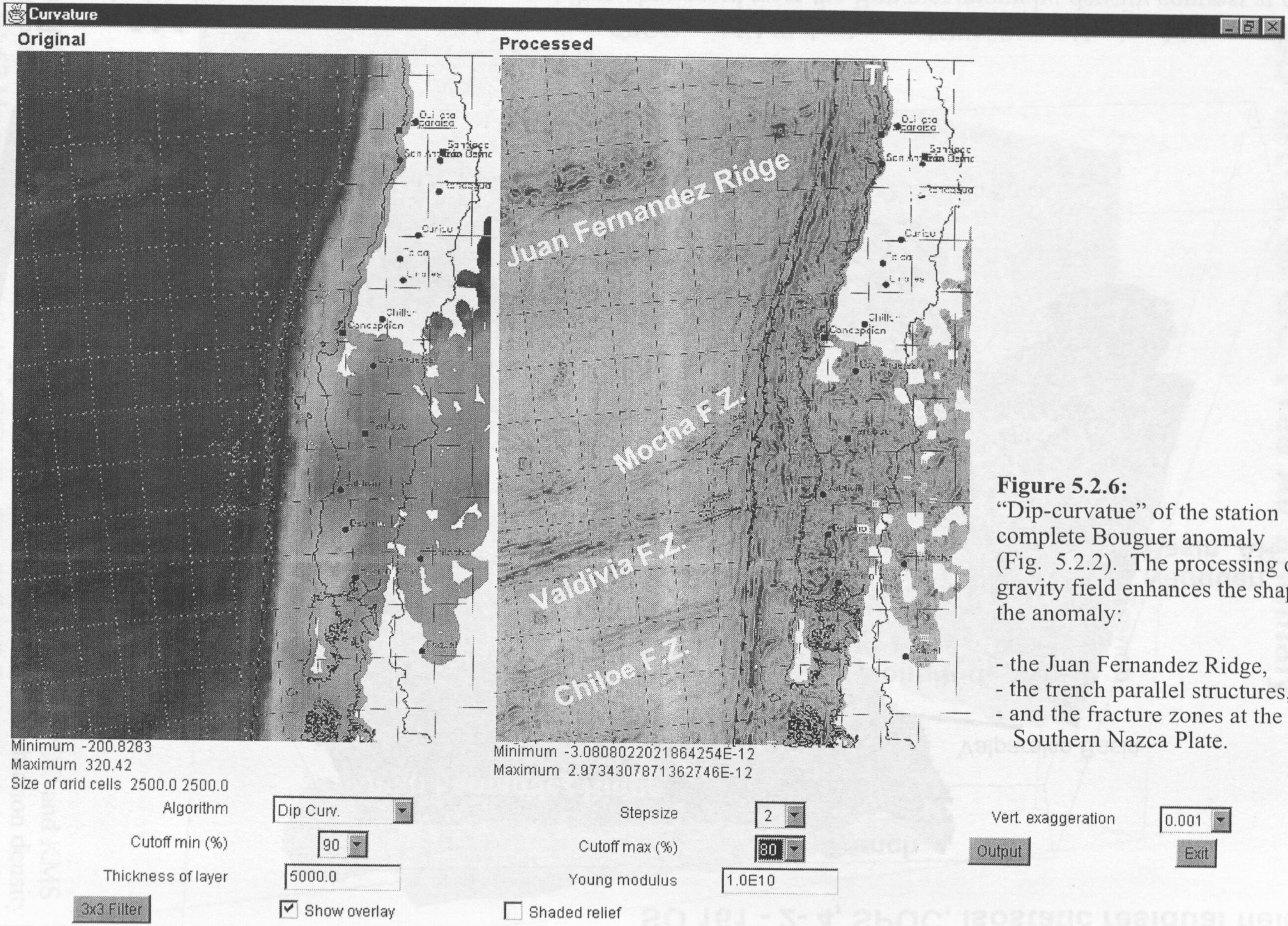

Minimum -200.8283
Maximum 320.42
Size of grid cells 2500.0 2500.0

Minimum -3.0808022021864254E-12
Maximum 2.9734307871362746E-12

Algorithm: Dip Curv.
Cutoff min (%): 90
Thickness of layer: 5000.0
☑ Show overlay
Stepsize: 2
Cutoff max (%): 80
Young modulus: 1.0E10
☐ Shaded relief
Vert. exaggeration: 0.001

**Figure 5.2.6:**
"Dip-curvatue" of the station complete Bouguer anomaly (Fig. 5.2.2). The processing of gravity field enhances the shape of the anomaly:

- the Juan Fernandez Ridge,
- the trench parallel structures,
- and the fracture zones at the Southern Nazca Plate.

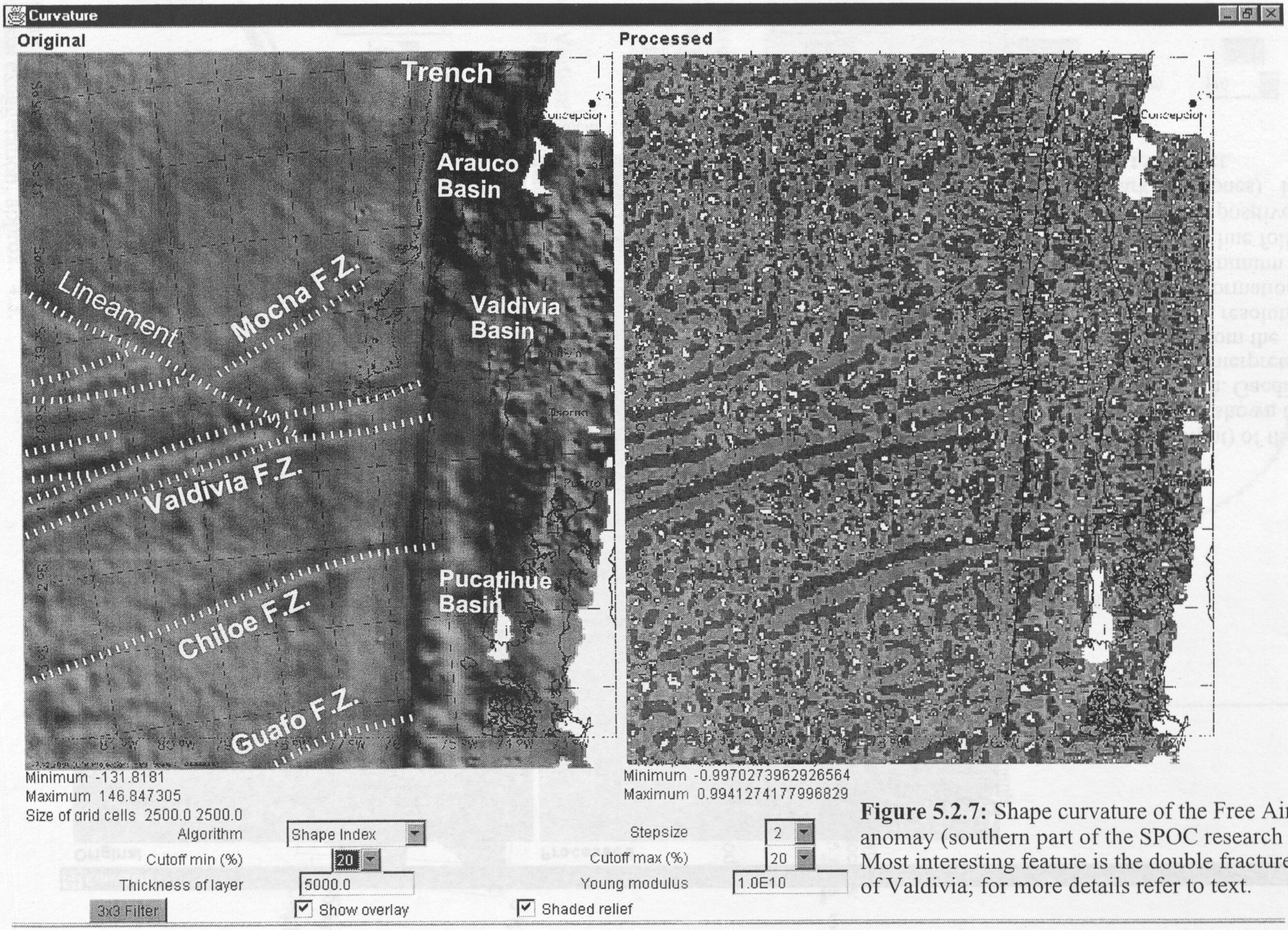

Minimum -131.8181
Maximum 146.847305
Size of grid cells 2500.0 2500.0
Algorithm: Shape Index
Cutoff min (%): 20
Thickness of layer: 5000.0
☑ Show overlay

Minimum -0.9970273962926564
Maximum 0.9941274177996829
Stepsize: 2
Cutoff max (%): 20
Young modulus: 1.0E10
☑ Shaded relief

**Figure 5.2.7:** Shape curvature of the Free Air anomay (southern part of the SPOC research area). Most interesting feature is the double fracture zone of Valdivia; for more details refer to text.

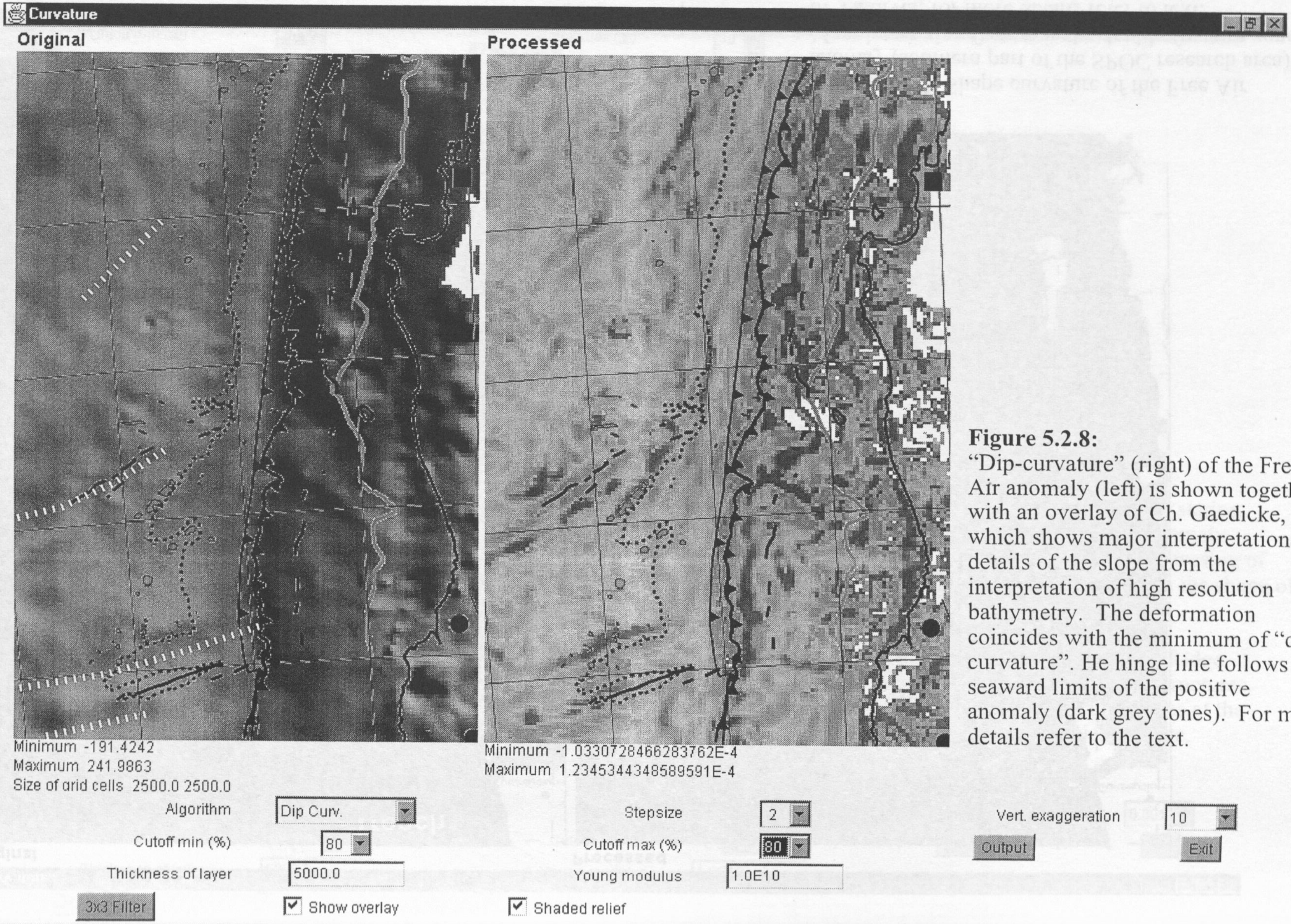

Minimum -191.4242
Maximum 241.9863
Size of grid cells 2500.0 2500.0

Minimum -1.0330728466283762E-4
Maximum 1.2345344348589591E-4

Algorithm: Dip Curv.
Cutoff min (%): 80
Thickness of layer: 5000.0
Stepsize: 2
Cutoff max (%): 80
Young modulus: 1.0E10
Vert. exaggeration: 10
☑ Show overlay
☑ Shaded relief

**Figure 5.2.8:**
"Dip-curvature" (right) of the Free Air anomaly (left) is shown together with an overlay of Ch. Gaedicke, which shows major interpretational details of the slope from the interpretation of high resolution bathymetry. The deformation coincides with the minimum of "dip-curvature". He hinge line follows the seaward limits of the positive anomaly (dark grey tones). For more details refer to the text.

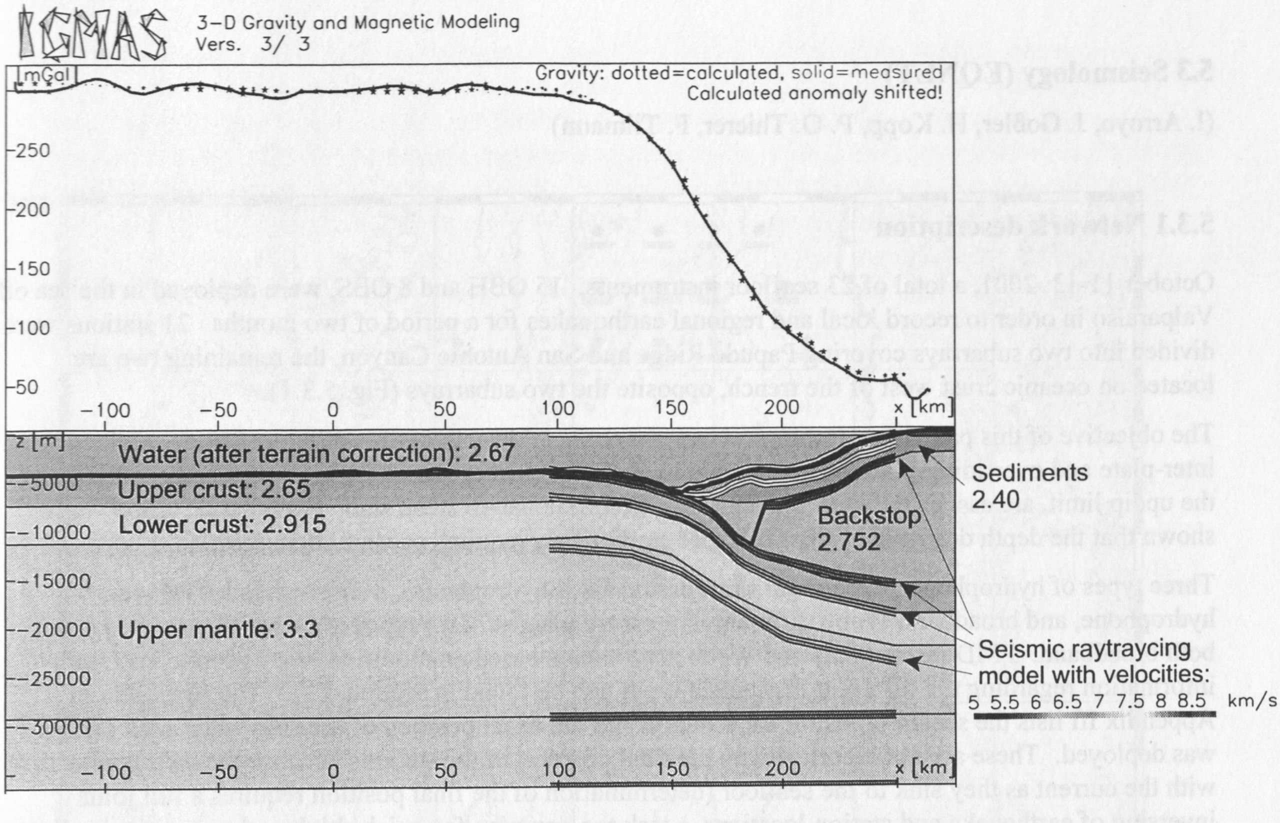

**Figure 5.2.9**: West/East vertical cross section 5 cutting through the preliminary density model along profile 02. Densities are given in $Mg/m^3$. Vertical exaggeration: approx. 4.3
Top: Profile lines of Bouguer Anomaly (solid) and calculated gravity field (dotted).

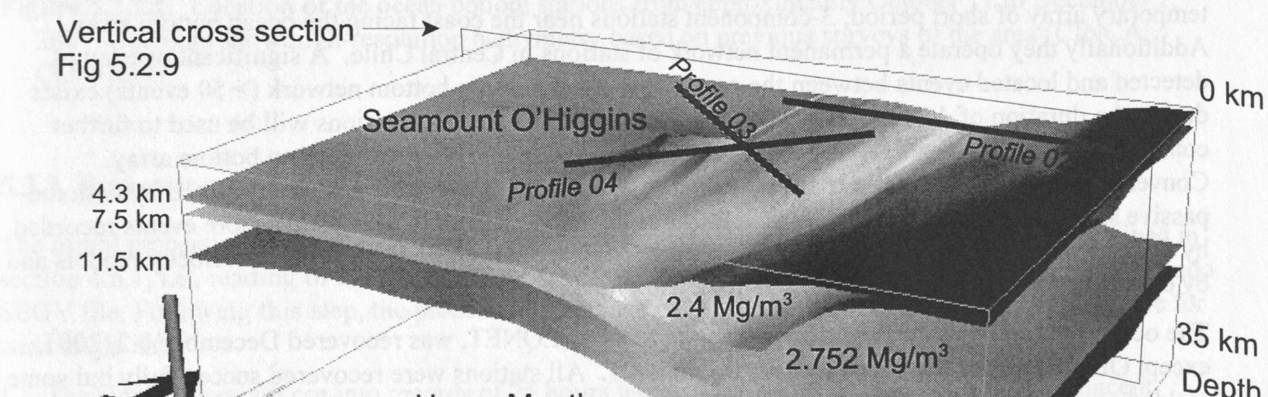

**Figure 5.2.10**: Perspective view of the preliminary density model along profile 02. Vertical exaggeration: approx. 4.3.

## 5.3 Seismology (EQNET)

(I. Arroyo, J. Goßler, H. Kopp, P. O. Thierer, F. Tilmann)

### 5.3.1 Network description

October 11-13, 2001, a total of 23 seafloor instruments, 15 OBH and 8 OBS, were deployed in the sea off Valparaíso in order to record local and regional earthquakes for a period of two months. 21 stations were divided into two subarrays covering Papudo Ridge and San Antonio Canyon, the remaining two are located on oceanic crust west of the trench, opposite the two subarrays (Fig. 5.3.1).

The objective of this passive seismological experiment is to detect possible effects of ridge subduction on inter-plate and overriding-plate seismicity and to observe whether any changes in seismicity, even near the updip limit, are associated with the transition from flat slab to steep slab. Husen et al. (1999) have shown that the depth determination of offshore earthquakes requires ocean bottom stations.

Three types of hydrophones were used: short period OAS hydrophones, a short-period AWI type hydrophone, and broadband Webb differential pressure gauges. Two types of seismometers were used, both broadband: PMD instruments and Webb instruments based on modified Mark geophones (more information regarding the different instrument types can be found in section 4.3). The first table in Appendix III lists the sensor types for each station and the exact position of the ship when each station was deployed. These are not identical with the final position of the stations because the instruments drift with the current as they sink to the seafloor (determination of the final position requires a full joint inversion of earthquake and station locations, a task too complex for quick shipboard processing). Some of the stations recorded shots from reflection profiles shot during leg 2 and 3 of this cruise, which will further help to constrain the locations of the stations. The sites for OBS01, and OBH02-03 were (approximately) reoccupied for wide-angle profile 02, giving us additional structural information for the northern sub-network.

Contemporaneously with the ocean bottom deployment, the Universidad de Chile at Santiago, deployed a temporary array of short period, 3-component stations near the coast facing the ocean bottom array. Additionally they operate a permanent network of stations in Central Chile. A significant overlap of detected and located events between the permanent and the ocean bottom network (> 50 events) exists during the duration of deployment. The additional data from the land stations will be used to further constrain earthquake locations and focal mechanisms within and nearby the ocean bottom array. Conversely, it is planned that our collaborators in Santiago will use the information gained by both the passive seismological experiment as well as the wide angle profiles to relocate offshore events recorded by the permanent network over the previous years (e.g., by using improved offshore velocity models and by employing a joint hypocentre determination approach).

The ocean bottom array, in the following called SO-161 EQNET, was recovered December 1-2, 2001, except OBS13, which was recovered on December 7. All stations were recovered successfully but some yielded no or faulty data due to recorder problems, premature exhaustion of batteries and mechanical failure of the seismometer release mechanism (see section 5.3.3).

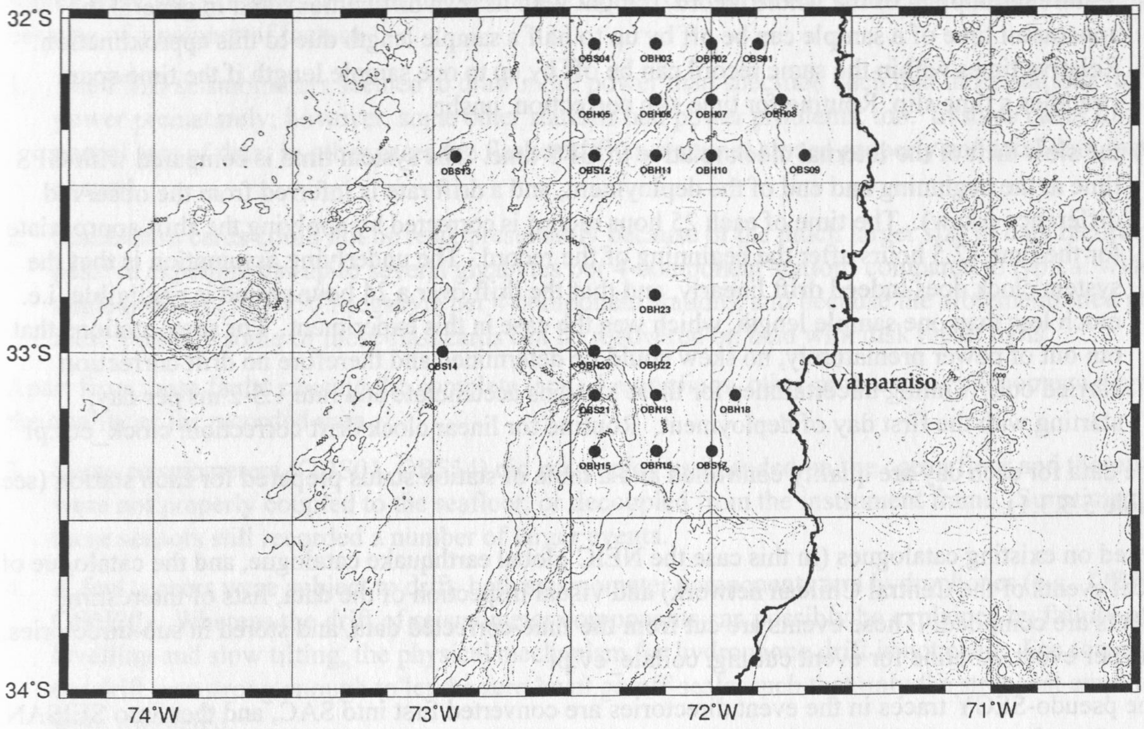

**Figure 5.3.1.1:** Location of the ocean bottom stations from approximately October 11 to December 1, 2001. Contours show high-resolution bathymetry based on previous surveys of the area (CINCA, CONDOR).

## 5.3.2. Processing

The initial processing of the data is identical to the processing sequence for wide angle data described in section 4.6.1, i.e., reading of the flashcards, conversion into a REFTEK file, and conversion into a pseudo SEGY file. Following this step, the processing sequence of the earthquake data diverges from the one for wide angle data.

1. The single traces are cut into records of 25 hours length with one hour overlap between adjacent records, such that each record begins at 0:00:01 (except on the first day of recording, of course). The reason for this cutting is (a) to make file sizes smaller and hence the data more manageable, and (b) to be able to apply the time corrections on a daily basis. Routine for cutting: split_segy.pl
2. The timing of each 25 hour section of the data is corrected. Two timing errors need to be taken account of:
   (a) the occurence of time slips (extra or missing samples) due to a mismatch of the desired and actual sample rates (see section 4.6.1 for a more detailed discussion of time slips). The approach for correcting time slips differs from the approach used for the wide angle data because seismological analysis needs to refer back to the continuous data stream throughout. The

occurrence time of all time slips is read out from the send2pas log file. The time slips before the beginning of the record are added up and applied as static shift to the start time of the record. For time slips during the record a sample is added (positive time slips) or removed (negative time slips) at the appropriate time. This procedure is only approximate (a correct treatment would require resampling of the whole record, fraught with its own difficulties), and in general the appararent time of a sample can be off by up to half a sample length due to this approximation. Relative times within the same record can be off by up to one sample length if the time span straddles a time slip. Routine for time slip correction: unslip

(b) the slow drift of the internal clock relative to GPS time. The system time is compared with GPS time at the beginning and end of the deployment, and a drift rate is inferred from the observed difference (skew). The time of each 25 hour record is corrected by applying the shift appropriate for the time 12.5 hours after the beginning of the record. The underlying assumption is that the system clock does indeed drift linearly, and that the drift over a 24 hour period is negligible, i.e. much less than one sample length, which was the case in this experiment. For some stations that ran out of power prematurely, no skew could be determined and therefore no drift correction carried out. Timing uncertainties for these stations accumulate at a rate 1.5-2 ms per day, starting with the first day of deployment. Routine for linear clock drift correction: clock_cor.pl

3. The data for each day are quality controlled and a table of station status prepared for each station (see Table 5.3.3.1).
4. Based on existing catalogues (in this case the NEIC global earthquake catalogue, and the catalogue of local events of the Central Chilean network) and visual inspection of the data, lists of interesting events are compiled. These events are cut from the time-corrected data, and stored in sub-directories, one per event. Routine for event cutting: collate_ev.pl
5. The pseudo-SEGY traces in the event directories are converted first into SAC, and then into SEISAN waveform format, which makes it possible to store all traces associated with an event in one file. The data are again inspected, bad events deleted, and good events registered into the SEISAN database (Havskov and Ottemöller, 2001). Events are also inspected for traces, which are unusable for a particular event, e.g. because they contain only noise. Routines for conversion: segy2sac_all.csh, sacsei.sh, seisei.sh
6. At last, P and where possible S phases are picked and events preliminarily located with the program HYP, which employ an iterative solution to the nonlinear localisation problem (Lienert, 1994). For the sake of simplicity of onboard processing, a one-dimensional model is assumed based on CONDOR wide angle profiles shot nearby (Flüh et al., 1997, Table 5.4.1) but with the low velocity zone and the sediment layer removed (Table 5.3..2.1). The coda magnitude is also determined for each event.

**Table 5.3.2.1:** 1D-Velocity model for earthquake localisation

| Vp(km/s) | Depth(km) |
|---|---|
| 4.0 | 0.0 |
| 5.2 | 5.0 |
| 5.3 | 14.0 |
| 5.9 | 21.0 |
| 6.4 | 23.0 |
| 7.0 | 26.0 |
| 8.0 | 28.0 |
| 8.2 | 50.0 |

### 5.3.3. Data Quality and Noise characteristics

As mentioned above, all stations of the network were recovered successfully. Most of the stations operated as intended and recorded a large number of local and regional earthquakes as well as the airgun source from MCS profiles shot during leg 2 and 3 of SO161. However, data recovery was not complete because of a number of factors.

1. The PMD seismometers seemed to draw more power than specified such that those stations ran out of power prematurely; however, some other stations had power problems, too. In some cases this lead to partial loss of data, in other cases the flashcard files were not closed properly and total data loss ensued.
2. Some flash cards could not be read, presumably because of the much larger size of data recorded in passive experiments (up to several gigabytes per 4-component station) compared to typical wide angle profiles (100-150 Megabyte per 4-component station), and because the aforementioned power loss. Possibly some of these flashcards can be recovered on land with disk repair tools.

Apart from these faults causing the complete lack of recordings, other problems or phenomena degraded the quality of the recorded data.

3. Some seismometers (OBS01, OBS14) did not deploy as intended on the ocean floor and therefore were not properly coupled to the seafloor, or decoupled from the instrument frame. Surprisingly, these sensors still recorded a number of larger events.
4. A few sensors were subject to drift, both seismometer components and hydrophones (e.g., OBH10, OBH20). Whereas the drift of seismometer components can possibly be explained by failure of levelling and slow tilting, the physical mechanism for hydrophone drift is not clear. For some sensors the drift was strong enough to let the zero level go off-scale, such that only the strongest amplitudes were registered.
5. The gain of the seismometers was generally too low such that for many stations the noise level was below the amplitude represented by one bit, whereas even strong earthquakes only use a small portion (less than 10%) of the range available. Unfortunately, the gain is hardwired into a modular board of the MLS recorders and could therefore not be changed for the subsequent wide-angle deployments. In spite of the non-optimal gain, many phases could be read from seismometer components.
6. The gain of the hydrophones was generally somewhat too high such that many arrivals were clippped, including some of those from moderately sized events (e.g., see Figure 5.3.4.8).
7. Some of the stations are affected by spikes, and more mysteriously, by bursts of almost monochromatic noise with a fundamental frequency close to 5 Hz, often supplemented by overtones (Fig. 5.3.3.1). The noisy periods can last up to several hours. Because of its relative monochromaticity this type of noise can be relatively easily removed by filtering, but only at the cost of filtering in a band where signal energy from local earthquakes is also strong.

Overall, data recovery (as measured by the fraction of usable data actually recovered versus the amount that would have been recovered if all stations had operated perfectly) was ~60% for pressure components, and 30% for seismometer velocity components. Table 5.3.3.1 gives a summary which stations operated on which day.

In order to compare the frequency response of the different sensor types we computed representative ambient noise spectra for each instrument type and compare them to the spectra of a typical local event recorded at the same instrument (Figure 5.3.4.5-7). The spectra are raw spectra, i.e. they have not been corrected for instrument response. The amplitude units can be considered arbitrary (really they are voltage multiplied by a recorder-dependent pre-amplifier constant). The polarity of each recorder-instrument combination was different and has to be reconstructed from the data.

| | Oktober | | | | | | | | | | | | | | | | | | | | | November | | | | | | | | | | | | | | | | | | | | | | | | | | | | | | Dezember | | Remarks |
|---|---|---|---|---|---|---|---|---|---|---|---|---|---|---|---|---|---|---|---|---|---|---|---|---|---|---|---|---|---|---|---|---|---|---|---|---|---|---|---|---|---|---|---|---|---|---|---|---|---|---|---|---|---|---|
| Day of month | 11 | 12 | 13 | 14 | 15 | 16 | 17 | 18 | 19 | 20 | 21 | 22 | 23 | 24 | 25 | 26 | 27 | 28 | 29 | 30 | 31 | 1 | 2 | 3 | 4 | 5 | 6 | 7 | 8 | 9 | 10 | 11 | 12 | 13 | 14 | 15 | 16 | 17 | 18 | 19 | 20 | 21 | 22 | 23 | 24 | 25 | 26 | 27 | 28 | 29 | 30 | 1 | 2 | |
| Julian day | | 285 | | | | | 290 | | | | | 295 | | | | | 300 | | | | | 305 | | | | | 310 | | | | | 315 | | | | | 320 | | | | | 325 | | | | | 330 | | | | | 335 | | |
| OBS01 | | | s | o | o | o | o | o | o | o | o | o | o | | | | | | | | | | | | | | | | | | | | | | | | | | | | | | | | | | | | | | | | | Channel 3,4 sometimes clipped after Julian Day 290, seismometer deployment failure causes insufficient coupling to seafloor |
| OBH02 | | s | x | x | x | x | x | x | x | x | x | x | x | x | x | x | x | x | x | x | x | x | x | x | x | x | x | x | x | x | x | x | x | x | x | x | x | x | x | x | x | x | s | | | | | | | | | | | |
| OBH03 | s | o | x | x | x | x | x | o | o | x | x | x | x | x | x | x | x | o | x | x | x | x | x | x | x | x | x | x | | | | | | | | | | | | | | | | | | | | | | | | | | |
| OBS04 | | | | | | | | | | | | | | | | | o | | | | | | | | | | | | | | | | | | | | | | | | | | | | | | | | | | | | | clipped for part of the day |
| OBH05 | s | s | x | x | x | x | x | x | x | x | x | x | x | x | x | x | x | x | x | x | x | x | x | x | x | x | x | x | x | x | x | x | x | x | x | x | x | x | x | x | x | x | x | x | x | x | x | x | x | x | s | | | |
| OBH06 | | s | x | x | x | x | x | x | x | x | x | x | x | x | x | x | x | x | x | x | x | x | x | x | x | x | x | x | x | x | x | x | x | x | x | x | x | x | x | x | | | | | | | | | | | | | | |
| OBH07 | | s | x | x | x | x | x | x | x | x | x | x | x | x | x | x | x | x | x | x | x | x | x | x | x | x | x | x | x | x | x | x | x | x | x | x | x | x | x | x | x | x | x | x | x | x | x | x | x | x | x | s | | |
| OBH08 | | s | x | o | o | o | o | o | o | o | o | o | o | - | - | - | - | - | - | - | - | - | - | - | - | - | - | - | - | - | - | - | - | - | - | - | - | - | - | - | - | - | - | - | - | - | - | - | - | - | - | - | | clipped or signal out of range |
| OBS09 | | | s | x | o | x | x | x | x | o | x | x | x | x | x | x | x | o | x | | | | | | | | | | | | | | | | | | | | | | | | | | | | | | | | | | | only hydrophone, ch. 2-4 bad. |
| OBH10 | | s | o | o | x | x | x | o | x | x | o | x | x | x | x | o | - | - | - | - | - | - | - | - | - | - | - | - | - | - | - | - | - | - | - | - | - | - | - | - | - | - | - | - | - | - | - | - | - | - | - | - | | clipped or signal out of range |
| OBH11 | | s | x | x | x | x | x | x | x | x | x | x | x | x | x | x | x | x | x | x | x | x | x | x | x | x | x | x | x | x | x | x | x | x | x | x | x | x | x | x | x | x | x | x | x | x | x | x | x | x | x | | | |
| OBS12 | | | | s | x | x | x | x | x | x | x | x | x | | | | | | | | | | | | | | | | | | | | | | | | | | | | | | | | | | | | | | | | | Ch. 3 bad |
| OBS13 | | | s | o | o | o | o | o | o | o | o | o | o | o | o | o | o | o | o | o | o | o | o | o | o | o | o | o | o | o | o | o | o | o | o | o | o | o | o | o | o | o | o | o | o | o | o | o | o | o | o | o | o ... | Ch. 2 down, Ch. 3, 4 gain low, levelling every 10 days, data recording continues until Julian day 341 |
| OBS14 | | s | s | o | o | o | o | o | o | o | o | o | o | o | o | o | o | o | o | o | o | o | o | o | o | o | o | o | o | o | o | o | o | o | o | o | o | o | o | o | o | o | o | o | o | o | o | o | o | o | o | o | o | Ch. 2 down, Ch. 3, 4 gain low, levelling every 10 days, seismometer deployment failure causes insufficient decoupling from instrument frame |
| OBH15 | | s | x | x | x | x | x | x | x | x | x | x | x | x | x | x | x | x | x | x | x | x | x | x | x | x | x | x | x | x | x | x | x | x | x | x | x | x | x | x | x | x | x | x | x | x | x | x | x | x | x | x | s | |
| OBH16 | | s | x | x | x | x | x | x | x | x | x | x | x | x | x | x | x | x | x | x | x | x | x | x | x | x | x | x | x | x | x | x | x | x | x | x | x | x | x | x | x | x | x | x | x | x | x | x | x | x | x | x | s | |
| OBS17 | | s | x | x | x | x | x | x | x | x | x | x | x | x | x | x | x | x | x | x | x | x | x | x | x | x | x | x | x | x | x | x | x | x | x | x | x | x | x | x | x | x | x | x | x | x | x | x | x | x | x | x | s | hydrophone signal not 'clean' on a few days |
| OBH18 | | s | x | x | x | x | x | x | x | x | x | x | x | x | x | x | x | x | x | x | x | x | x | x | x | x | x | x | x | x | x | x | x | x | x | x | x | x | x | x | x | x | x | x | x | x | x | x | x | x | x | x | s | |
| OBH19 | | | s | x | x | x | x | x | x | x | x | x | x | x | x | x | x | x | x | x | x | x | x | x | x | x | x | x | x | x | x | x | x | x | x | x | x | x | x | x | x | x | | | | | | | | | | | | |
| OBH20 | | | | s | x | x | x | x | x | x | x | x | x | - | - | - | - | - | - | - | - | - | - | - | - | - | - | - | - | - | - | - | - | - | - | - | - | - | - | - | - | - | - | o | o | x | x | x | o | - | - | o | o | off scale |
| OBS21 | | | | | | | | | | | | | | | | | | | | | | | | | | | | | | | | | | | | | | | | | | | | | | | | | | | | | | no data, recorder problem |
| OBH22 | | | s | x | x | x | x | x | x | x | x | x | x | x | x | x | x | x | x | x | x | x | x | x | x | x | x | x | x | x | x | x | x | x | x | x | x | x | x | x | x | x | x | x | x | x | x | x | x | x | x | x | s | |
| OBH23 | | | | | | | | | | | | | | | | | | | | | | | | | | | | | | | | | | | | | | | | | | | | | | | | | | | | | | no data, recorder problem |

| | |
|---|---|
| x | data |
| o | data with specific problems but at least one component usable (see comment column) |
| s | start or stop of data recording (deployment and recovery) |
| - | recording present, but no useful data |
| blank | not recorded |

**Table 5.3.3.1:** Station Status

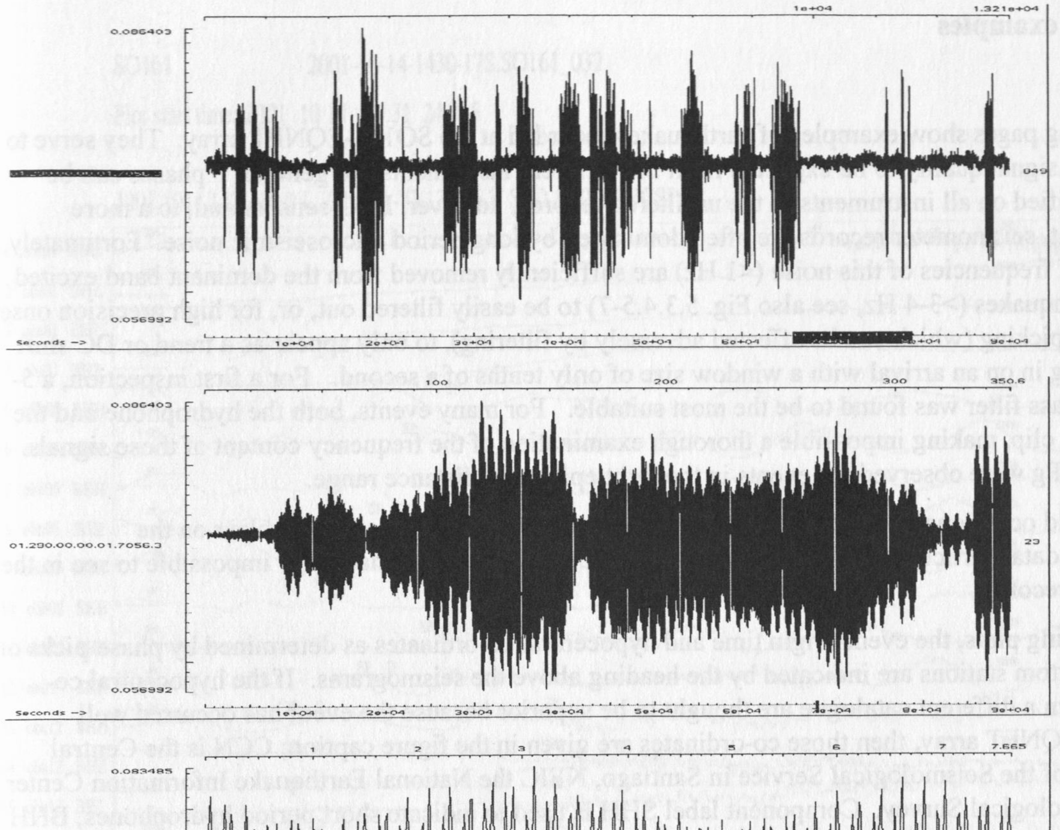

**Figure 5.3.3.1:** Series of 5 Hz bursts with overtones from an unknown source registered on the seismometer channels of obs14 on Oct. 17, 2001 from 18:16 to 21:55 (top). Details of noise bursts with window length of ~6 min (2nd from top) and 8 s (3rd from top). Frequency spectrum of the previous sequence (bottom): large peaks at about 5 Hz, 10 Hz, 15 Hz and 20 Hz are visible. The time series exhibits beating, corresponding to split peaks in the frequency domain.

### 5.3.4. Data examples

The following pages show examples of earthquakes recorded at the SO161-EQNET array. They serve to illustrate the signal quality to be expected from the different instruments. In general, P phases can be clearly identified on all instruments in the unfiltered records, however, DPG sensors and, to a more limited extent, seismometer records are often dominated by long period microseismic noise. Fortunately, the dominant frequencies of this noise (<1 Hz) are sufficiently removed from the dominant band excited by local earthquakes (>3-4 Hz, see also Fig. 5.3.4.5-7) to be easily filtered out, or, for high precision onset and polarity picking (which can be affected adversely by filtering), to only appear as a trend or DC shift after zooming in on an arrival with a window size of only tenths of a second. For a first inspection, a 5-20 Hz bandpass filter was found to be the most suitable. For many events, both the hydrophone and the DPG records clip, making impossible a thorough examination of the frequency content of those signals. Both Pn and Pg were observed for events in the right epicentral distance range.

S-waves could occasionally be picked, too. As expected, these phases were quite clear on the seismometer data, particularly on the horizontal components, but much harder or impossible to see in the hydrophone records.

In the following plots, the event origin time and hypocentral co-ordinates as determined by phase picks on the ocean bottom stations are indicated by the heading above the seismograms. If the hypocentral co-ordinates from a different catalogue are thought to be superior because the event has occurred well outside the EQNET array, then those co-ordinates are given in the figure caption; CCN is the Central Chilean Net of the Seismological Service in Santiago, NEIC the National Earthquake Information Center of the US Geological Survey. Component label SHH is used to indicate short period hydrophones, BHH for DPG sensors, and BHZ, BH1, and BH2 are the vertical and two horizontal seismometer components. Amplitude and polarity of all data are 'raw', i.e., uncorrected for instrumental response, preamplifier gain, and polarity flips. All times are UTC. First, examples of local events are shown, then regional events.

### Local events

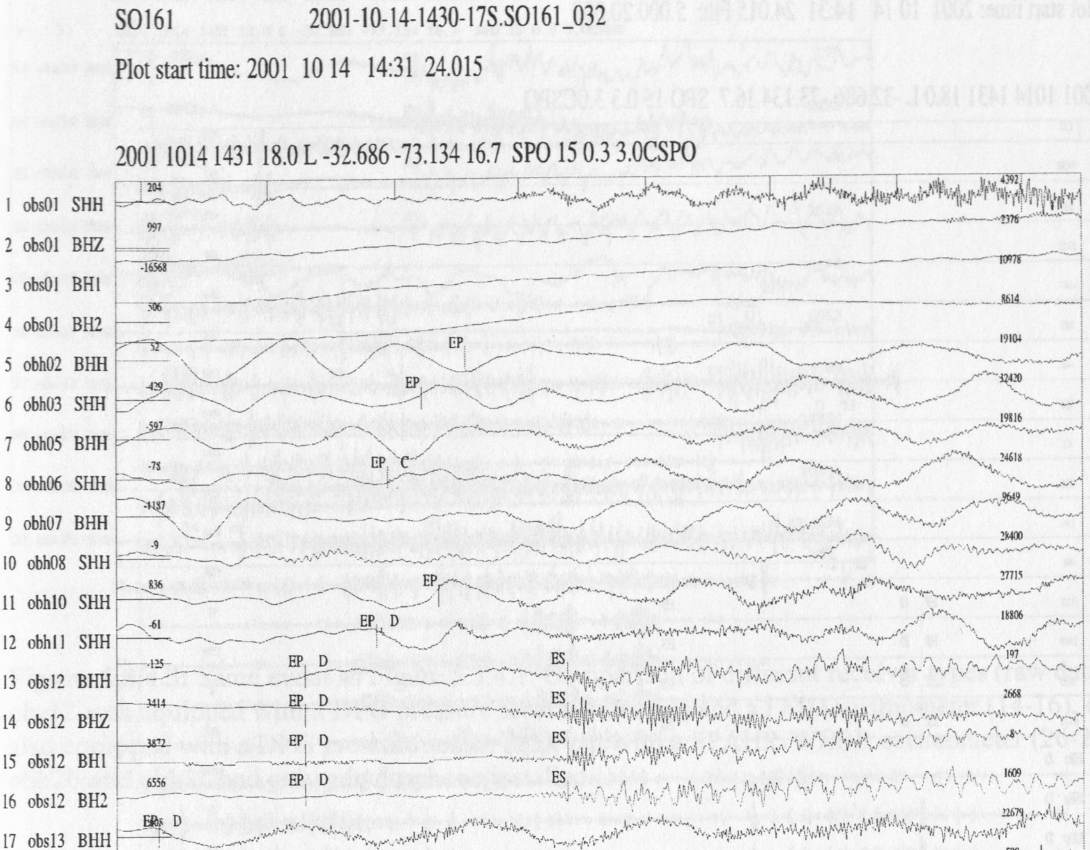

**Figure 5.3.4.1:** $M_L$=3.8 local earthquake from Oct. 14, 2001 14:31:28 located at 32.73° S, 73.04° W, depth 26 km (CCN), between OBS positions 13 and 14 at the western margin of the EQNET area.

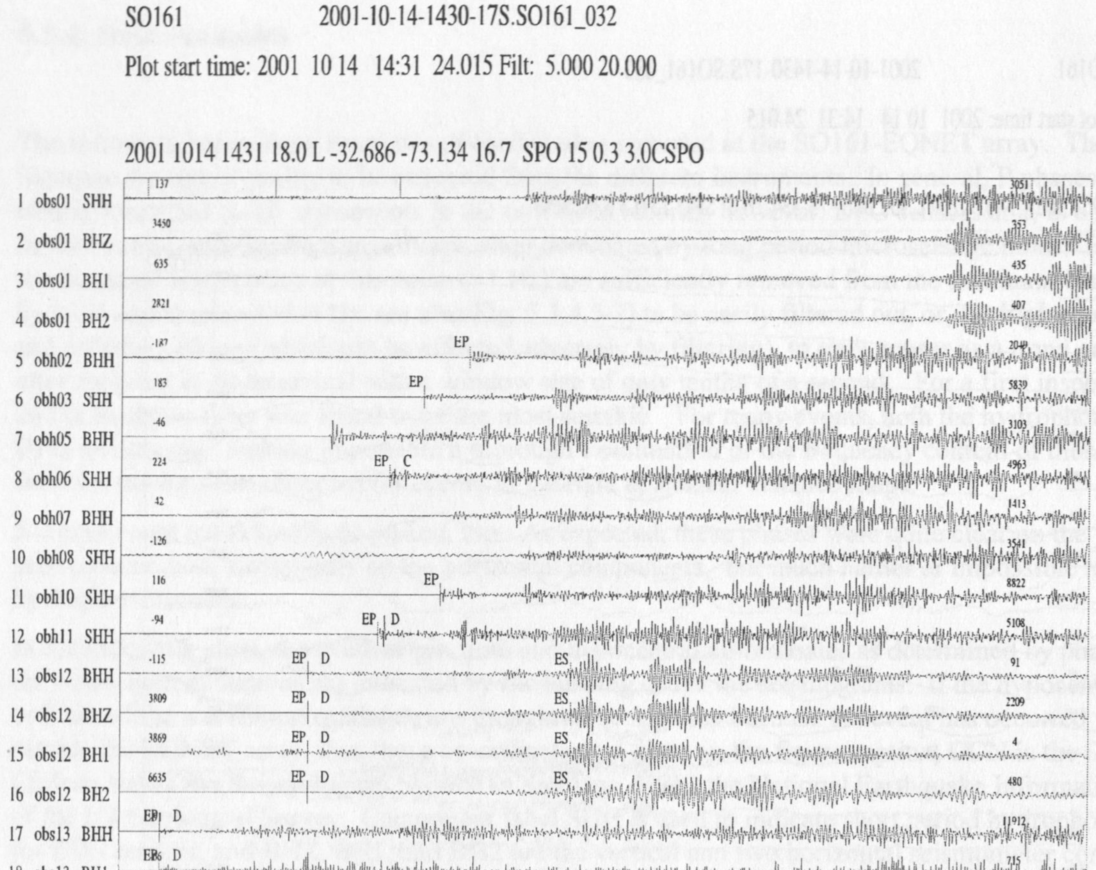

**Figure 5.3.4.2:** Same event as Figure 5.3.4.1. A bandpass filter from 5 to 20 Hz has been applied, so that the earthquake wavelets show up much clearer than in the raw data, especially at the northern stations which are further away from the epicenter (traces 1-12).

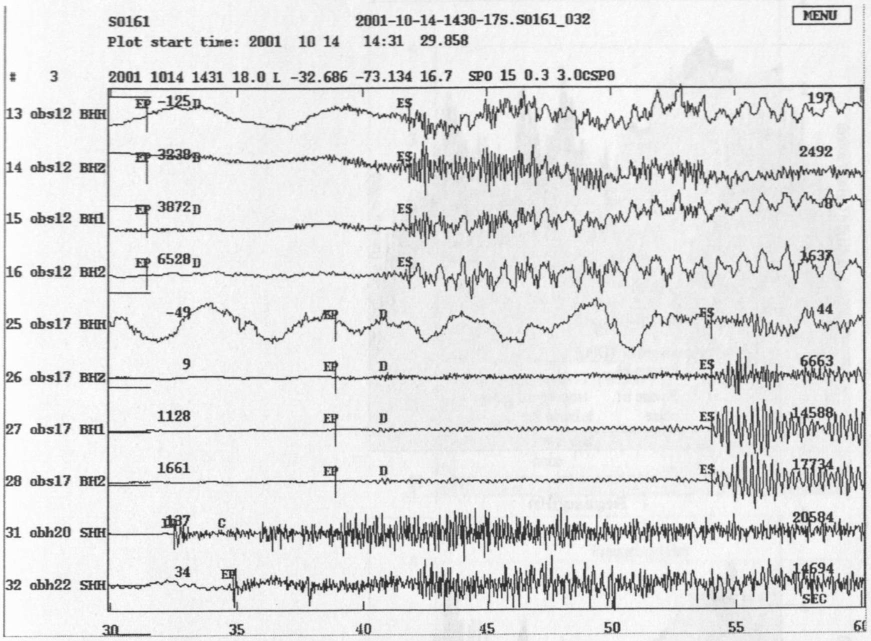

**Figure 5.3.4.3:** Same event as Figure 5.3.4.1. Comparison of different receiver types (raw data): Station obs12 was equipped with a DPG pressure sensor (trace 13) and a PMD seismometer (14-16), obs17 was also equipped with a DPG pressure sensor (25), but with a SPAHR-WEBB seismometer (26-28). Stations obh20 and obh22 had only a hydrophone installed.

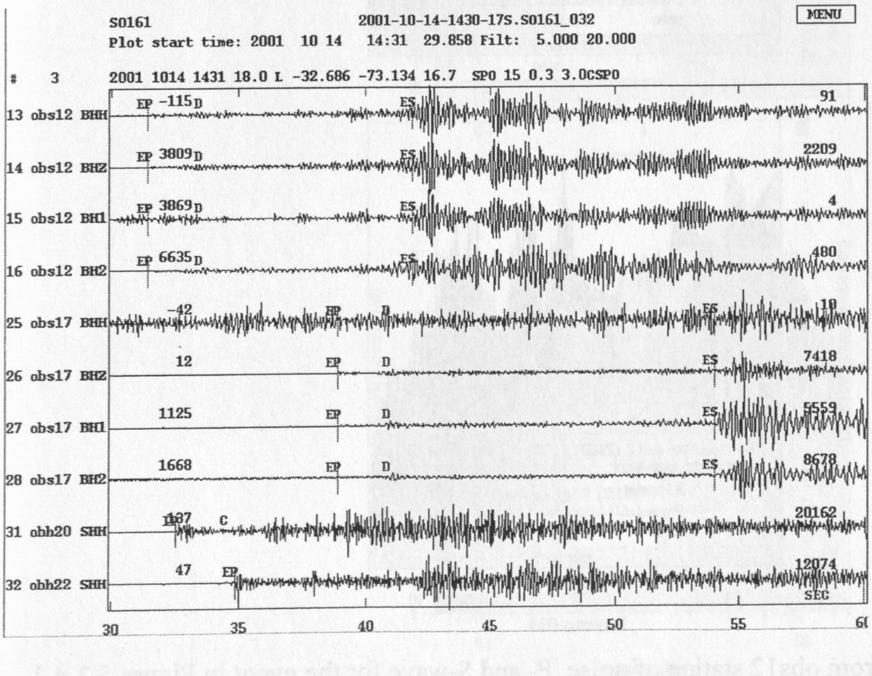

**Figure 5.3.4.4:** The same seismograms as in figure 5.3.4.4, but filtered with a 5 to 20 Hz bandpass. Pressure and seismometer channels from obs12 (traces 13-16) look very similar, whereas the pressure sensor at obs17 (25) resolves the signal only very poorly.

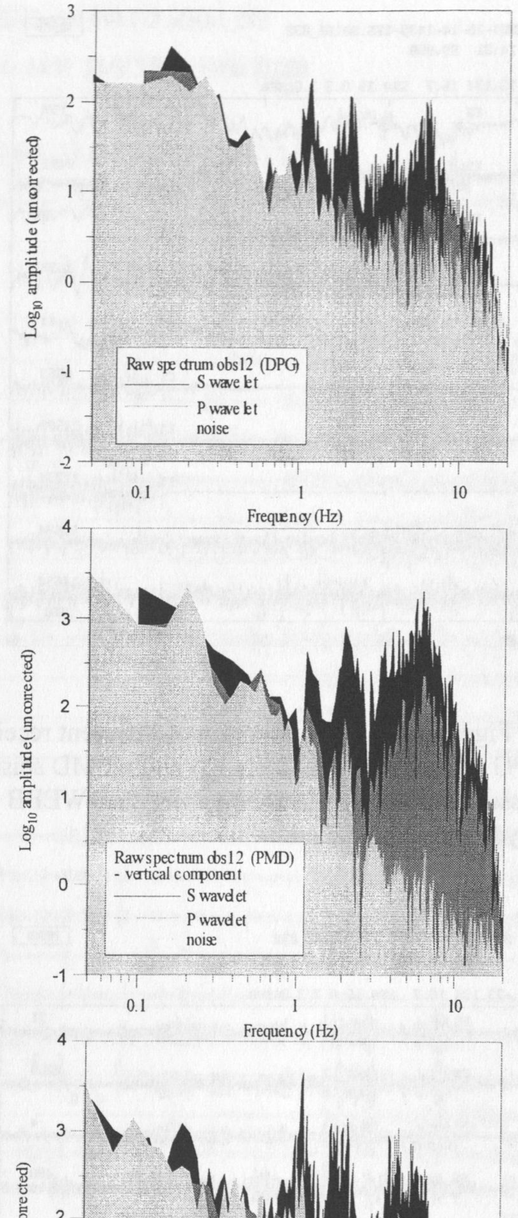

**Figure 5.3.4.5:** Raw spectra from obs12 station of noise, P- and S-wave for the event in Figure 5.3.4.1, epicentral distance 74 km. The upper panel shows the DPG pressure sensor channel, the two other panels show the PMD seismometer channels. The seismometer clearly has a better signal-to-noise ratio than the pressure sensor.

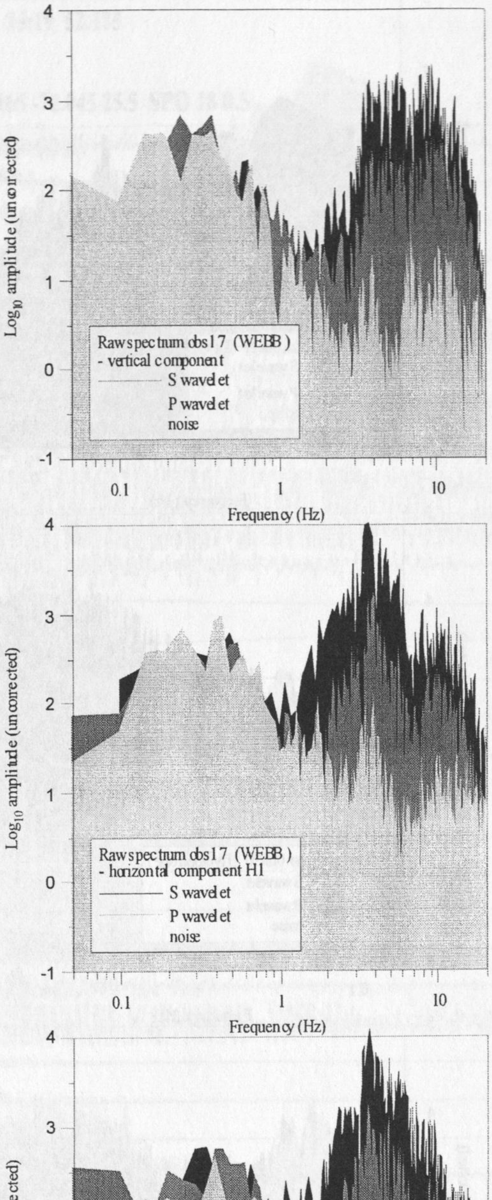

**Figure 5.3.4.6:** Raw spectra for the event in Figure 5.3.4.1., recorded on obs17, epicentral distance 126 km. Noise, P- and S-wave spectra are displayed for the vertical (top panel), first horizontal (center) and second horizontal component (bottom). The horizontals have a prominent maximum at about 2.5 Hz.

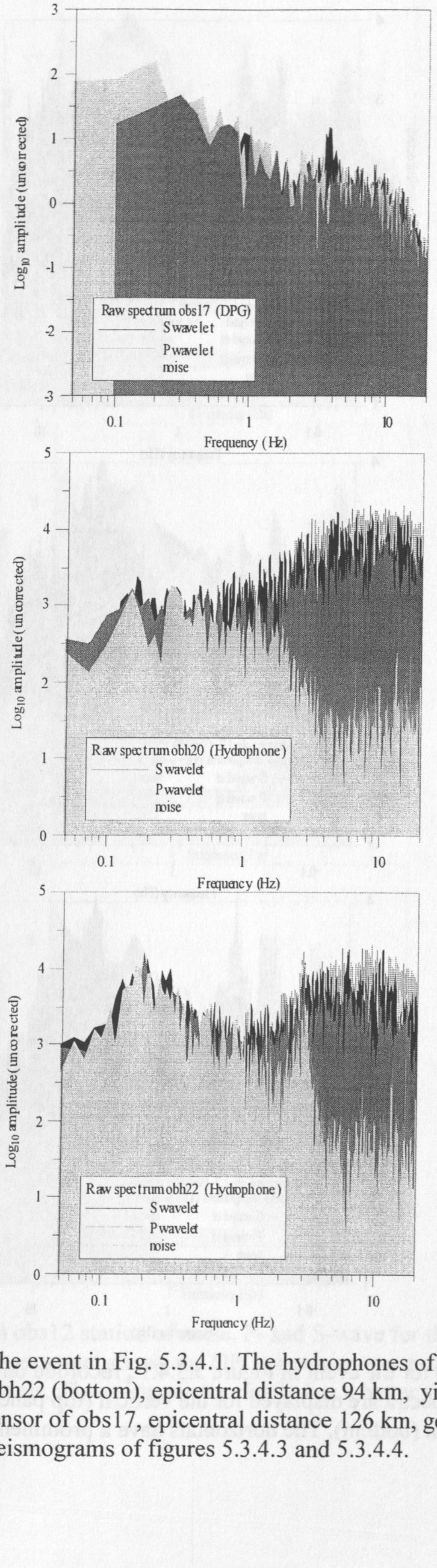

**Figure 5.3.4.7:** OBH spectra of the event in Fig. 5.3.4.1. The hydrophones of station obh20 (center), epicentral distance 76 km, and obh22 (bottom), epicentral distance 94 km, yield good signal-to-noise ratios, while the DPG pressure sensor of obs17, epicentral distance 126 km, gets only a poor signal. This can also be seen directly on the seismograms of figures 5.3.4.3 and 5.3.4.4.

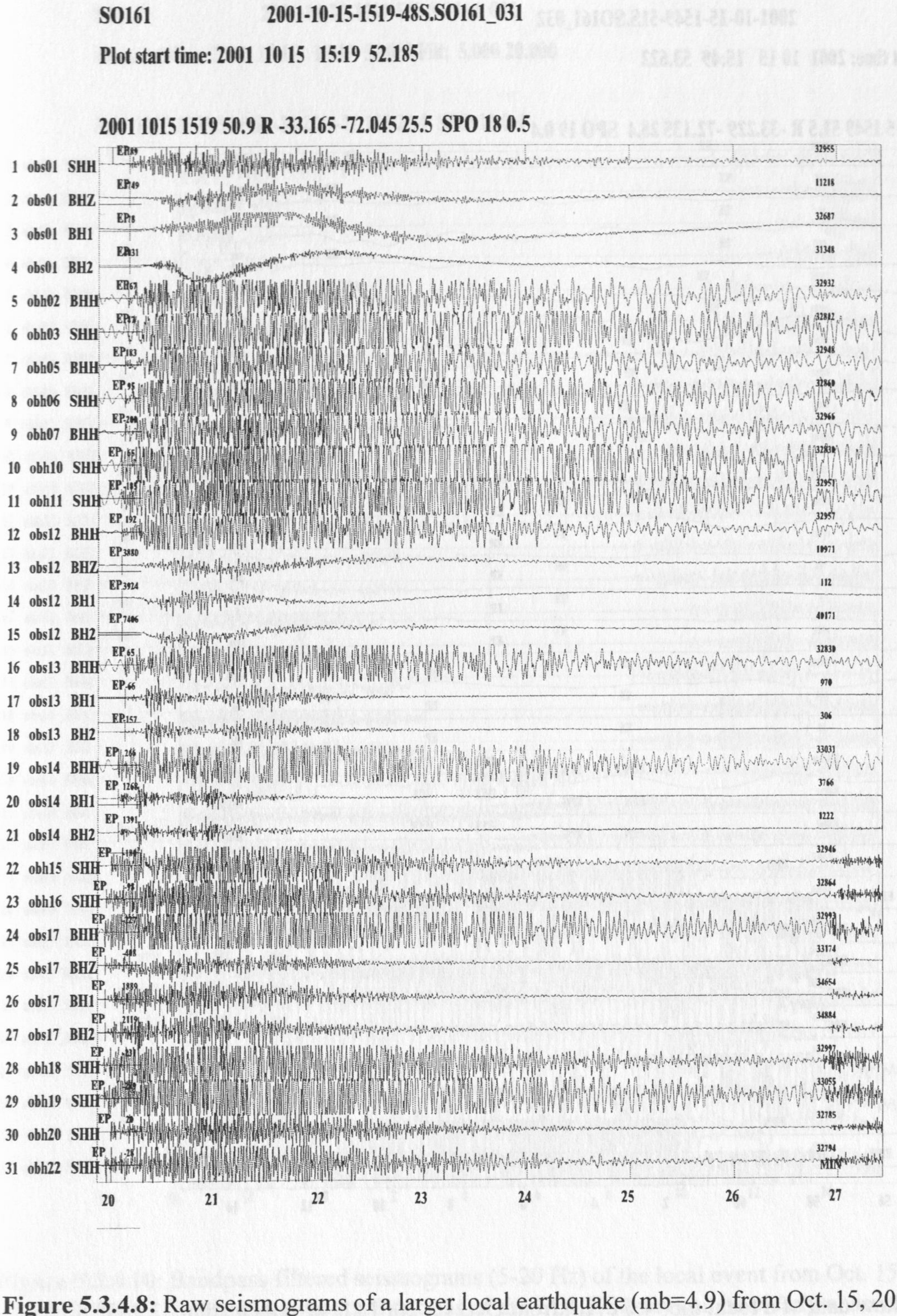

**Figure 5.3.4.8:** Raw seismograms of a larger local earthquake (mb=4.9) from Oct. 15, 2001 15:19:52 relocated at 33.165° S, 72.045° W, depth 25 km (EQNET), which lies in the southern part of the EQNET area. All hydrophone channels are clipped, except obs01 SHH which is located in the north-western corner of the EQNET array. The seismometers registered the full signal.

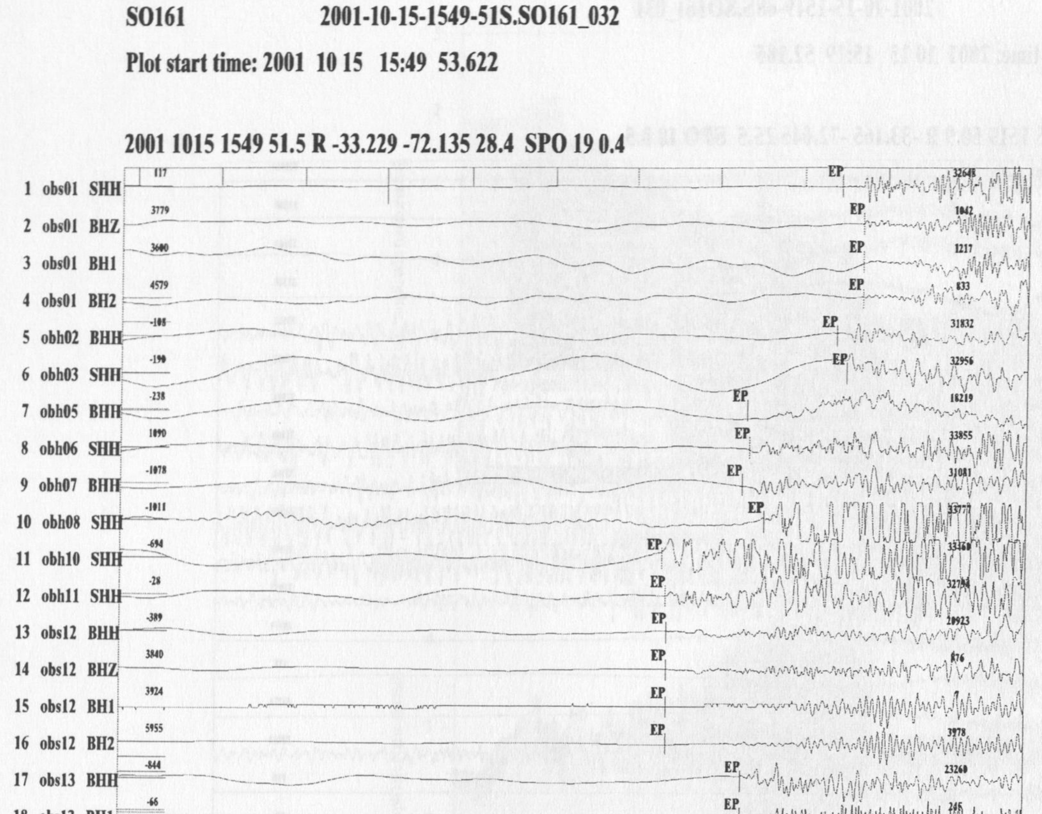

SO161 2001-10-15-1549-51S.SO161_032

Plot start time: 2001 10 15 15:49 53.622

2001 1015 1549 51.5 R -33.229 -72.135 28.4 SPO 19 0.4

**Figure 5.3.4.9:** Raw data of a local mb=4.6 event from Oct. 15, 2001 15:49 relocated at 33.229° S, 72.135° W, depth 28 km (EQNET), which is very close to the larger event from 15:19 (Figure 5.3.4.8). Here only the southern hydrophone stations, and obh08, obh10, obh11 which are closest to the epicenter from the northern part of the array, are clipped.

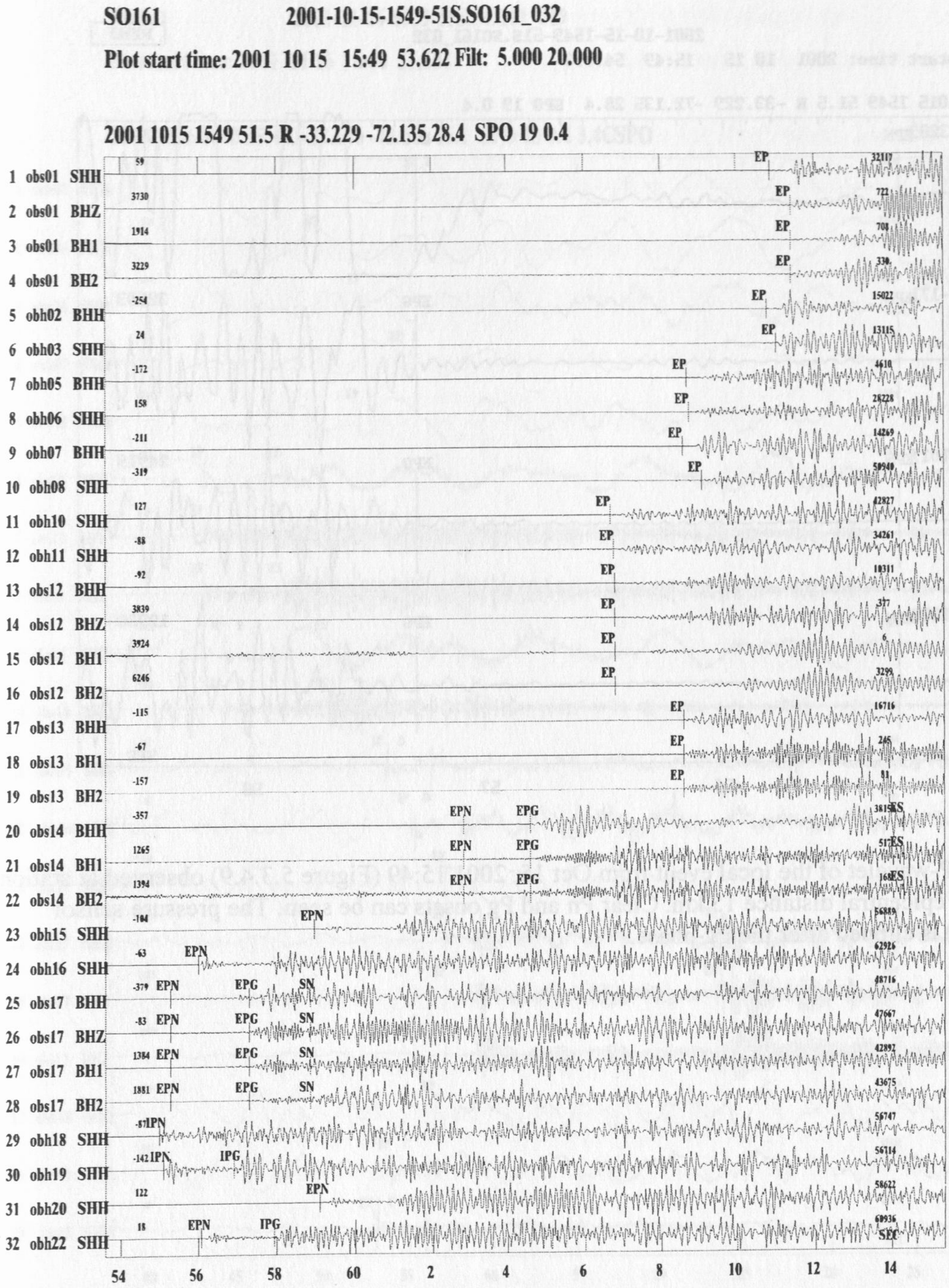

**Figure 5.3.4.10:** Bandpass filtered seismograms (5-20 Hz) of the local event from Oct. 15, 2001 15:49 (Figure 5.3.4.9). The first arrival at all stations of the EQNET array can be clearly observed.

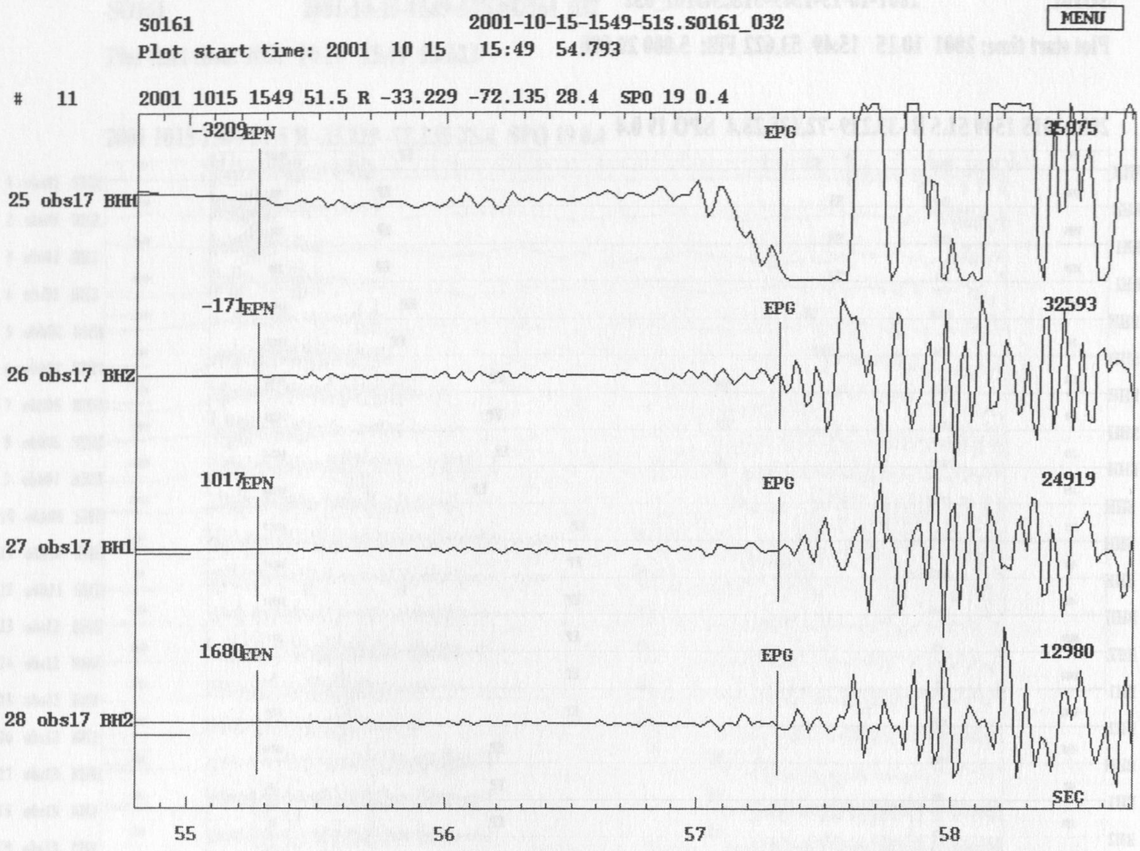

**Figure 5.3.4.11:** P-wavelet of the local event from Oct 15, 2001 15:49 (Figure 5.3.4.9) observed at station obs17 (raw data), epicentral distance 15 km. Clear Pn and Pg onsets can be seen. The pressure sensor channel (trace 25) is clipped after the Pg-phase.

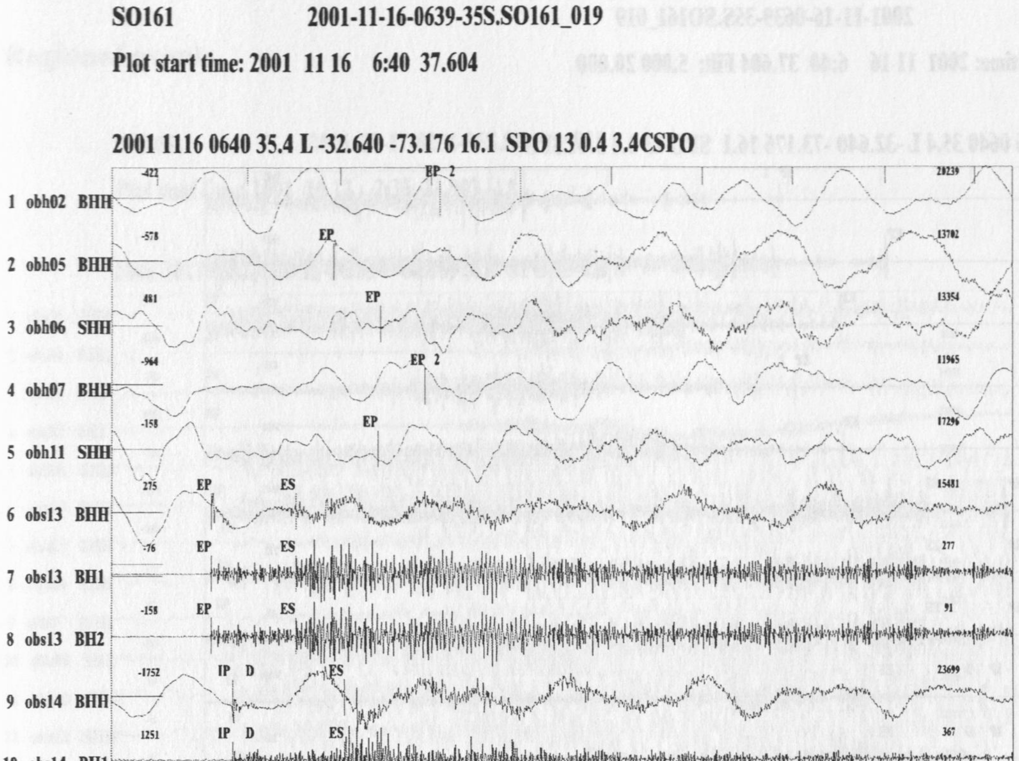

**Figure 5.3.4.12:** Raw seismograms of a $M_L$=3.6 local earthquake at Nov. 16, 2001 06:40 relocated at 32.640° S, 73.176° W. The epicenter was close to the obs13 and obs14 stations in oceanic crust. Clear signals are obtained at these stations and in the southern part of the array (trace 6-19).

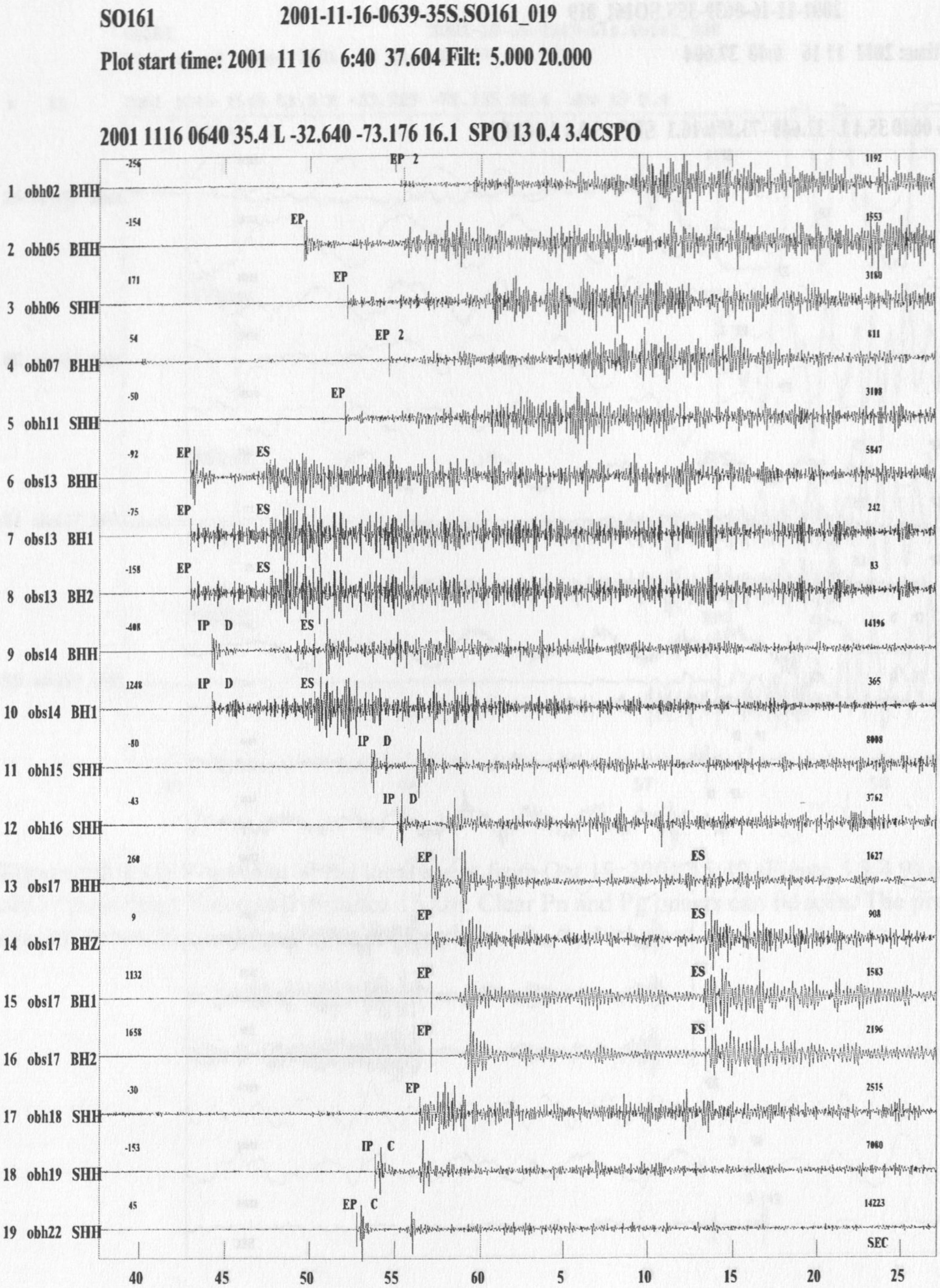

**Figure 5.3.4.13:** Bandpass filtered seismograms (5-20 Hz) of the local event in Fig. 5.3.4.12. Very good signals can be observed at all operating stations of the EQNET seismic network. Missing stations have been down because of power outage or other technical problems, so that they did not register reliable signals.

## Regional events

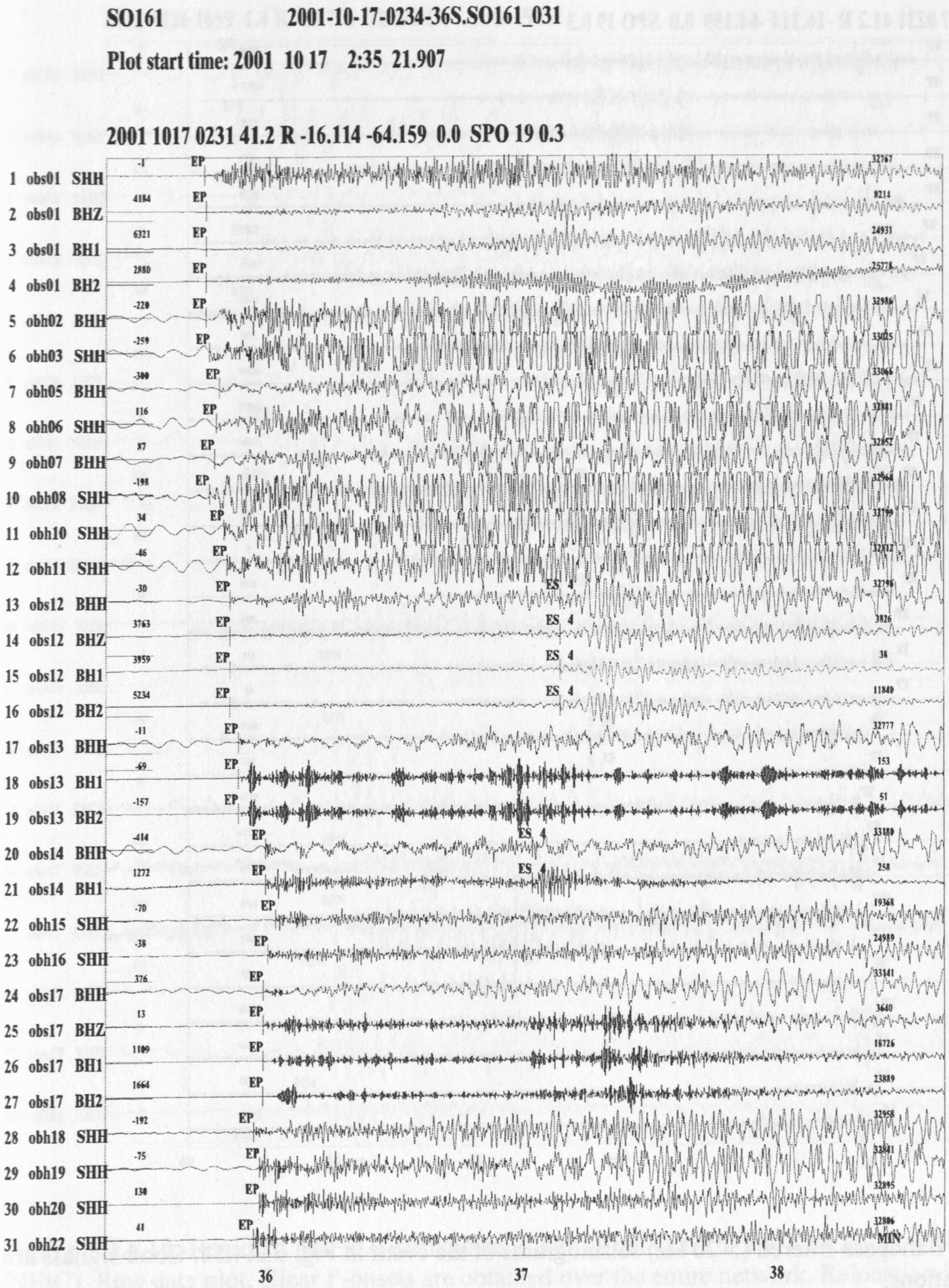

**Figure 5.3.4.14:** Regional $M_W$=5.4 earthquake in Northern Chile from Oct. 17, 2001 02:34:38 at 28.30° S, 68.71° W, depth 81 km (NEIC). Raw data plot. Accurate relocation is impossible because the epicentre is too far away from the EQNET network, which was designed for local earthquake studies.

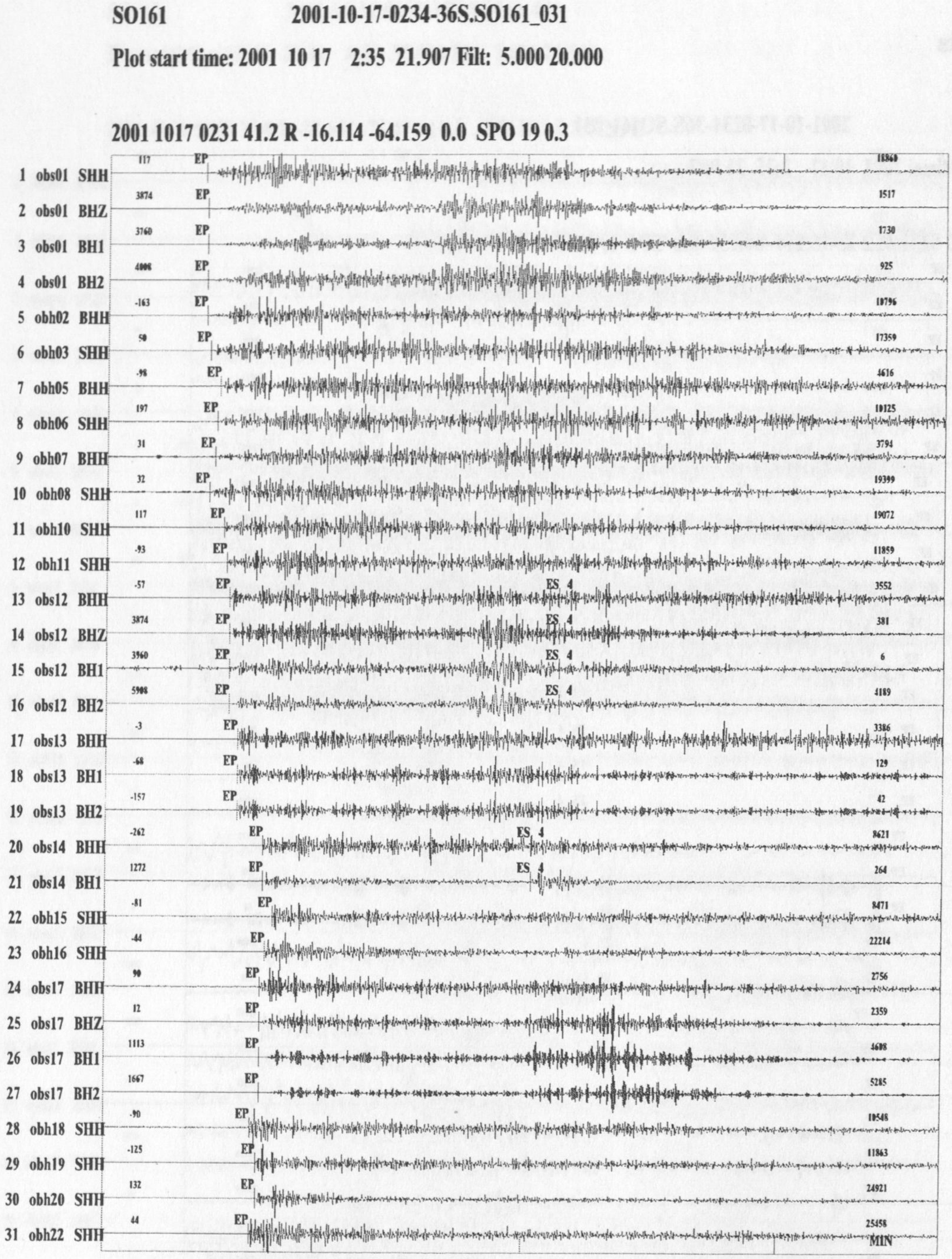

**Figure 5.3.4.15:** Bandpass filtered (5-20 Hz) seismograms of the event in Fig. 5.3.4.14. Good signals are obtained at all stations.

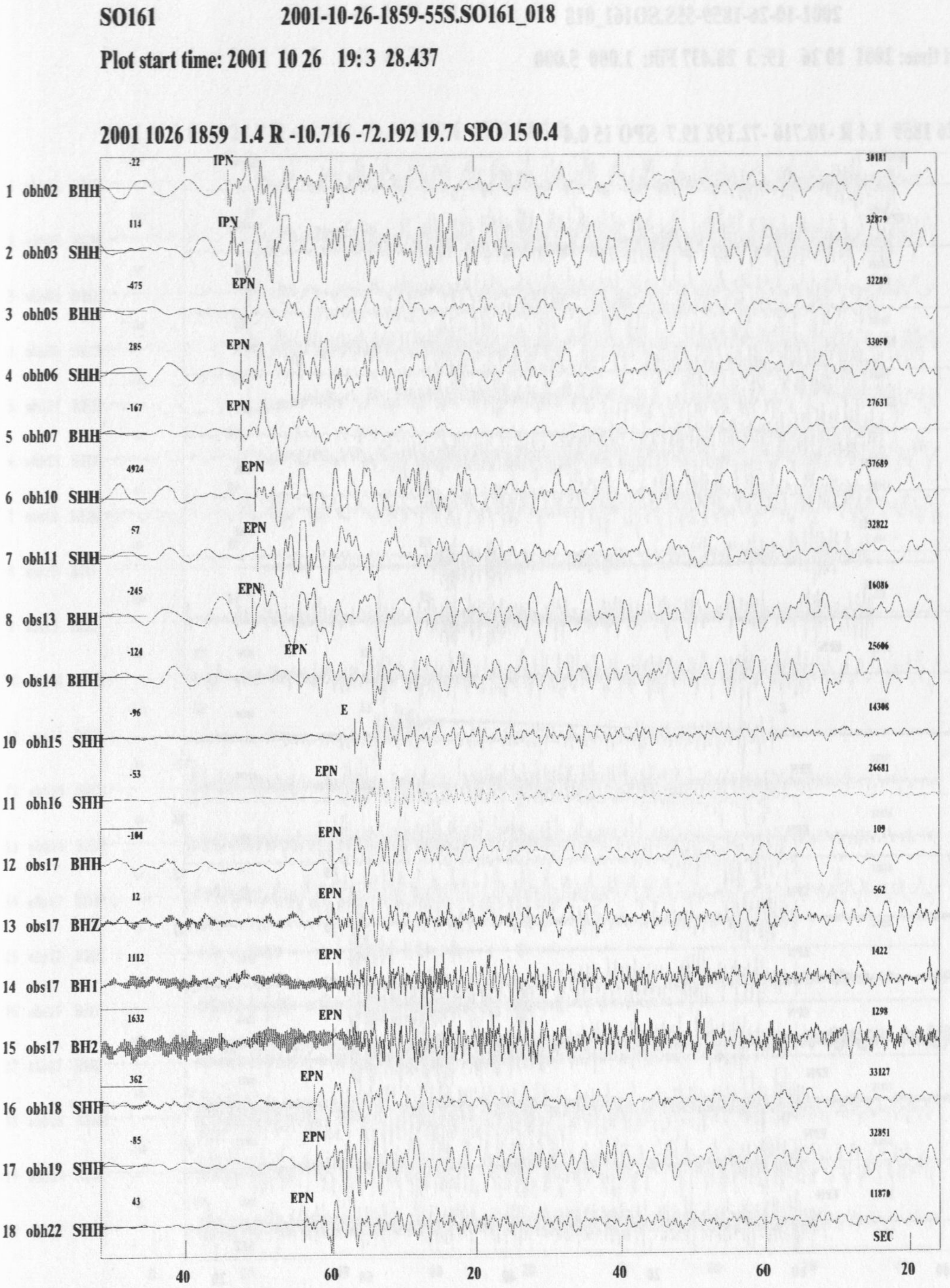

**Figure 5.3.4.16:** Regional $M_W$=6.0 earthquake in Peru from Oct. 26, 2001 18:59:56 at 14.79° S, 70.50° W (NEIC). Raw data plot. Clear P-onsets are obtained over the entire network. Relocation is inaccurate because the epicentre is far from the network, and only first arrivals has been picked.

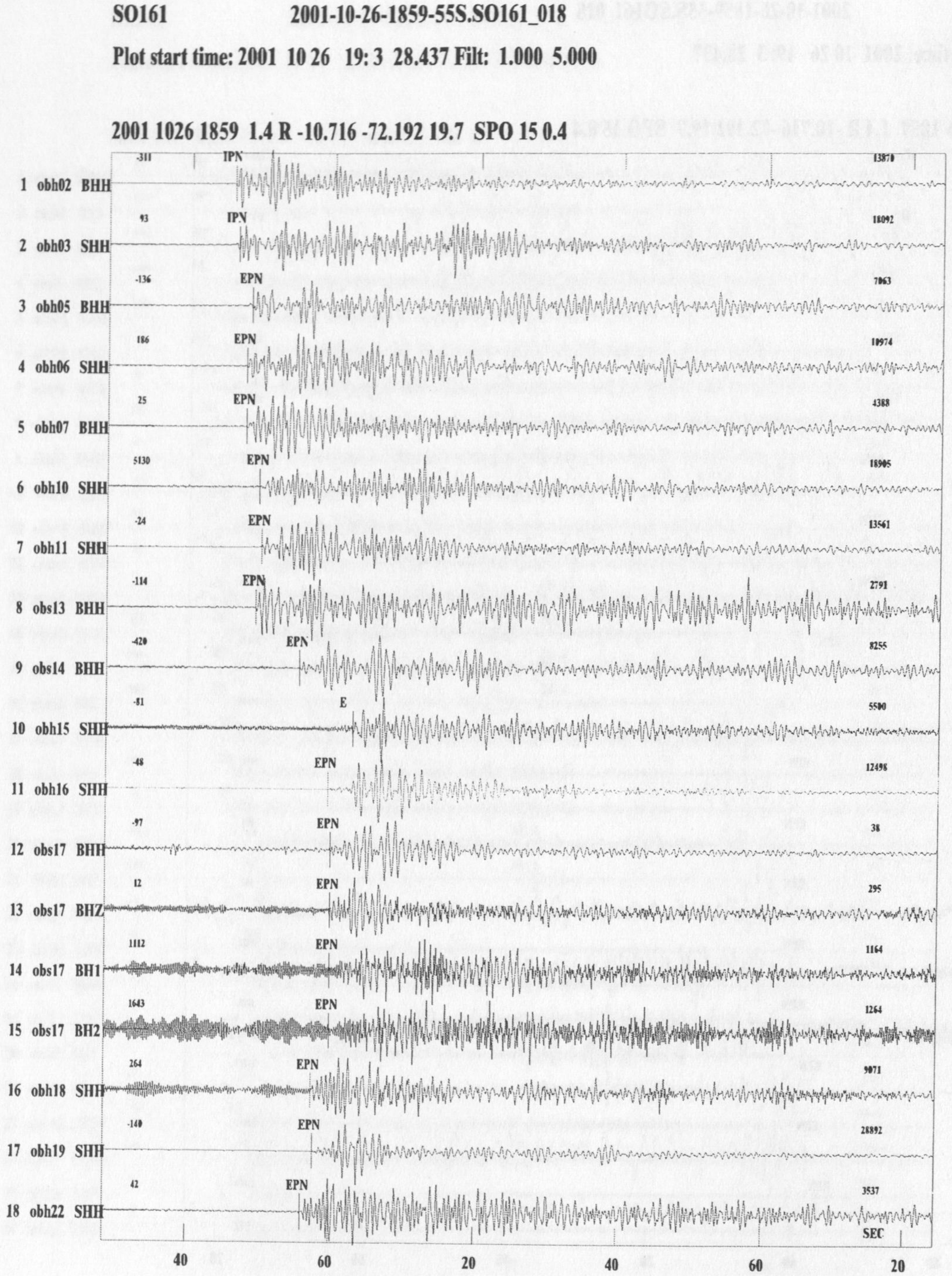

**Figure 5.3.4.17:** Bandpass filtered (1-5 Hz) seismograms of the Oct. 26, 2001 regional event in Figure 5.3.4.15. Good signals are obtained at all stations. At obs17 the horizontal components show higher frequency noise. It was the only seismometer which was operating correctly at the time of the event.

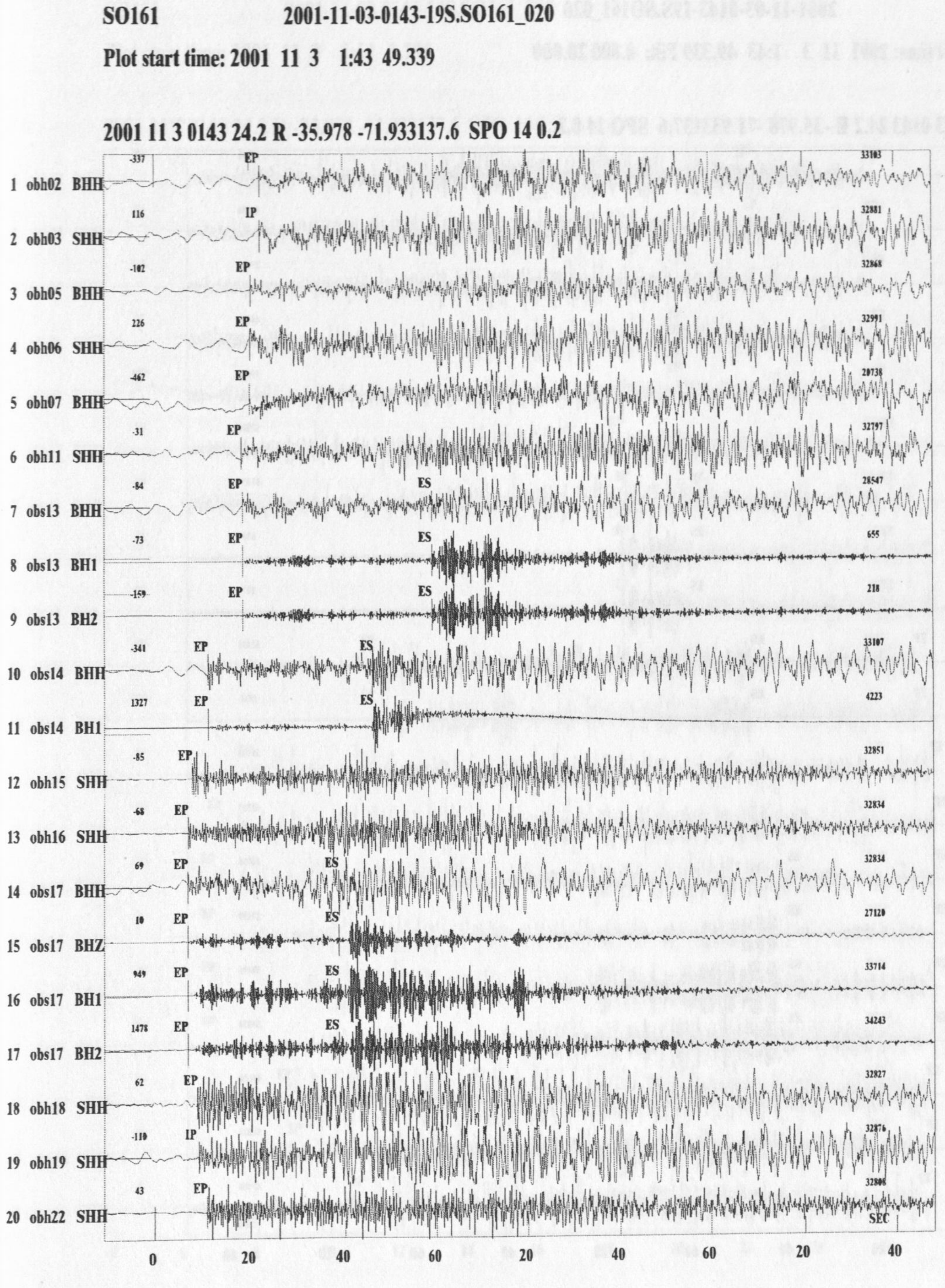

**Figure 5.3.4.18:** Raw seismograms of an event south of the EQNET array from Nov. 03, 2001 01:43 with mb=4.8 at 36.12° S, 71.38° W. The seismometer channels (traces 8, 9, 11, 15-17) show good S-waves, which cannot be observed with pressure sensors (HH channels). The vertical components of obs13 and obs14 where down, and the horizontal channels of obs13 (8,9) are identical. Relocation is much better than for the previous regional events. This is because of shorter epicentral distances and the usage of S-wave picks.

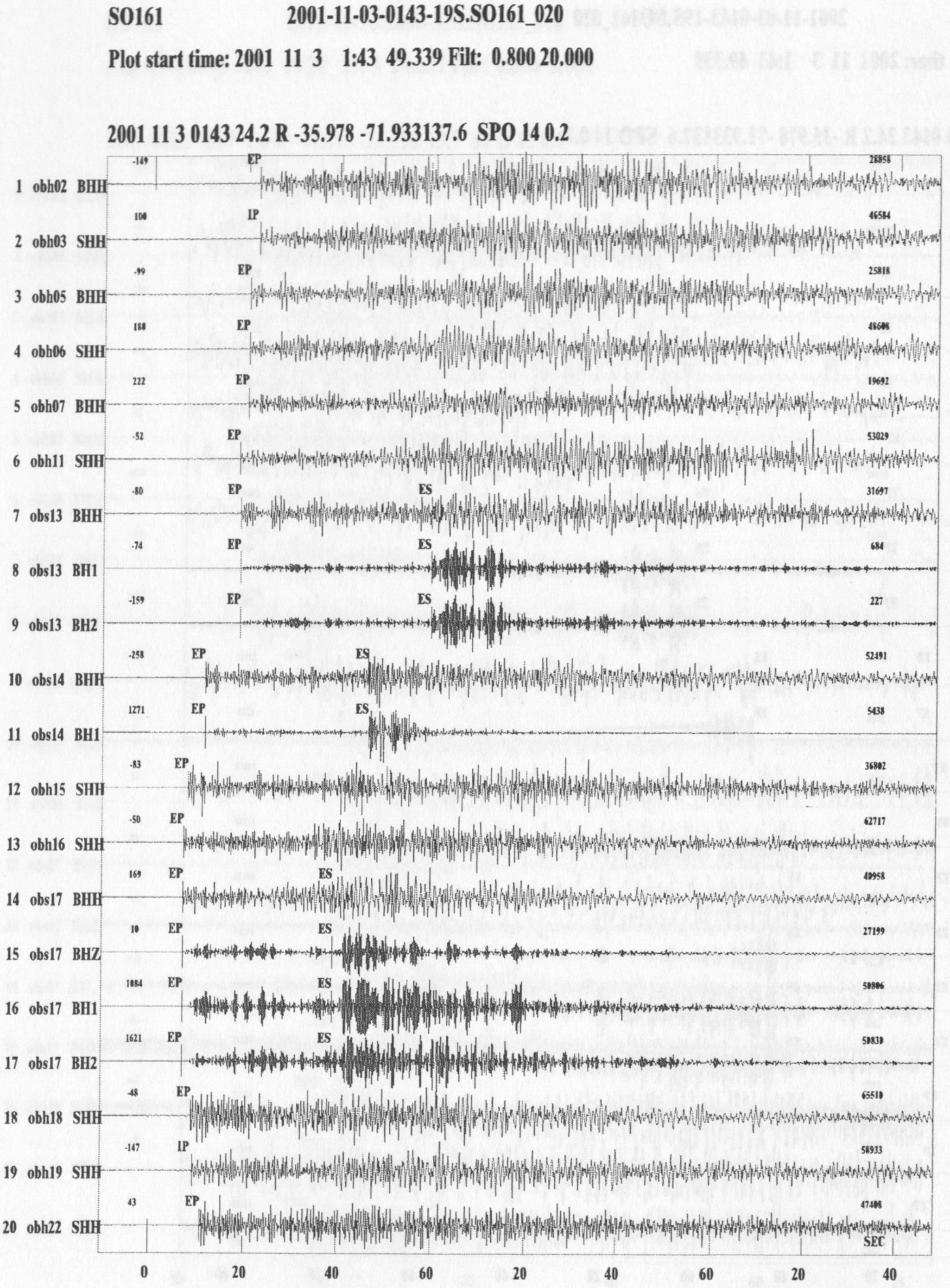

Figure 5.3.4.19: Bandpass filtered (0.8-20 Hz) seismograms of the Nov. 3, 2001 event in Fig. 5.3.4.17.

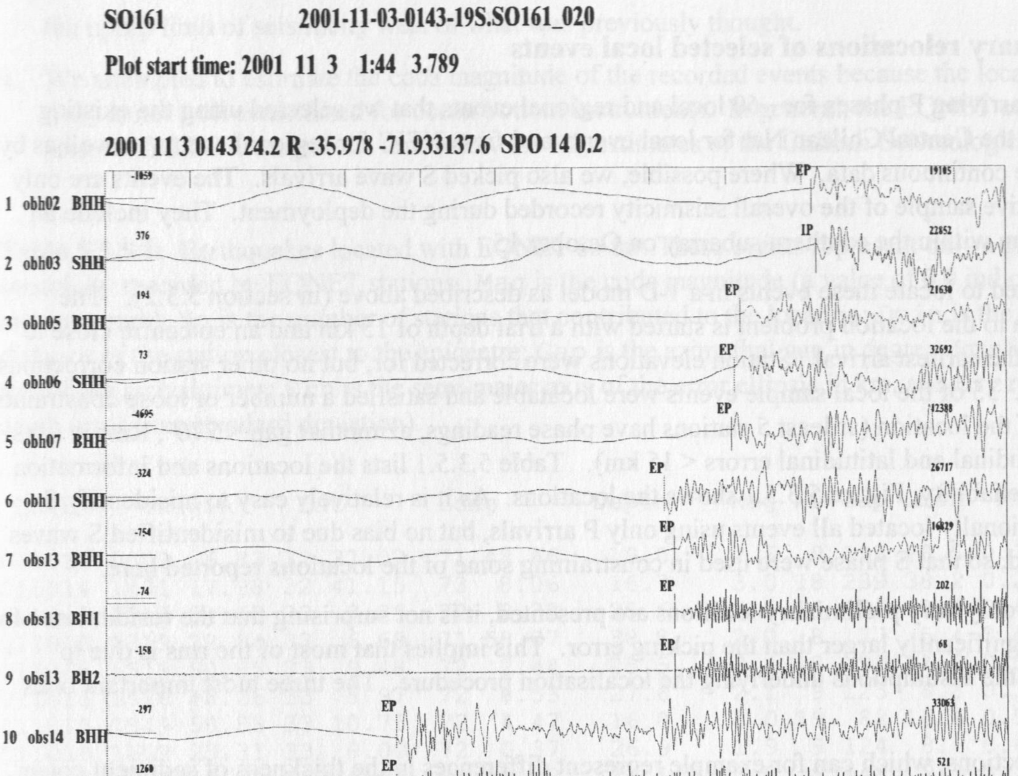

**Figure 5.3.4.20:** Zoomed-in view of the P-wavelets of the Nov. 03, 2001 event in Fig. 5.3.4.18 (raw data). Station obh18 is clipped. The signals on the horizontal components of obs17 are extremely narrow band. This can also be observed on the signal spectra of figure 5.3.4.6, where the horizontals have a stronger peak around 2.5 Hz than the vertical.

### 5.3.5. Preliminary relocations of selected local events

We picked first arriving P phases for ~60 local and regional events that we selected using the existing catalogues from the Central Chilean Net for local events and from NEIC for regional events as well as by inspection of the continuous data. Where possible, we also picked S wave arrivals. The events are only an unrepresentative sample of the overall seismicity recorded during the deployment. They include an earthquake swarm within the southern subarray on October 15.

We then attempted to locate these events in a 1-D model as described above (in section 5.3.2). The iterative solution to the location problem is started with a trial depth of 15 km and an epicentre close to the station with the earliest arrival. Station elevations were corrected for, but no other station corrections were carried out. 35 of the local sample events were locatable and satisfied a number of loose constraints on the quality of the location (at least 5 stations have phase readings, azimuthal gap < 270°, Rms < 1.0 s, estimated longitudinal and latitudinal errors < 15 km). Table 5.3.5.1 lists the locations and information regarding their reliability, Figure 5.3.5.1 shows the locations. As it is relatively easy to misidentify S phases, we additionally located all events using only P arrivals, but no bias due to misidentified S waves could be detected, so that S phase were used in constraining some of the locations reported here.

As in this report only very preliminary locations are presented, it is not surprising that the residual rms for most events is significantly larger than the picking error. This implies that most of the rms is due to shortcomings of the assumptions underlying the localisation procedure. The three most important ones are likely to be:

- Station corrections, which can for example represent differences in the thickness of sediment cover, have not been determined.
- The assumption of a one-dimensional velocity model is clearly inappropriate in a subduction zone.
- Station locations are not quite correct because of the drift of the stations as they sink to the seafloor.

For this reason, all results are suggestive rather than conclusive. Nevertheless, we can make a few first order observations.

1. The events of the October 15 swarm cluster tightly together (with only one exception), i.e., they are likely to have occurred on the same fault or within the same fault system. The mutual proximity of the locations shows that the location procedure produces at least internally consistent results, even though a different set of stations contributed to the location of each event in the swarm.
2. Earthquakes in the EQNET area occur predominantly between 15 and 30 km depth below sea-level (Figure 5.3.5.2). Those events that fall outside this range belong to the least well located events in the sample set, and not too much significance should be attached to their depths (the formal standard deviation for depth exceeds 13 km for each of the three events located well below 30 km). It is well known that the nonlinear problem of earthquake location can, under certain circumstances, be sensitive to the starting depth assumed in the iterative solution. In order to assess the robustness of the depths obtained by us, we tried a number of starting depths between 5 and 40 km. The 15-30 km depth limits occured for all starting depths within this range.
3. For 29 events in the sample set, locations are also available from the catalogue of the Central Chile Net. Histograms of the differences in location between both catalogues are presented in Figure 5.2.5.3, and the horizontal differences are also shown in Figure 5.2.5.1. No particular trend is observed for the difference in North-South direction, and there is only a slight tendency towards deeper locations in the EQNET catalogue. The most striking result is that EQNET locations of events in the northern subarray are displaced ~8-12 km westward with regard to the Central Chile Net locations. The reason for this bias is not yet clear, but we can speculate that it is due to lateral heterogeneity. Assuming this trend is confirmed by a more comprehensive analysis, this would move

the updip limit of seismicity west of what was previously thought.

4. We attempted to estimate the coda magnitude of the recorded events because the local Richter scale ($M_L$) is not well established for ocean bottom instruments. In general, the EQNET coda magnitudes seem to fall 0.5-1 magnitude unit below the $M_L$ estimates of the Chilean Seismological Service.

**Table 5.3.5.1:** Earthquakes located with EQNET so far. These events represent only a part of the seismicity recorded by EQNET stations. `Mag` is the coda magnitude (a value of 0.0 indicates no measurement); `No` is the number of stations that contributed to the location; `Dmin` is the epicentral distance of the station closest to the epicentre; `Gap` is the azimuthal gap in degree; `Rms` is the residual rms of the arrival times; `Erh` is the semi-major axis of the error ellipsis in km, and `Erzr` is the estimated depth error (one standard deviation).

| Date | Origin | Lat | Long | Depth | Mag | No | Gap | Dmin | Rms | Erh | Erzr |
|---|---|---|---|---|---|---|---|---|---|---|---|
| 011013 | 0503 6.83 | 32 37.02 | 71 48.66 | 19.0 | 2.6 | 9 | 198 | 28.5 | 0.31 | 7.9 | 4.00 |
| 011014 | 1431 17.98 | 32 41.15 | 73 8.06 | 16.7 | 3.0 | 18 | 239 | 38.2 | 0.28 | 8.8 | 2.60 |
| 011015 | 1307 54.13 | 33 9.29 | 72 2.32 | 25.6 | 3.1 | 19 | 89 | 11.6 | 0.48 | 8.8 | 5.11 |
| 011015 | 1319 22.04 | 33 6.69 | 71 58.07 | 38.8 | 2.0 | 8 | 177 | 5.4 | 0.44 | 15.8 | 16.40 |
| 011015 | 1519 50.85 | 33 9.48 | 72 2.44 | 25.5 | 3.4 | 18 | 90 | 11.9 | 0.51 | 8.4 | 4.41 |
| 011015 | 1526 46.26 | 33 8.97 | 72 0.53 | 27.6 | 2.1 | 9 | 125 | 8.8 | 0.39 | 7.4 | 6.60 |
| 011015 | 1549 50.88 | 33 10.75 | 72 4.47 | 16.8 | 3.0 | 19 | 82 | 15.6 | 0.52 | 7.5 | 3.11 |
| 011015 | 1602 23.31 | 33 9.00 | 72 0.37 | 26.9 | 1.9 | 9 | 124 | 8.6 | 0.45 | 11.8 | 6.80 |
| 011015 | 1635 43.72 | 33 6.97 | 72 1.22 | 24.1 | 0.0 | 9 | 148 | 9.9 | 0.37 | 9.5 | 8.40 |
| 011015 | 1856 25.70 | 33 7.99 | 72 1.50 | 24.1 | 2.6 | 17 | 83 | 10.1 | 0.39 | 7.5 | 4.61 |
| 011015 | 1941 38.90 | 33 7.84 | 72 2.68 | 30.1 | 2.2 | 9 | 137 | 14.5 | 0.51 | 15.2 | 16.50 |
| 011016 | 0023 56.23 | 33 9.40 | 72 3.32 | 26.1 | 2.5 | 16 | 83 | 13.2 | 0.56 | 10.4 | 6.81 |
| 011020 | 0443 34.10 | 32 42.09 | 71 38.02 | 19.7 | 2.6 | 14 | 220 | 46.7 | 0.20 | 7.4 | 2.50 |
| 011021 | 1006 27.39 | 32 28.94 | 71 46.97 | 25.9 | 2.8 | 23 | 183 | 21.7 | 0.69 | 9.0 | 4.71 |
| 011021 | 1639 11.64 | 32 16.27 | 71 54.47 | 22.2 | 2.6 | 18 | 162 | 9.0 | 0.62 | 6.7 | 3.81 |
| 011022 | 0625 40.54 | 32 17.24 | 72 46.01 | 23.8 | 3.2 | 22 | 203 | 20.1 | 0.31 | 4.4 | 2.90 |
| 011024 | 2108 30.22 | 32 16.16 | 71 57.81 | 28.2 | 3.1 | 13 | 202 | 21.0 | 0.72 | 14.3 | 10.21 |
| 011025 | 1848 33.72 | 32 23.85 | 71 52.23 | 24.5 | 2.8 | 13 | 206 | 12.4 | 0.79 | 13.3 | 5.51 |
| 011027 | 0641 38.74 | 32 22.56 | 71 55.22 | 26.0 | 0.0 | 8 | 197 | 15.8 | 0.61 | 17.4 | 10.01 |
| 011102 | 1207 48.70 | 32 37.42 | 72 13.69 | 19.7 | 2.6 | 12 | 144 | 23.0 | 0.43 | 8.0 | 3.41 |
| 011103 | 1017 56.41 | 32 28.88 | 71 58.68 | 23.6 | 2.5 | 11 | 178 | 25.7 | 0.49 | 8.0 | 4.81 |
| 011104 | 0854 54.91 | 32 36.64 | 72 7.71 | 21.6 | 2.8 | 12 | 144 | 22.5 | 0.58 | 11.0 | 6.51 |
| 011107 | 0124 46.97 | 32 17.07 | 72 1.29 | 26.7 | 2.6 | 7 | 216 | 17.3 | 0.46 | 14.9 | 7.81 |
| 011107 | 0150 31.80 | 32 14.65 | 71 57.12 | 21.8 | 2.6 | 16 | 197 | 4.6 | 0.74 | 9.4 | 4.91 |
| 011107 | 0155 26.82 | 32 15.33 | 71 56.26 | 19.8 | 0.0 | 12 | 200 | 5.9 | 0.48 | 7.0 | 4.31 |
| 011107 | 1347 6.74 | 32 14.38 | 71 55.14 | 22.2 | 2.6 | 13 | 204 | 7.7 | 0.68 | 10.8 | 4.71 |
| 011110 | 1756 55.29 | 32 10.93 | 71 53.81 | 25.4 | 2.7 | 10 | 226 | 14.7 | 0.59 | 13.3 | 4.31 |
| 011115 | 1805 35.34 | 32 45.27 | 71 26.76 | 15.1 | 2.6 | 8 | 263 | 60.8 | 0.18 | 12.7 | 2.50 |
| 011116 | 0316 54.67 | 32 16.28 | 71 55.84 | 24.0 | 2.6 | 11 | 201 | 6.9 | 0.68 | 14.5 | 6.01 |
| 011116 | 0640 35.35 | 32 38.39 | 73 10.61 | 16.1 | 3.4 | 16 | 251 | 34.7 | 0.37 | 9.4 | 2.70 |
| 011118 | 1651 47.56 | 32 8.59 | 71 58.16 | 44.9 | 3.2 | 18 | 201 | 7.3 | 0.86 | 17.5 | 13.21 |
| 011118 | 2046 24.92 | 32 30.82 | 71 51.74 | 25.5 | 3.0 | 14 | 200 | 32.0 | 0.66 | 14.1 | 9.11 |
| 011118 | 2314 56.66 | 32 43.81 | 71 57.29 | 16.3 | 2.8 | 13 | 180 | 44.8 | 0.92 | 16.6 | 7.81 |
| 011121 | 1342 32.64 | 32 41.19 | 72 2.13 | 18.2 | 2.8 | 11 | 163 | 33.6 | 0.62 | 15.3 | 4.41 |
| 011122 | 1111 30.61 | 32 21.96 | 71 40.80 | 50.2 | 2.4 | 6 | 240 | 32.8 | 0.13 | 11.7 | 13.40 |

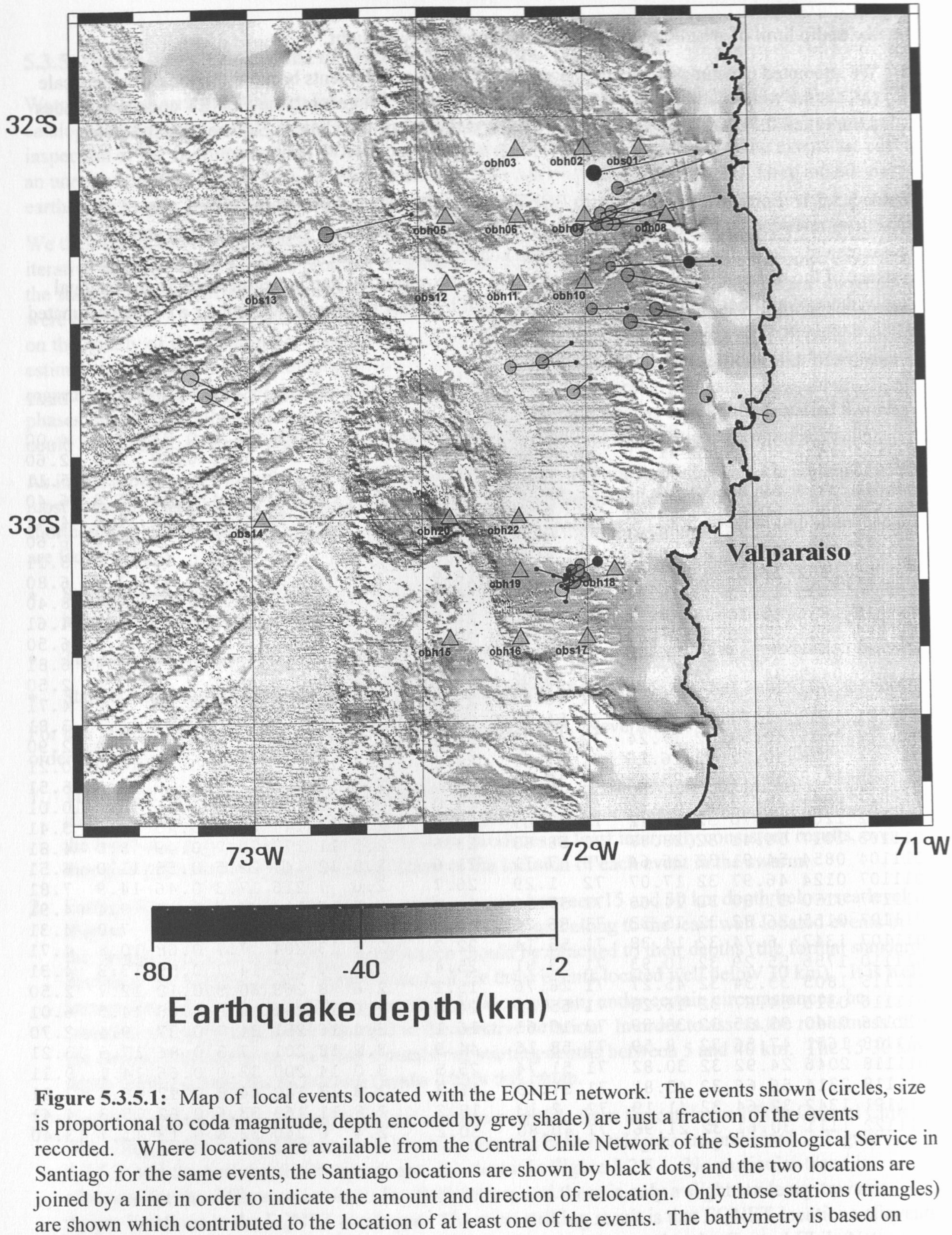

**Figure 5.3.5.1:** Map of local events located with the EQNET network. The events shown (circles, size is proportional to coda magnitude, depth encoded by grey shade) are just a fraction of the events recorded. Where locations are available from the Central Chile Network of the Seismological Service in Santiago for the same events, the Santiago locations are shown by black dots, and the two locations are joined by a line in order to indicate the amount and direction of relocation. Only those stations (triangles) are shown which contributed to the location of at least one of the events. The bathymetry is based on hydrosweep mapping during this cruise and the CONDOR survey.

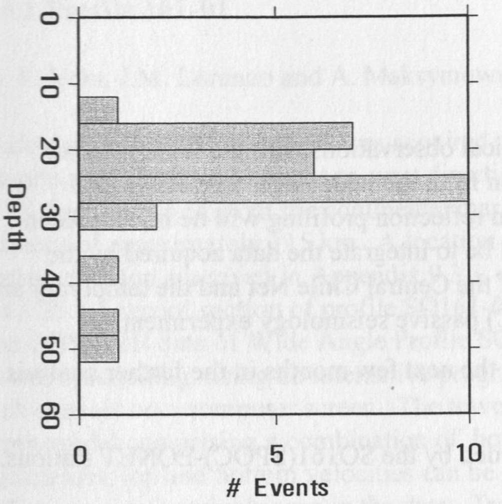

**Figure 5.3.5.2:** Depth distribution of located earthquakes

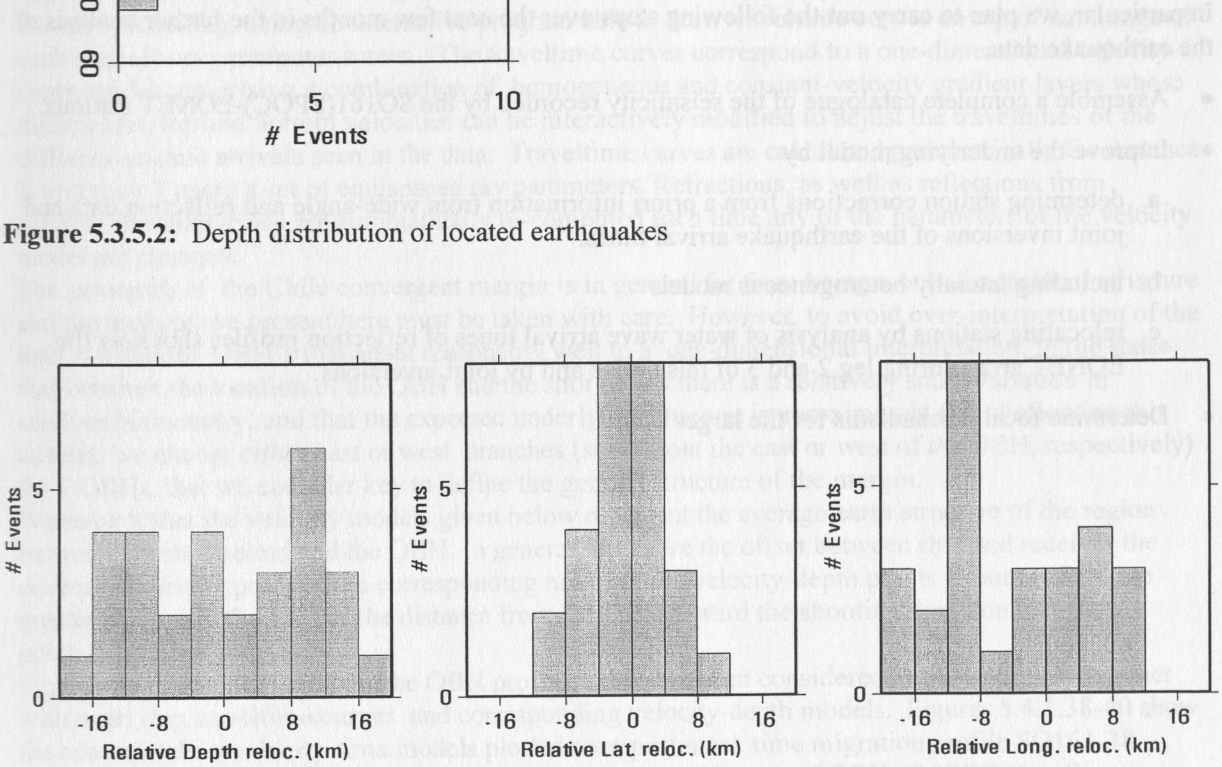

**Figure 5.3.5.3:** Histograms of latitude, longitude, and depth components of relocation vectors of events located with SO161-EQNET relative to the locations obtained by the Chilean Seismological Service using only land stations of the Central Chilean Net.

### 5.3.6. Future Work

The most important task will be to integrate the seismological observations with the work of other participating groups. In particular, the velocity information from the wide-angle modelling and information about the thickness of the sediment cover from reflection profiling will be invaluable in improving earthquake locations. Of equal importance will be to integrate the data acquired by the University of Santiago with both the permanent stations of the Central Chile Net and the temporary array located near the coast for the duration of the SO161(SPOC) passive seismology experiment.

In particular, we plan to carry out the following steps over the next few months in the further analysis of the earthquake data.

- Assemble a complete catalogue of the seismicity recorded by the SO161(SPOC)-EQNET stations.
- Improve the underlying model by
  a. determing station corrections from a priori information from wide-angle and reflection data and joint inversions of the earthquake arrival times.
  b. including laterally heterogeneous models
  c. relocating stations by analysis of water wave arrival times of reflection profiles shot near the EQNET array during leg 2 and 3 of this cruise and by joint inversions.
- Determine focal mechanisms for the larger events

## 5.4 Wide angle seismics

### 5.4.1 Profile 161-01

(E. E. Vera, J.M. Lorenzo and A. Maksymowicz)

Wide Angle Profile SO 161-01 was acquired along multichannel reflection line SO 161-038, shot on the previous Leg along an east-to-west direction at aproximately 38°S (See Fig. 1.6.2). OBS/OBH 24 to 47 were deployed from the continental margin to the outer rise east of the trench, covering a total distance of aproximately 115 km. A location map is given in Figure 5.4.1.1. Details regarding instrumentation are given in Appendix 9.3.1, all record sections are shown in Figures 5.4.1.2 to 5.4.1.25. A record section of profile SO161-038 is shown in Figures 5.4.1.26 to 5.4.1.29.

The OBS/OBH data of Wide Angle Profile SO 161-01, are analyzed by one-dimensional traveltime forward modelling, using an interactive program able to draw traveltime curves on top of an image of each data set on a computer screen. The traveltime curves correspond to a one-dimensional velocity-depth model comprising a combination of homogeneous and constant-velocity gradient layers whose thicknesses, top and bottom velocities can be interactively modified to adjust the traveltimes of the different seismic arrivals seen in the data. Traveltime curves are calculated parametrically for distance X and time T using a set of equispaced ray parameters. Refractions, as well as reflections from velocity discontinuities are automatically re-computed each time any of the parameters of the velocity model are changed.

The geometry of the Chile convergent margin is in general far from being a one-dimensional structure and the analysis we present here must be taken with care. However, to avoid over-interpretation of the data, we choose OBH's that adapt reasonably well to a one-dimensional interpretation, in the sense that between the location of the OBH and the shot points there is a relatively small variation in seafloor bathymetry, and that the expected underlying structure is aproximately flat. Following this criteria, we choose either east or west branches (shots from the east or west of the OBH, respectively) for 7 OBHs, that we consider key to define the general structure of the margin.

We remark that the velocity models given below represent the average earth structure of the region between the shot points and the OBH. In general, the more the offset between shot and receiver the deeper the turning point of the corresponding ray. For the velocity-depth points in our models, the greater the depth, the greater the distance from the OBH toward the shooting direction that these points represent.

Figures 5.4.1.30-5.4.1.37 show the OBH profiles that have been considered in this analysis, together with overlying traveltime curves and corresponding velocity-depth models. Figures 5.4.1.38-40 show the corresponding velocity-time models plotted over post-stack time migration profile SO161-38.

Two cases are worth discussing in closer detail, the western branch of OBH 46 (OBH46w, Fig. 5.4.1.30), and the eastern branch of OBH 25 (OBH25e, Fig. 5.4.1.37) , corresponding to pure oceanic crust and continental margin, respectively. These OBH's then give the two structural extremes of the margin: The oceanic crust being subducted, and the continental structure far from the deformation front.

OBH46w samples a segment 40-60 km west of the deformation front, over an almost horizontal oceanic crust overlain by only a few hundred meters of sediments, and underlain by a distinct Moho reflection at the classical ~2s below its top (Figure 5.4.1.38) . This profile is very well suited for a one-dimensional velocity model analysis, and results in a classic 6.5 km-thick oceanic crustal structure where layers 2a-c and 3 are clearly identifiable. Figure 5.4.1.31 is a close-up of Figure 5.4.1.30 showing a bright spot for the amplitude of the refractions, at an offset of about 6.5 km, and 3.8 s reduced time. This bright spot is typical of marine refraction profiles (e.g., Vera et al., 1990) and is due to a relatively rapid increase in velocity with depth that marks the layer 2-3 transition zone, that is, the transition from extrusive basalts and sheeted dykes above to massive gabbros below. The lower limit of this zone also marks the level of the top of the axial magma chamber at the moment of crust formation. In the OBH46w velocity-depth model, this transition is represented by a linear velocity increase from 5 to 6.5 km/s between 0.53 and 1.73 km below the top of the oceanic crust. Another remarkable feature of OBH46w are the continuous Moho reflections that range from normal incidence to postcritical, with the critical point indicated by an amplitude bright spot around 25 km. The location of this critical point allows us to estimate an upper mantle velocity of about 8 km/s.

OBH25w samples a segment of the continental margin 40-70 km east of the deformation front (Fig. 5.4.1.40). Its velocity-depth modeling indicates an almost 20 km-thick layer with velocities between 4 and 6 km/s, that we interpret as continental crust, underlying an approximately ~0.5 km-thick layer of superficial, unconsolidated sediments. This interpreted continental crust is underlain by a ~6 km thick layer with an average velocity of 6.5 km/s that we interpret as subducted oceanic crust. The 20 km-thick continental crust can be divided into a 5 km upper crust with velocities of 4-5 km/s, and a 15 km-thick, 6 km/s lower crust. An important detail that supports this interpretation are the reflections seen around 17 km and 6 s reduced time. These reflections are used to calibrate the thickness and velocity of the ~15 km layer that forms the main structure of the continental lower crust at this point. The results from the rest of the OBH's present a somewhat intermediate situation between those of OBH25w and OBH46w. OBH41w and OBH43w give basically the same oceanic crust structure shown by the OBH46w velocity-depth model. Additionally they give the thickness and velocity of trench sediments. OBH37e and OBH38e over the accretionary prism, are the most complex to interpret since the velocity structure is definitely not one dimensional in this section of the margin. Although the velocities may be biased particularly by the seafloor slope, these OBH's show a transition from relatively low-velocity material (< 4.5 km/s) to a region where velocities are larger than 6.5 km/s, and that we interpret as oceanic crust. OBH32e presents an upper structure similar to that of OBH25w, about 30 km to the west, but with a lower continental crust about 10 km thinner than the one inferred from OBH26w.

The interpretation of Wide Angle Profile SO 161-01 based on the results of the one-dimensional velocity-depth model discussed above is summarized in the depth section shown in Figure 5.4.1.41. This section is drawn using the seafloor bathymetry and the geometry of the upper sediments seen in multichannel reflection line SO161-38, and the one-dimensional velocity depth models discussed above. Our interpretation shows a subducting oceanic crust with a slope that increases eastward from ~2.5° under the sediment-filled trench, to ~13°, 70 km east of the deformation front at 20 km depth. It is interesting to note that this overall geometry is very similar to that found at 33° S, ~500 km to the north, during the CONDOR experimemt (von Huene et al., 1997, Flueh et al., 1998). Our interpretation would distinguish between a relatively slow upper continental crust, and a thicker and faster lower crust. The continental back stop would be located 15-25 km east of the deformation front under the middle-upper slope. This point would also mark the onset of the highly coupled seismogenic zone at ~12 km depth, where the oceanic and continental crust first enter into direct contact.

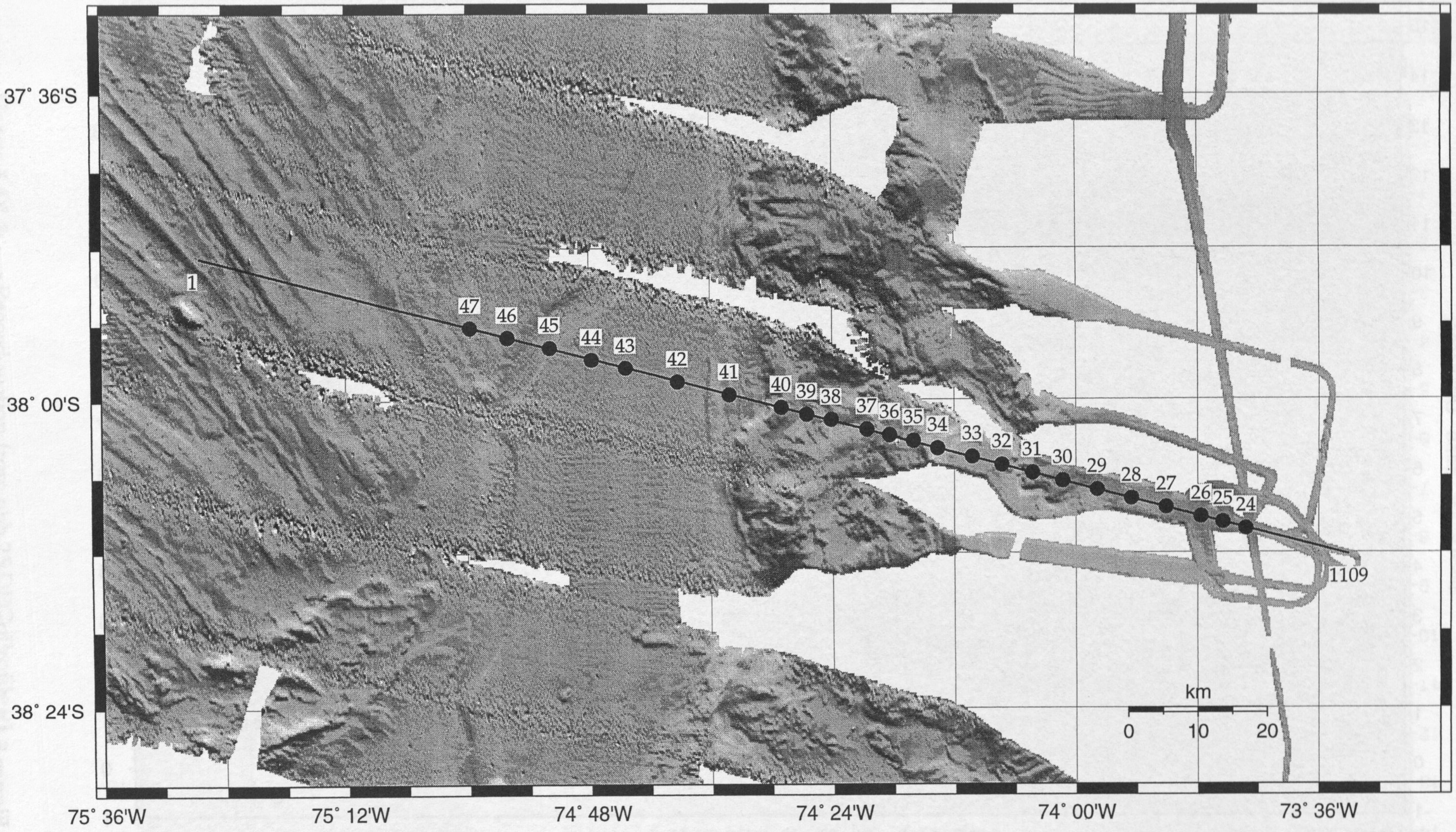

**Figure 5.4.1.1:** Location map of profile 1 and illuminated multibeam bathymetry. Superimposed the obh/obs locations, the first, and last shotpoint number.

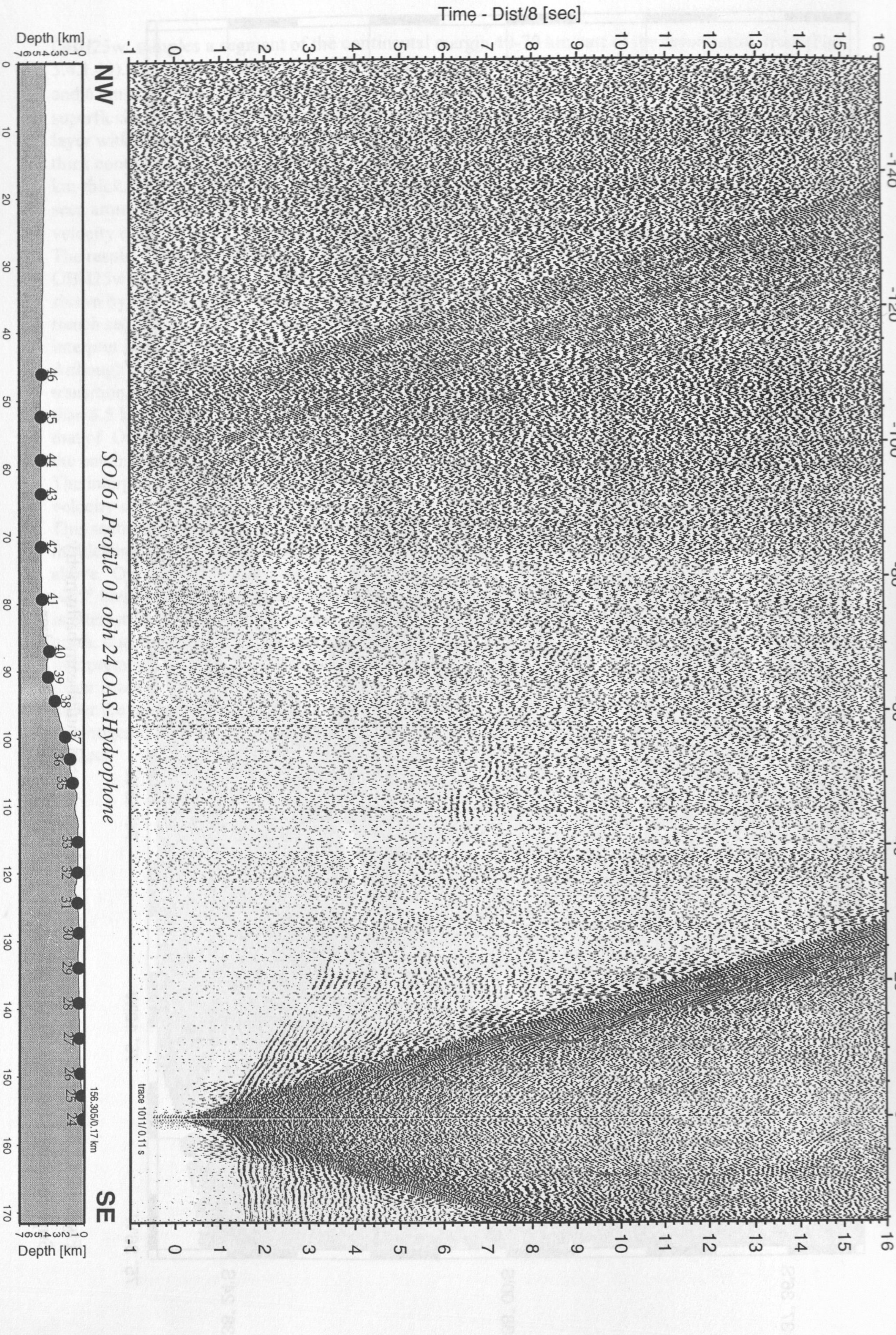

Figure 5.4.1.2: Record section from obh 24 OAS-Hydrophone, Profile 01.

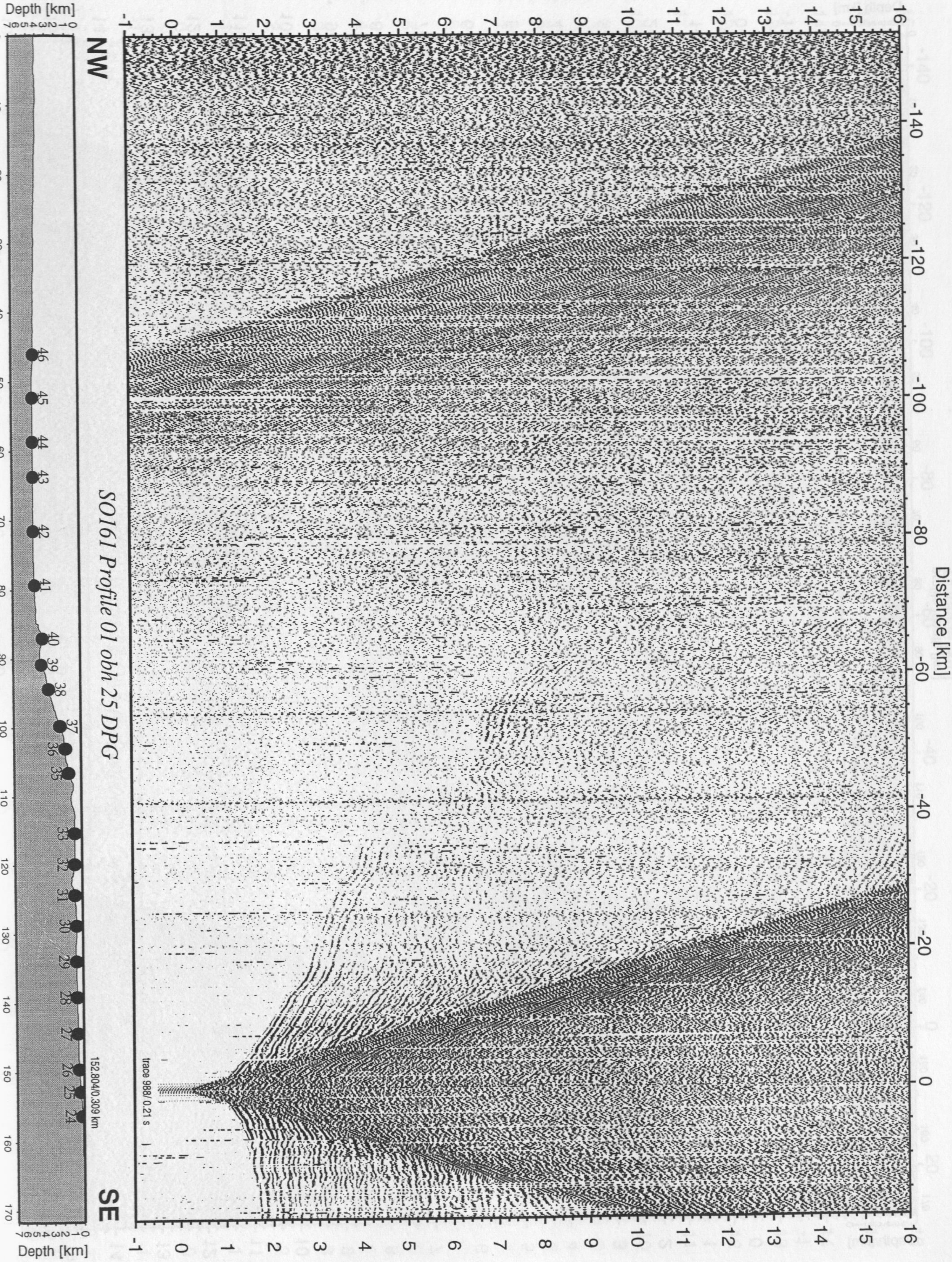

**Figure 5.4.1.3:** Record section from obh 25 DPG, Profile 01.

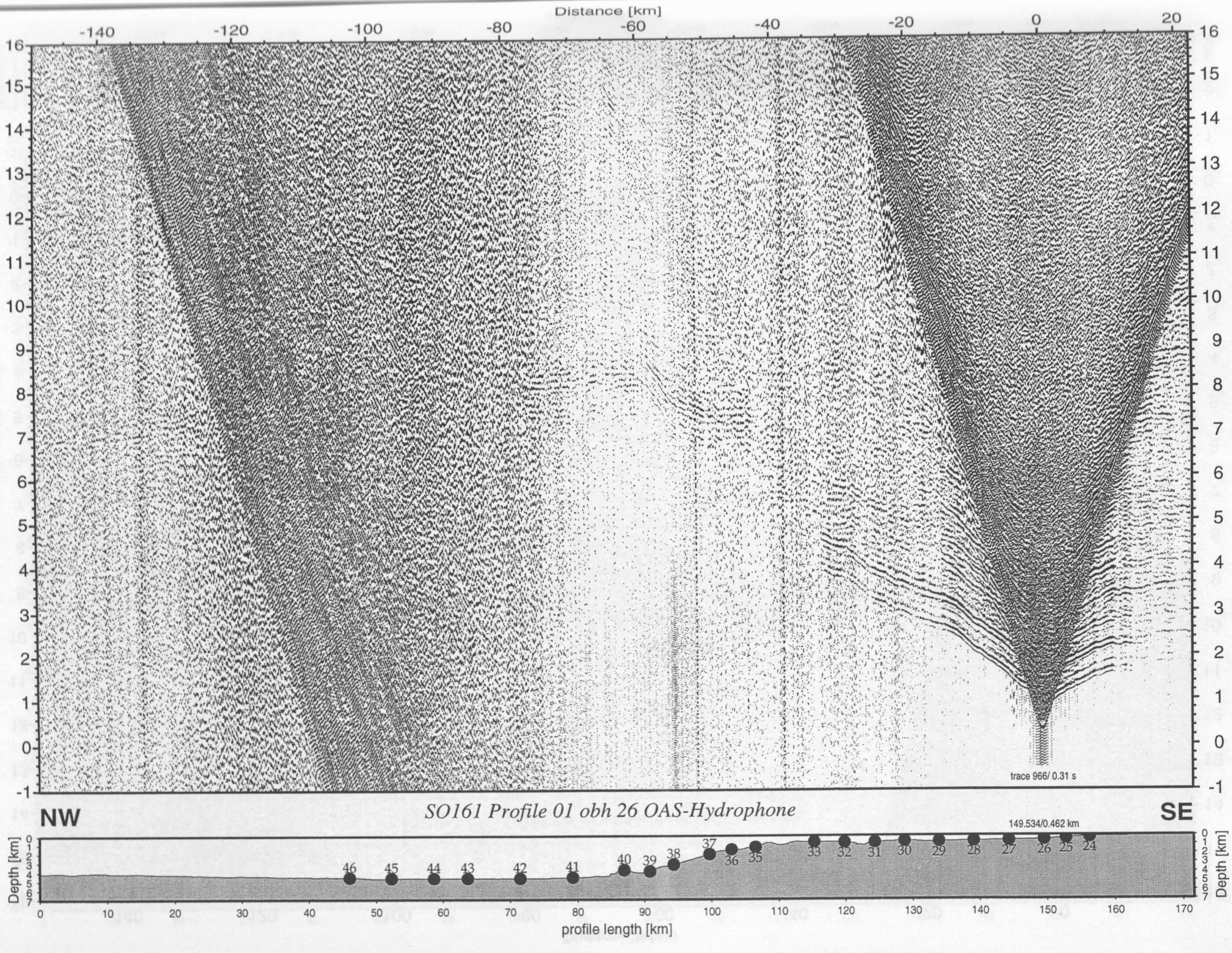

**Figure 5.4.1.4:** Record section from obh 26 OAS-Hydrophone, Profile 01.

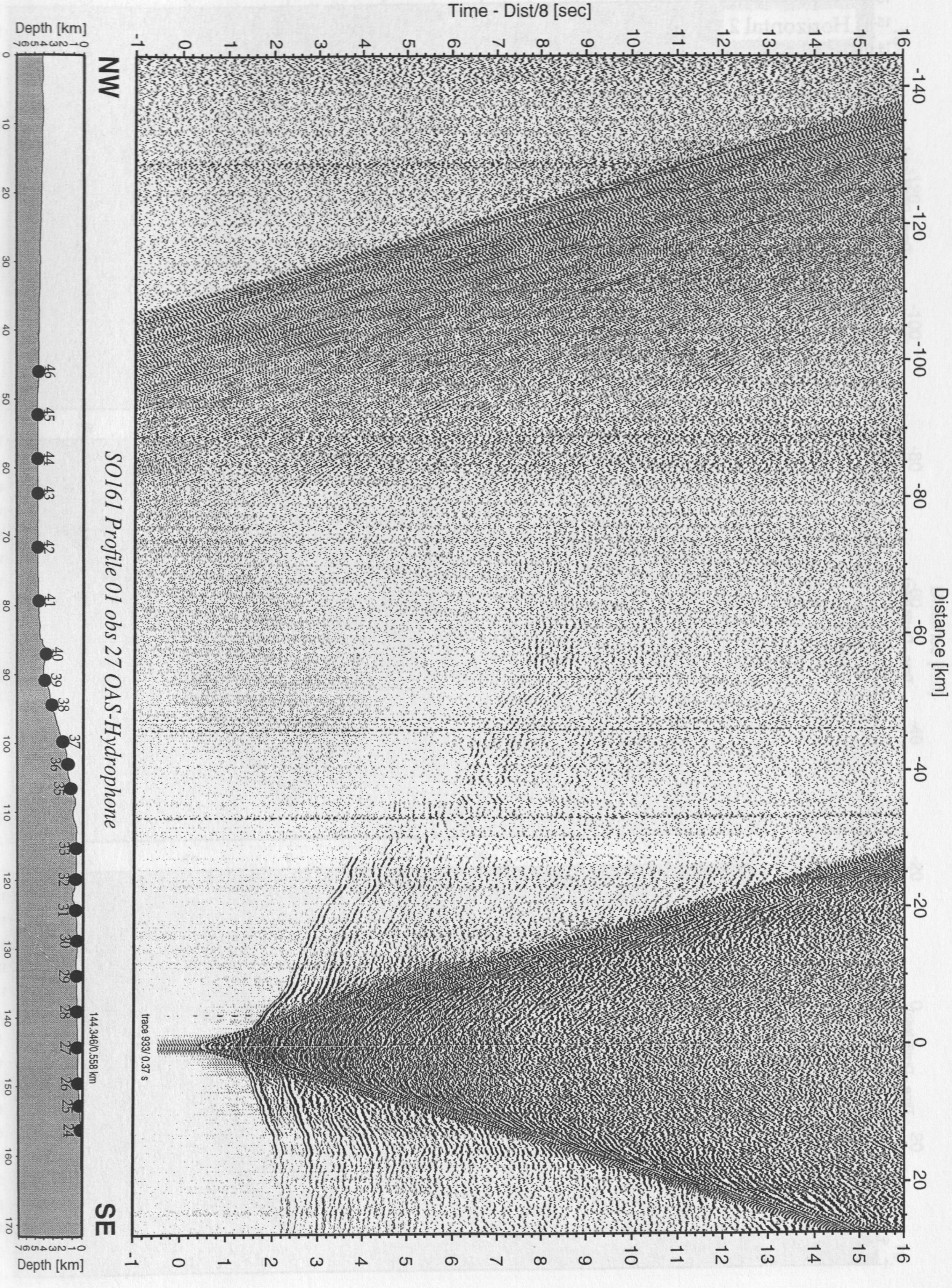

**Figure 5.4.1.5:** Record section from obs 27 OAS-Hydrophone, Profile 01.

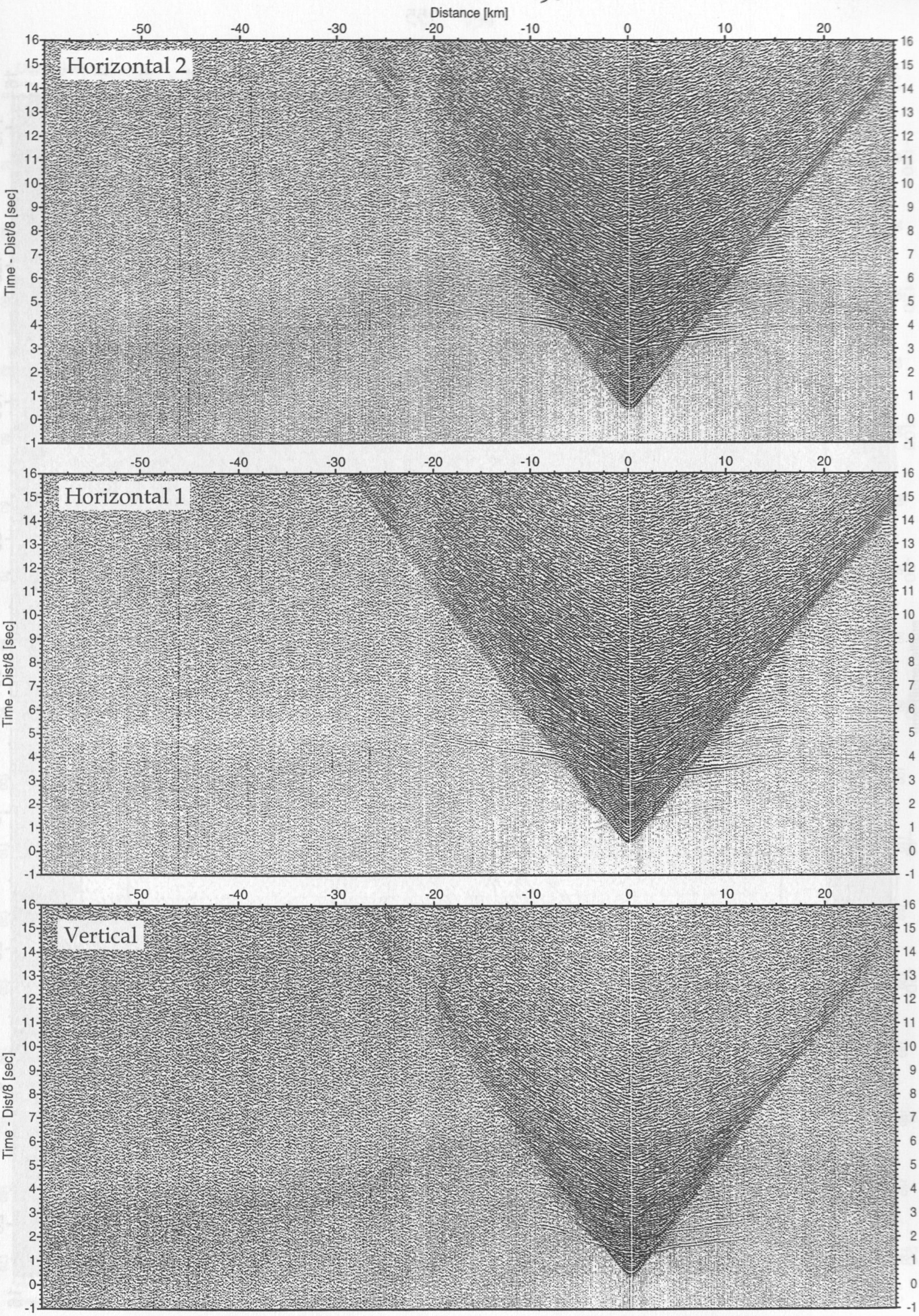

**Figure 5.4.1.6:** Record sections from obs 27 OAS/Owen-4.5Hz, SO161 Profile 01.

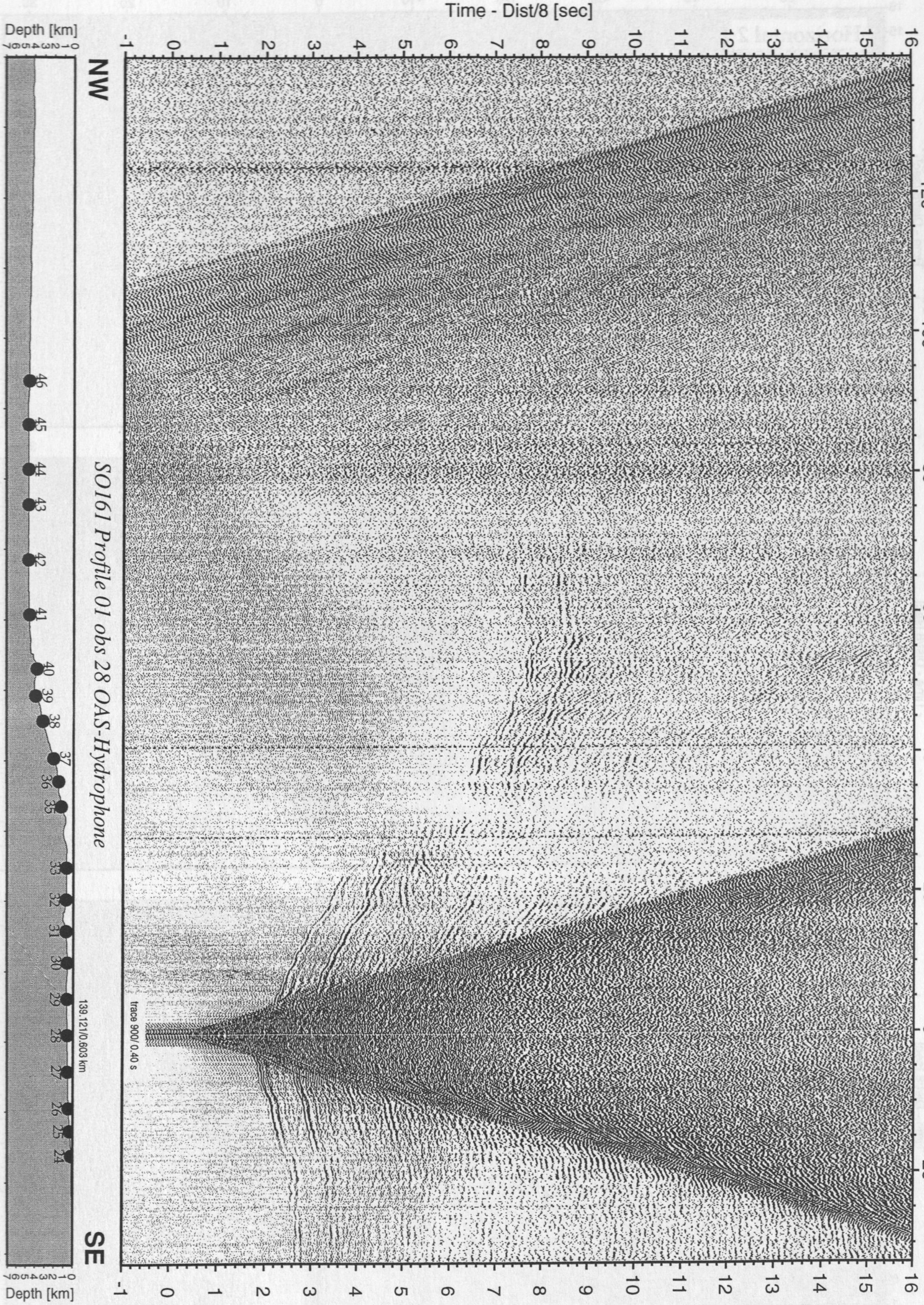

**Figure 5.4.1.7:** Record section from obs 28 OAS-Hydrophone, Profile 01.

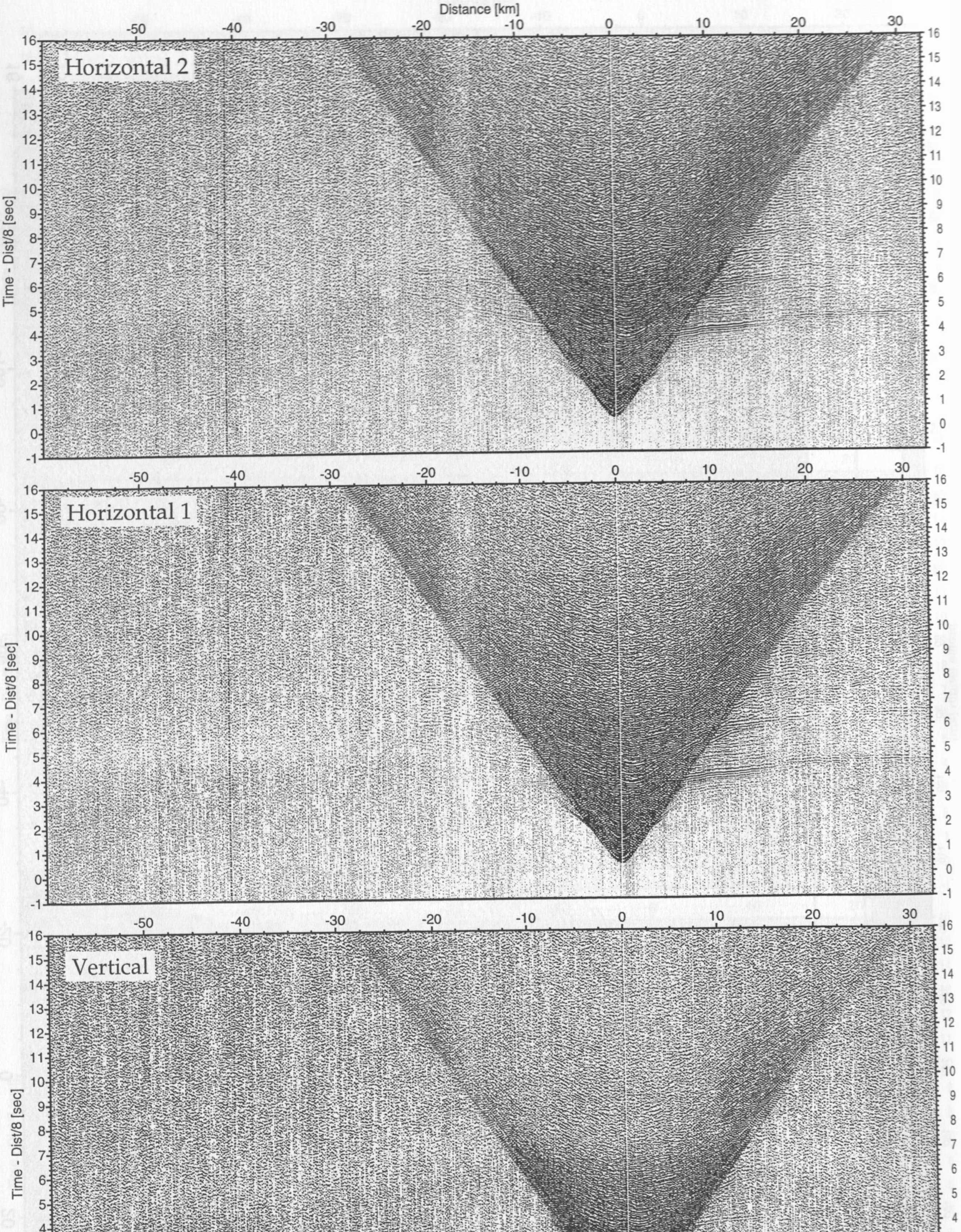

**Figure 5.4.1.8:** Record sections from obs 28 OAS/Owen-30Hz, SO161 Profile 01.

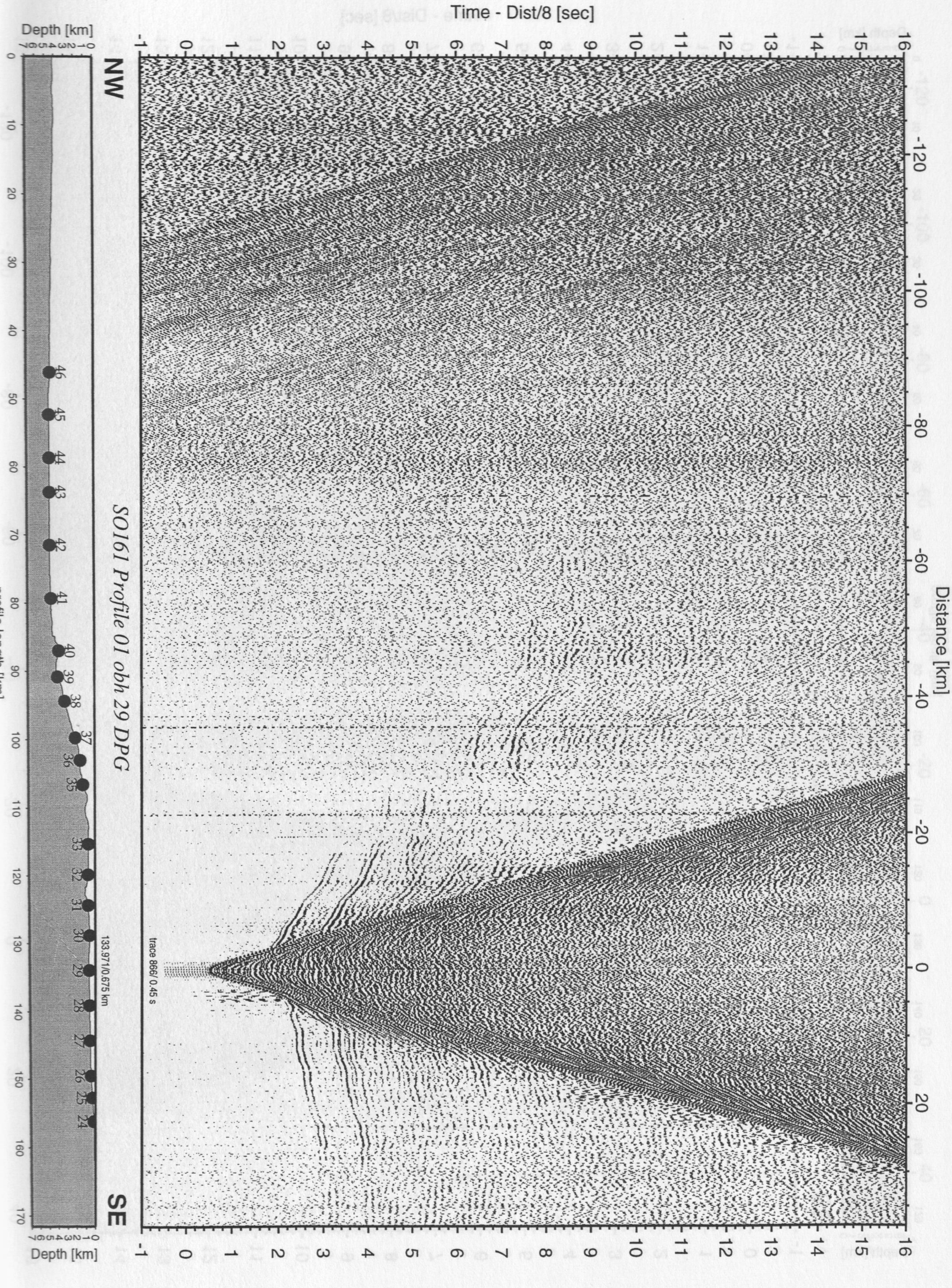

**Figure 5.4.1.9:** Record section from obh 29 DPG, Profile 01.

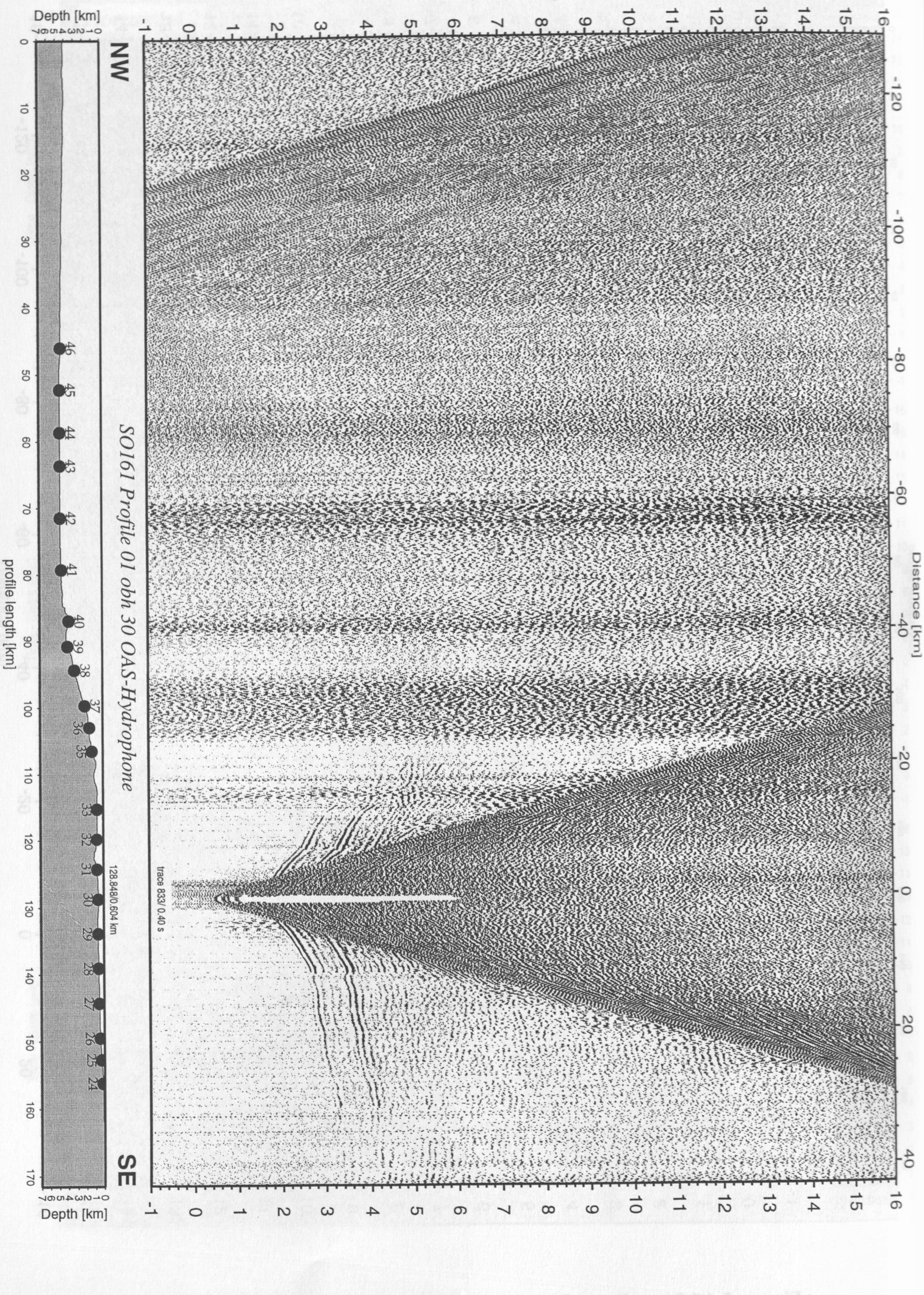

**Figure 5.4.1.10:** Record section from obh 30 OAS-Hydrophone, Profile 01.

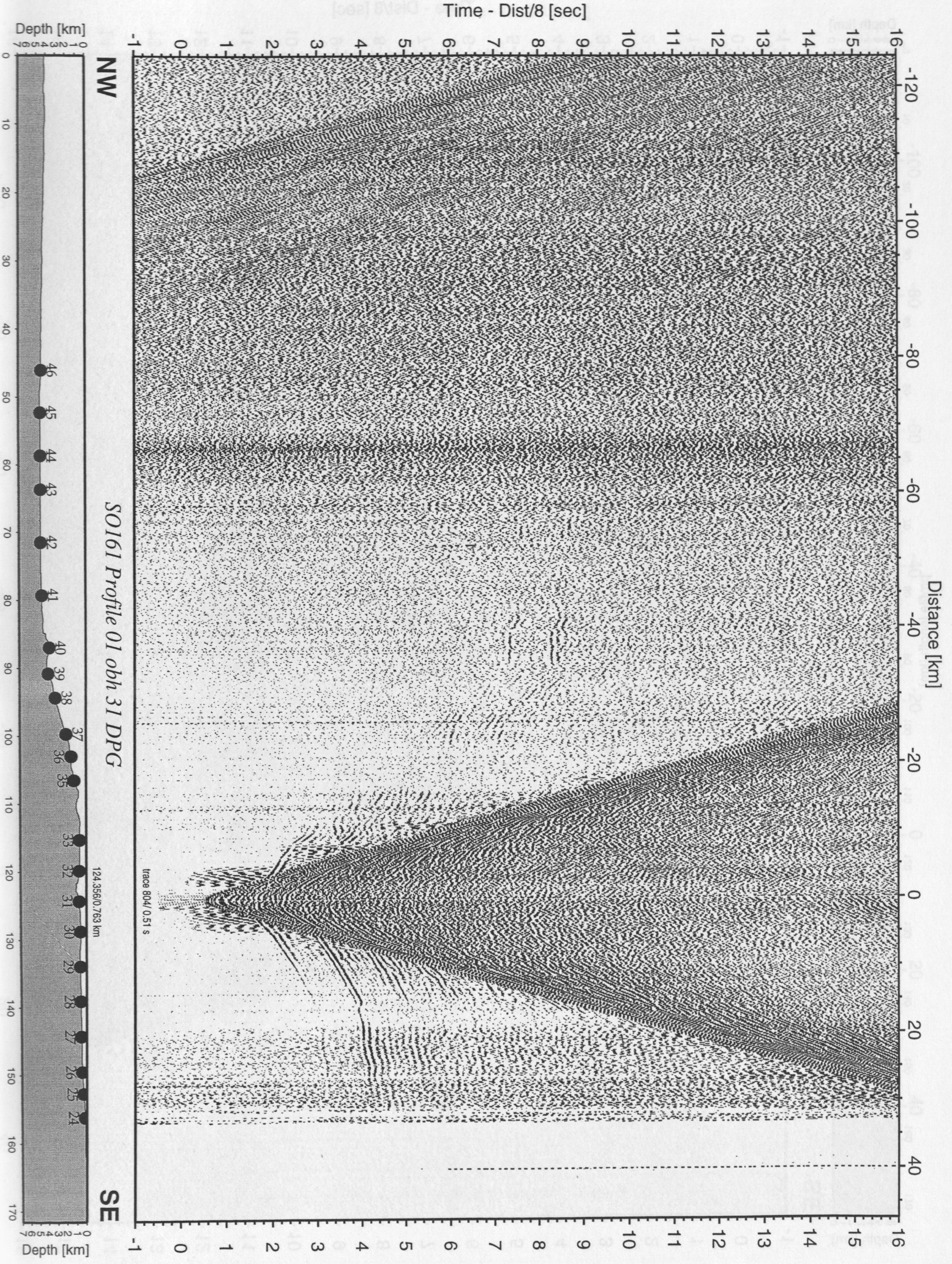

**Figure 5.4.1.11:** Record section from obh 31 DPG, Profile 01.

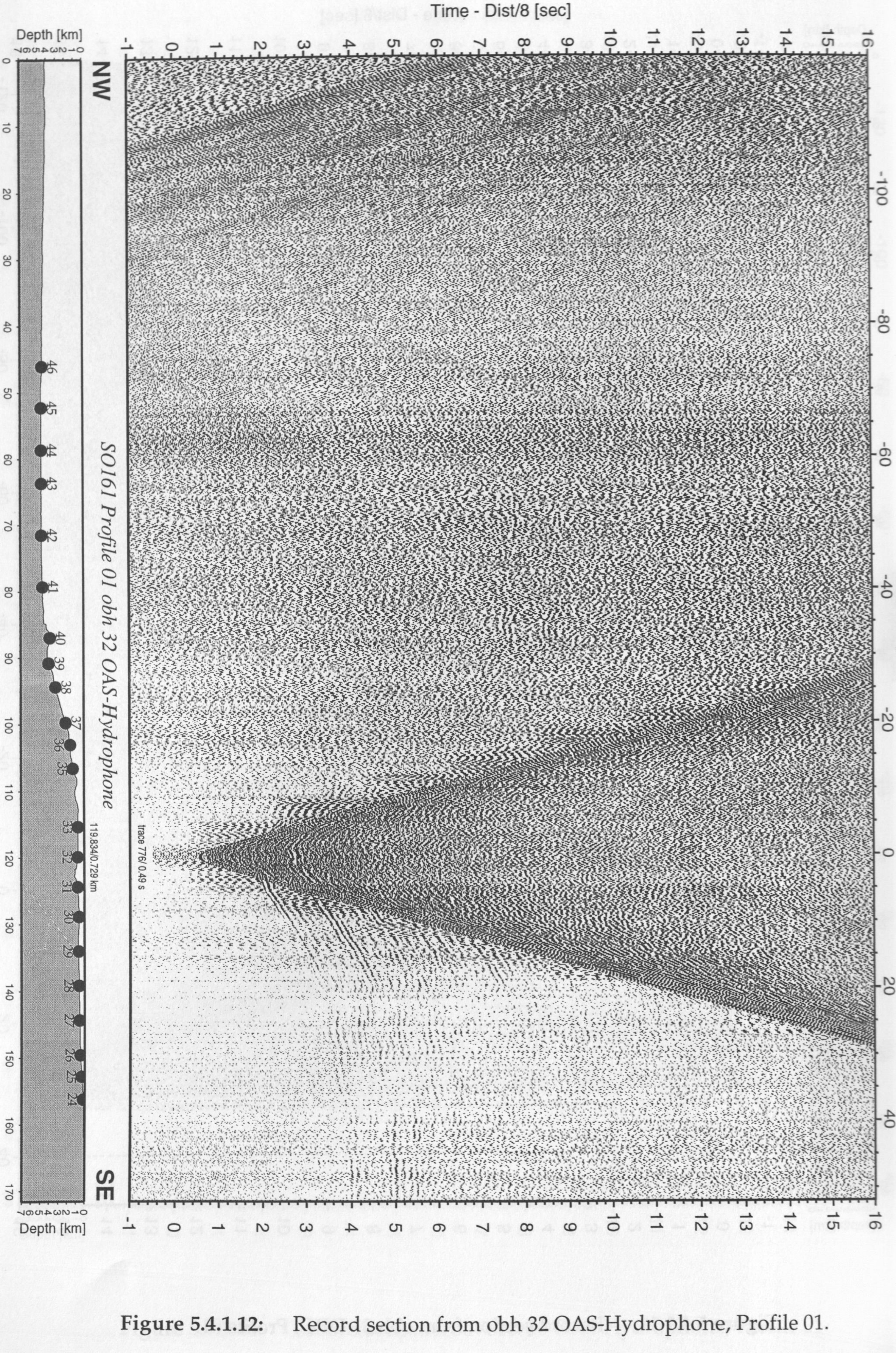

**Figure 5.4.1.12:** Record section from obh 32 OAS-Hydrophone, Profile 01.

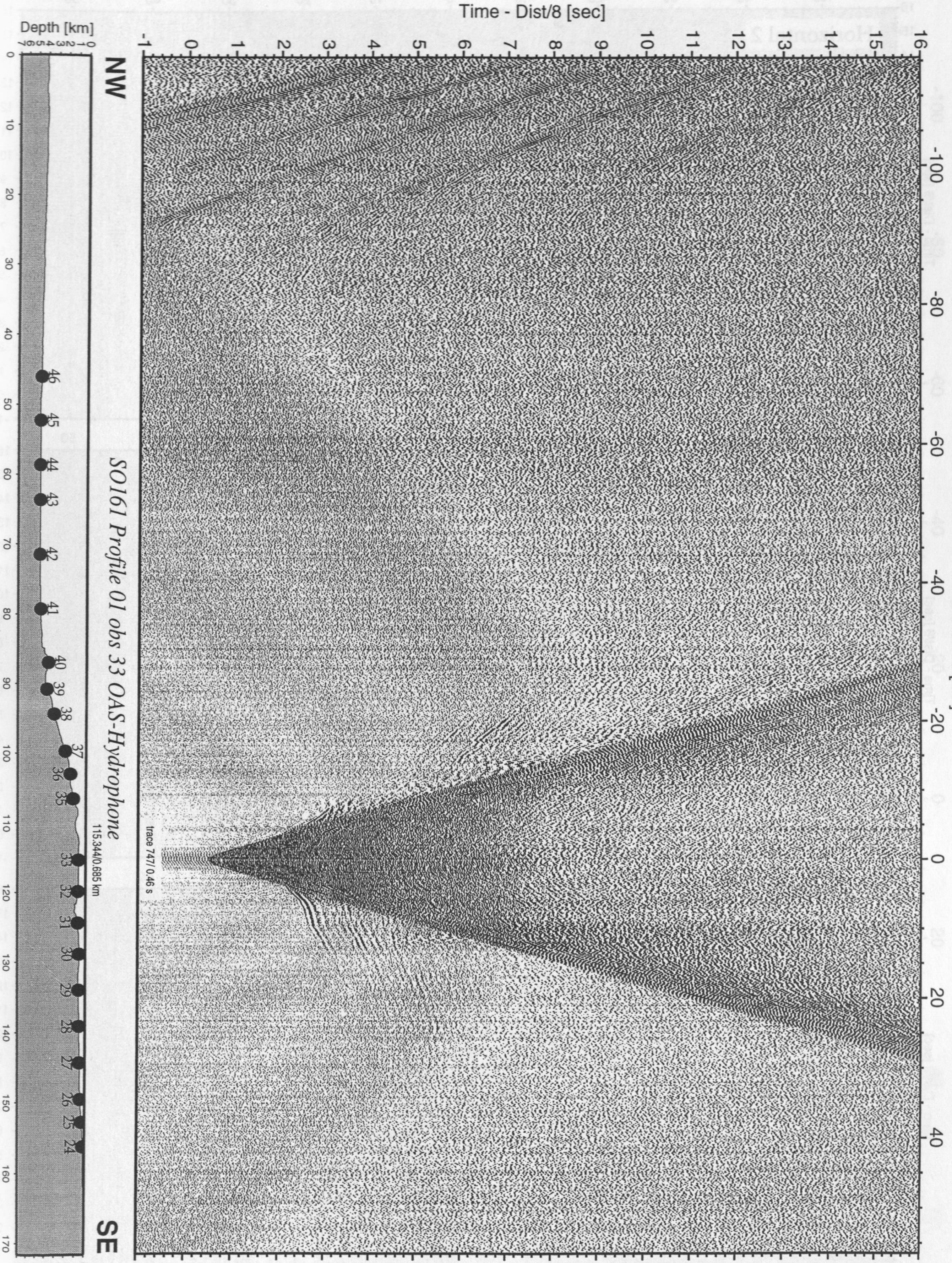

**Figure 5.4.1.13:** Record section from obs 33 OAS-Hydrophone, Profile 01.

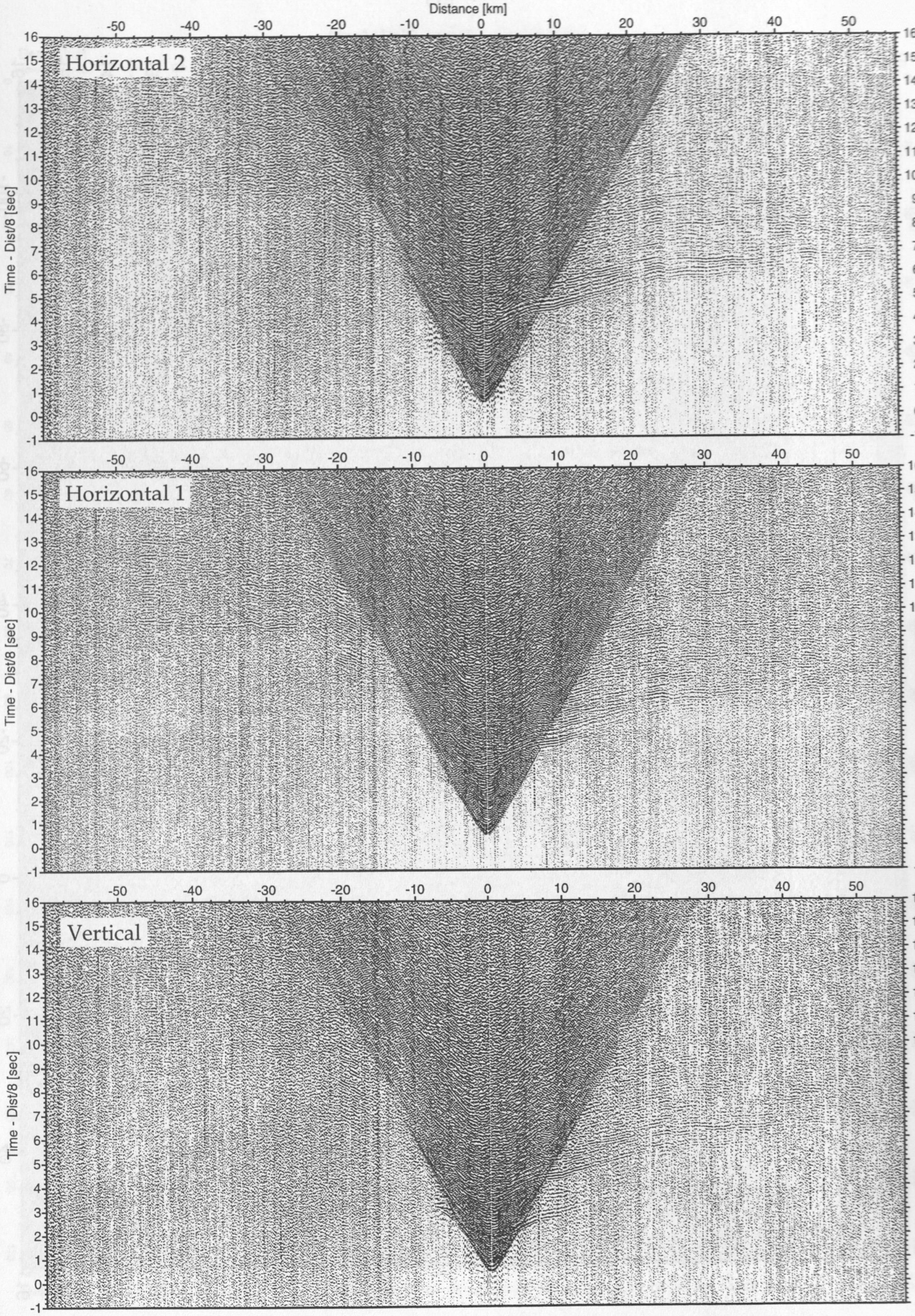

**Figure 5.4.1.14:** Record sections from obs 33 OAS/A01-4.5Hz, SO161 Profile 01.

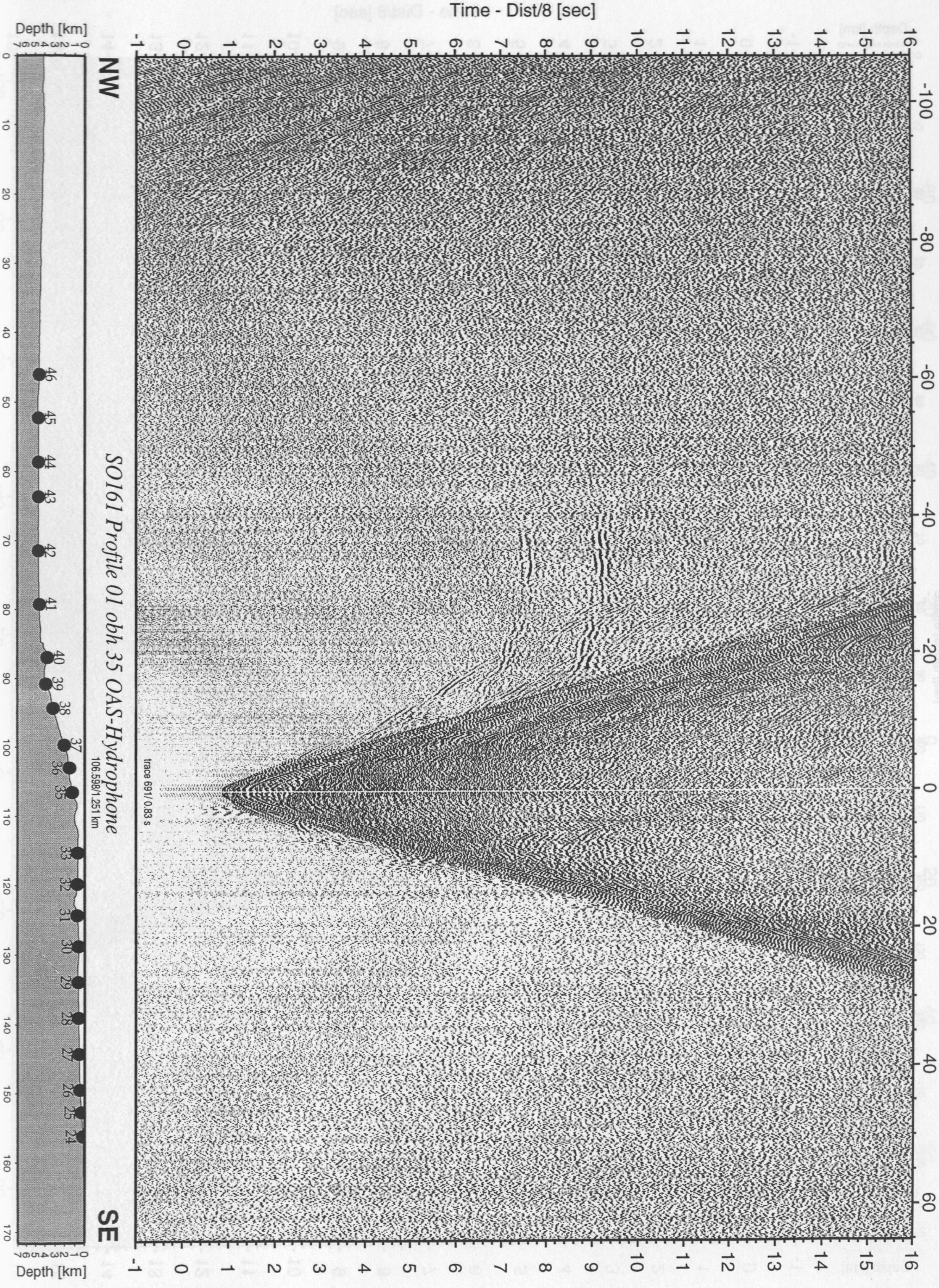

**Figure 5.4.1.15:** Record section from obh 35 OAS-Hydrophone, Profile 01.

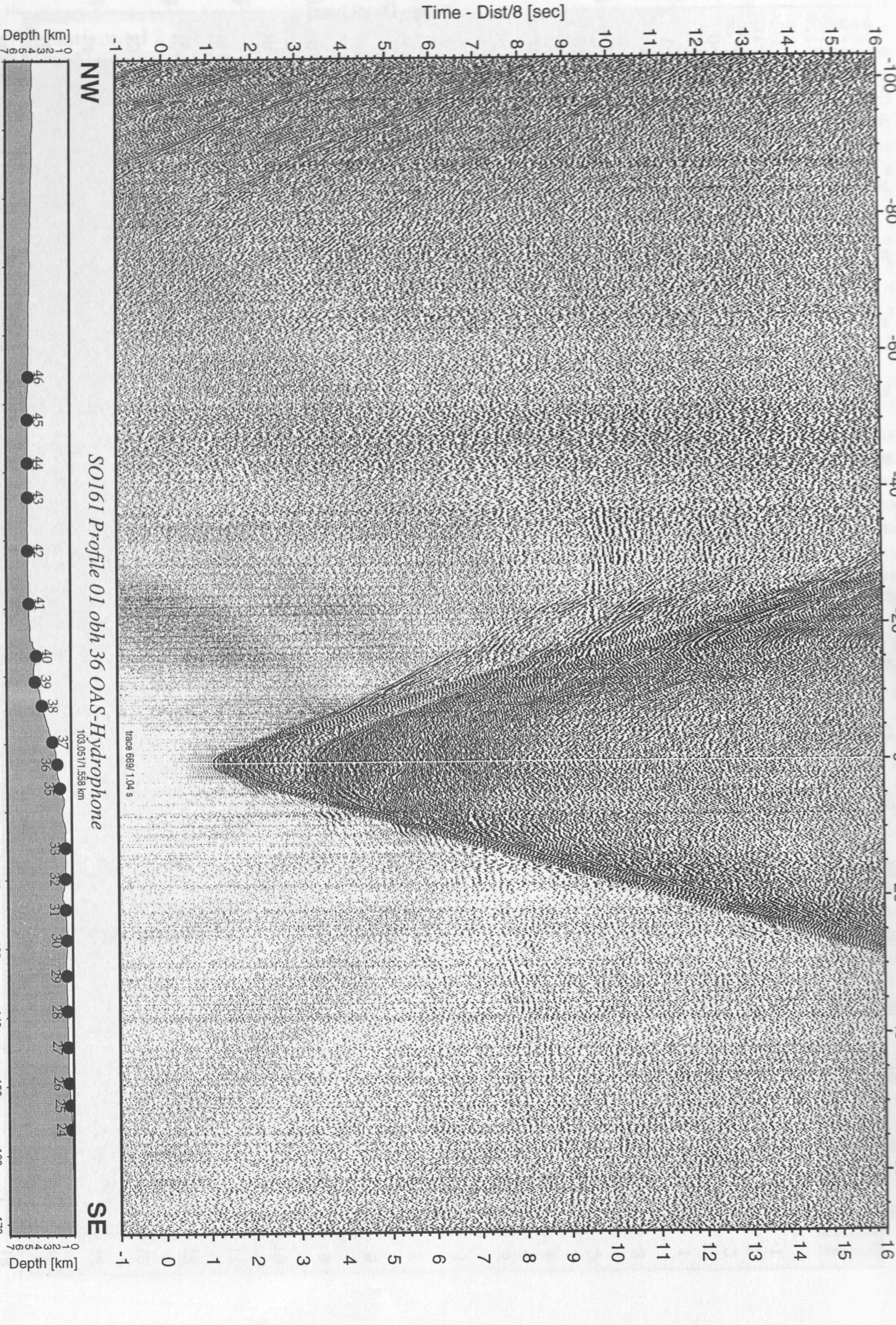

**Figure 5.4.1.16:** Record section from obh 36 OAS-Hydrophone, Profile 01.

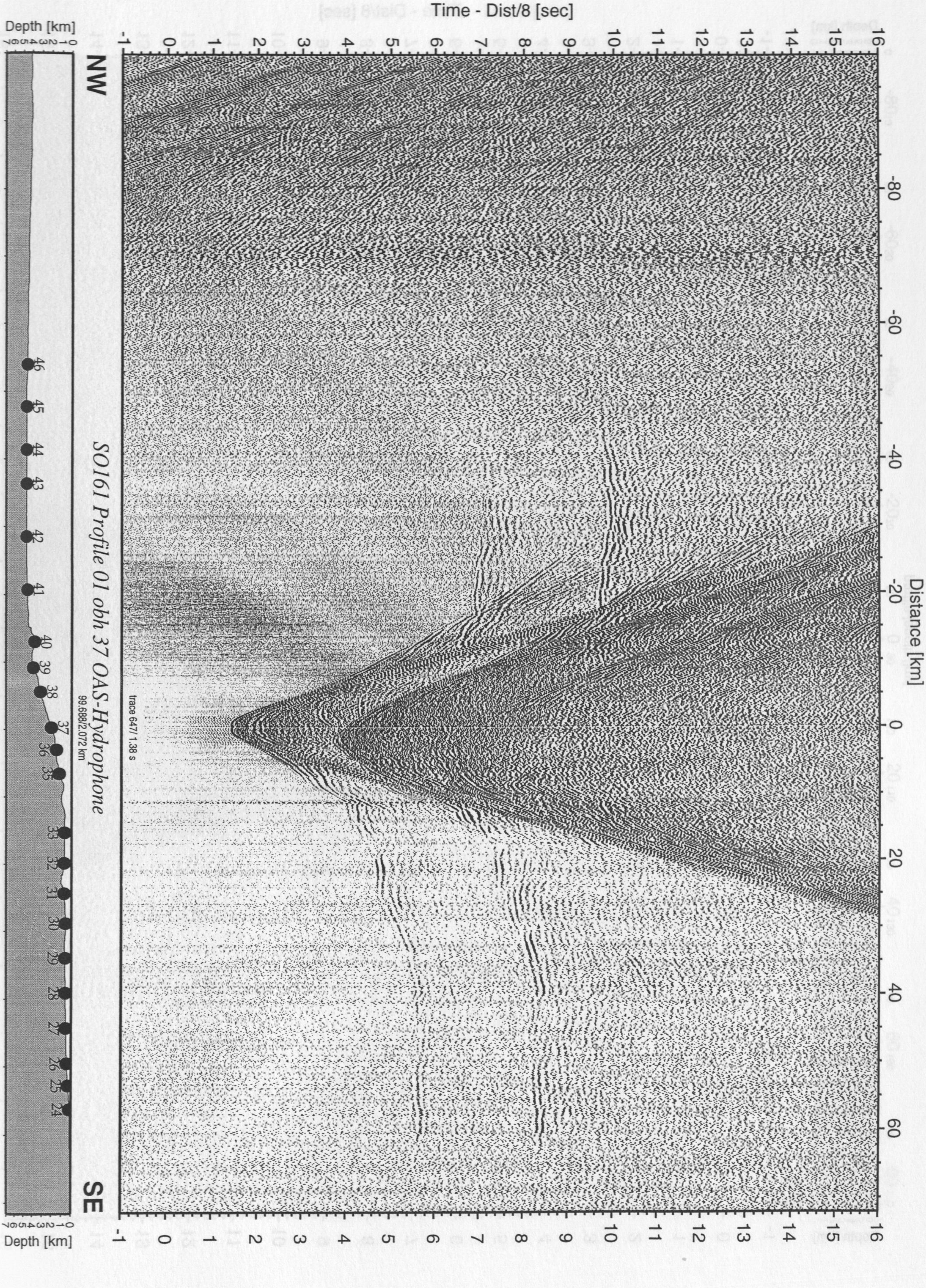

**Figure 5.4.1.17:** Record section from obh 37 OAS-Hydrophone, Profile 01.

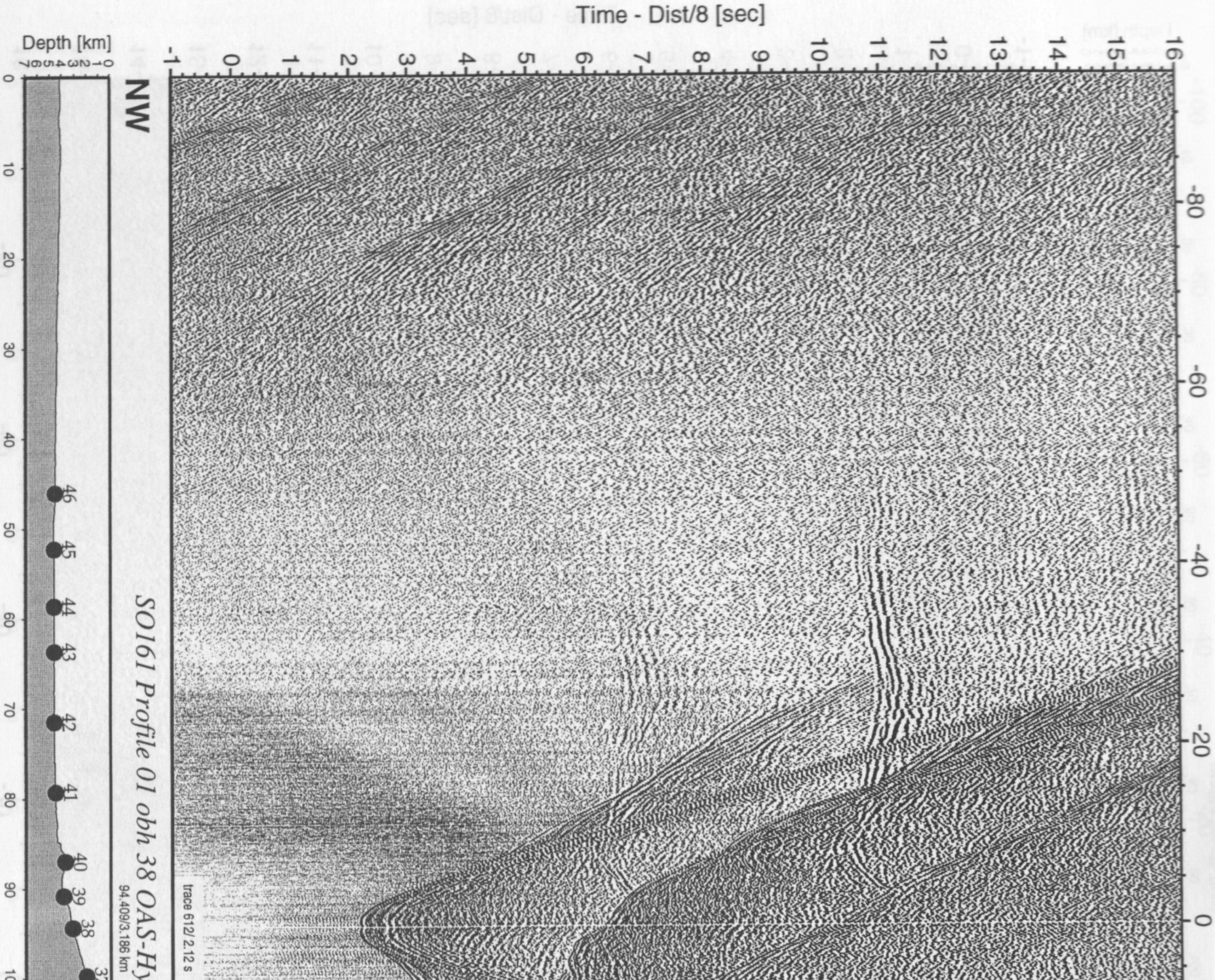

Figure 5.4.1.18: Record section from obh 38 OAS-Hydrophone, Profile 01.

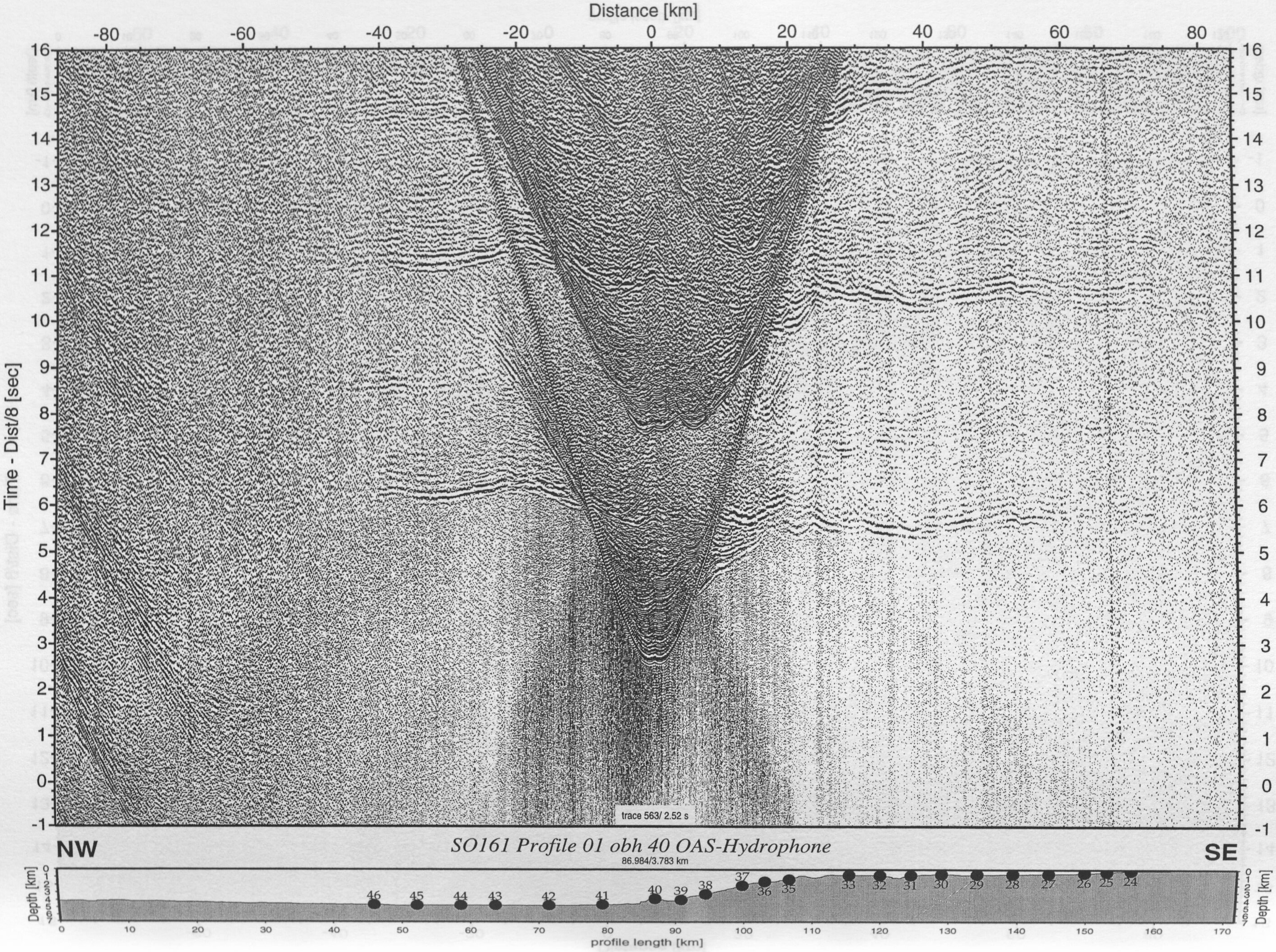

**Figure 5.4.1.19:** Record section from obh 40 OAS-Hydrophone, Profile 01.

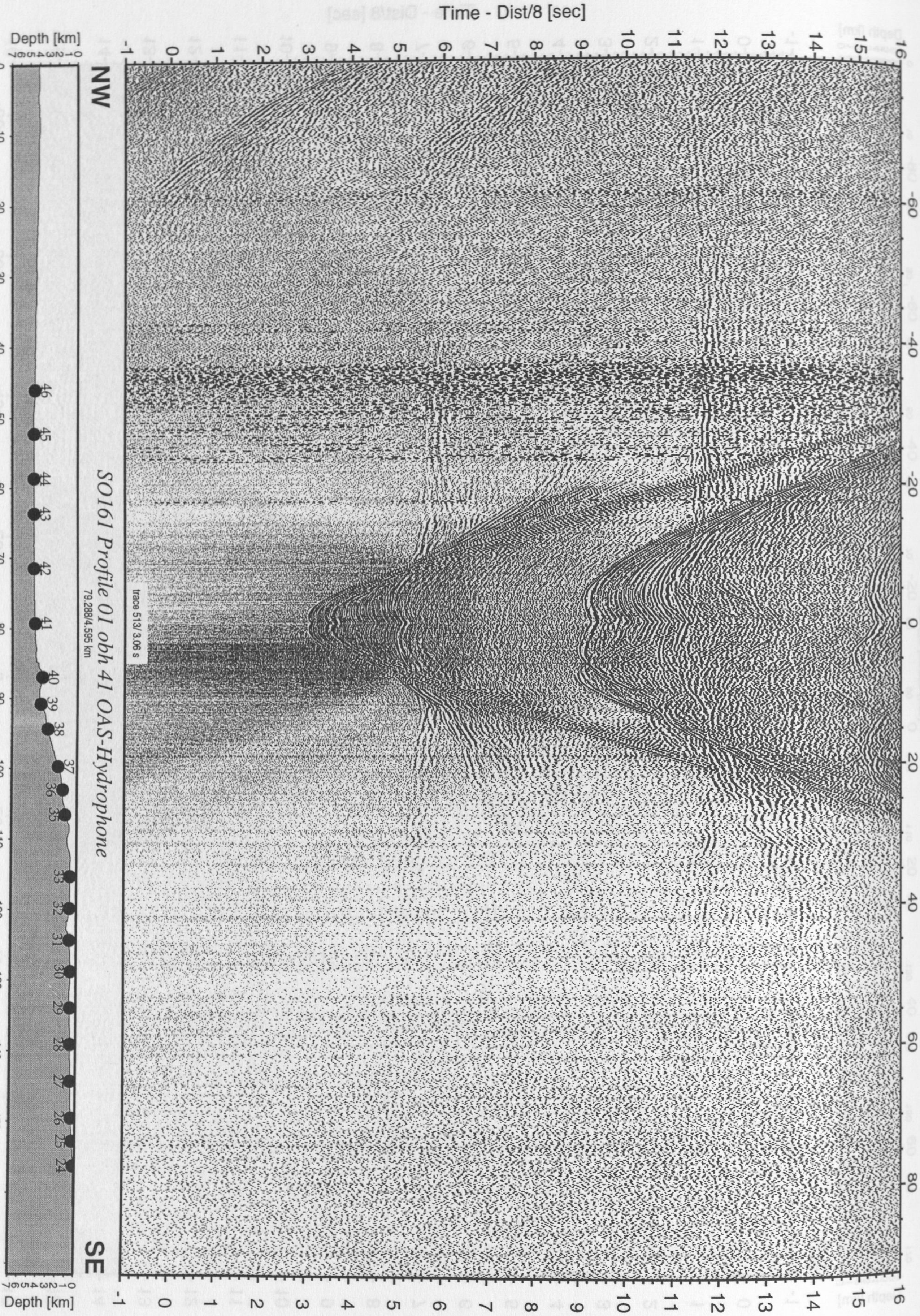

**Figure 5.4.1.20:** Record section from obh 41 OAS-Hydrophone, Profile 01.

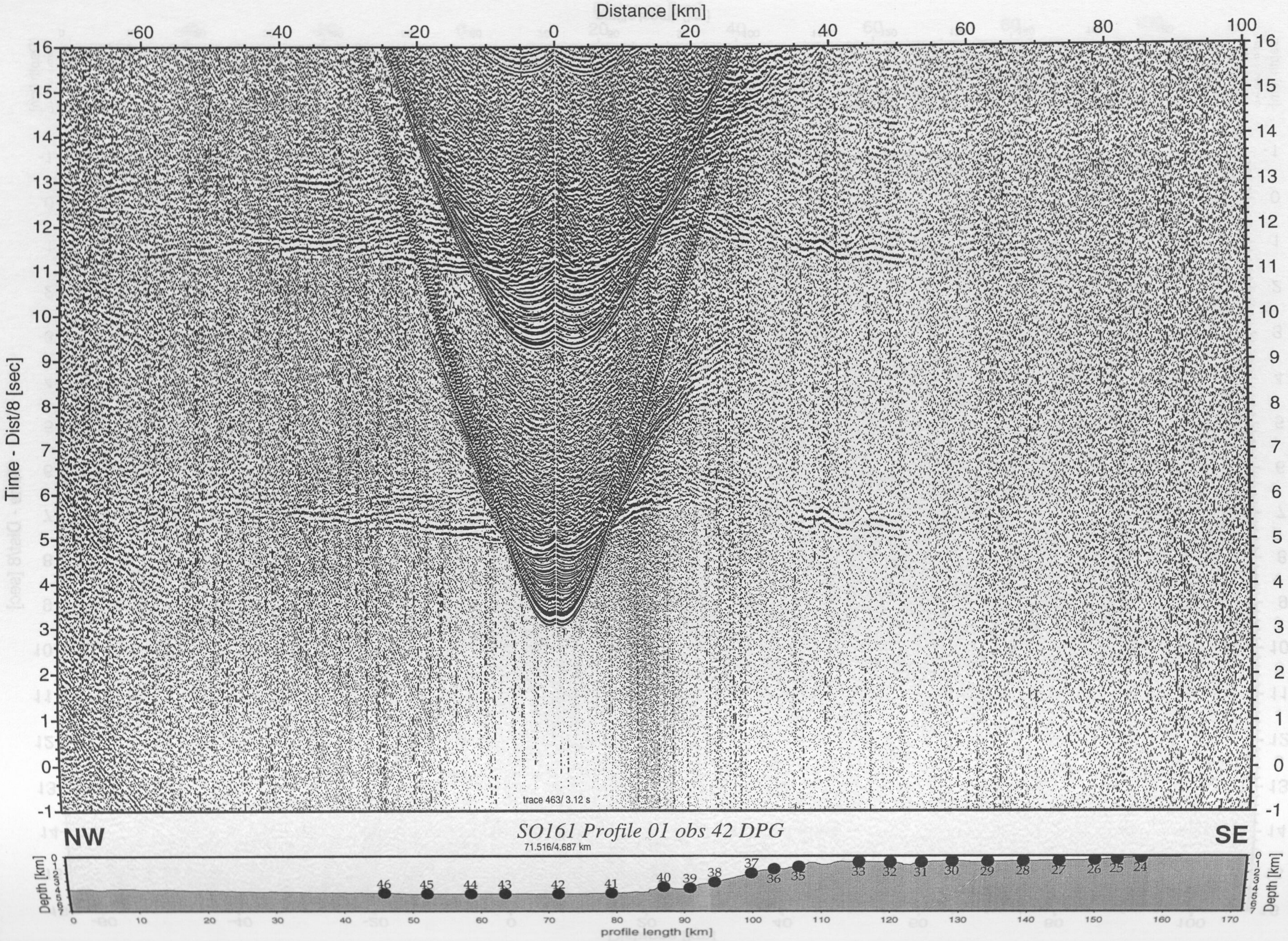

**Figure 5.4.1.21:** Record section from obs 42 DPG, Profile 01.

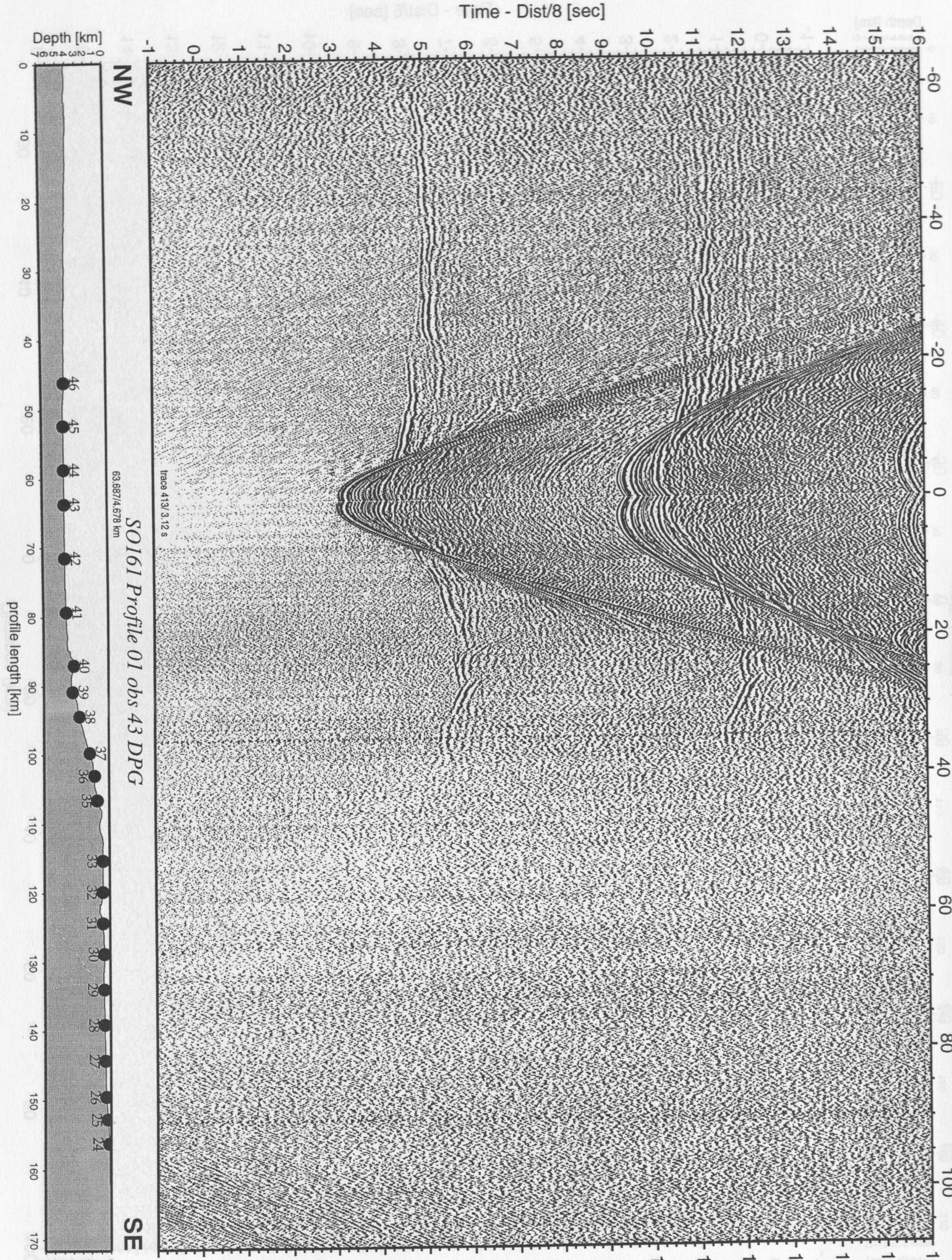

Figure 5.4.1.22: Record section from obs 43 DPG, Profile 01.

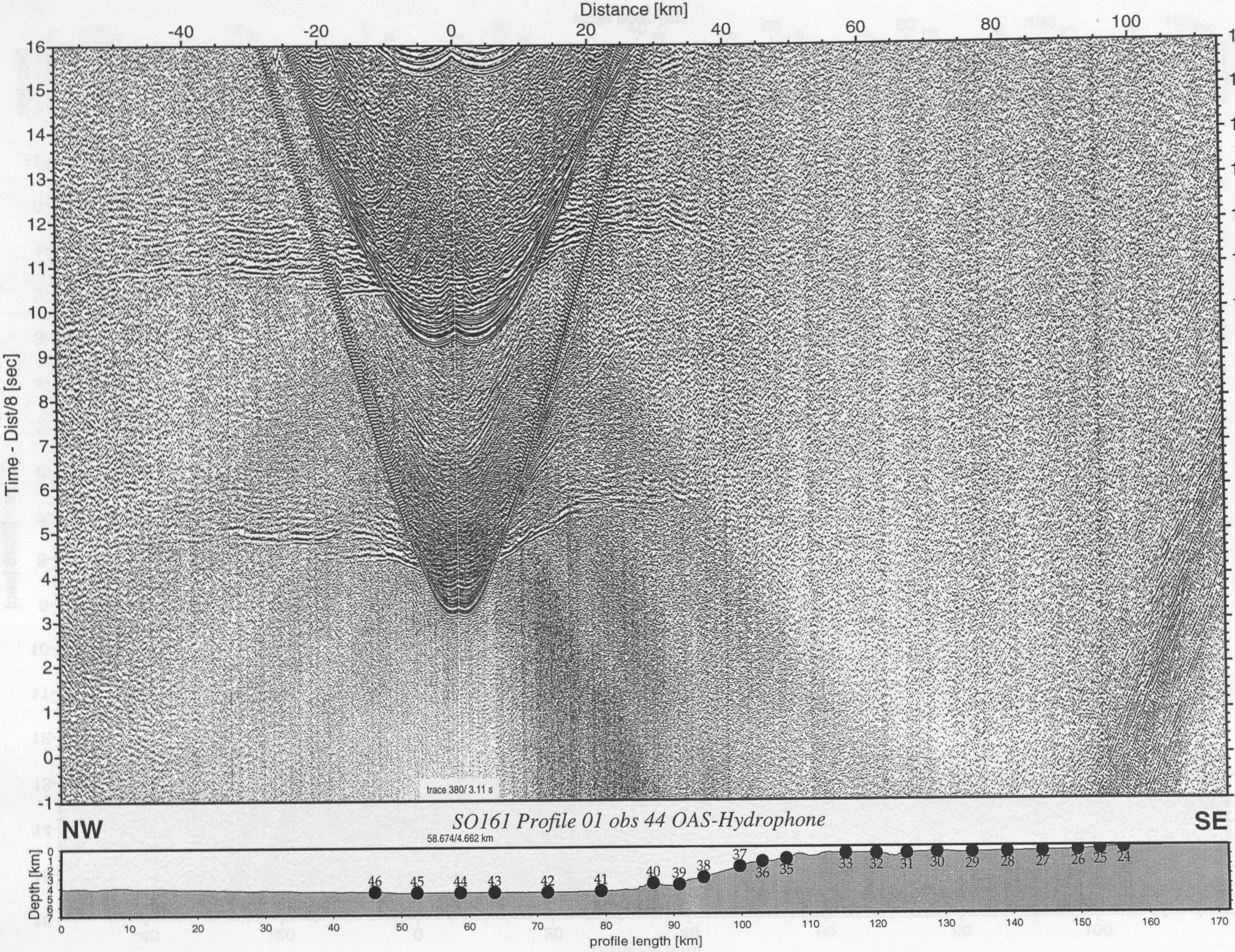

**Figure 5.4.1.23:** Record section from obs 44 OAS-Hydrophone, Profile 01.

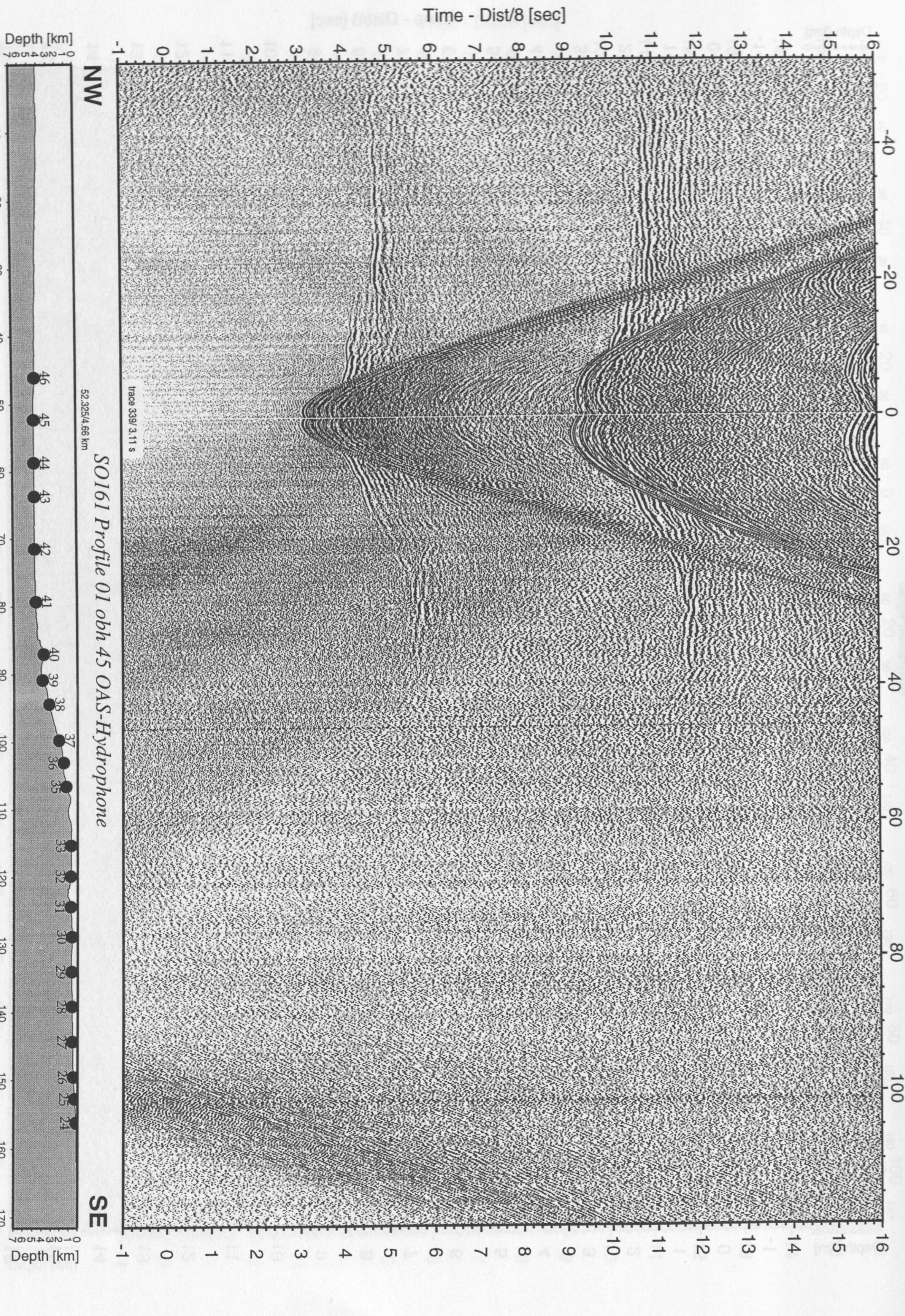

**Figure 5.4.1.24:** Record section from obh 45 OAS-Hydrophone, Profile 01.

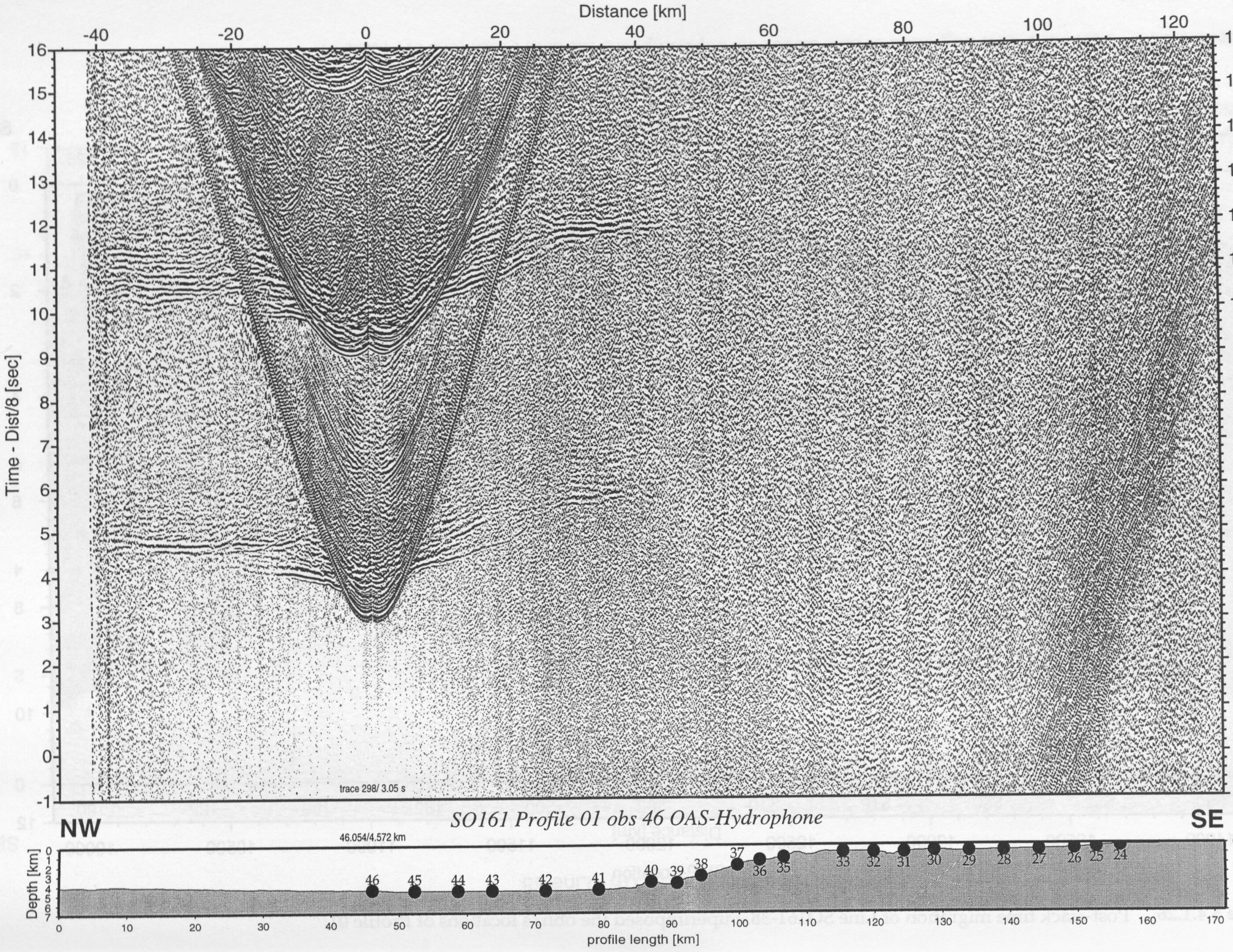

**Figure 5.4.1.25:** Record section from obs 46 OAS-Hydrophone, Profile 01.

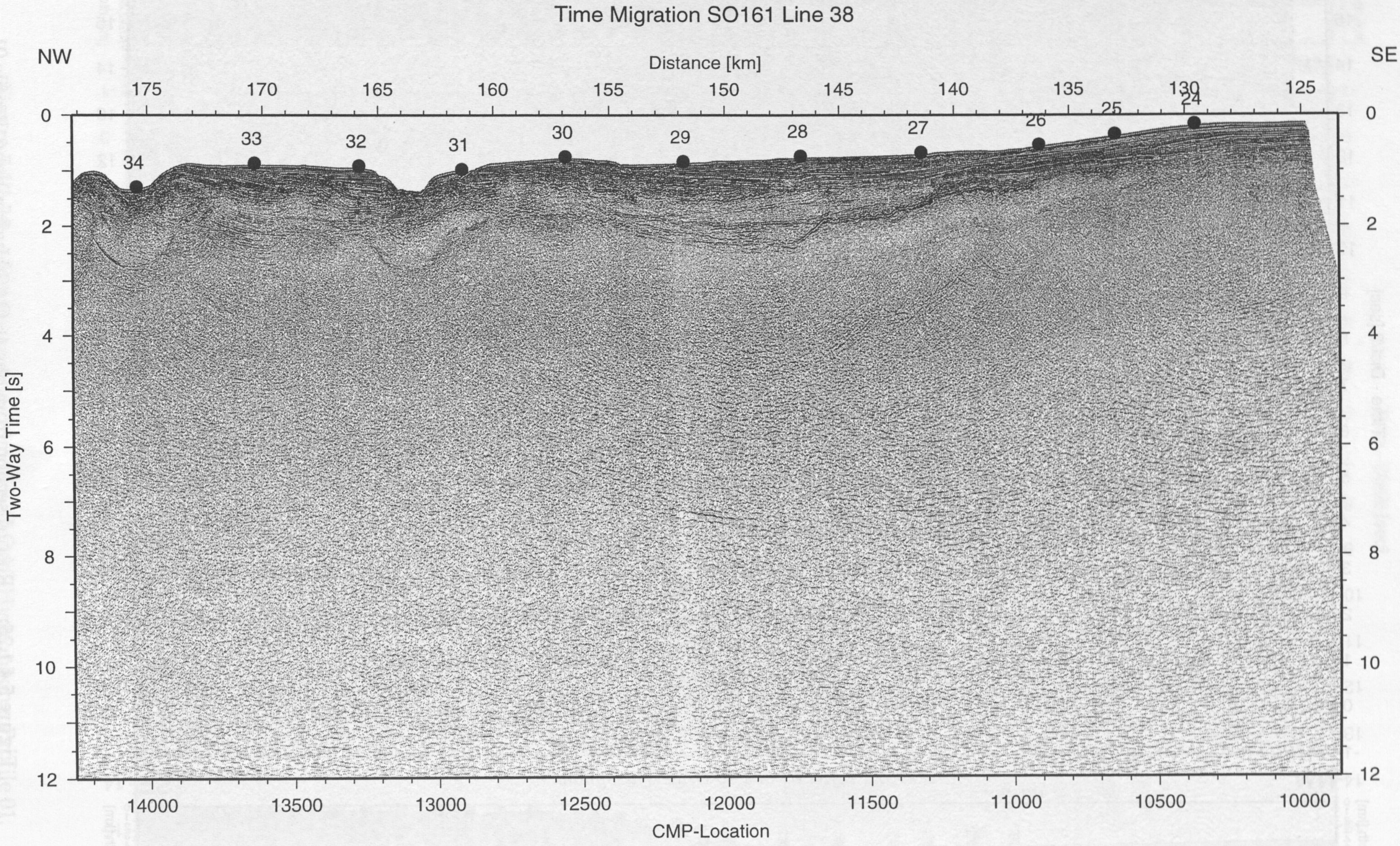

**Figure 5.4.1.26:** Post-stack time migration of Line SO161-38. Superimposed the obh/s locations of Profile 01.

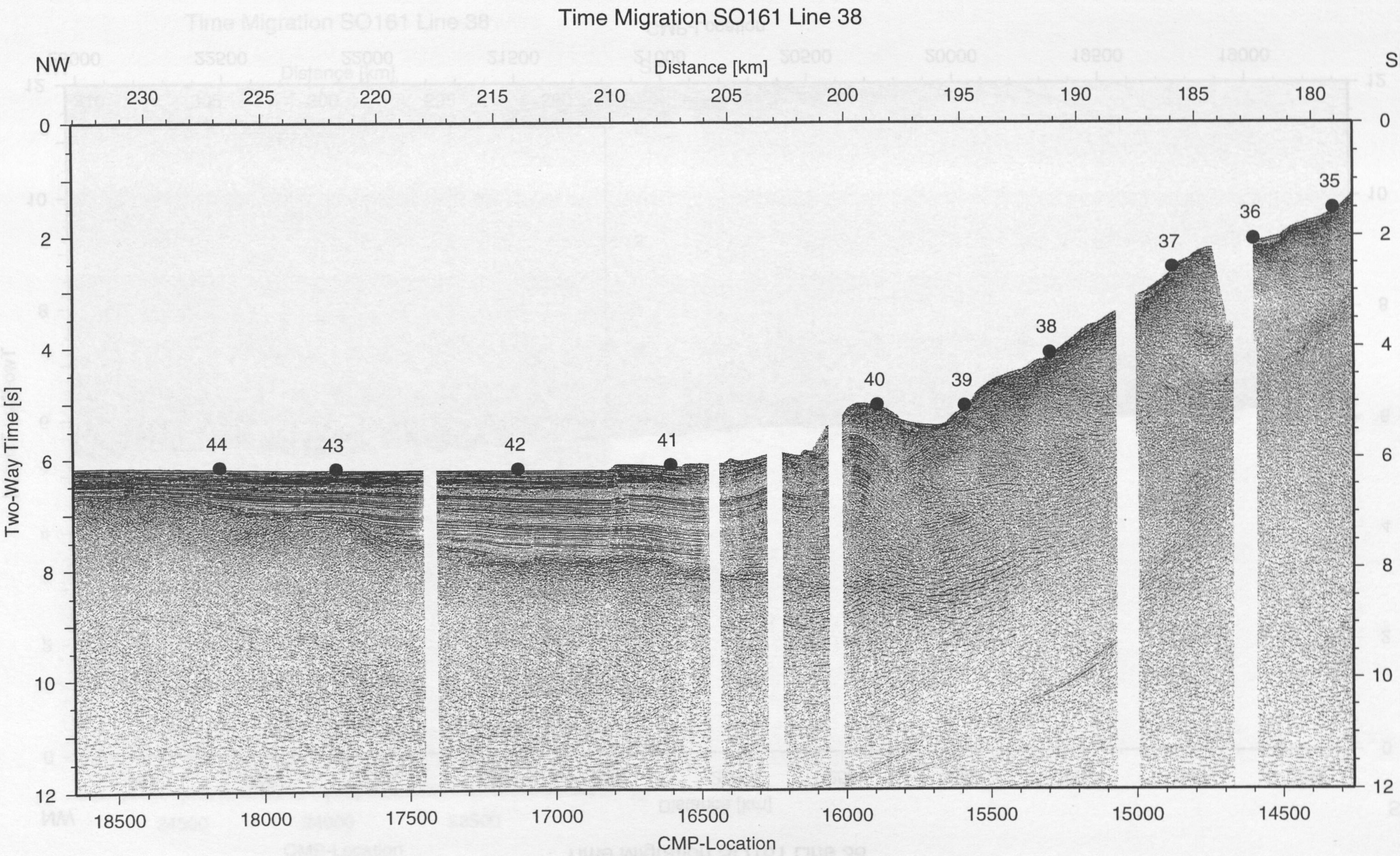

**Figure 5.4.1.27:** Post-stack time migration of Line SO161-38. Superimposed the obh/s locations of Profile 01.

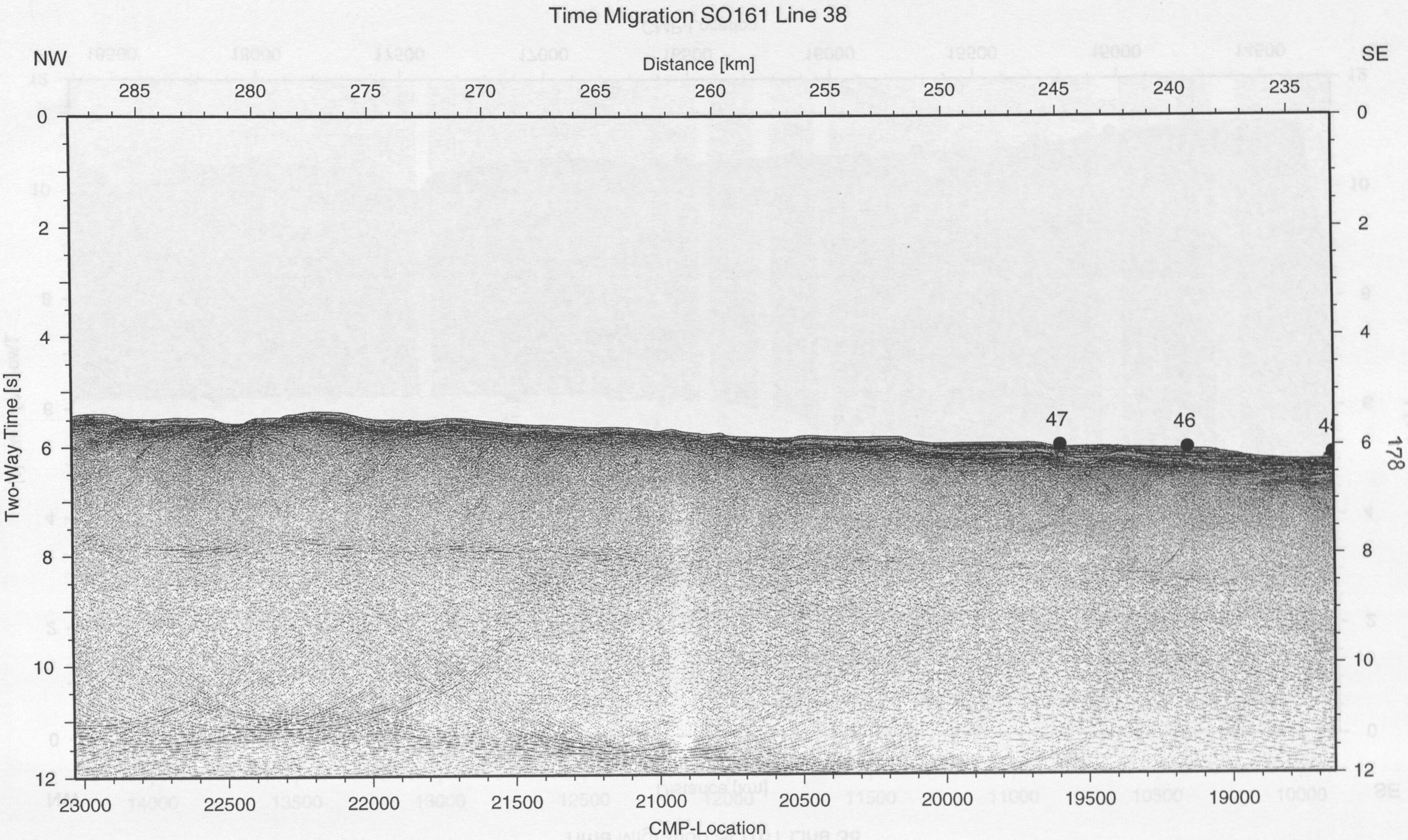

**Figure 5.4.1.28:** Post-stack time migration of Line SO161-38. Superimposed the obh/s locations of Profile 01.

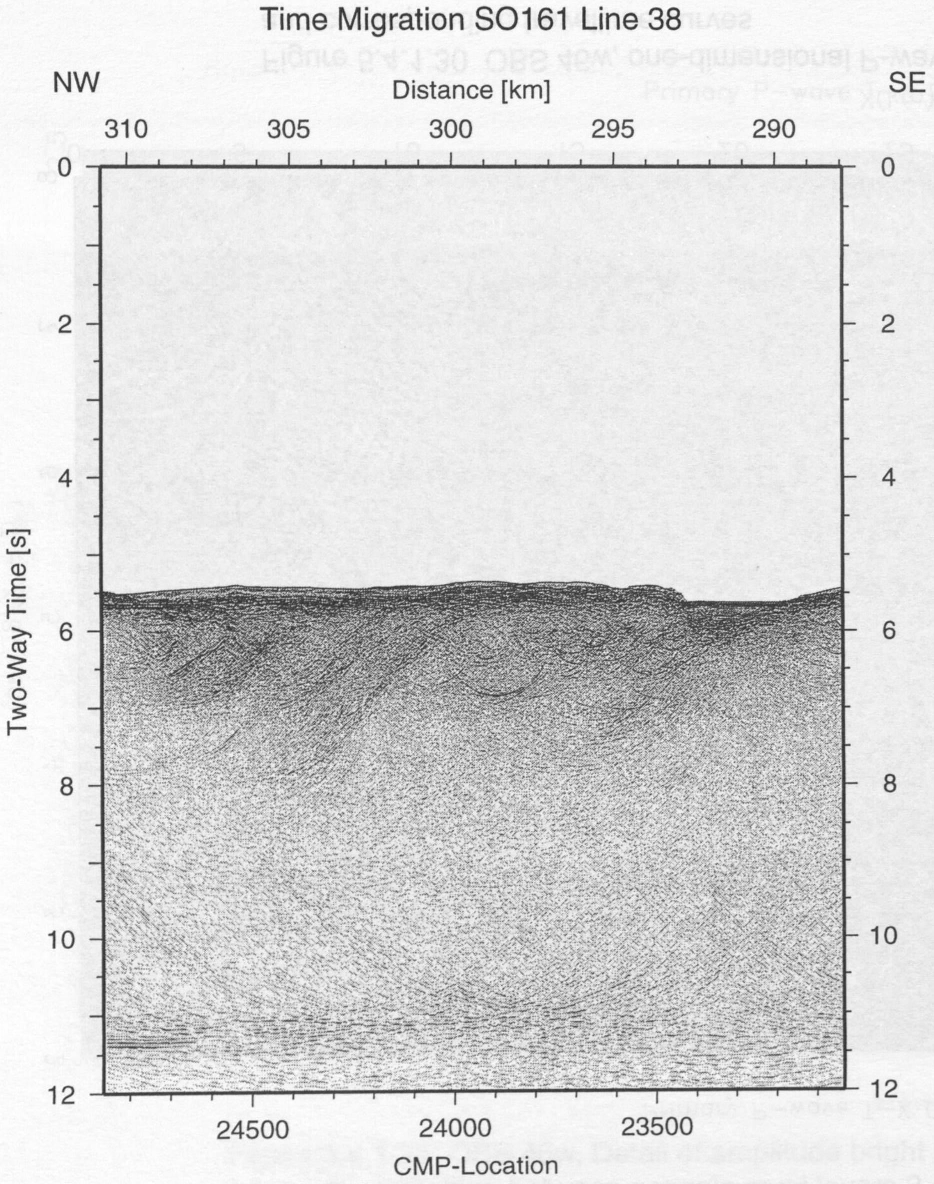

**Figure 5.4.1.29:** Post-stack time migration of Line SO161-38. Superimposed the obh/s locations of Profile 01.

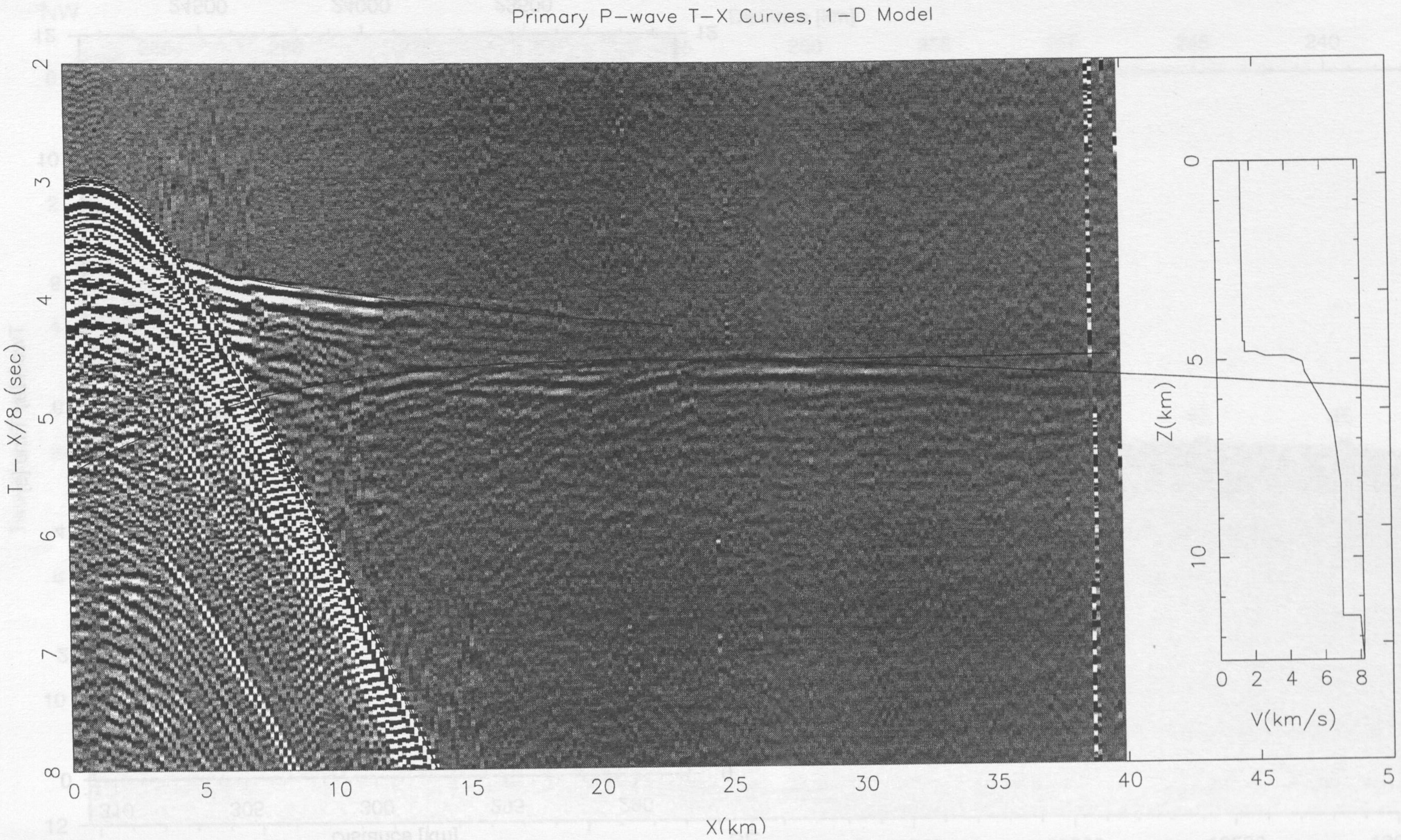

Figure 5.4.1.30 OBS 46w, one-dimensional P-wave velocity-depth model, and corresponding traveltime curves

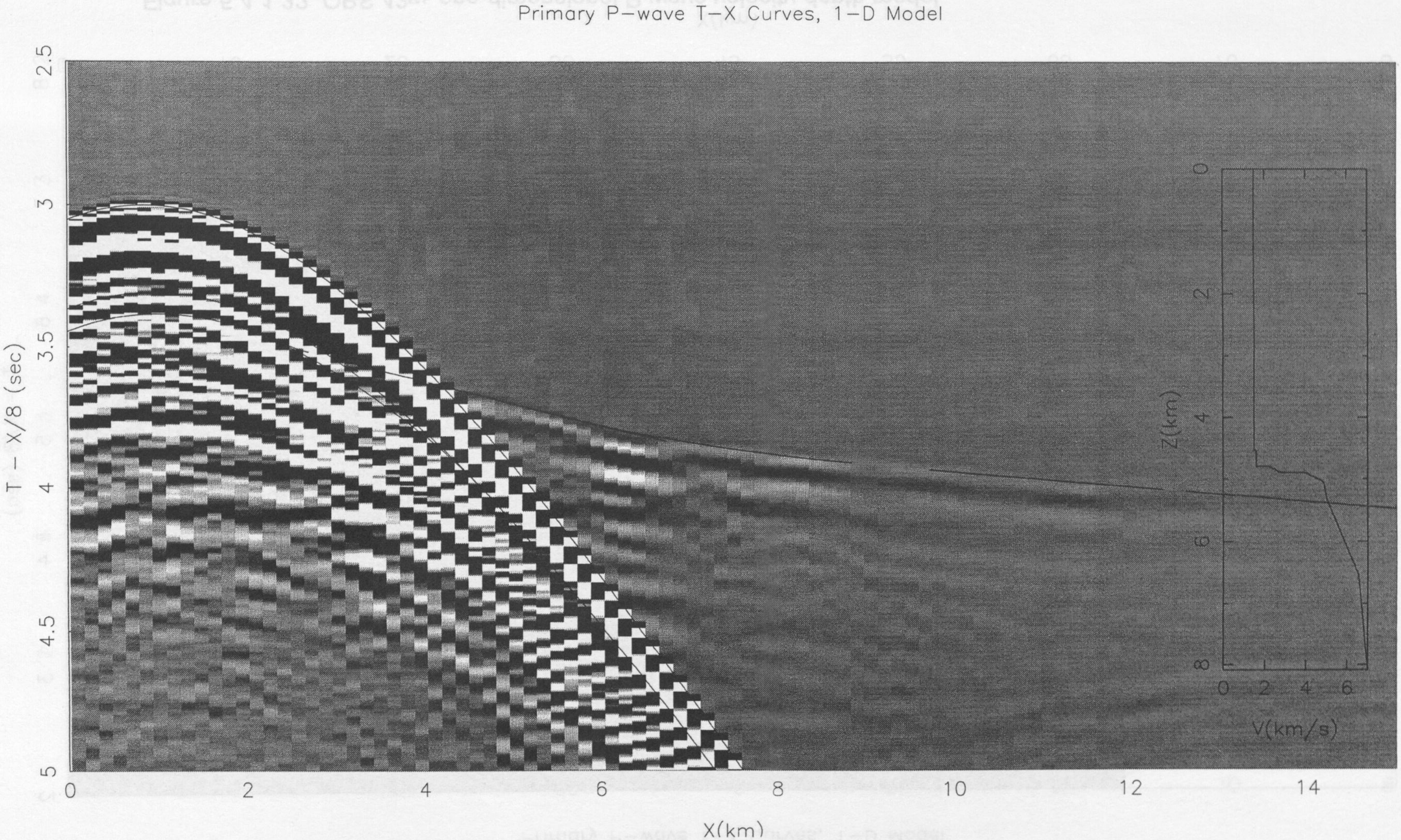

Figure 5.4.1.31 OBS 46w, Detail of amplitude bright spot around 6.5 km and 3.8 s of reduced time that makes the transition between oceanic crust layers 2 and 3.

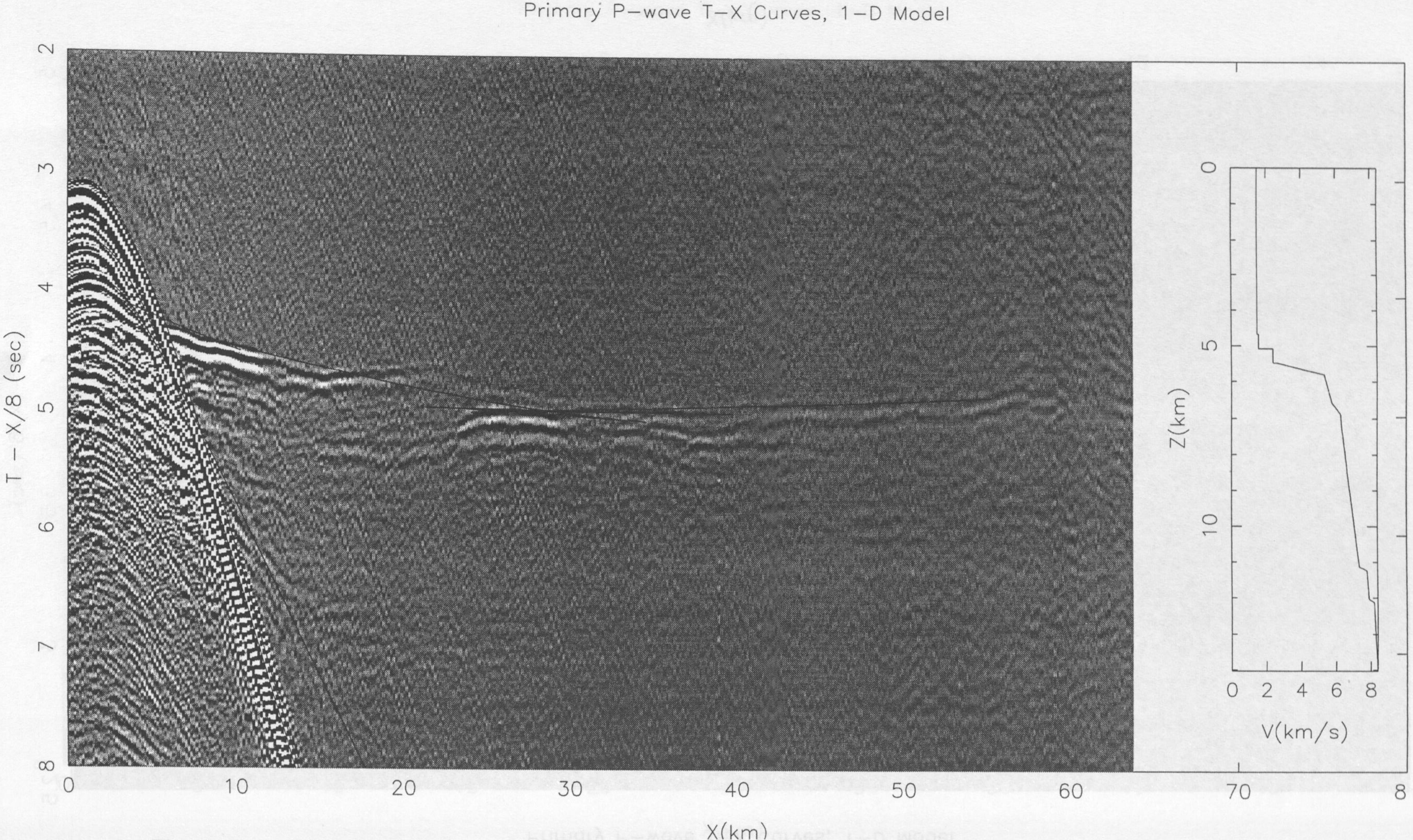

Figure 5.4.1.32 OBS 43w, one-dimensional P-wave velocity-depth model, and corresponding traveltime curves

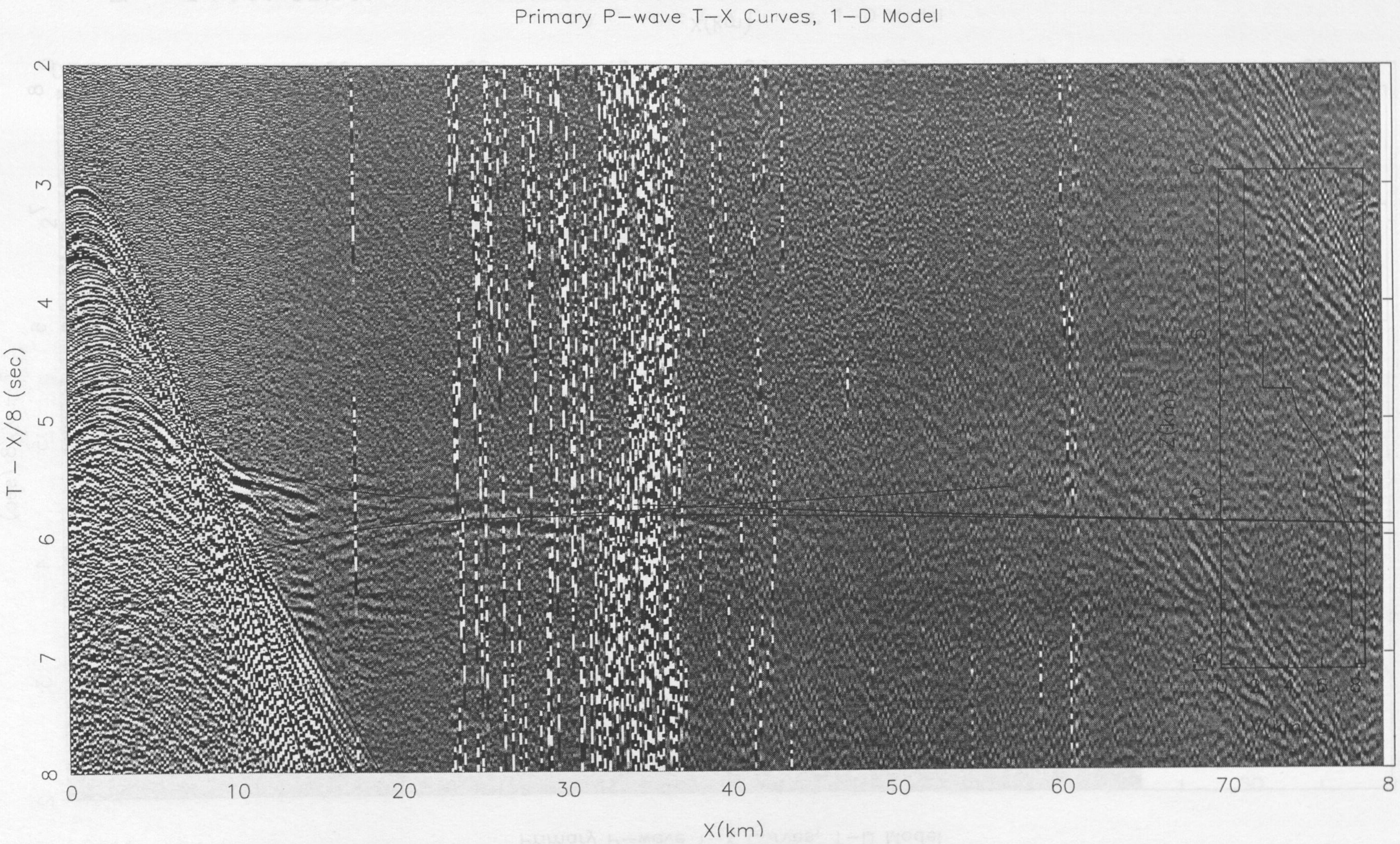

Figure 5.4.1.33 OBH 41w, one-dimensional P-wave velocity-depth model, and corresponding traveltime curves

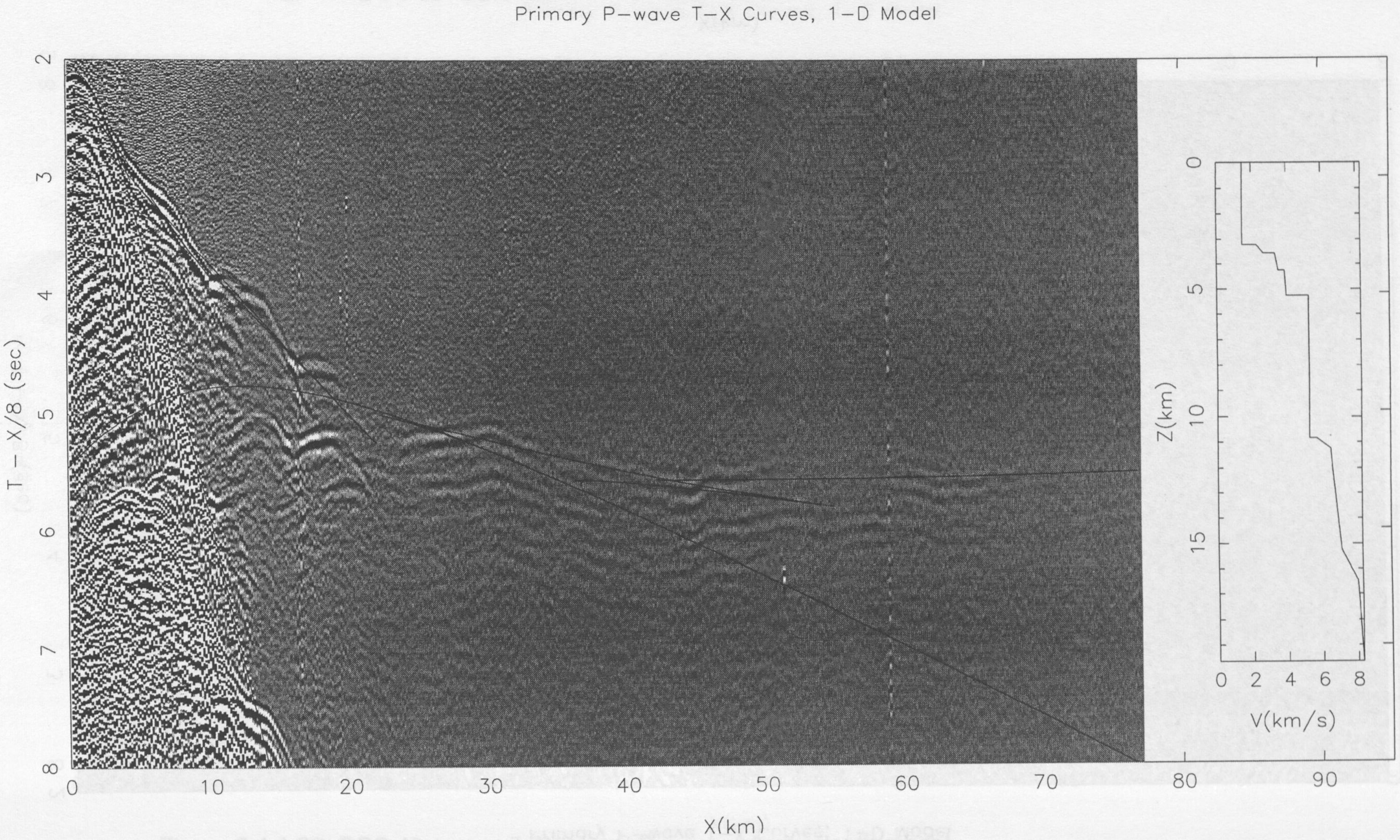

Figure 5.4.1.34 OBH 38e, one-dimensional P-wave velocity-depth model, and corresponding traveltime curves

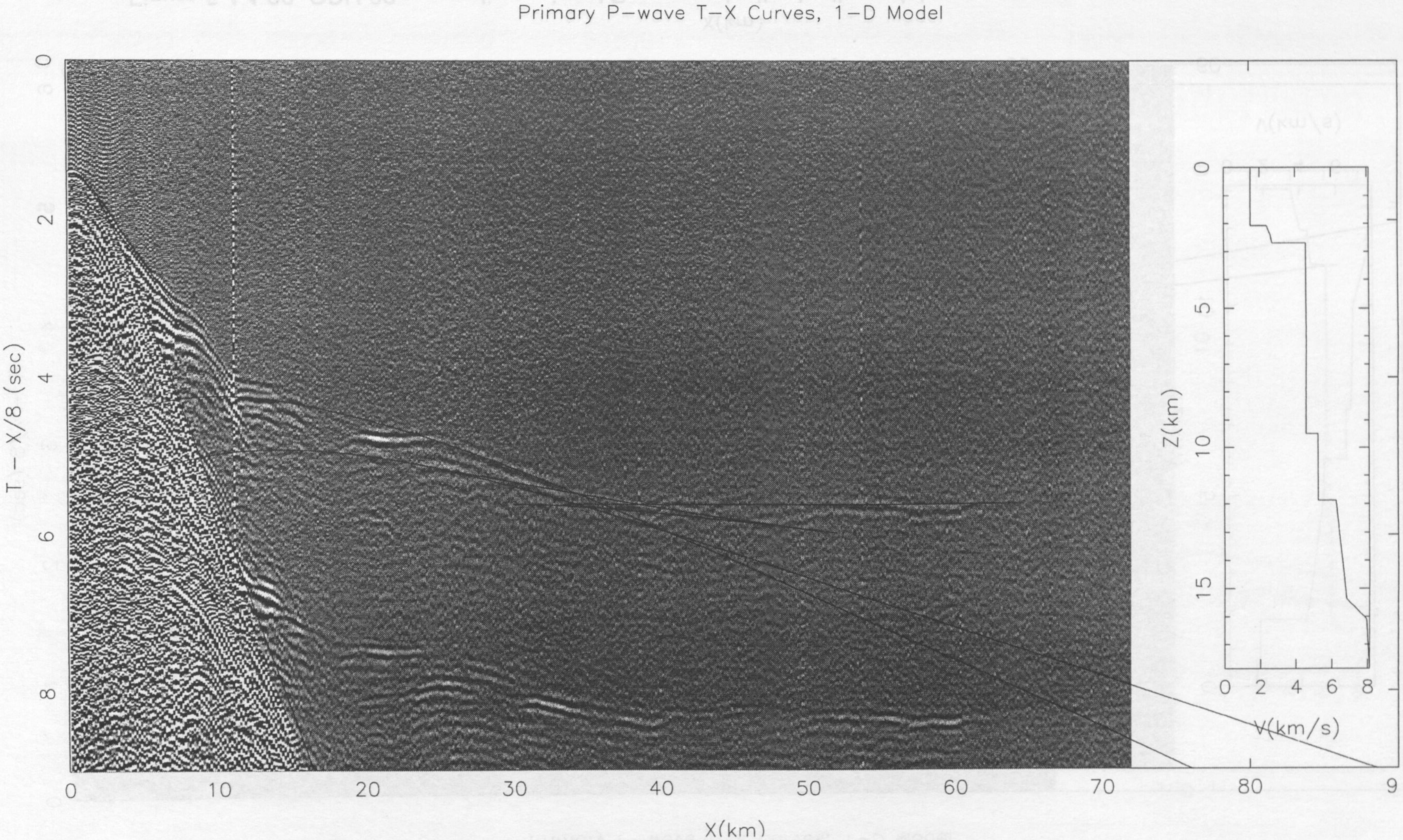

Primary P–wave T–X Curves, 1–D Model

Figure 5.4.1.35 OBH 37e, one-dimensional P-wave velocity-depth model, and corresponding traveltime curves

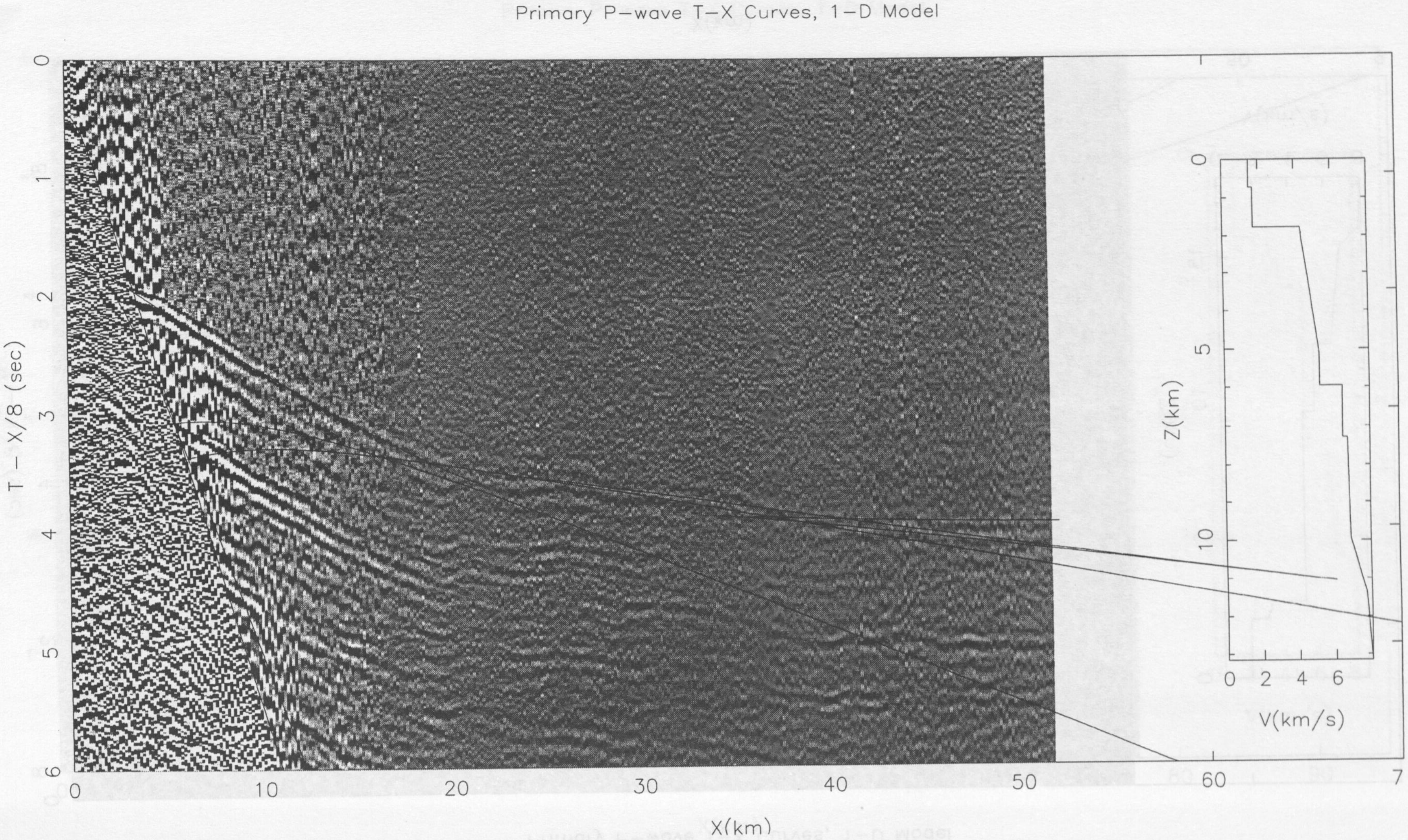

Figure 5.4.1.36 OBH 32e, one-dimensional P-wave velocity-depth model, and corresponding traveltime curves

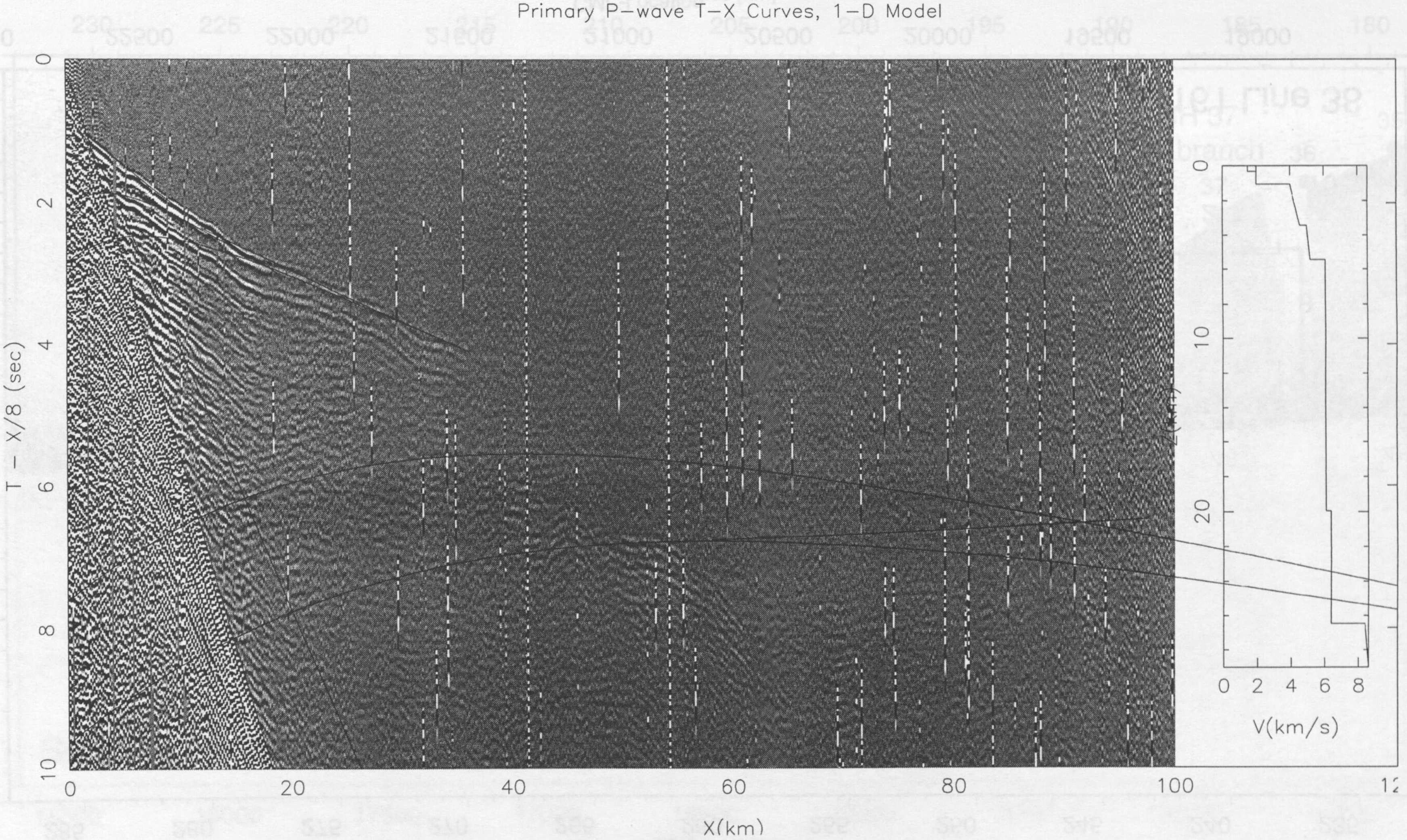
Primary P–wave T–X Curves, 1–D Model

Figure 5.4.1.37 OBH 25w, one-dimensional P-wave velocity-depth model, and corresponding traveltime curves

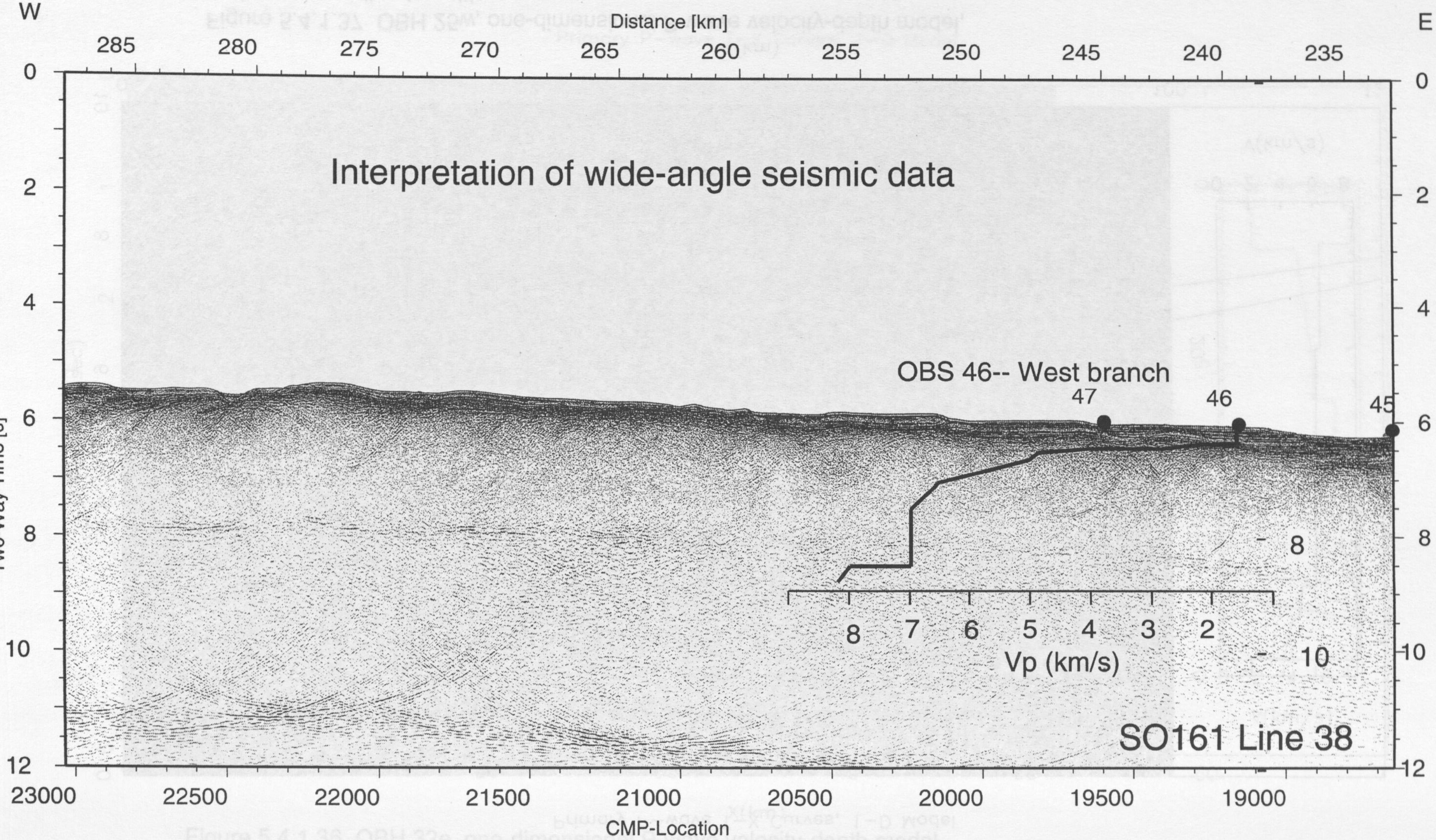

**Figure 5.4.1.38** One-dimensional compressional-wave velocity (Vp) versus two-way traveltime solutions, plotted over post-stack time migration profile SO161-38, shot along approximately 38 degrees S latitude. The locations of OBS/OBH 24-47 deployed along the line are also shown.

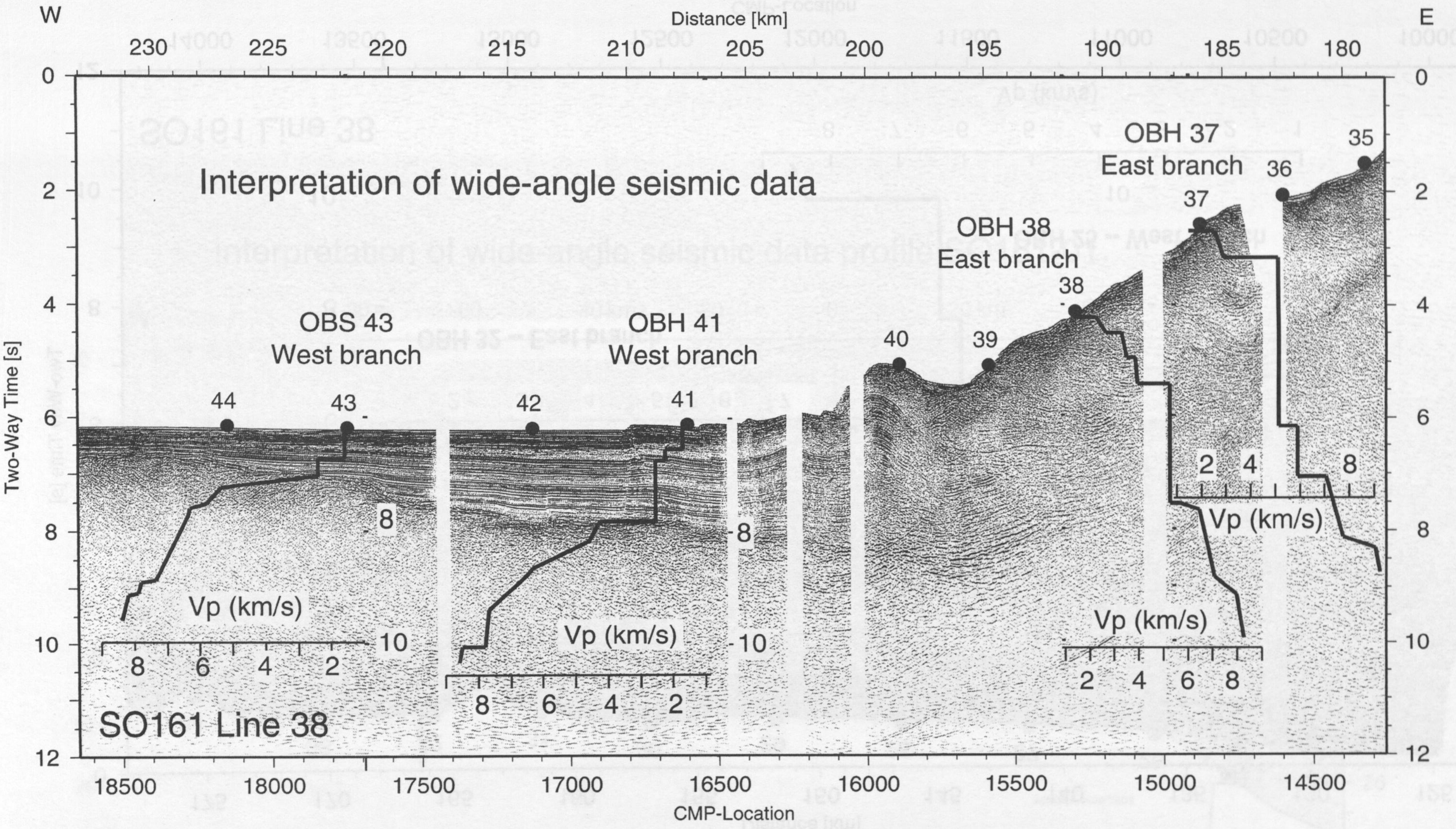

**Figure 5.4.1.39** One-dimensional compressional-wave velocity (Vp) versus two-way traveltime (s) solutions, plotted over post-stack time migration profile SO161-38, shot along approximately 38 degrees S latitude

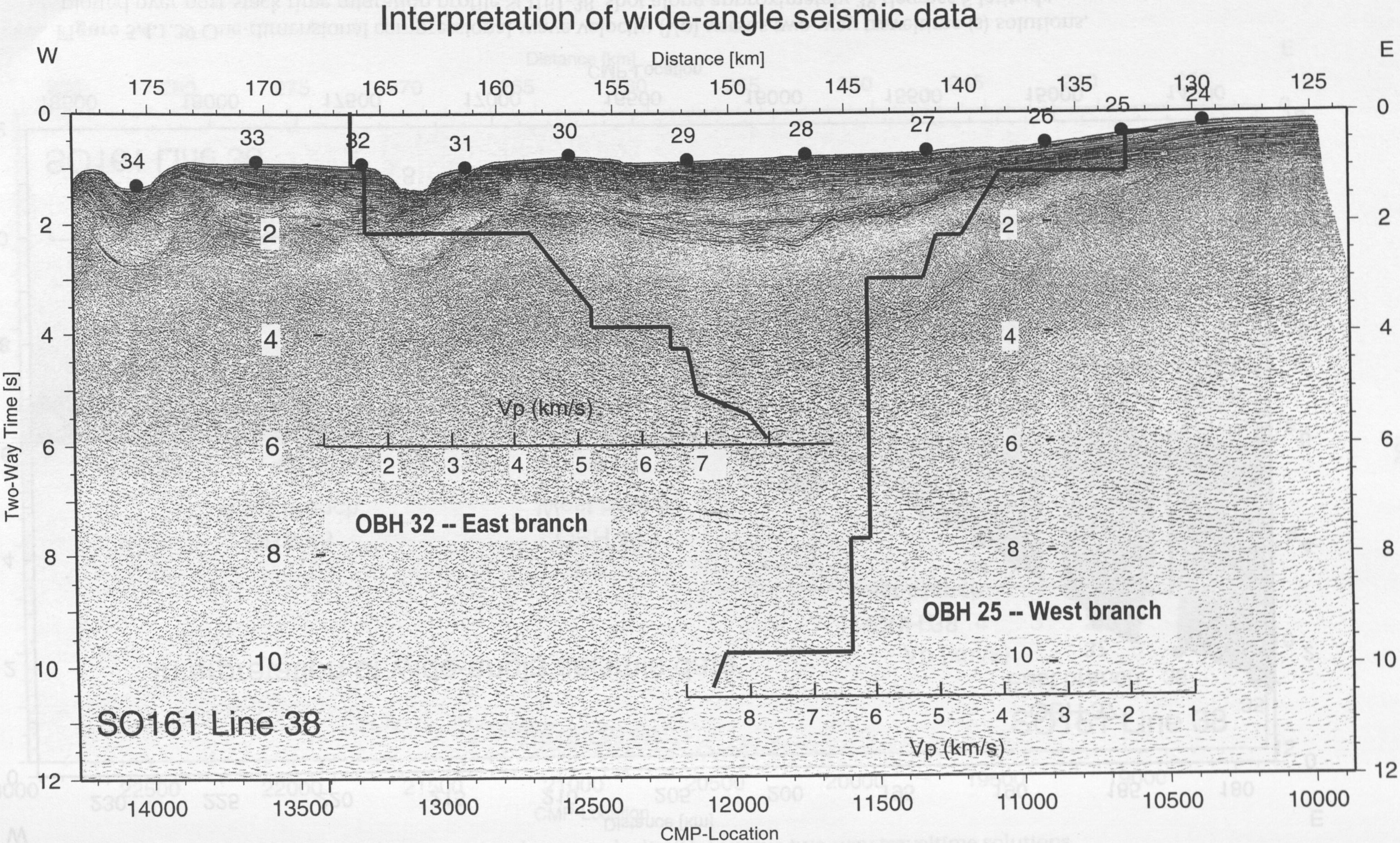

**Figure 5.5.1.40** One-dimensional compressional-wave velocity (Vp) versus two-way traveltime (s) solutions, plotted over post-stack time migration profile SO161-38, shot along approximately 38 degrees S latitude

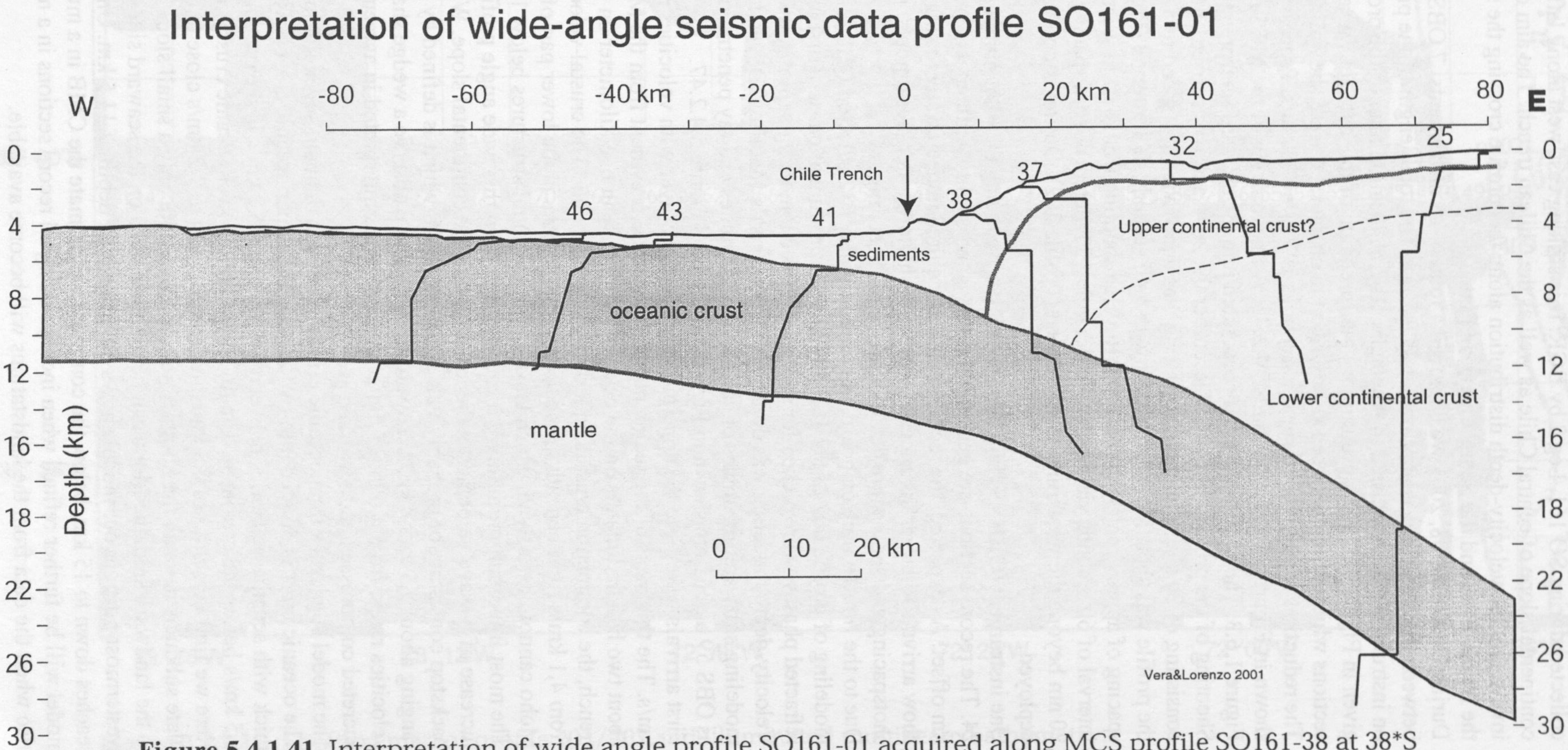

Interpretation of wide-angle seismic data profile SO161-01

**Figure 5.4.1.41** Interpretation of wide angle profile SO161-01 acquired along MCS profile SO161-38 at 38*S based on one dimensional Vp versus depth solutions for OBHs 25w, 32e, 37e, 38e, 41w, 43w, and 46w also shown in the figure. The vertical arrow marks the position of the deformation front.

### 5.4.2 Profile P02, SO 161-04

(Peter Oliver Thierer)

The wide angle profile P02 is coincident with the multichannel seismic reflection line No. 18, collected during SO 161, Leg 2 by BGR. It is striking east-west along latitude 32° S and crosses the continental slope of central Chile as well as the Chilean trench. The aim of the experiment was to investigate the velocity-depth distribution along this profile crossing the subduction zone formed by the Nazca Plate and the South American Plate.

During December 08, 2001 we deployed a total of 25 instruments; 7 OBS and 18 OBH. The spacing between the stations was approximately 2,5 nm. The total length of the profile is about 180 km. Detail on instrumentátion are listed in Appendix III.2. A location map of the profile including bathymetry is given in Figure 5.4.2.1. A preliminary interpretation of this data set was attempted at sea. The record sections which were processed as described in chapter 4.6.1 are shown in Figures 5.4.2.2 to 5.4.2.40. The reduction velocity of all seismic sections is $V_{red}$ = 8000 m/s. Processed sections of line 18 are shown in Figure 5.4.2.41 to Figure 5.4.2.45. A line drawing of the MCS data is also presented in Figure 1.6.3. These results were incorporated into the onboard interpretation.

Shooting of the profile started on December 09, 2001 and was carried out using the BGR air gun array consisting of 20 single air guns. Shooting was done twice at a speed of 5 kn. First, the eastern part of the profile was shot from west to east with a 40 seconds shot interval (Profile 201), yielding a shot spacing of approximately 100 meters. Reverse shooting from east to west was done with a shot interval of 60 seconds yielding approximately 150 meters of shot spacing and was extended for about 20 nm beyond the westernmost instrument (Profile 202). During shooting the magnetometer was also deployed.

One instrument (OBH 49) failed to record data, reducing the total number of usable seismic sections to 24. The record sections are generally of very good quality, with energy penetration in excess of 100 km offset. As expected, the record sections acquired in deep waters using 60 seconds shot intervals show arrivals to larger distances. In contrast, shallow water instruments, profit from the shorter shotspacing and show more detail in the near offset ranges.

Due to the limited time on board, only the arrivals of 12 selected OBS/H instruments were used for modeling of profile P02 of SO 161-4. The most prominent phases (first arrivals, plus the reflected and refracted phases) were picked for every record section, using xzplot software (Zelt and Smith, 1992). Velocity-depth modeling was done using J. Luetgert's MacRay 2D, version 2.0.1, (Luetgert, 1992) modeling software. Examples of calculated traveltimes and ray penetration of OBH 50 and 51 as well as OBS 59 and 61 are shown in Figure 5.4.2.46 and Figure 5.4.2.47.

First arrivals were fit to the uppermost sedimentary layer with velocities ranging from 1.8 km/s to 2.5 km/s. The thickness of the sedimentary layer varies as evident from the MCS data. It ranges from about two hundred meters on the oceanic crust to about one kilometer on the slope. To the east of the trench, the continental crust is underlying the sediments. The crustal velocities used in the model range from 4,1 km/s right beneath the sediments to 5,9 km/s in the lower part of the crust. The continental Moho cannot be resolved, which leaves the continental structures below 15 km undefined.

The most important preliminary result deduced from this wide angle profile concerns the lateral increase of p-wave velocities at the lower part of the continental slope. We can clearly observe a backstop consisting of probably Paleozoic basement, which is defined by relatively high velocities, ranging about 5,5 to 5,8 km/s. Toward the trench, we observe a wedge shaped body. There, p-wave velocities range from 4.6 to 5.5 km/s. This body was interpreted in agreement with the MCS data as accreted compressed and reworked sediment.

The model suggests a total oceanic crustal thickness of about seven kilometers seawards of the trench. The oceanic crust is divided into two layers. The upper oceanic crust (Layer 2 and 3a) is about 2,5 km thick with seismic velocities between 4,8 km/s and 6,2 km/s in the oceanic domain and 5,9 km/s and 6,5 km/s below the continent. The thickness of the lower oceanic crust (Layer 3b) is about 4,5 km. Here we find velocities of 6,5 km/s in the upper part to 7,2 km/s close to the CMB. The oceanic Nazca Plate subducts beneath the South American Plate with only a small slope inclination angle. In contrast to the landward side, the Moho can be well observed on the seaward side of the trench. In the westermost portion, our model shows the Moho in a depth of 11,5 km. Underneath the trench it reaches down to 15 km, below the continent we estimate the CMB in a much deeper position. This model will be further refined when incorporating all record sections in a more detailed analysis, and also when the data from the landstations will become available.

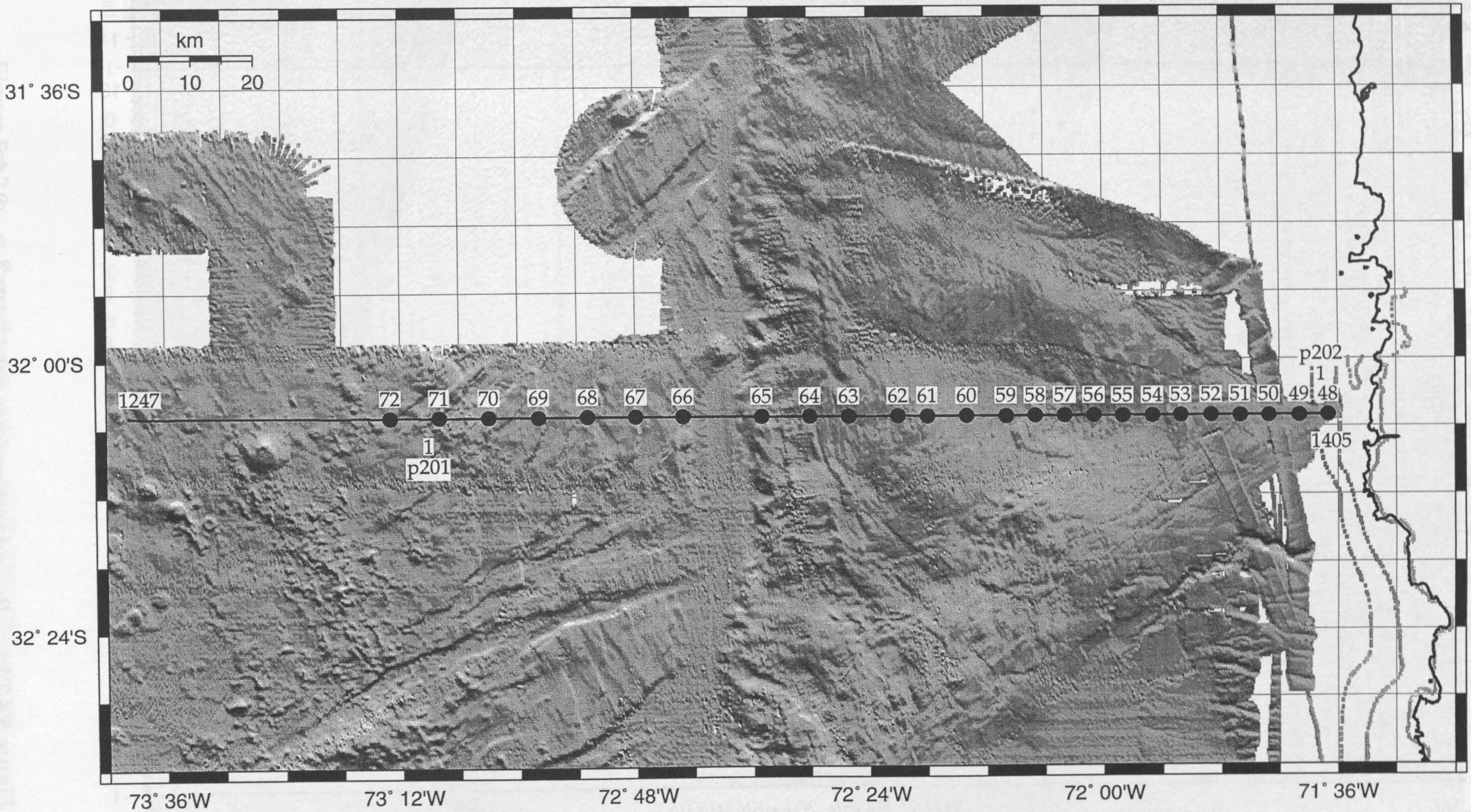

**Figure 5.4.2.1:** Location map of profile 201/202 and illuminated multibeam bathymetry. Superimposed the obh/obs locations, the first, and last shotpoint numbers.

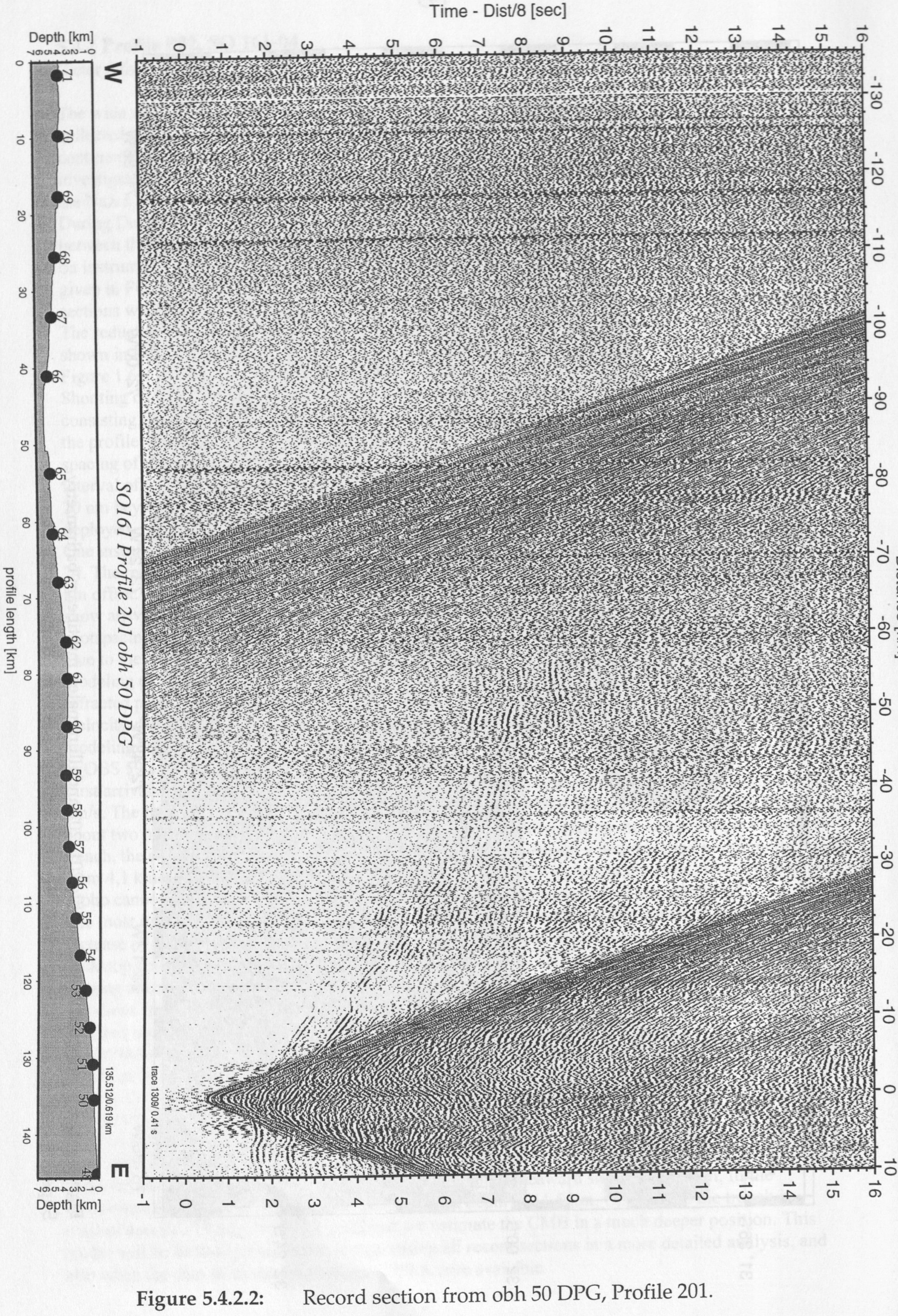

**Figure 5.4.2.2:** Record section from obh 50 DPG, Profile 201.

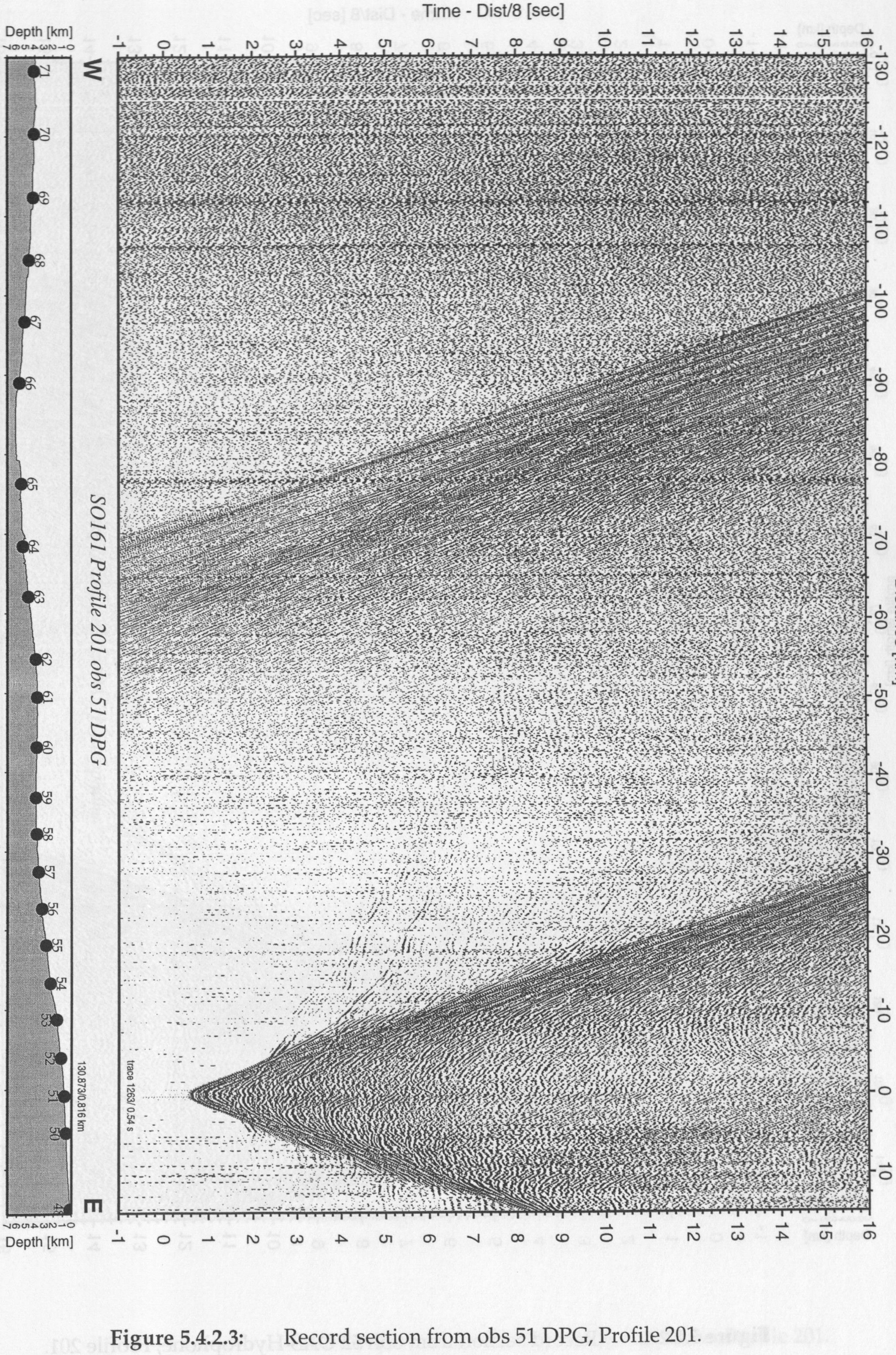

Figure 5.4.2.3: Record section from obs 51 DPG, Profile 201.

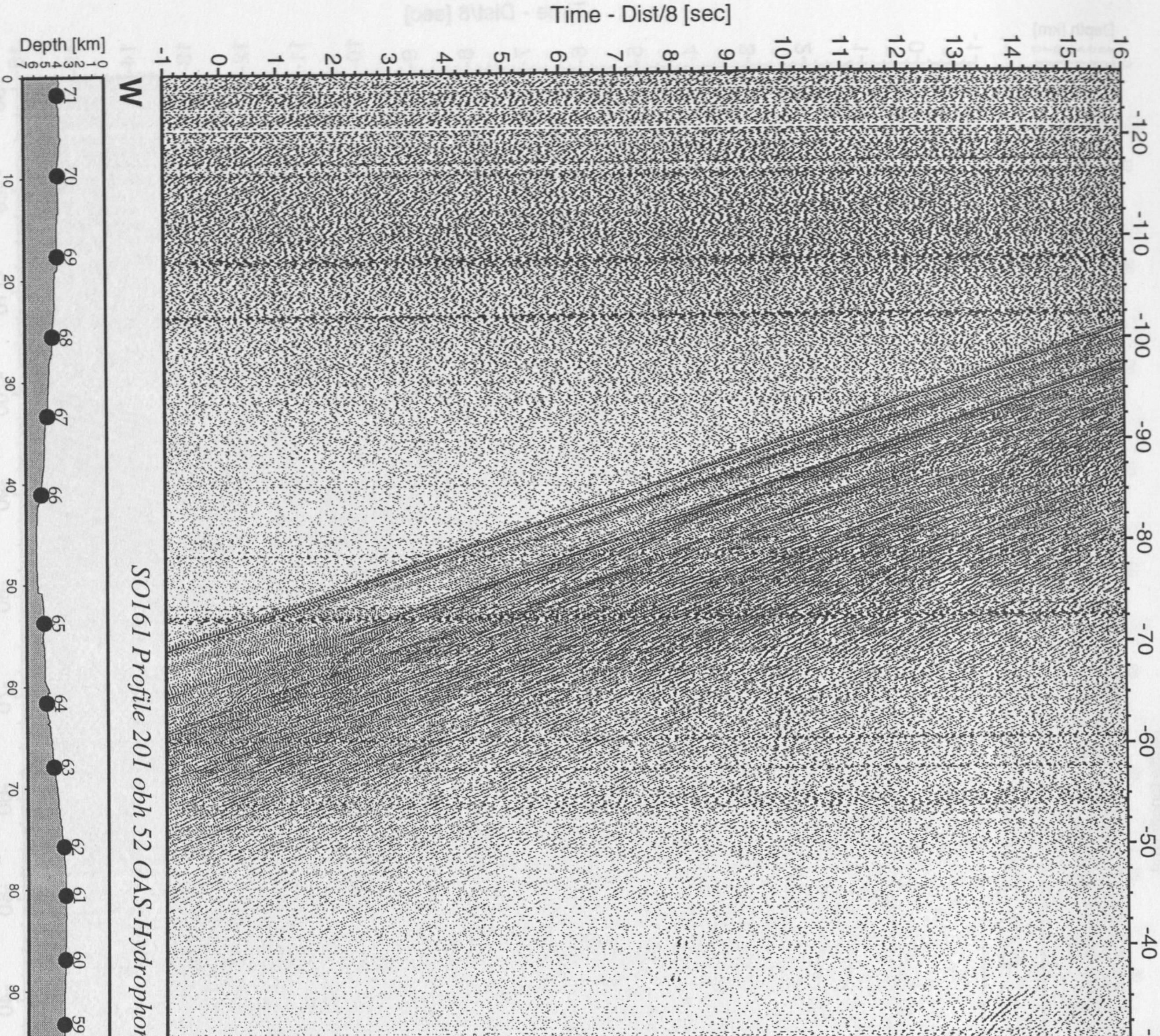

**Figure 5.4.2.4:** Record section from obh 52 OAS-Hydrophone, Profile 201.

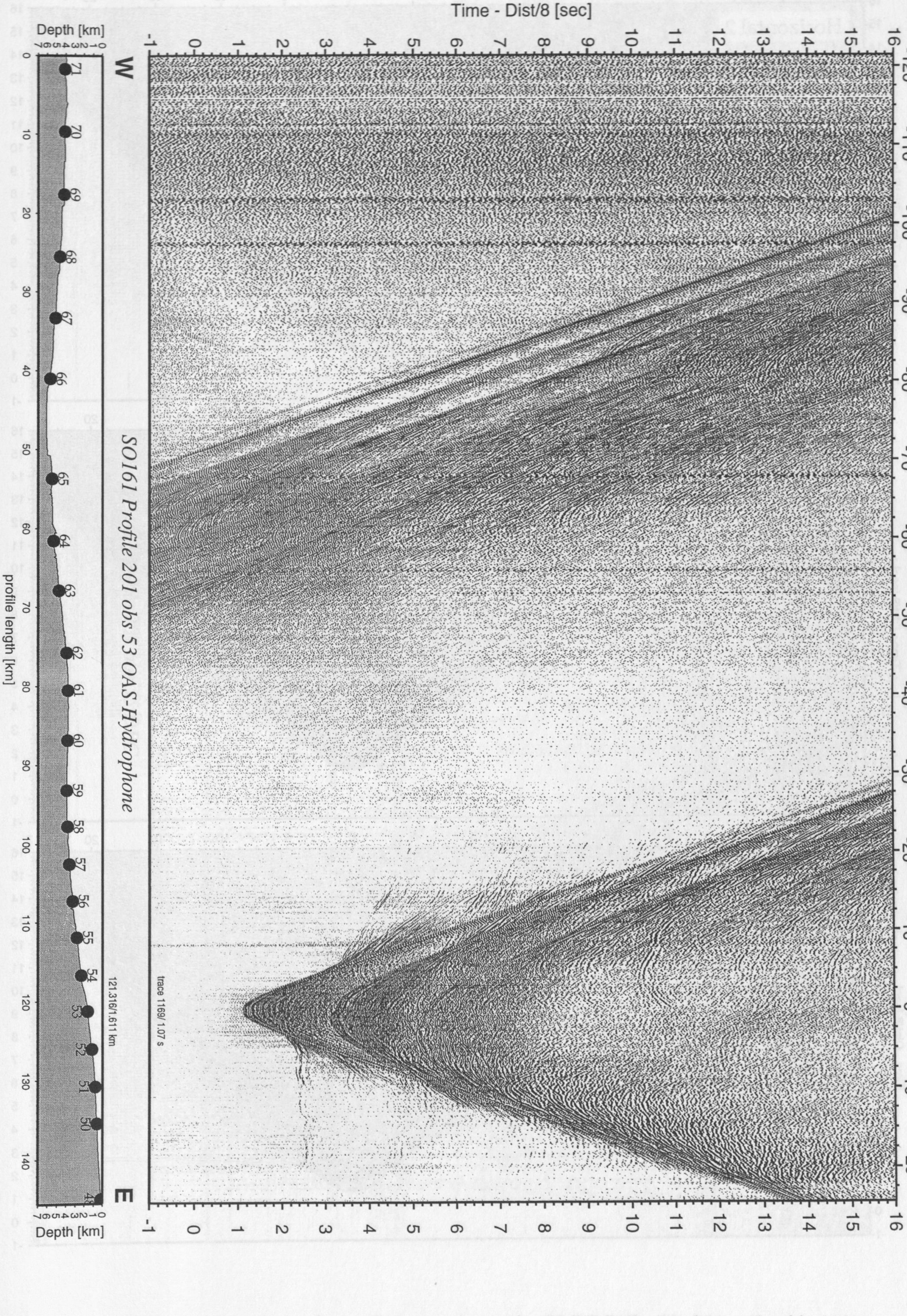

**Figure 5.4.2.5:** Record section from obs 53 OAS-Hydrophone, Profile 201.

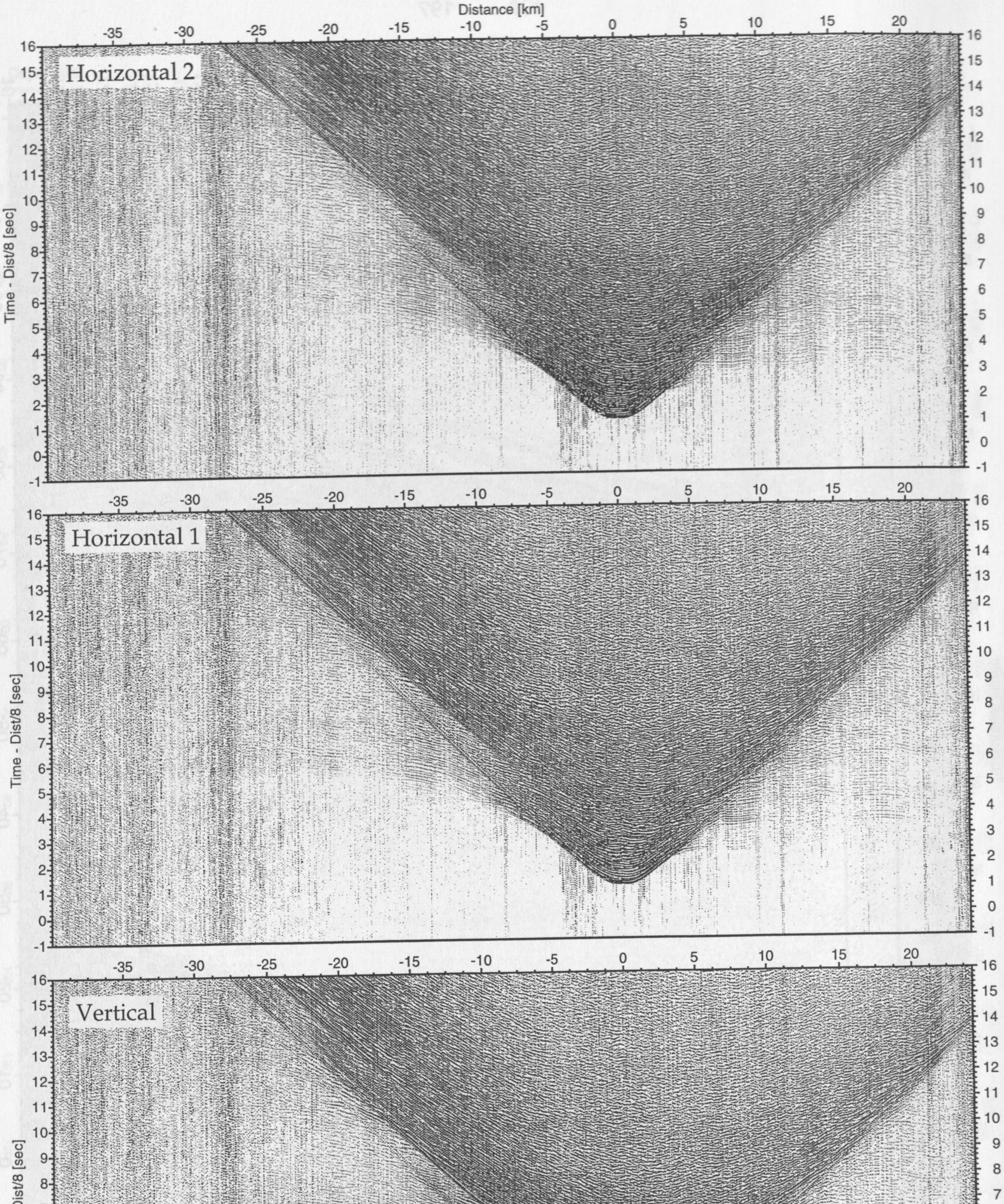

**Figure 5.4.2.6:** Record sections from obs 53 OAS/A01-4.5Hz, SO161 Profile 201.

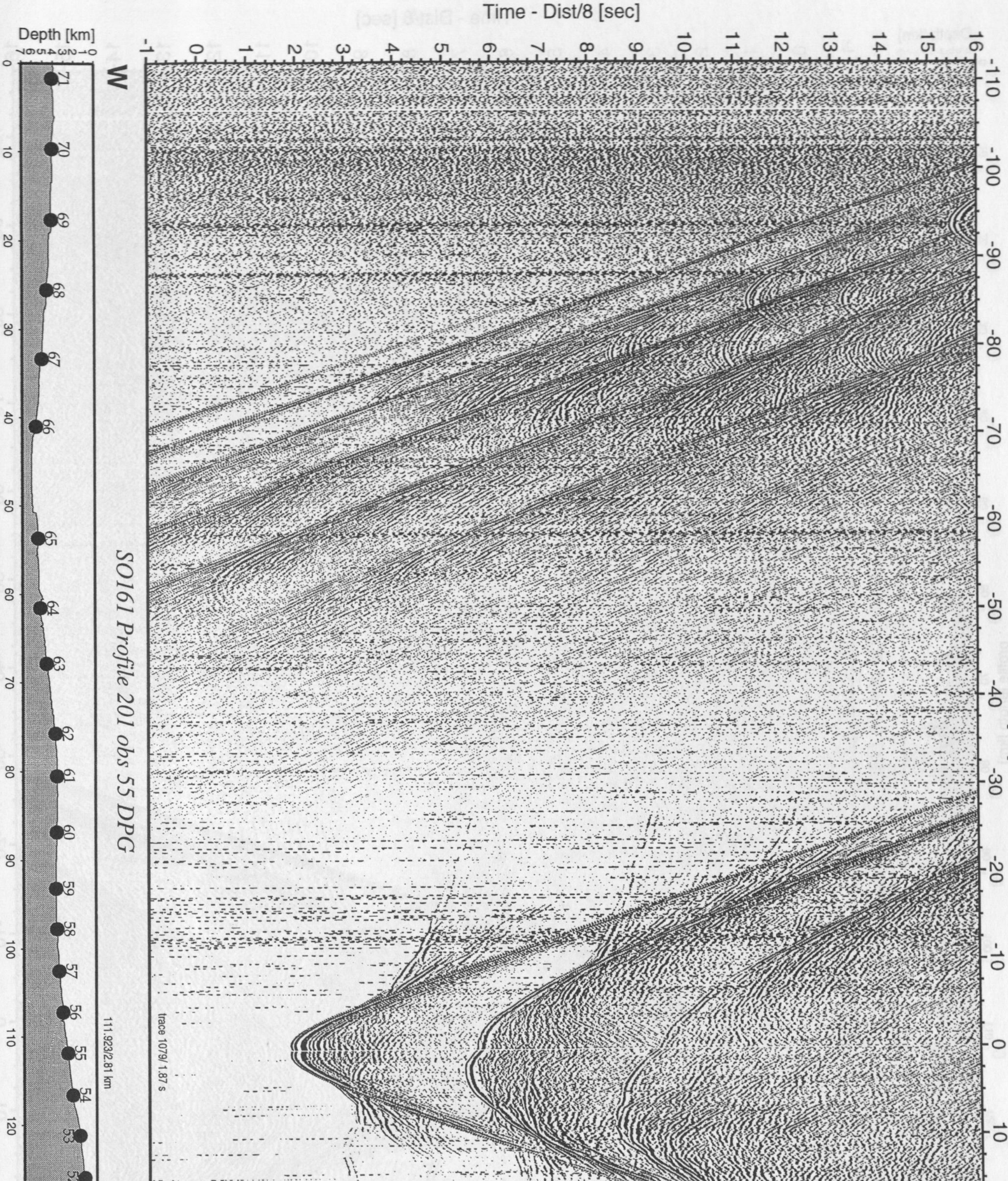

**Figure 5.4.2.7:** Record section from obs 55 DPG, Profile 201.

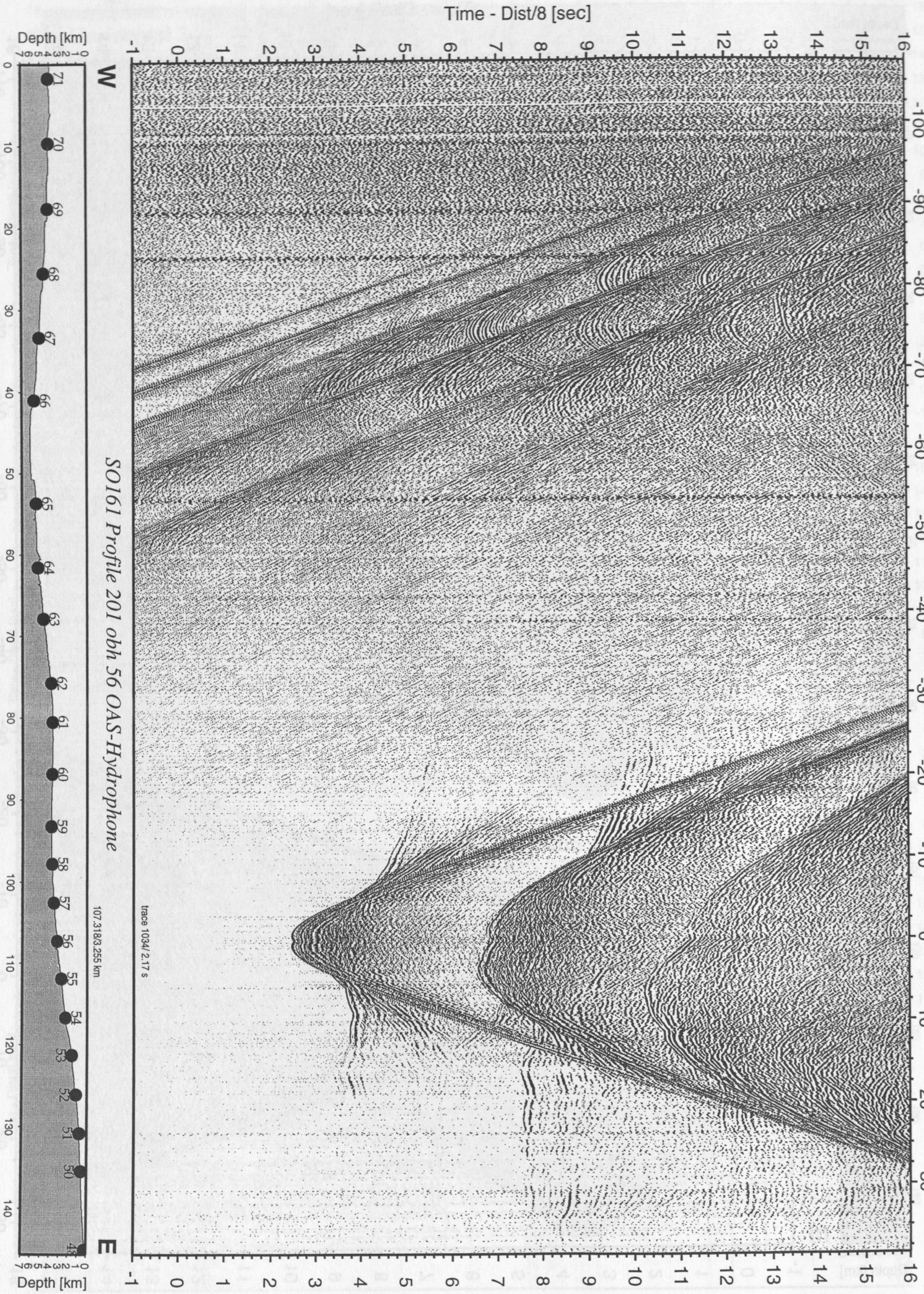

**Figure 5.4.2.8:** Record section from obh 56 OAS-Hydrophone, Profile 201.

2o1

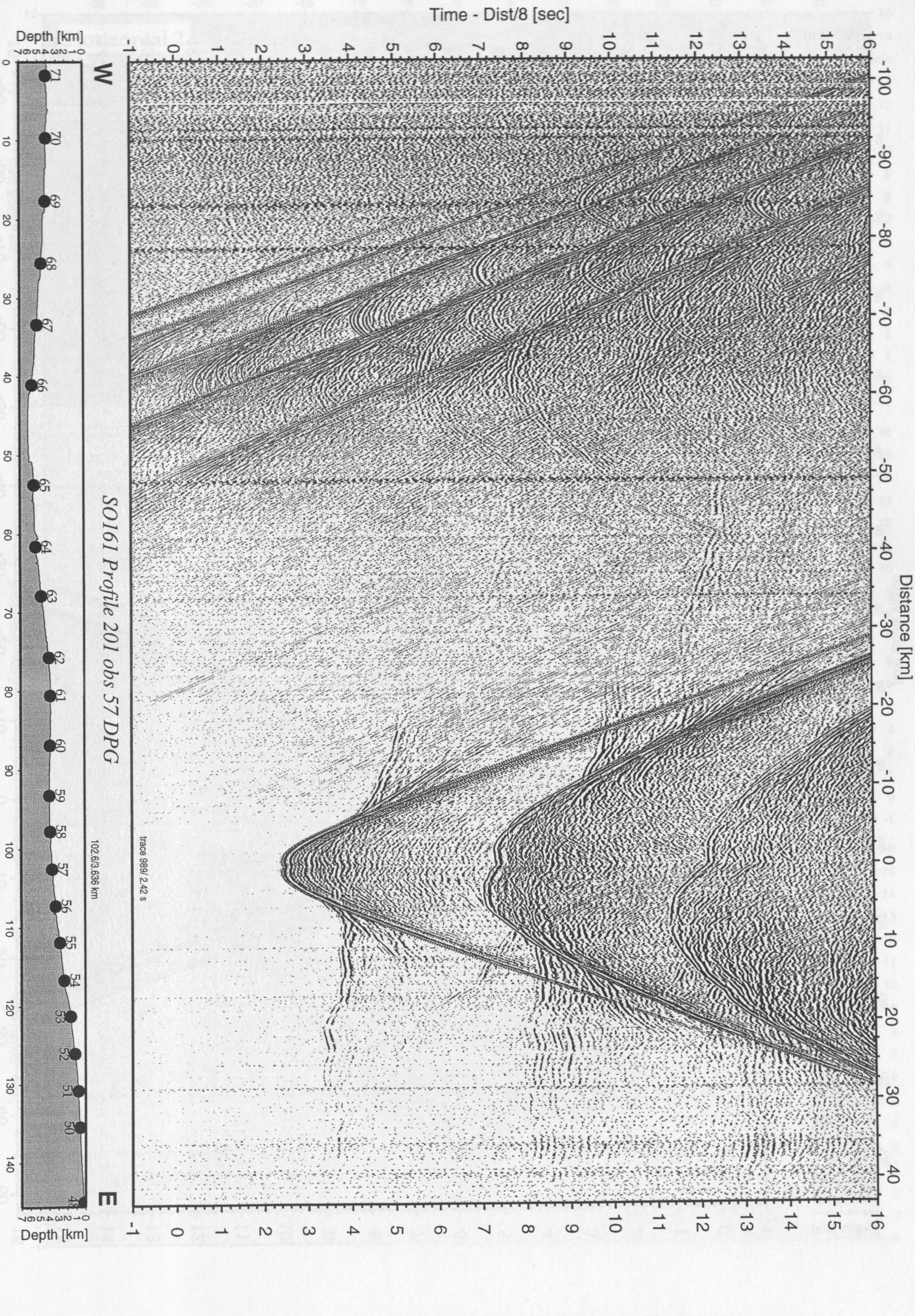

**Figure 5.4.2.9:** Record section from obs 57 DPG, Profile 201.

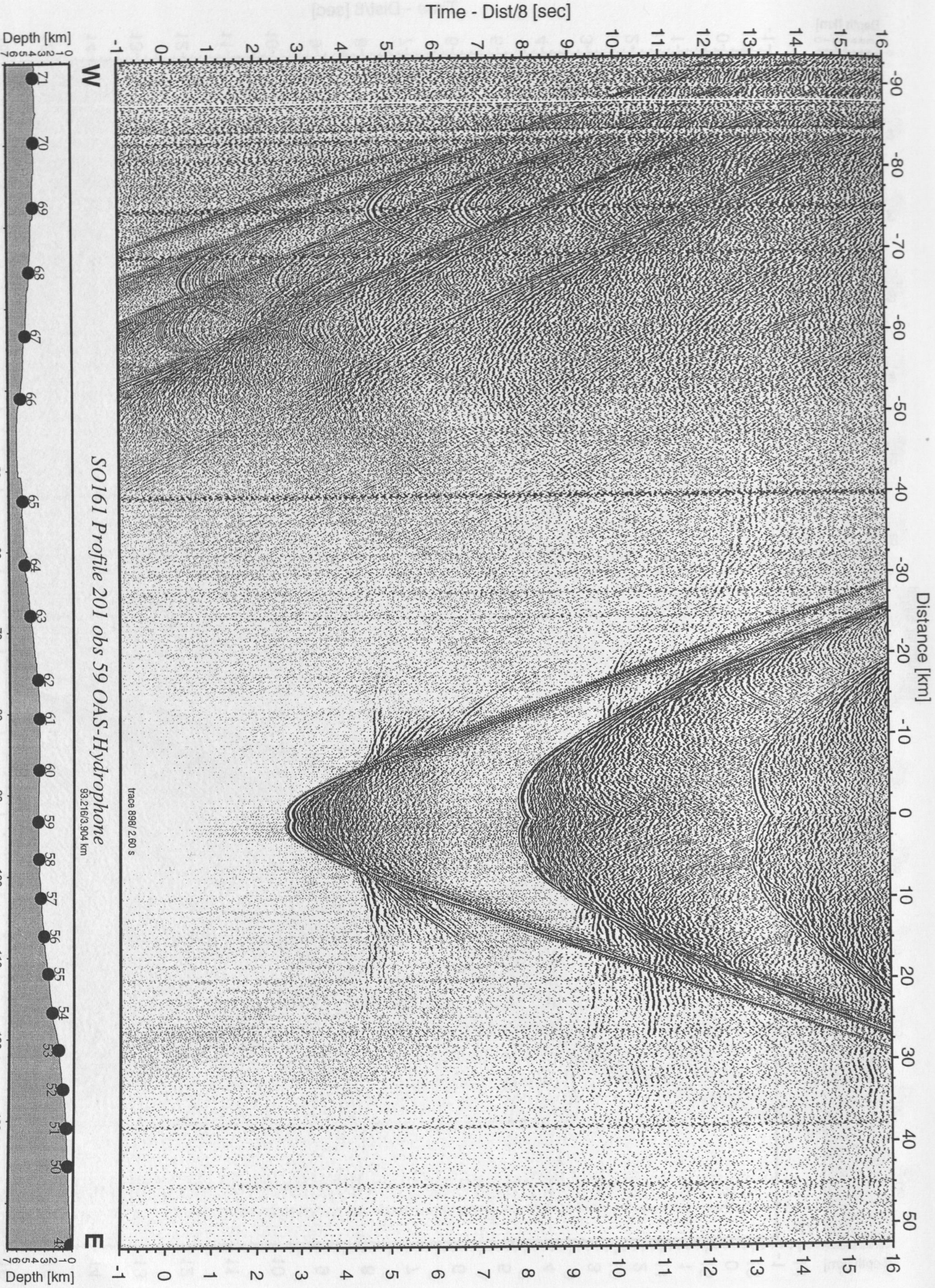

**Figure 5.4.2.10:** Record section from obs 59 OAS-Hydrophone, Profile 201.

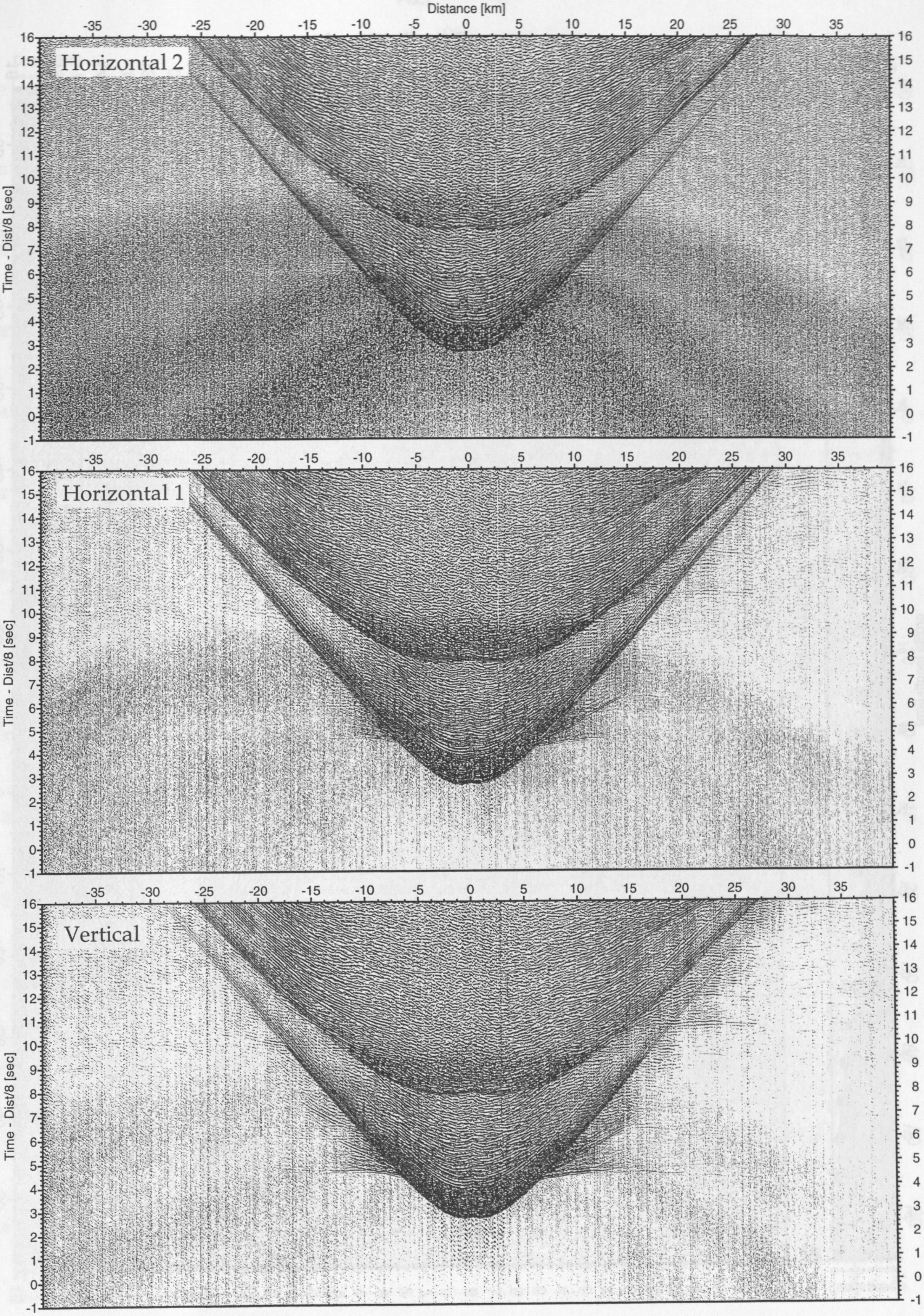

**Figure 5.4.2.11:** Record sections from obs 59 OAS/WEBB, SO161 Profile 201.

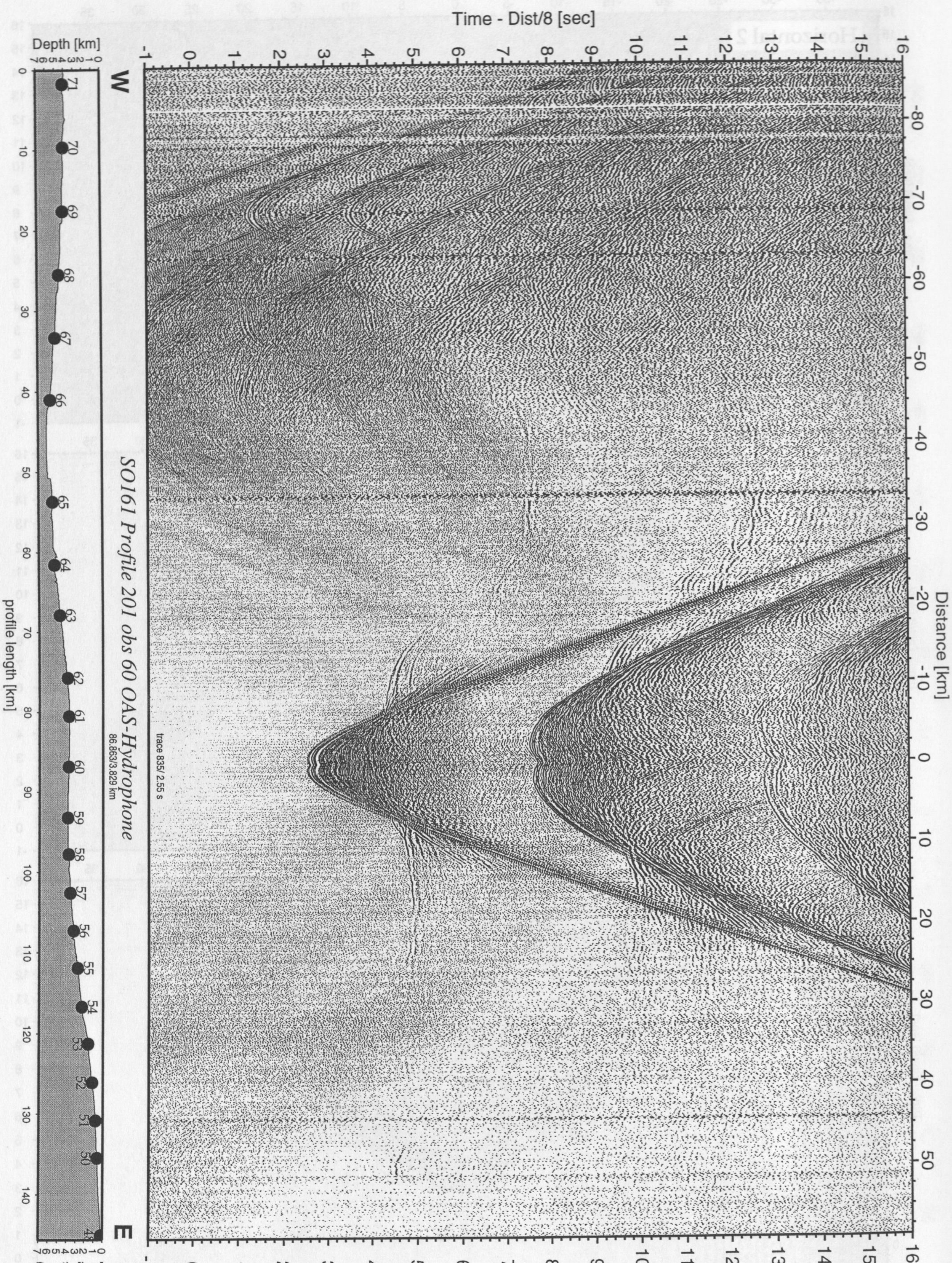

**Figure 5.4.2.12:** Record section from obs 60 OAS-Hydrophone, Profile 201.

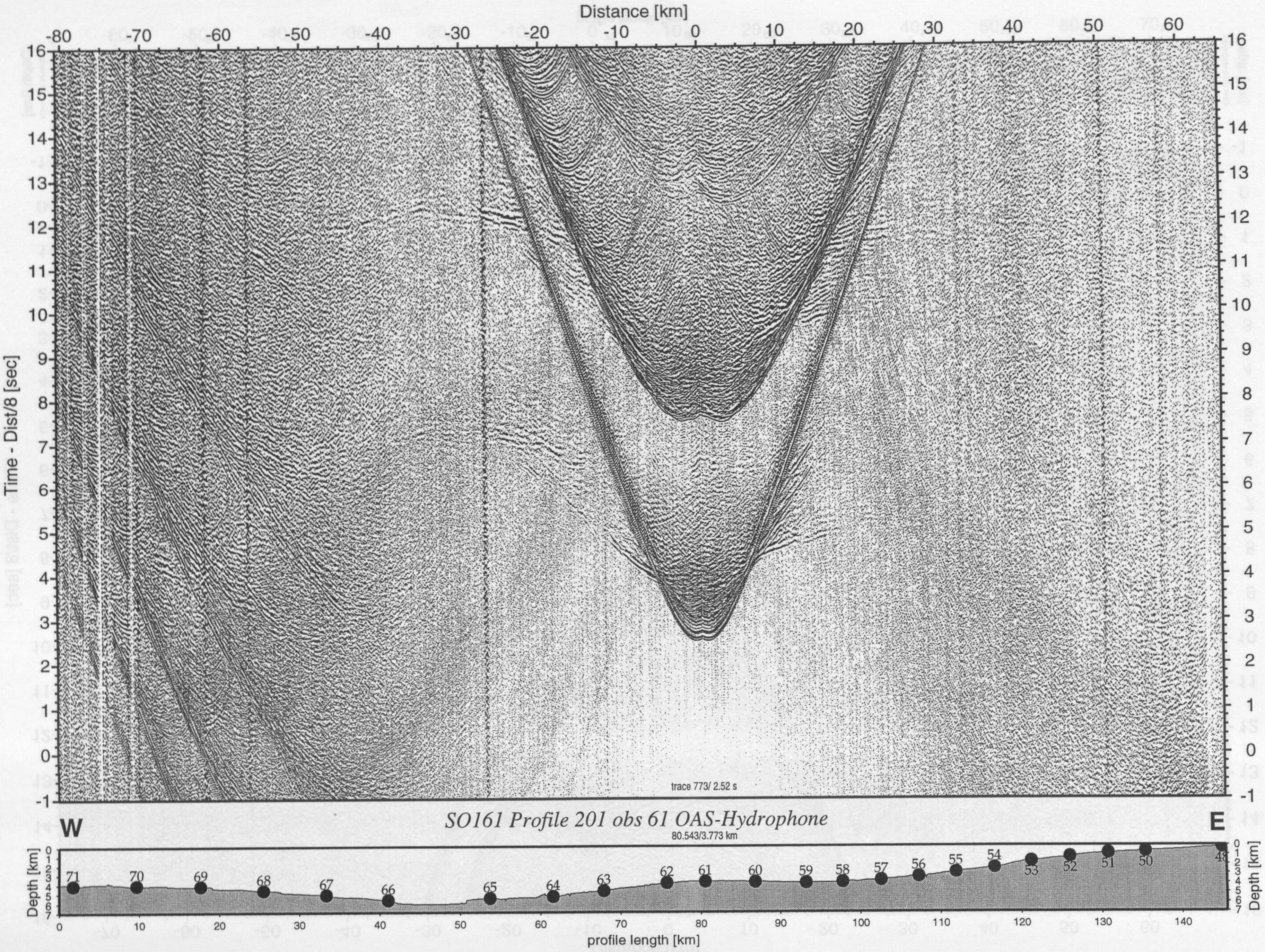

**Figure 5.4.2.13:** Record section from obs 61 OAS-Hydrophone, Profile 201.

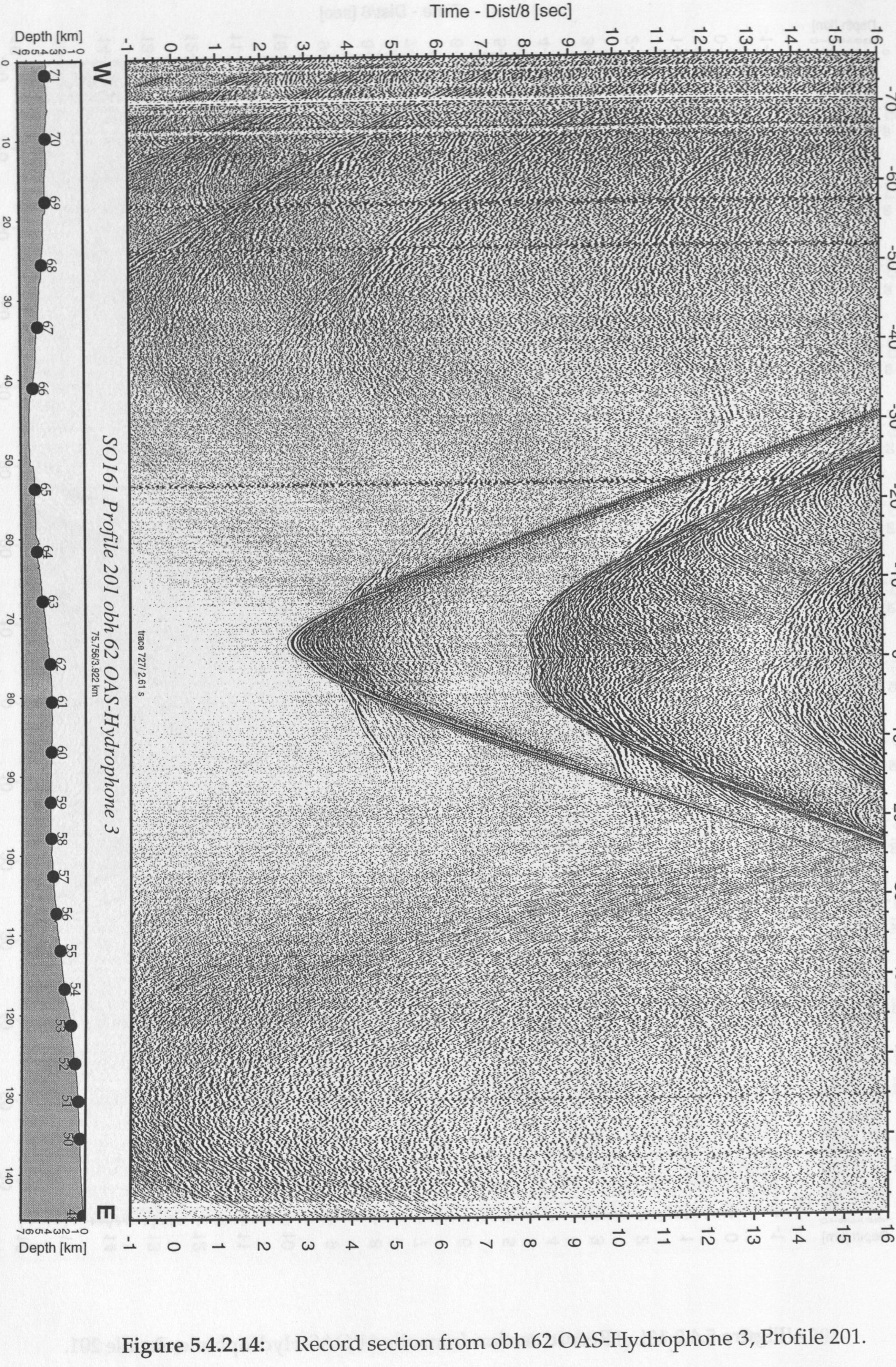

**Figure 5.4.2.14:** Record section from obh 62 OAS-Hydrophone 3, Profile 201.

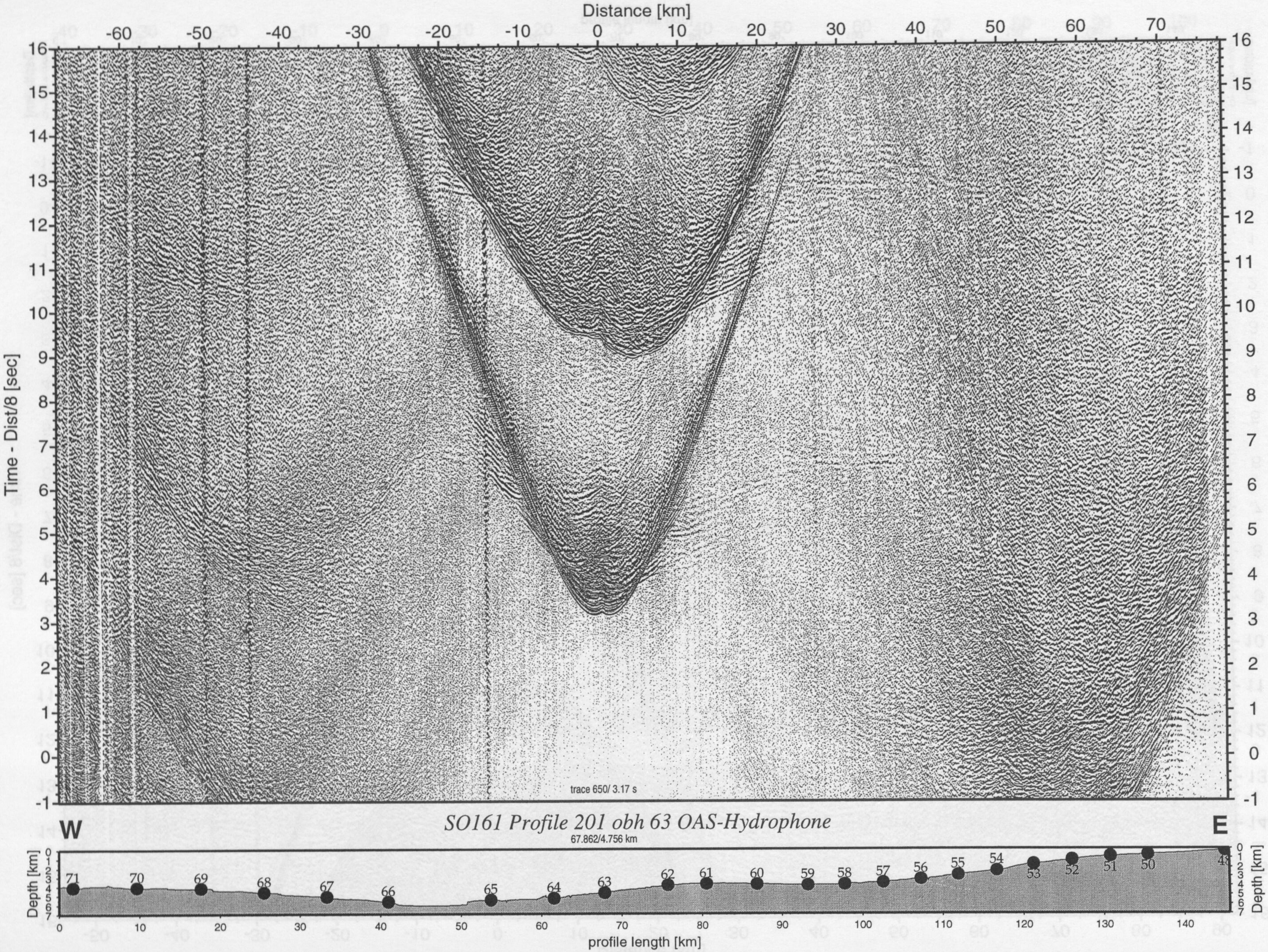

**Figure 5.4.2.15:** Record section from obh 63 OAS-Hydrophone, Profile 201.

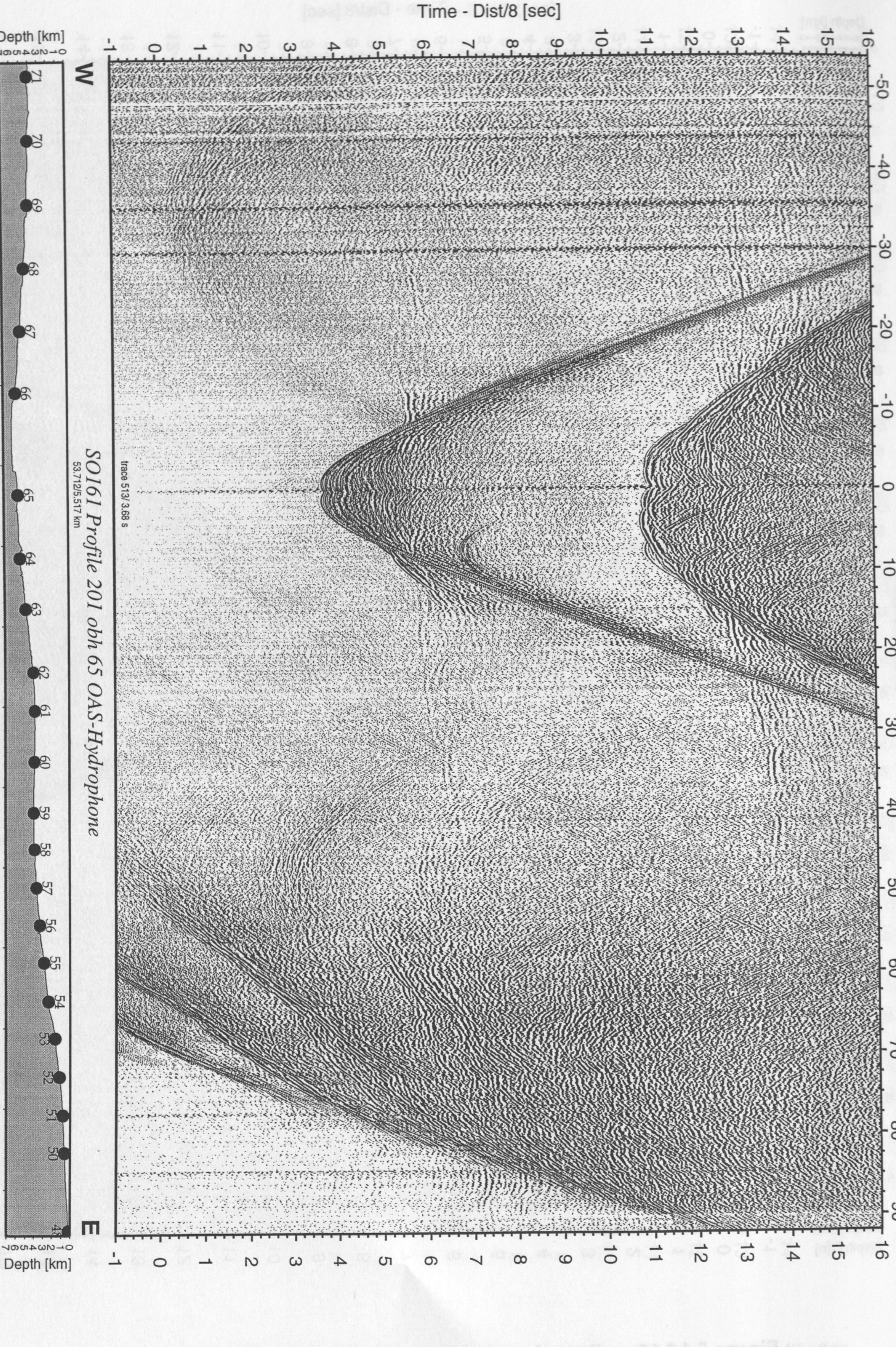

**Figure 5.4.2.16:** Record section from obh 65 OAS-Hydrophone, Profile 201.

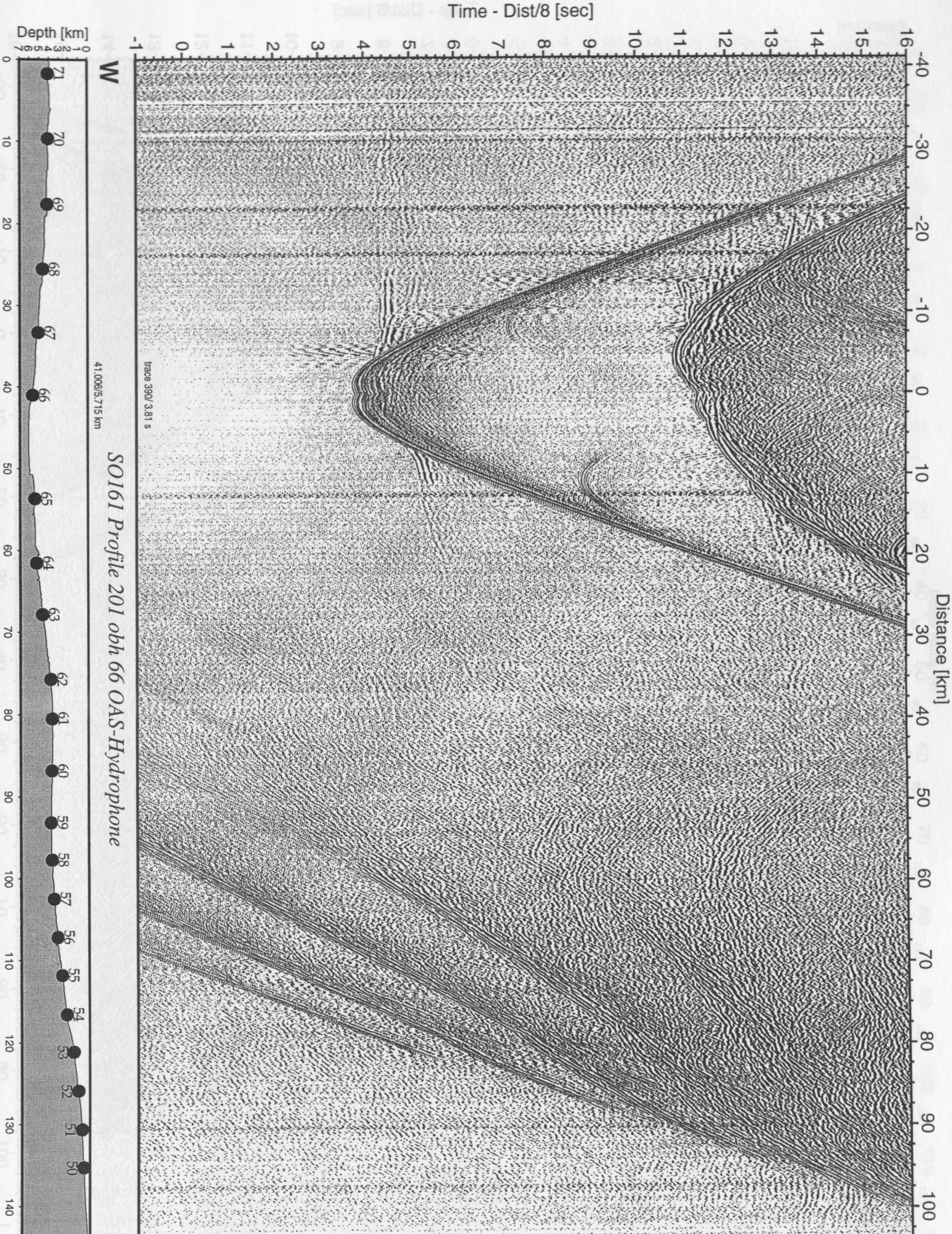

**Figure 5.4.2.17:** Record section from obh 66 OAS-Hydrophone, Profile 201.

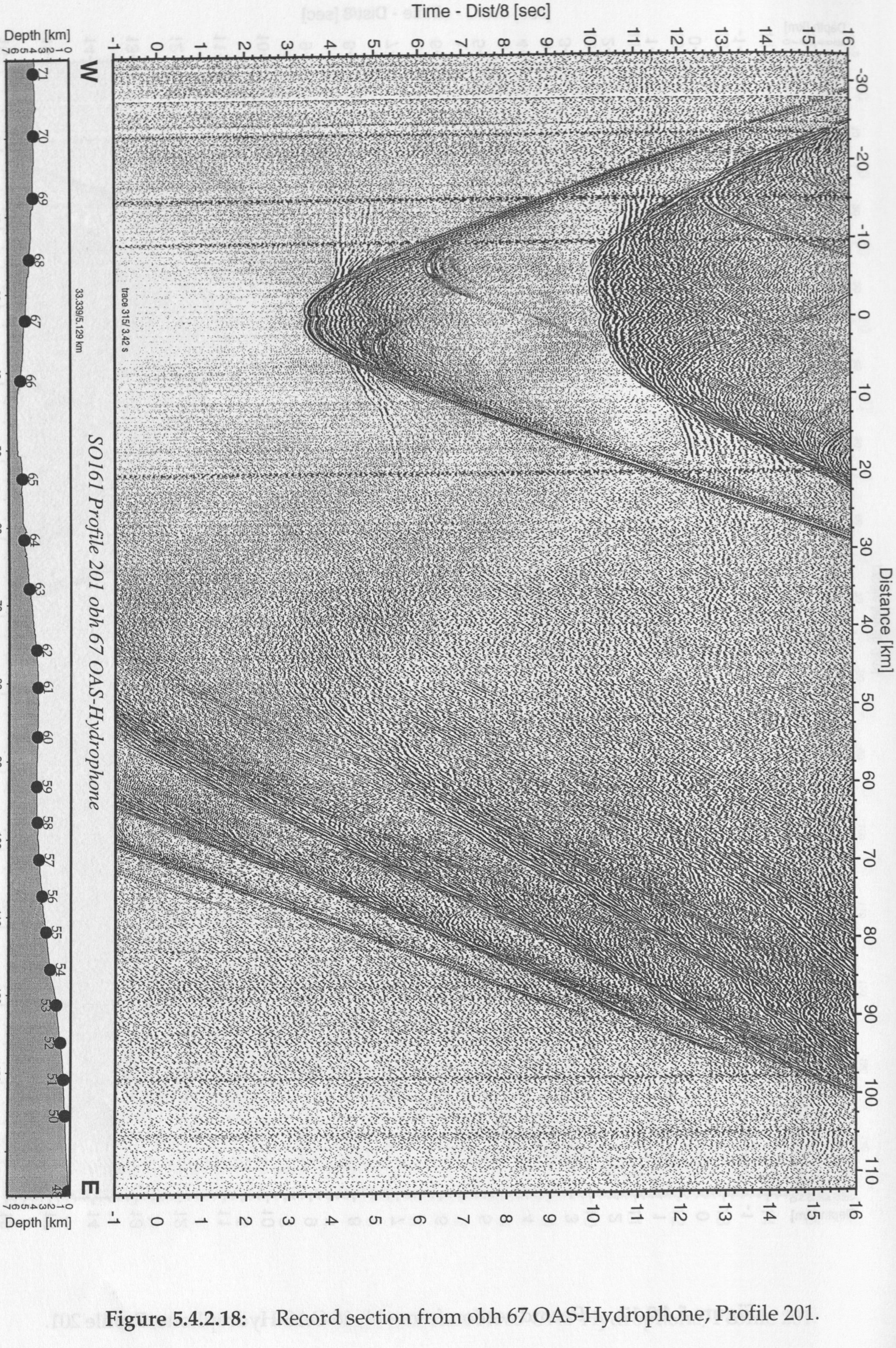

Figure 5.4.2.18: Record section from obh 67 OAS-Hydrophone, Profile 201.

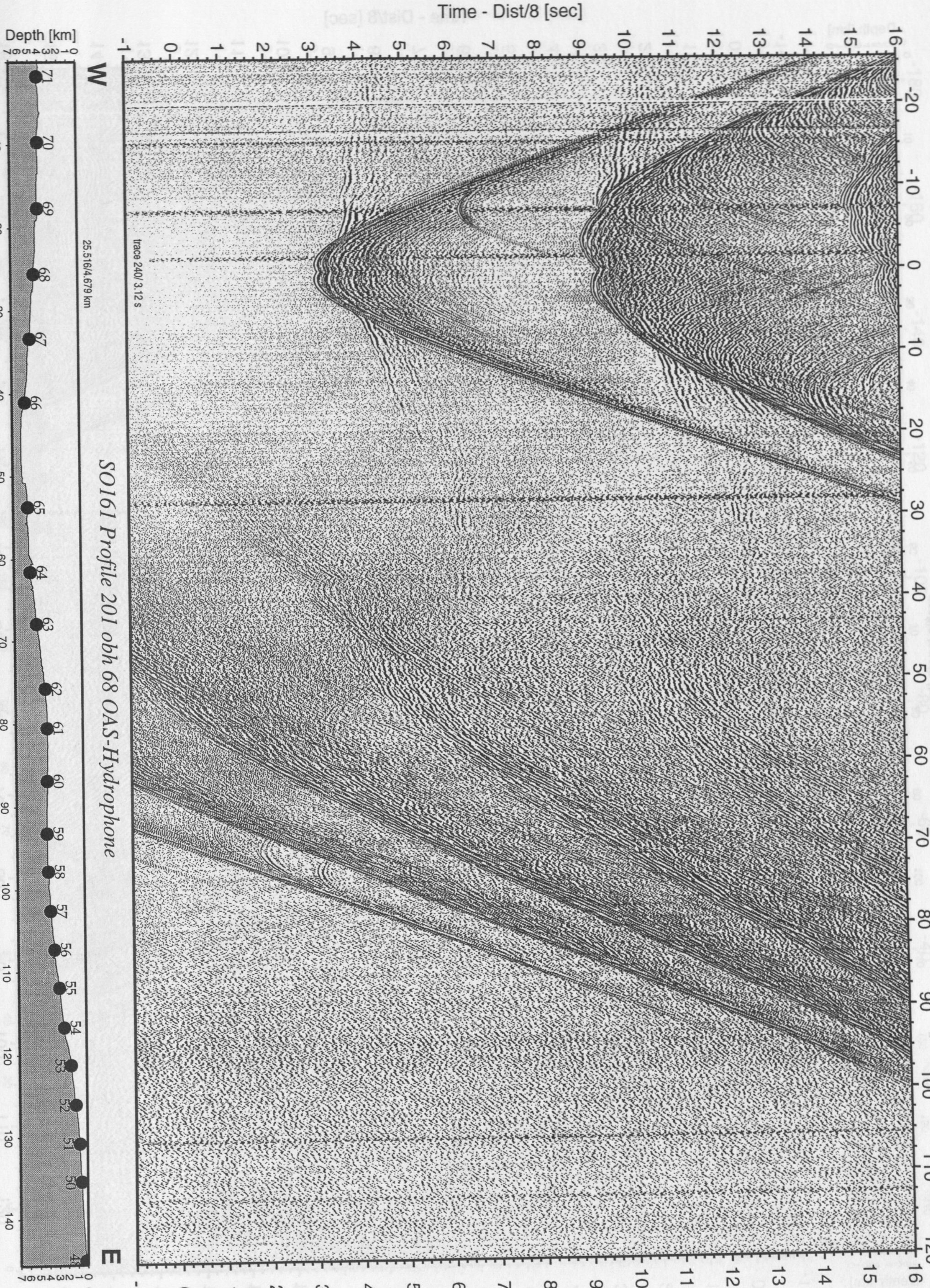

**Figure 5.4.2.19:** Record section from obh 68 OAS-Hydrophone, Profile 201.

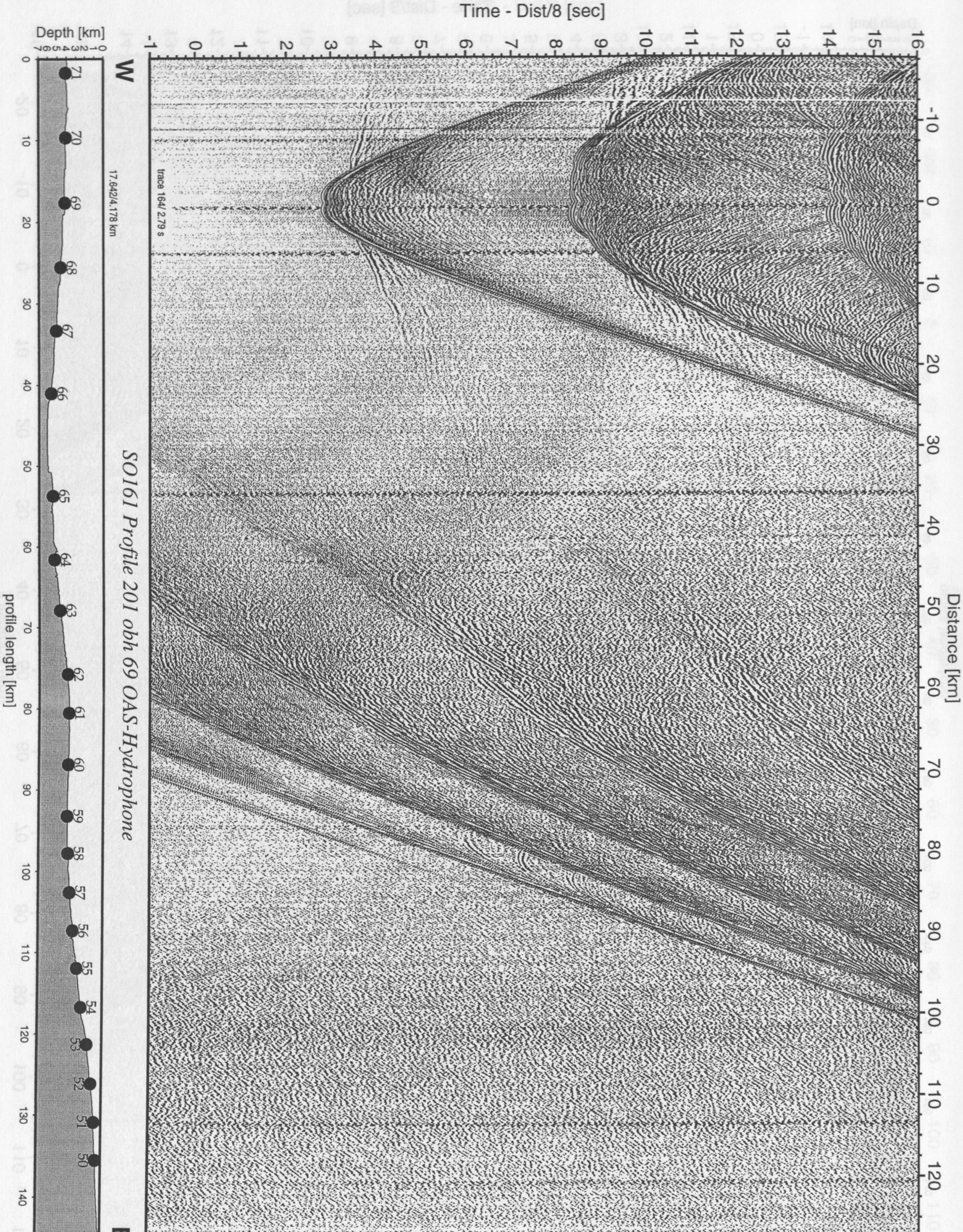

**Figure 5.4.2.20:** Record section from obh 69 OAS-Hydrophone, Profile 201.

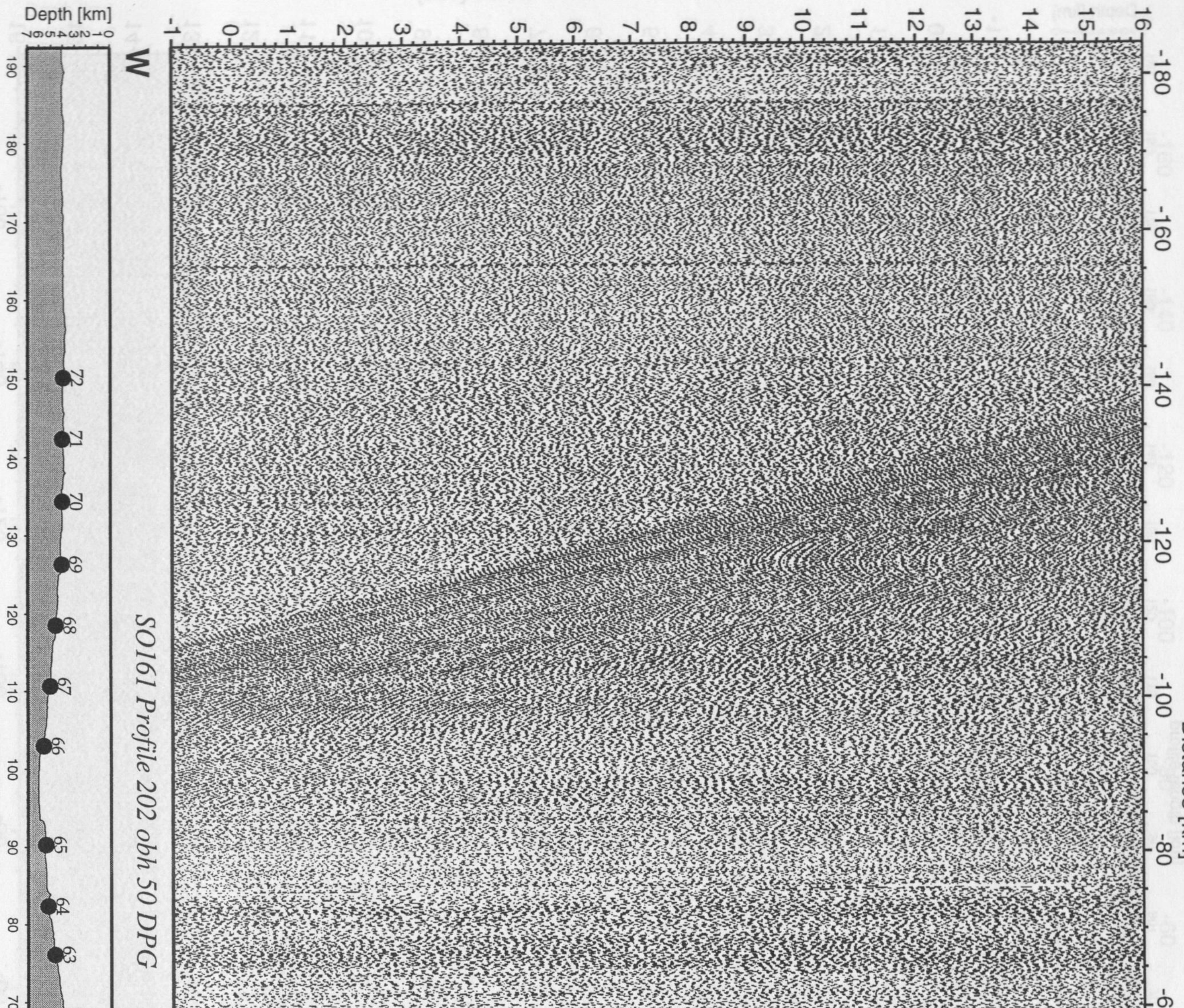

Figure 5.4.2.21: Record section from obh 50 DPG, Profile 202.

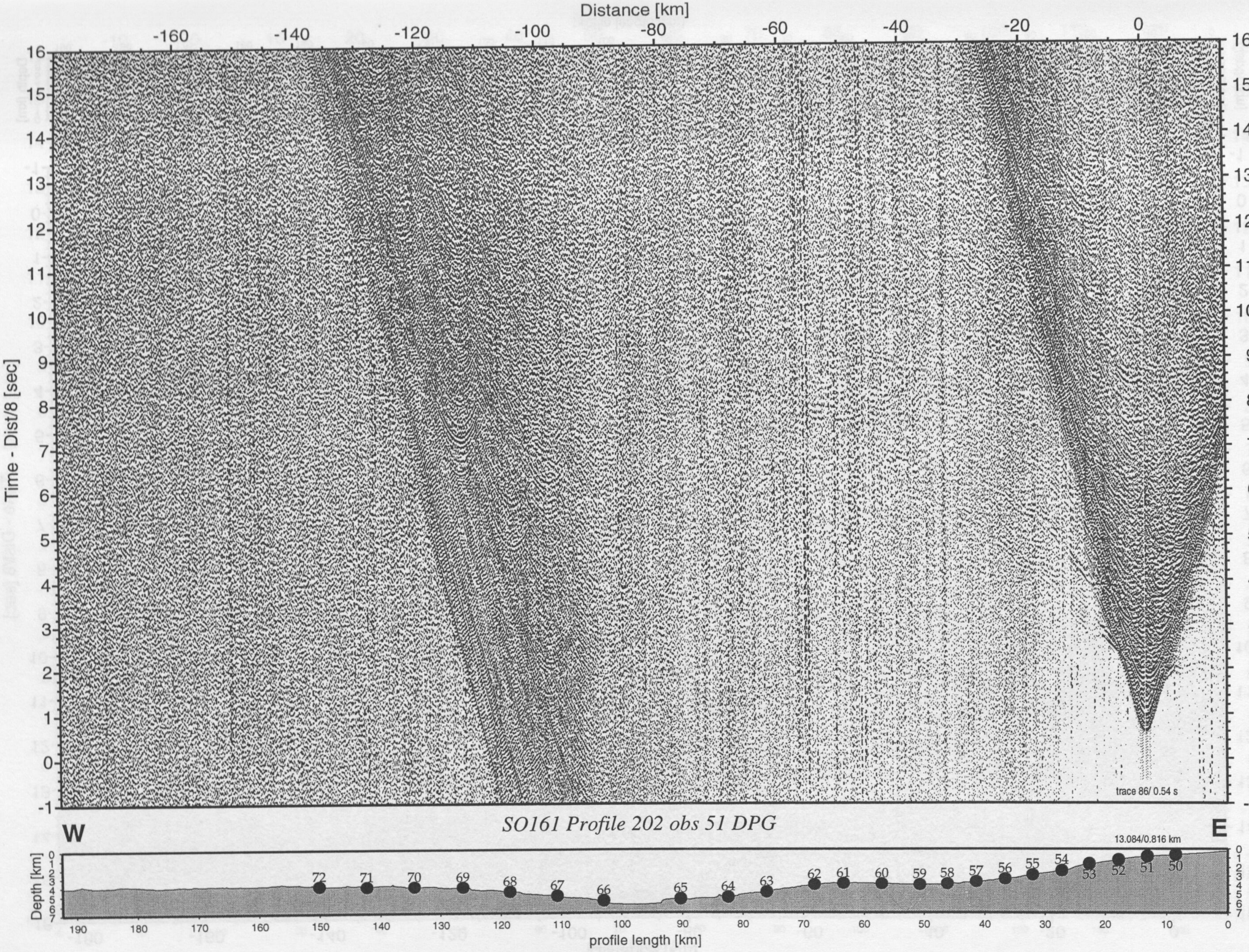

**Figure 5.4.2.22:** Record section from obs 51 DPG, Profile 202.

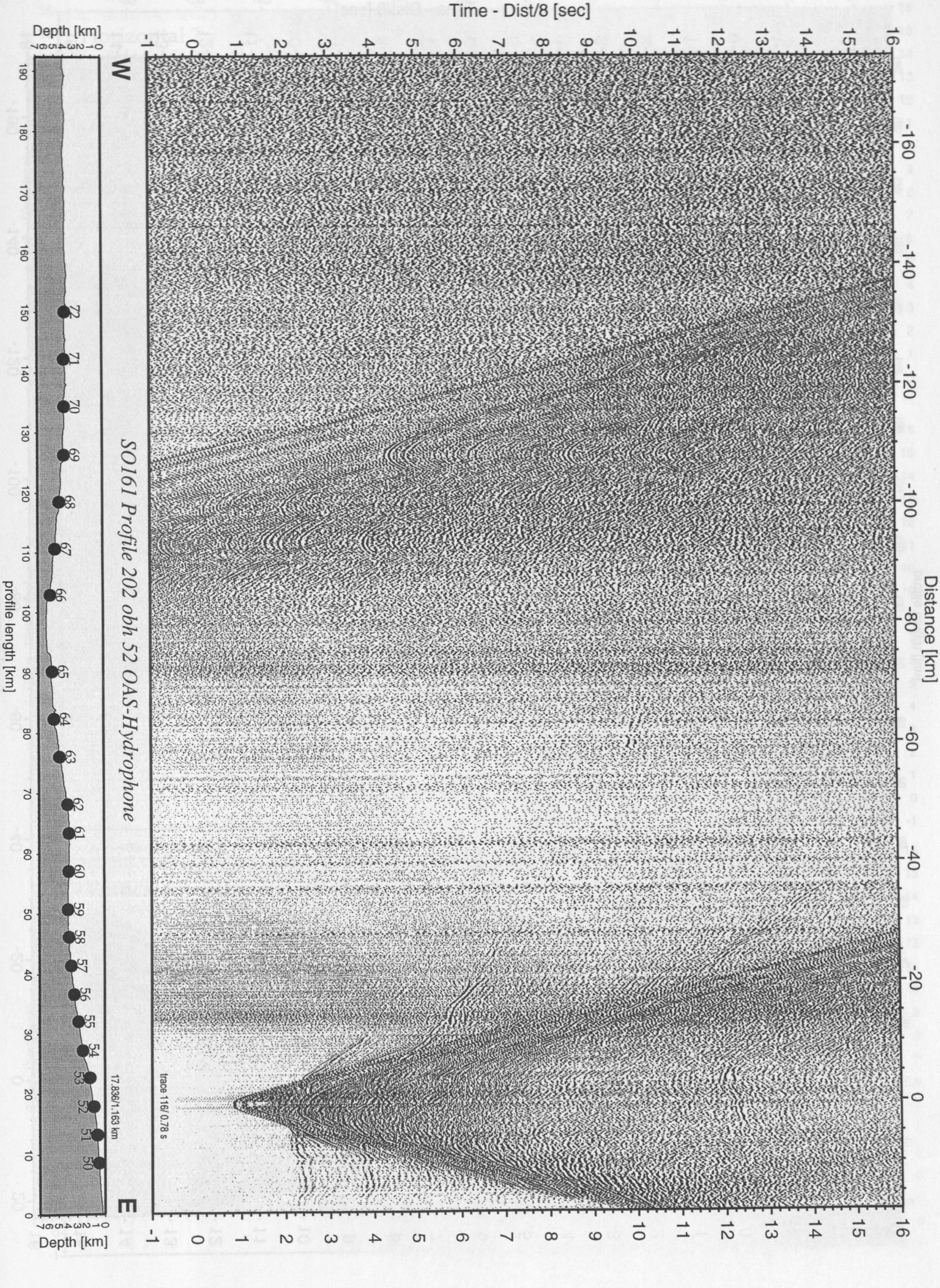

**Figure 5.4.2.23:** Record section from obh 52 OAS-Hydrophone, Profile 202.

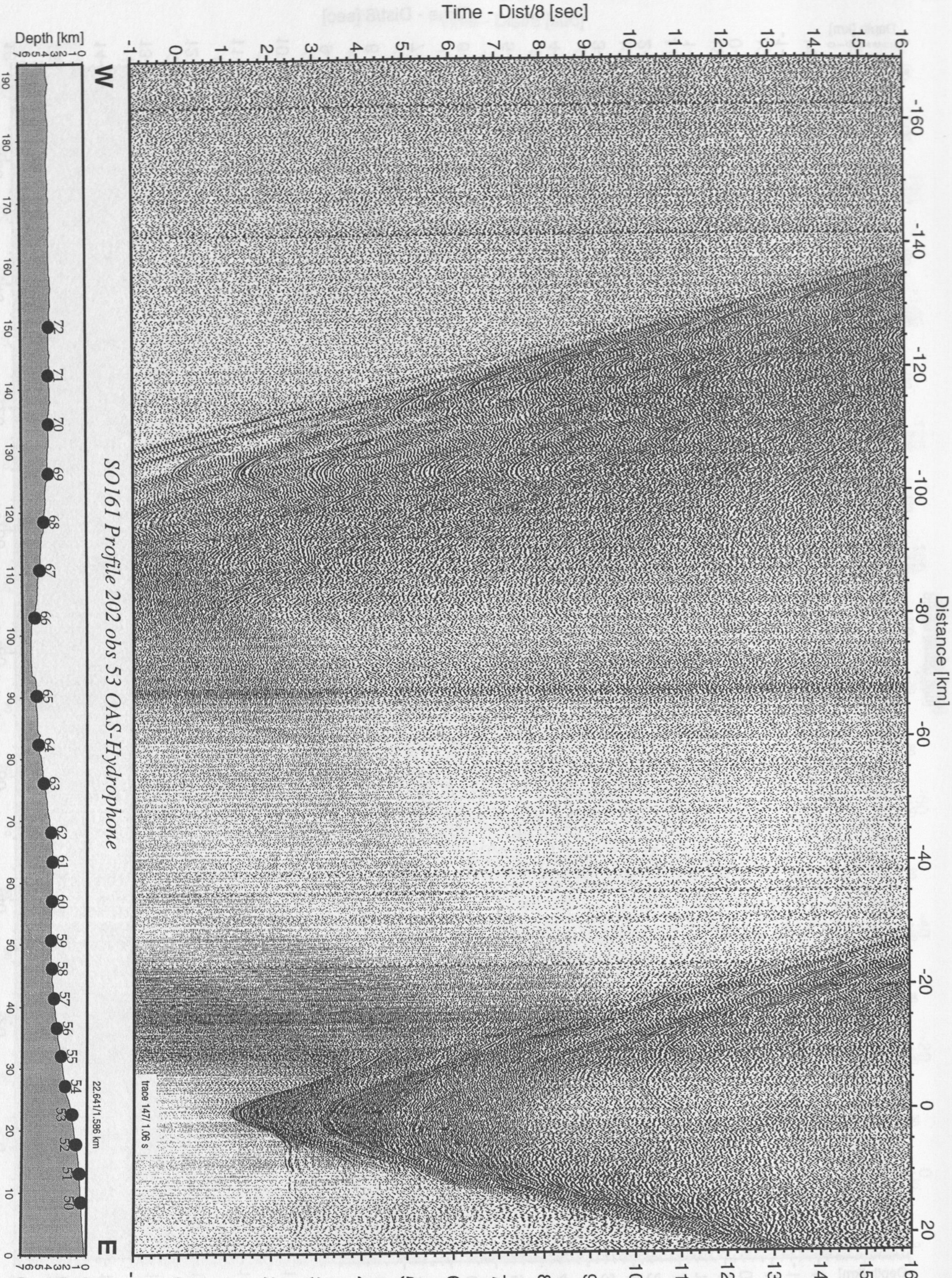

**Figure 5.4.2.24:** Record section from obs 53 OAS-Hydrophone, Profile 202.

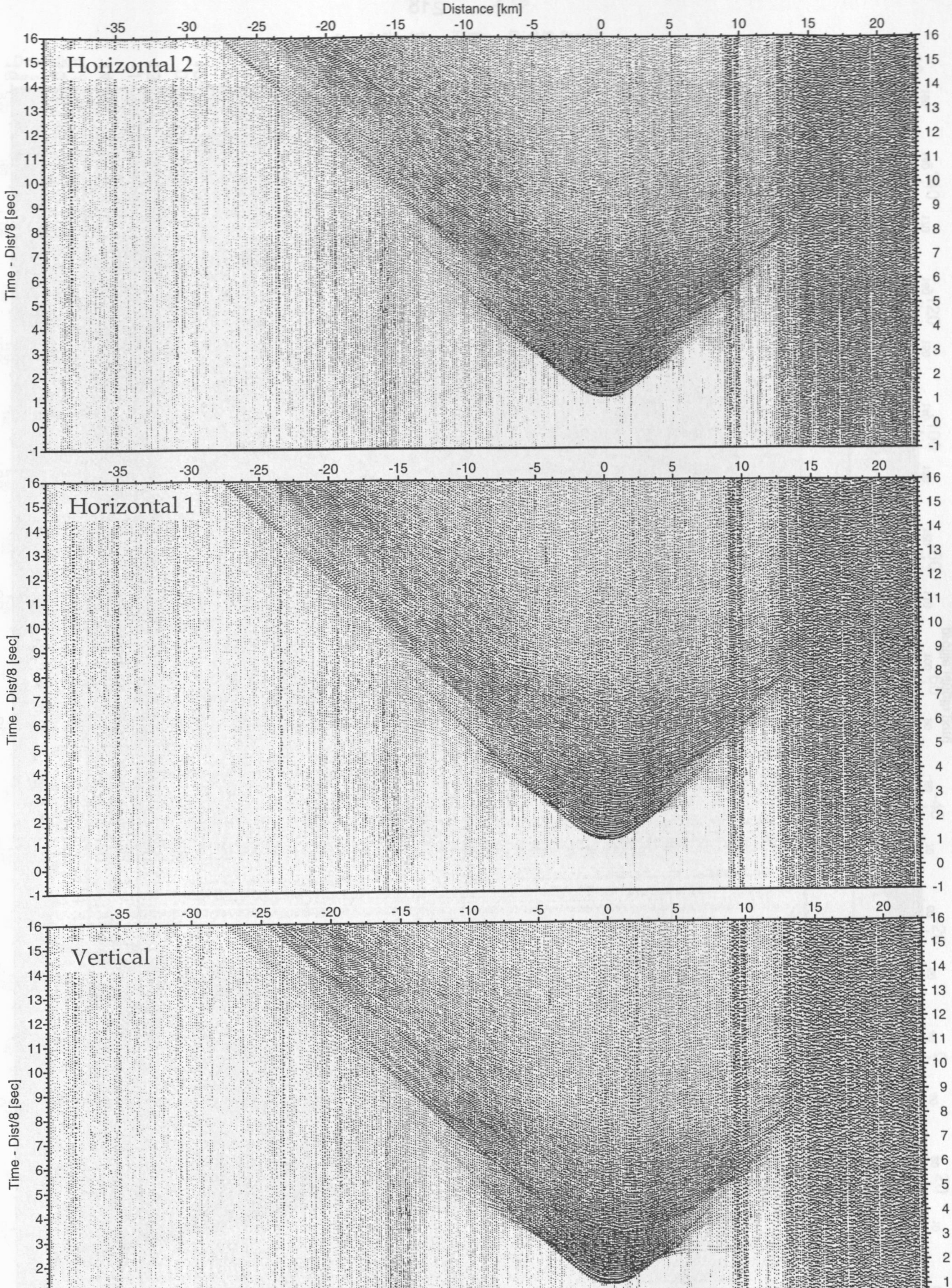

**Figure 5.4.2.25:** Record sections from obs 53 OAS/A01-4.5Hz, SO161 Profile 202.

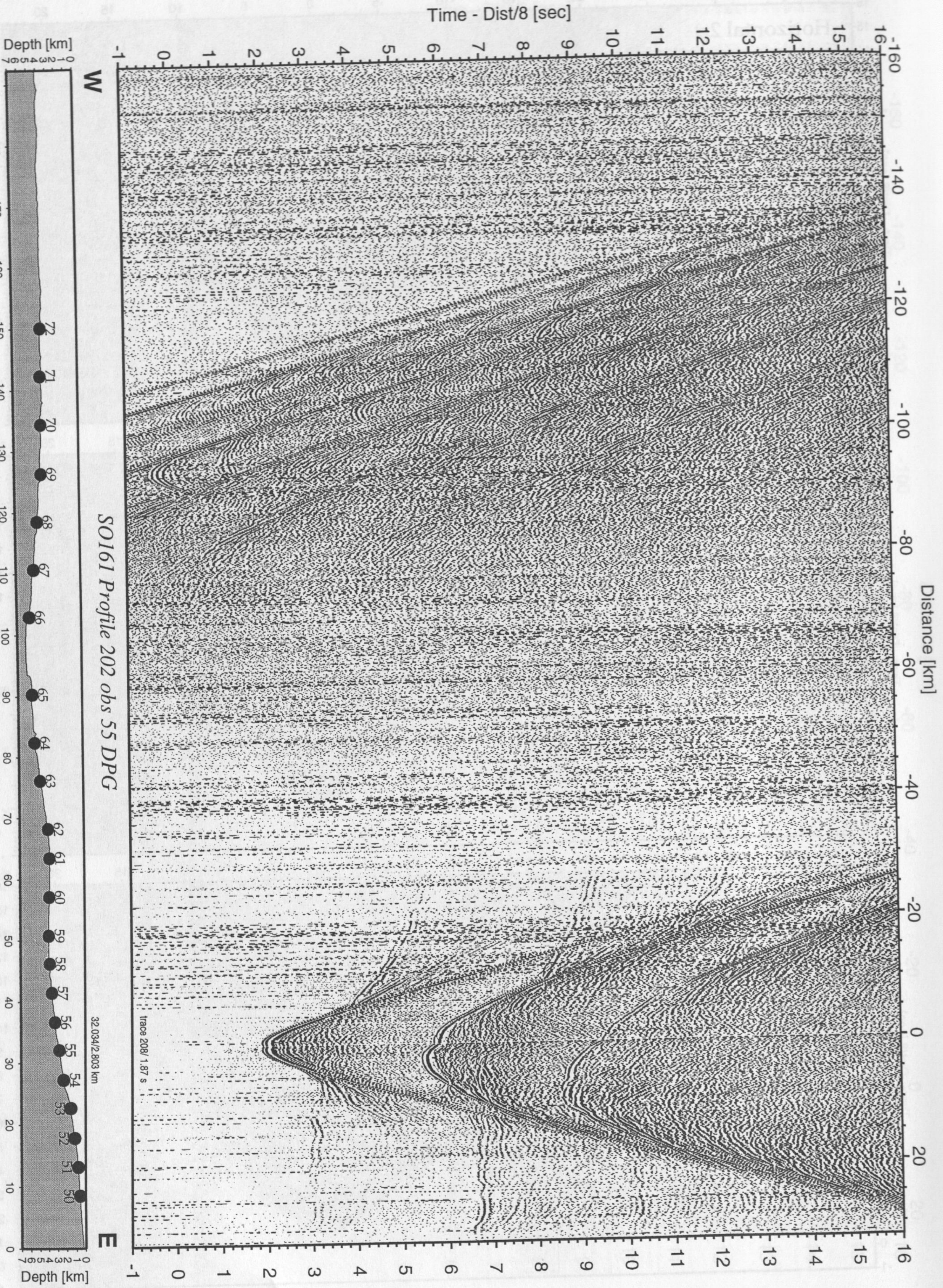

Figure 5.4.2.26: Record section from obs 55 DPG, Profile 202.

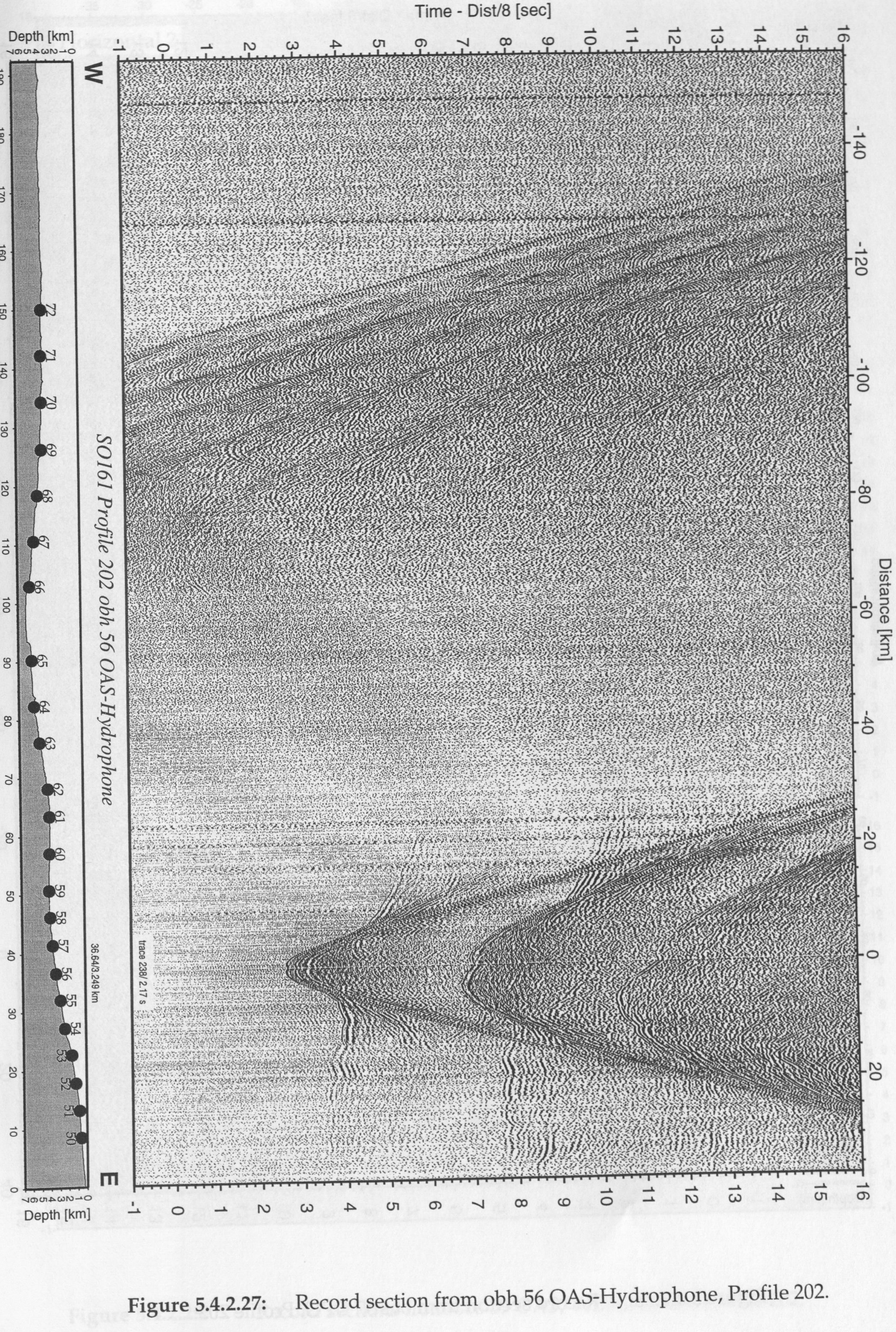

**Figure 5.4.2.27:** Record section from obh 56 OAS-Hydrophone, Profile 202.

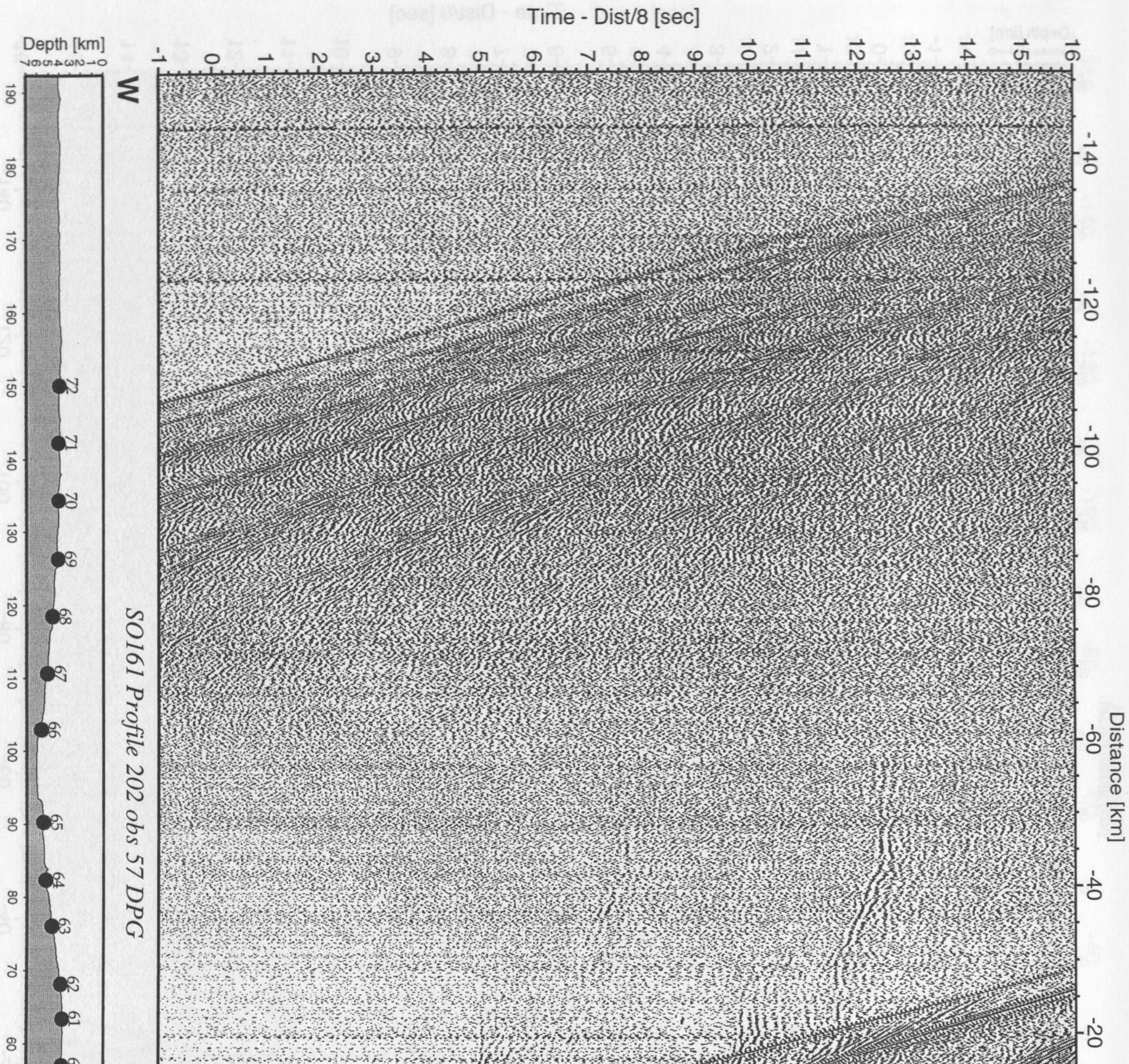

**Figure 5.4.2.28:** Record section from obs 57 DPG, Profile 202.

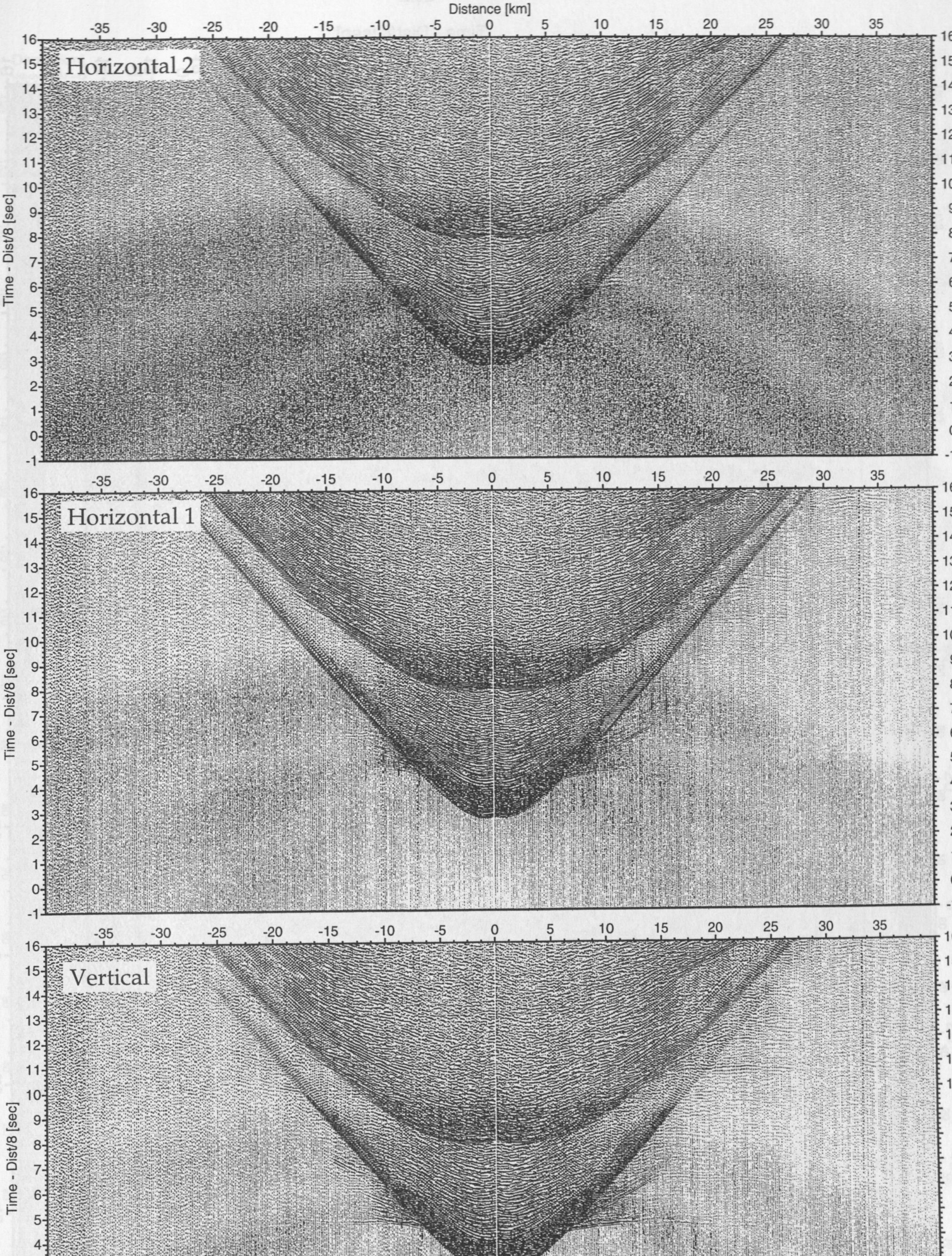

**Figure 5.4.2.29:** Record sections from obs 59 OAS/WEBB, SO161 Profile 202.

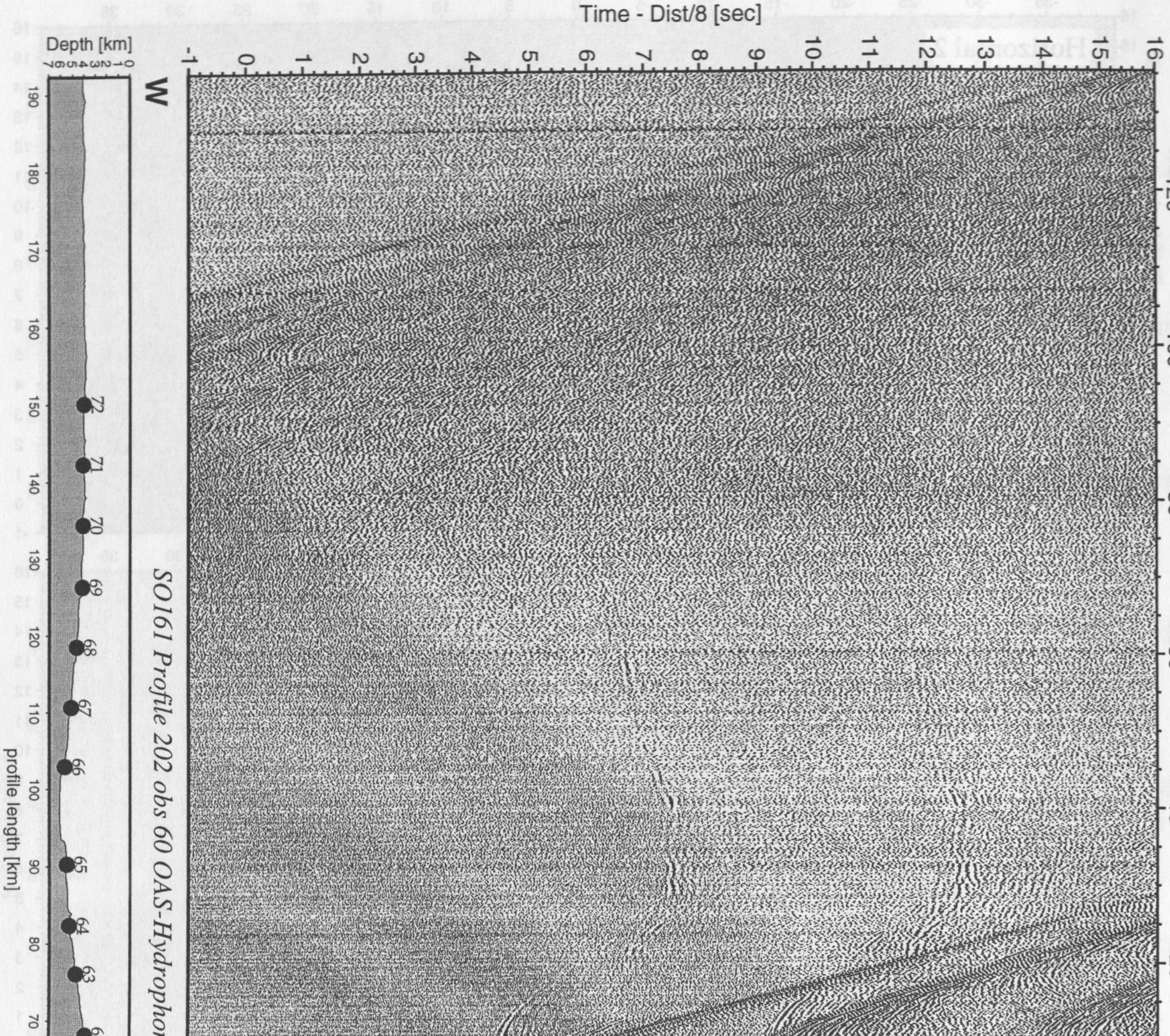

**Figure 5.4.2.30:** Record section from obs 60 OAS-Hydrophone, Profile 202.

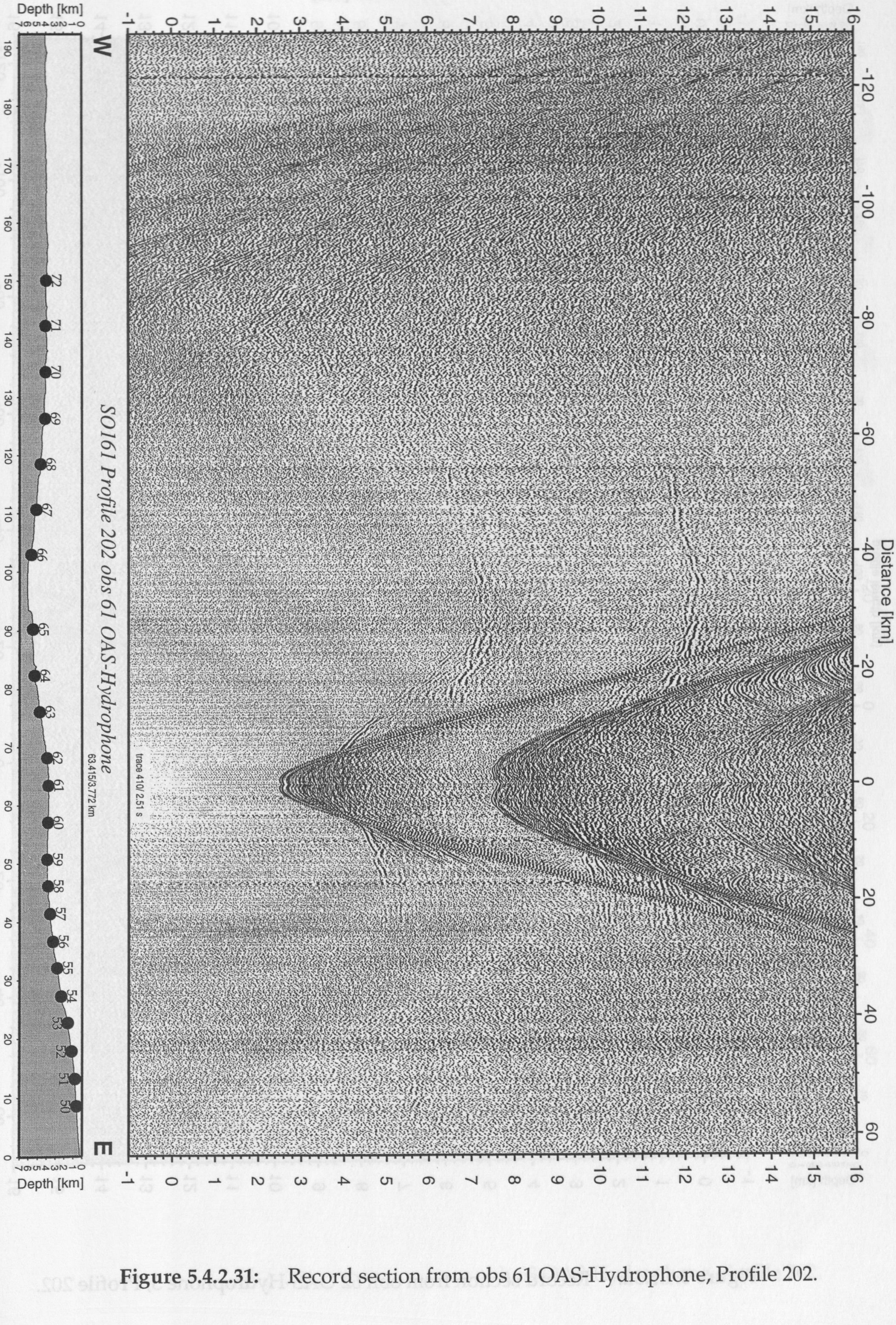

**Figure 5.4.2.31:** Record section from obs 61 OAS-Hydrophone, Profile 202.

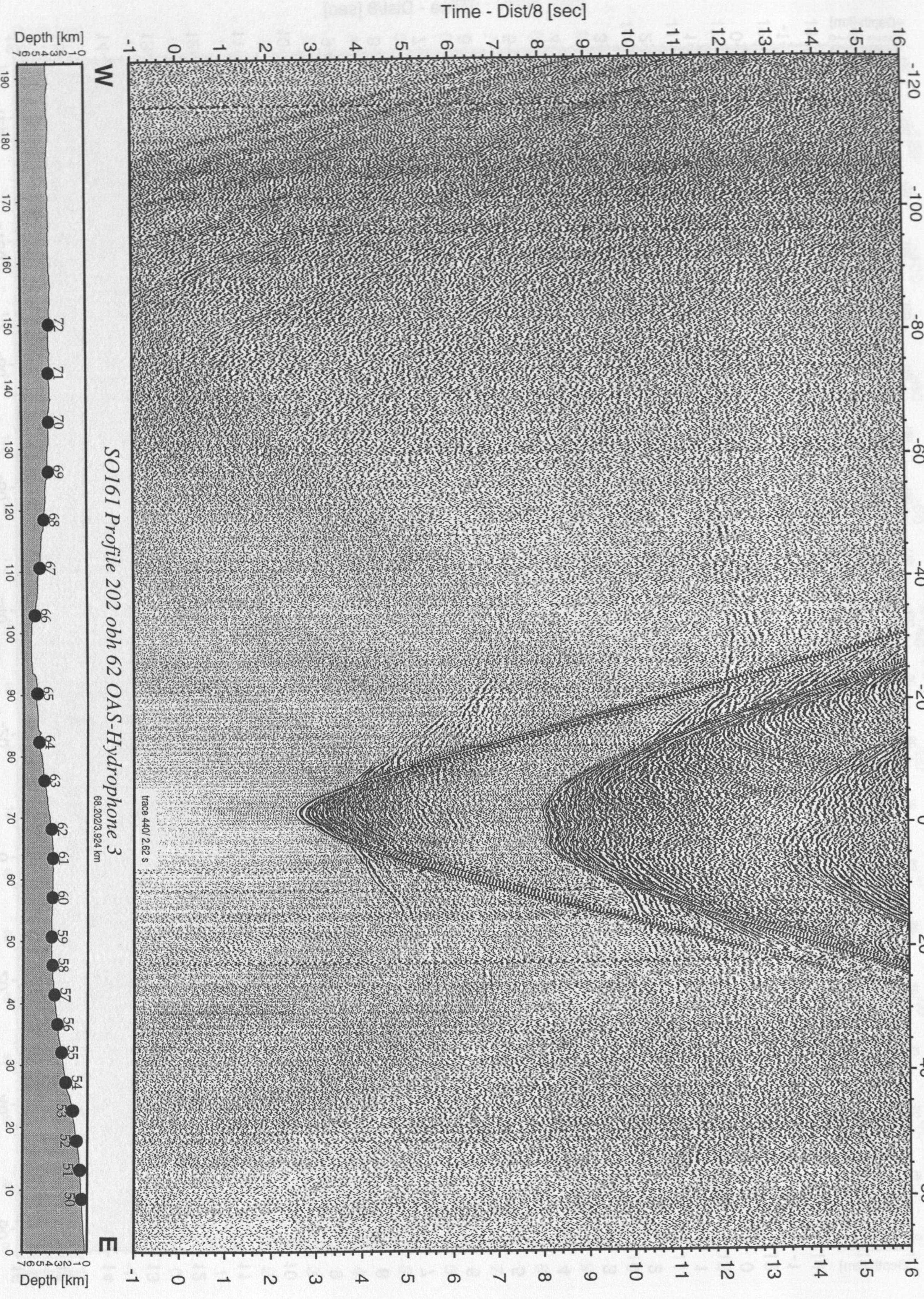

**Figure 5.4.2.32:** Record section from obh 62 OAS-Hydrophone 3, Profile 202.

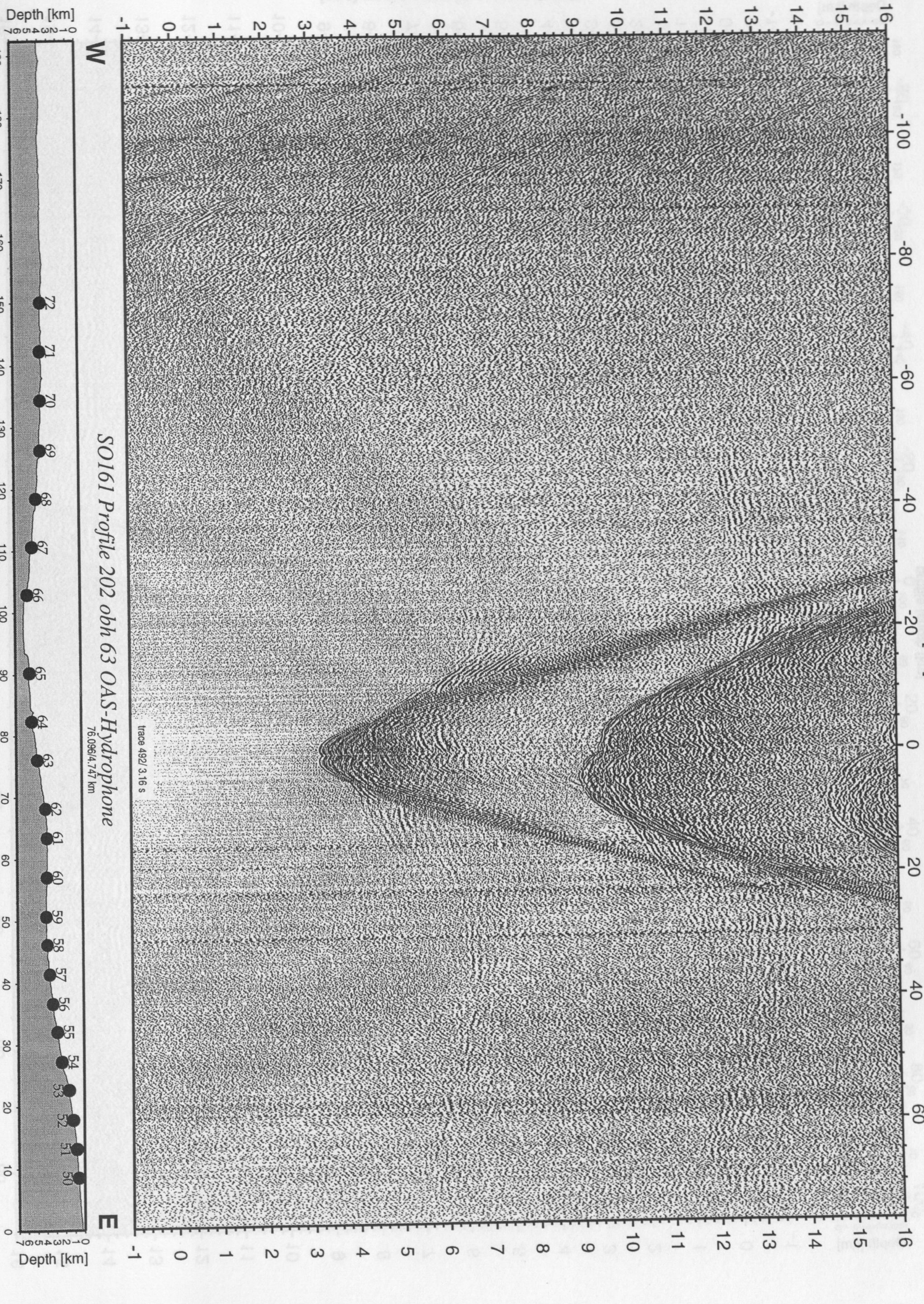

**Figure 5.4.2.33:** Record section from obh 63 OAS-Hydrophone, Profile 202.

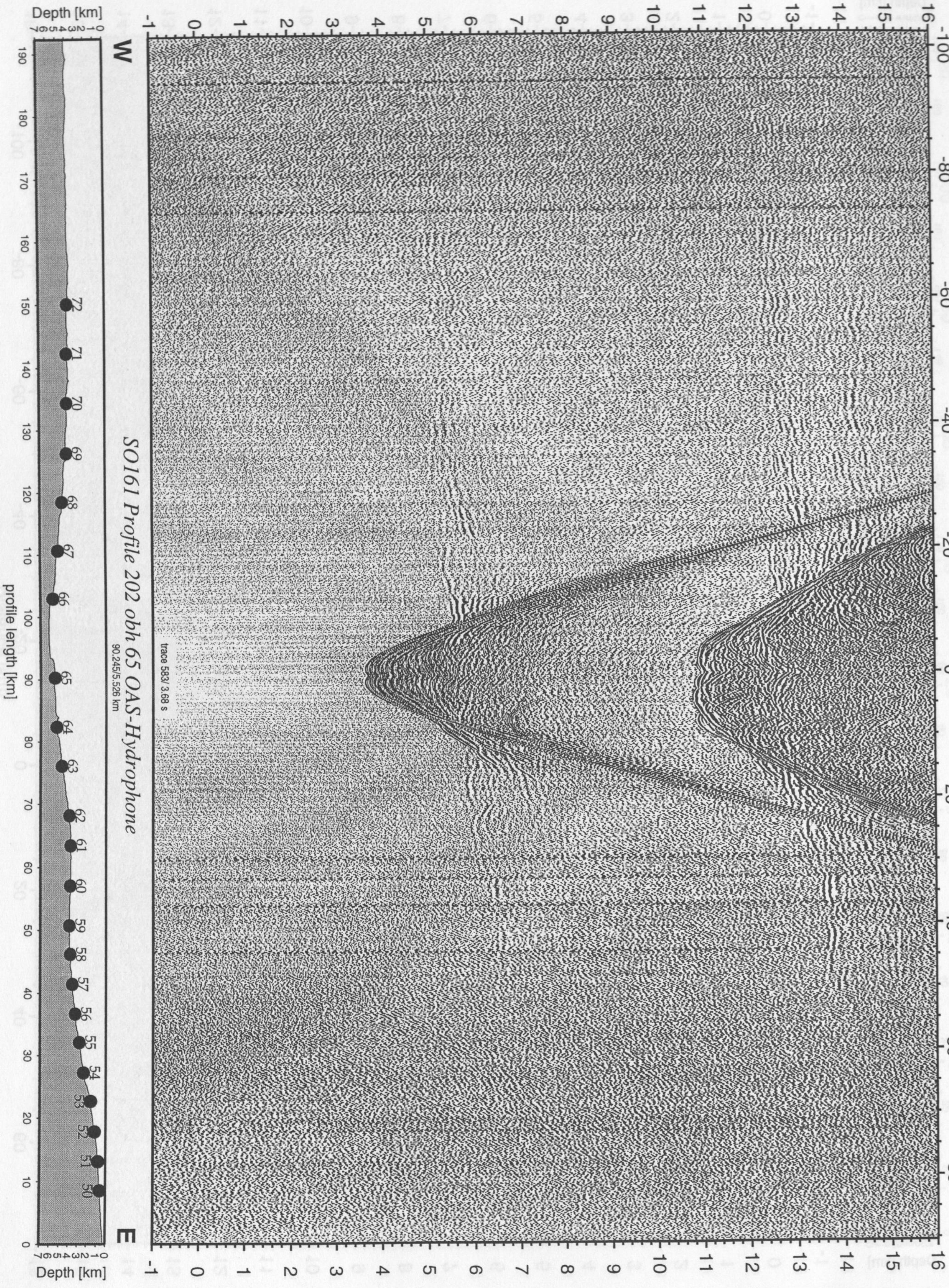

**Figure 5.4.2.34:** Record section from obh 65 OAS-Hydrophone, Profile 202.

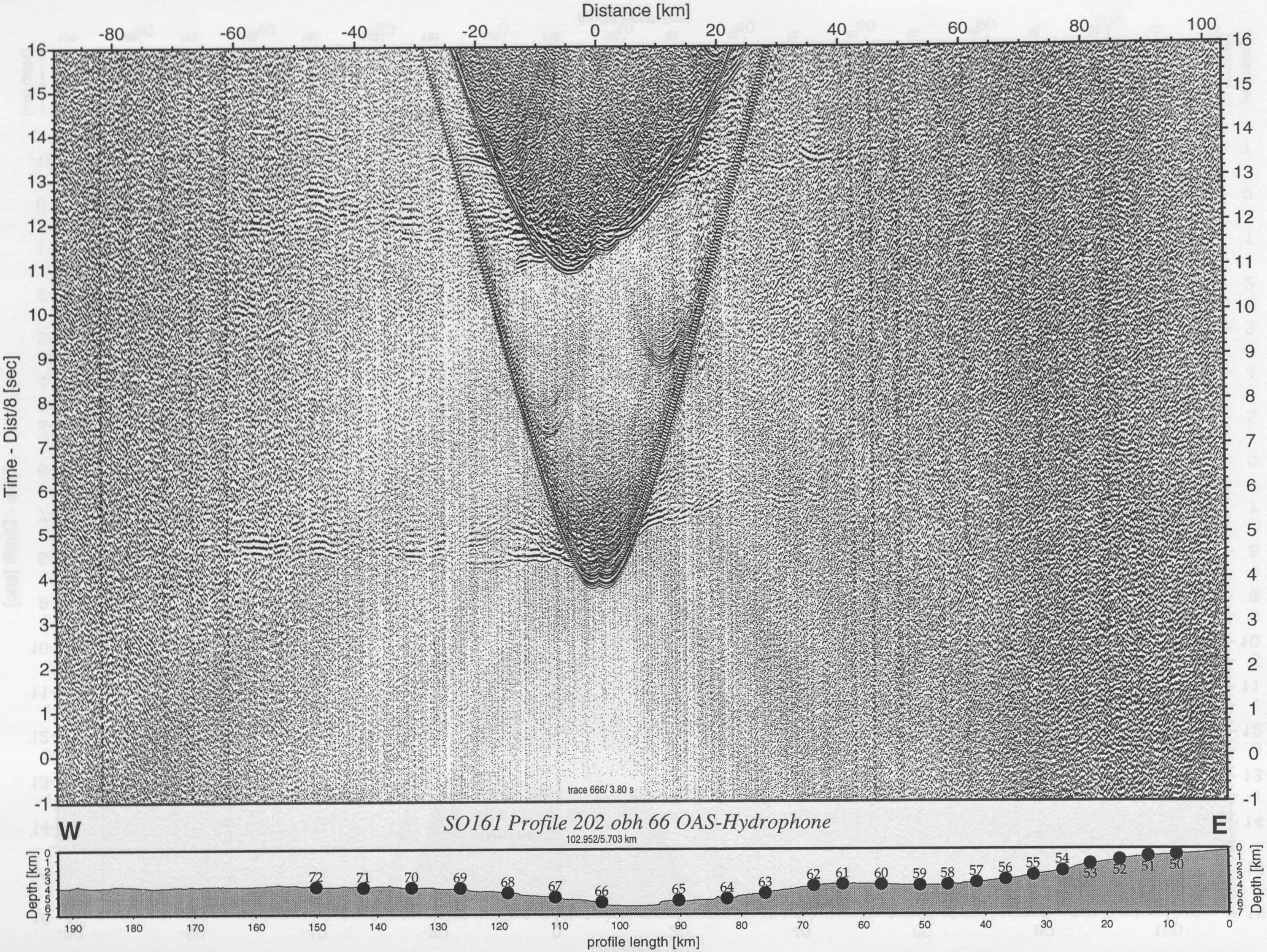

**Figure 5.4.2.35:** Record section from obh 66 OAS-Hydrophone, Profile 202.

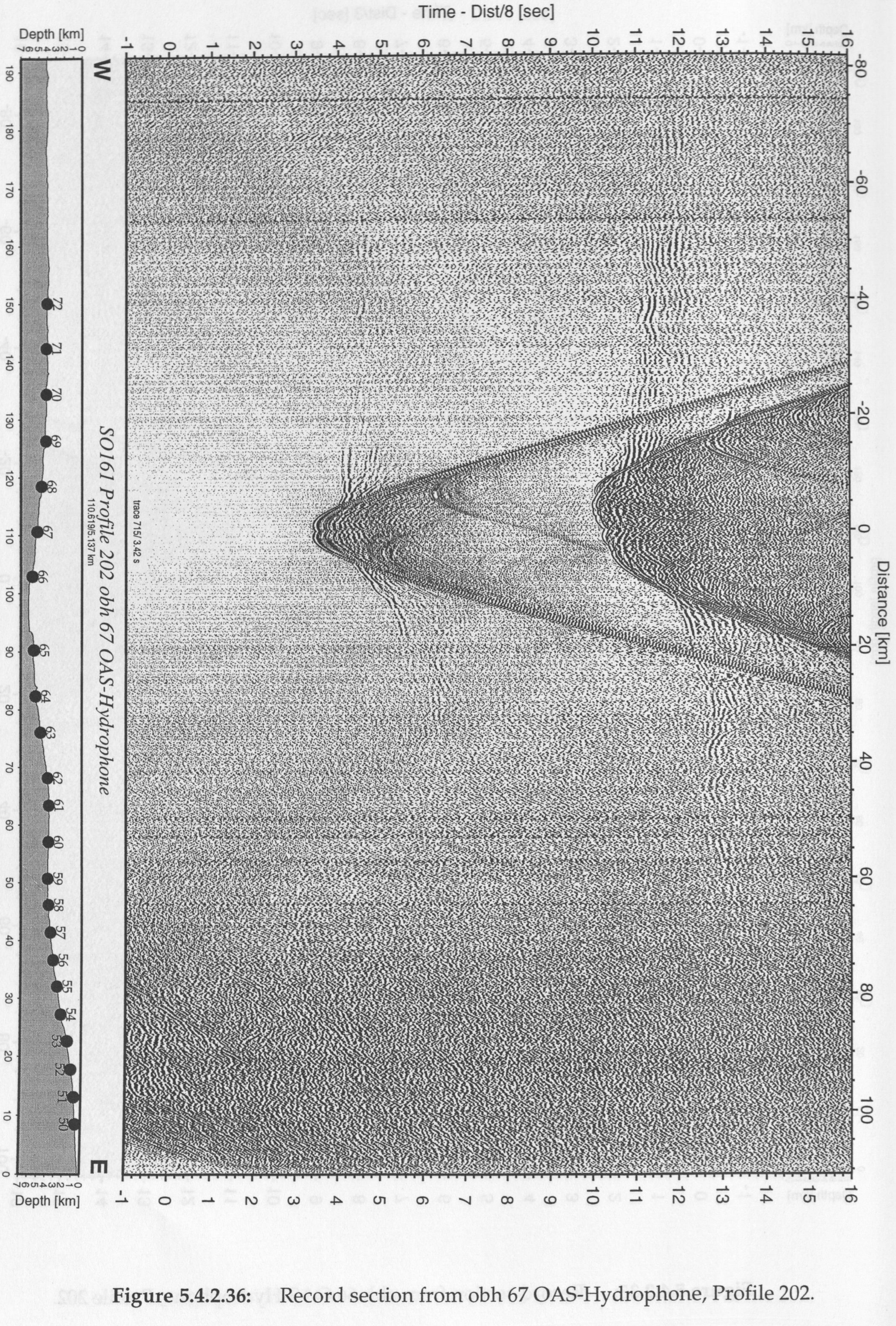

**Figure 5.4.2.36:** Record section from obh 67 OAS-Hydrophone, Profile 202.

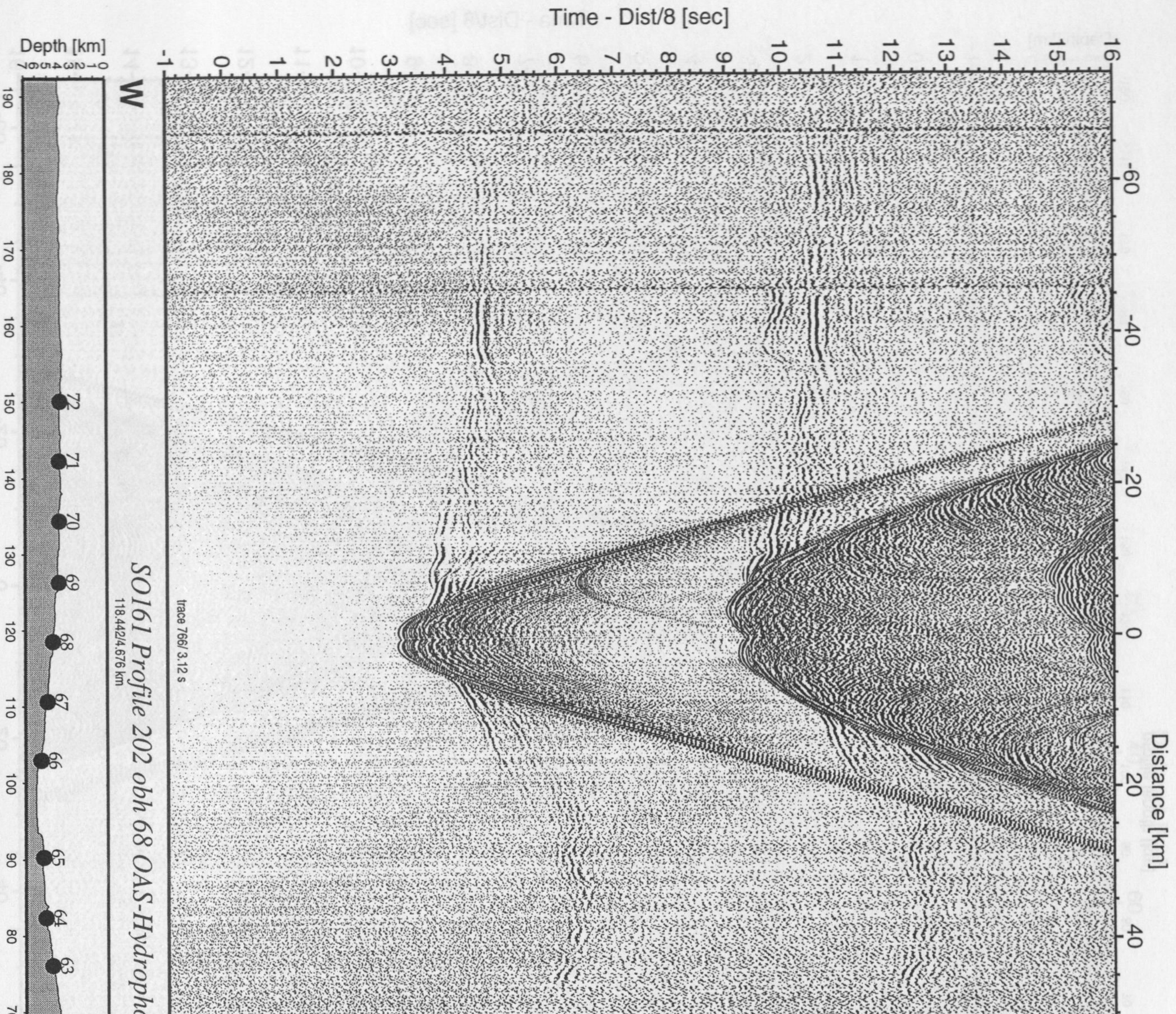

**Figure 5.4.2.37:** Record section from obh 68 OAS-Hydrophone, Profile 202.

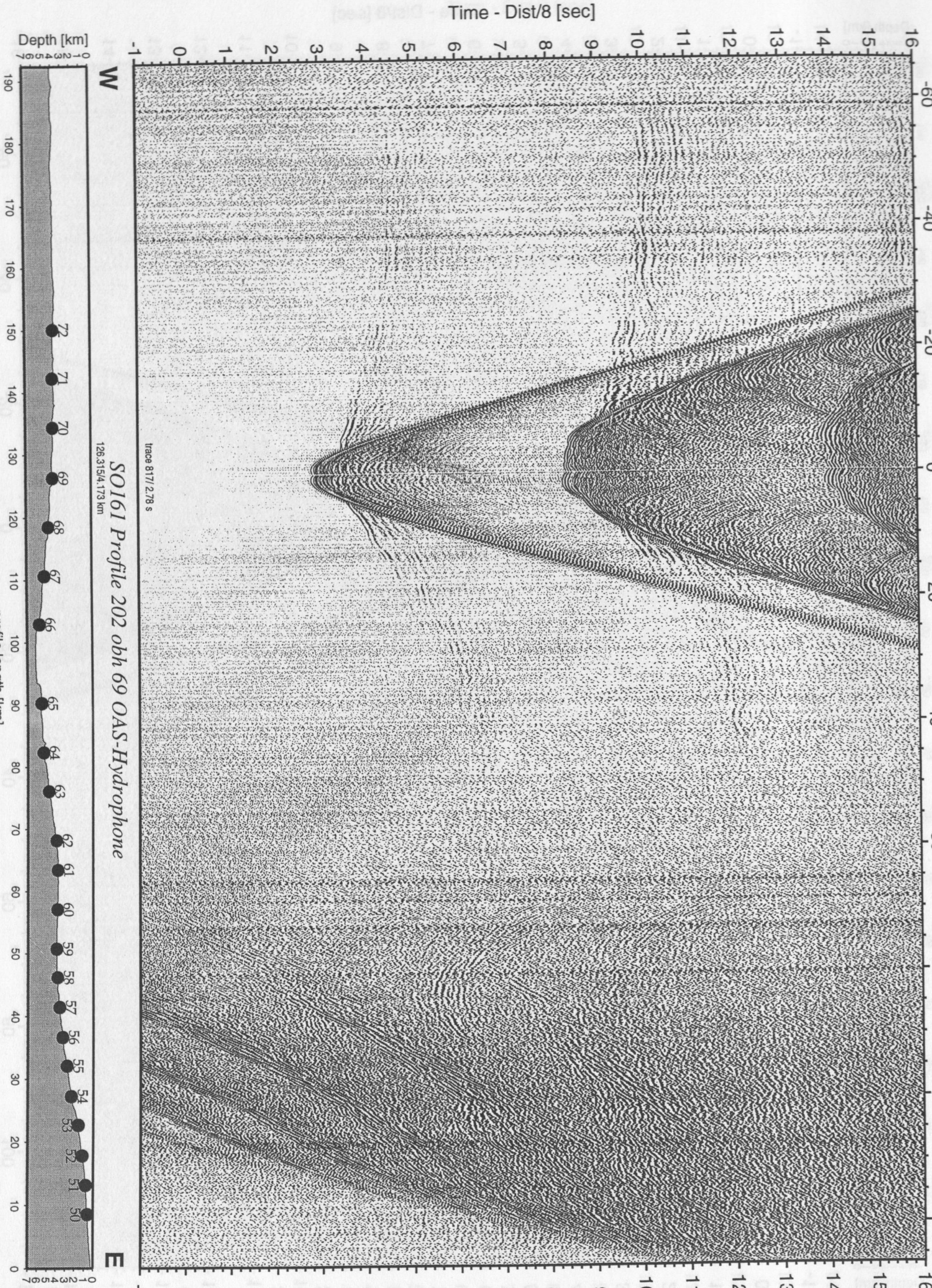

**Figure 5.4.2.38:** Record section from obh 69 OAS-Hydrophone, Profile 202.

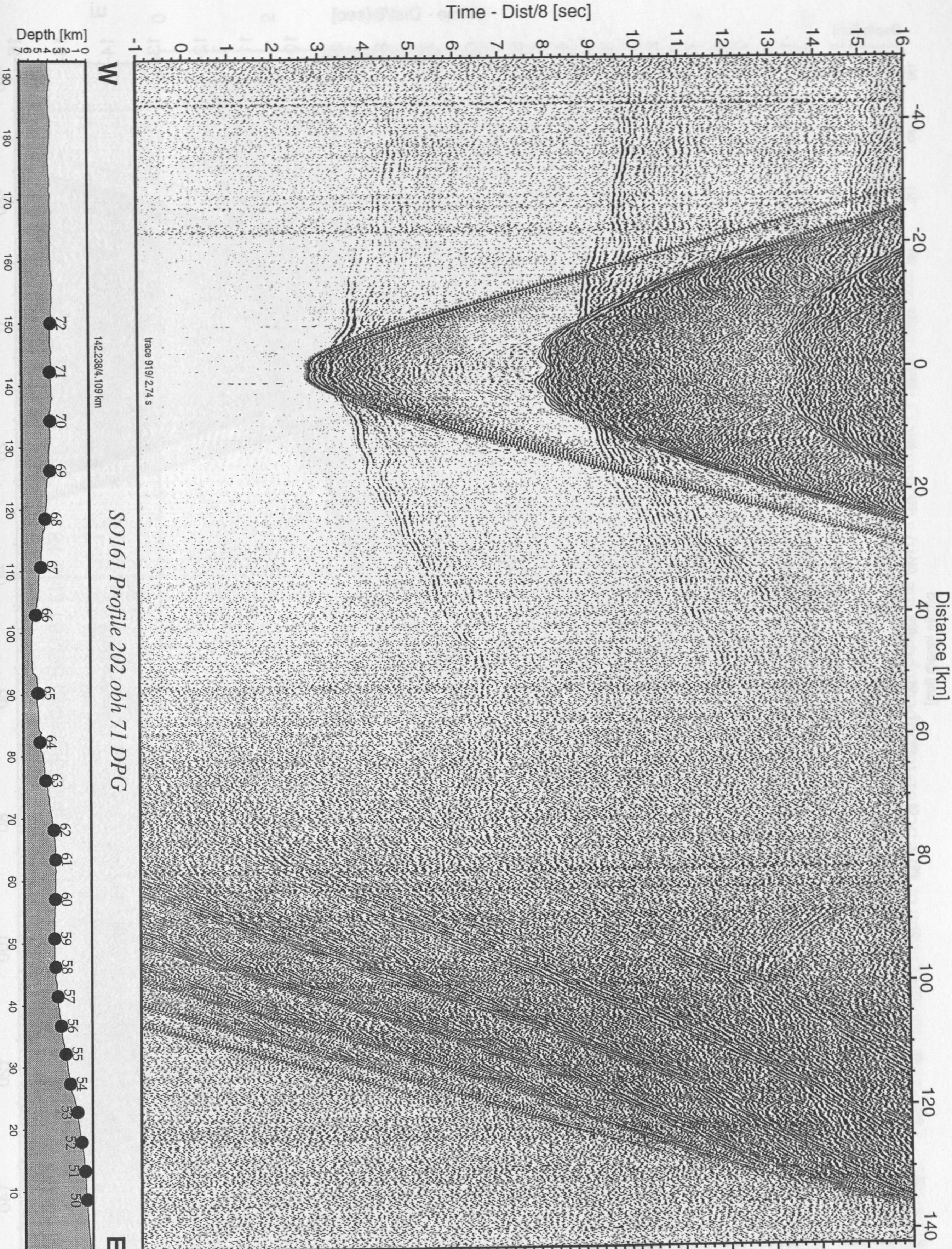

**Figure 5.4.2.39:** Record section from obh 71 DPG, Profile 202.

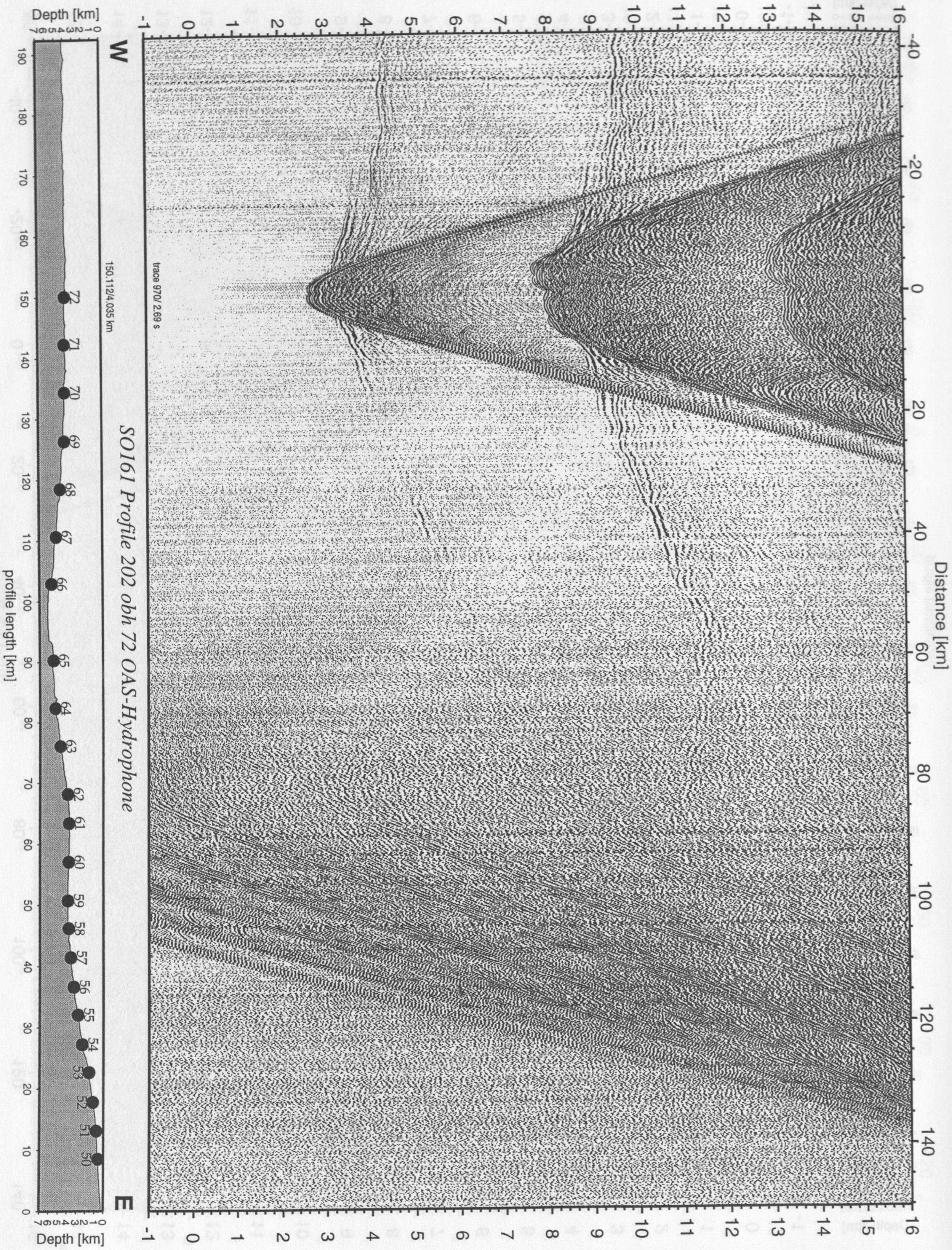

**Figure 5.4.2.40:** Record section from obh 72 OAS-Hydrophone, Profile 202.

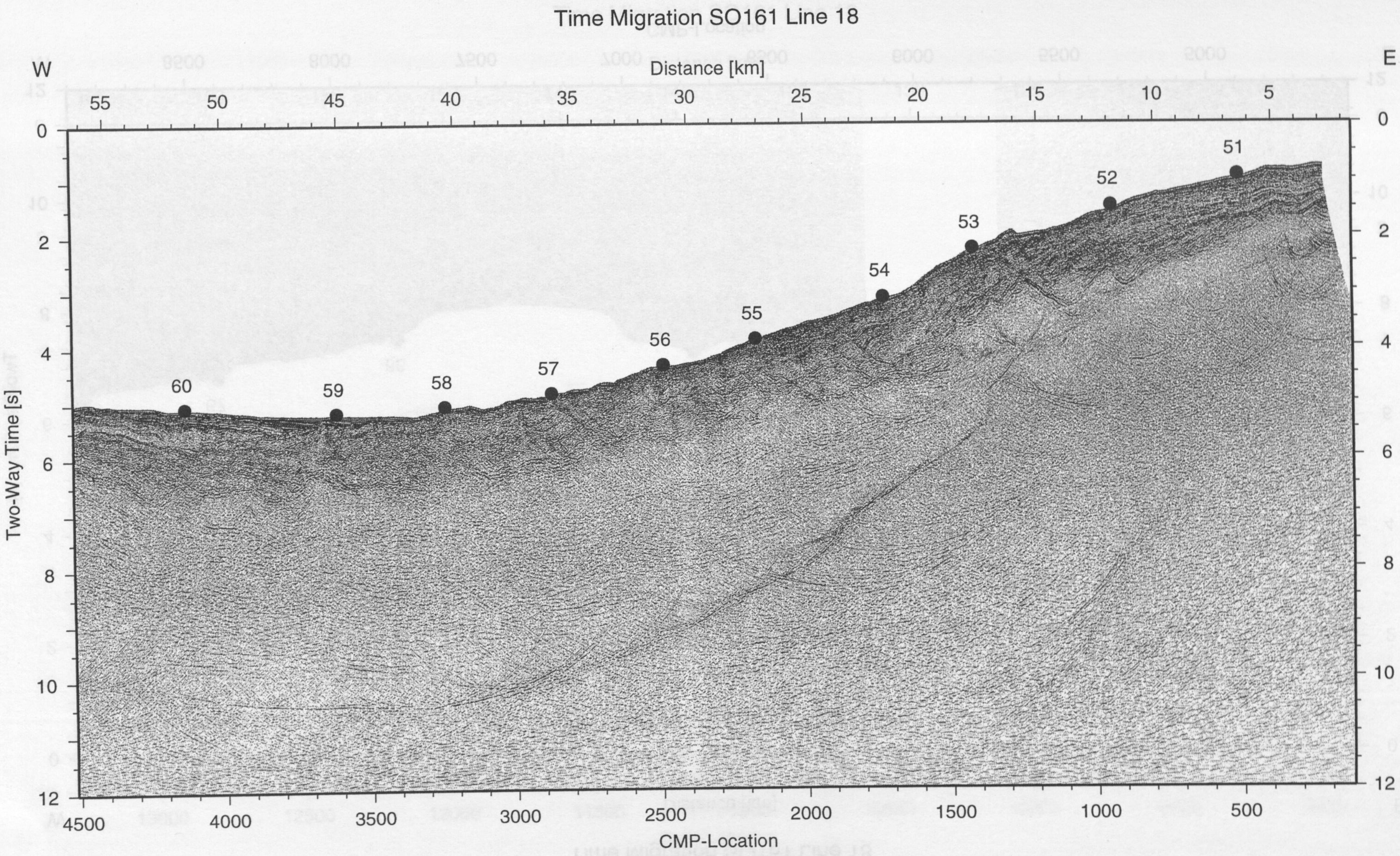
Time Migration SO161 Line 18

**Figure 5.4.2.41:** Post-stack time migration of Line SO161-18. Superimposed the obh/s locations of Profile 201/202.

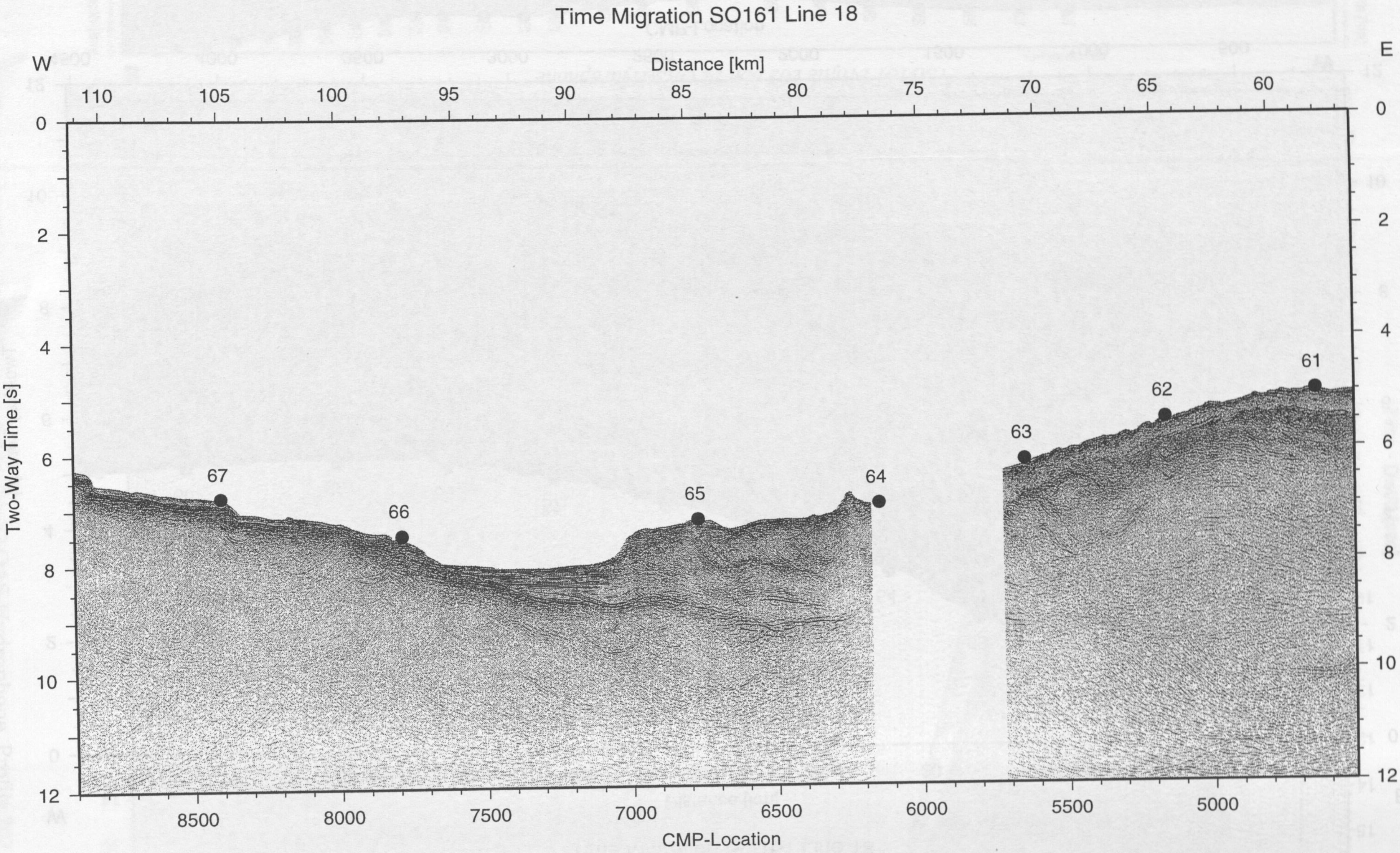

**Figure 5.4.2.42:** Post-stack time migration of Line SO161-18. Superimposed the obh/s locations of Profile 201/202.

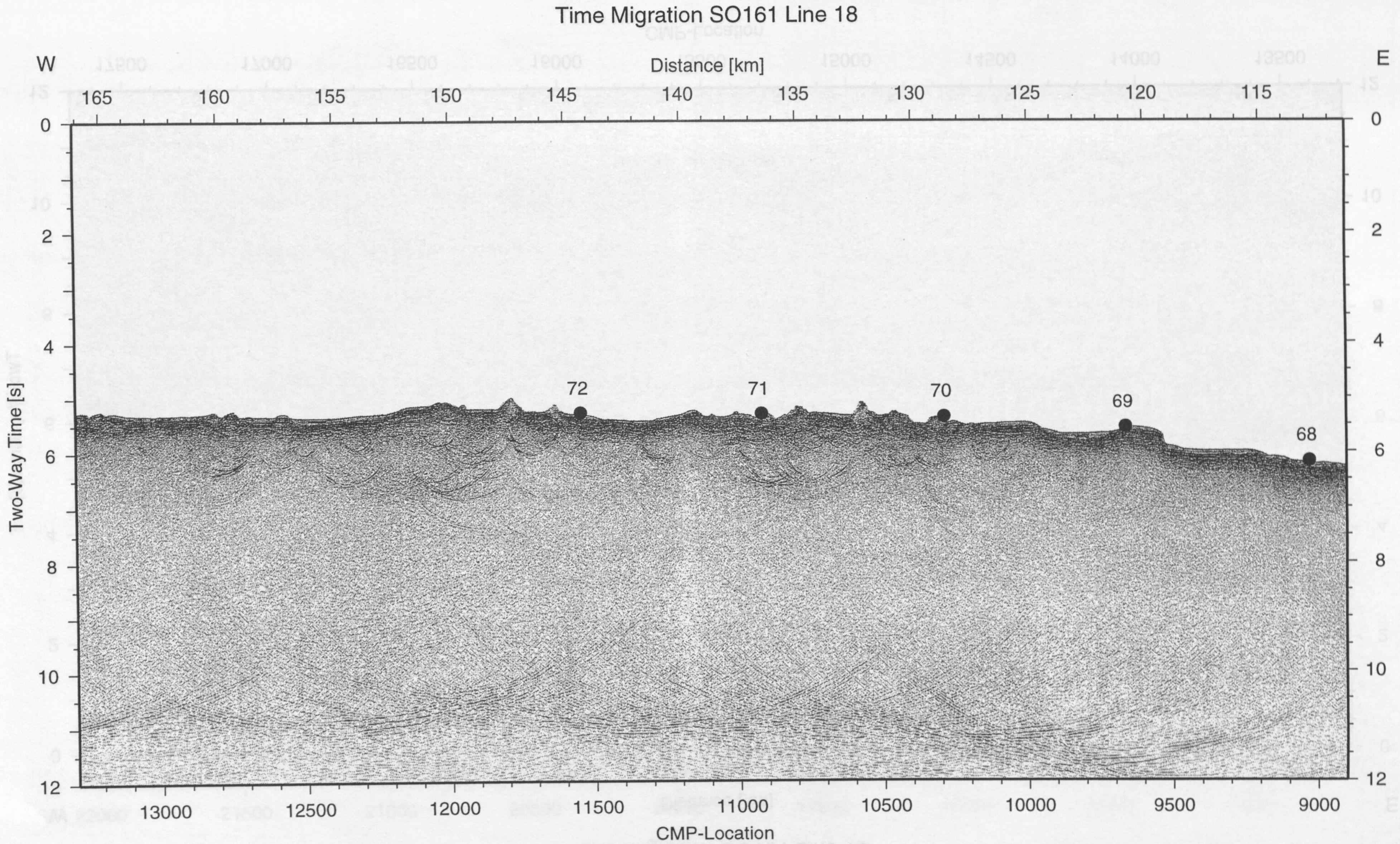

**Figure 5.4.2.43:** Post-stack time migration of Line SO161-18. Superimposed the obh/s locations of Profile 201/202.

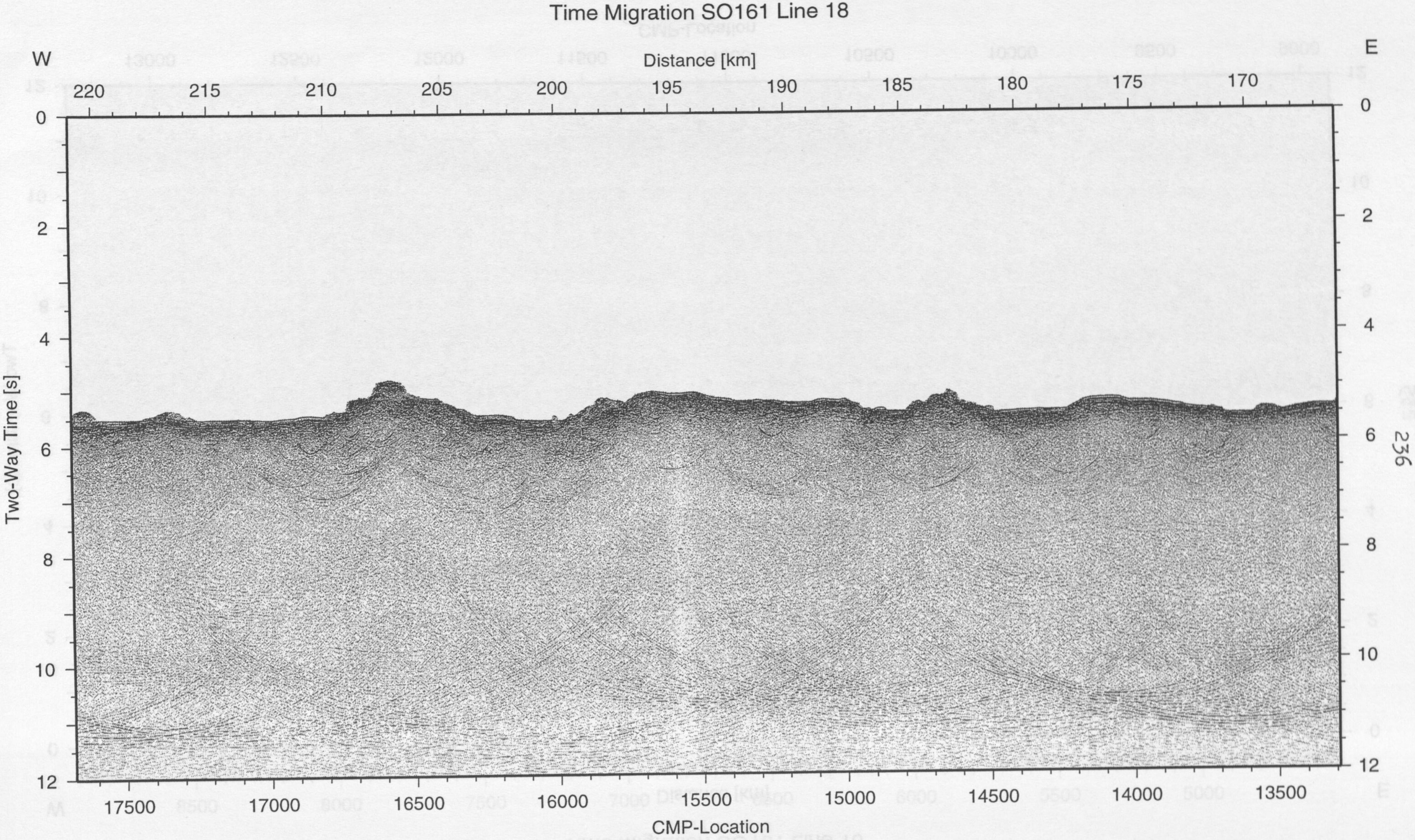

**Figure 5.4.2.44:** Post-stack time migration of Line SO161-18. Superimposed the obh/s locations of Profile 201/202.

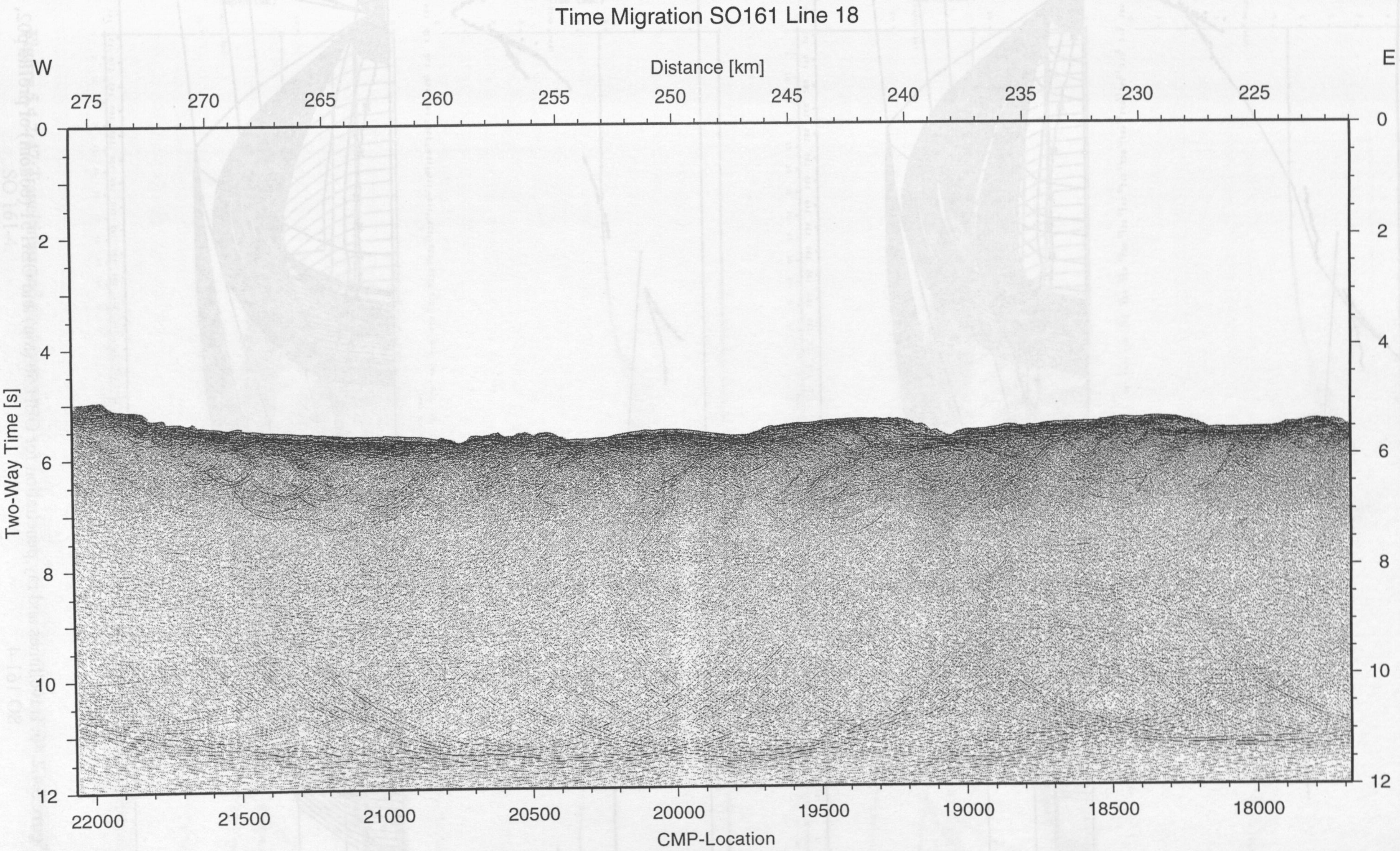

**Figure 5.4.2.45:** Post-stack time migration of Line SO161-18. Superimposed the obh/s locations of Profile 201/202.

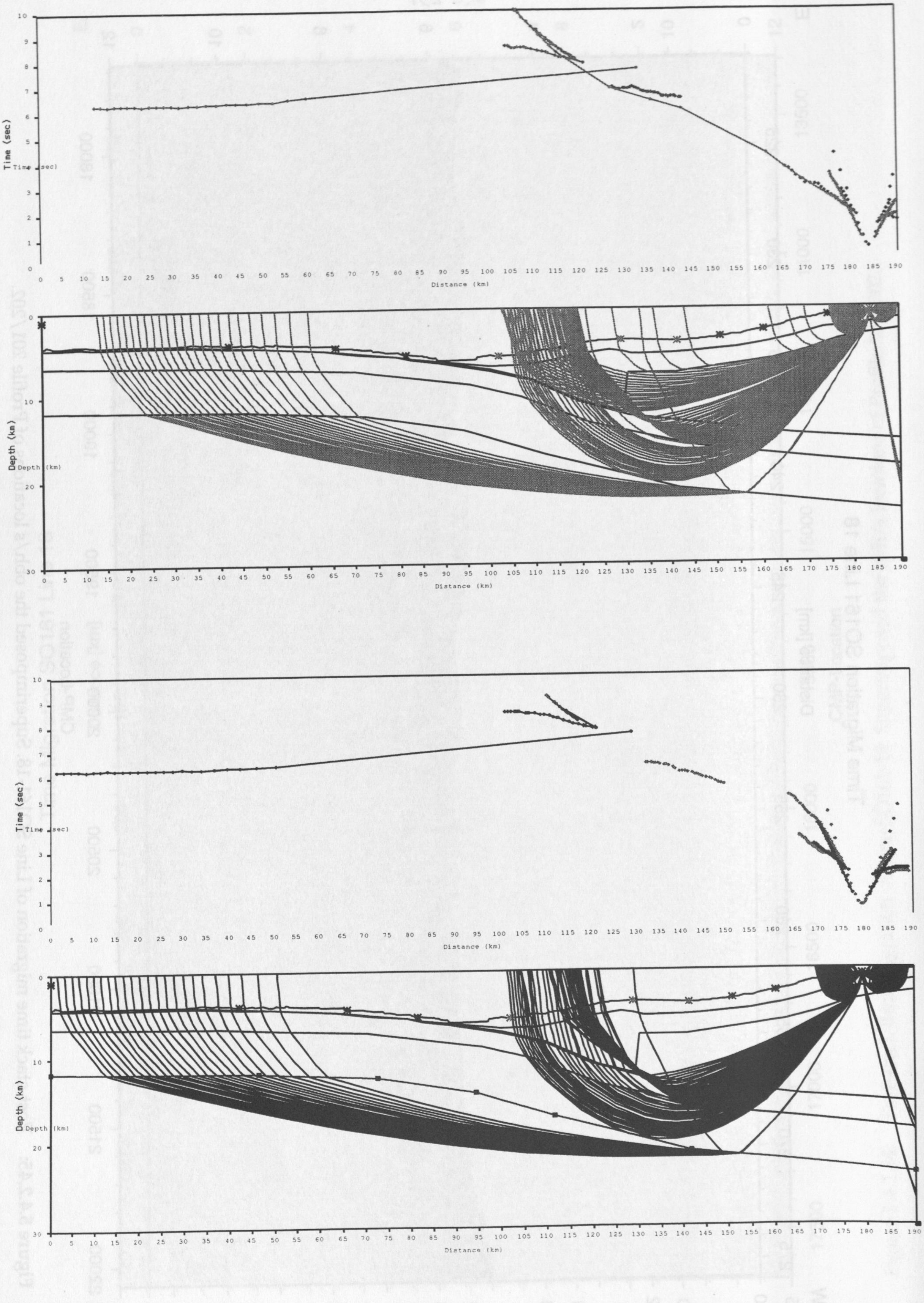

**Figure 5.4.2.46:** Traveltimes and ray penetration for OBH 50 (top) and OBH 51 (bottom) of profile p02, SO 161-4.

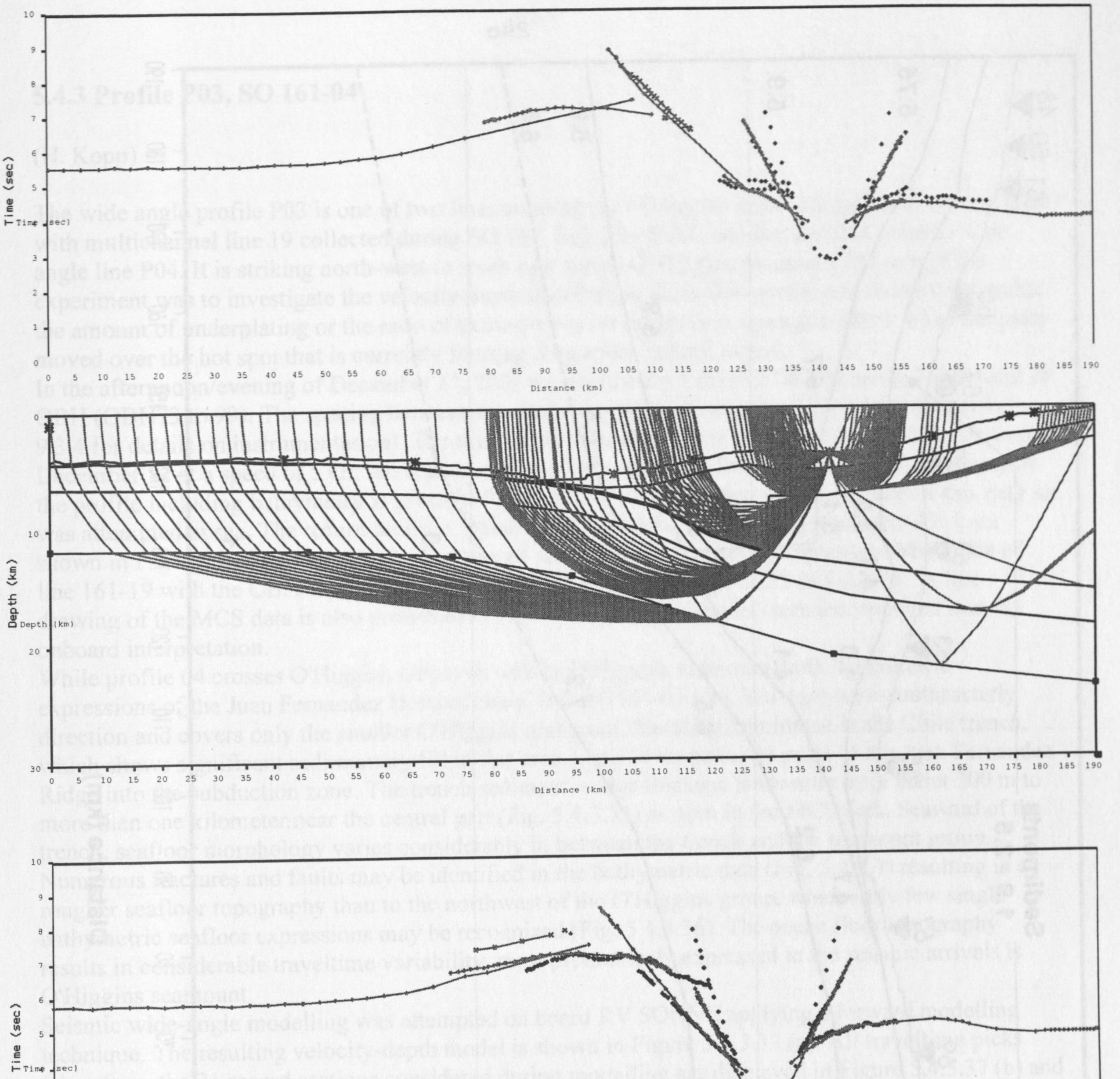

**Figure 5.4.2.47:** Traveltimes and ray penetration for OBS 51 (top) and OBS 61 (bottom) of profile p02, SO 161-4.

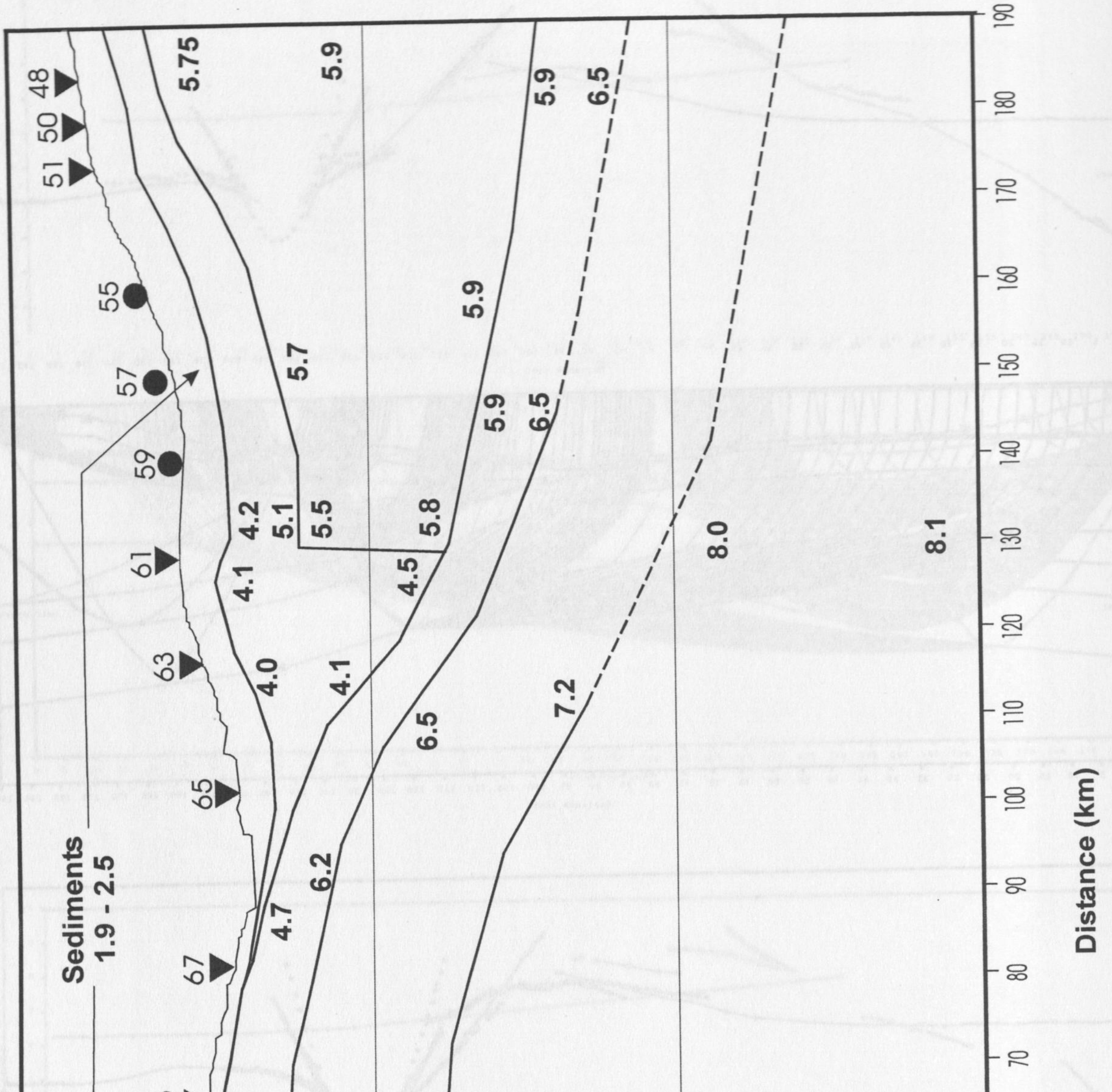

**Figure 5.4.2.48**: Velocity-depth model of profile 02, SO 161-4. Velocities given are in km/s

### 5.4.3 Profile P03, SO 161-04

(H. Kopp)

The wide angle profile P03 is one of two lines crossing the O'Higgins seamount group. It is coincident with multichannel line 19 collected during SO 161, Leg 2 by BGR. and lies perpendicular to wide-angle line P04. It is striking north-west to south east across O´Higgins seamount The aim of the experiment was to investigate the velocity-depth distribution along this profile and thereby determine the amount of underplating or the ratio of extrusive versus intrusive magma generated when the plate moved over the hot spot that is currently forming Alexander Selkirk Island.
In the afternnoon/evening of December 11, 2001 we deployed a total of 27 instruments; 7 OBS and 20 OBH (OBH73 to 99). The spacing between the stations was approximately 2,2 nm (see Appendix 9.3.4 for details on instrumentation). The total length of the profile is about 220 km and was shot on December 12 at a speed of 5 kn. All instruments were recovered on December 13. A location map of the profile including bathymetry is given in Figure 5.4.3.1. A preliminary interpretation of this data set was attempted at sea. The record sections which were processed as described in chapter 4.6.1 are shown in Figures 5.4.3.2 to 5.4.2.32. They are all reduced with 8 km/s. The processed MCS data of line 161-19 with the OBH/S positions indicated is given in Figures 5.4.3.33 to 5.4.3.36.. A line drawing of the MCS data is also presented in Figure 1.6.4. These results were incorporated into the onboard interpretation.
While profile 04 crosses O'Higgins Guyot as well as O'Higgins seamount, both bathymetric expressions of the Juan Fernandez Hotspot chain, line SO161-03 runs in a northwest-southeasterly direction and covers only the smaller O'Higgins seamount. Shooting terminated in the Chile trench, which shows significant sedimentary fill in this area south of the entrance point of the Juan Fernandez Ridge into the subduction zone. The trench sediment wedge thickens landwards from about 200 m to more than one kilometer near the central part (Fig. 5.4.3.33) as seen in the MCS data. Seaward of the trench, seafloor morphology varies considerably in between the trench and the seamount group. Numerous fractures and faults may be identified in the bathymetric data (Fig. 5.4.3.1) resulting in a rougher seafloor topography than to the northwest of the O'Higgins group, where only few single bathymetric seafloor expressions may be recognized (Fig. 5.4.3.36). The ocean floor topography results in considerable traveltime variability, most pronouncely expressed in the seismic arrivals is O'Higgins seamount.
Seismic wide-angle modelling was attempted on board RV SONNE applying a forward modelling technique. The resulting velocity-depth model is shown in Figure 5.4.3.37 (a). All traveltime picks taken from the 21 record sections considered during modelling are displayed in Figure 5.4.3.37 (b) and show a high coverage especially in the central part of the profile across the ridge. Traveltimes were calculated using a 'top-down' approach, modelling velocity and depth for each layer before moving to the next. Raytracing examples are shown for OBS 81 in Figure 5.4.3.37 (c) which like many other stations shows a clear Pn phase running to the northwest. As on most other stations along this 210 km long profile, the data are of high quality, displaying low ambient noise and a quality waveform which allows a high picking accuracy. While the stations deployed on O'Higgins seamount suffer from limited energy penetration, seismic arrivals in some cases of up to a distance of more than 120 km are recognized on numerous stations.
Only a thin pelagic sediment cover on the ocean basin is visible in the MCS data (Fig. 5.4.3.36) and was taken into consideration in the wide-angle modelling. Though no strong sedimentary refraction phases can be detected in the data, a time delay of the first refraction phases occurs on some stations located on the ocean basin. To account for this delay and the results from the MCS data, a 500 m thick layer with low seismic velocities ranging from 1.6 km/s to 1.7 km/s was introduced in the model to account for the pelagics (Fig. 5.4.3.37 (a)), thinning across the seamount.
A 1-2 km thick layer with seismic velocities ranging from 3.3-5.0 km/s was modelled underneath the pelagic sediment cover. This layer may include sequences of volcaniclastic material, which may have been deposited in a shallow water to submarine environment. These deposits show typical velocities ranging from about 3 km/s to 4 km/s and are thus difficult to separate from velocity values assigned to basement rocks. Preliminary modeling of this profile did not reveal the boundary between igenous basement and volcaniclast fill in sediments. Thus the resulting model may provide a reasonably thick oceanic crustal layer away from the vicinity of the seamount.

Within the volcanic edifice reasonably low velocities of less than 4.0 km/s are abundant. Typical velocities of gabbroic rocks are only encountered in a depth of more than 5 km beneath the tip of the seamount. A clearly expressed Moho deflection marked by a velocity increase from 7.2 km/s to 8.0 km/s at the crust-mantle boundary is present underneath the seamount, indicating a Moho depression of up to 4 km. Underneath the ridge, the Moho was modelled in a depth of approximately 13 to 14 km, which agrees well with results from Profile 04, striking perpendicular to this line. The exact extension of this crustal thickening and the geometry of the crustal root need to be constrained by further modelling and tomographic investigations.

Overall, a fairly smooth velocity field with little lateral velocity variations is proposed as a preliminary model. To conclude, the structure obtained from preliminary seismic data analysis is in reasonably good agreement with other structures deduced from geophysical data that are believed to be of similar origin (Flueh et al., 1998, Caress et al., 1995). A post-cruise data analysis considering all the data acquired across the Juan Fernandez Ridge will help constrain and improve these preliminary results.

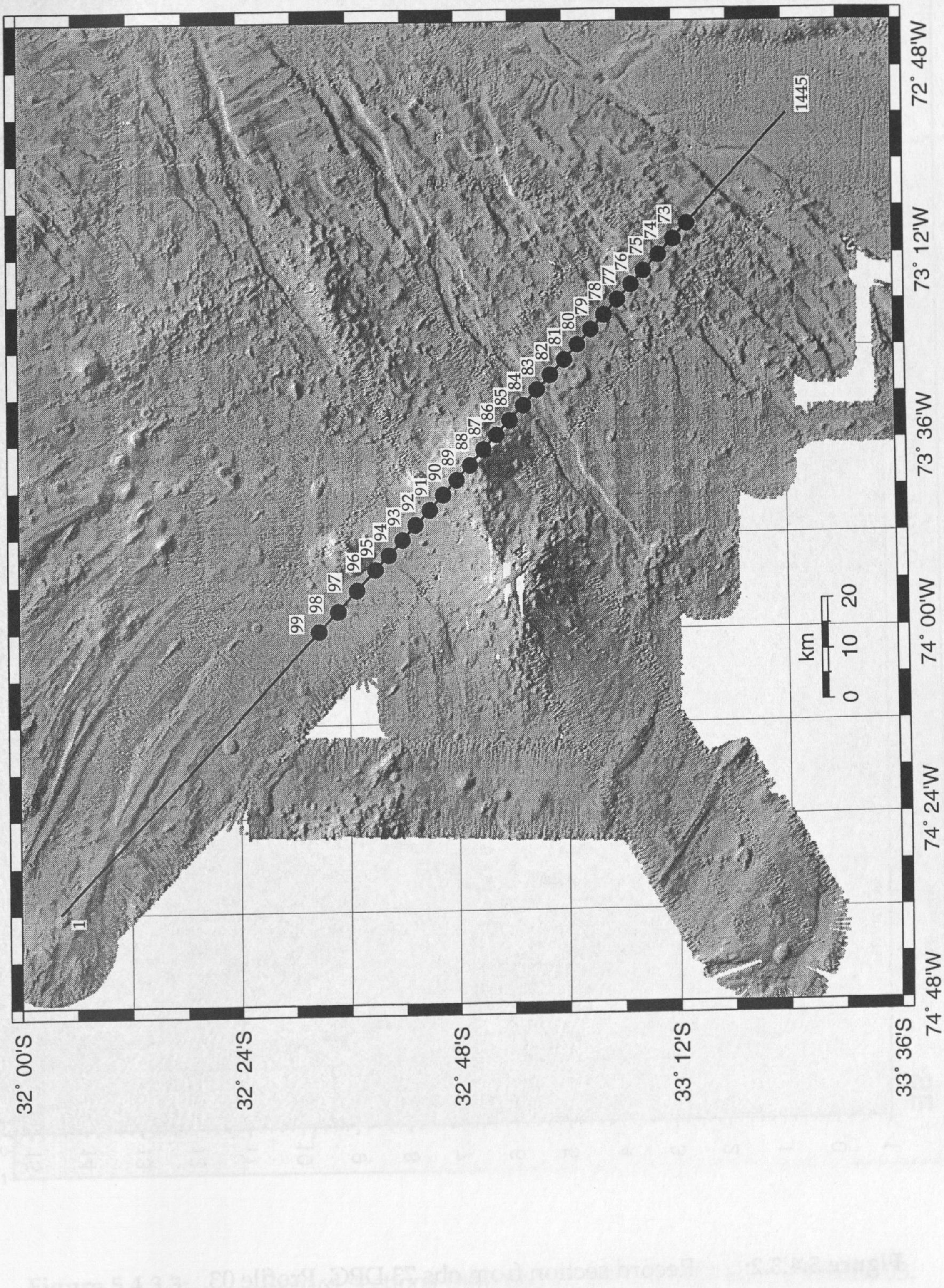

**Figure 5.4.3.1:** Location map of profile 3 and illuminated multibeam bathymetry. Superimposed the obh/obs locations, the first, and last shotpoint number.

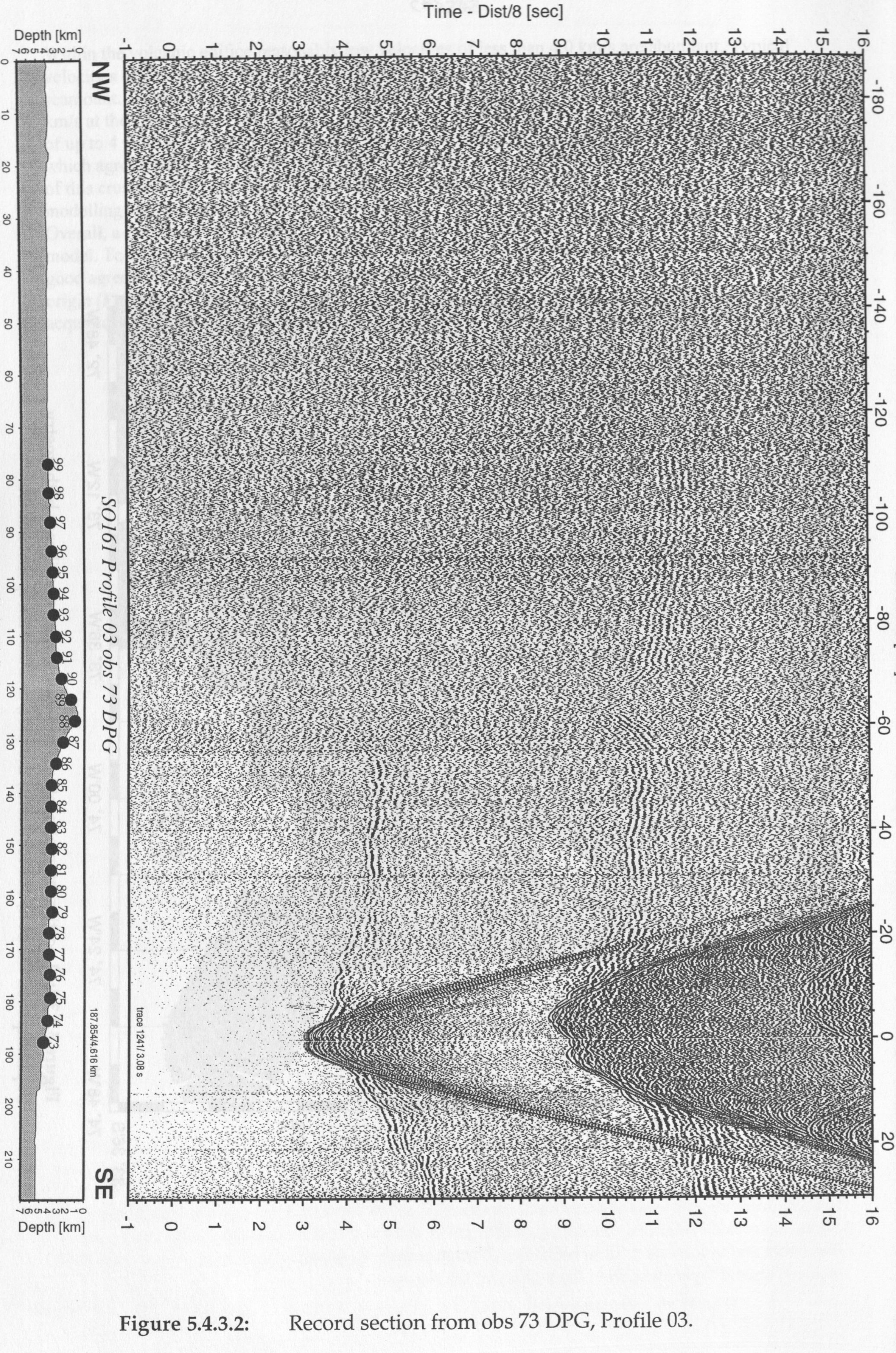

**Figure 5.4.3.2:** Record section from obs 73 DPG, Profile 03.

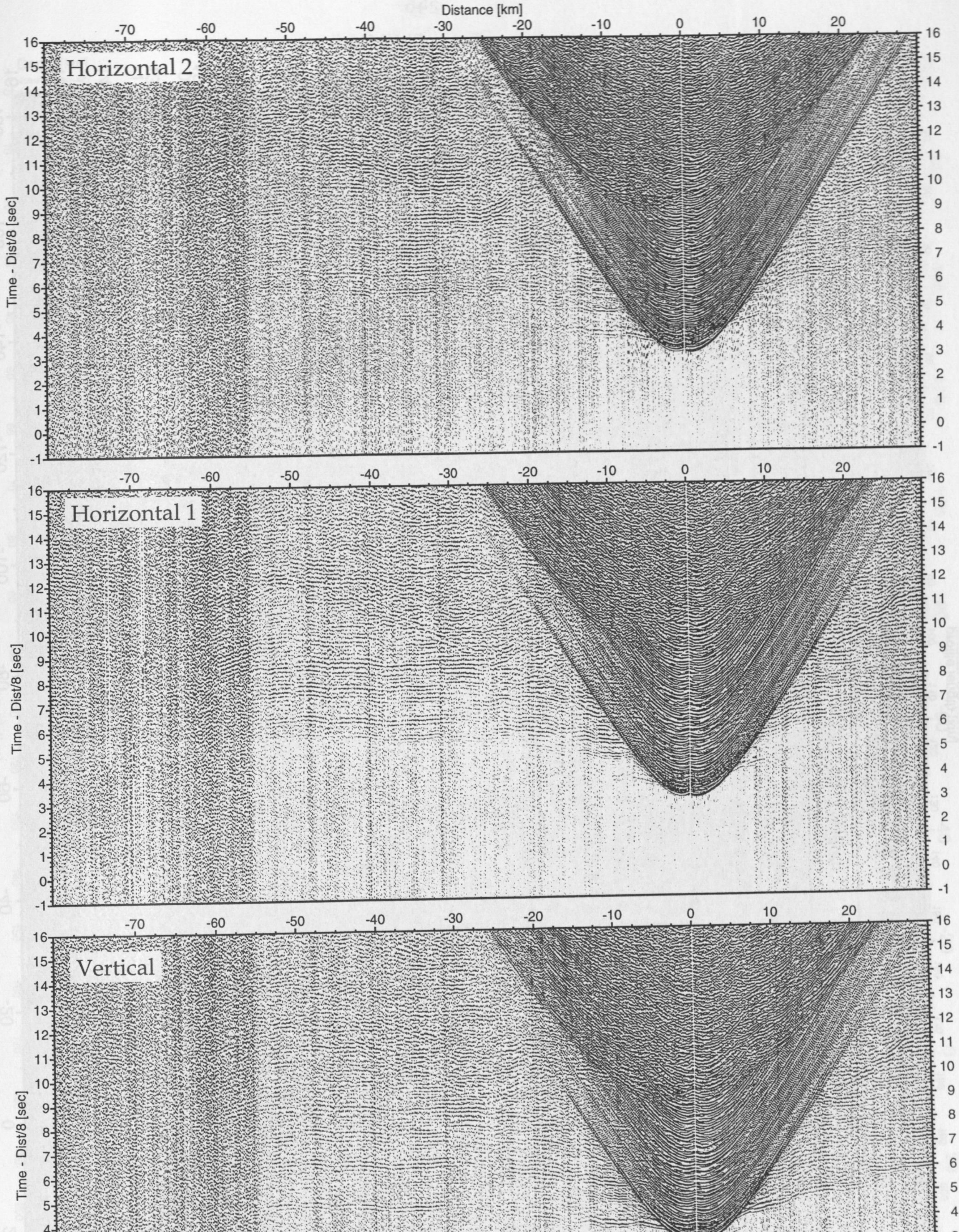

**Figure 5.4.3.3:** Record sections from obs 73 DPG/PMD, SO161 Profile 03.

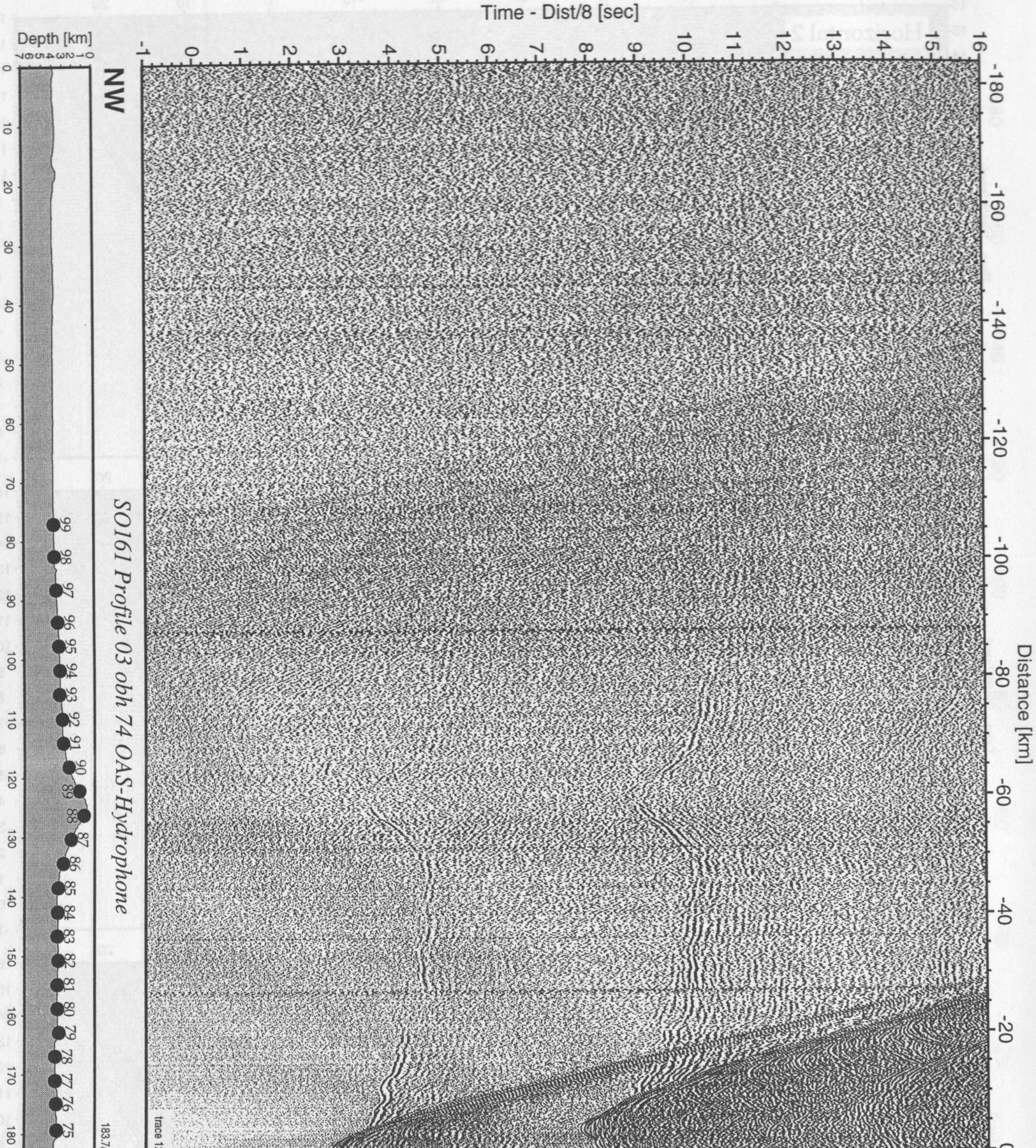

**Figure 5.4.3.4:** Record section from obh 74 OAS-Hydrophone, Profile 03.

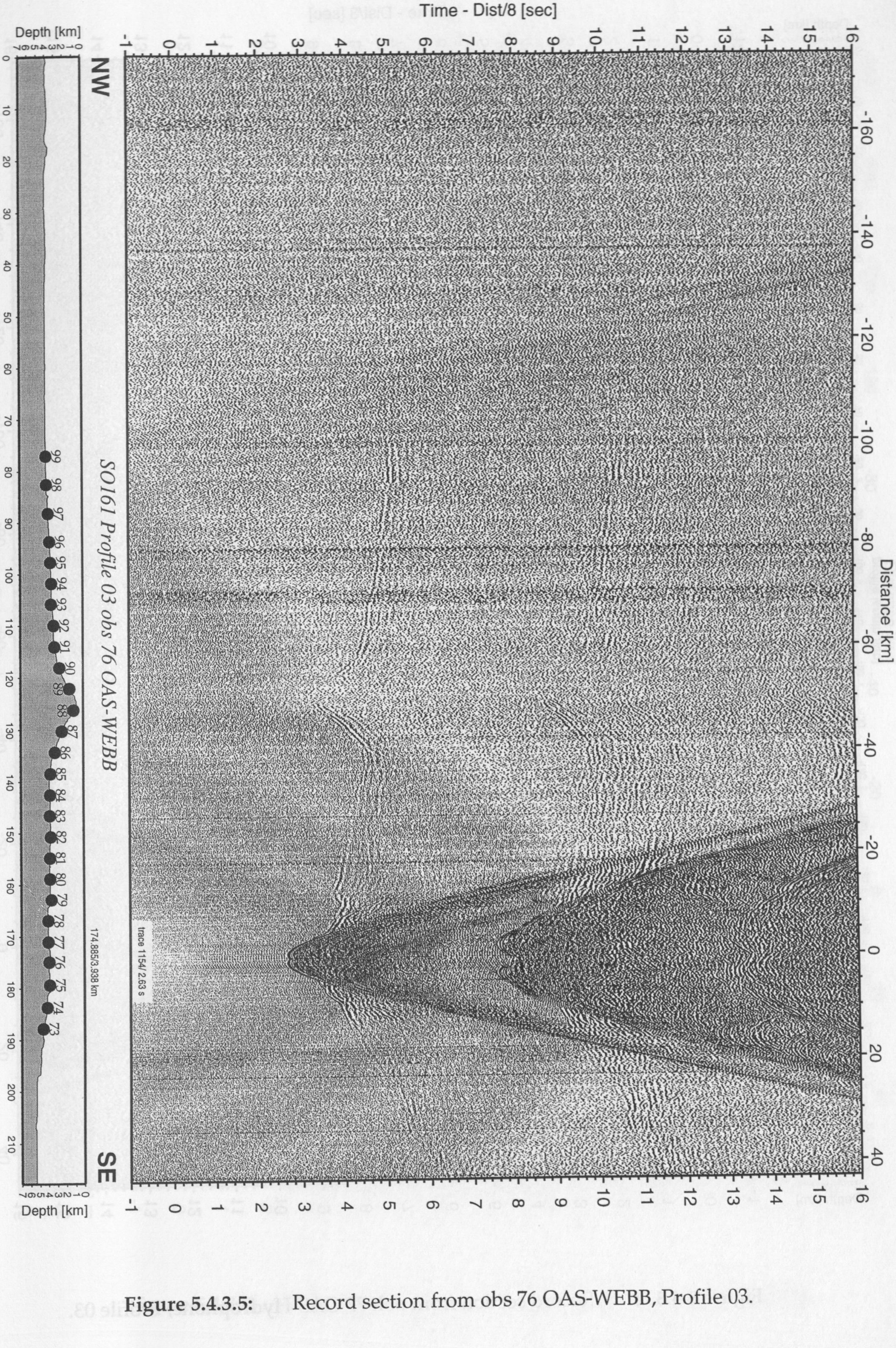

**Figure 5.4.3.5:** Record section from obs 76 OAS-WEBB, Profile 03.

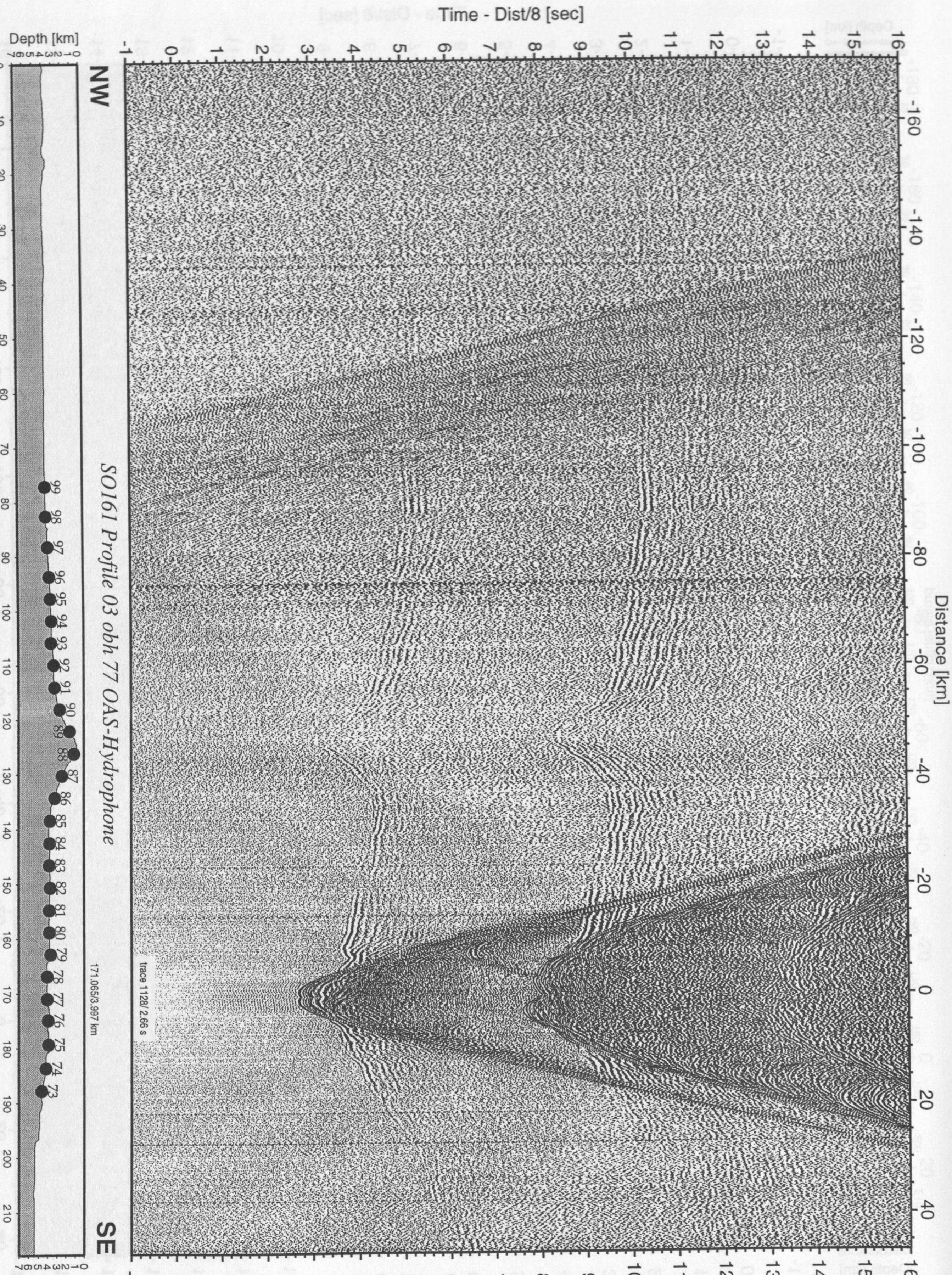

**Figure 5.4.3.6:** Record section from obh 77 OAS-Hydrophone, Profile 03.

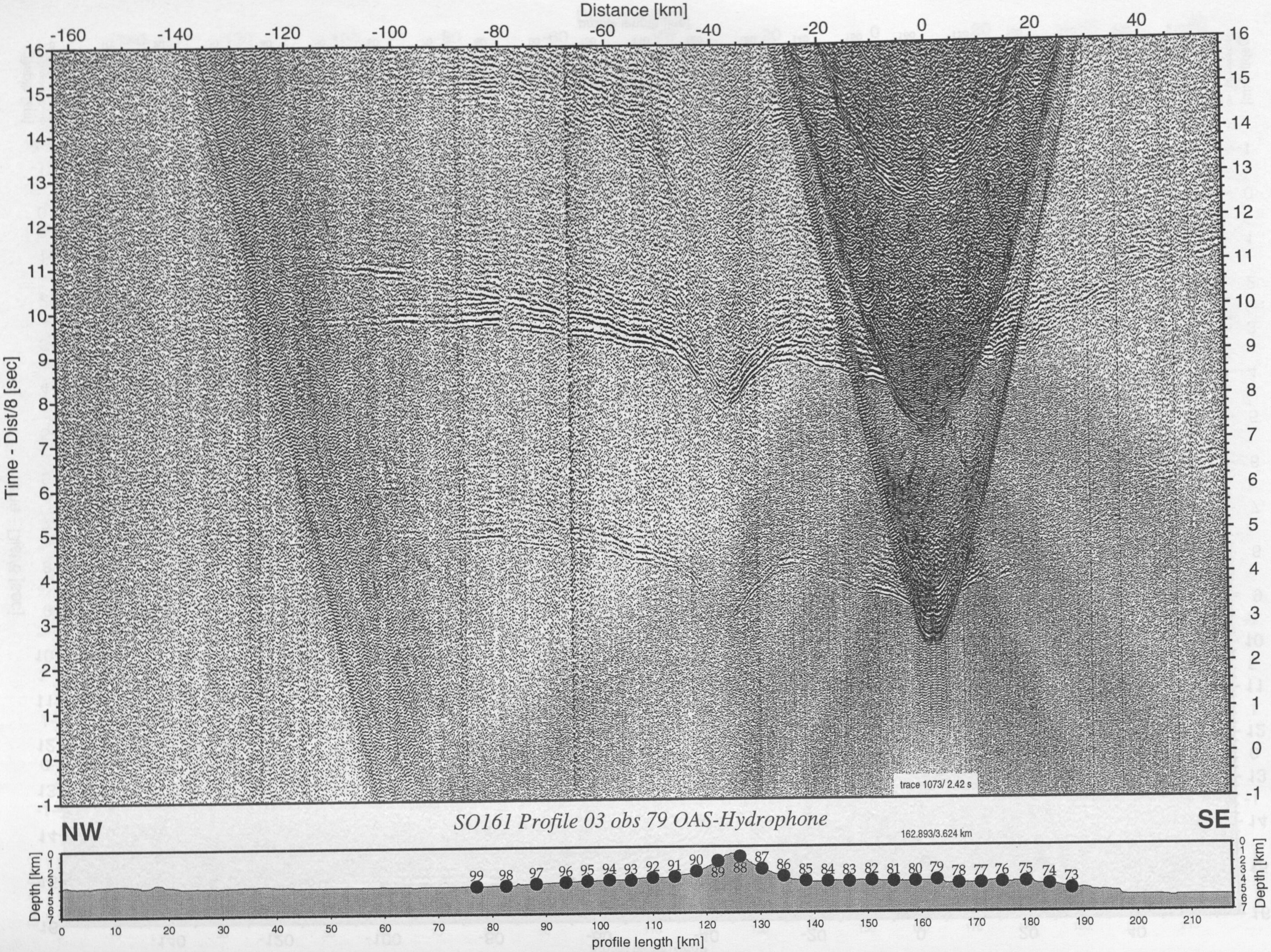

**Figure 5.4.3.7:** Record section from obs 79 OAS-Hydrophone, Profile 03.

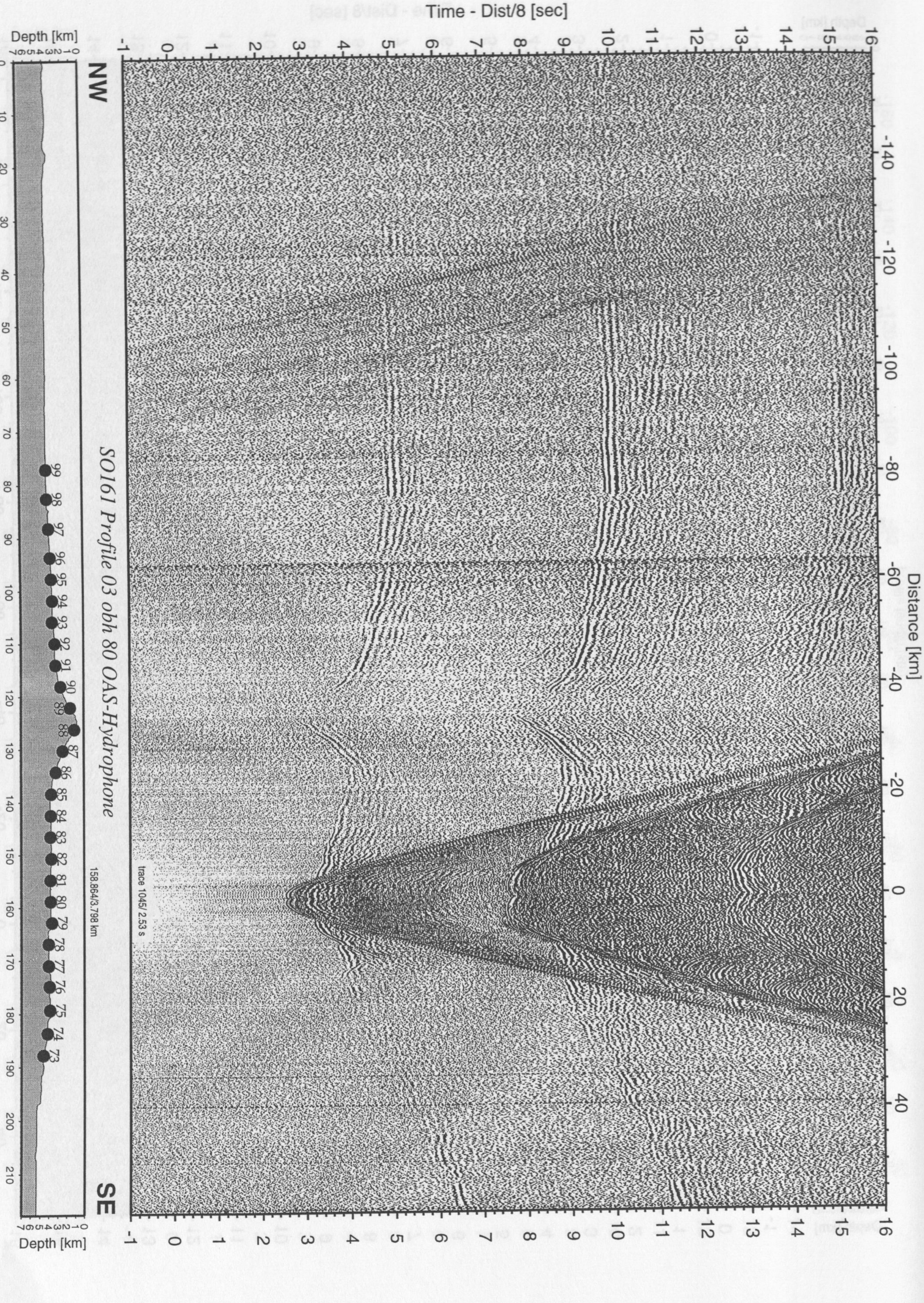

**Figure 5.4.3.8:** Record section from obh 80 OAS-Hydrophone, Profile 03.

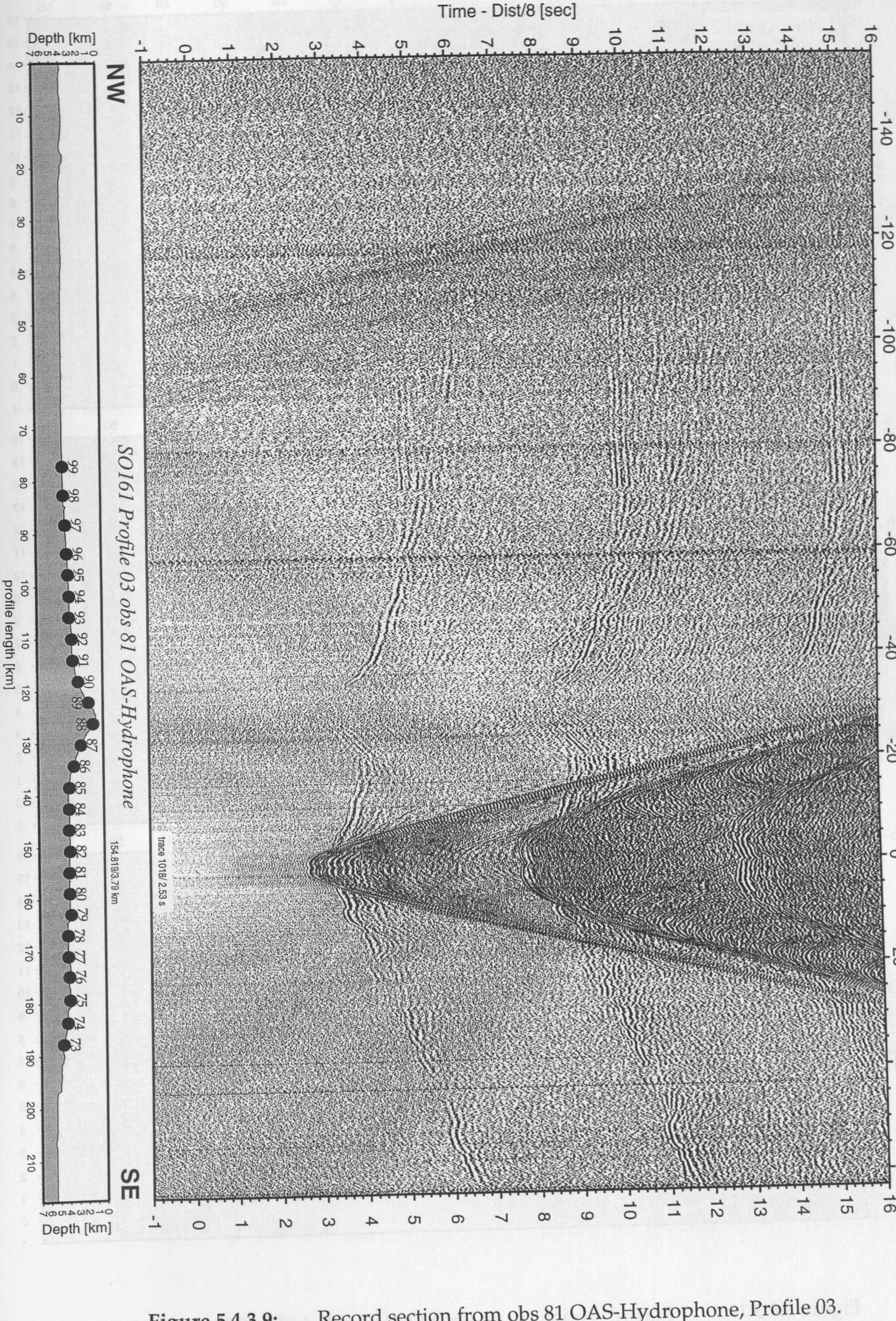

**Figure 5.4.3.9:** Record section from obs 81 OAS-Hydrophone, Profile 03.

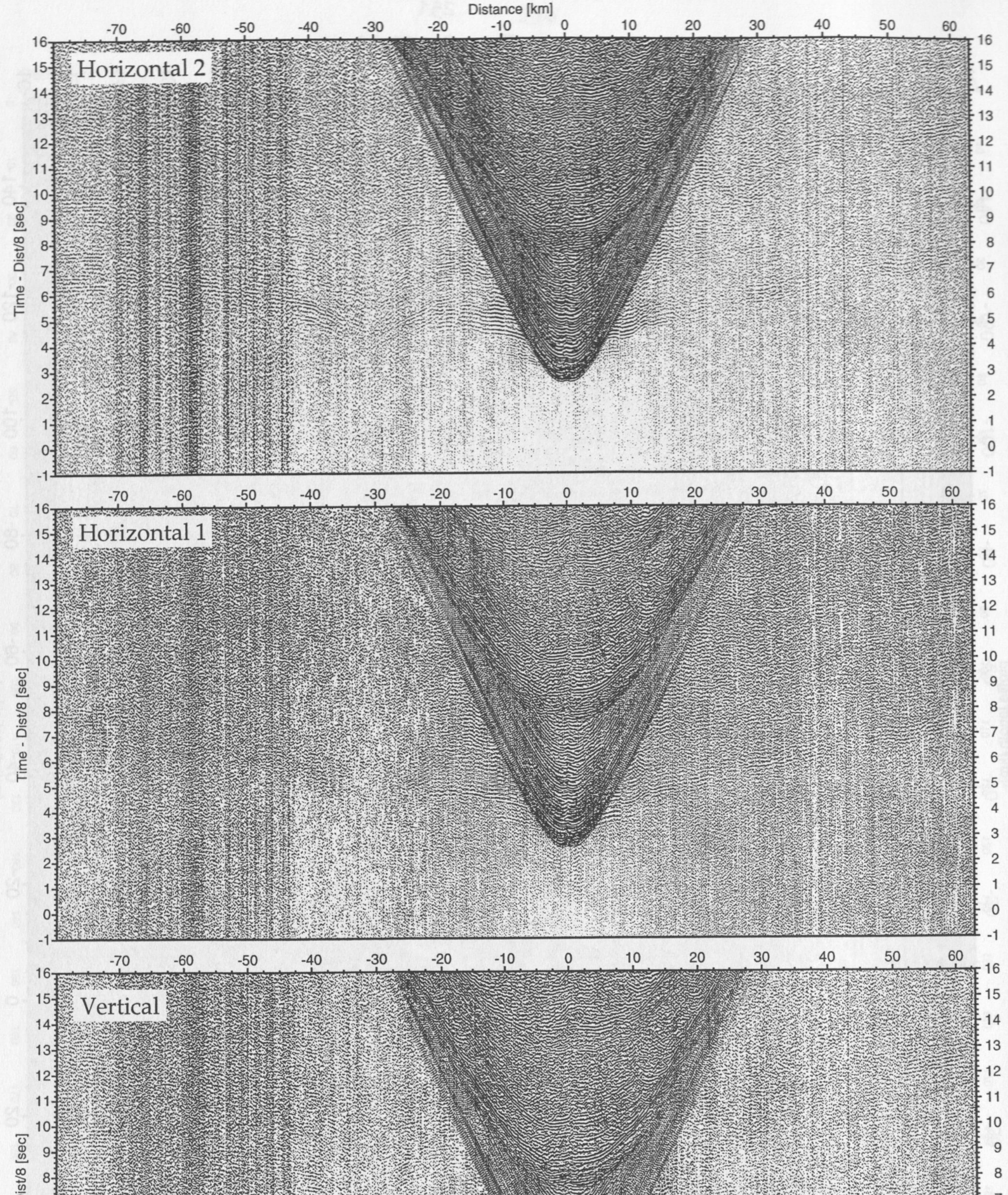

**Figure 5.4.3.10:** Record sections from obs 81 OAS/A01-4.5Hz, SO161 Profile 03.

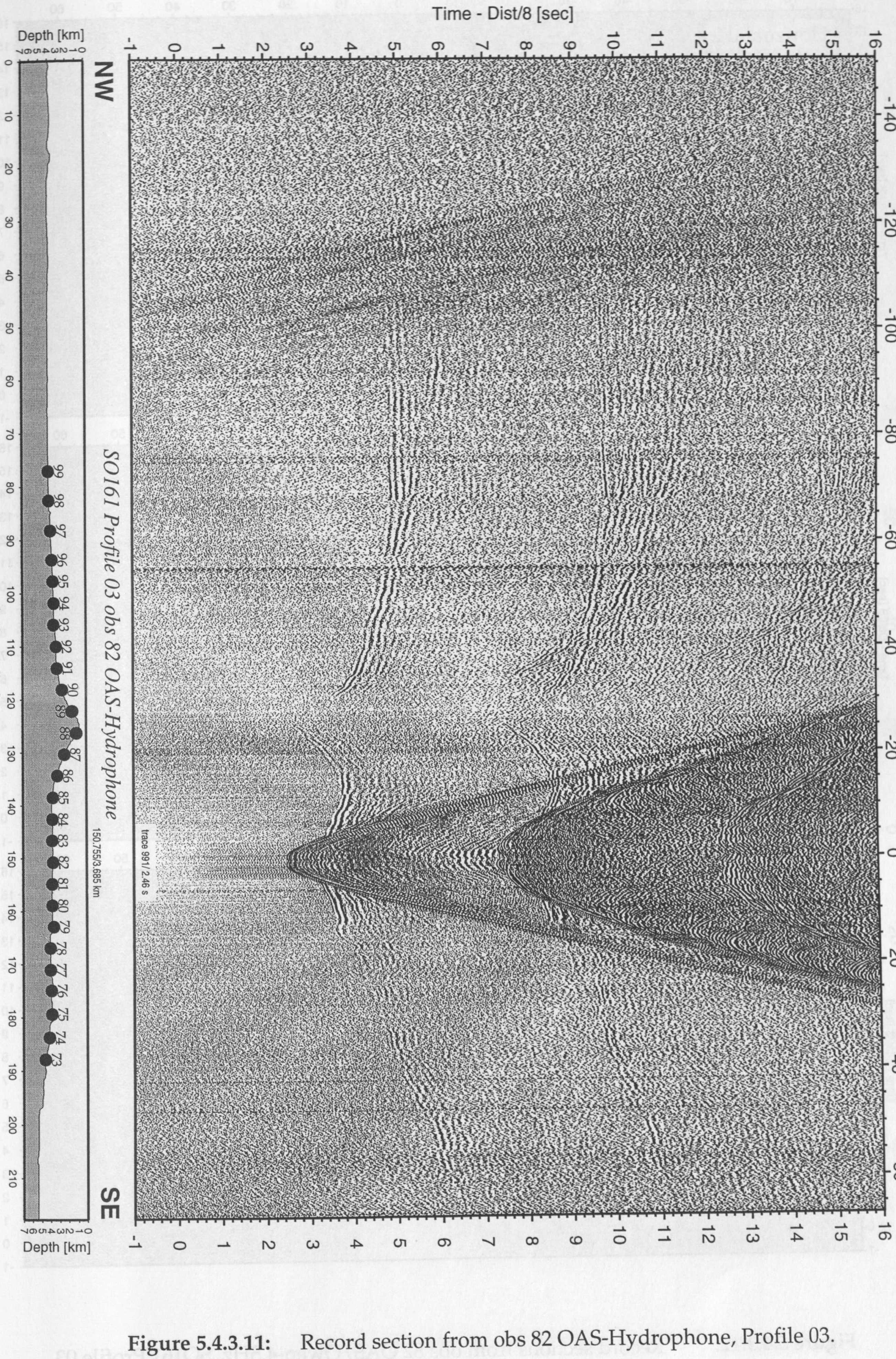

**Figure 5.4.3.11:** Record section from obs 82 OAS-Hydrophone, Profile 03.

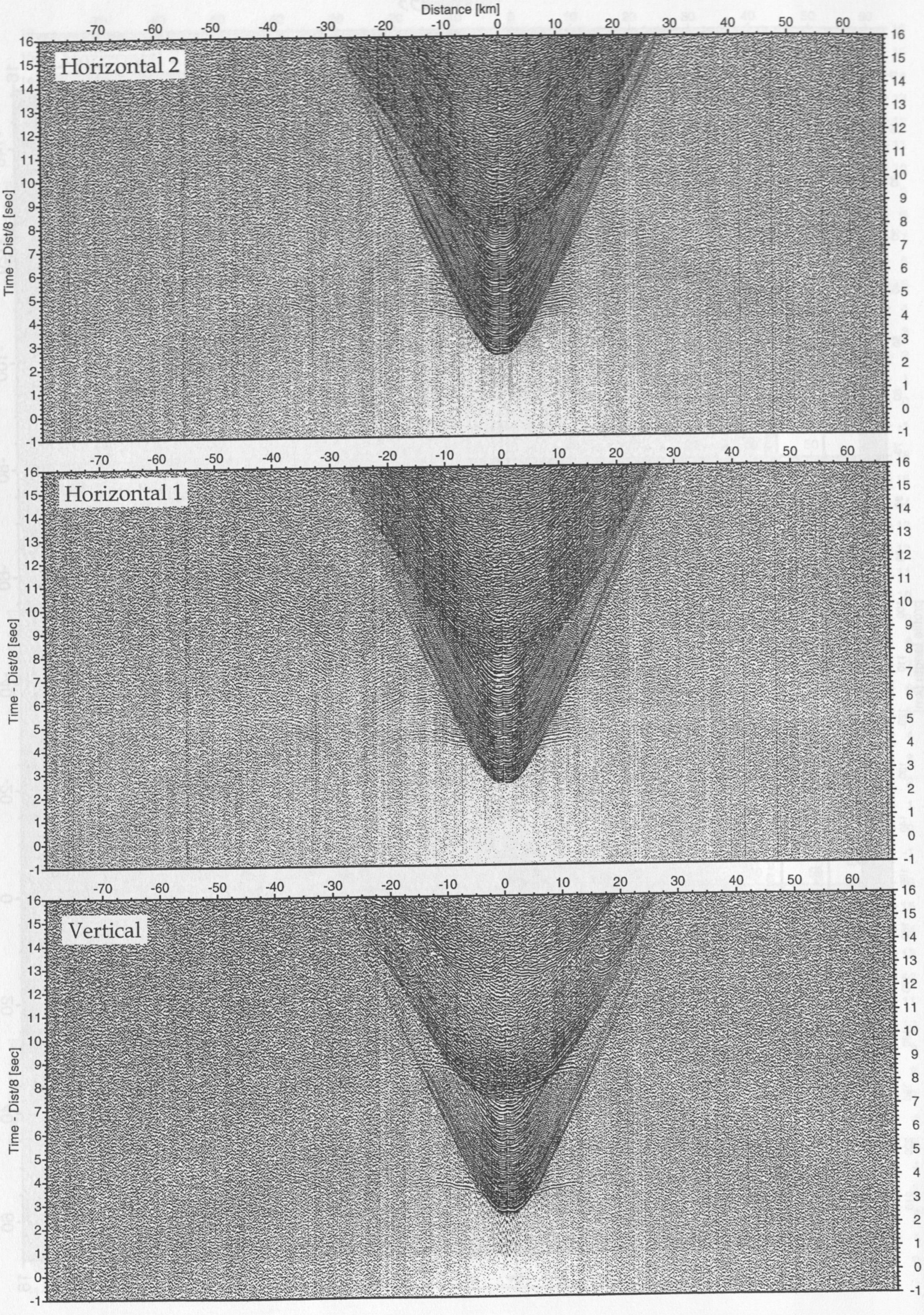

**Figure 5.4.3.12:** Record sections from obs 82 OAS/Owen-4.5Hz, SO161 Profile 03.

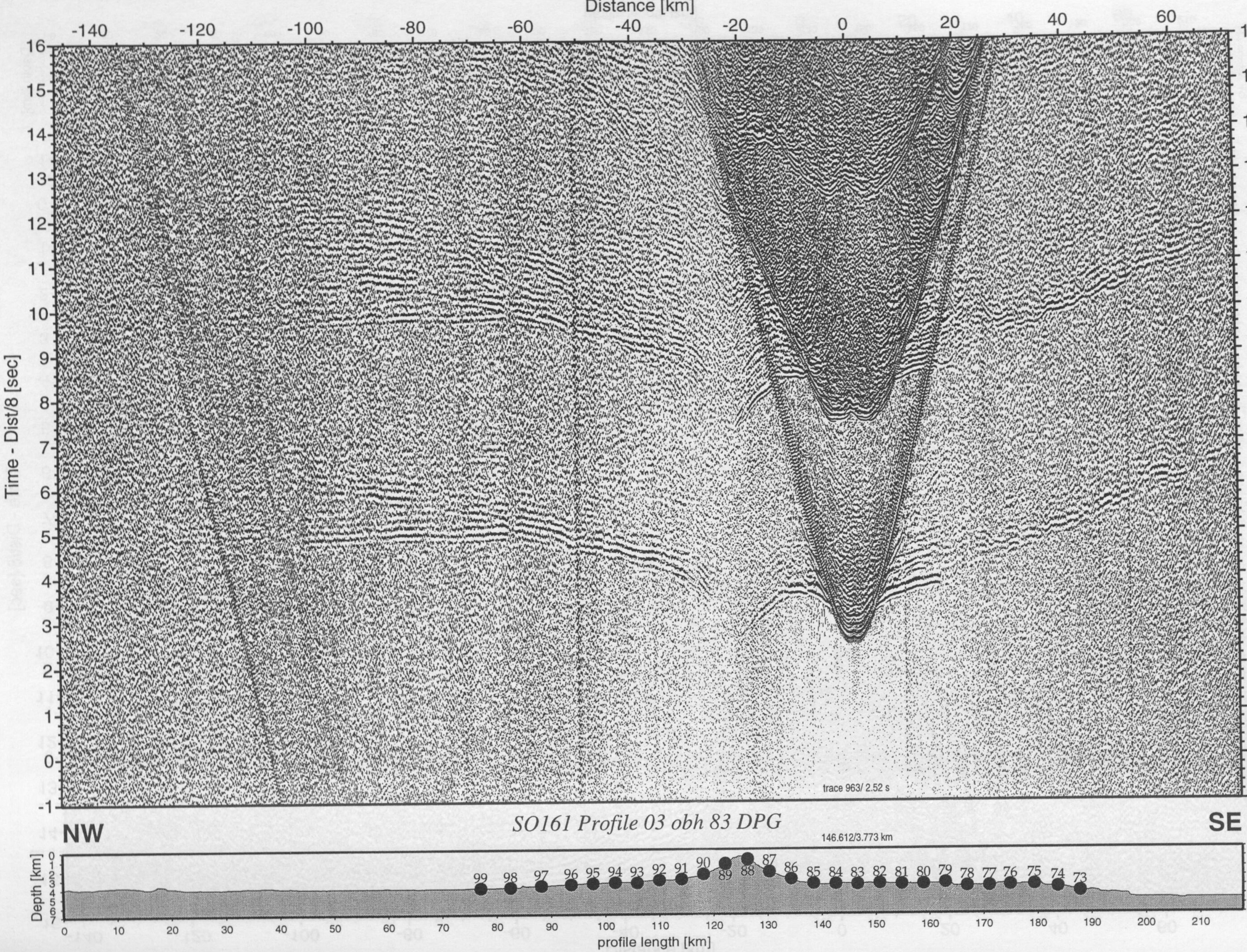

**Figure 5.4.3.13:** Record section from obh 83 DPG, Profile 03.

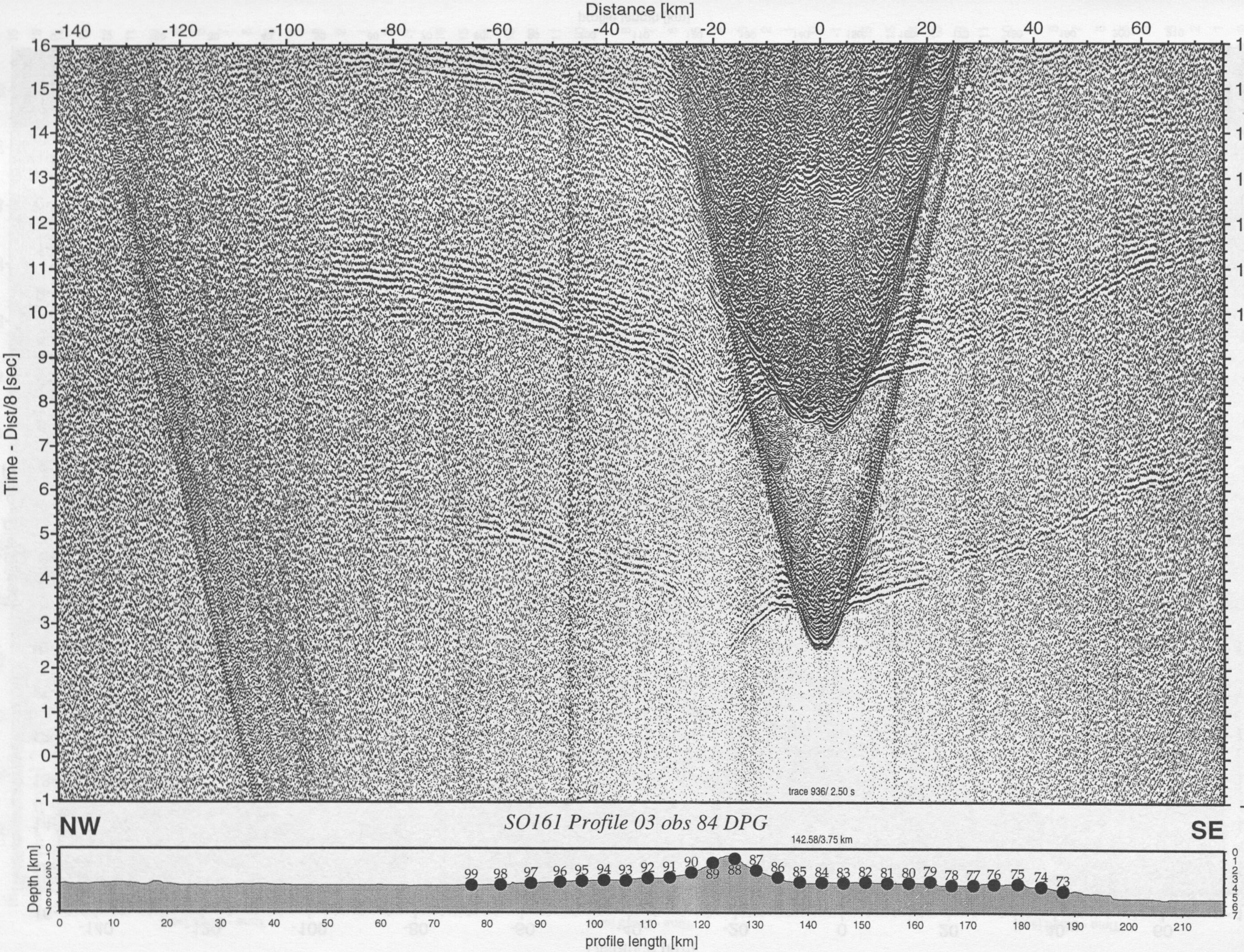

**Figure 5.4.3.14:** Record section from obs 84 DPG, Profile 03.

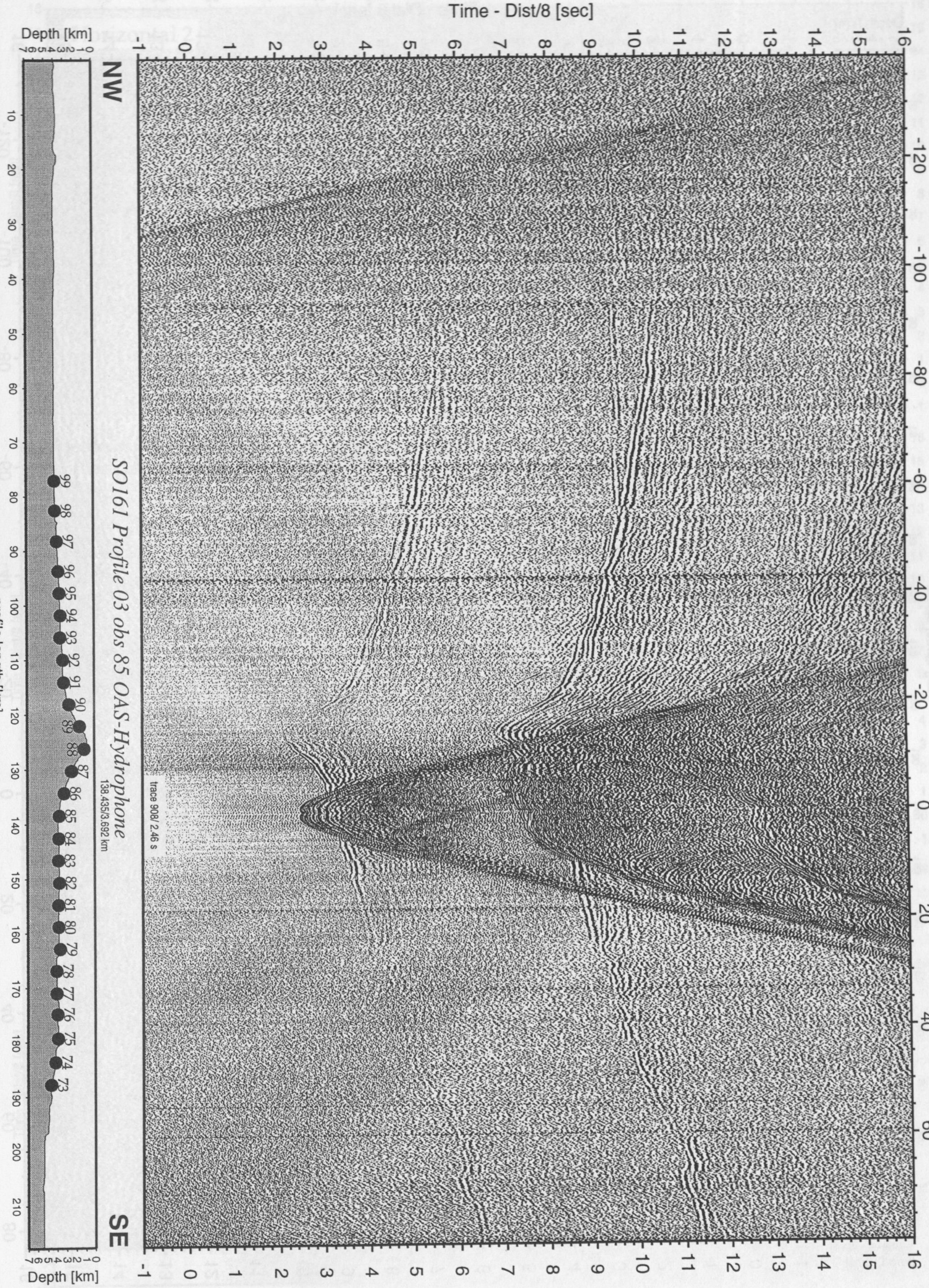

**Figure 5.4.3.15:** Record section from obs 85 OAS-Hydrophone, Profile 03.

258

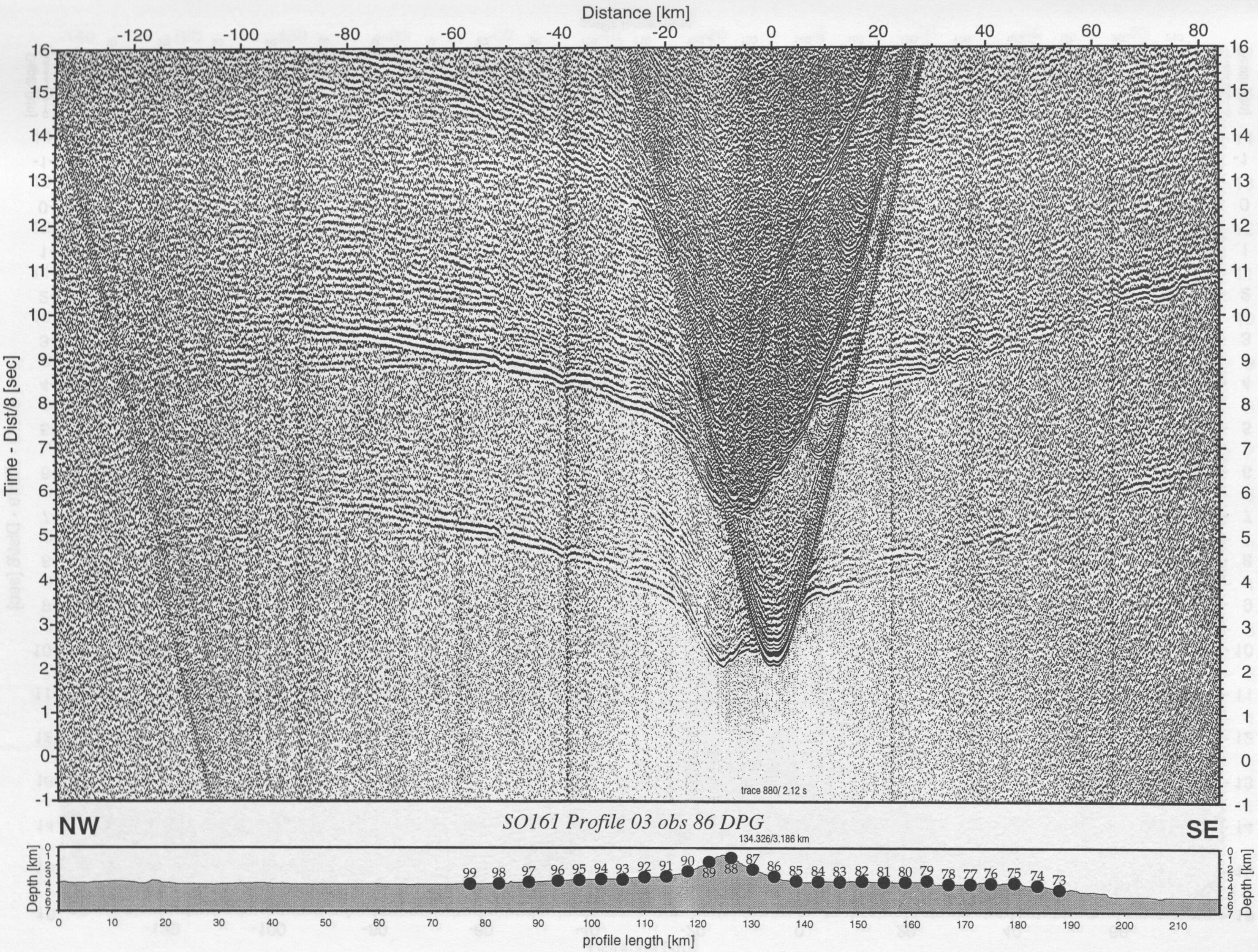

**Figure 5.4.3.16:** Record section from obs 86 DPG, Profile 03.

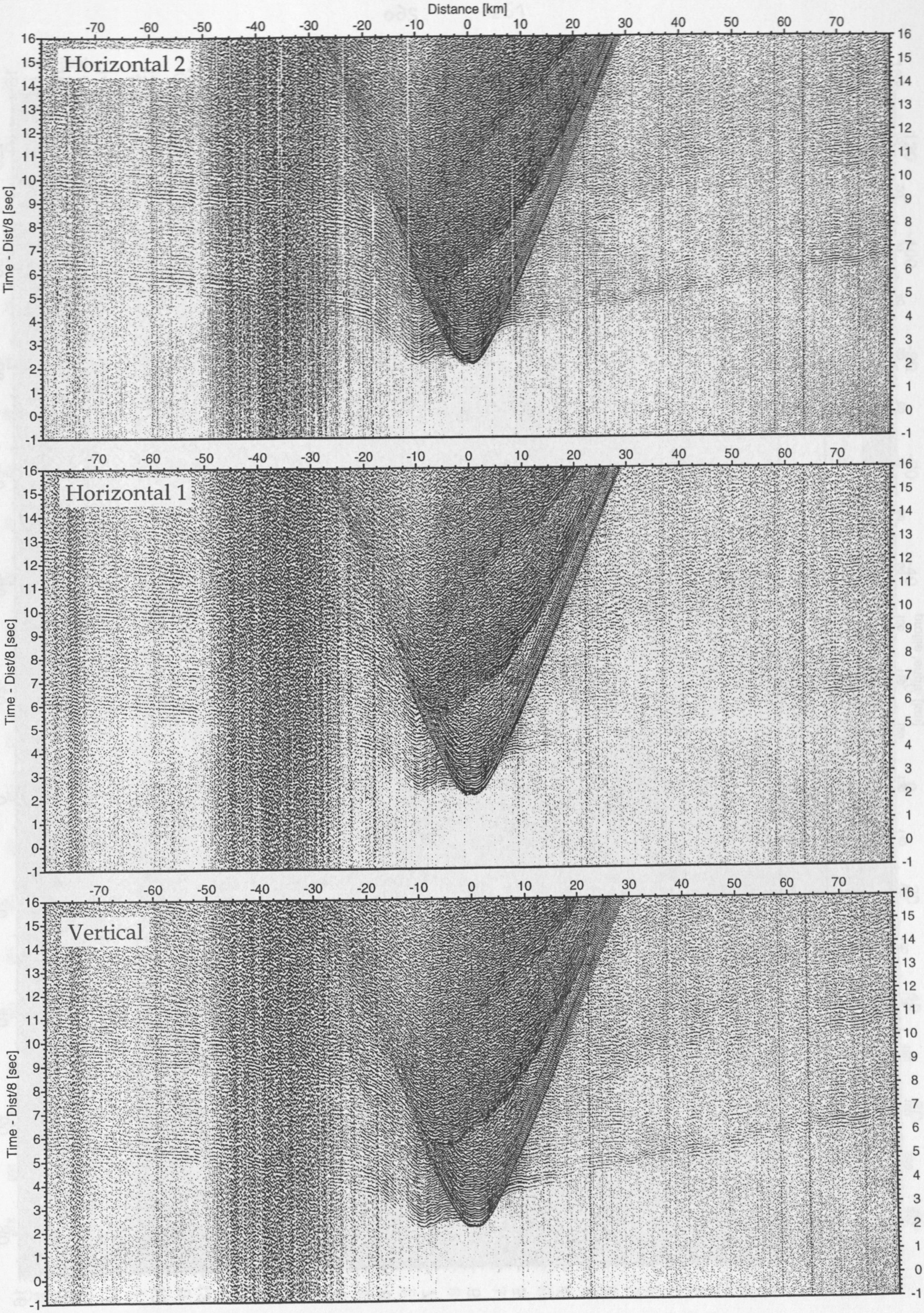

**Figure 5.4.3.17:** Record sections from obs 86 DPG/PMD, SO161 Profile 03.

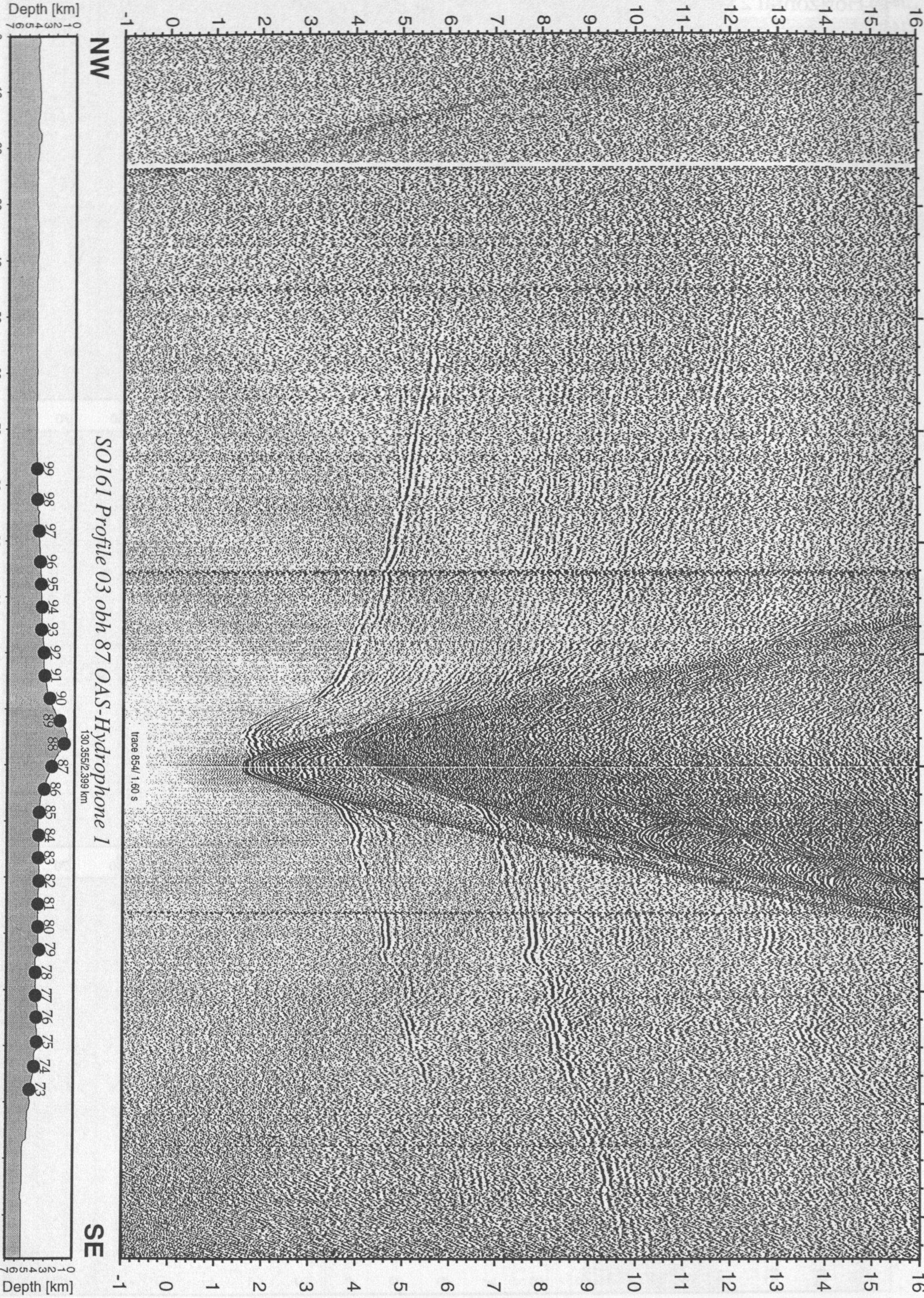

**Figure 5.4.3.18:** Record section from obh 87 OAS-Hydrophone 1, Profile 03.

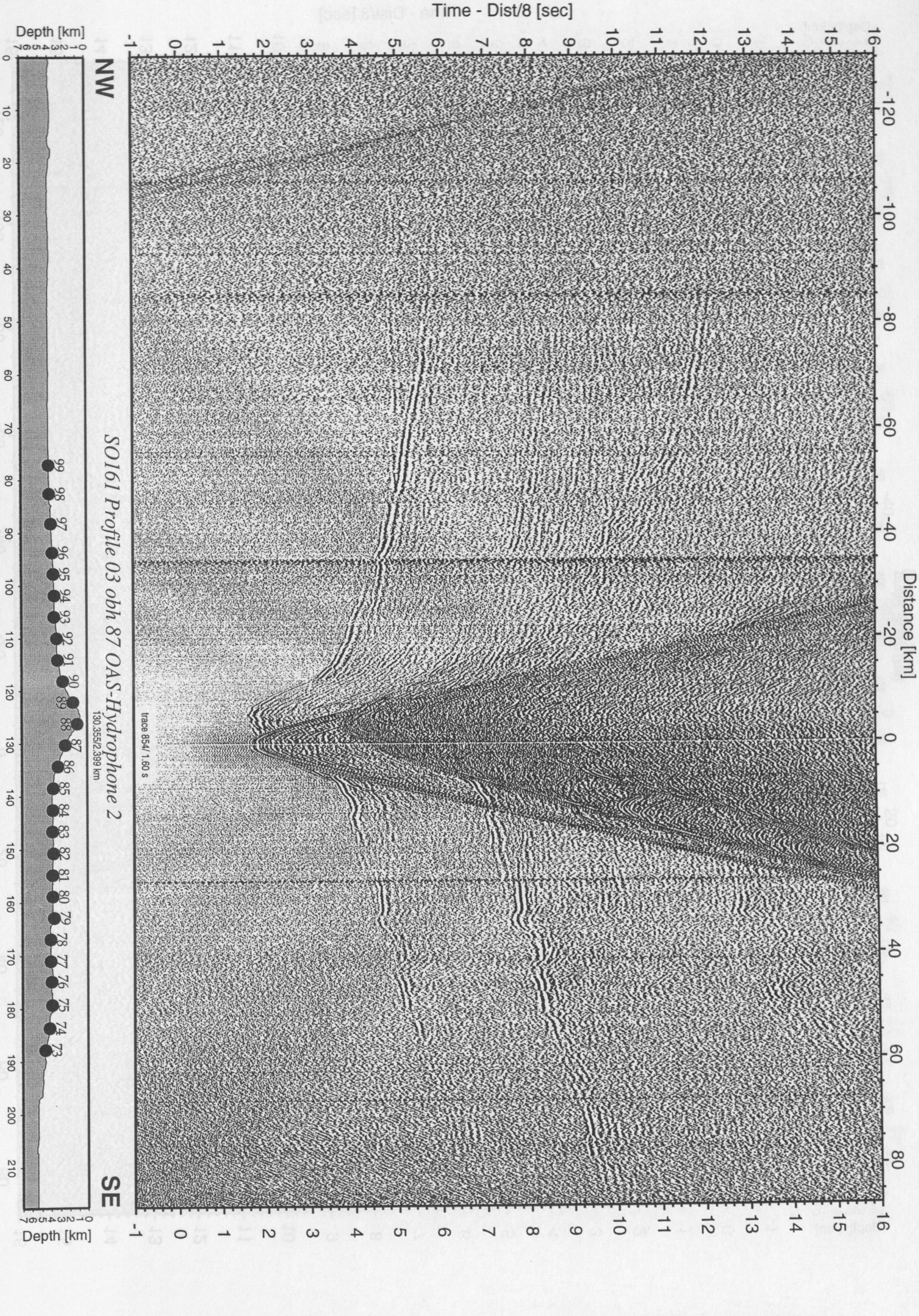

**Figure 5.4.3.19:** Record section from obh 87 OAS-Hydrophone 2, Profile 03.

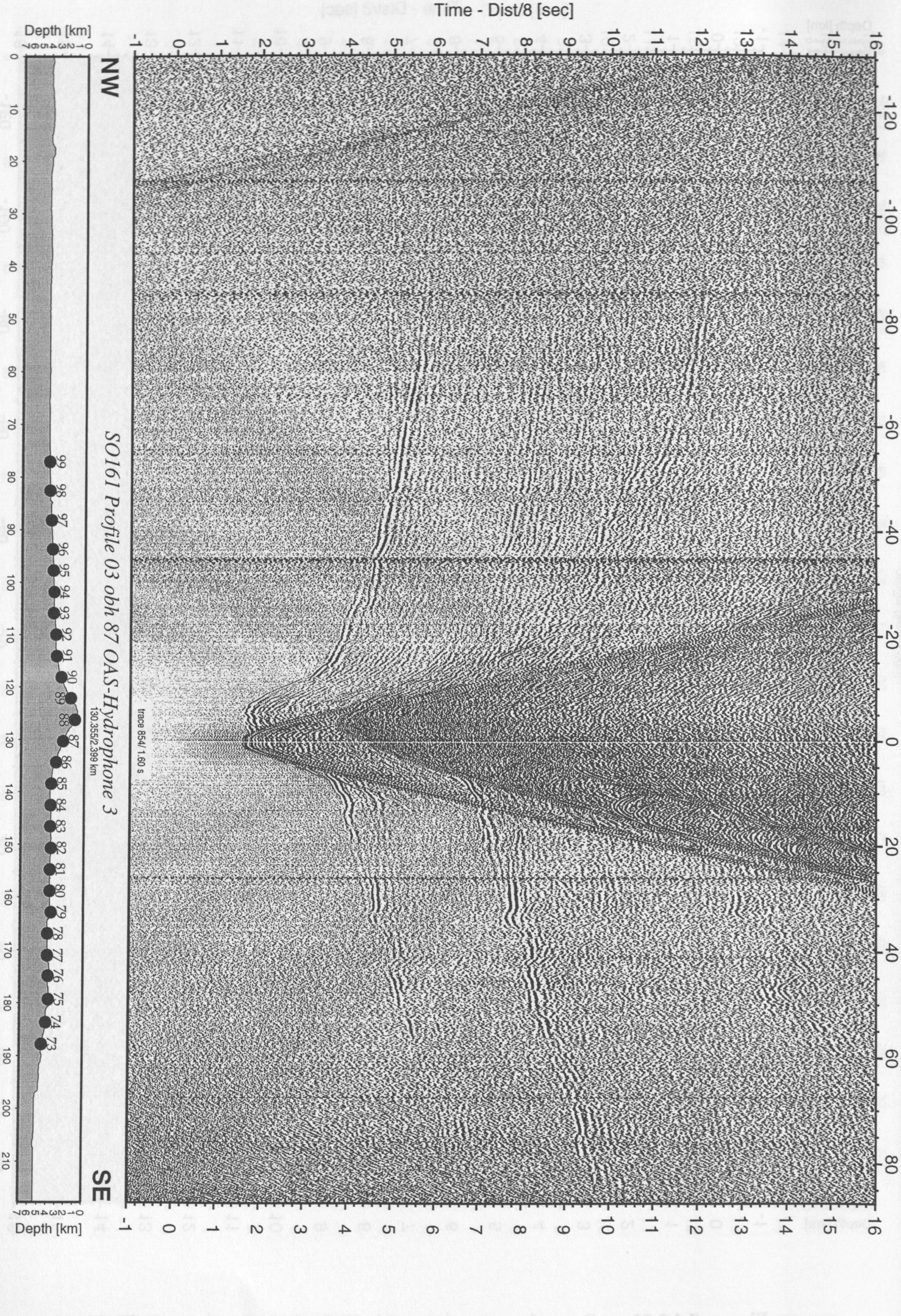

**Figure 5.4.3.20:** Record section from obh 87 OAS-Hydrophone 3, Profile 03.

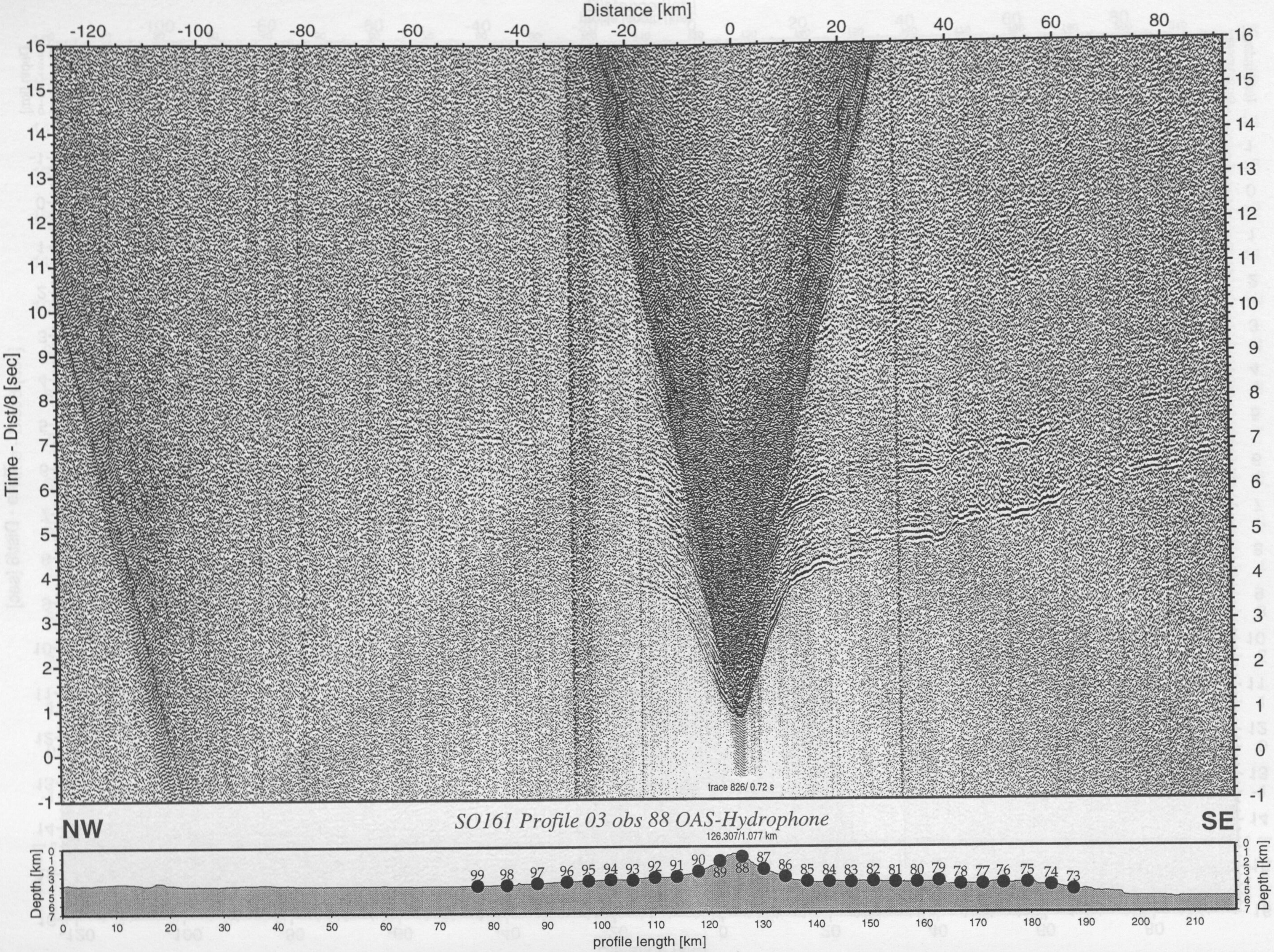

**Figure 5.4.3.21:** Record section from obs 88 OAS-Hydrophone, Profile 03.

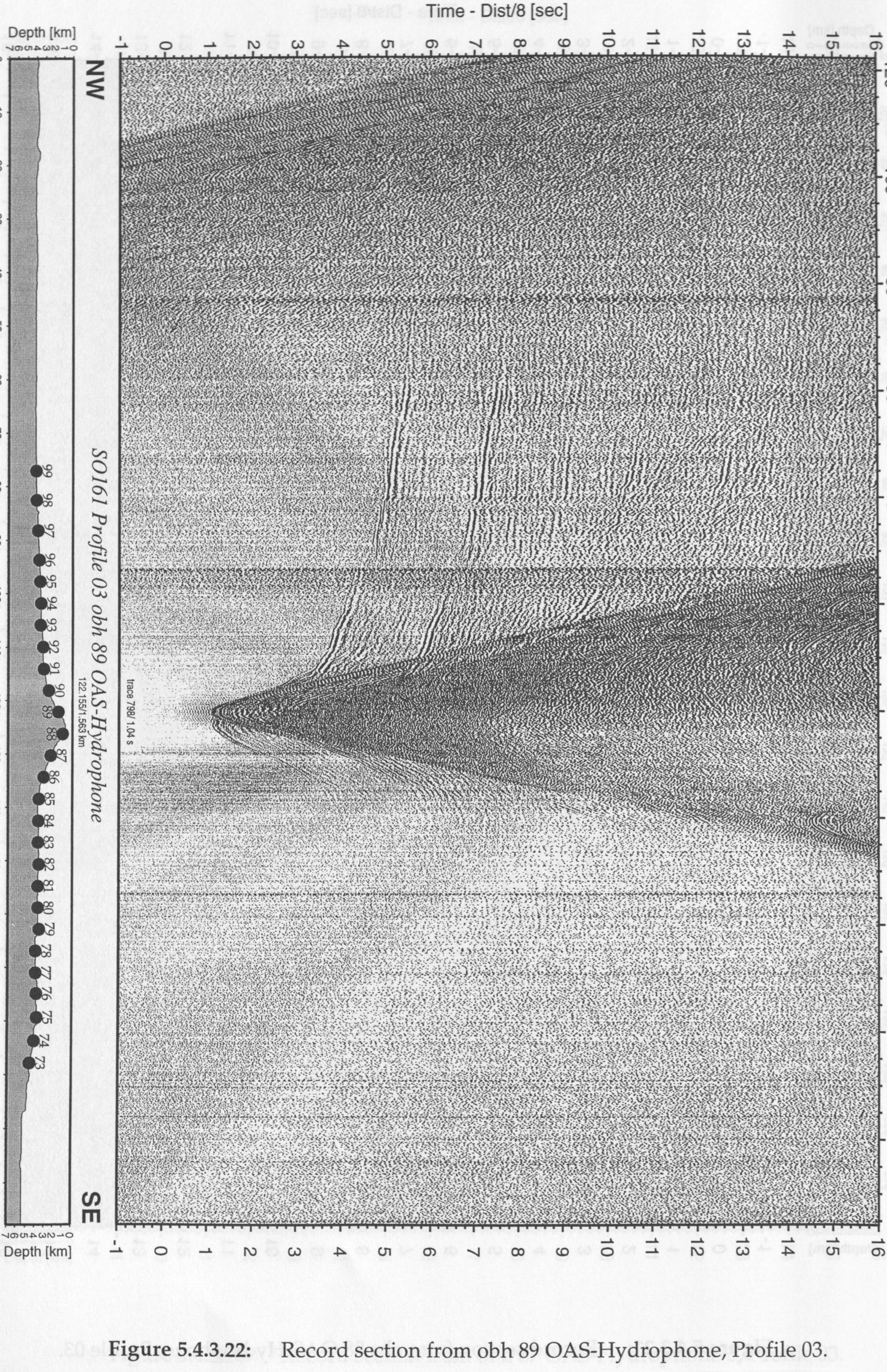

**Figure 5.4.3.22:** Record section from obh 89 OAS-Hydrophone, Profile 03.

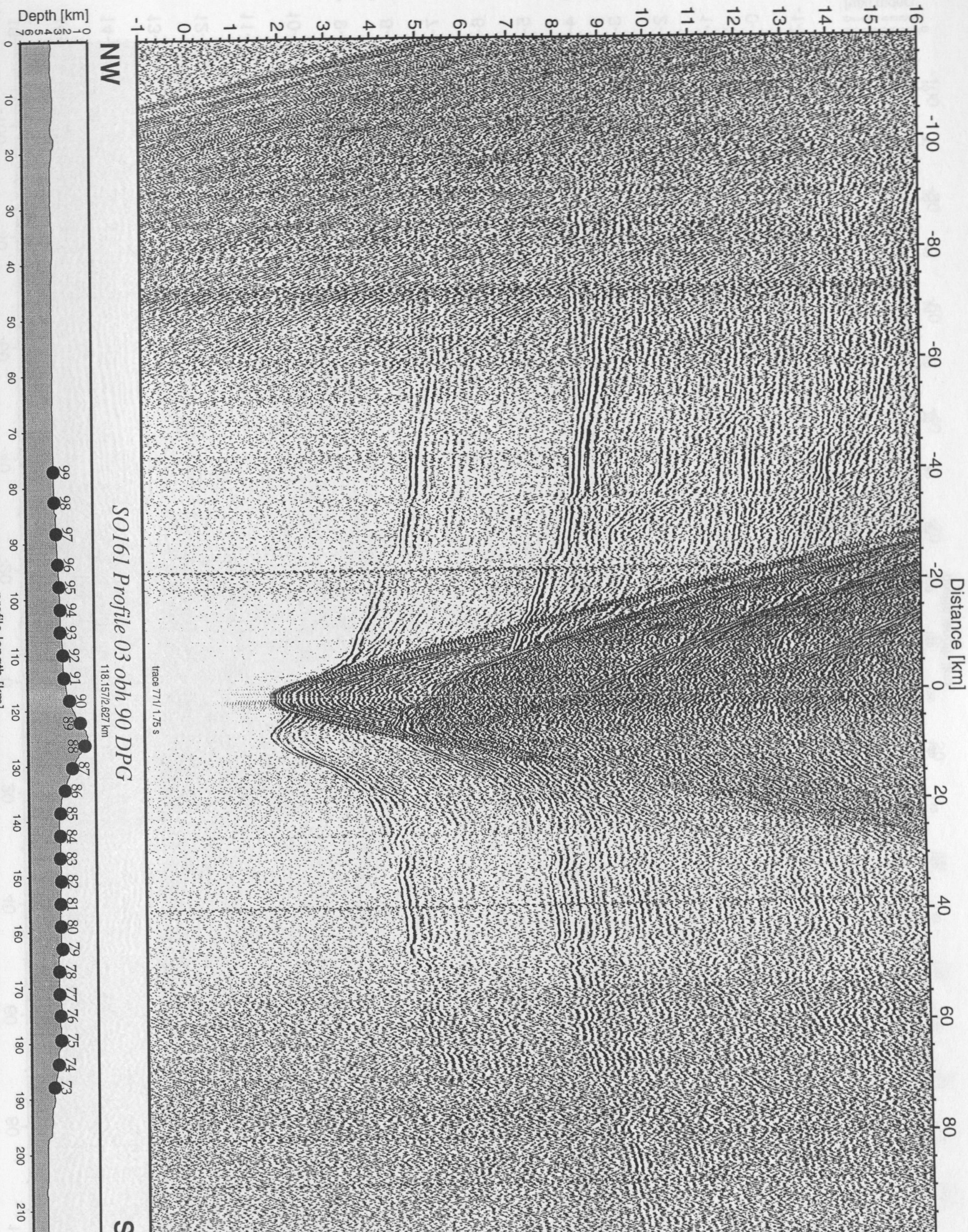

**Figure 5.4.3.23:** Record section from obh 90 DPG, Profile 03.

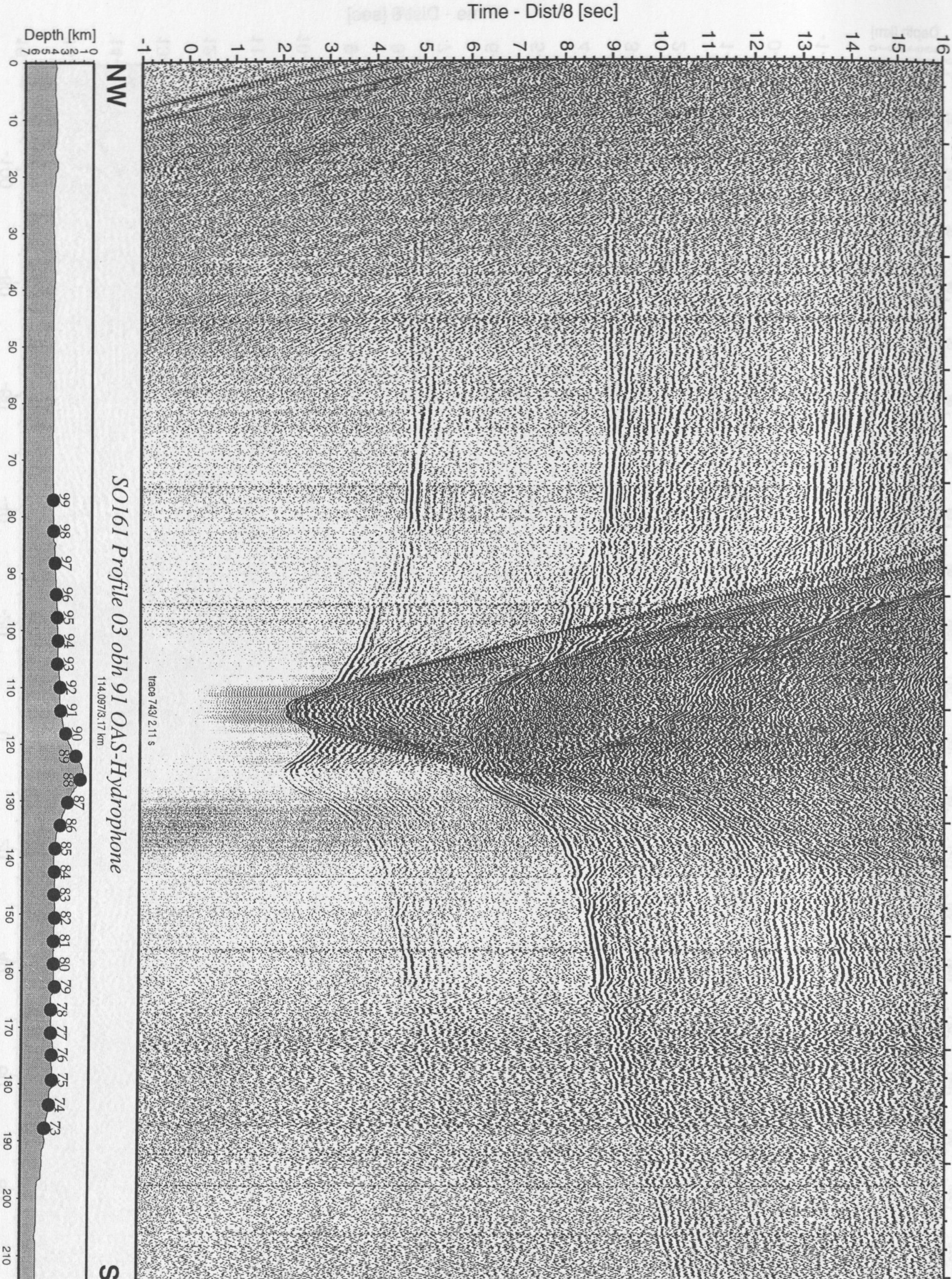

**Figure 5.4.3.24:** Record section from obh 91 OAS-Hydrophone, Profile 03.

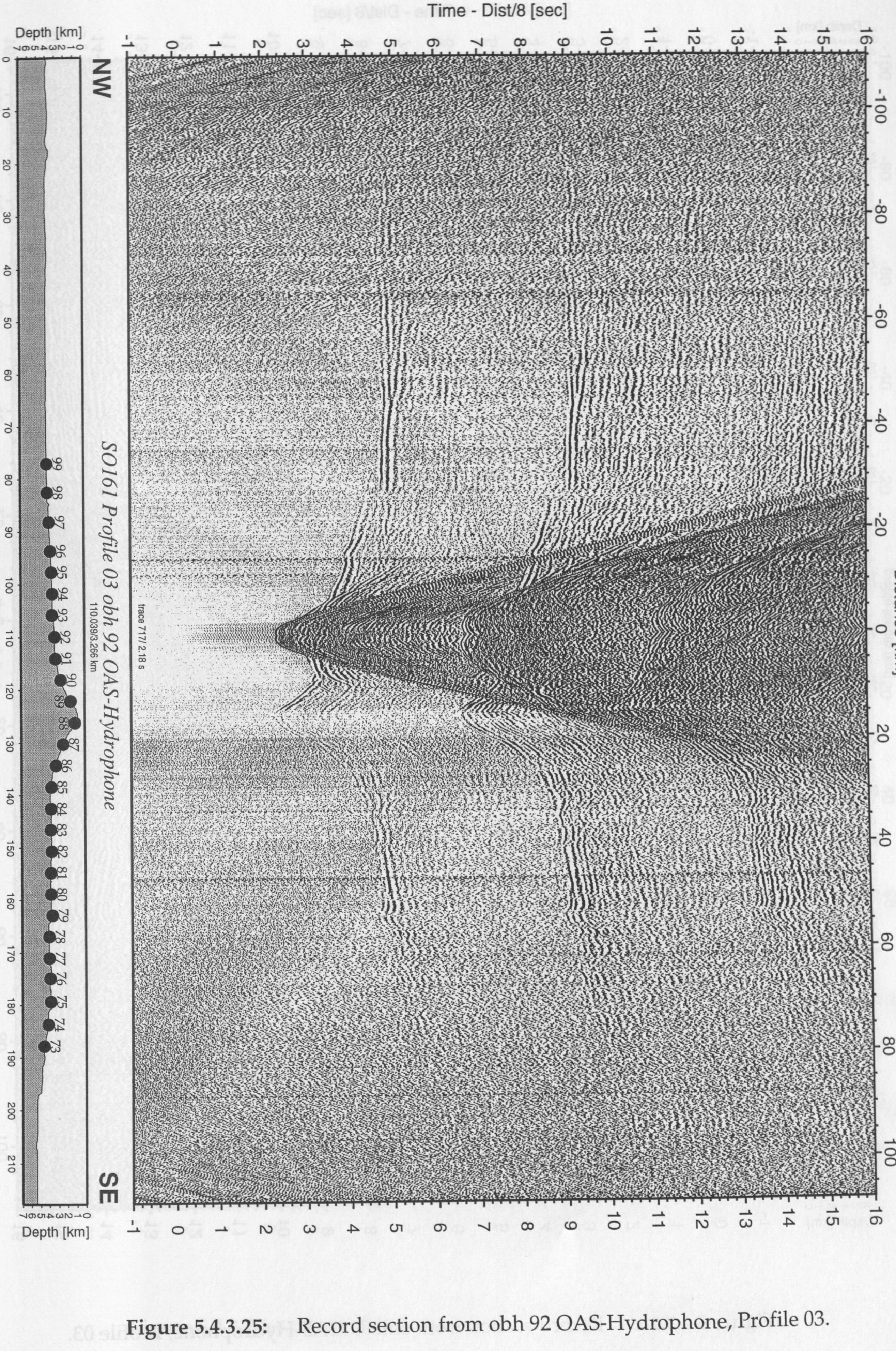

**Figure 5.4.3.25:** Record section from obh 92 OAS-Hydrophone, Profile 03.

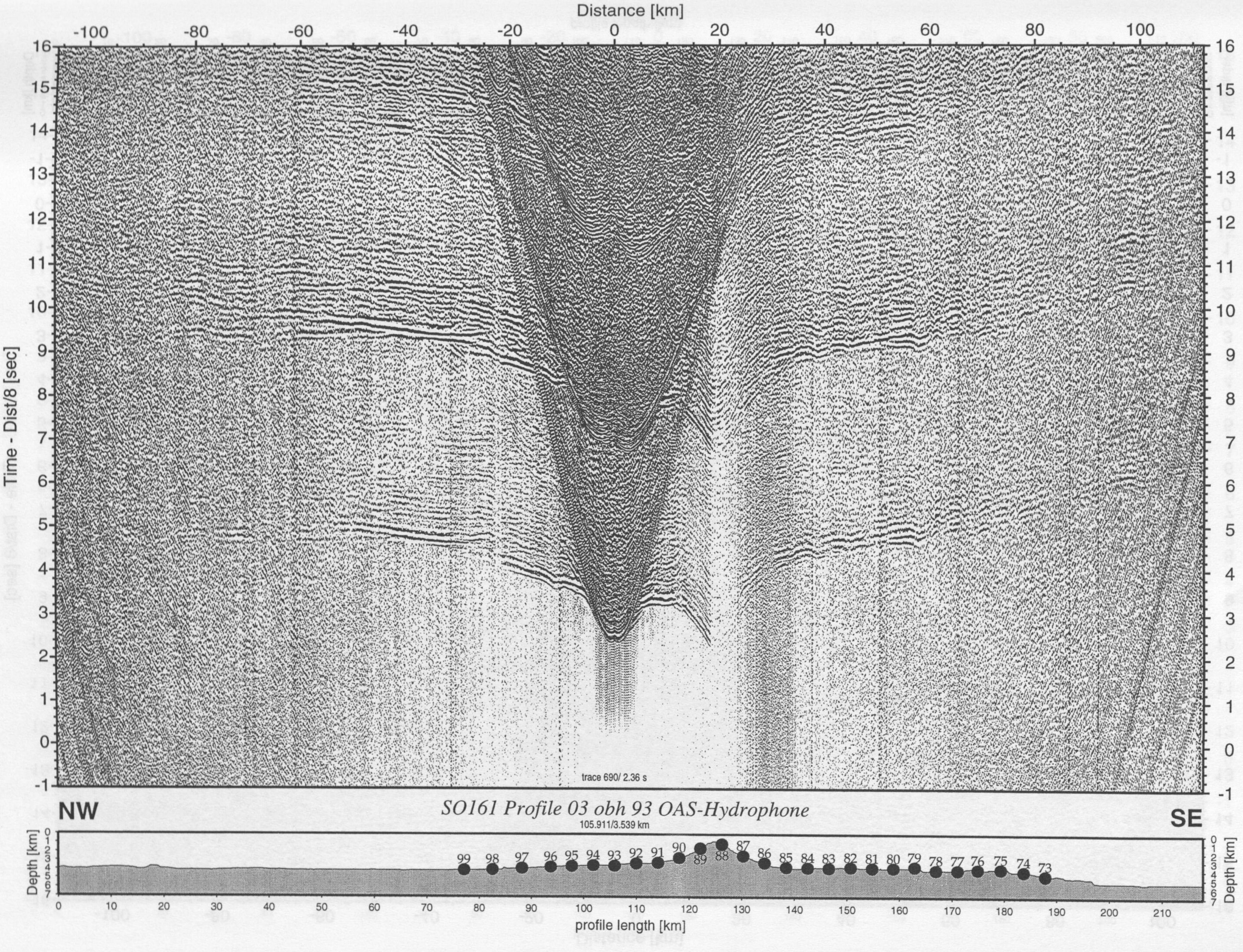

**Figure 5.4.3.26:** Record section from obh 93 OAS-Hydrophone, Profile 03.

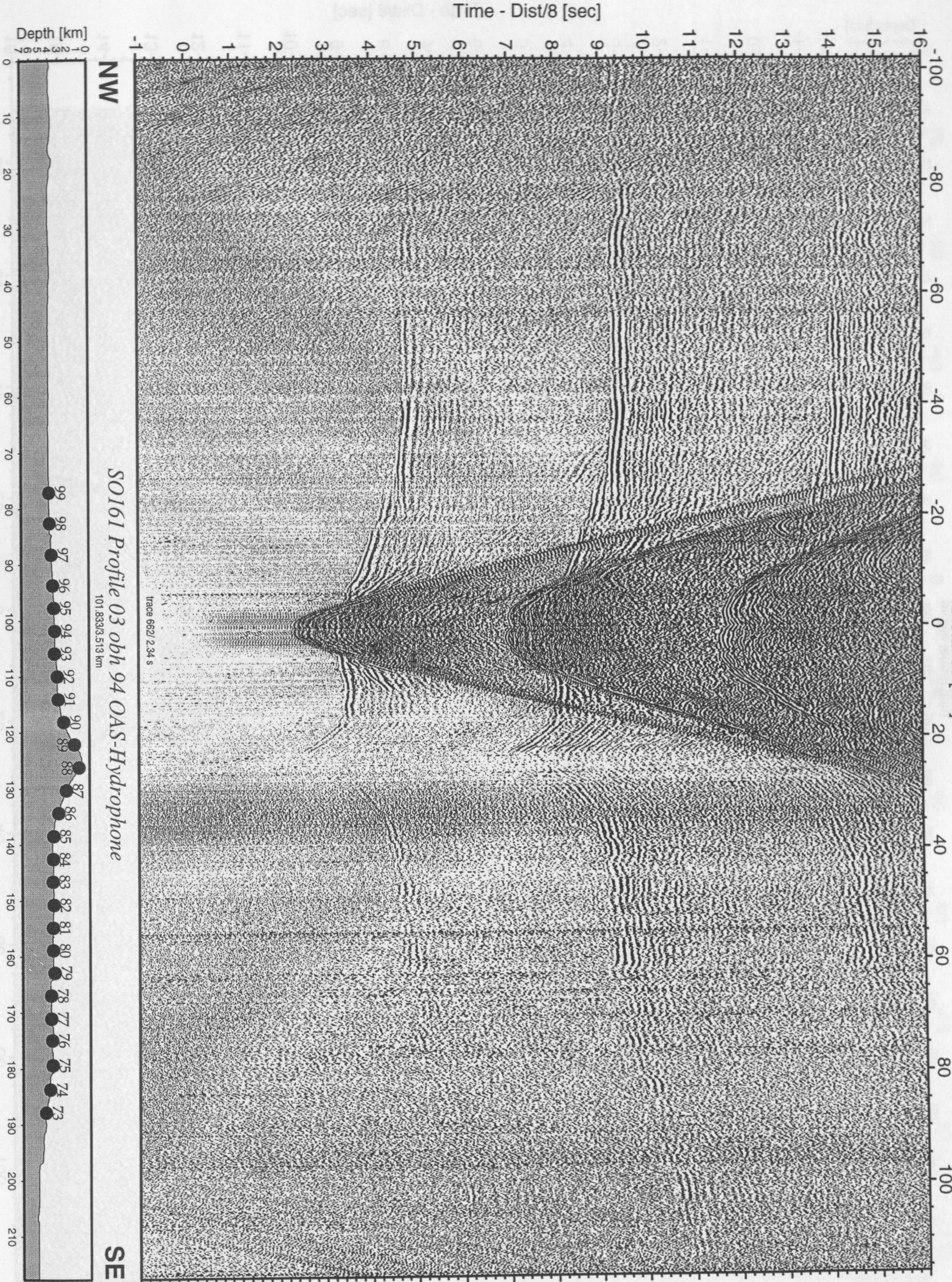

**Figure 5.4.3.27:** Record section from obh 94 OAS-Hydrophone, Profile 03.

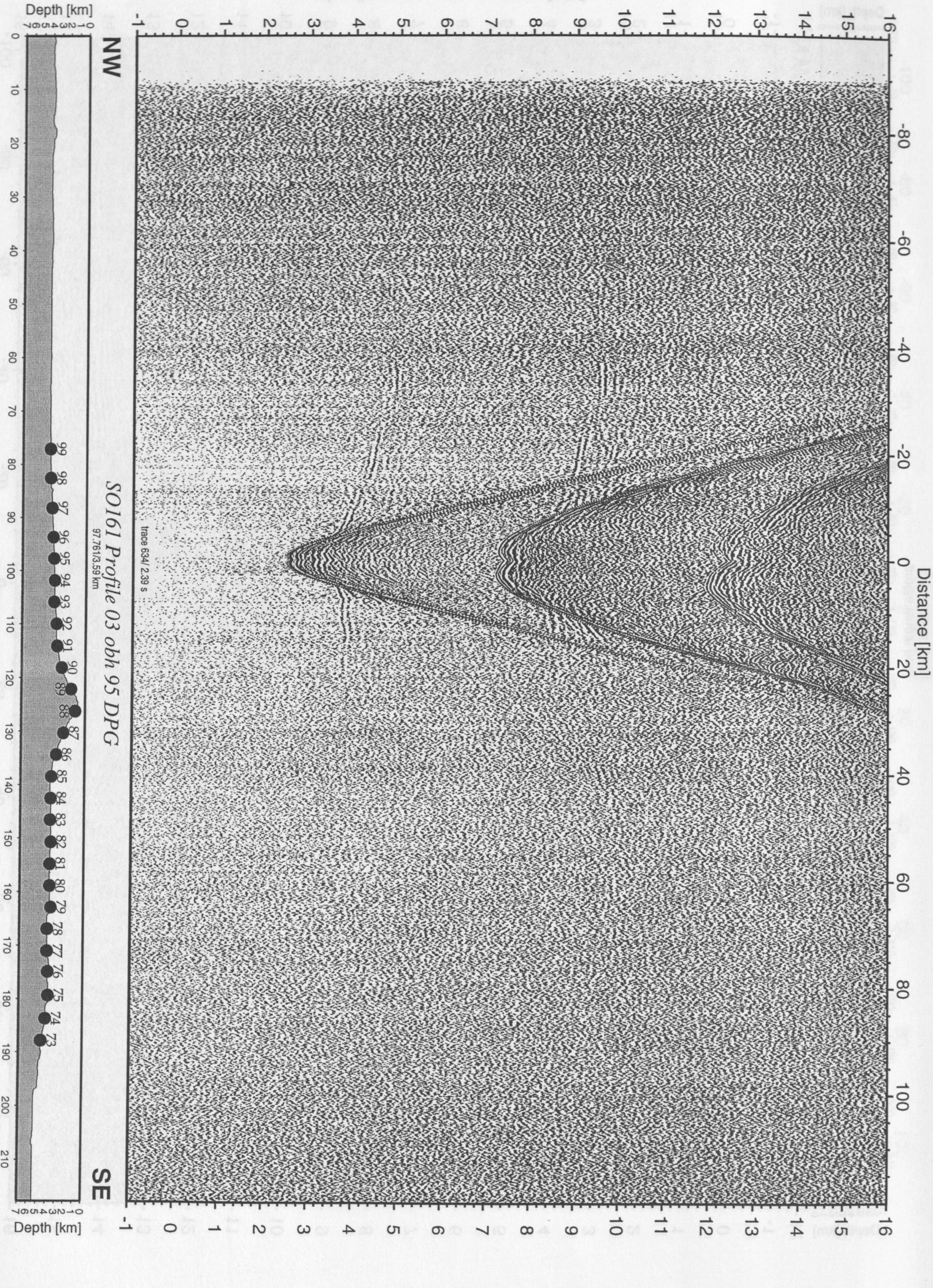

**Figure 5.4.3.28:** Record section from obh 95 DPG, Profile 03.

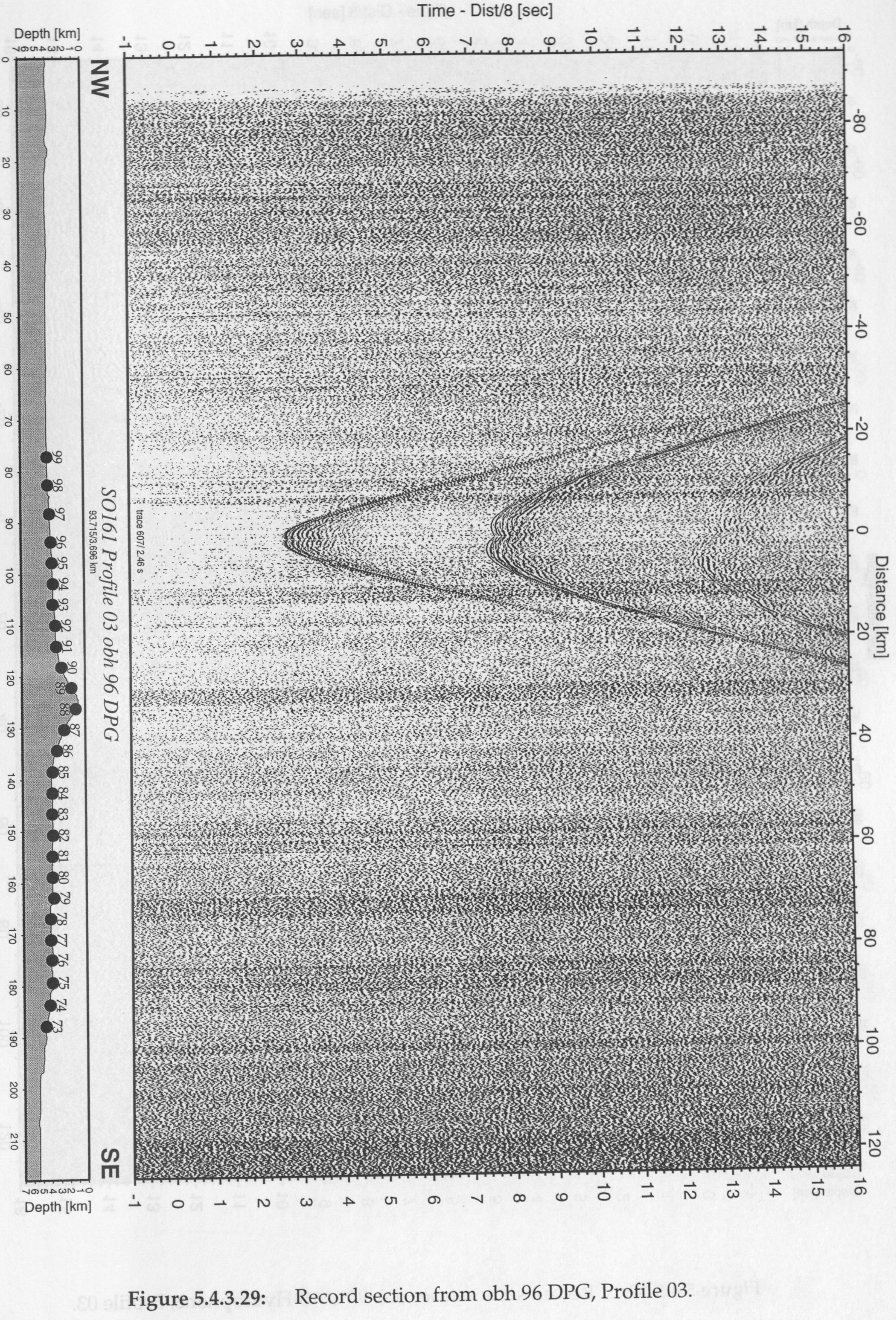

**Figure 5.4.3.29:** Record section from obh 96 DPG, Profile 03.

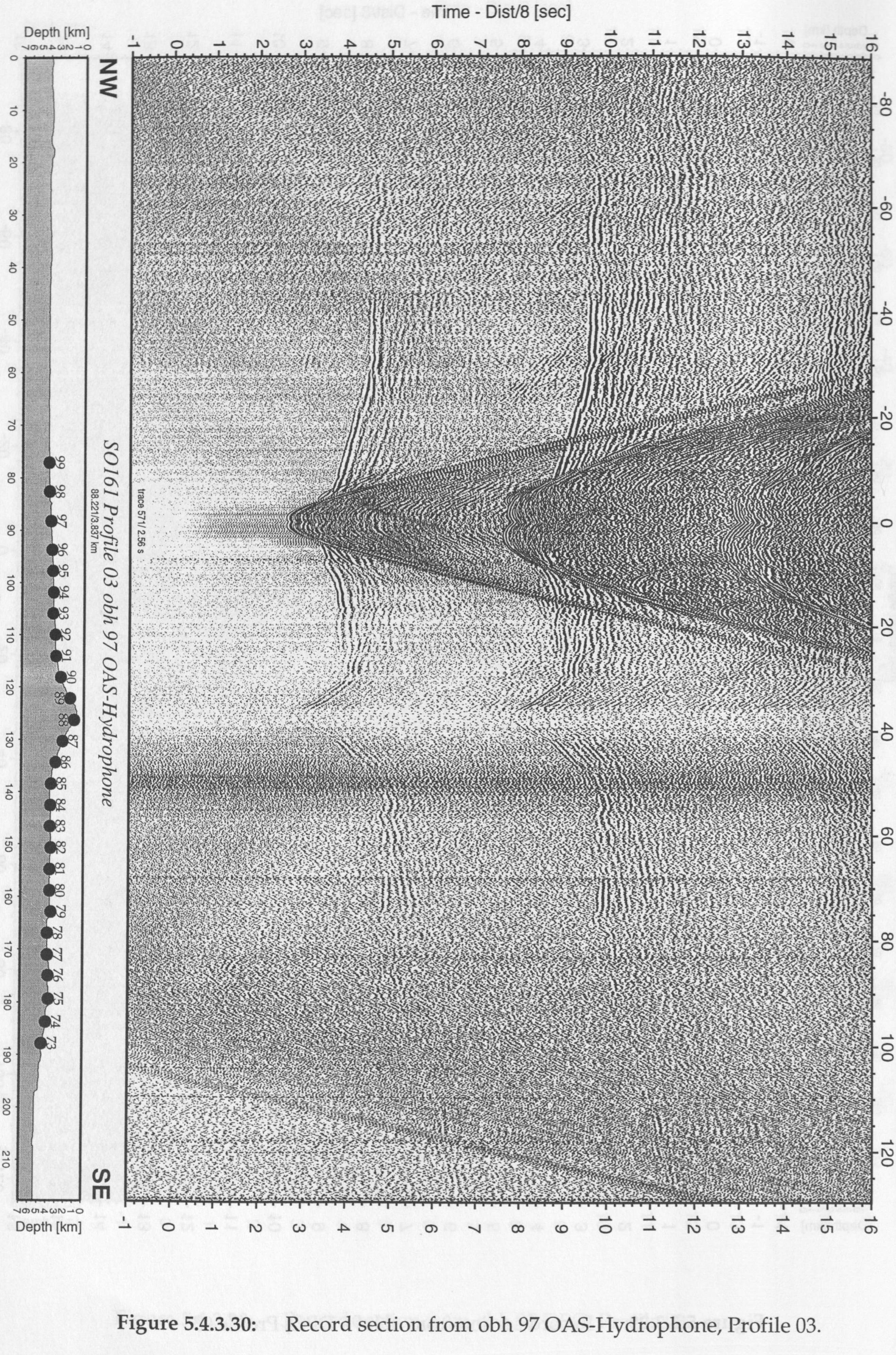

**Figure 5.4.3.30:** Record section from obh 97 OAS-Hydrophone, Profile 03.

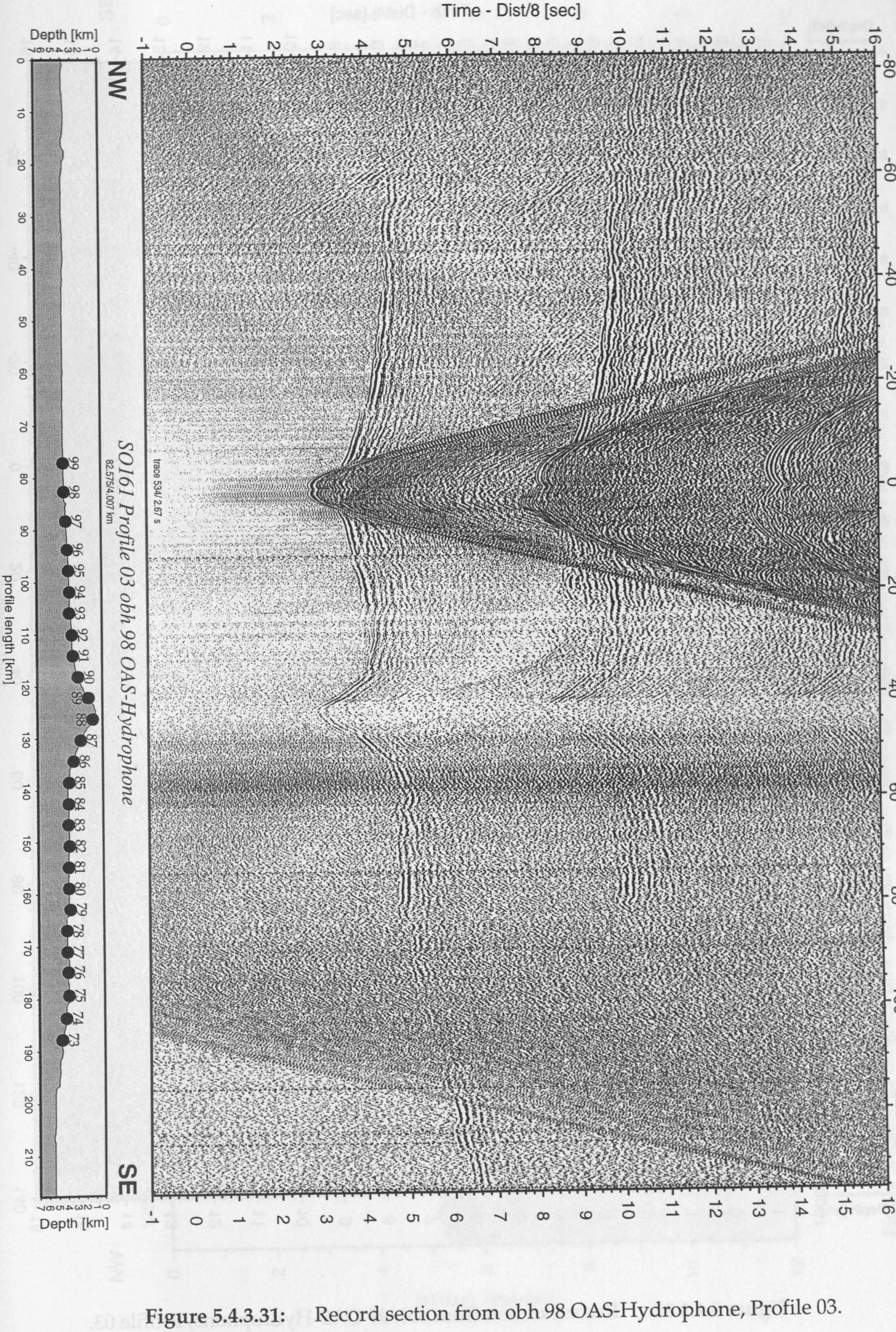

**Figure 5.4.3.31:** Record section from obh 98 OAS-Hydrophone, Profile 03.

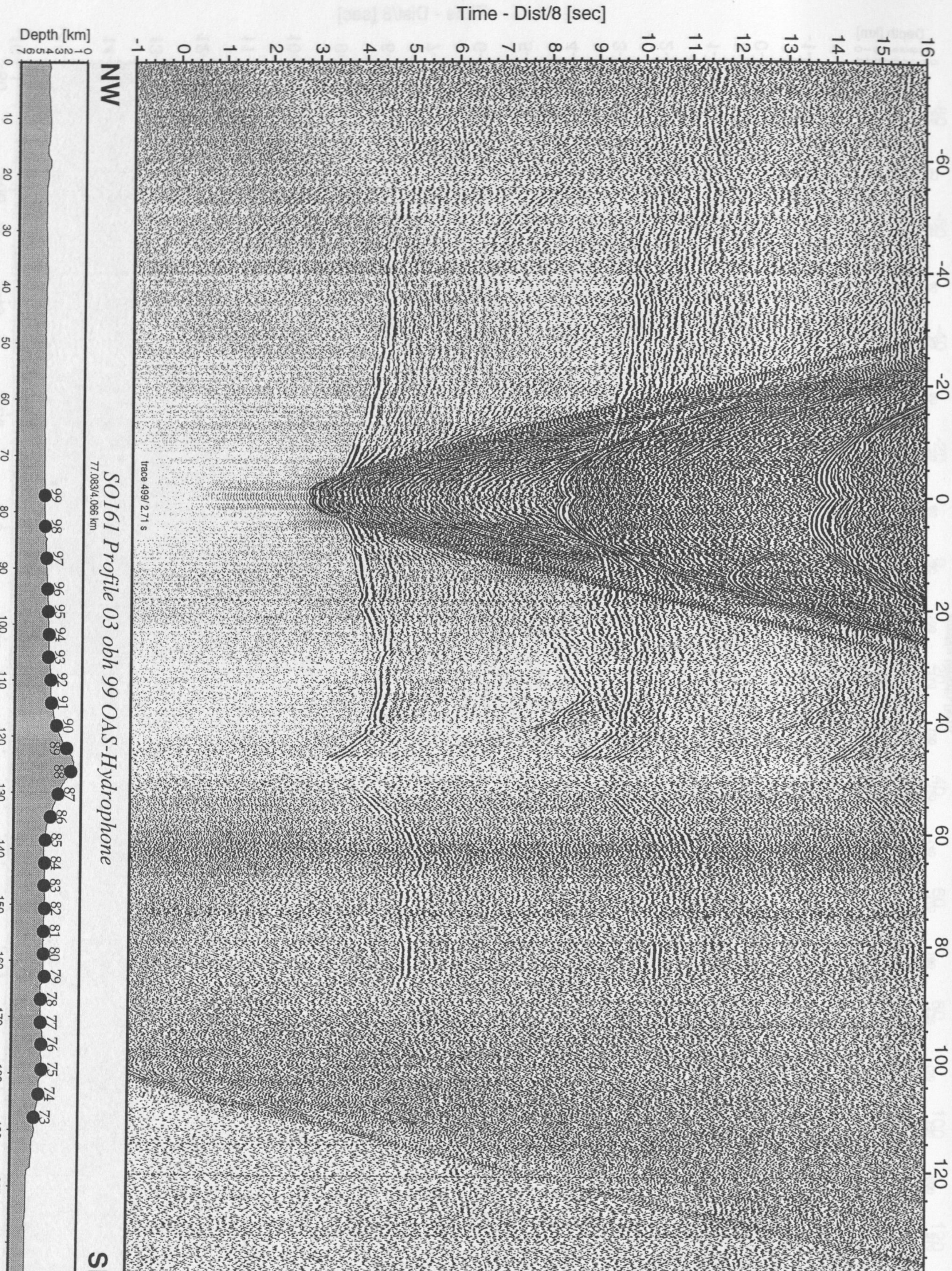

**Figure 5.4.3.32:** Record section from obh 99 OAS-Hydrophone, Profile 03.

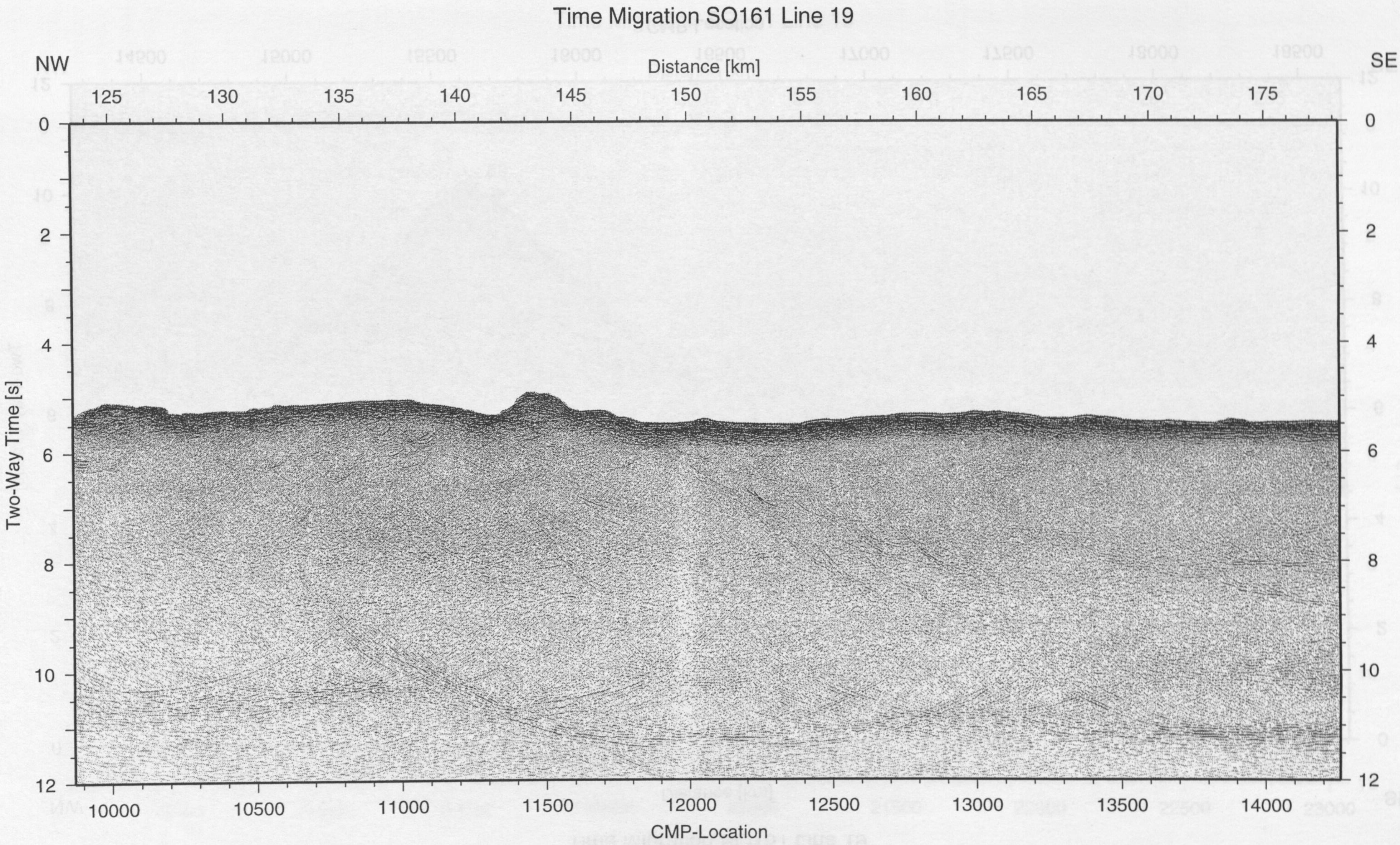

**Figure 5.4.3.33:** Post-stack time migration of Line SO161-19. Superimposed the obh/s locations of Profile 03.

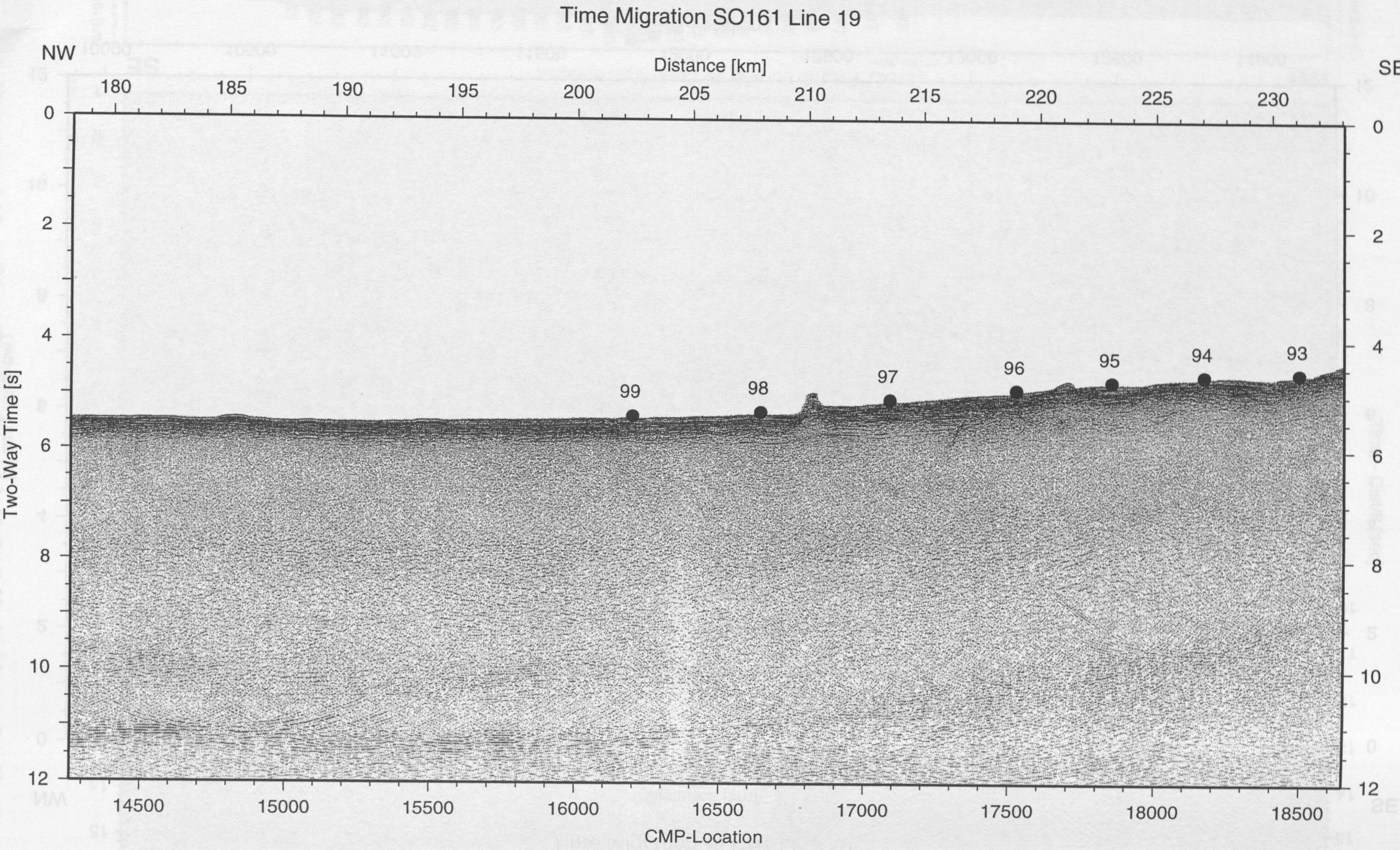

**Figure 5.4.3.34:** Post-stack time migration of Line SO161-19. Superimposed the obh/s locations of Profile 03.

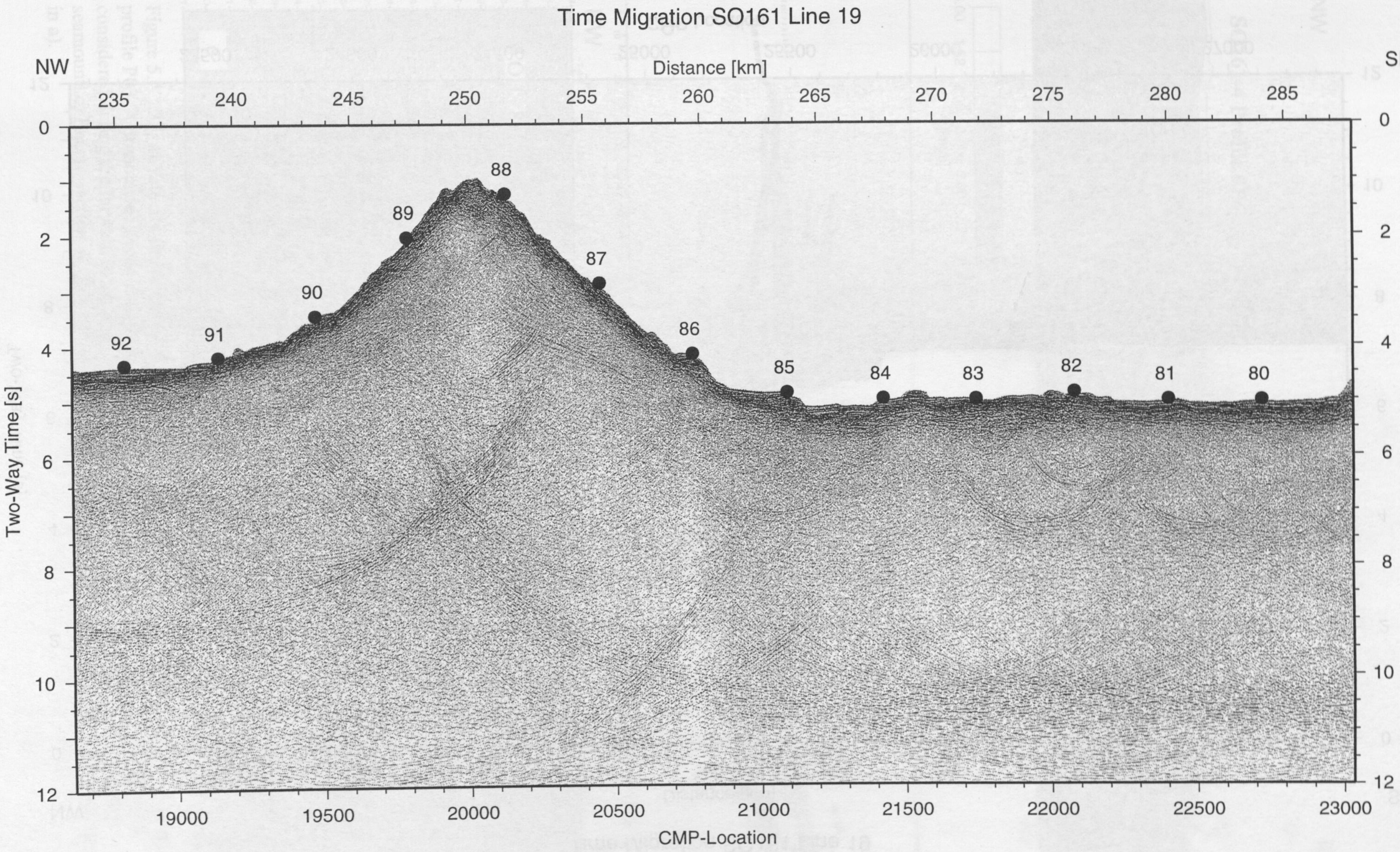

**Figure 5.4.3.35:** Post-stack time migration of Line SO161-19. Superimposed the obh/s locations of Profile 03.

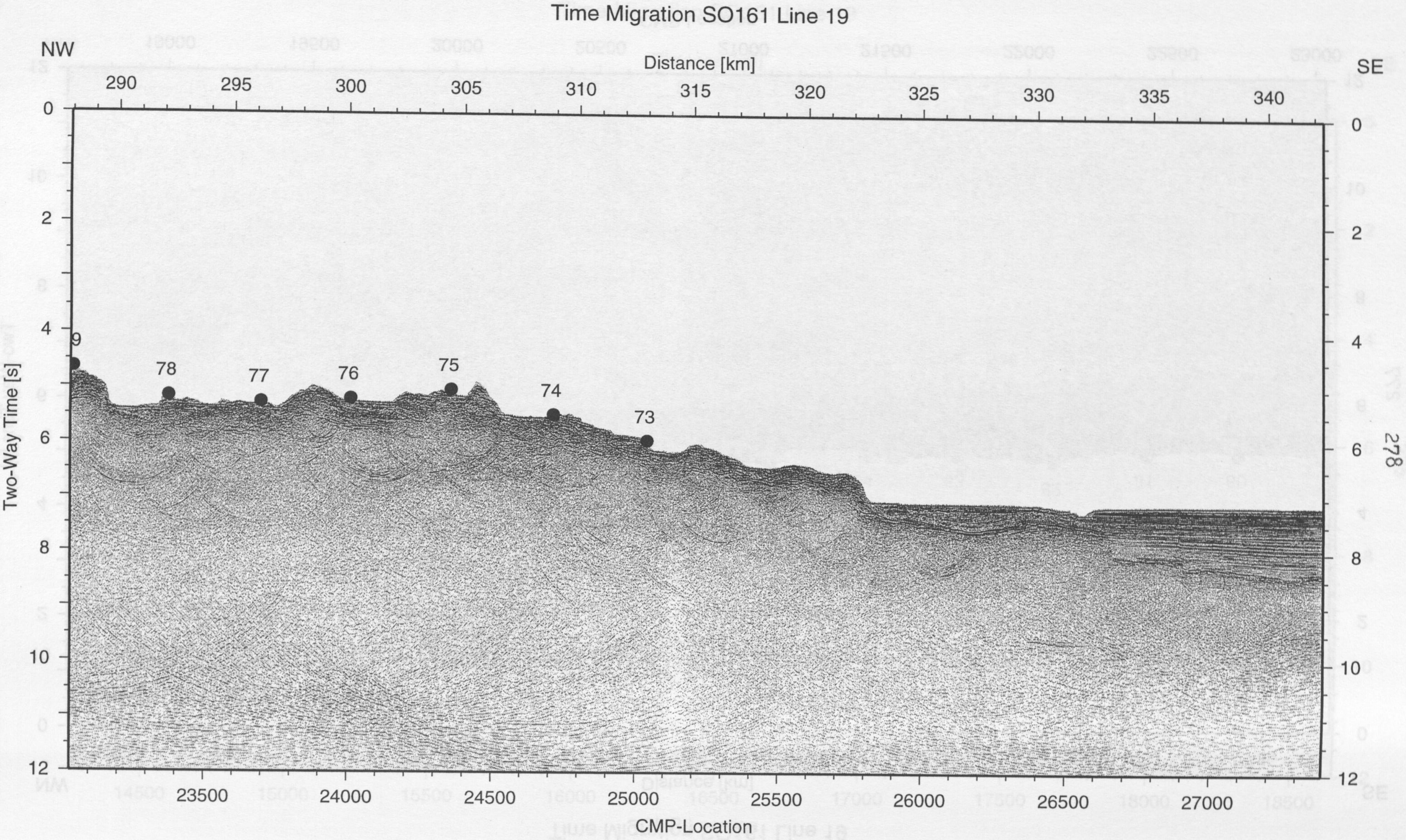

**Figure 5.4.3.36:** Post-stack time migration of Line SO161-19. Superimposed the obh/s locations of Profile 03.

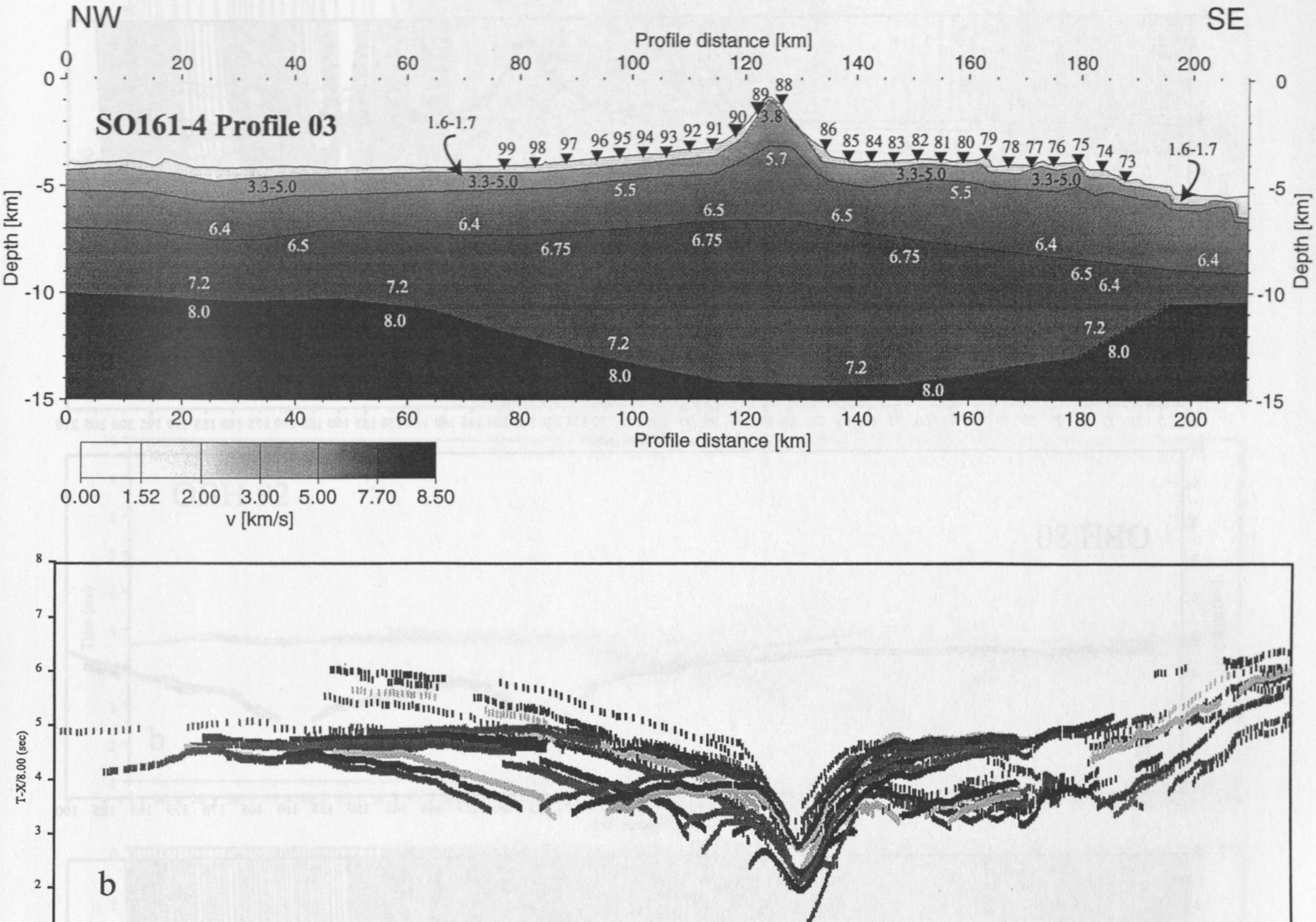

Figure 5.4.3.37: a) Velocity-depth model derived from forward modelling of 21 stations deployed along profile P03. A pronounced Moho deflection is present underneath O'Higgins Seamount. b) Data picks considered during the forward modelling. A good coverage is achieved especially around O'Higgins seamount. c) Record section of OBS 81 overlain by calculated traveltimes resulting from the model shown in a).

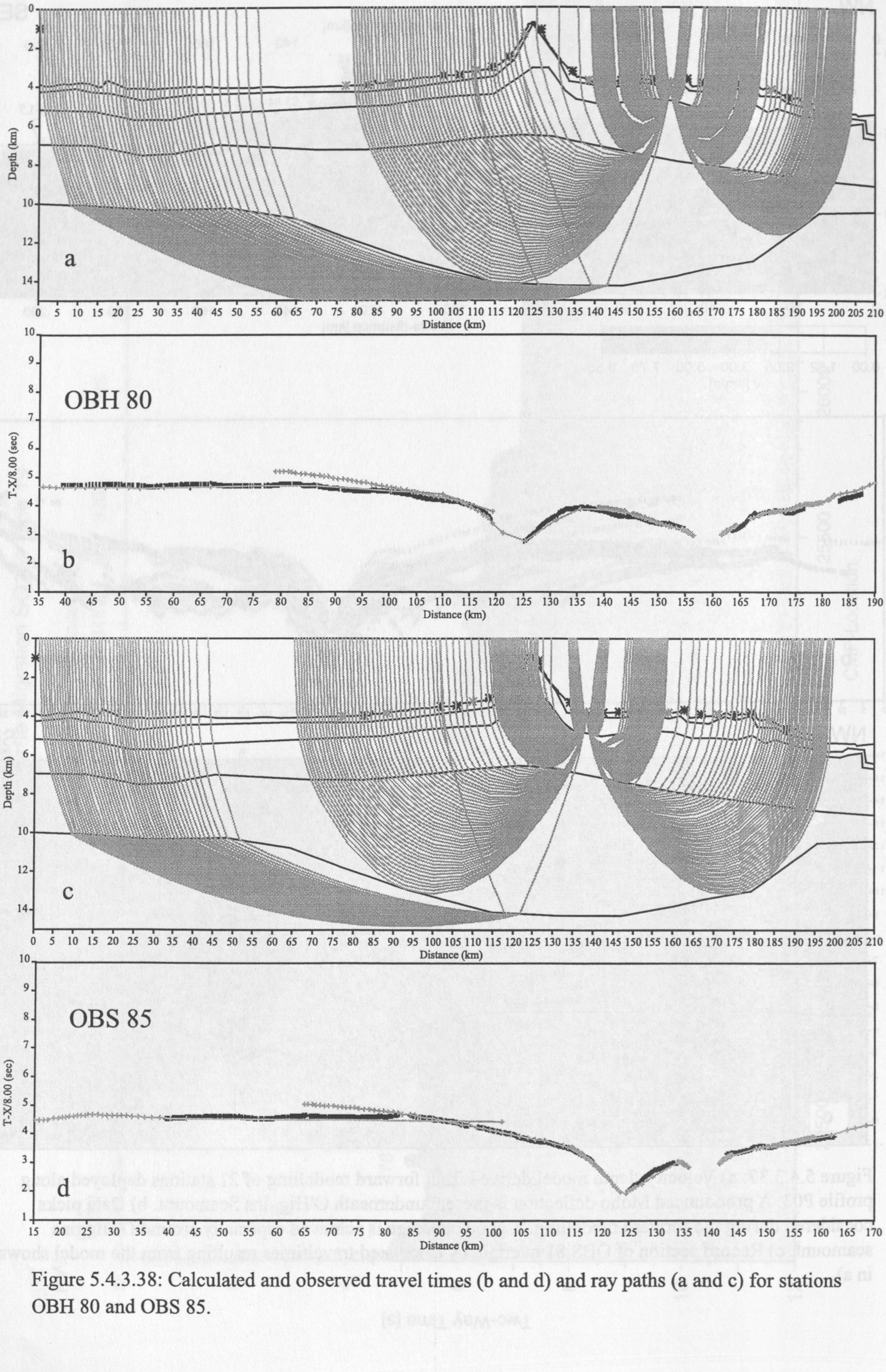

Figure 5.4.3.38: Calculated and observed travel times (b and d) and ray paths (a and c) for stations OBH 80 and OBS 85.

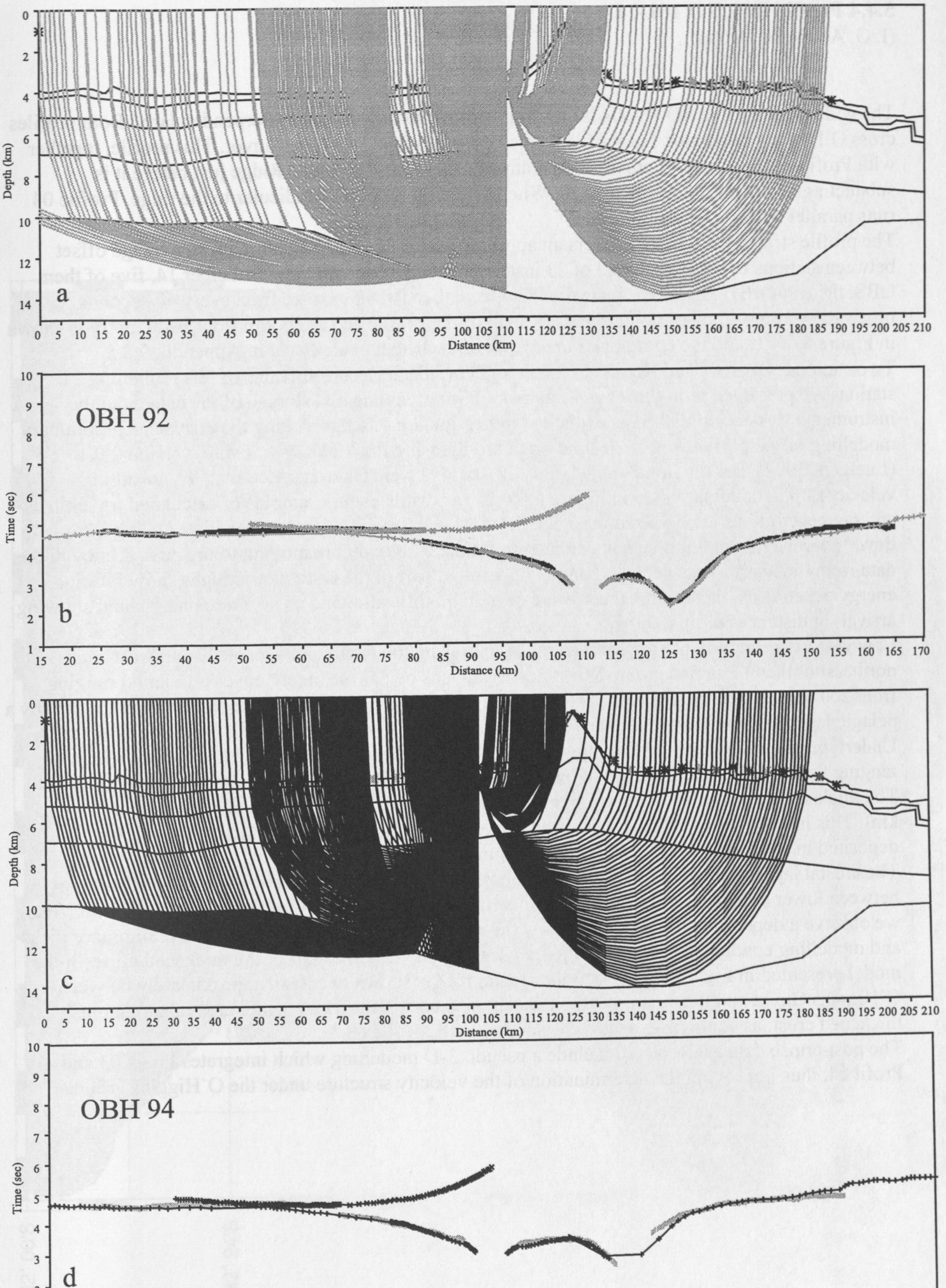

Figure 5.4.3.39: Calculated and observed travel times (b and d) and ray paths (a and c) for stations OBH 92 and OBH 94.

### 5.4.4 Profile P04, SO 161-04

(I. G. Arroyo, H. Kopp)

The wide angle Profile SO 161-04 is crossing Profile SO 161-03 nearly perpendicularly. Both profiles cross O´Higgins seamount, but Profile 04 also extends over O´Higgins Guyot. This profile, together with Profile 03, was shot to provide constraints on the Juan Fernández Ridge just before it is subducting beneath the Chilean margin. Whereas Profile 03 is perpendicular to the ridge, Profile 04 runs parallel to it.

The profile strikes SW-NE and covers an approximate distance of 140 km with an average offset between stations of 2.8 nm. A total of 23 instruments were deployed on December 14, five of them OBS, the rest OBH. They were recovered on December 16. Shots were fired every 60 seconds, proceeding from southwest to northeast. A map of the profile and the ocean floor bathymetry is shown in Figure 5.4.4.1, and the coordinates and depth of each station are listed in Appendix 9.3.5.

Two stations (OBS101 and OBH111) failed to record data. Record sections of the remaining 21 stations are presented in Figures 5.4.4.2 to 5.4.4.23. Processing and storage of the data from the instruments was accomplished as explained in Section 4.6.1. After picking the arrivals, a preliminary modelling of the profile was carried out on board by using the MacRay software, version 2.0.1 (Luetgert, 1992). For the initial model, only 12 stations were taken into account. The resulting velocity-depth model is shown in Figure 5.4.4.24 (a), while some examples of calculated traveltimes and ray penetrations are depicted in Figure 5.4.4.24 (b). Traveltimes were calculated using a 'top-down' approach, modelling velocity and depth for each layer before moving to the next. Although the data from the instruments deployed on the uppermost part of the bathymetric highs show inferior energy penetration, most of the records are of high quality, allowing an accurate picking and showing arrivals at distances of up to 80 km.

Low velocity refraction phases are seen in the data from the instruments located southwest and northeast of the O´Higgins group. We interpret them as pelagic sediment cover (1.6 km/s) ranging from 200 m to 500 m in thickness. The depression between the guyot and the seamount is covered by a pelagic layer with an average thickness of 250 m.

Underlying the sediment cover, an upper crustal layer with a thickness of 1-2 km and velocities ranging from 3.3-5.0 km/s, similar to the one described for Profile 03, was detected along Profile 04. The thickness of this layer increases significantly in the O´Higgins Guyot and Seamount area (~ 2.5 km). This layer is believed to be composed of volcanoclastic sequences, which may have been deposited in shallow water or subaerial environment.

The crustal layering closely follows the morphology of the guyot and the seamount. The boundary between lower and upper crust is uplifted underneath both the O´Higgins Guyot and Seamount. Also, we observe a depression of the Moho below these bathymetric highs. However, the preliminary picks and modelling conduced on board could not ascertain the lateral extent of the thickened crust. In the model presented in Figure 5.4.4.24 (a) the crustal root is shown to extend approximately between O´Higgins Guyot and Seamount but the data are also consistent with a wider area of anomalously thickened crust, as could be expected by analogy with Profile 03.

The post-cruise data analysis will include a pseudo 3-D modelling which integrates Profil 03 and Profil 04, thus improving the determination of the velocity structure under the O´Higgins group.

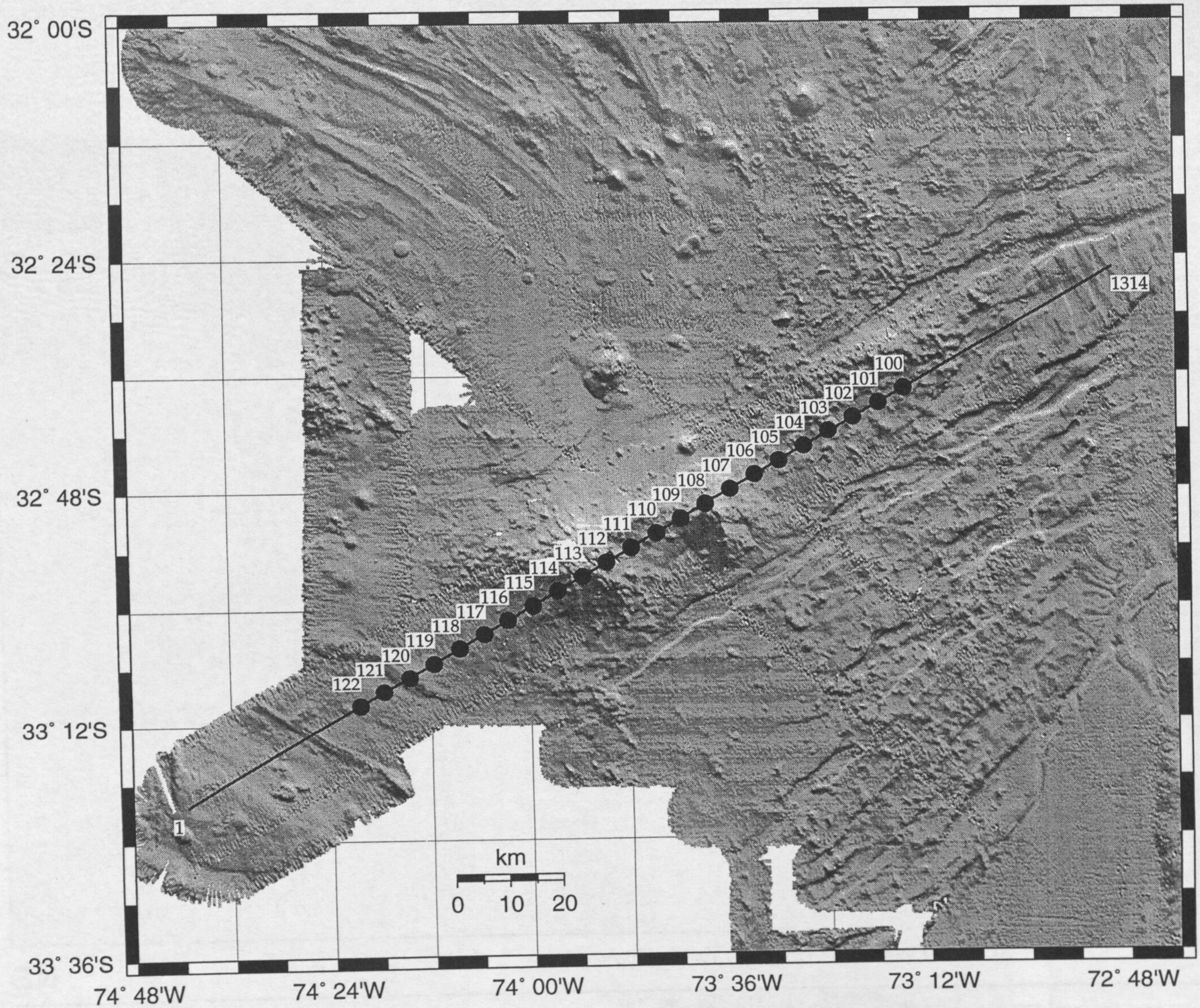

**Figure 5.4.4.1:** Location map of profile 4 and illuminated multibeam bathymetry. Superimposed the obh/obs locations, the first, and last shotpoint number.

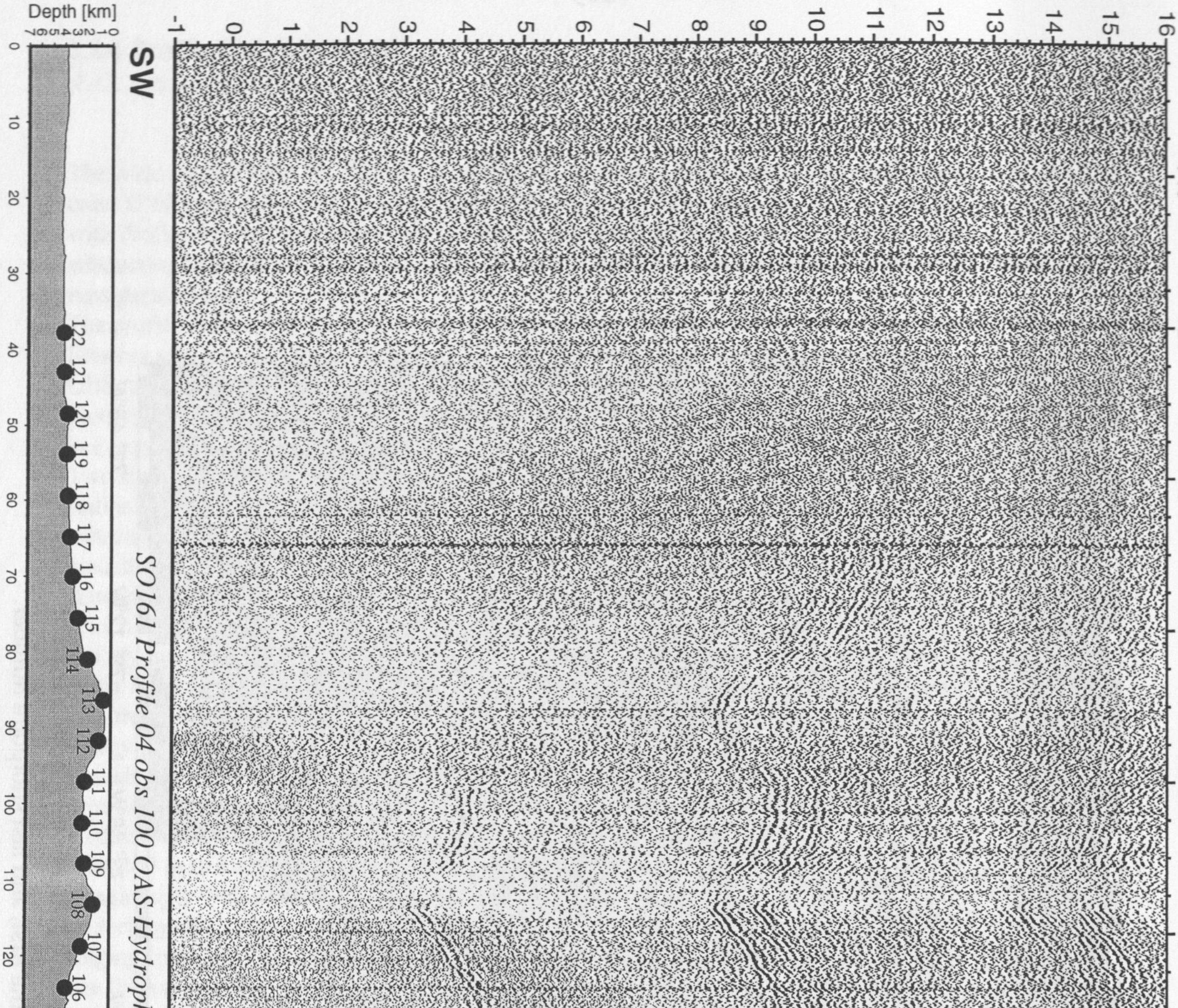

**Figure 5.4.4.2:** Record section from obs 100 OAS-Hydrophone, Profile 04.

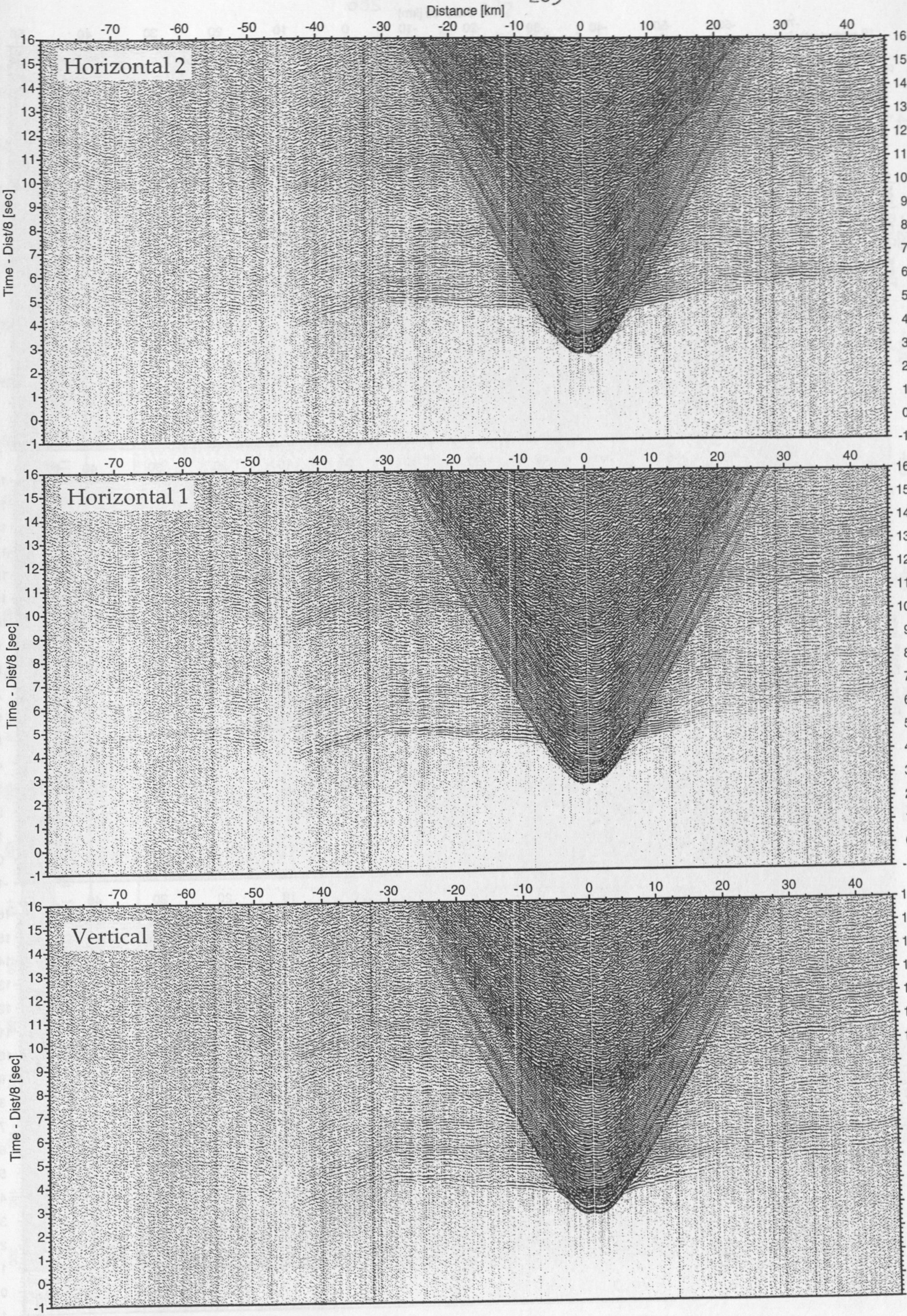

**Figure 5.4.4.3:** Record sections from obs 100 OAS/A01-4.5Hz, SO161 Profile 04.

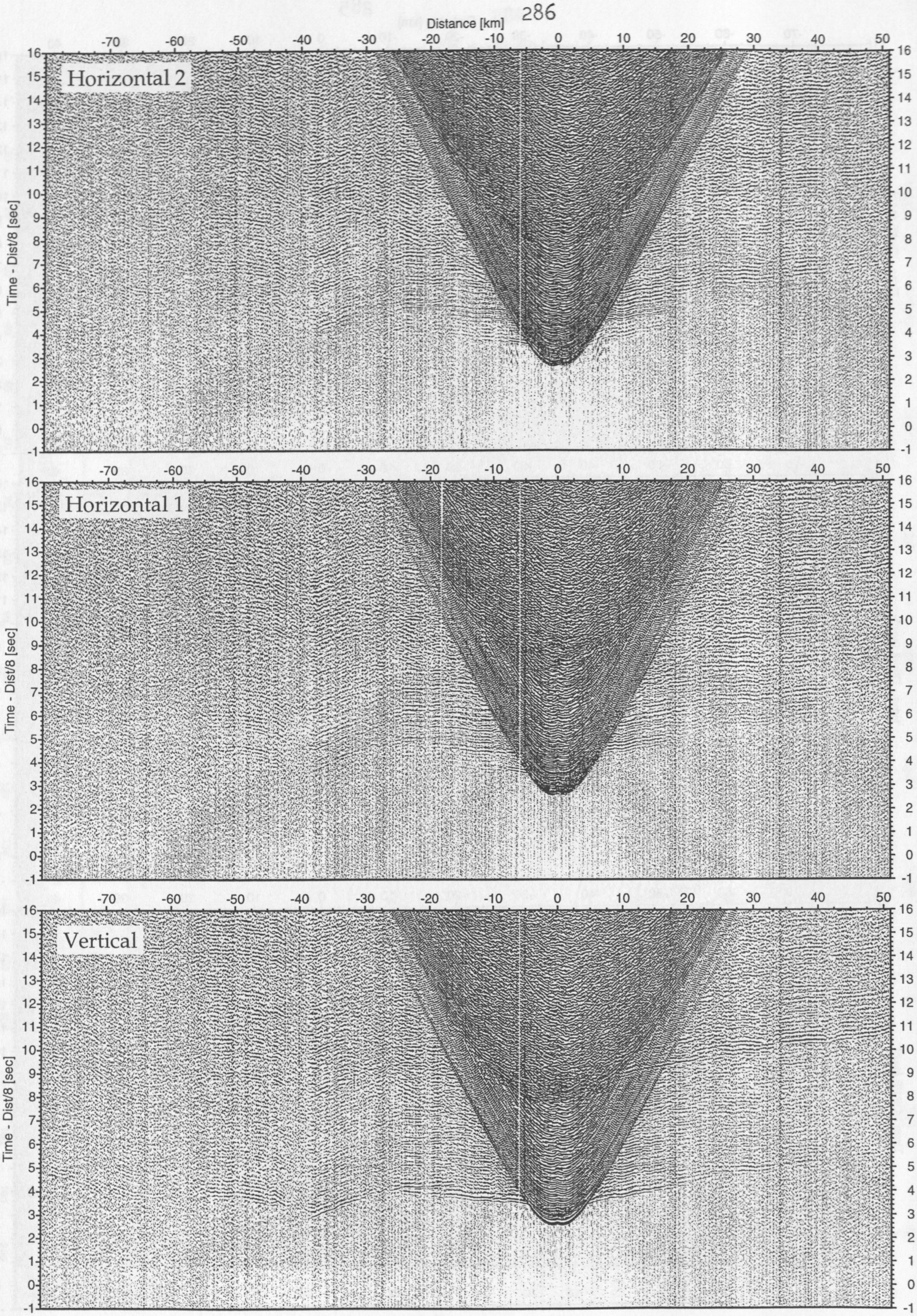

**Figure 5.4.4.4:** Record sections from obs 101 DPG/PMD, SO161 Profile 04.

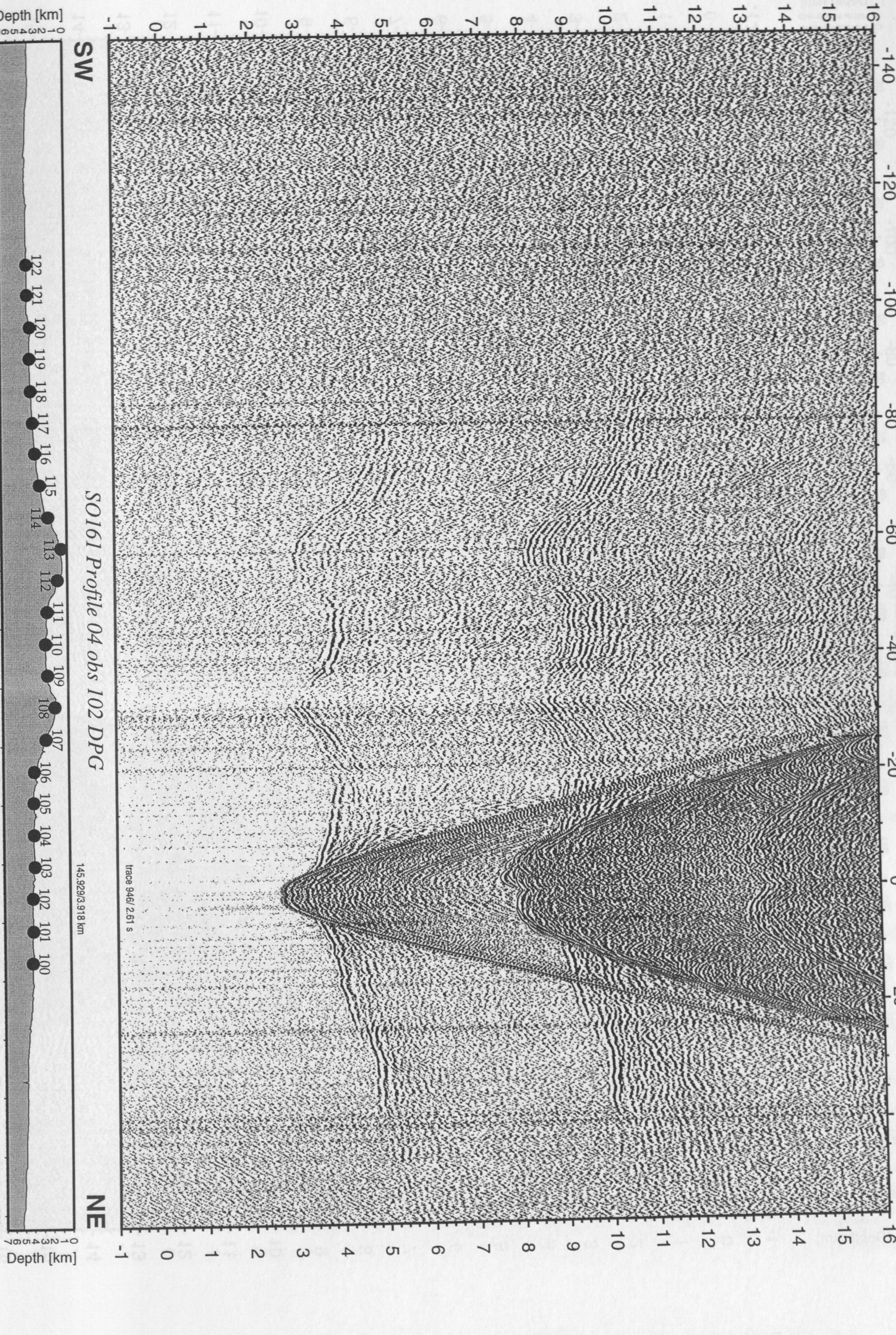

**Figure 5.4.4.5:** Record section from obs 102 DPG, Profile 04.

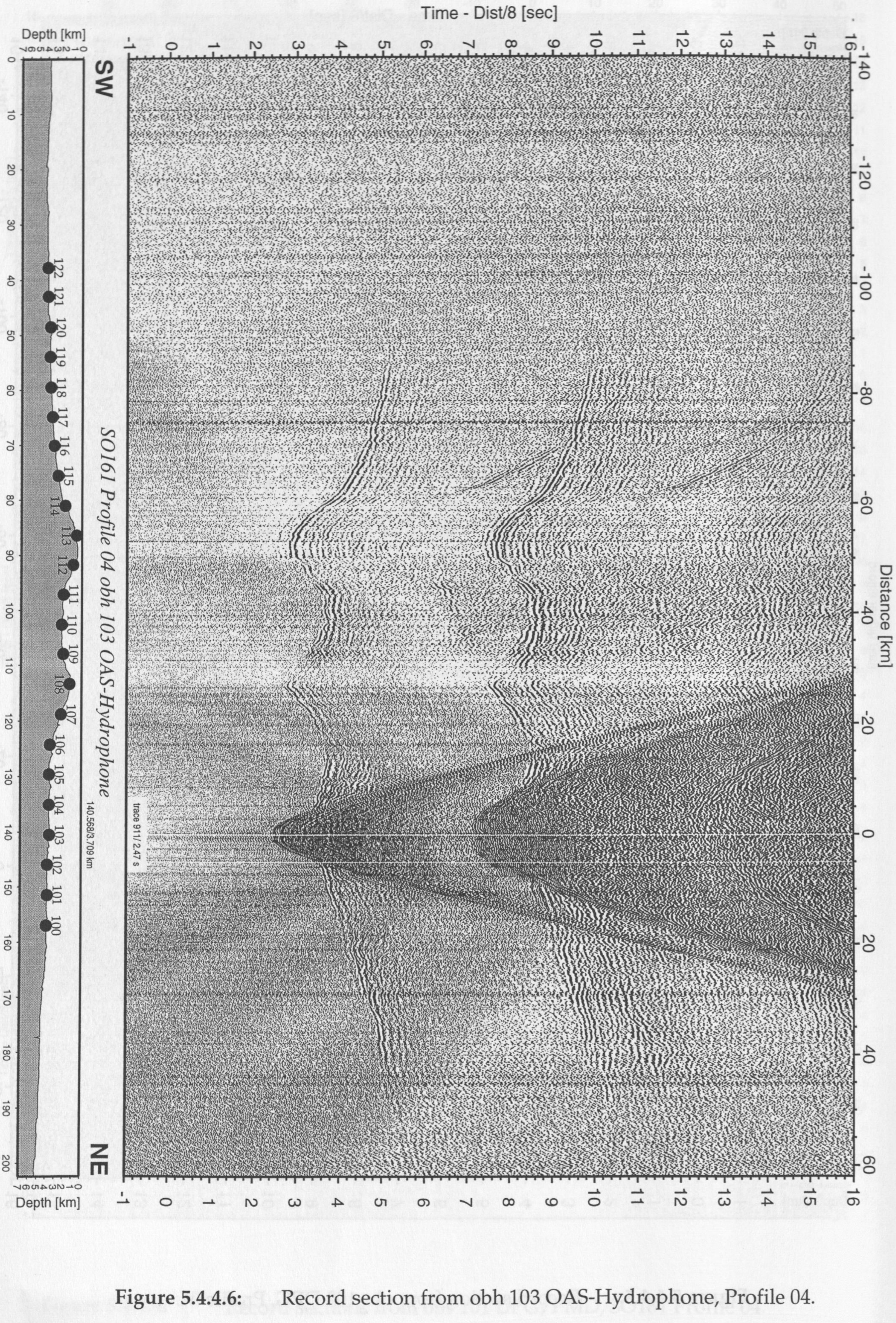

**Figure 5.4.4.6:** Record section from obh 103 OAS-Hydrophone, Profile 04.

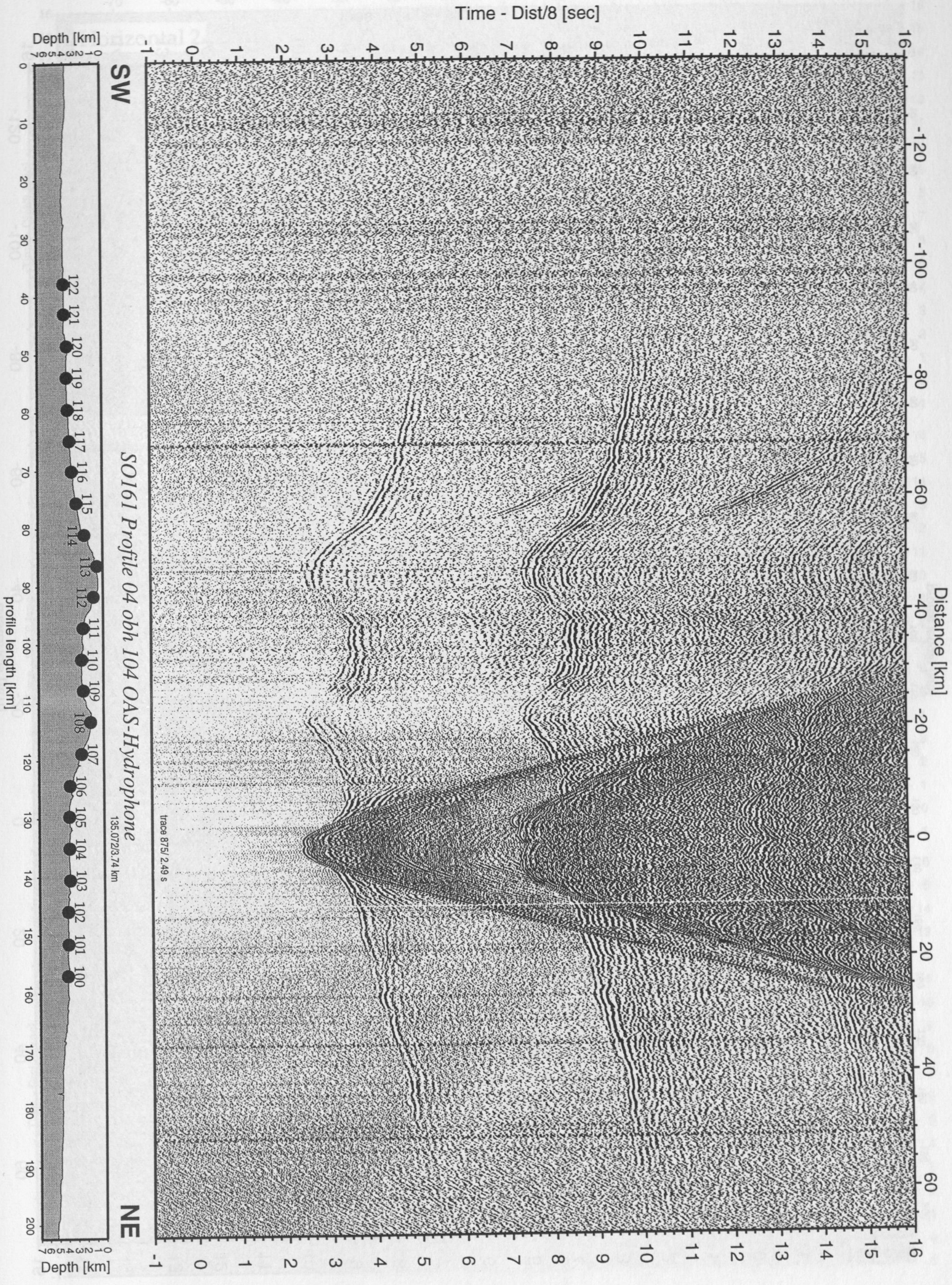

**Figure 5.4.4.7:** Record section from obh 104 OAS-Hydrophone, Profile 04.

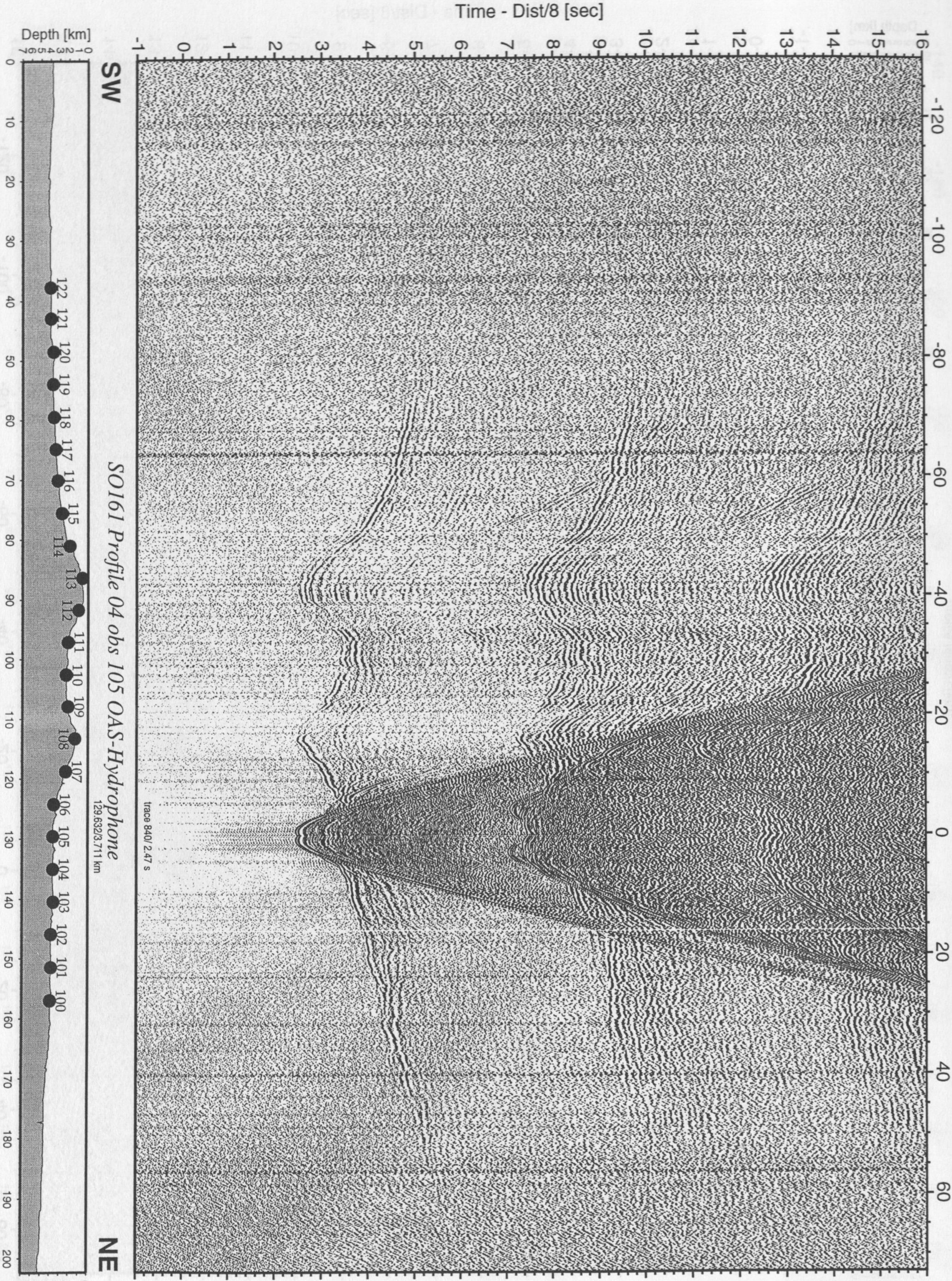

**Figure 5.4.4.8:** Record section from obs 105 OAS-Hydrophone, Profile 04.

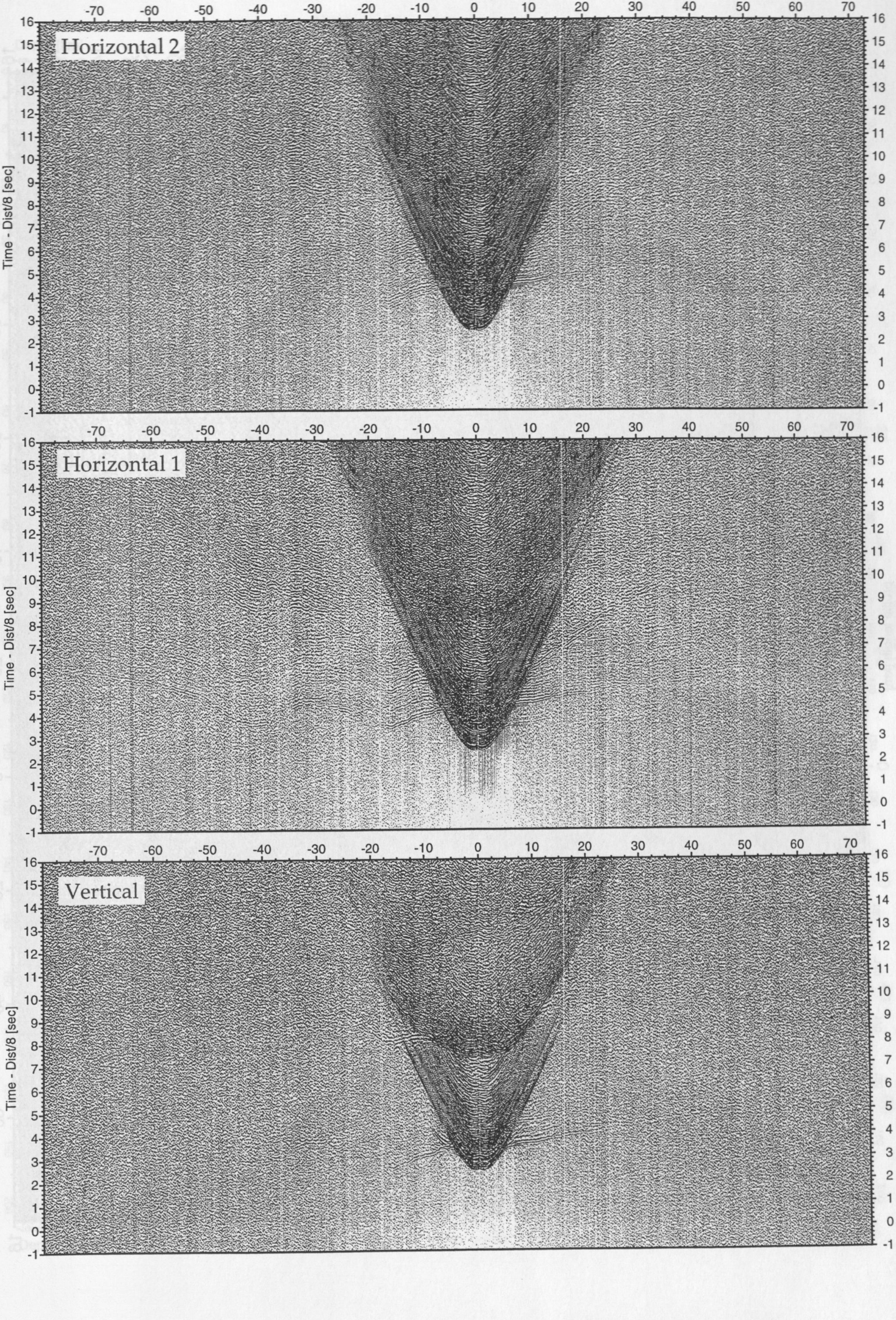

**Figure 5.4.4.9:** Record sections from obs 105 OAS/Owen-4.5Hz, SO161 Profile 04.

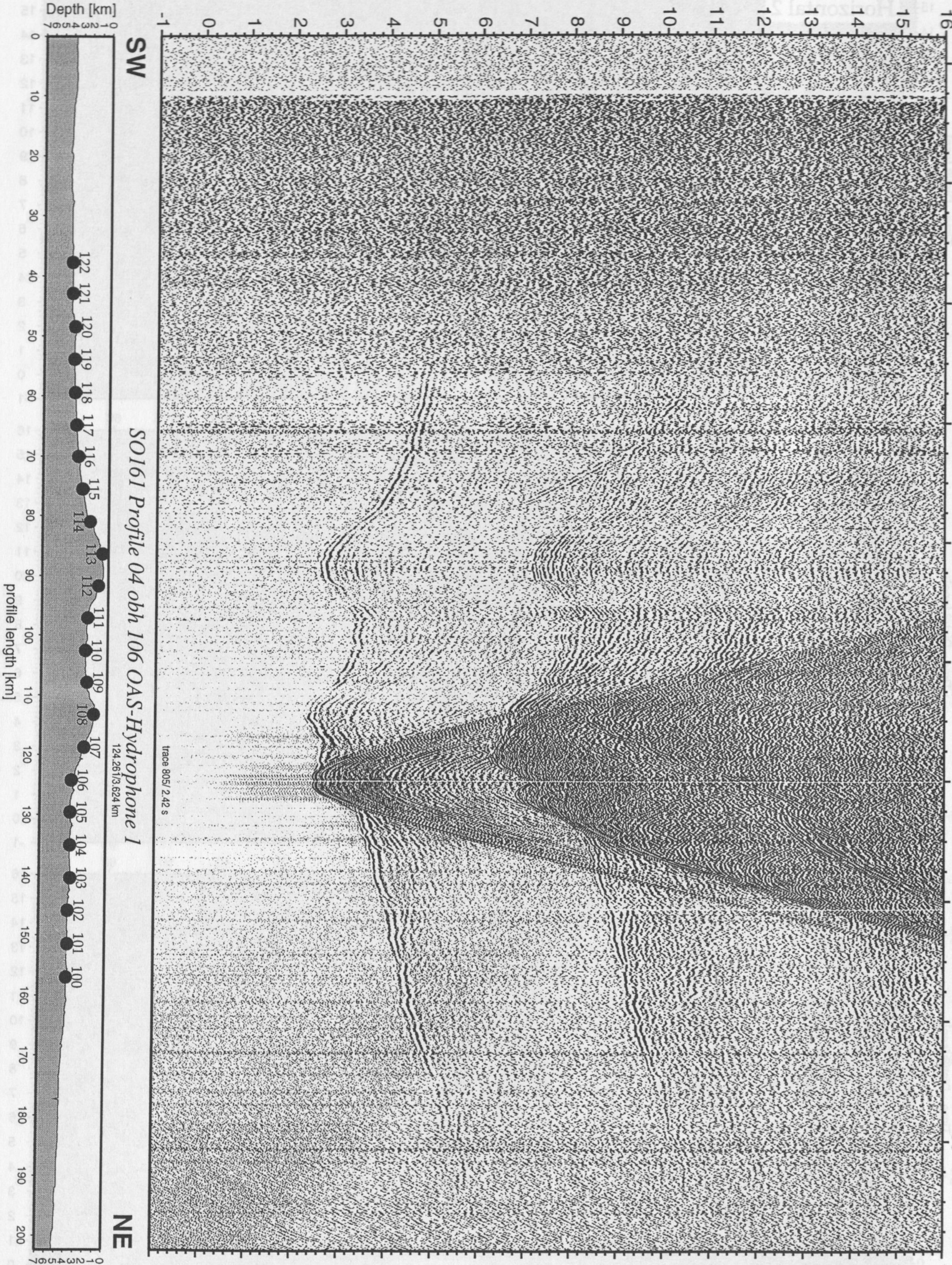

**Figure 5.4.4.10:** Record section from obh 106 OAS-Hydrophone 1, Profile 04.

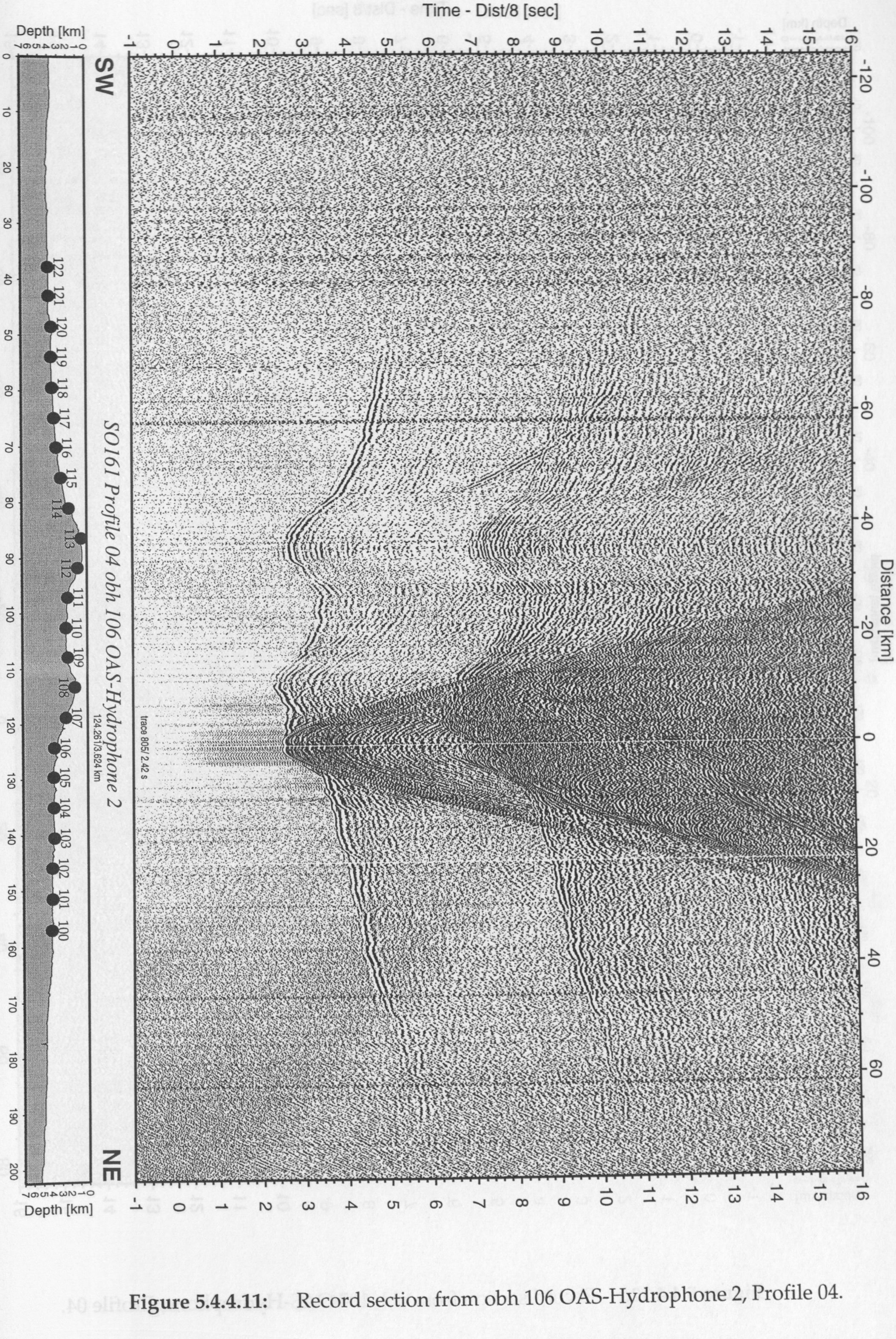

**Figure 5.4.4.11:** Record section from obh 106 OAS-Hydrophone 2, Profile 04.

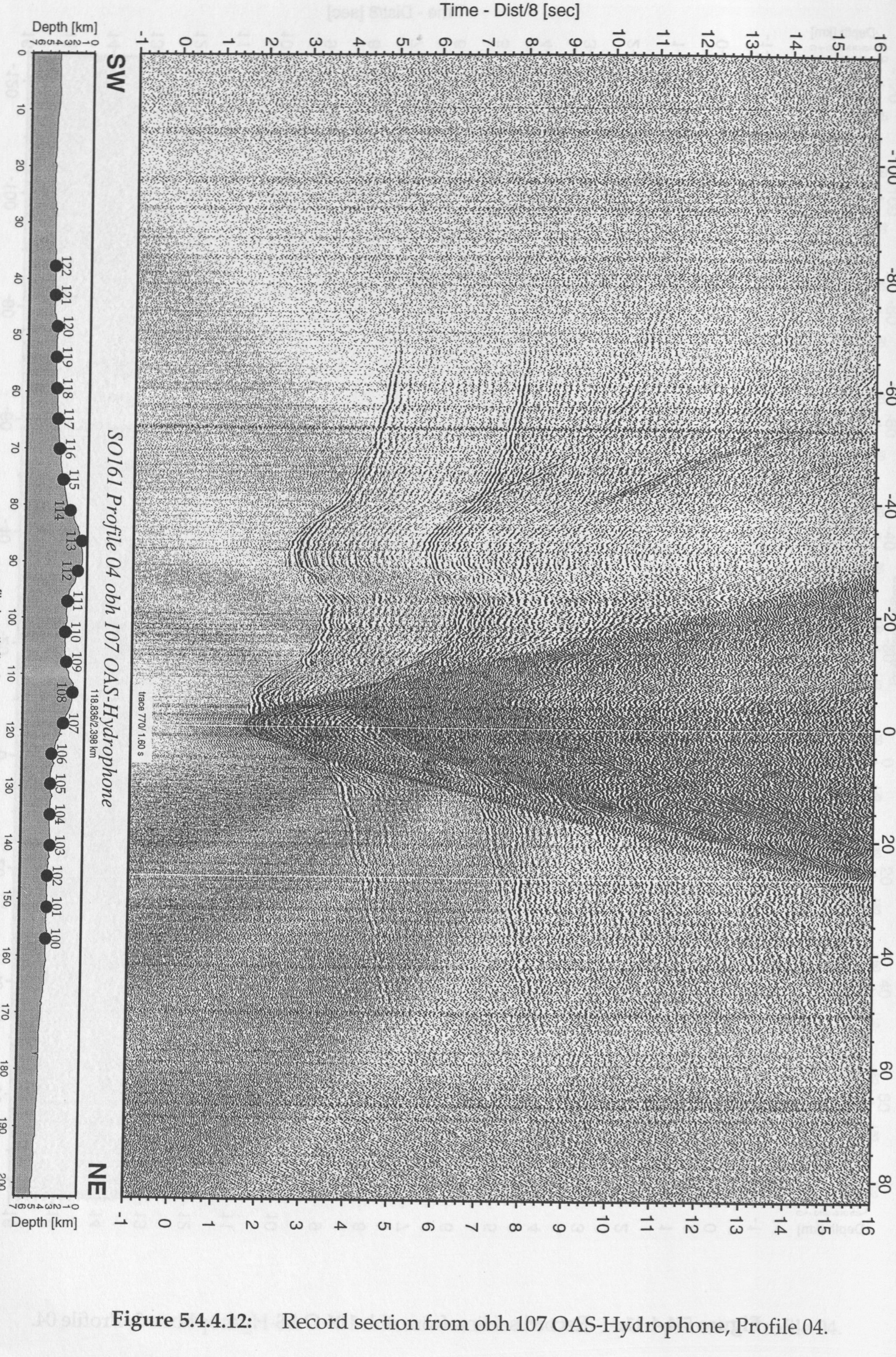

Figure 5.4.4.12: Record section from obh 107 OAS-Hydrophone, Profile 04.

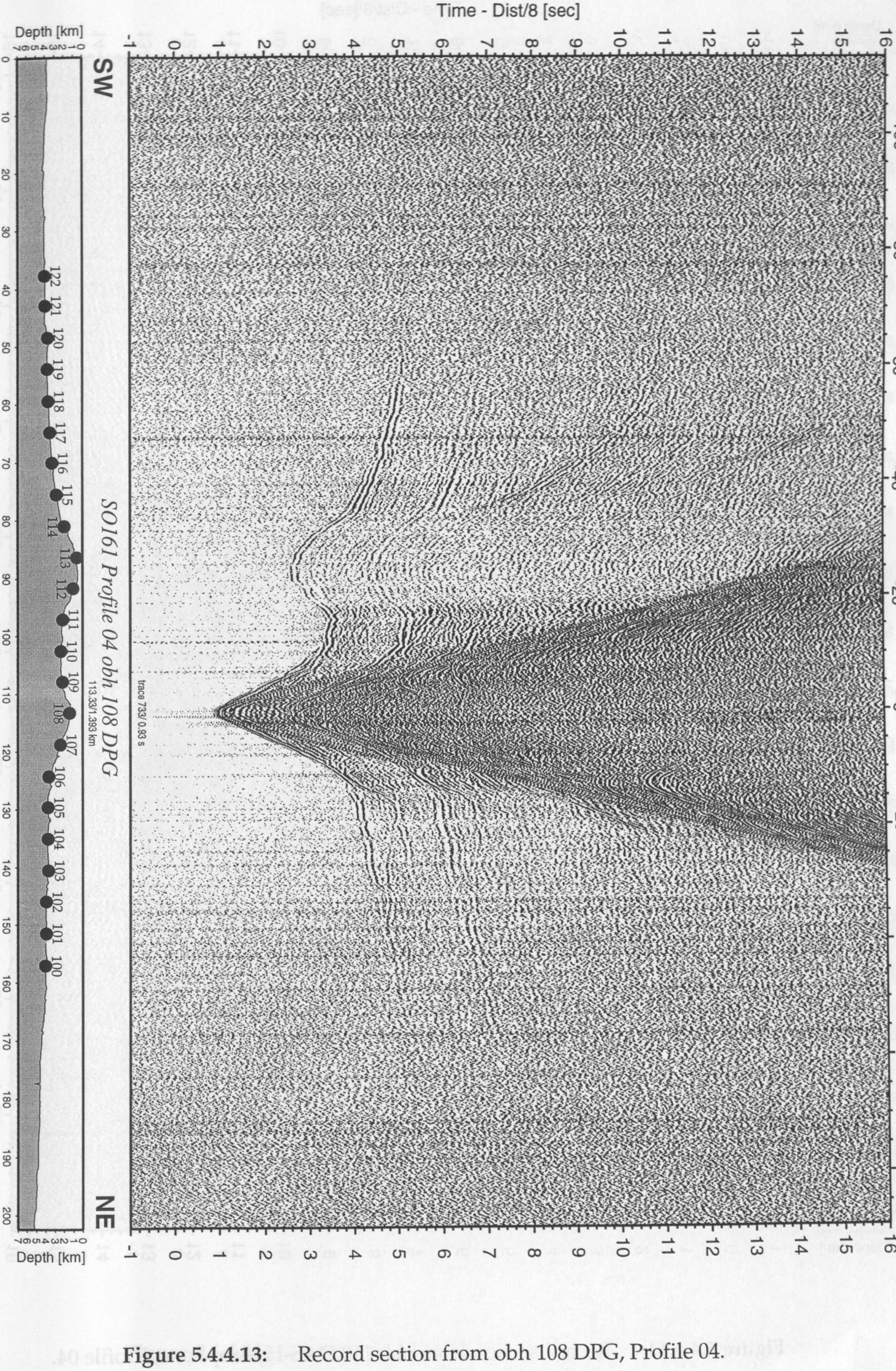

**Figure 5.4.4.13:** Record section from obh 108 DPG, Profile 04.

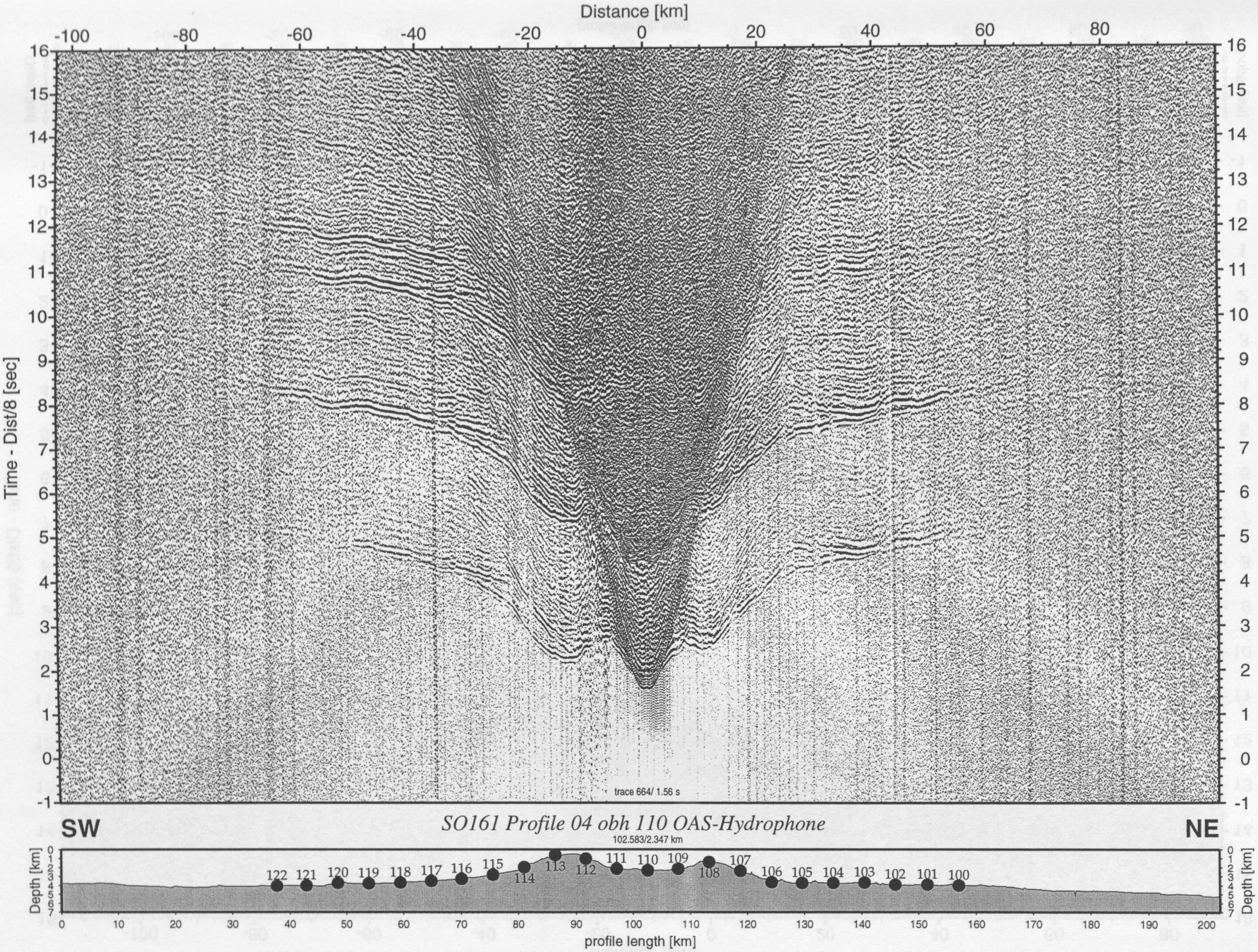

**Figure 5.4.4.14:** Record section from obh 110 OAS-Hydrophone, Profile 04.

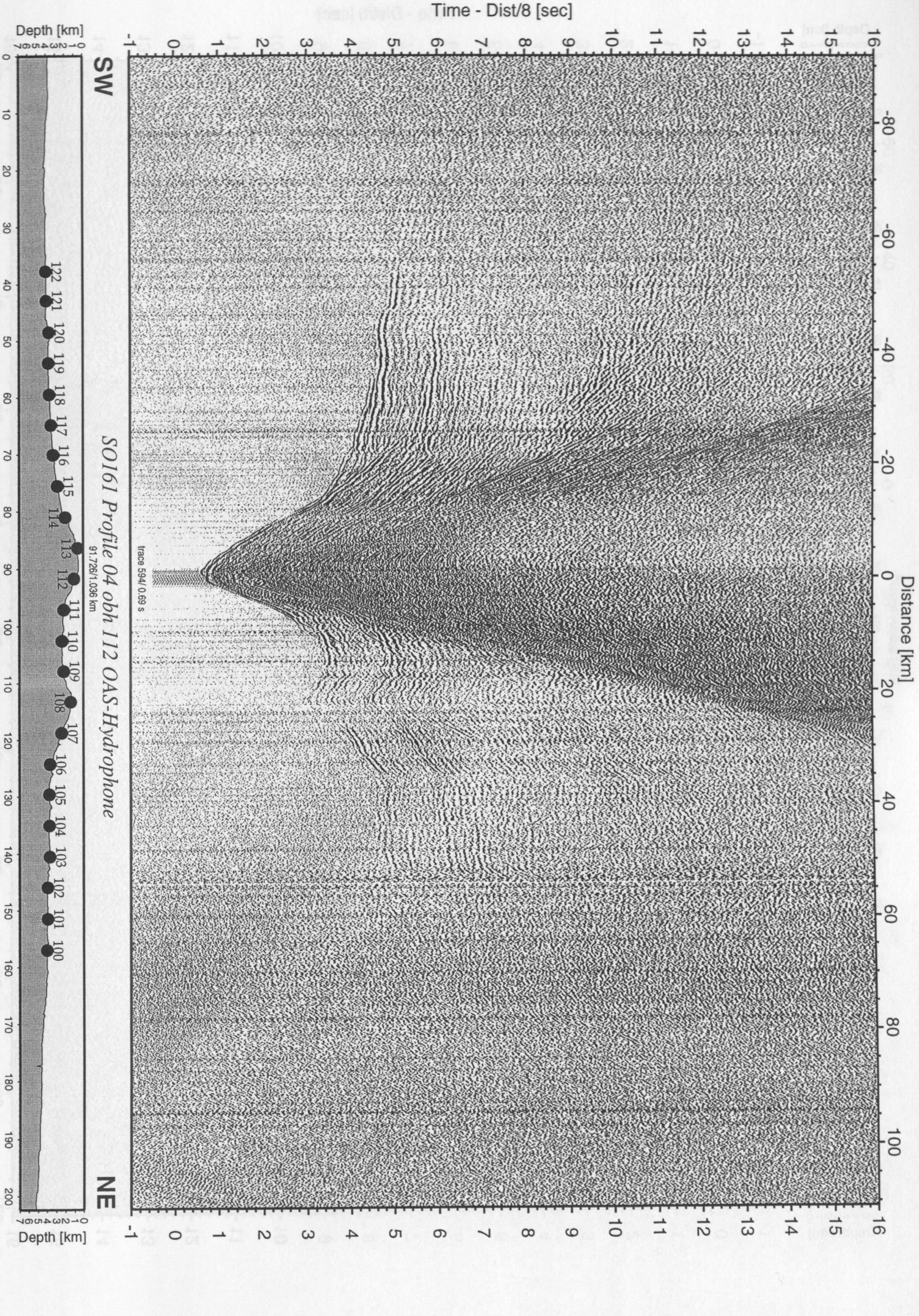

**Figure 5.4.4.15:** Record section from obh 112 OAS-Hydrophone, Profile 04.

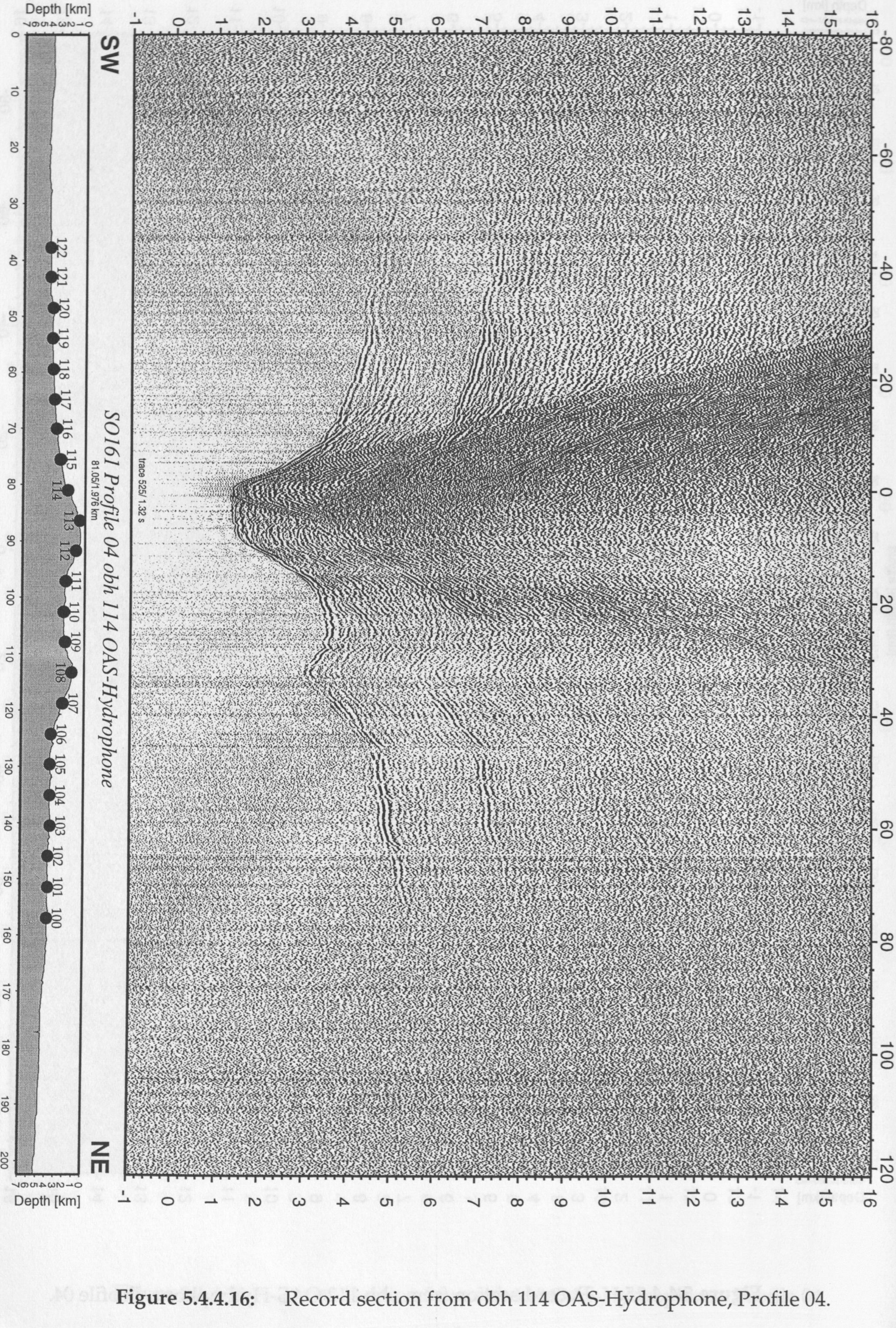

**Figure 5.4.4.16:** Record section from obh 114 OAS-Hydrophone, Profile 04.

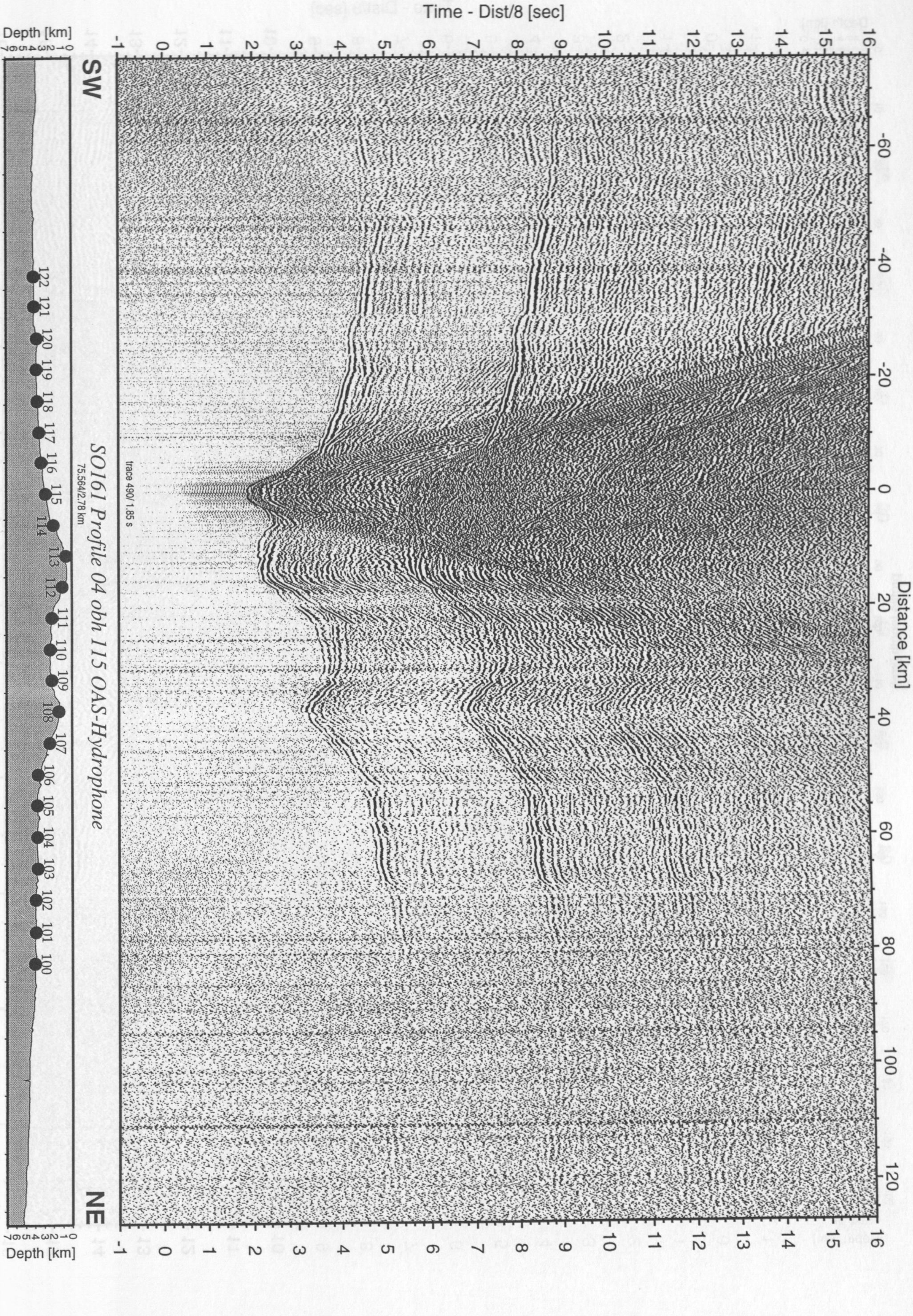

**Figure 5.4.4.17:** Record section from obh 115 OAS-Hydrophone, Profile 04.

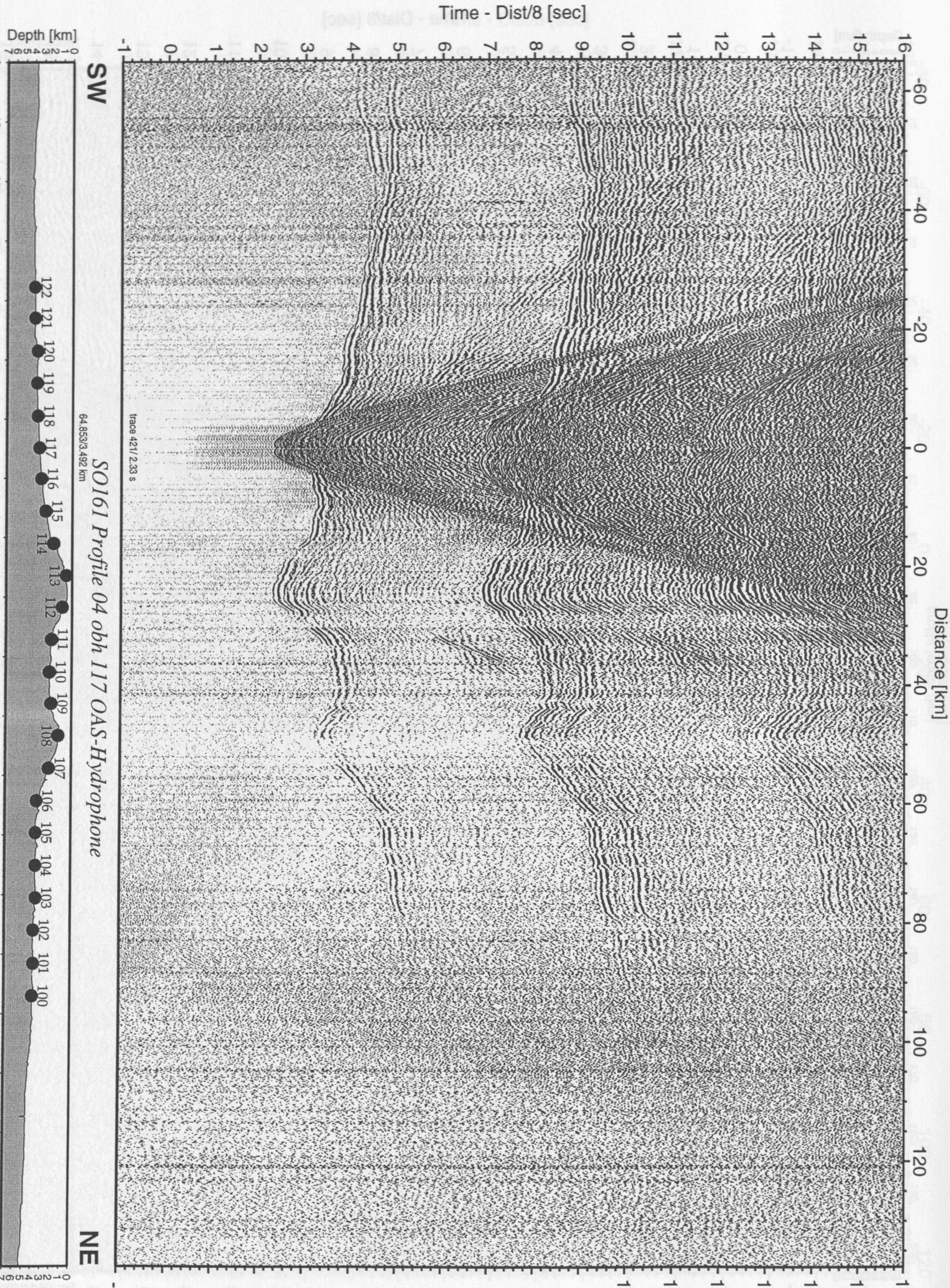

**Figure 5.4.4.18:** Record section from obh 117 OAS-Hydrophone, Profile 04.

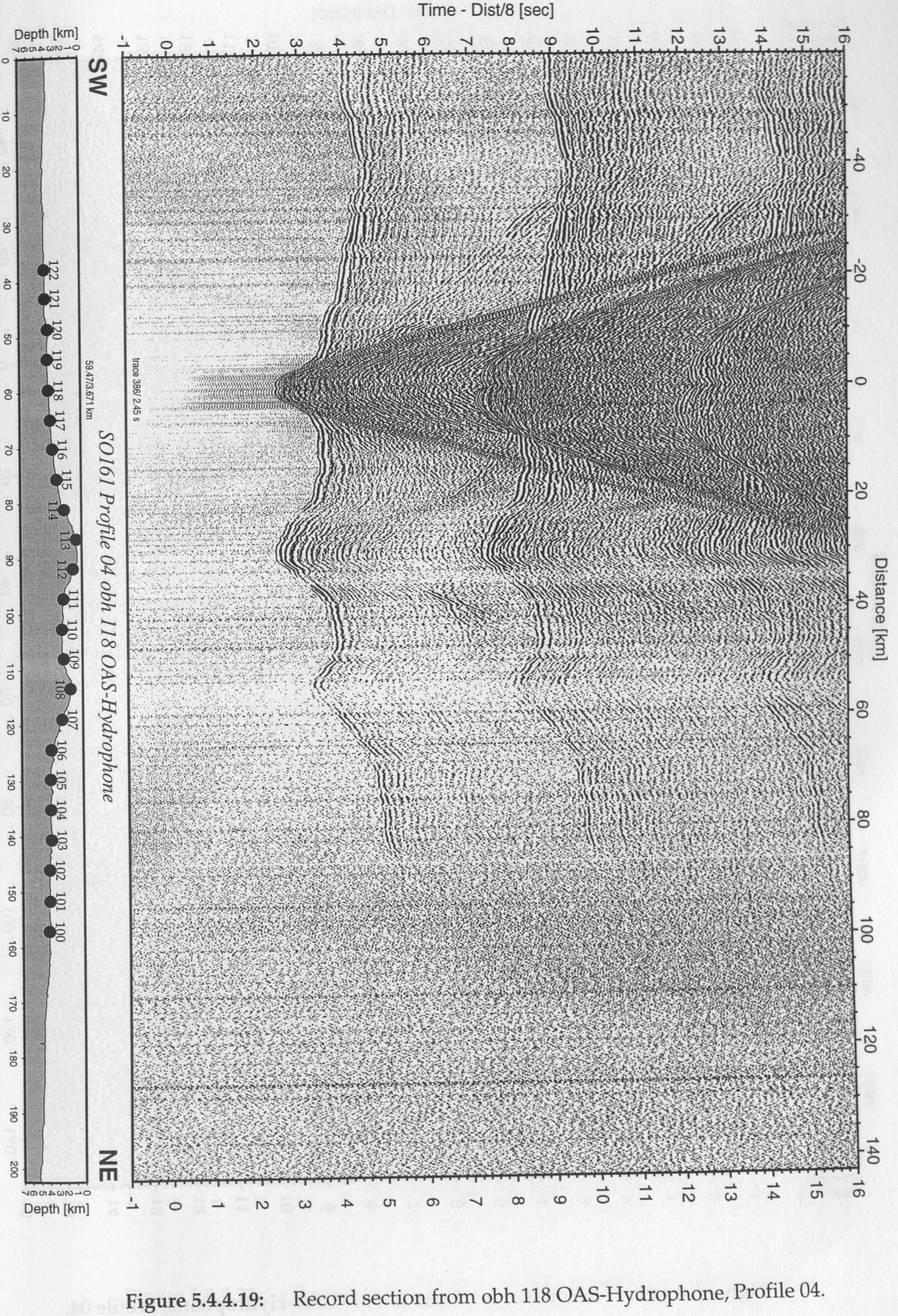

**Figure 5.4.4.19:** Record section from obh 118 OAS-Hydrophone, Profile 04.

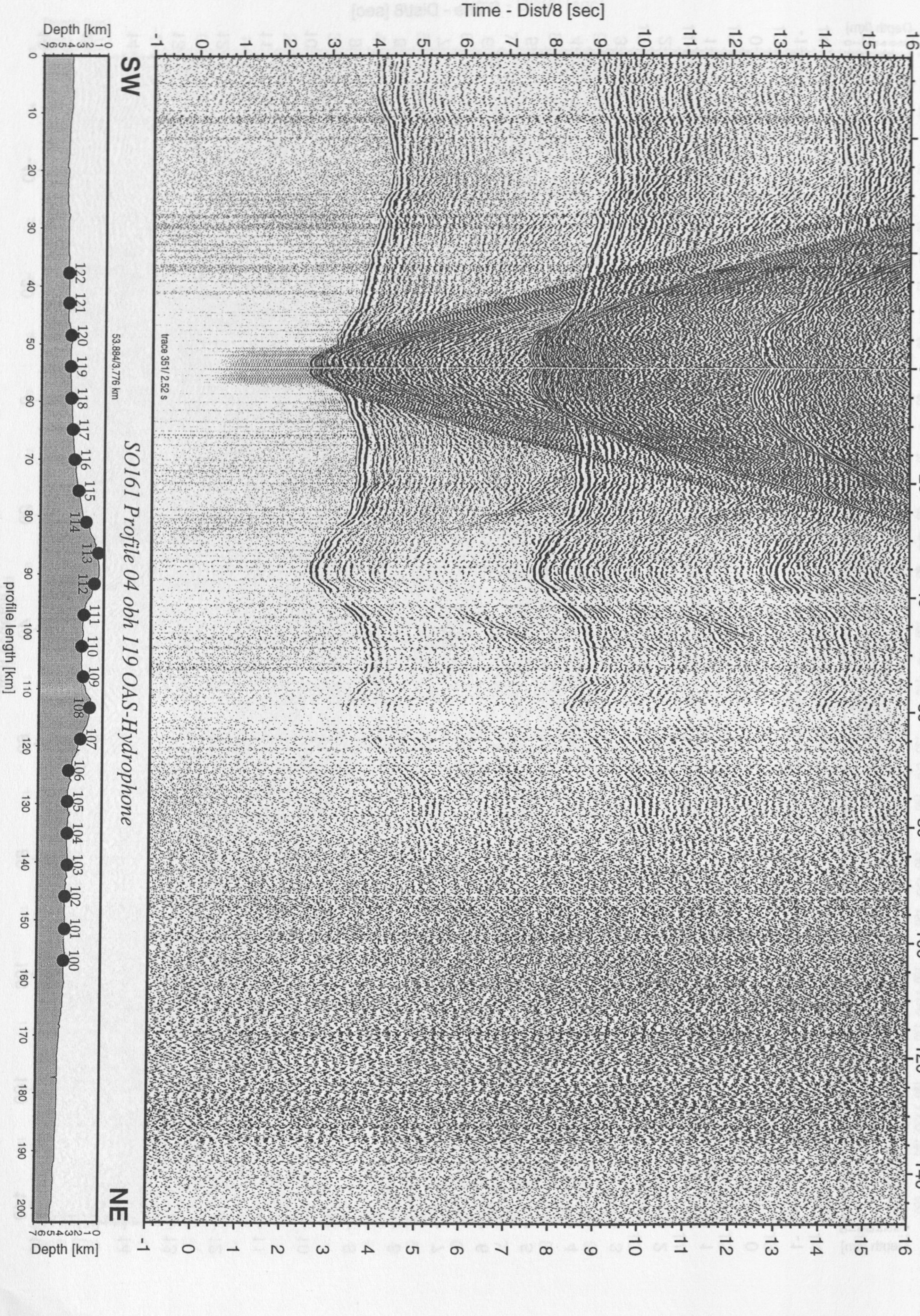

**Figure 5.4.4.20:** Record section from obh 119 OAS-Hydrophone, Profile 04.

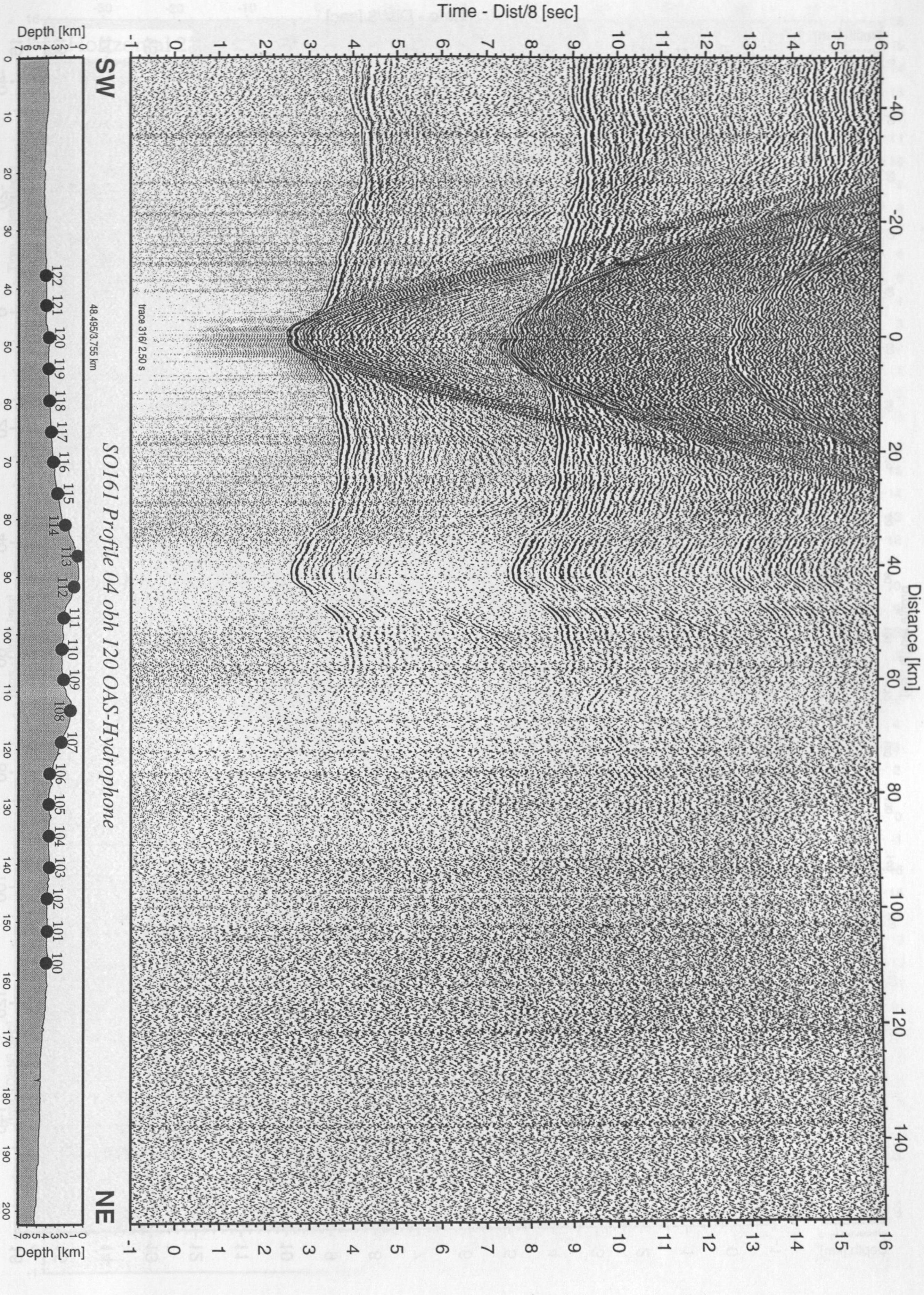

**Figure 5.4.4.21:** Record section from obh 120 OAS-Hydrophone, Profile 04.

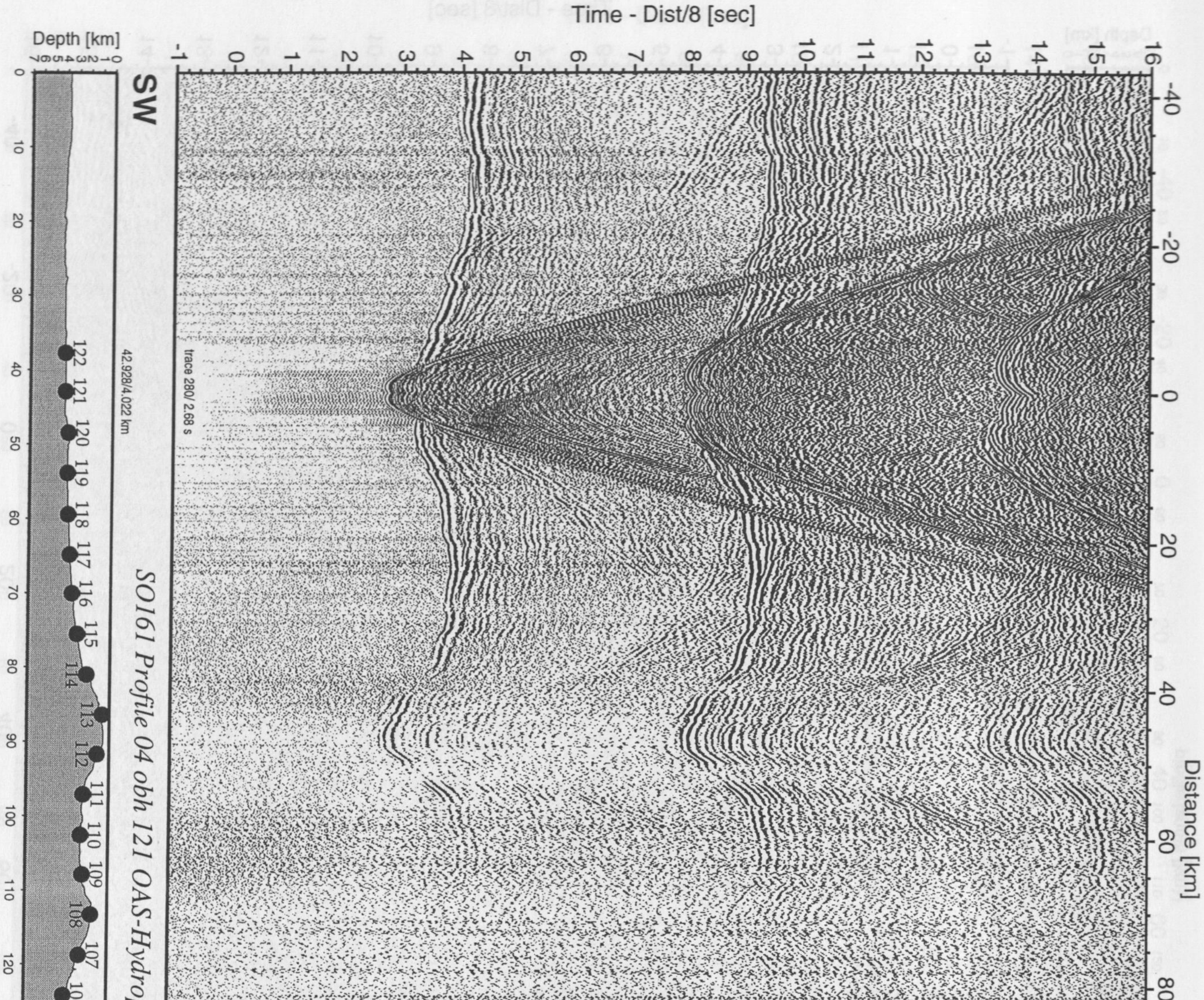

**Figure 5.4.4.22:** Record section from obh 121 OAS-Hydrophone, Profile 04.

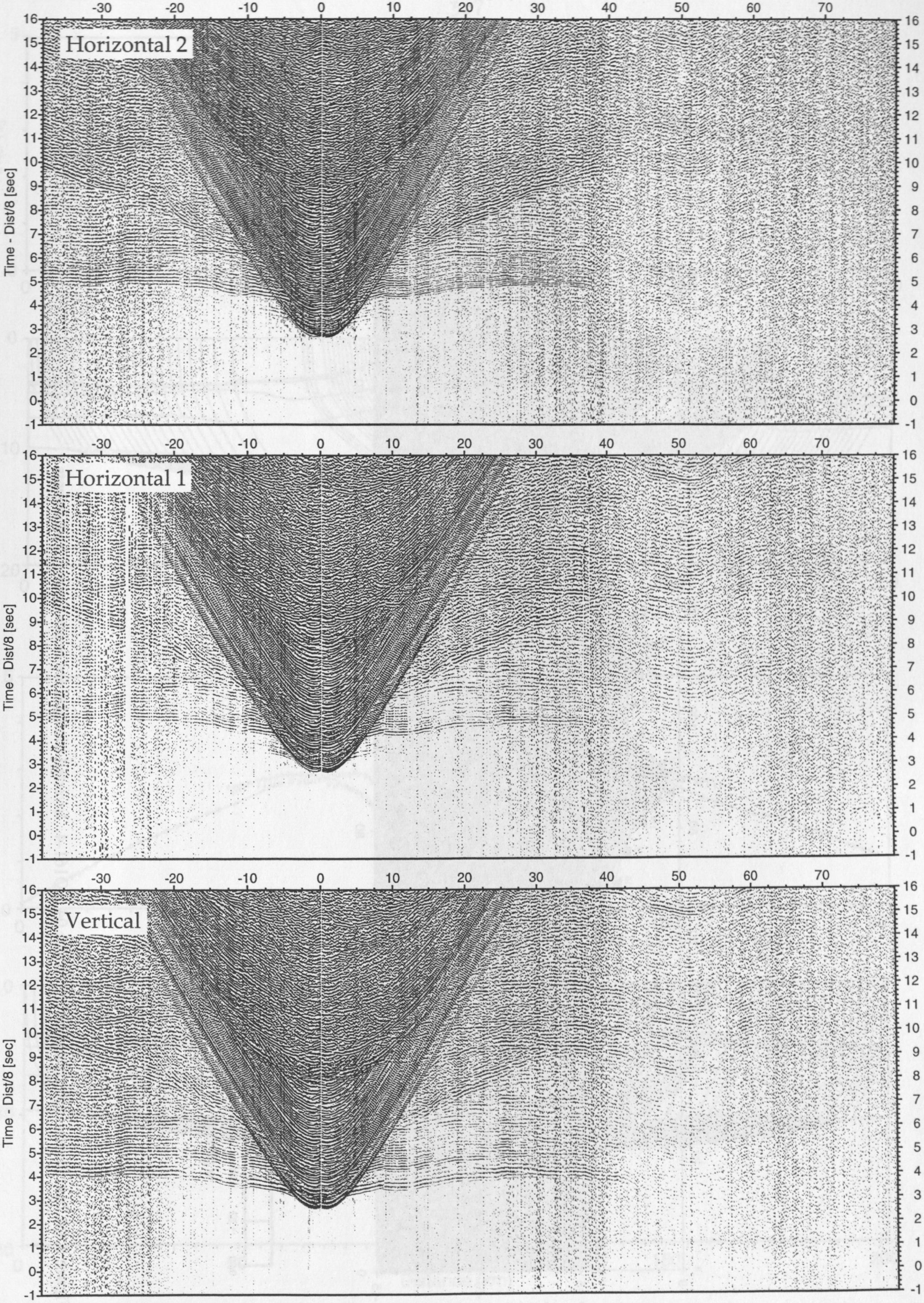

**Figure 5.4.4.23:** Record sections from obs 122 DPG/PMD, SO161 Profile 04.

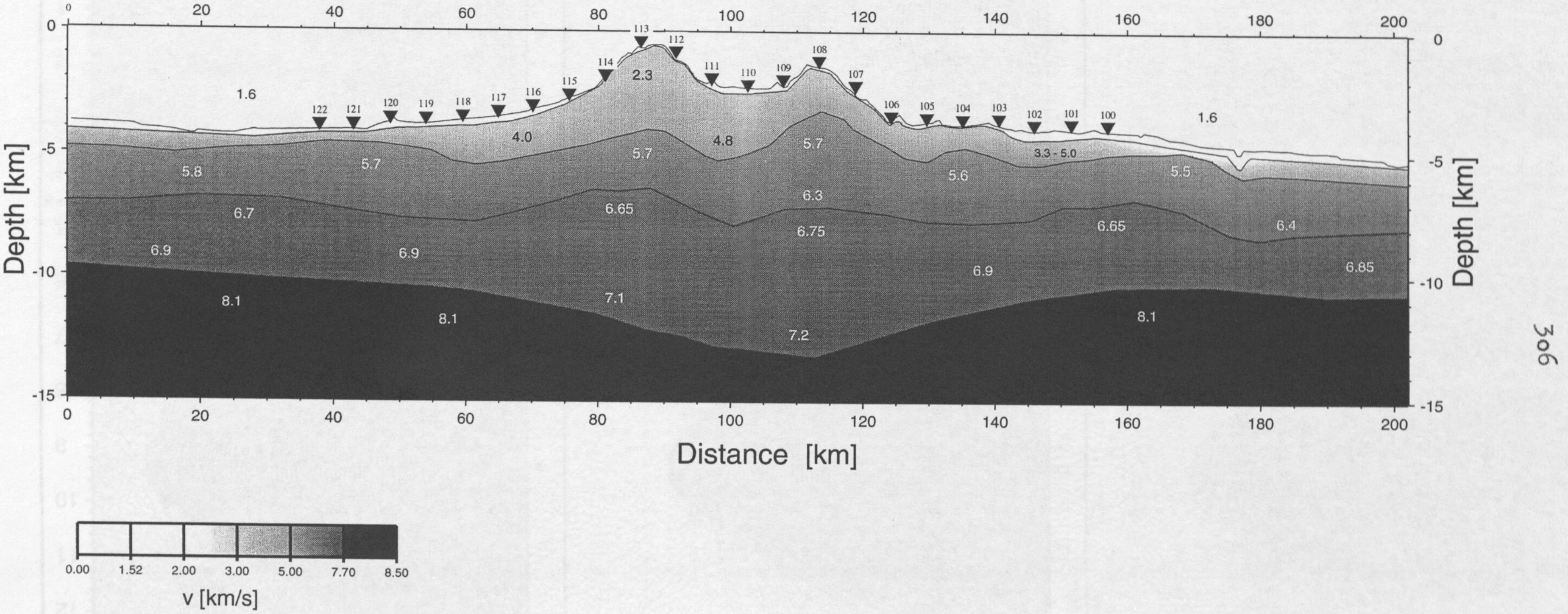

**Figure 5.4.4.24a:** Depth-velocity model for Profile 04, SO161-4. Inverted triangles are ocean-bottom instruments.

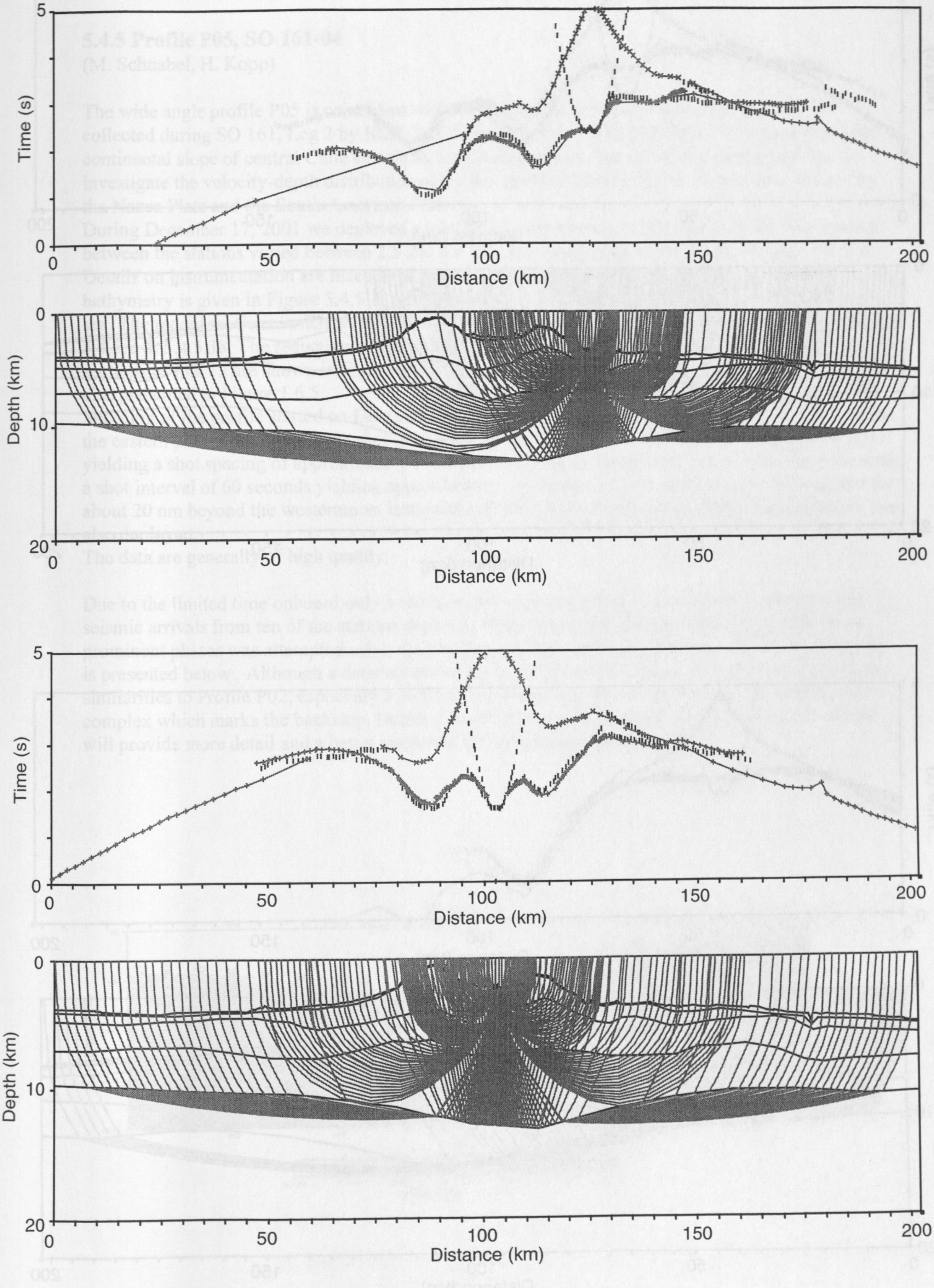

**Figure 5.4.4.24b:** Traveltimes and ray penetration for OBH106 (top) and OBH110 (bottom) of Profile 04, SO161-4

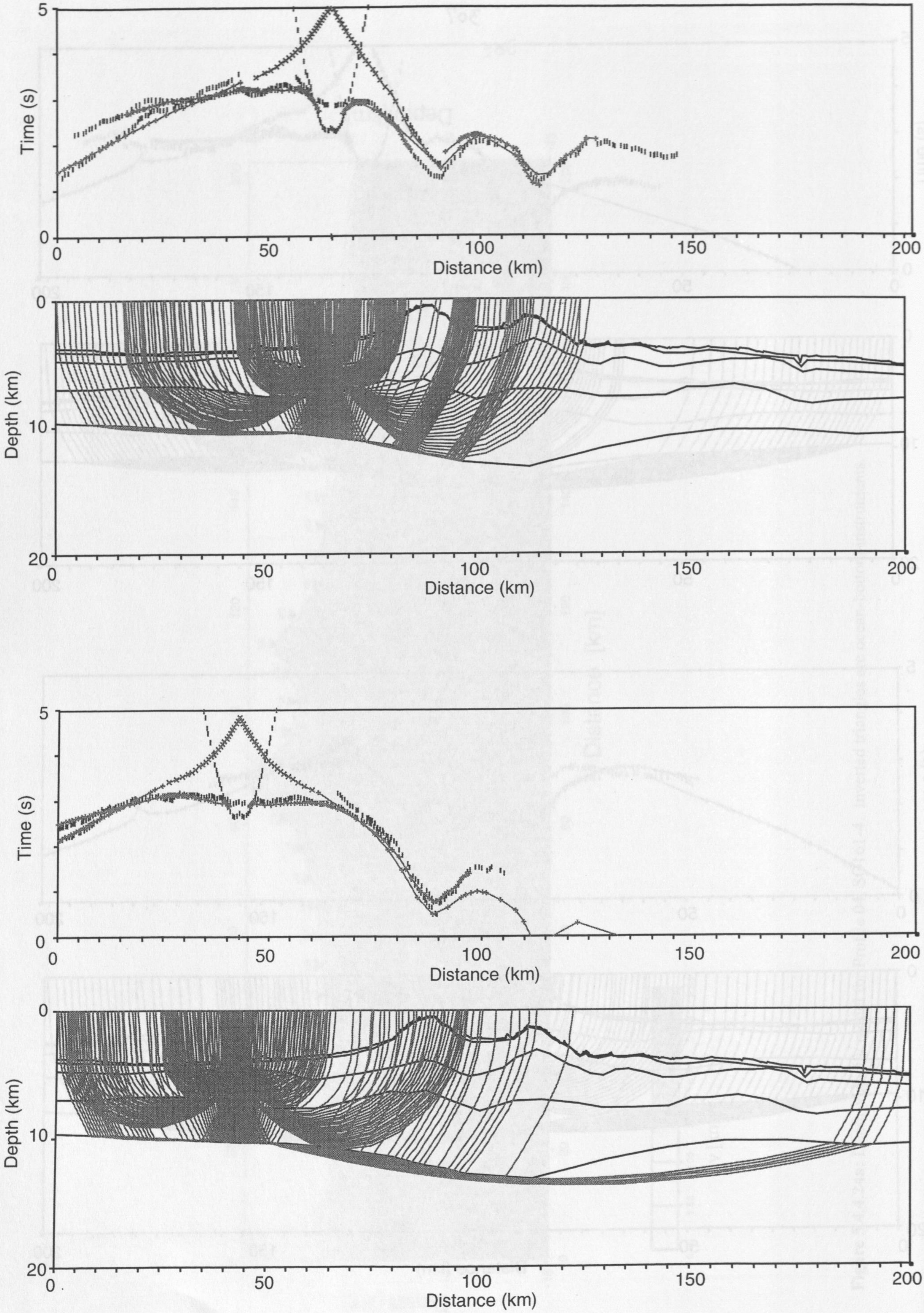

**Figure 5.4.4.24b:** Traveltimes and ray penetration for OBH117 (top) and OBH121 (bottom) of Profile 04, SO161-4

### 5.4.5 Profile P05, SO 161-04

(M. Schnabel, H. Kopp)

The wide angle profile P05 is coincident with the multichannel seismic reflection line No. 12, collected during SO 161, Leg 2 by BGR. It is striking east-west along latitude 31° S and crosses the continental slope of central Chile as well as the Chilean trench. The aim of the experiment was to investigate the velocity-depth distribution along this profile crossing the subduction zone formed by the Nazca Plate and the South American Plate.

During December 17, 2001 we deployed a total of 26 instruments; 5 OBS and 21 OBH. The spacing between the stations varied between 2,5 and 4.9 nm. The total length of the profile is about 190 km. Details on instrumentation are listed in Appendix III.6. A location map of the profile including bathymetry is given in Figure 5.4.5.1. A preliminary interpretation of this data set was attempted at sea. The record sections which were processed as described in chapter 4.6.1 are shown in Figures 5.4.5.2 to 5.4.5.38. The reduction velocity of all seismic sections is $V_{red}$ = 8000 m/s. Processed sections of line 12 are shown in Figure 5.4.5.39 to Figure 5.4.5.42. A line drawing of the MCS data is also presented in Figure 1.6.5.

Shooting of the profile started on December 18, 2001 and was was done twice at a speed of 5 kn. First, the eastern part of the profile was shot from west to east with a 30 seconds shot interval (Profile 501), yielding a shot spacing of approximately 75 meters. Reverse shooting from east to west was done with a shot interval of 60 seconds yielding approximately 150 meters of shot spacing and was extended for about 20 nm beyond the westernmost instrument (Profile 502). During shooting the magnetometer was also deployed.

The data are generally of high quality.

Due to the limited time onboard only a crude preliminary modelling was conducted onboard using seismic arrivals from ten of the stations deployed along the profile. Forward modelling of the most prominent phases was attempted using the MacRay software package (Luetgert, 1992) and the model is presented below . Although a detailed modelling was not possible at sea, we can already infer some similarities to Profile P02, especially a pronounced lateral velocity increase within the accretionary complex which marks the backstop. Detailed modelling using all stations deployed along the profile will provide more detail and a better resolution of the velocity-depth structure.

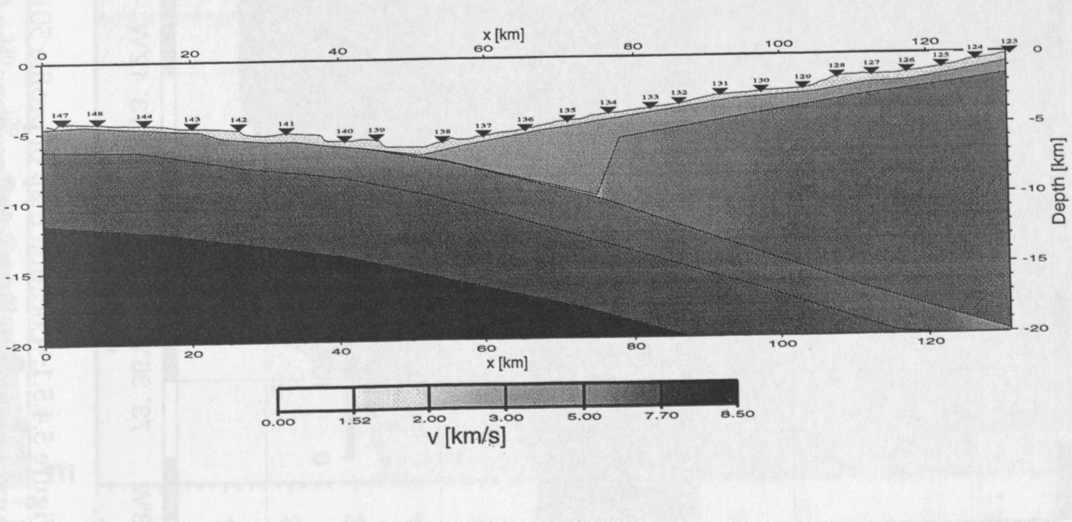

Figure 5.4.5.43.: Preliminary velocity-depth model of Profile P05.

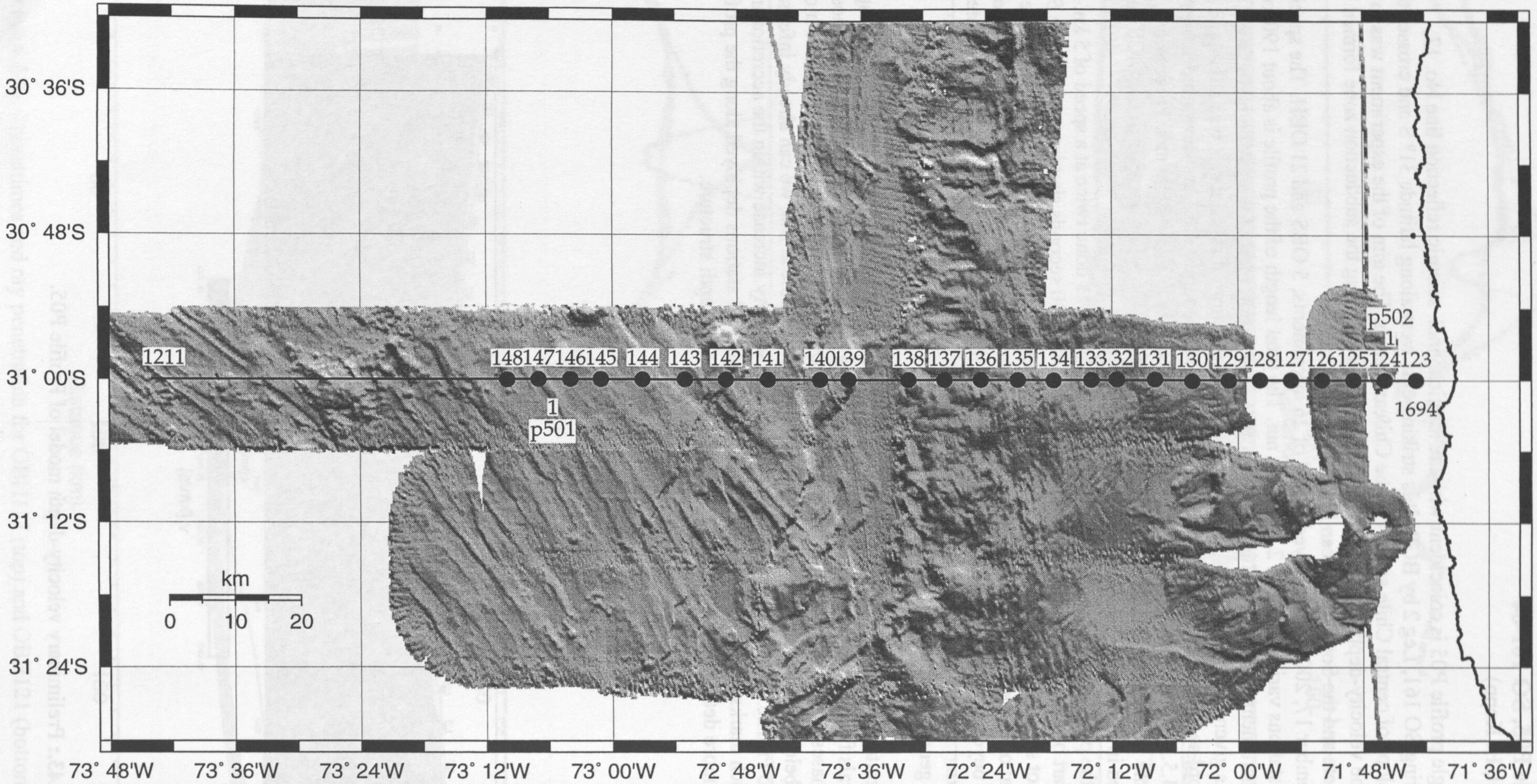

**Figure 5.4.5.1:** Location map of profile 501/502 and illuminated multibeam bathymetry. Superimposed the obh/obs locations, the first, and last shotpoint numbers.

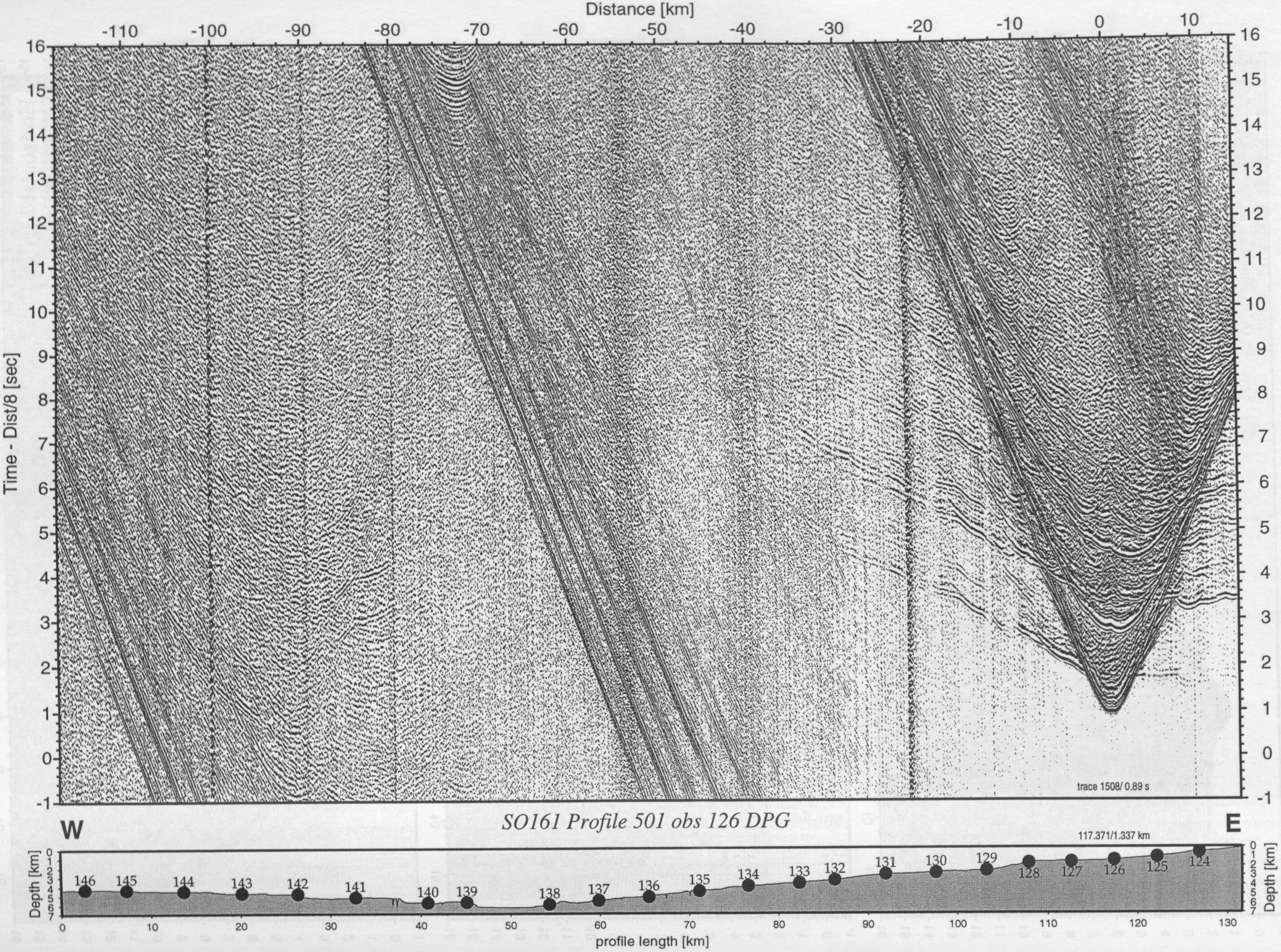

**Figure 5.4.5.2:** Record section from obs 126 DPG, Profile 501.

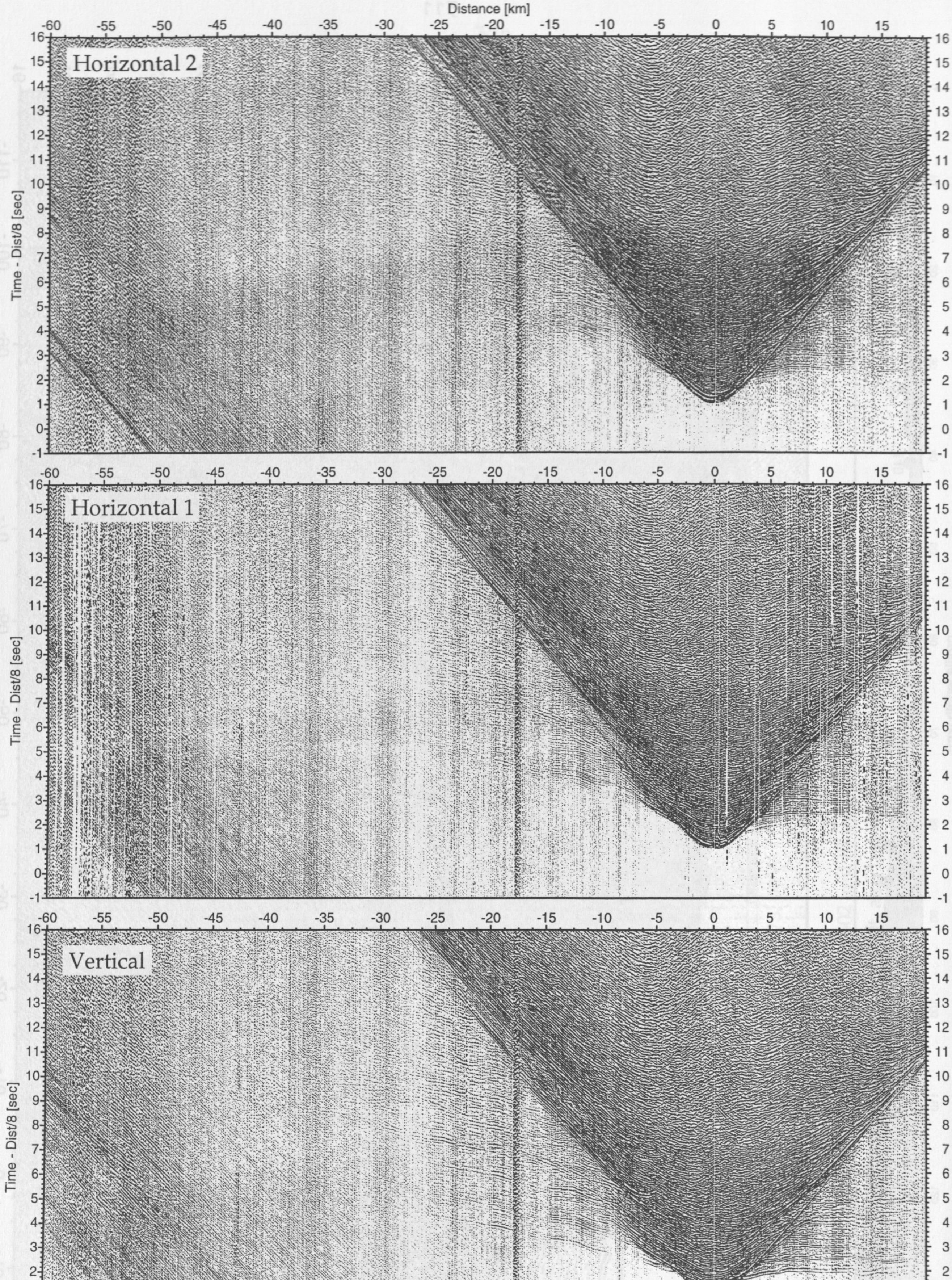

**Figure 5.4.5.3:** Record sections from obs 127 OAS/PMD, SO161 Profile 501.

313

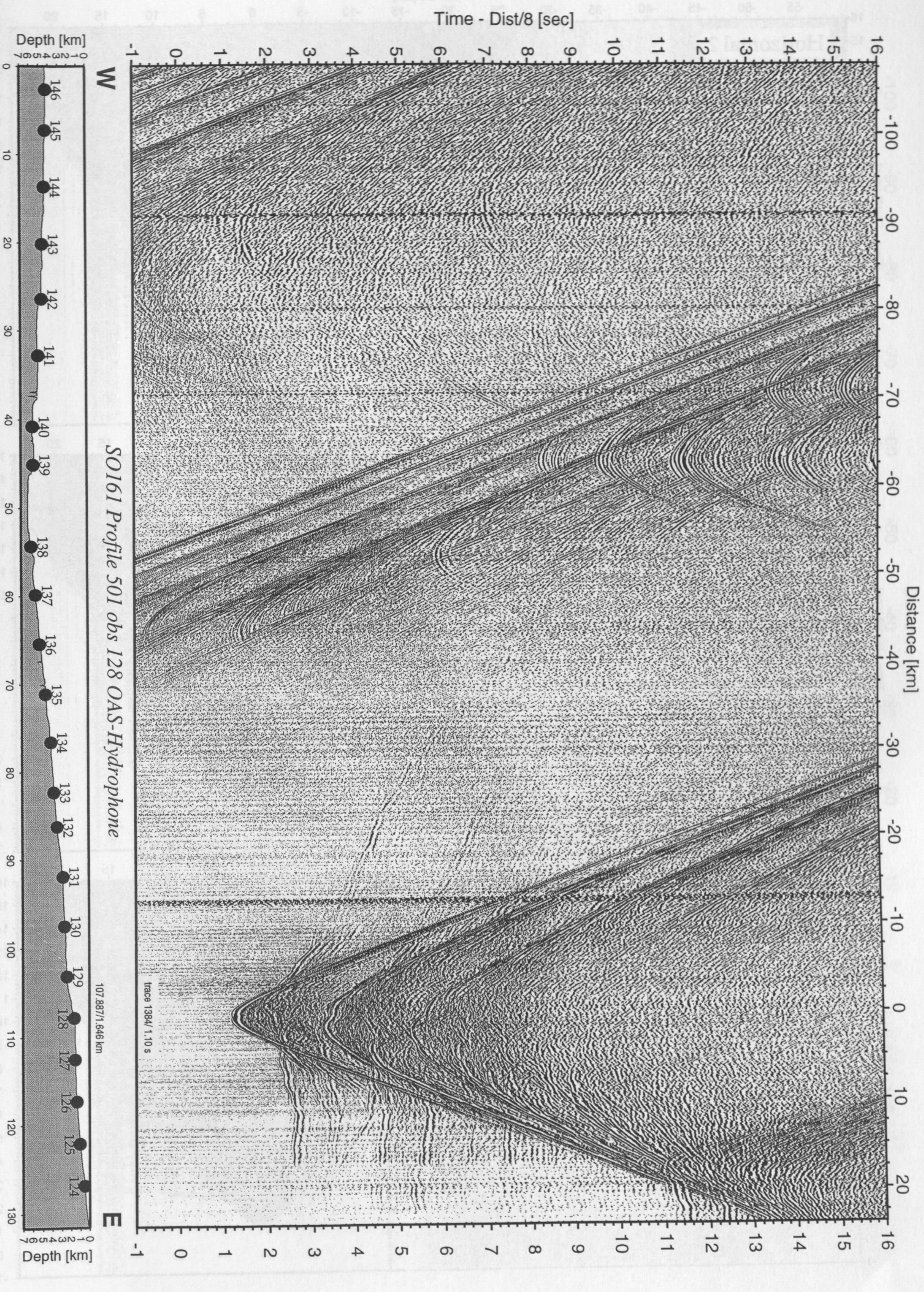

**Figure 5.4.5.4:** Record section from obs 128 OAS-Hydrophone, Profile 501.

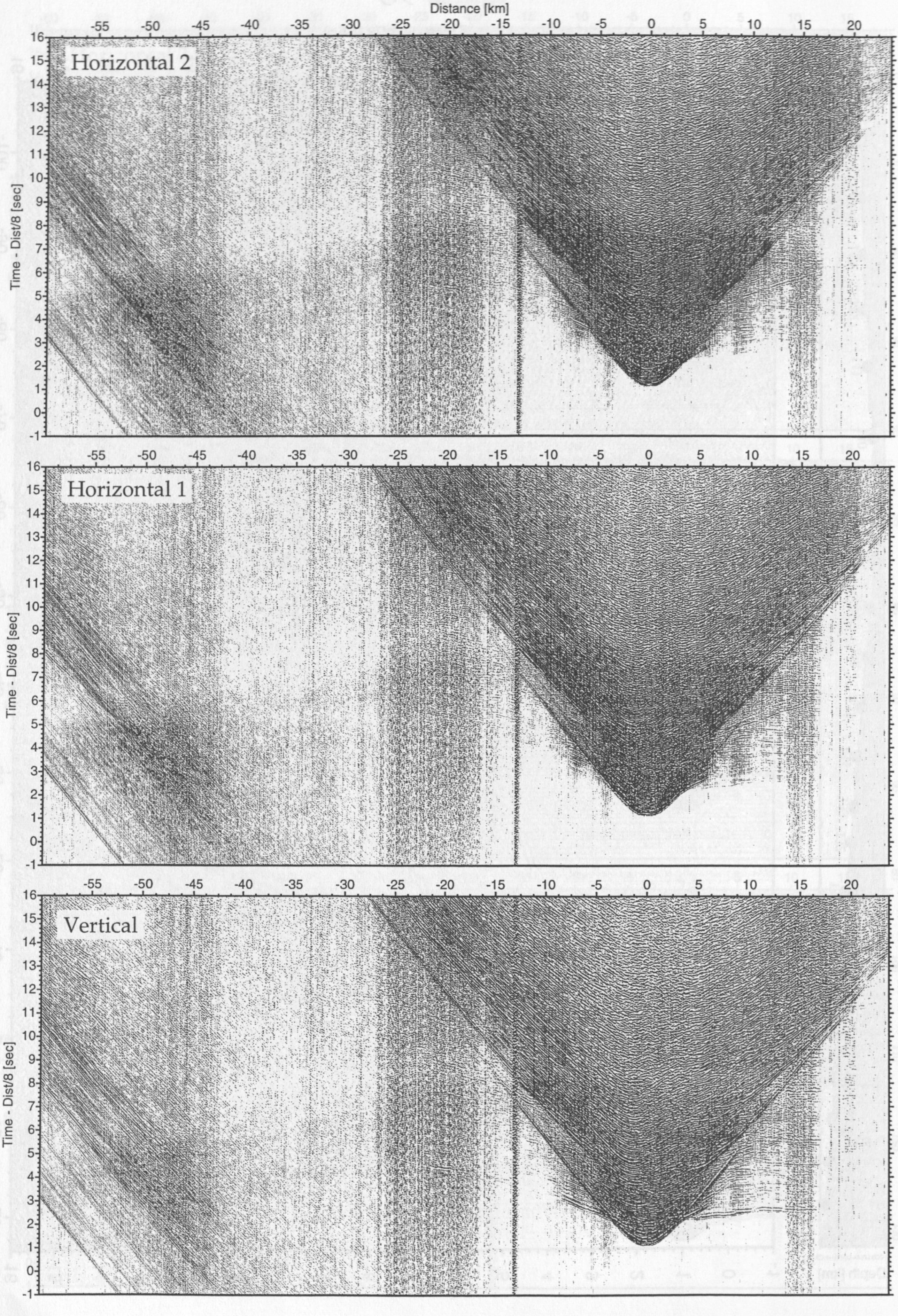

**Figure 5.4.5.5:** Record sections from obs 128 OAS/A01-4.5Hz, SO161 Profile 501.

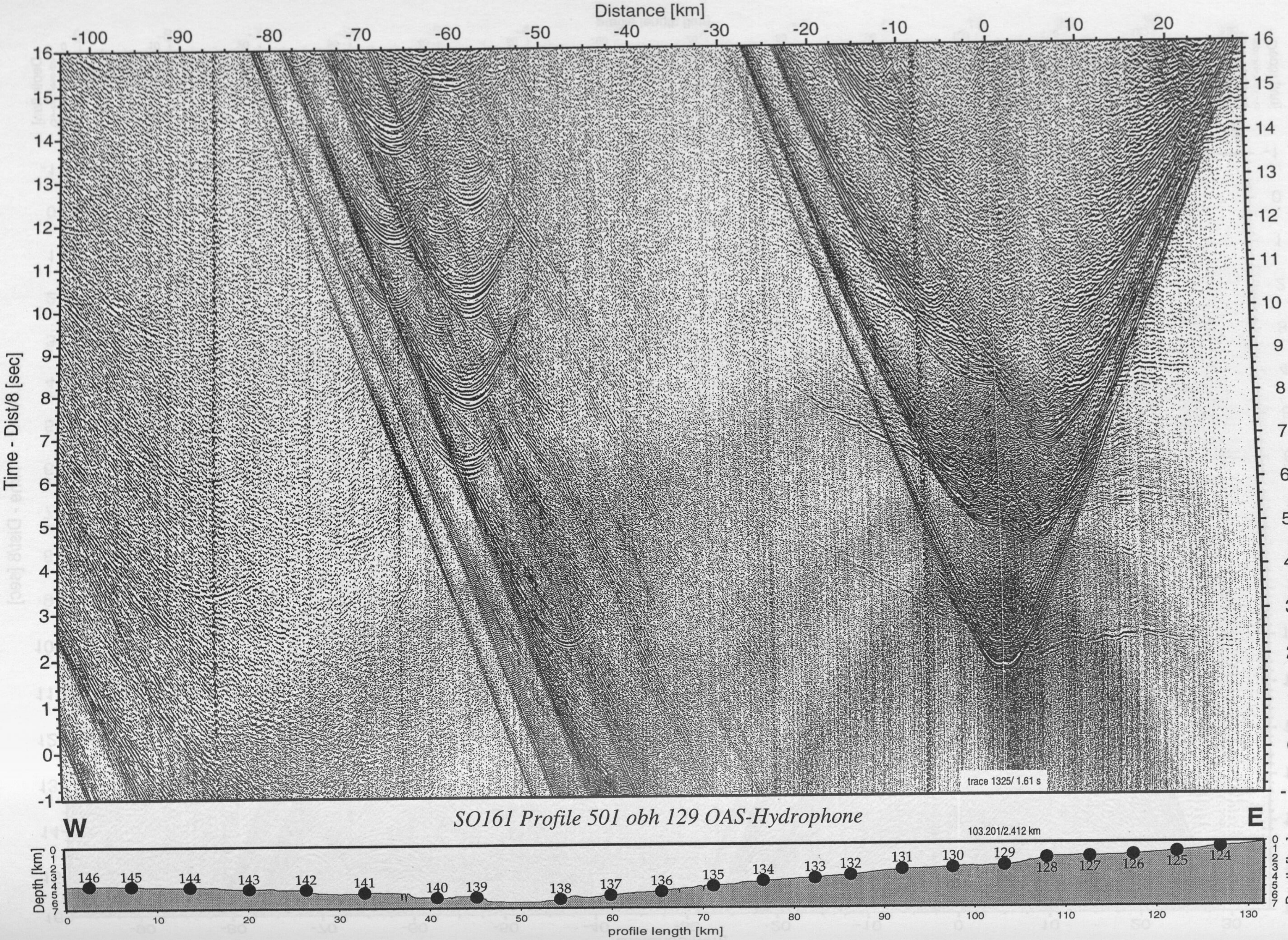

**Figure 5.4.5.6:** Record section from obh 129 OAS-Hydrophone, Profile 501.

**Figure 5.4.5.7:** Record section from obh 130 OAS-Hydrophone, Profile 501.

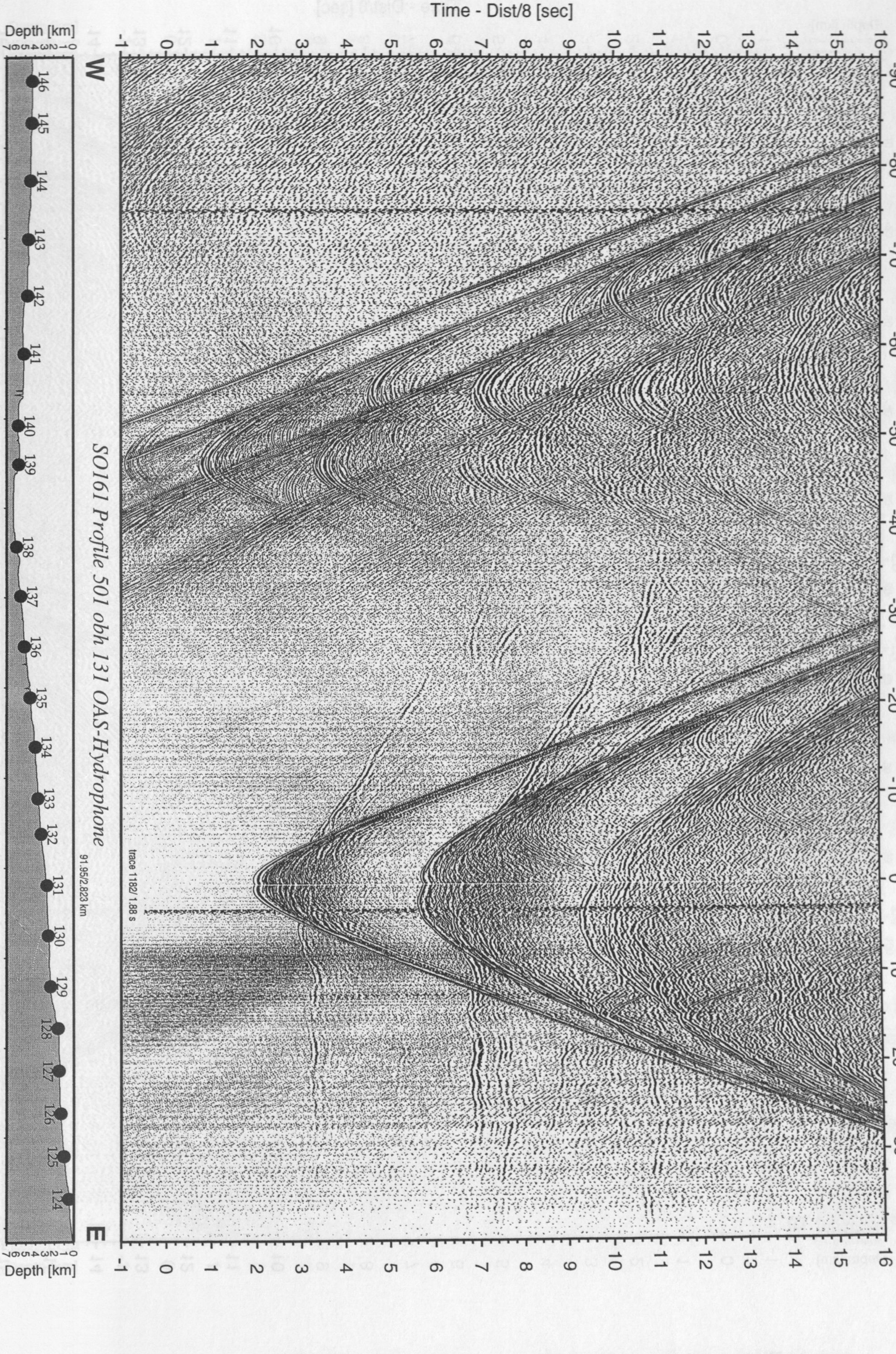

**Figure 5.4.5.8:** Record section from obh 131 OAS-Hydrophone, Profile 501.

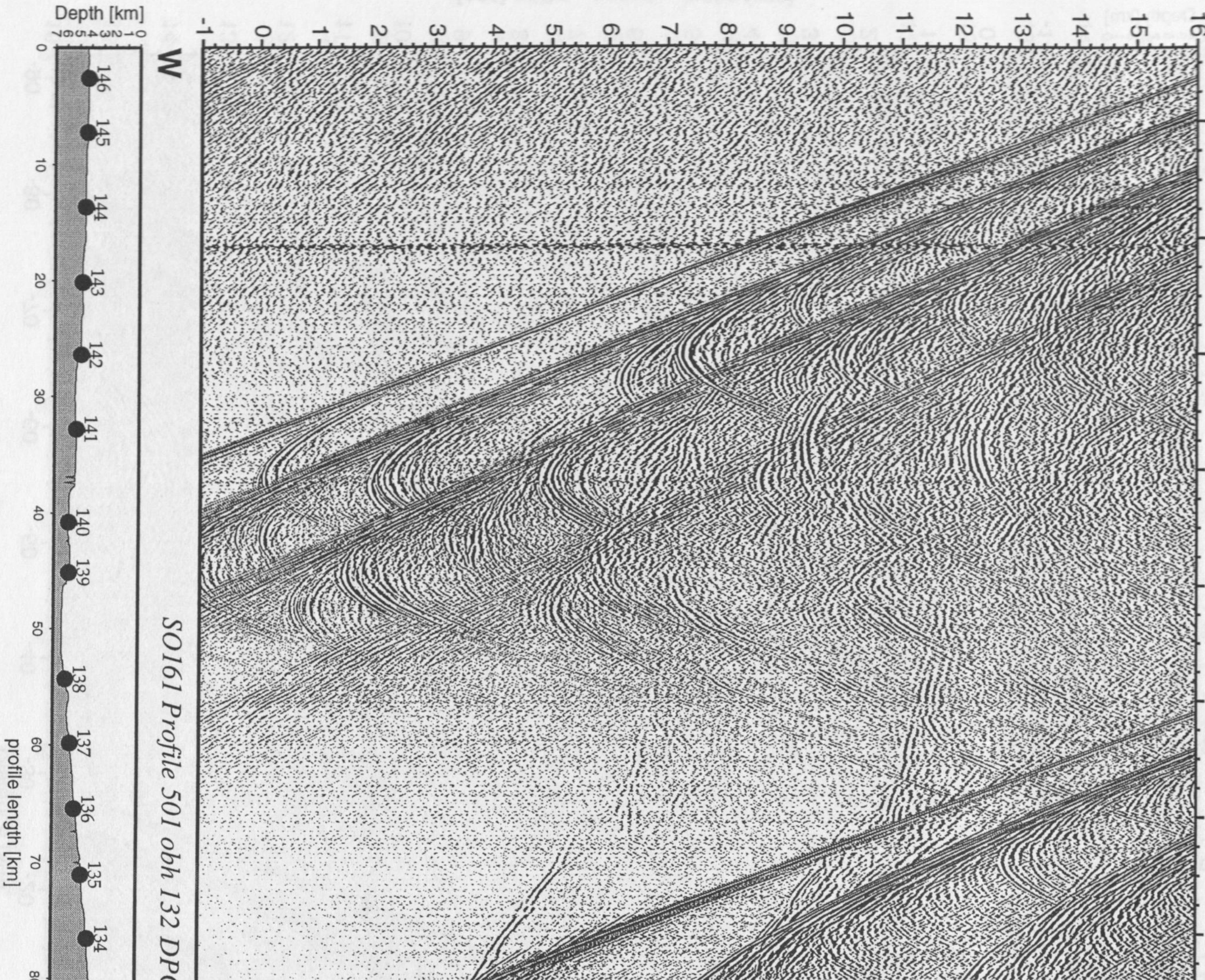

**Figure 5.4.5.9:** Record section from obh 132 DPG, Profile 501.

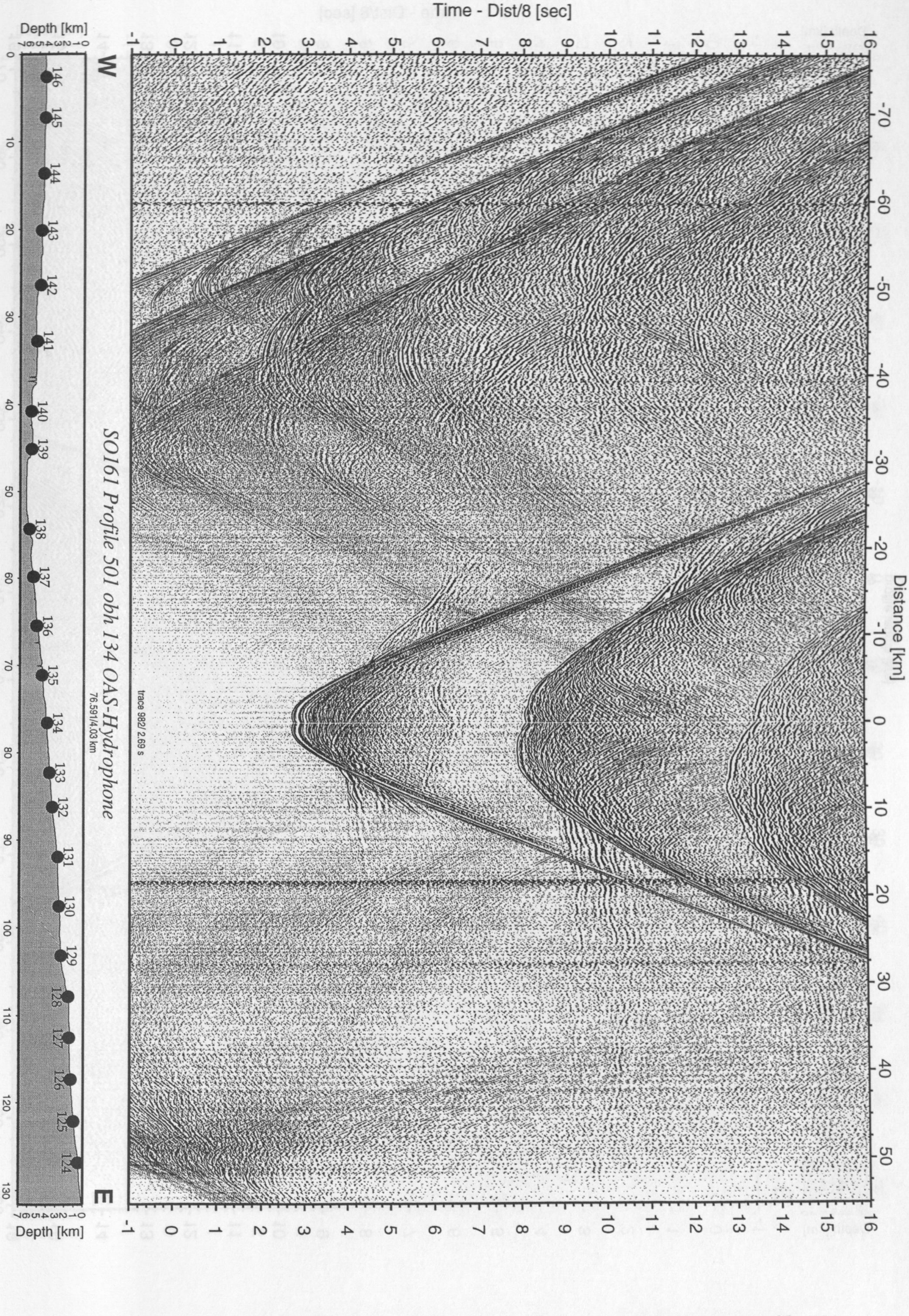

**Figure 5.4.5.10:** Record section from obh 134 OAS-Hydrophone, Profile 501.

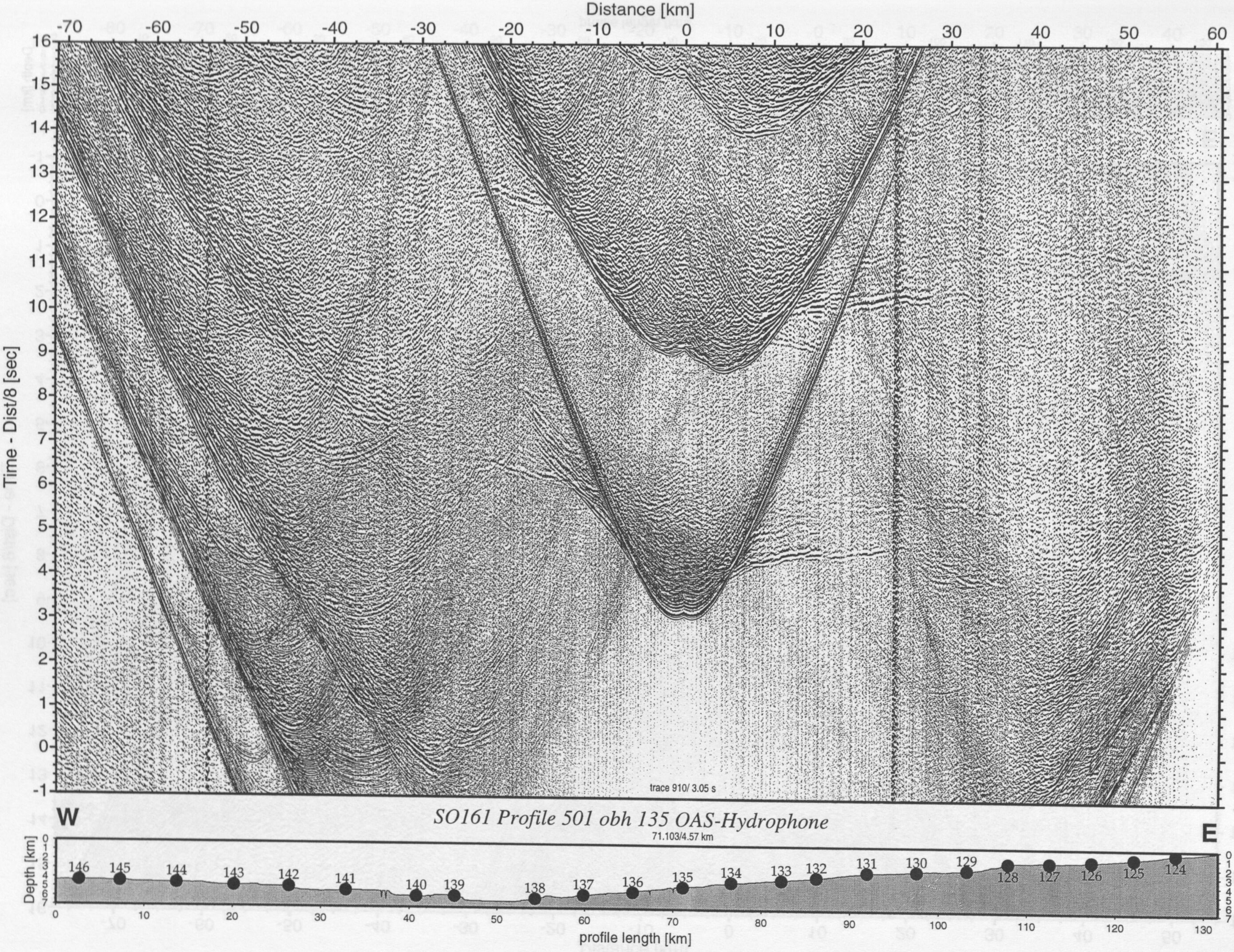

**Figure 5.4.5.11:** Record section from obh 135 OAS-Hydrophone, Profile 501.

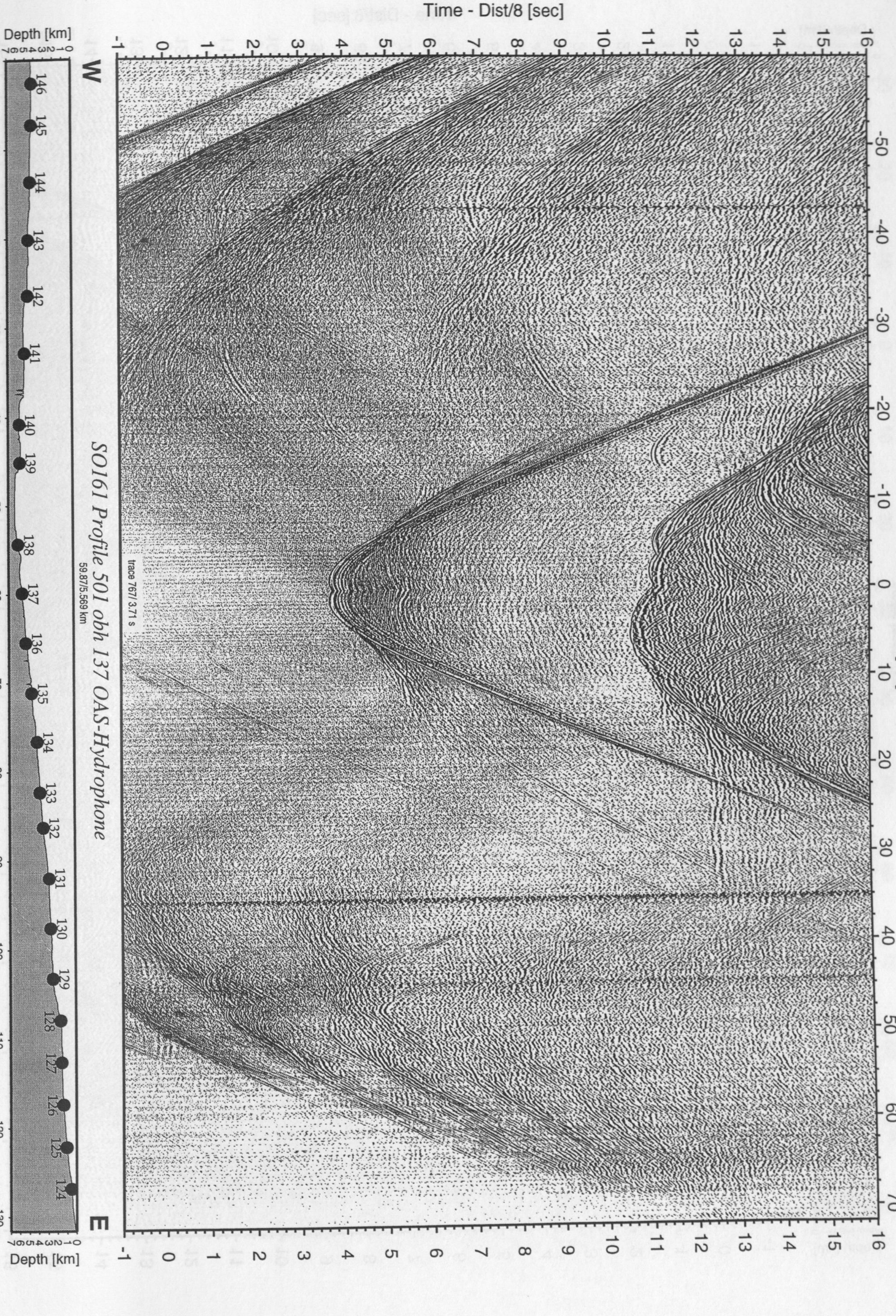

**Figure 5.4.5.12:** Record section from obh 137 OAS-Hydrophone, Profile 501.

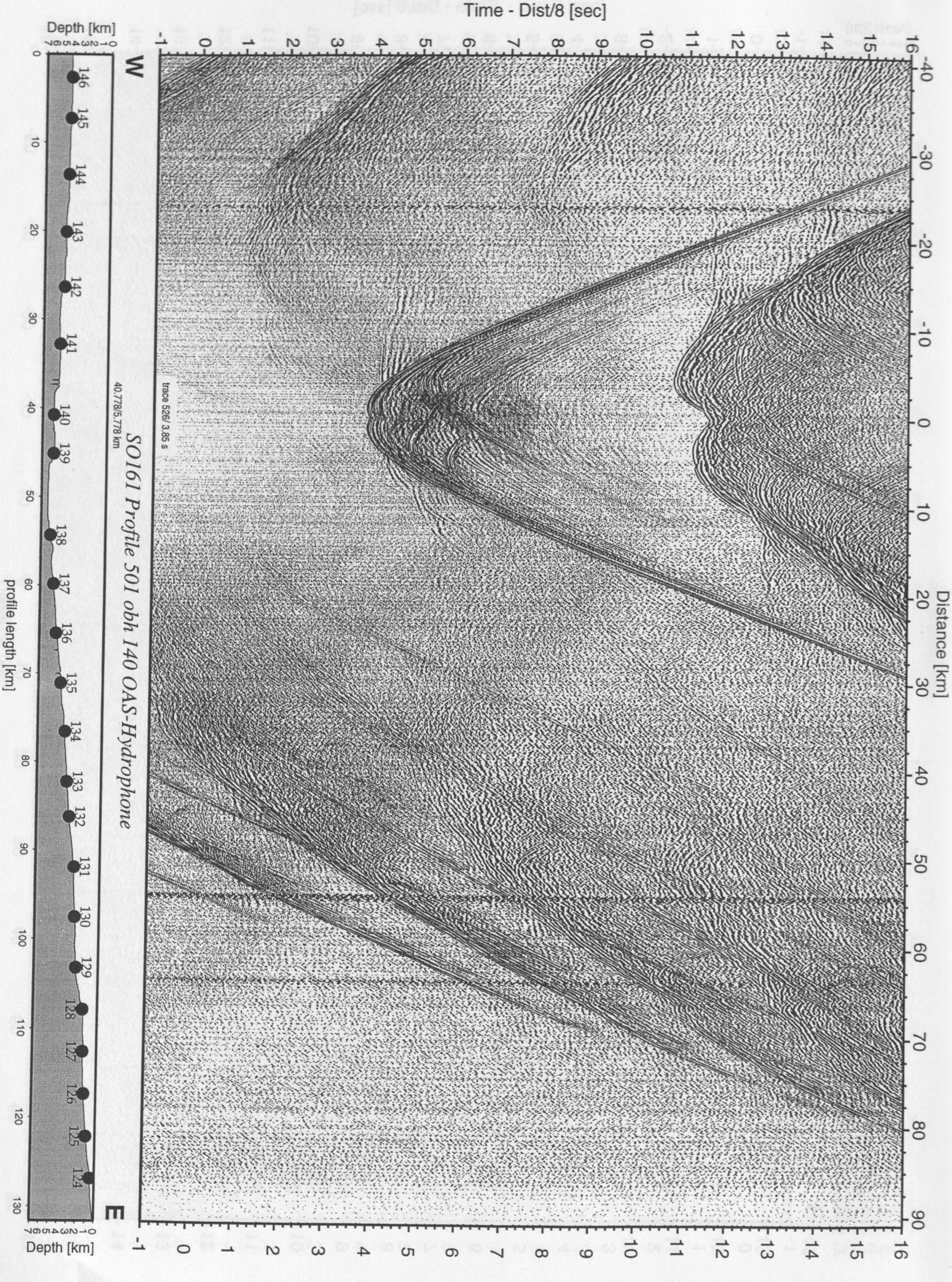

**Figure 5.4.5.13:** Record section from obh 140 OAS-Hydrophone, Profile 501.

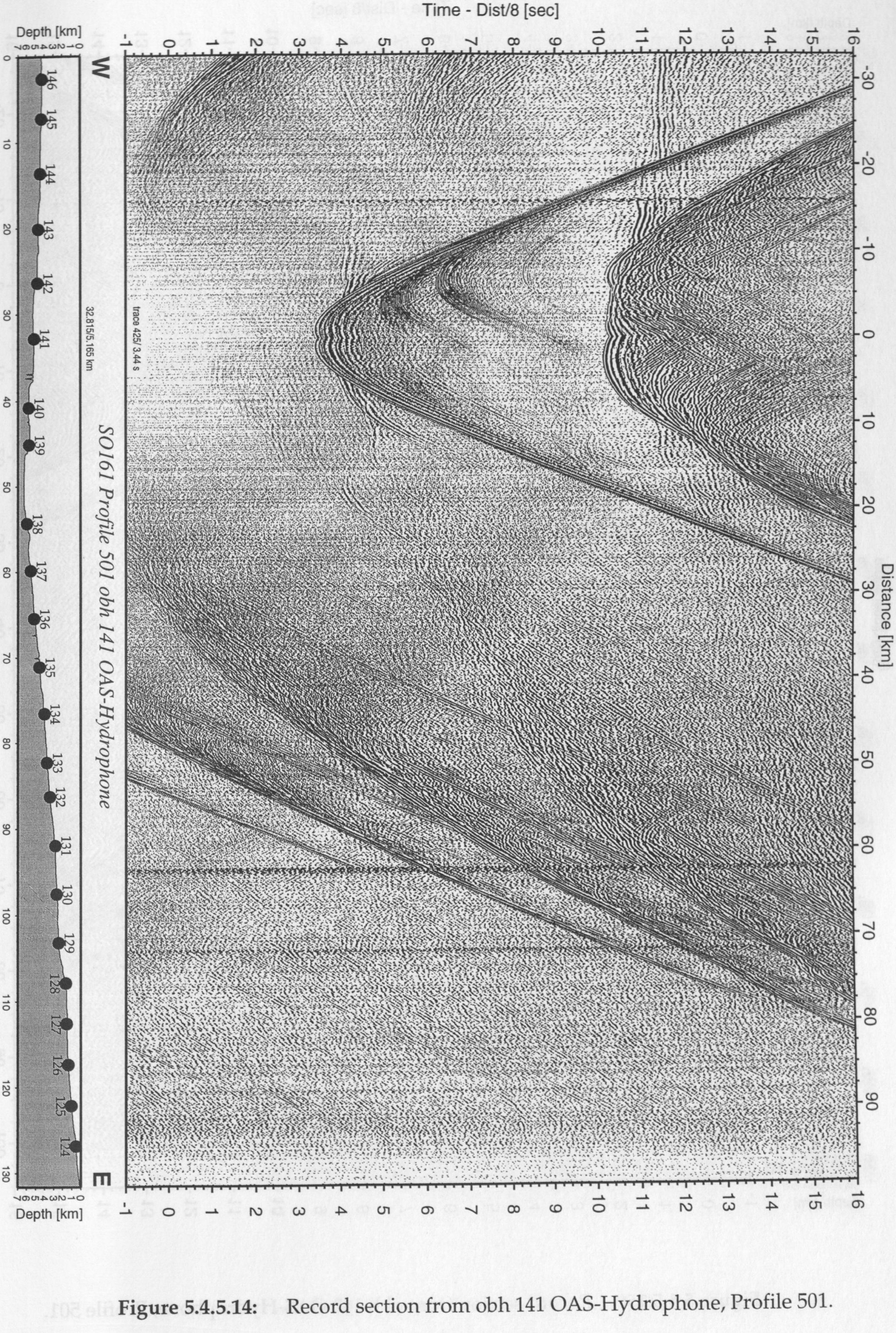

Figure 5.4.5.14: Record section from obh 141 OAS-Hydrophone, Profile 501.

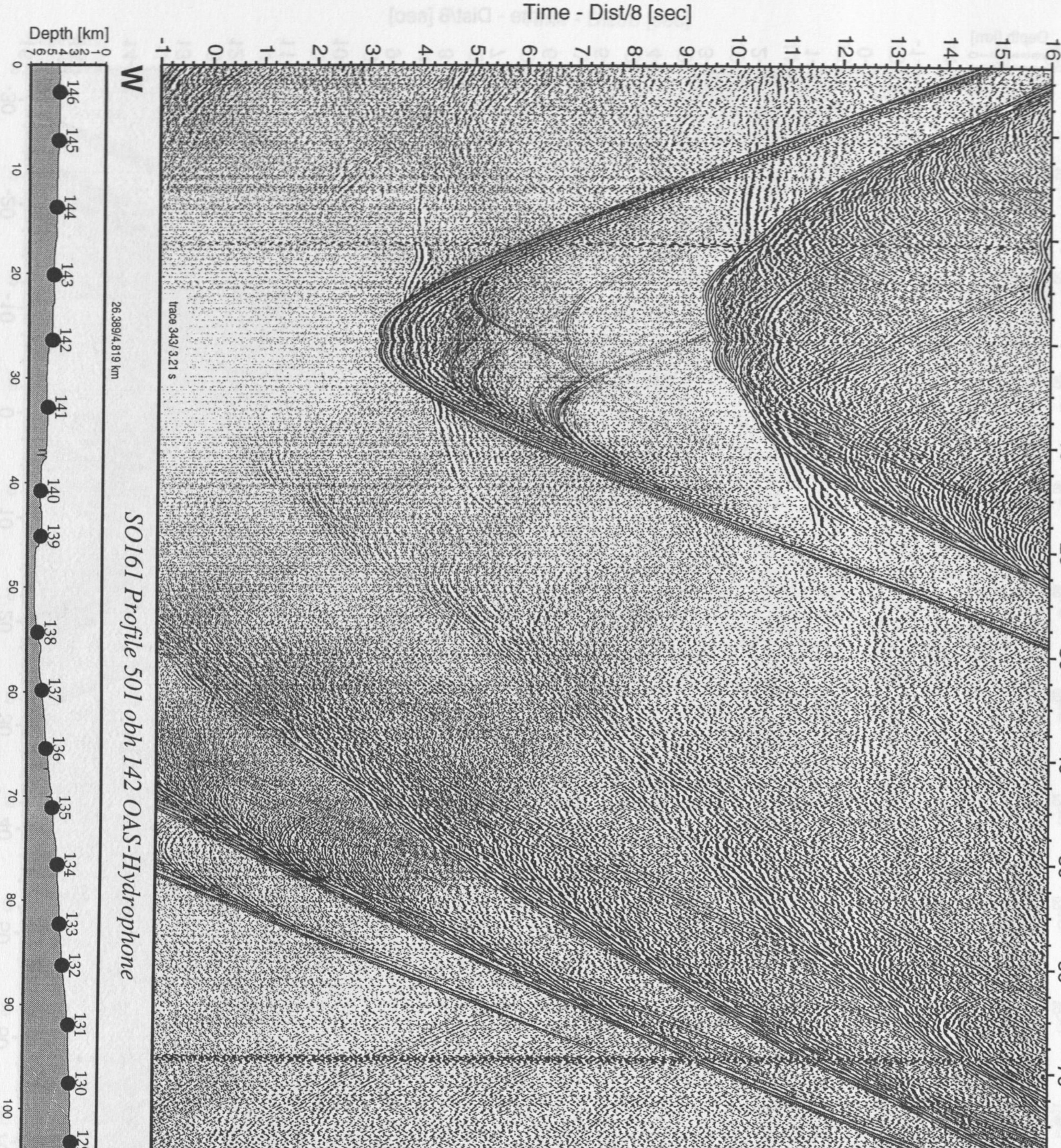

**Figure 5.4.5.15:** Record section from obh 142 OAS-Hydrophone, Profile 501.

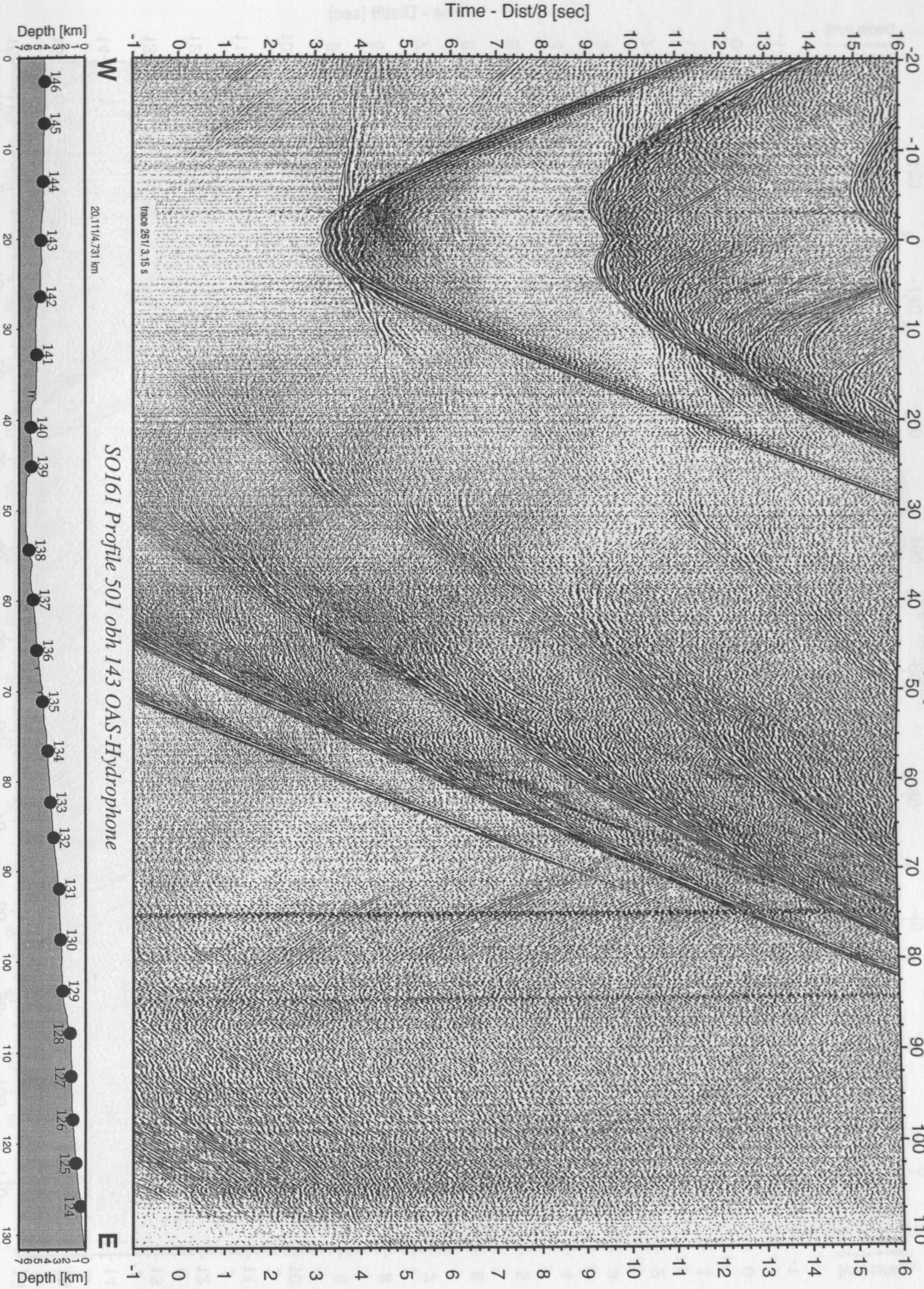

**Figure 5.4.5.16:** Record section from obh 143 OAS-Hydrophone, Profile 501.

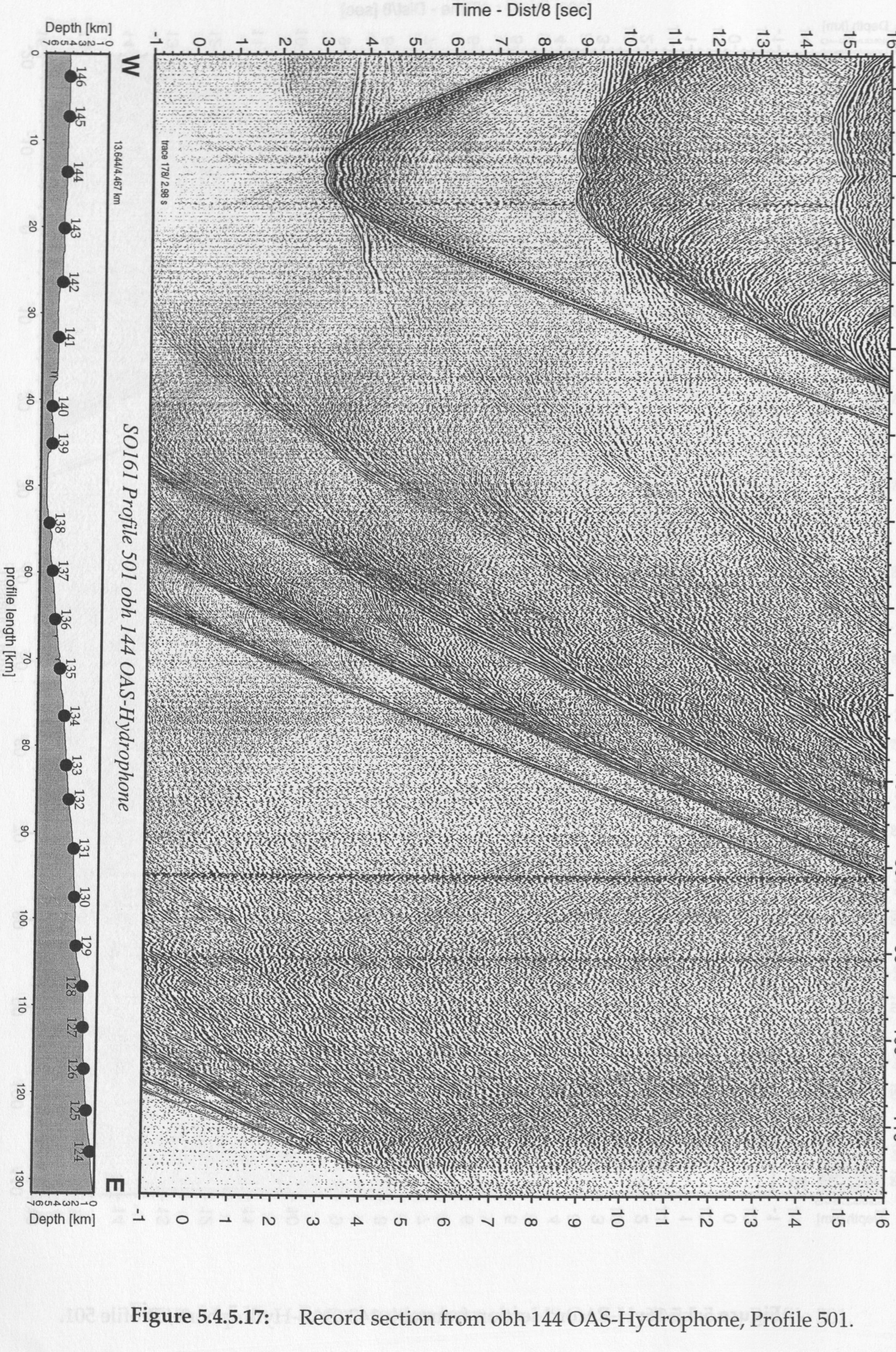

**Figure 5.4.5.17:** Record section from obh 144 OAS-Hydrophone, Profile 501.

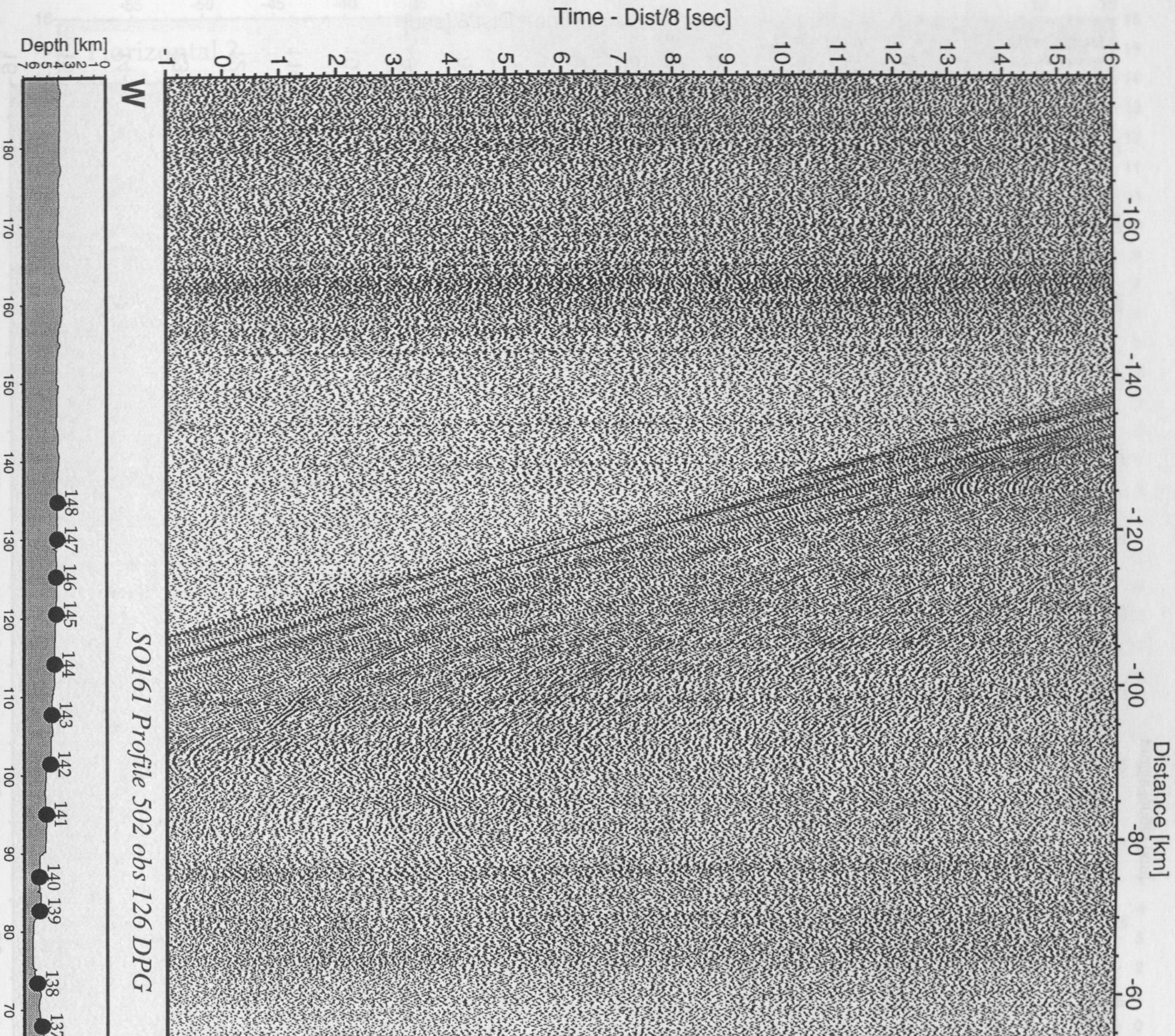

Figure 5.4.5.18: Record section from obs 126 DPG, Profile 502.

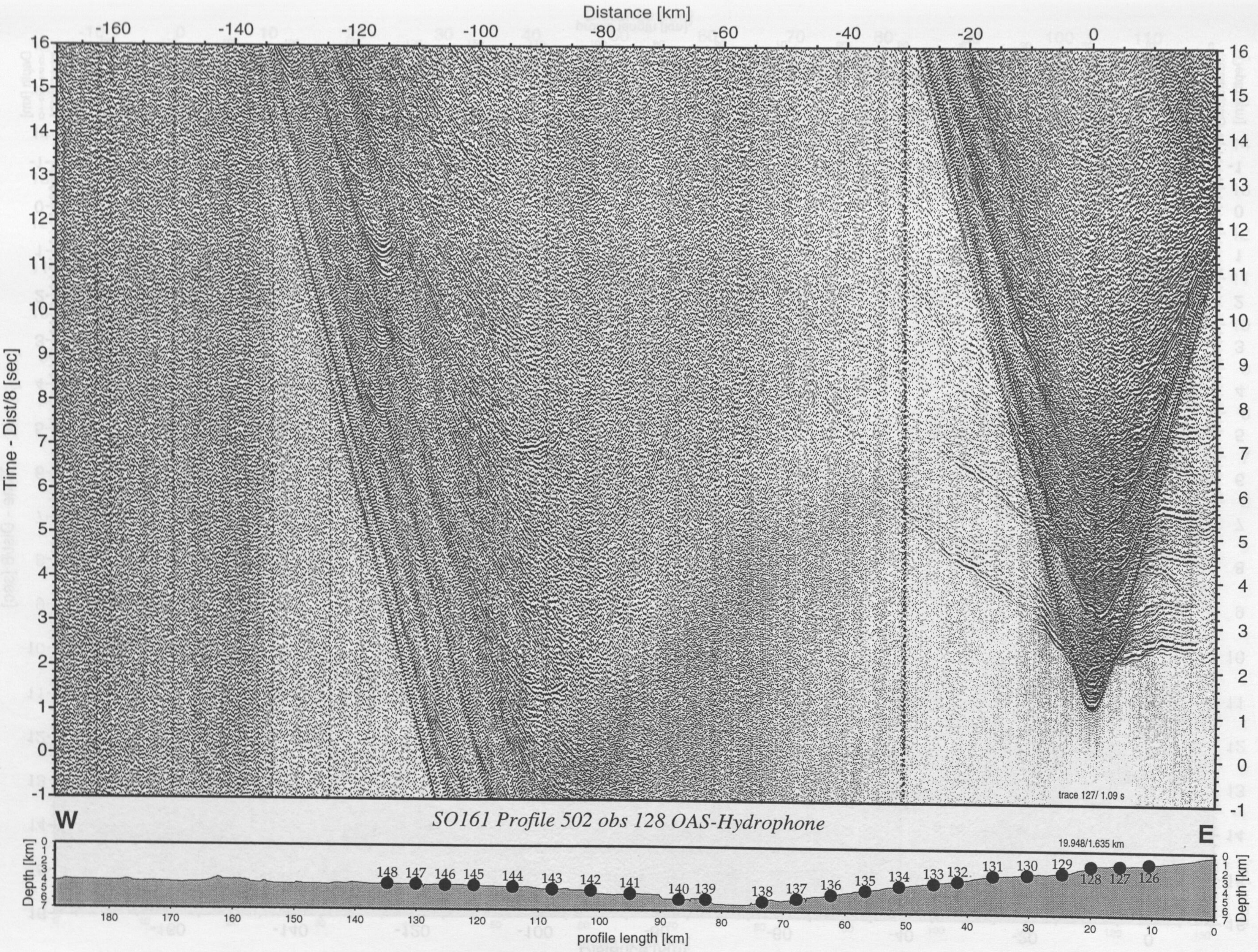

**Figure 5.4.5.20:** Record section from obs 128 OAS-Hydrophone, Profile 502.

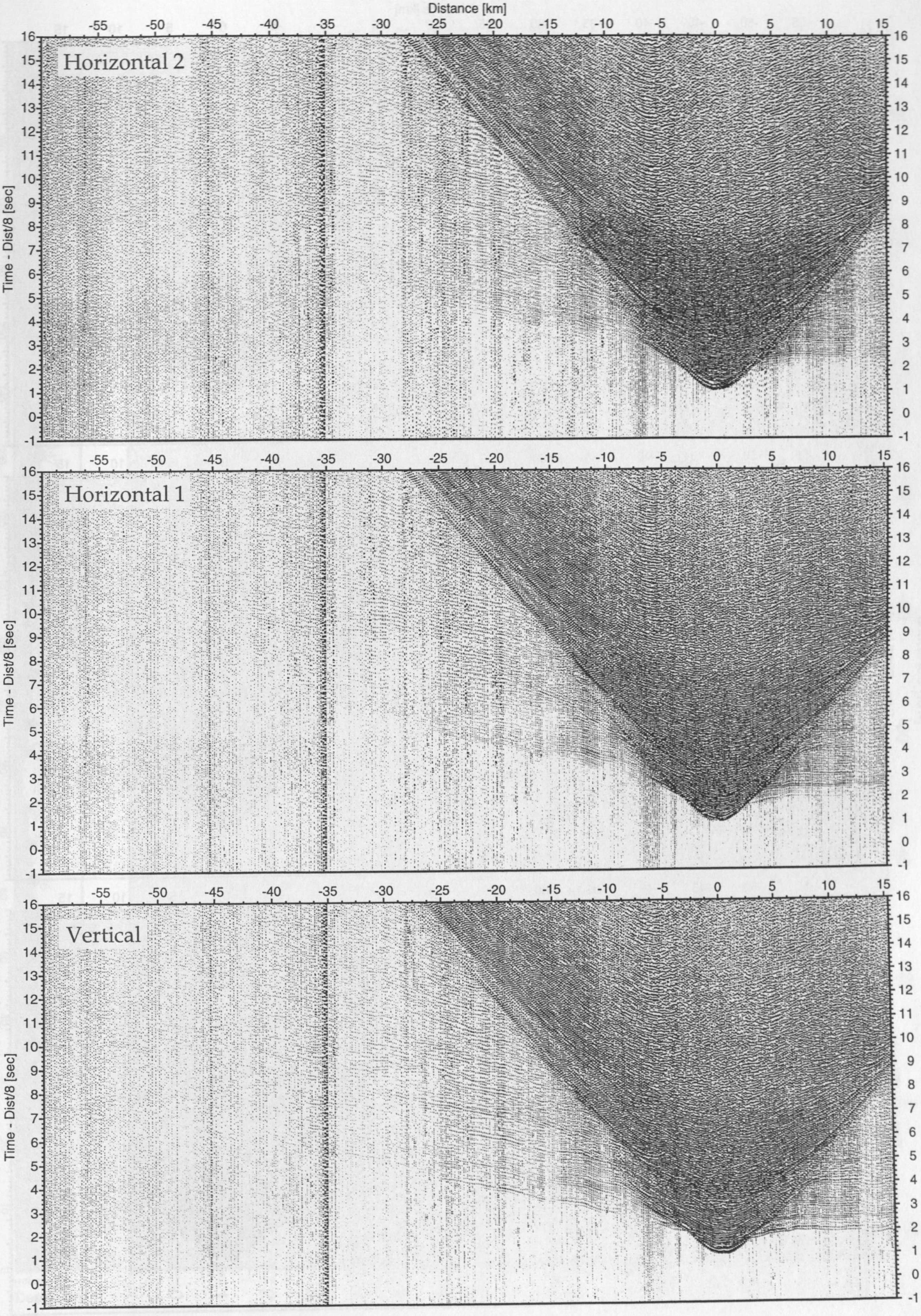

**Figure 5.4.5.19:** Record sections from obs 127 OAS/PMD, SO161 Profile 502.

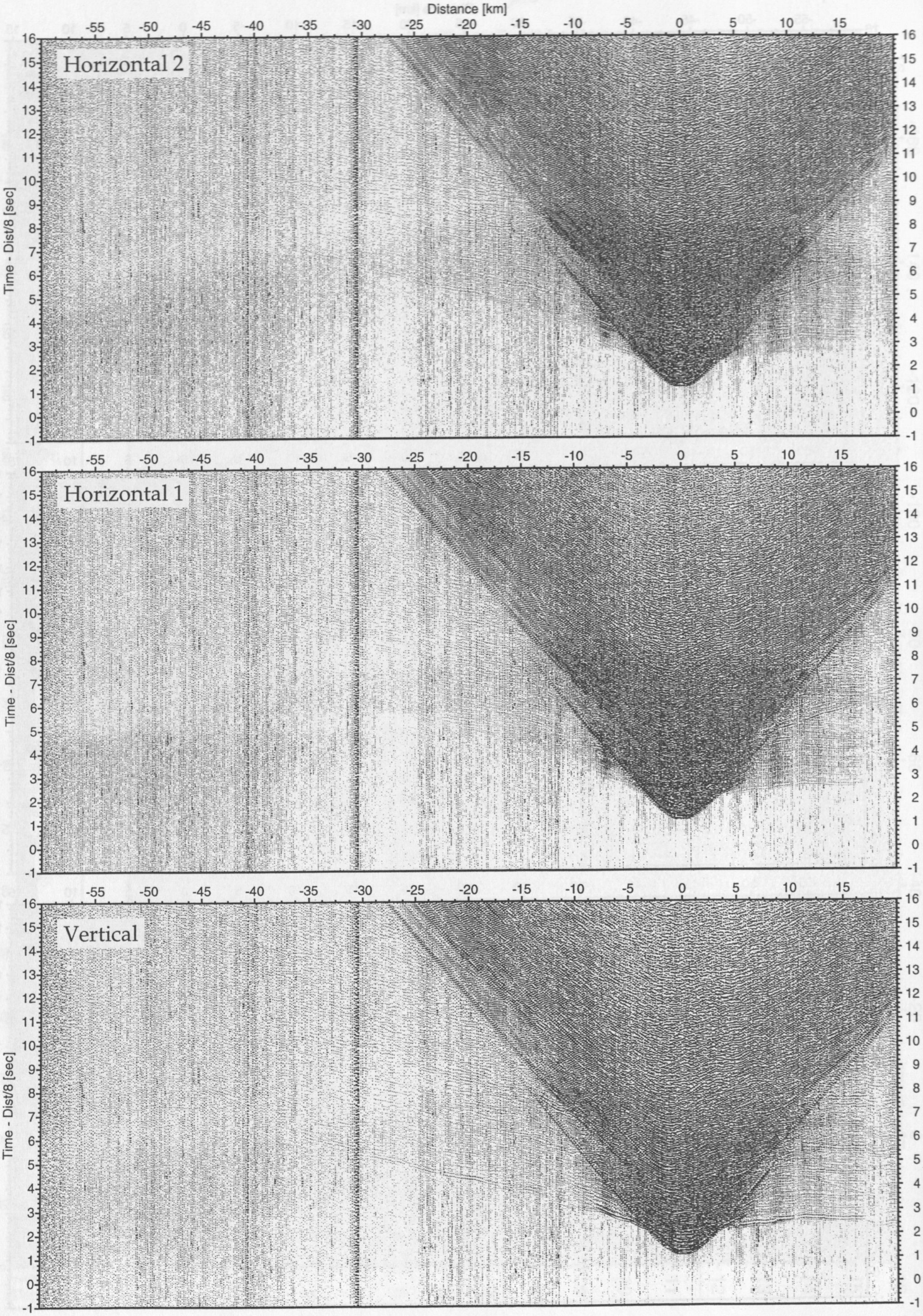

**Figure 5.4.5.21:** Record sections from obs 128 OAS/A01-4.5Hz, SO161 Profile 502.

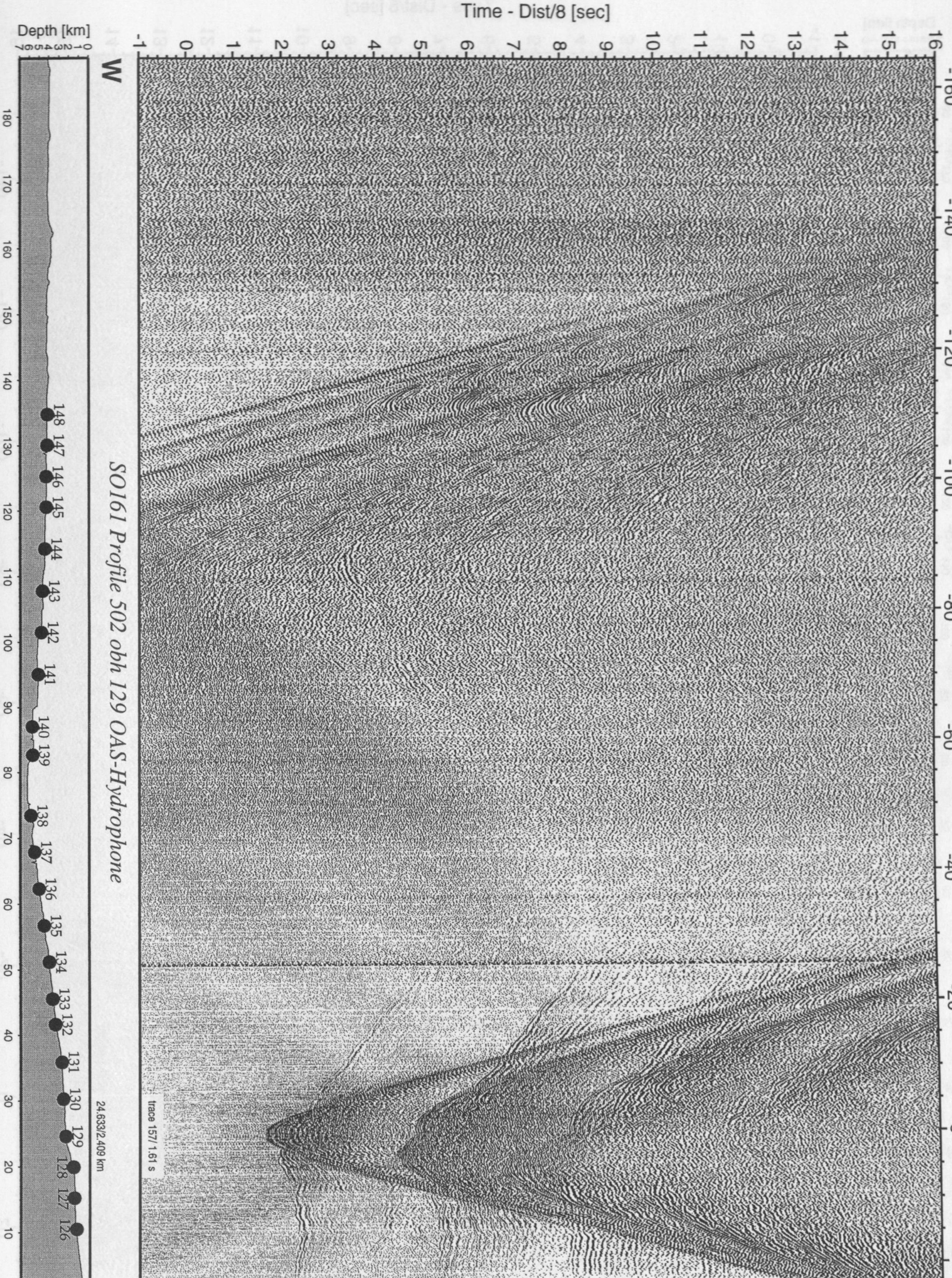

**Figure 5.4.5.22:** Record section from obh 129 OAS-Hydrophone, Profile 502.

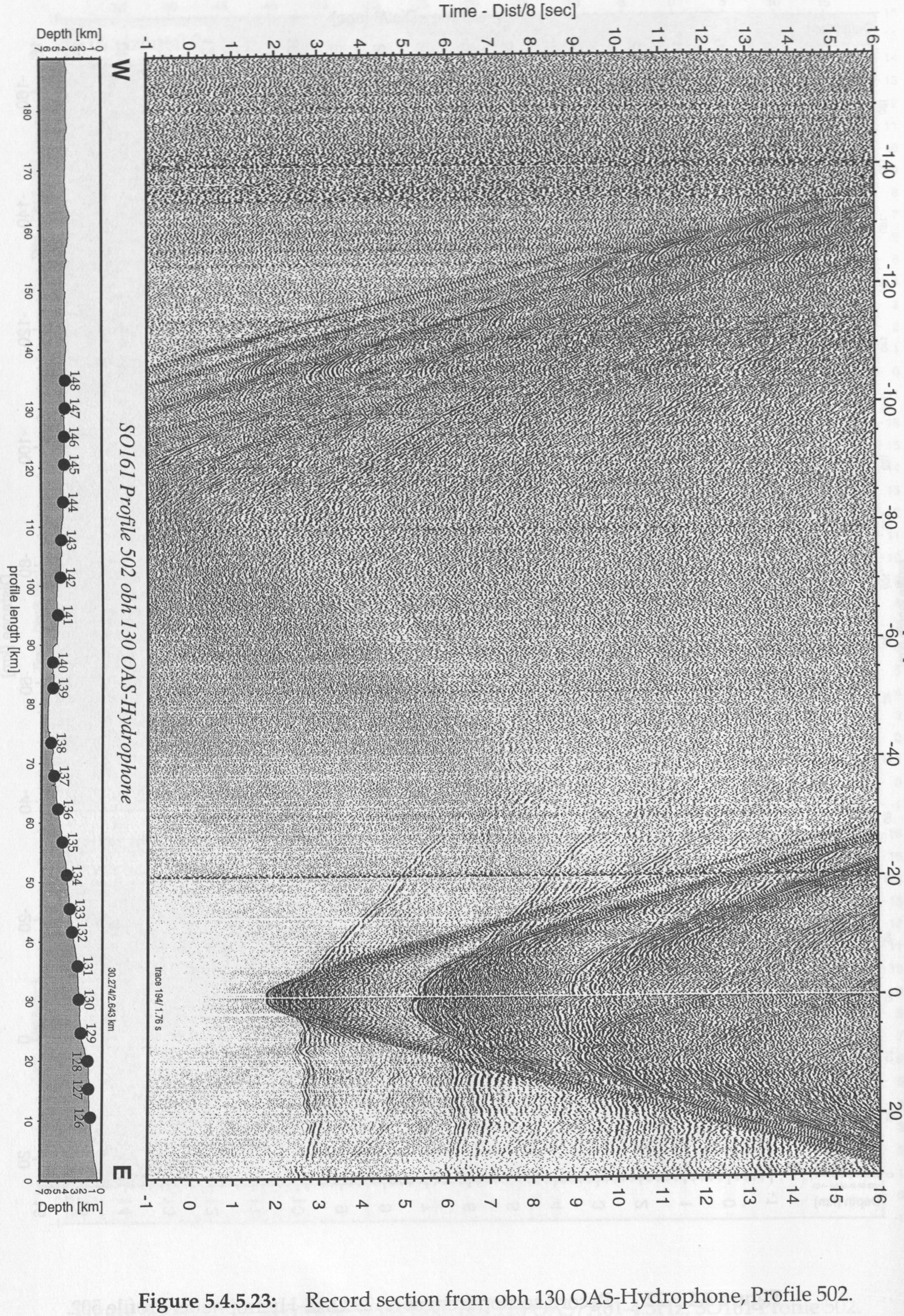

**Figure 5.4.5.23:** Record section from obh 130 OAS-Hydrophone, Profile 502.

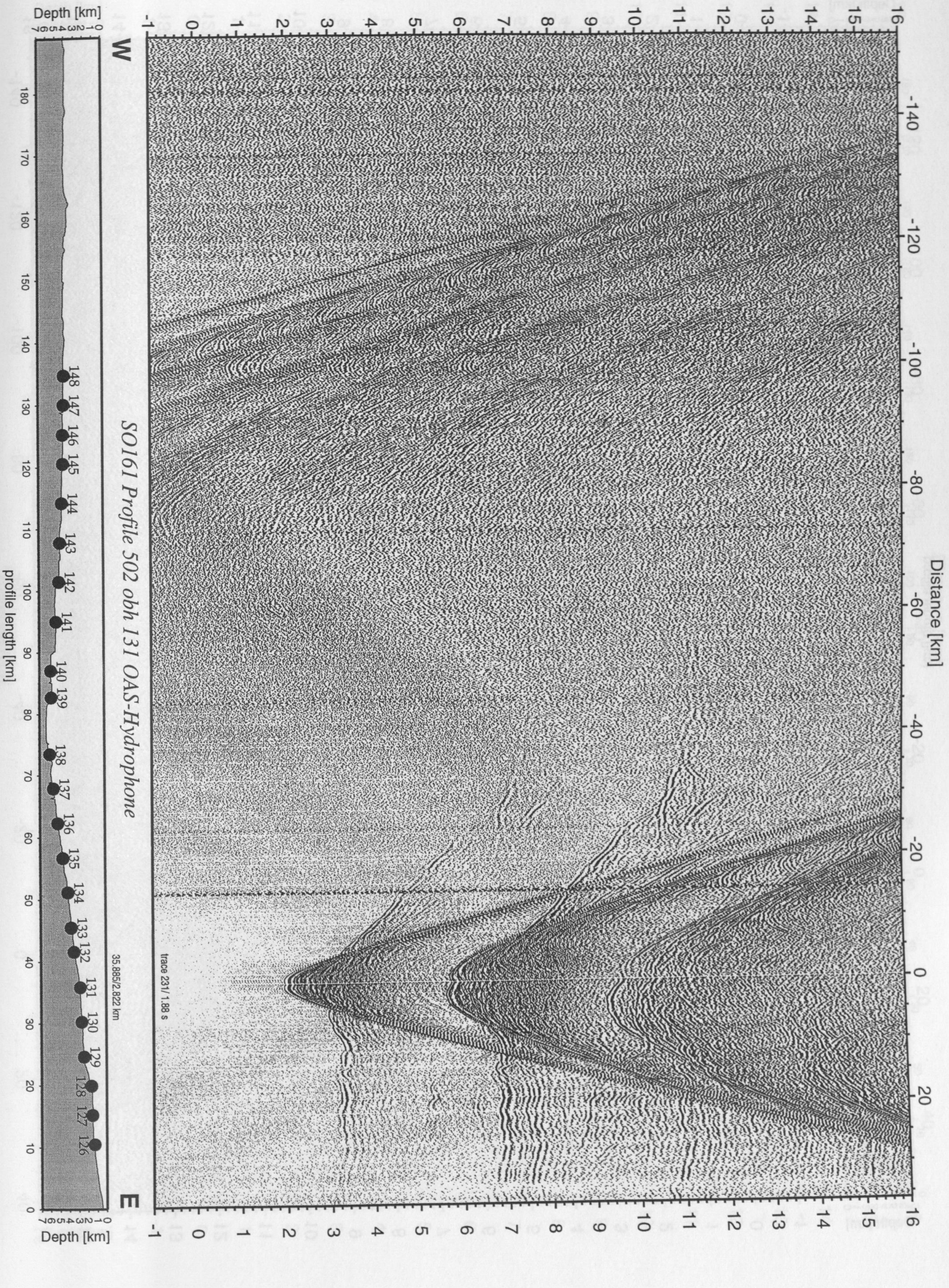

**Figure 5.4.5.24:** Record section from obh 131 OAS-Hydrophone, Profile 502.

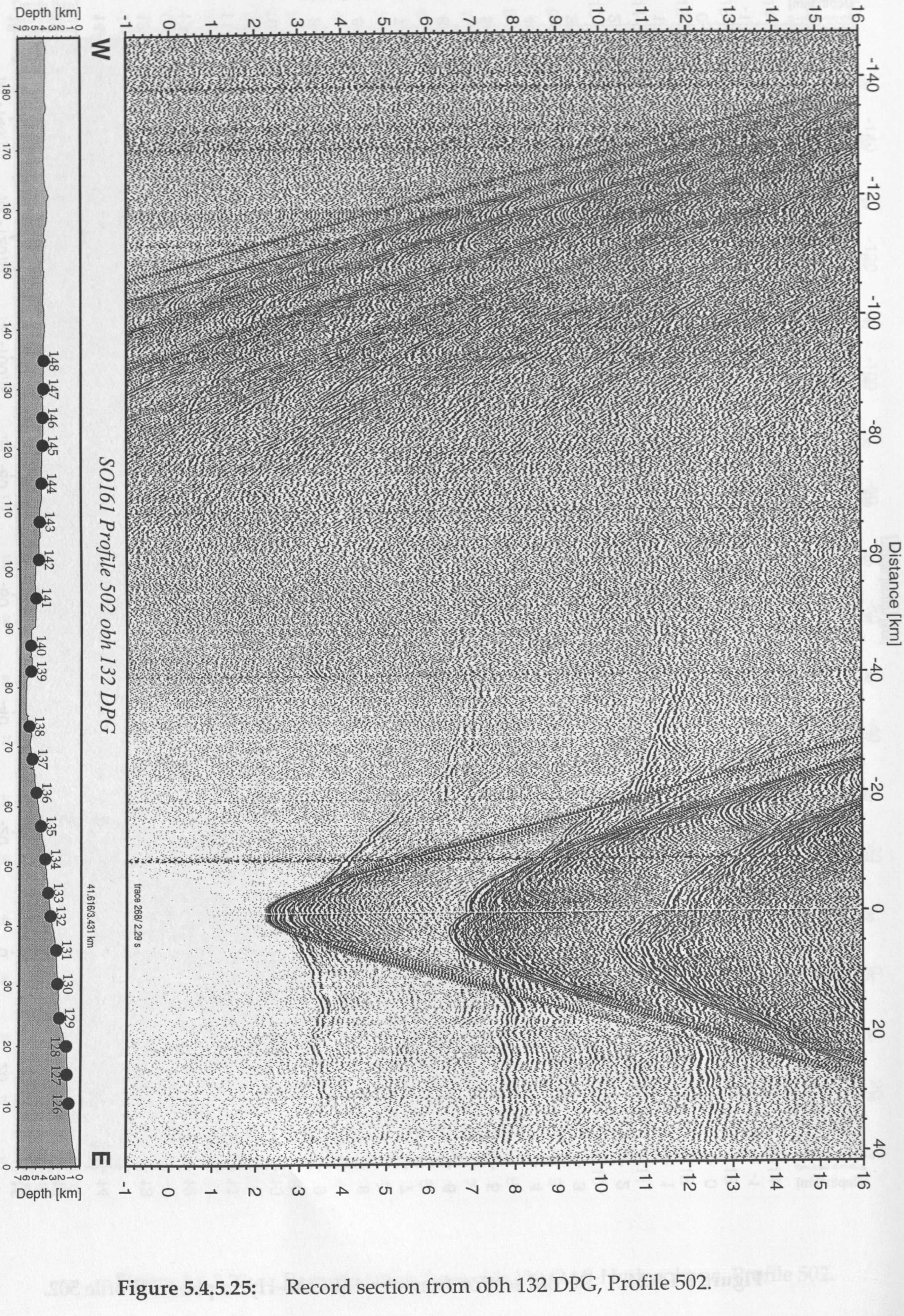

**Figure 5.4.5.25:** Record section from obh 132 DPG, Profile 502.

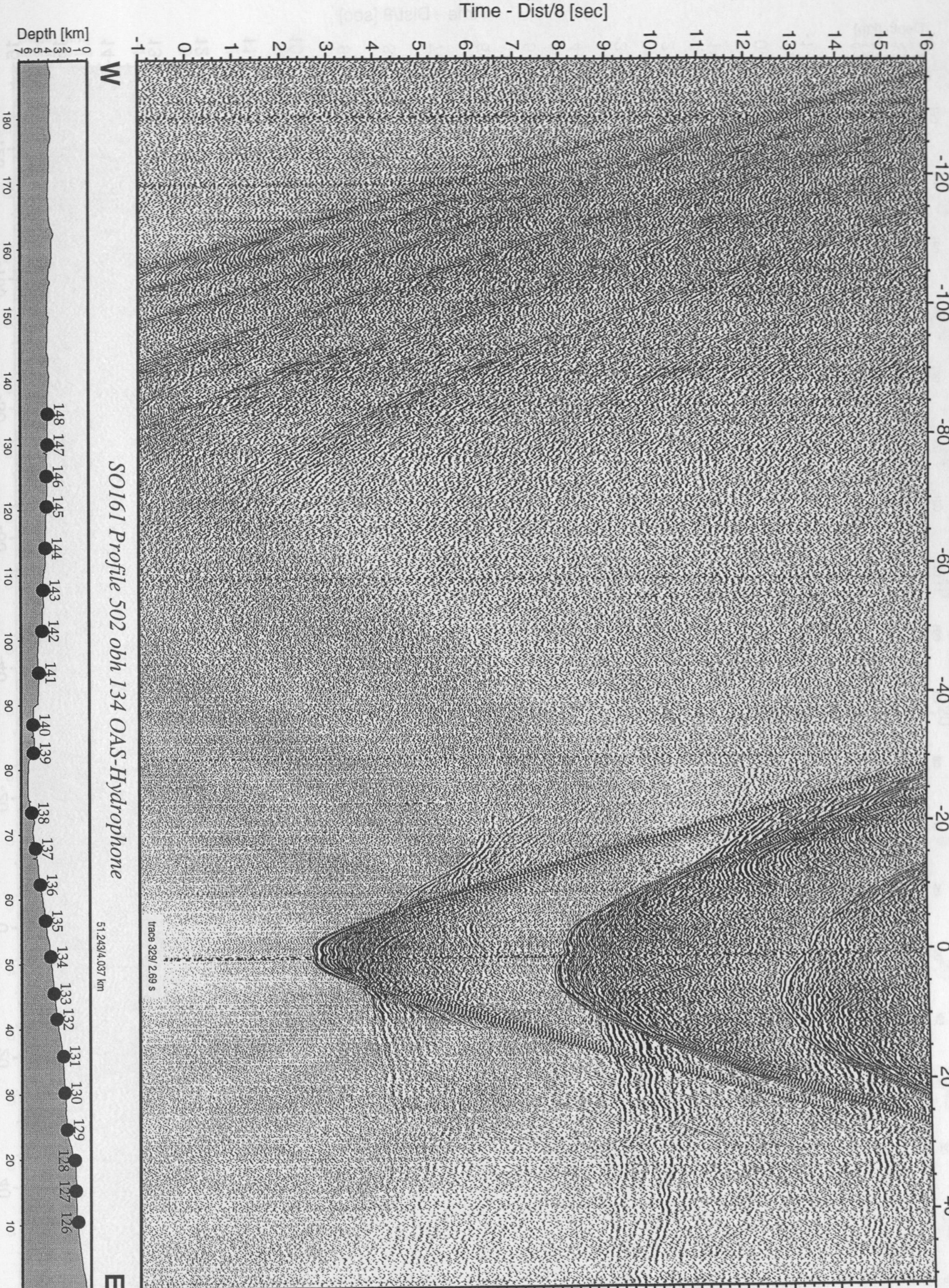

**Figure 5.4.5.26:** Record section from obh 134 OAS-Hydrophone, Profile 502.

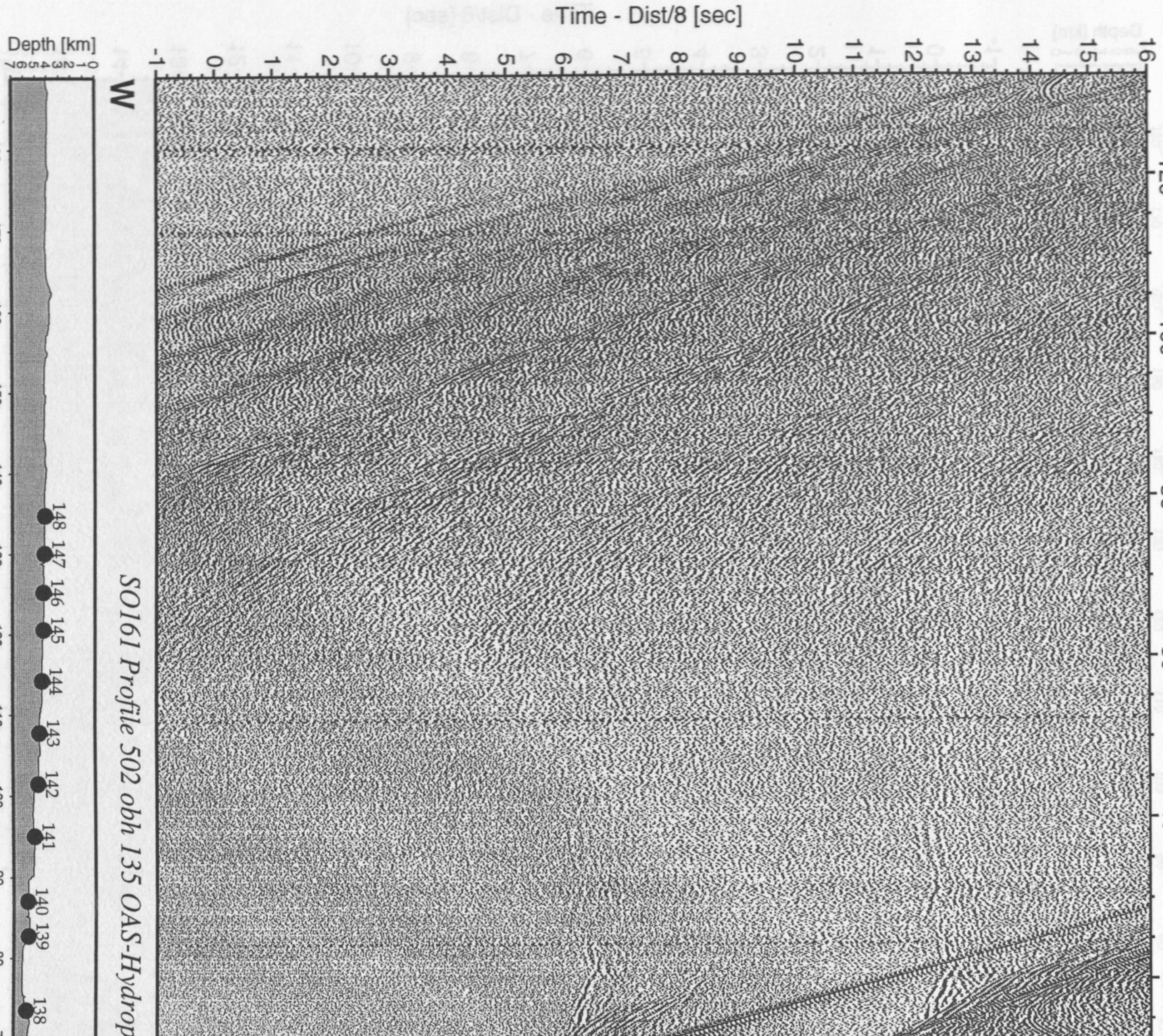

**Figure 5.4.5.27:** Record section from obh 135 OAS-Hydrophone, Profile 502.

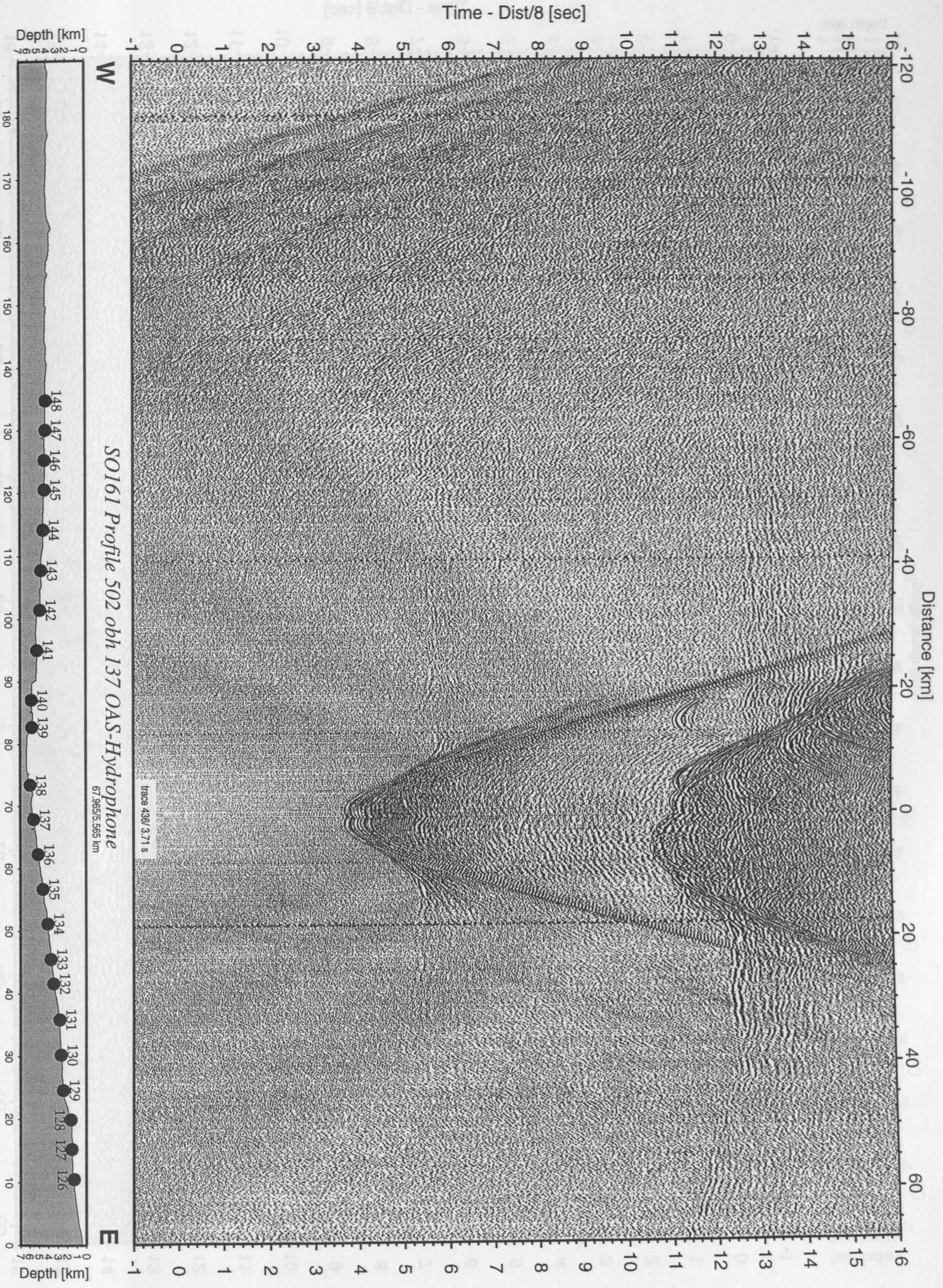

**Figure 5.4.5.28:** Record section from obh 137 OAS-Hydrophone, Profile 502.

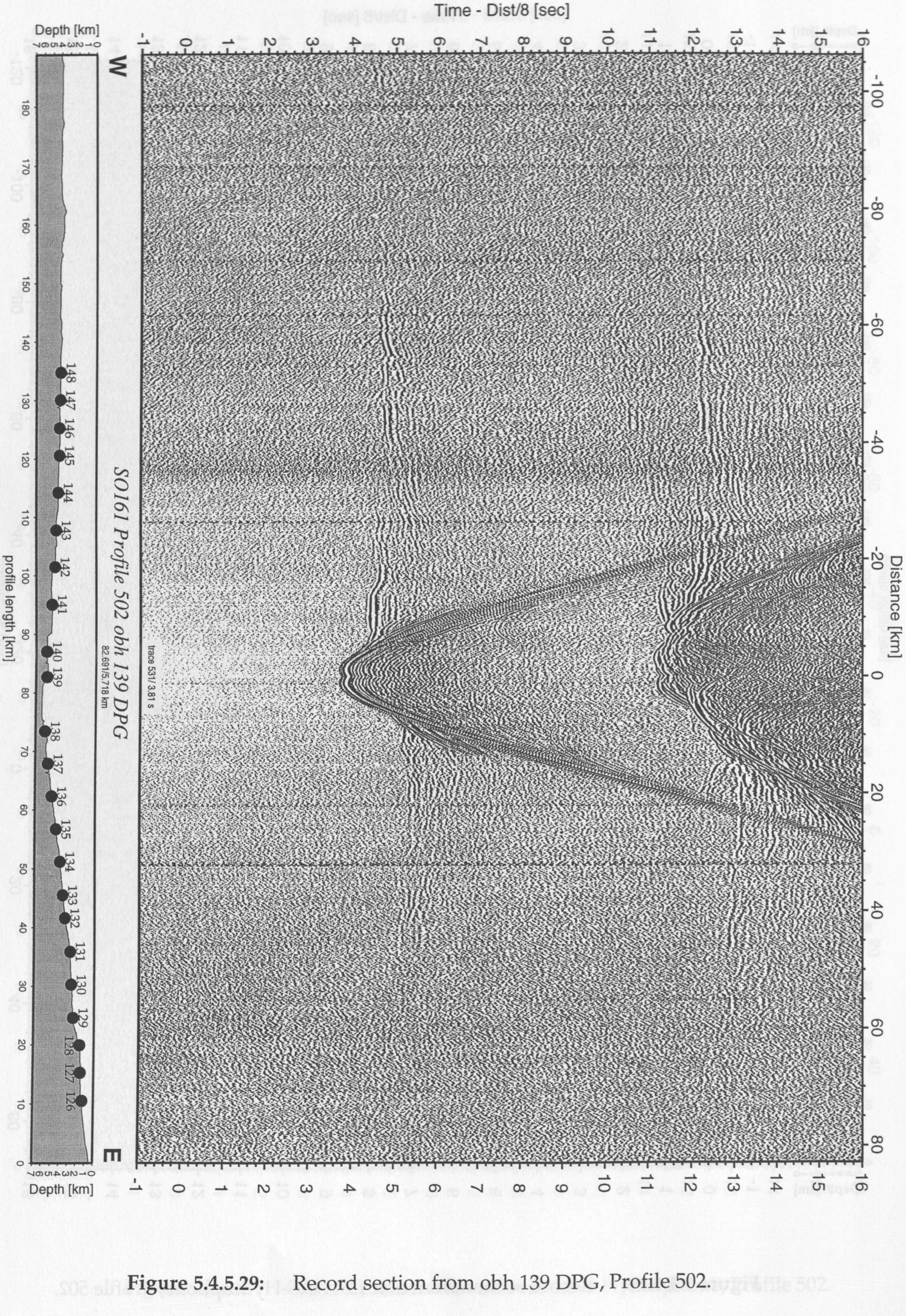

Figure 5.4.5.29: Record section from obh 139 DPG, Profile 502.

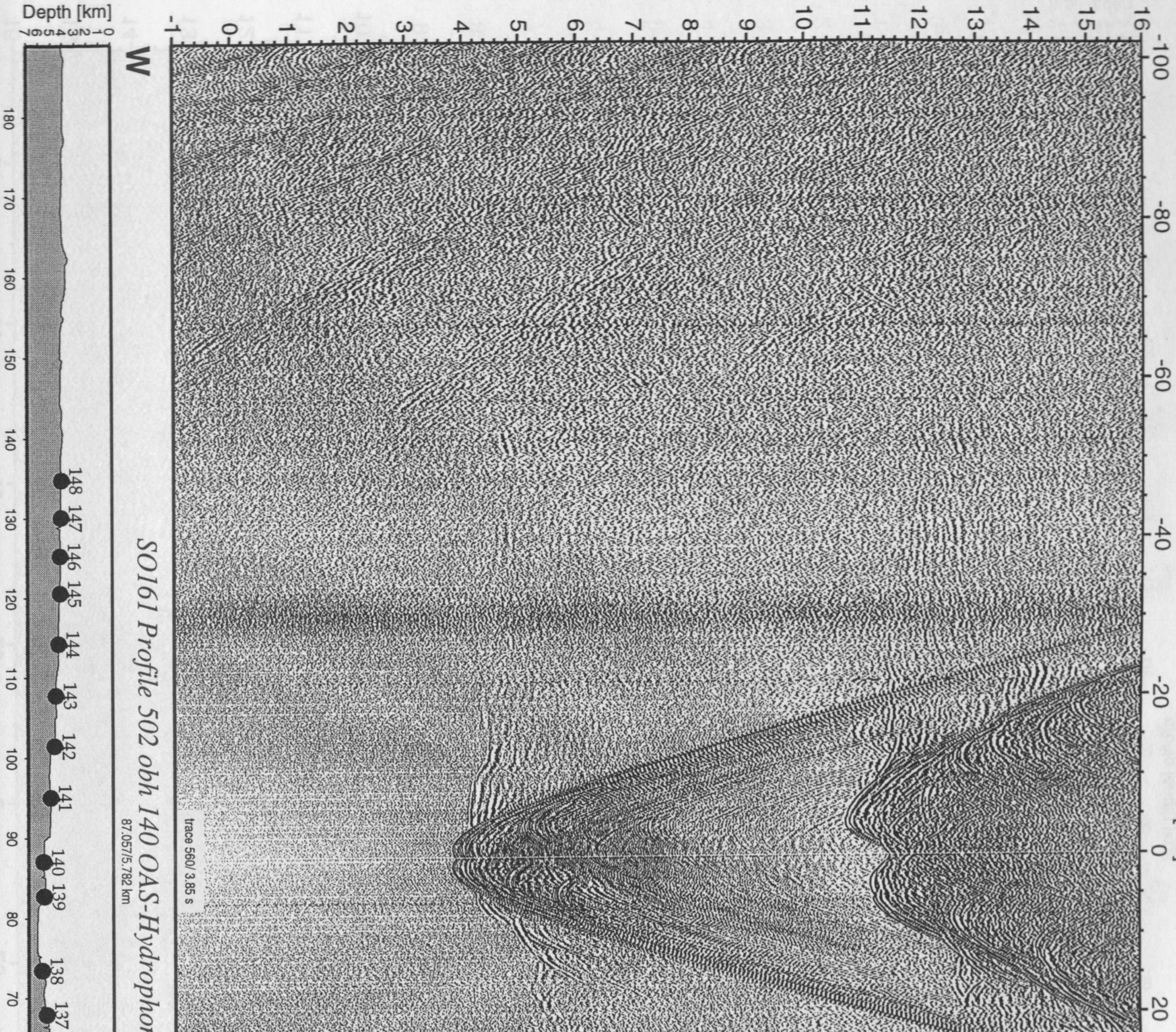

**Figure 5.4.5.30:** Record section from obh 140 OAS-Hydrophone, Profile 502.

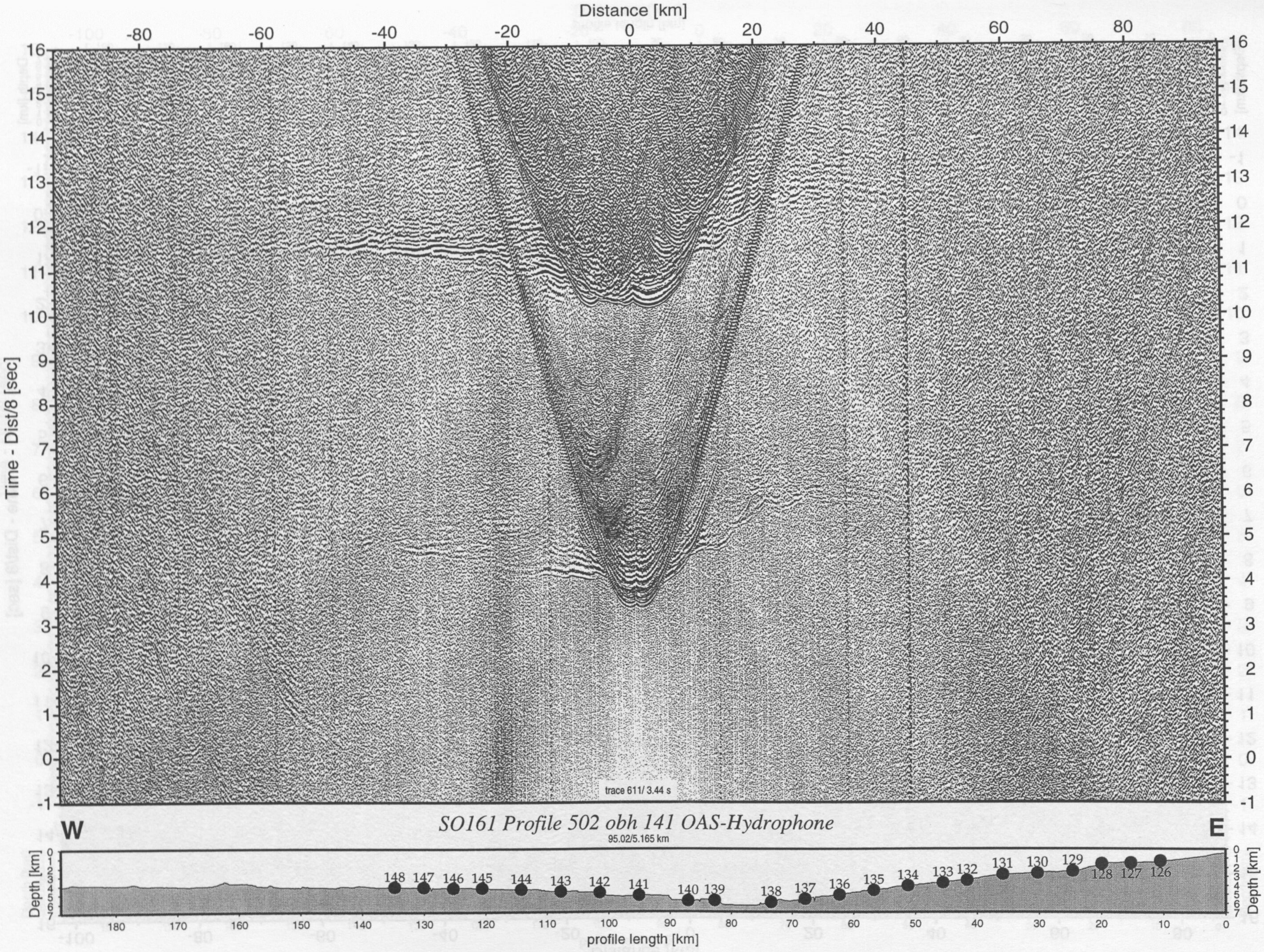

**Figure 5.4.5.31:** Record section from obh 141 OAS-Hydrophone, Profile 502.

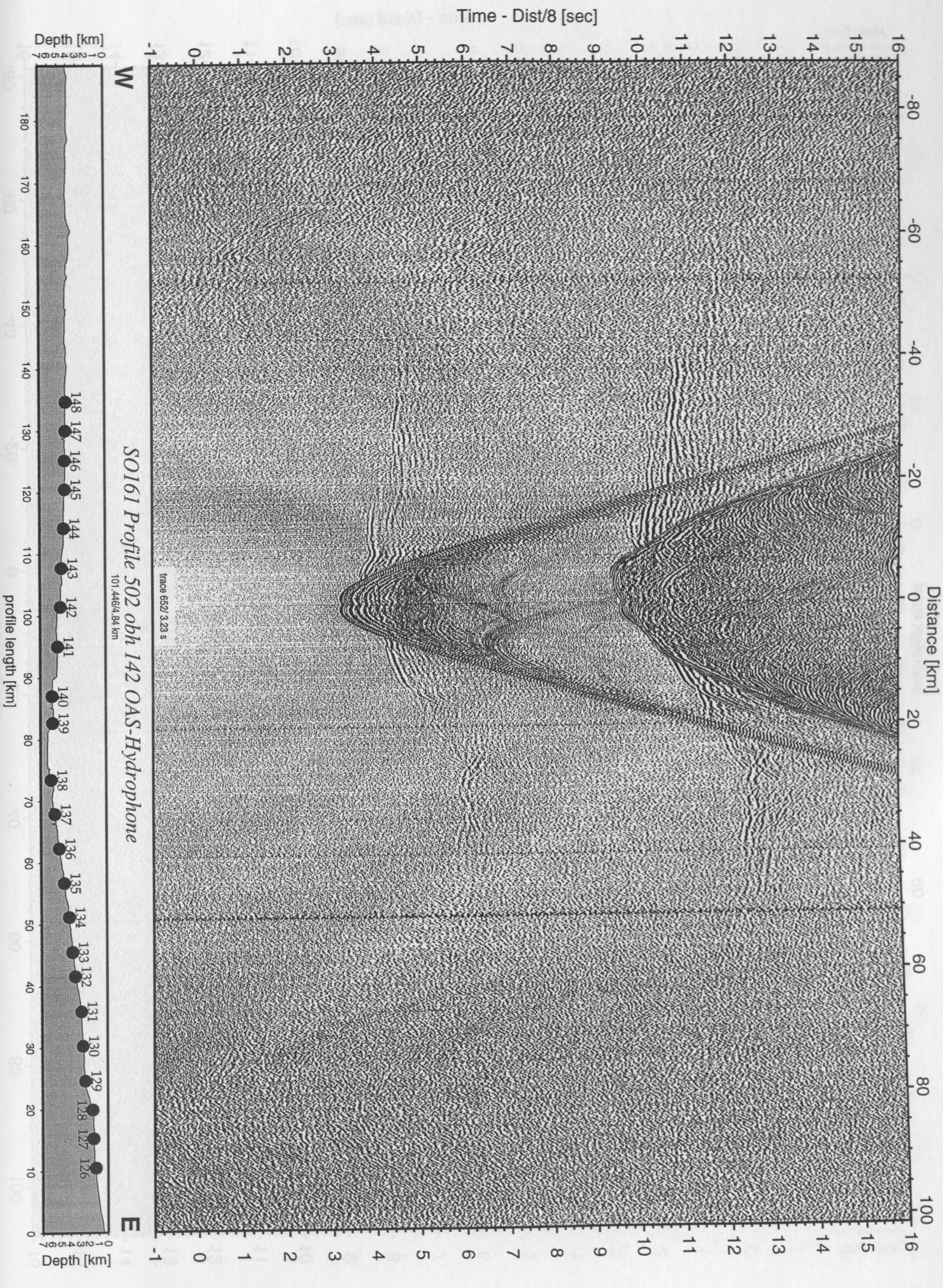

**Figure 5.4.5.32:** Record section from obh 142 OAS-Hydrophone, Profile 502.

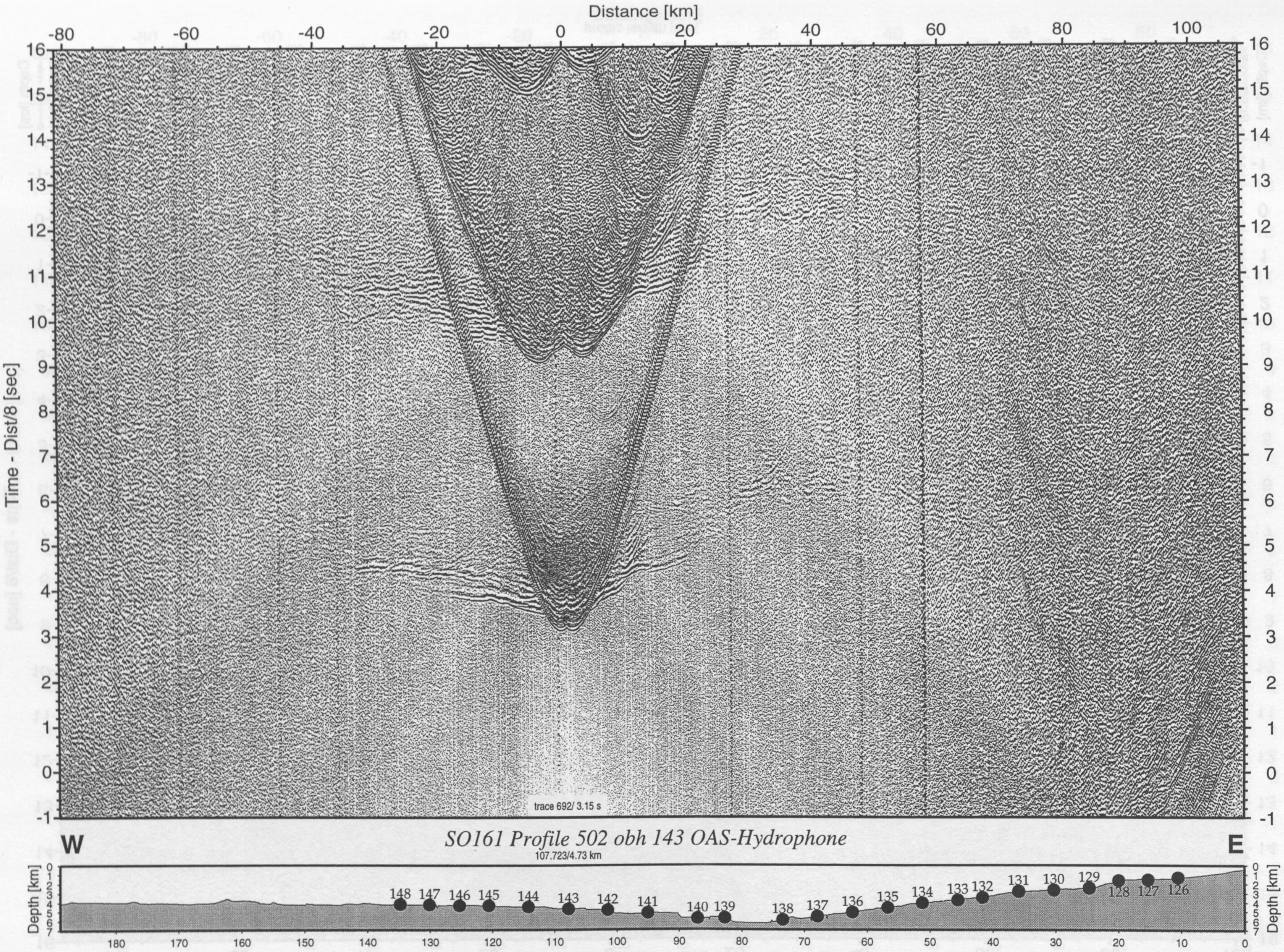

**Figure 5.4.5.33:** Record section from obh 143 OAS-Hydrophone, Profile 502.

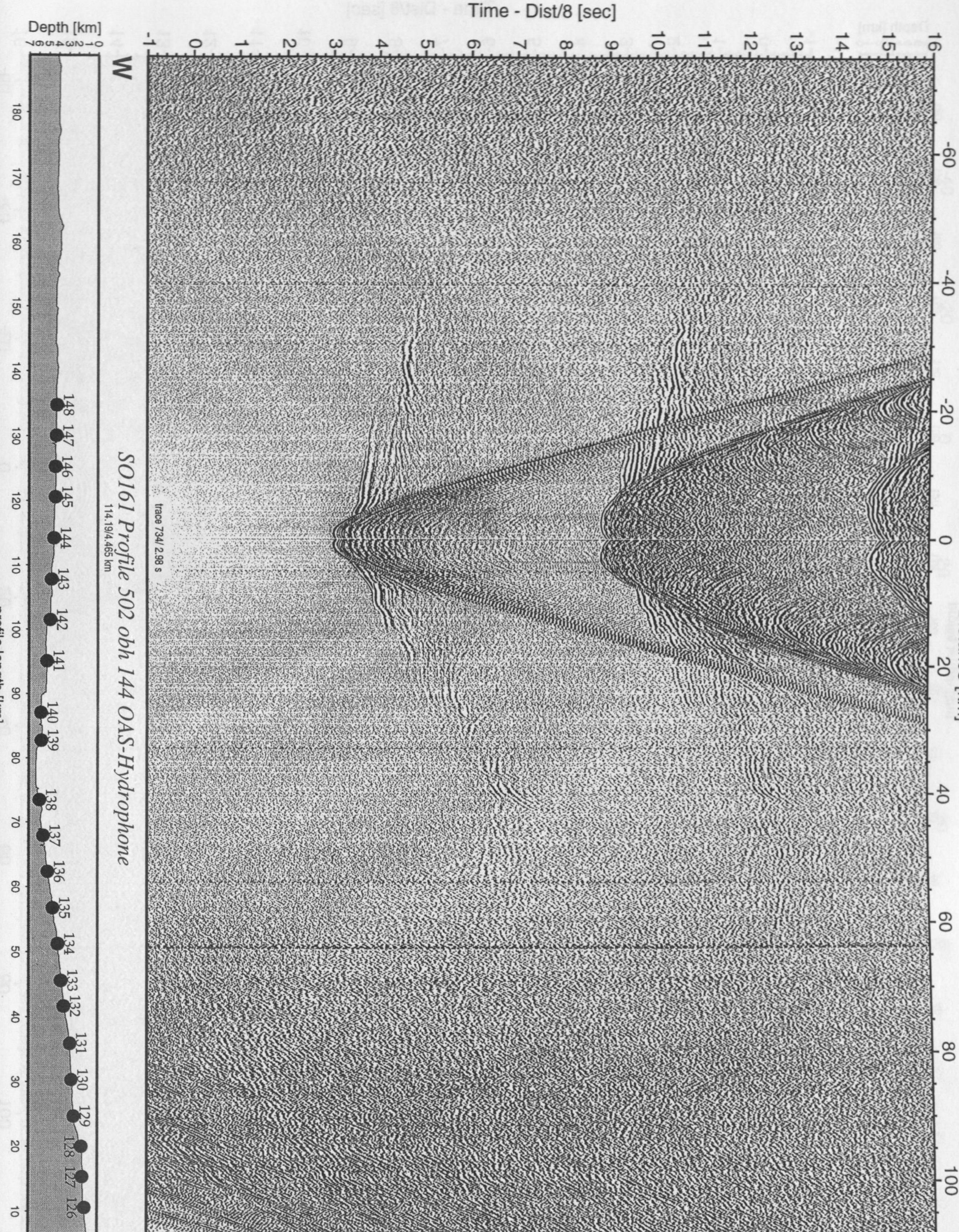

**Figure 5.4.5.34:** Record section from obh 144 OAS-Hydrophone, Profile 502.

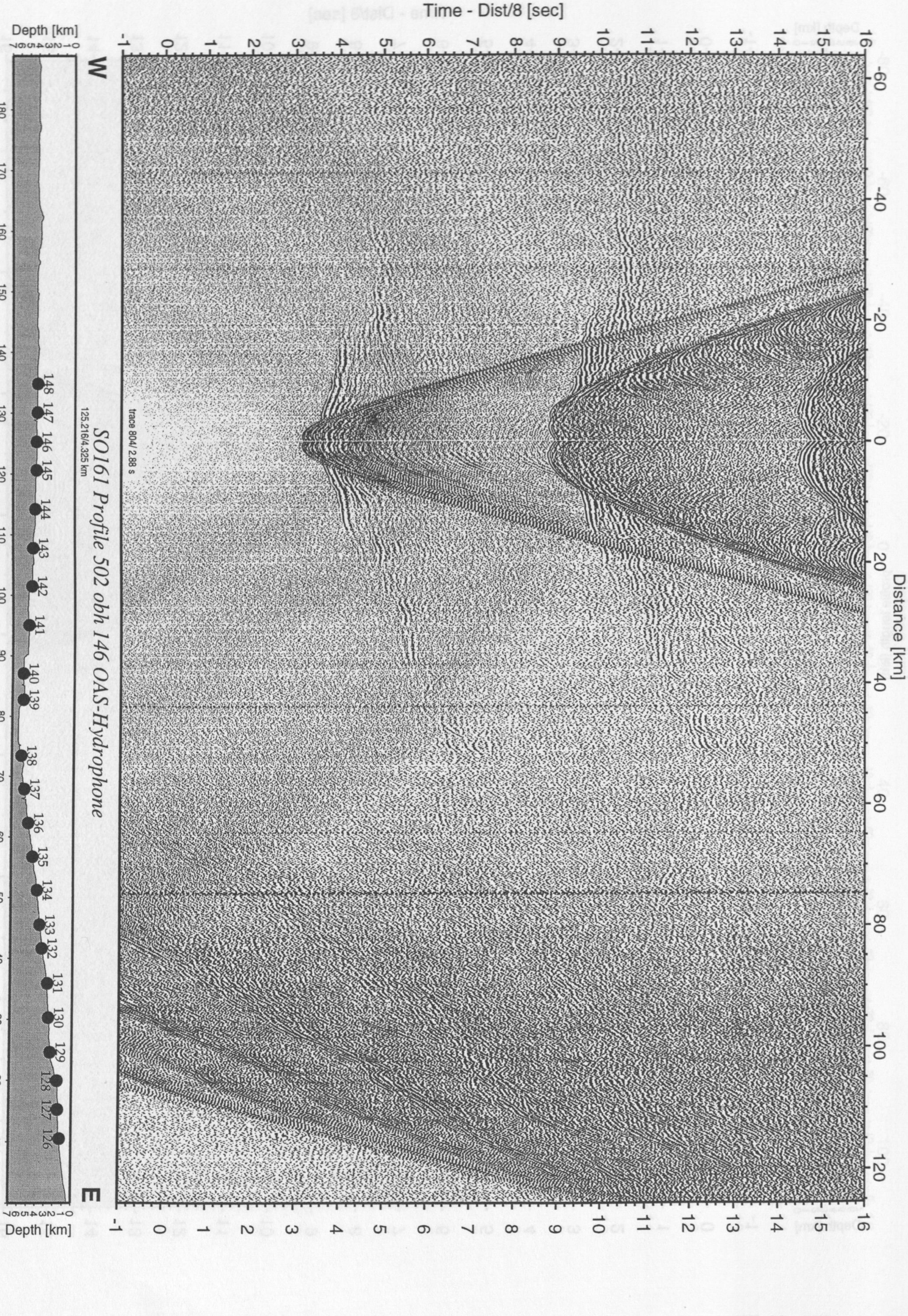

**Figure 5.4.5.35:** Record section from obh 146 OAS-Hydrophone, Profile 502.

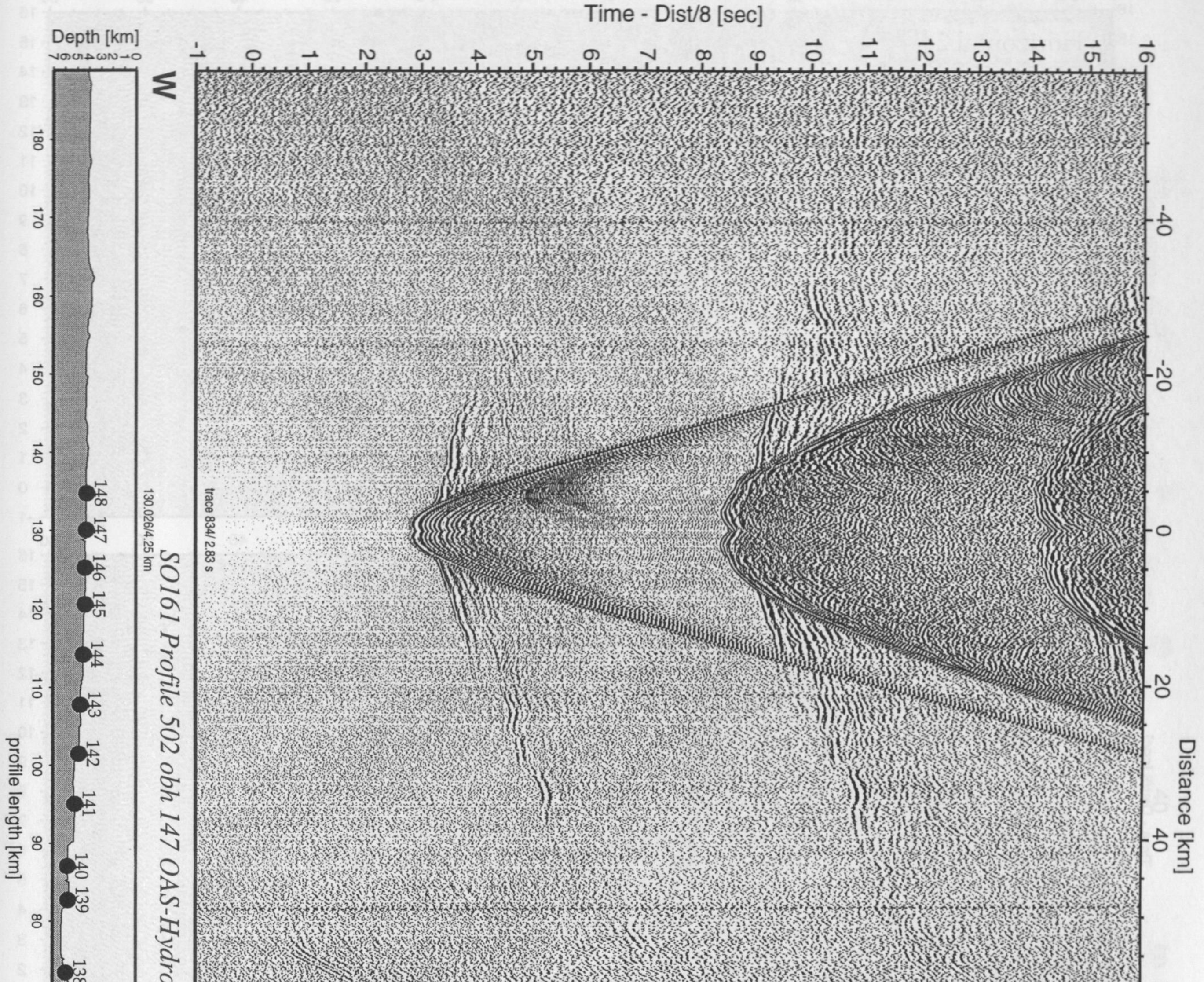

**Figure 5.4.5.36:** Record section from obh 147 OAS-Hydrophone, Profile 502.

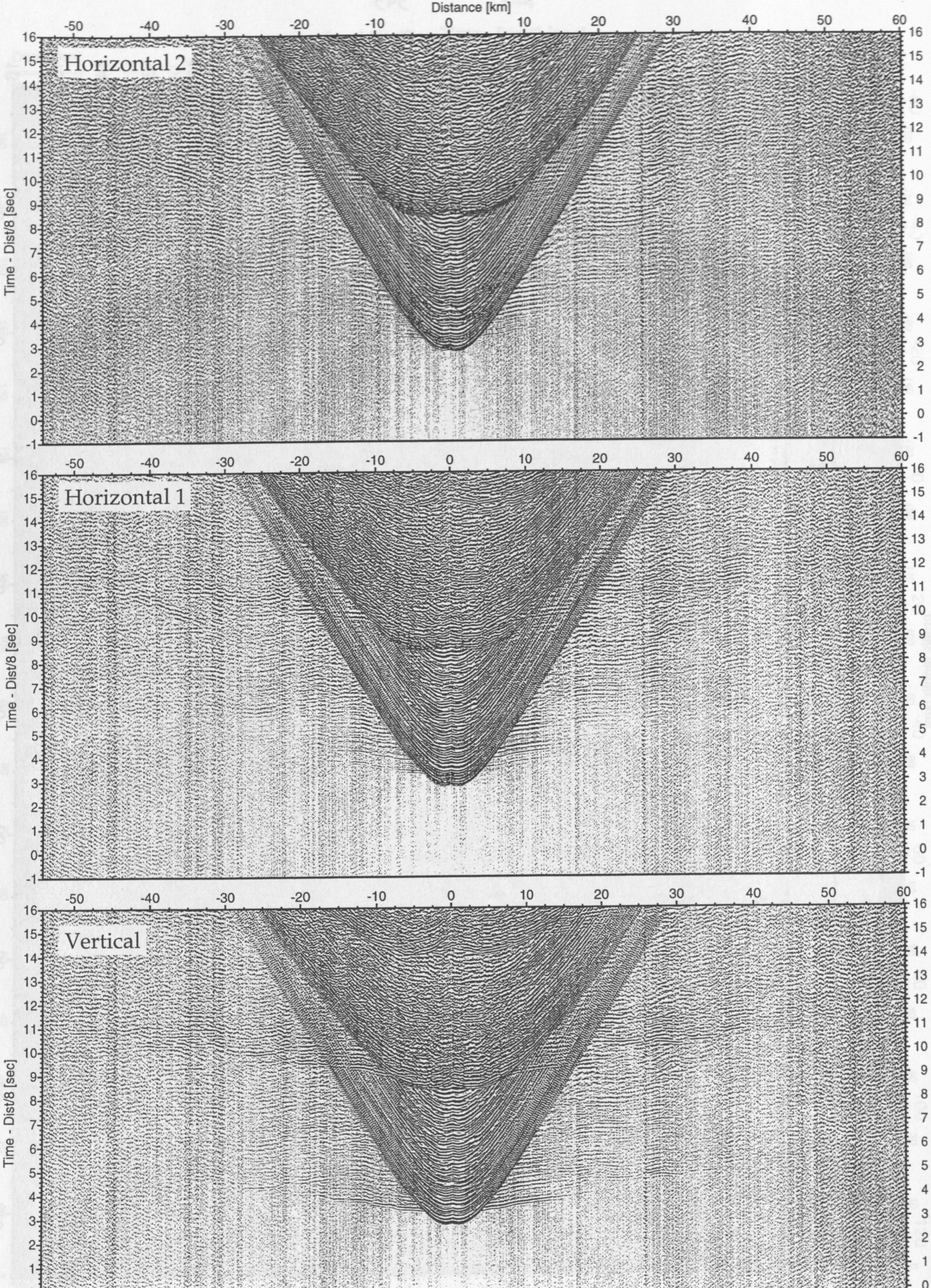

**Figure 5.4.5.38:** Record sections from obs 148 DPG/PMD, SO161 Profile 502.

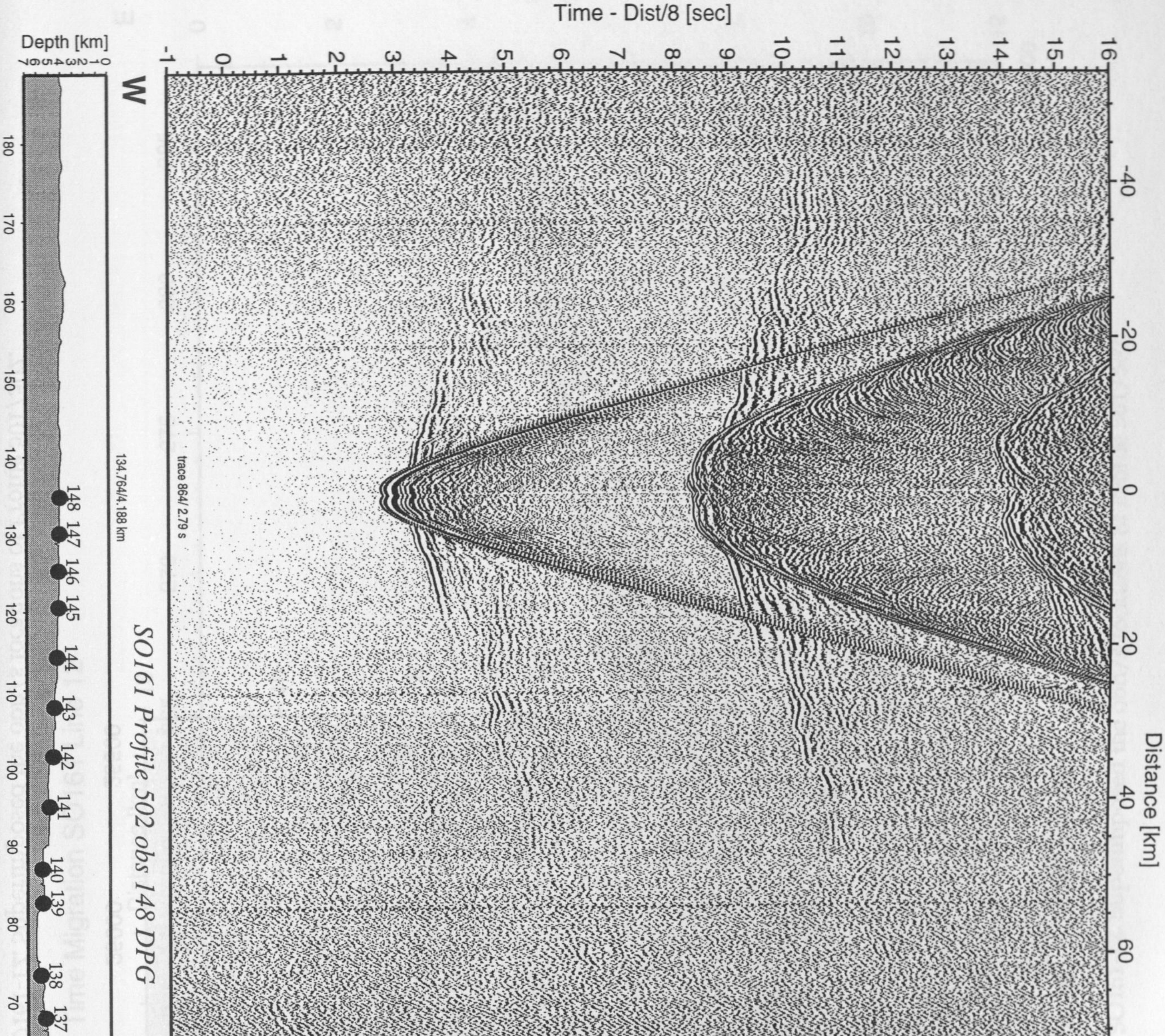

**Figure 5.4.5.37:** Record section from obs 148 DPG, Profile 502.

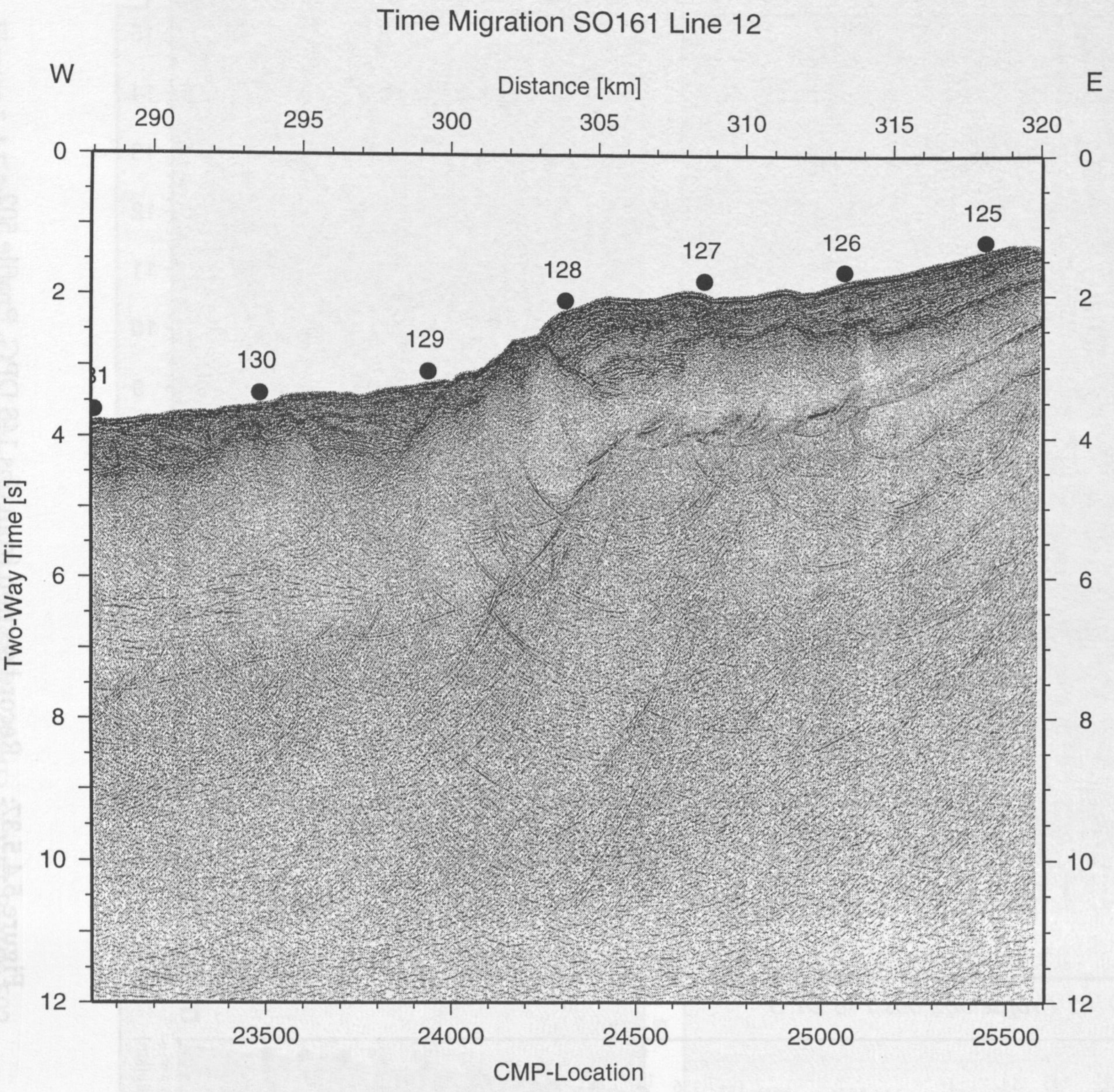

**Figure 5.4.5.39:** Post-stack time migration of Line SO161-12. Superimposed the obh/s locations of Profile 501/502.

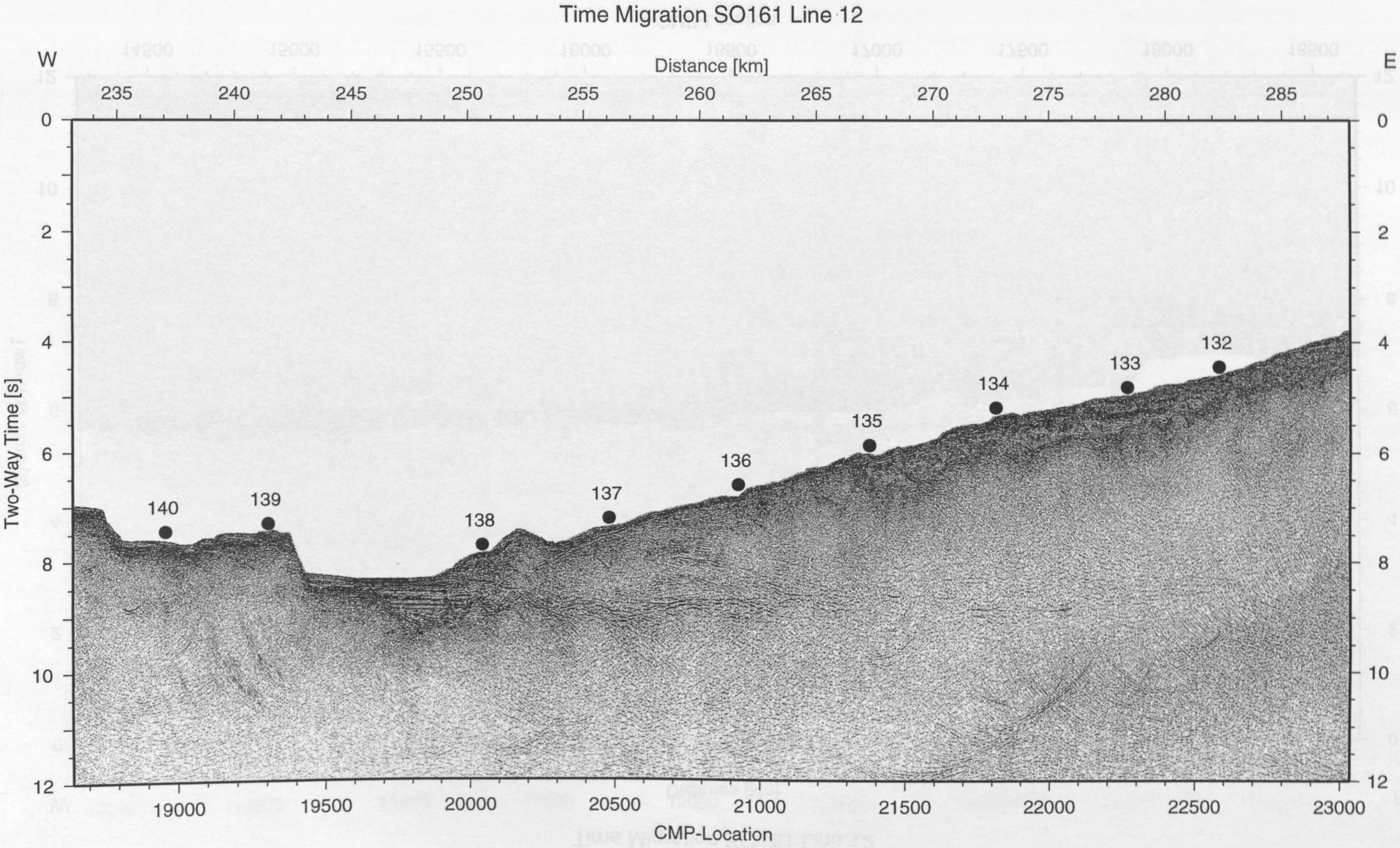

**Figure 5.4.5.40:** Post-stack time migration of Line SO161-12. Superimposed the obh/s locations of Profile 501/502.

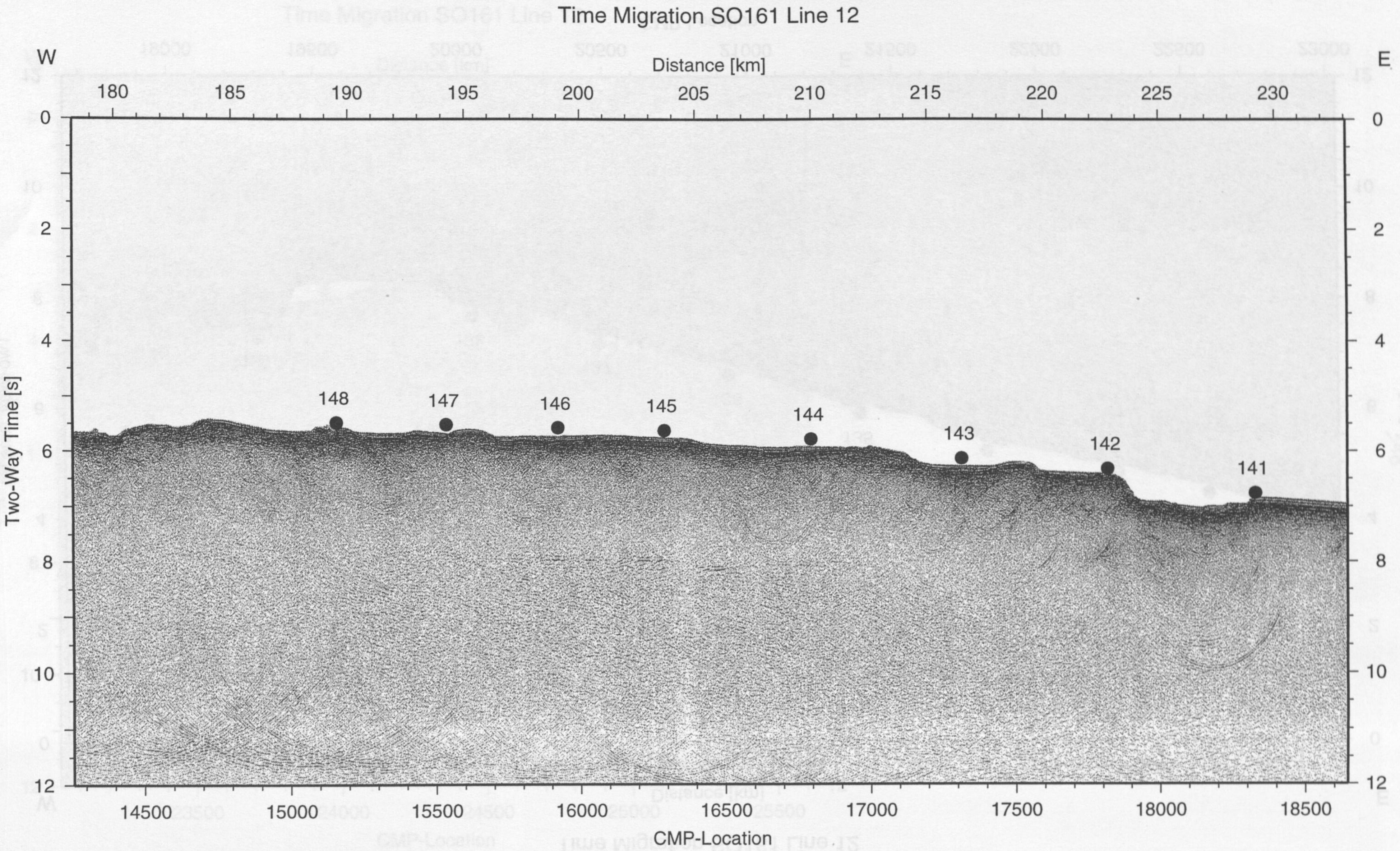

**Figure 5.4.5.41:** Post-stack time migration of Line SO161-12. Superimposed the obh/s locations of Profile 501/502.

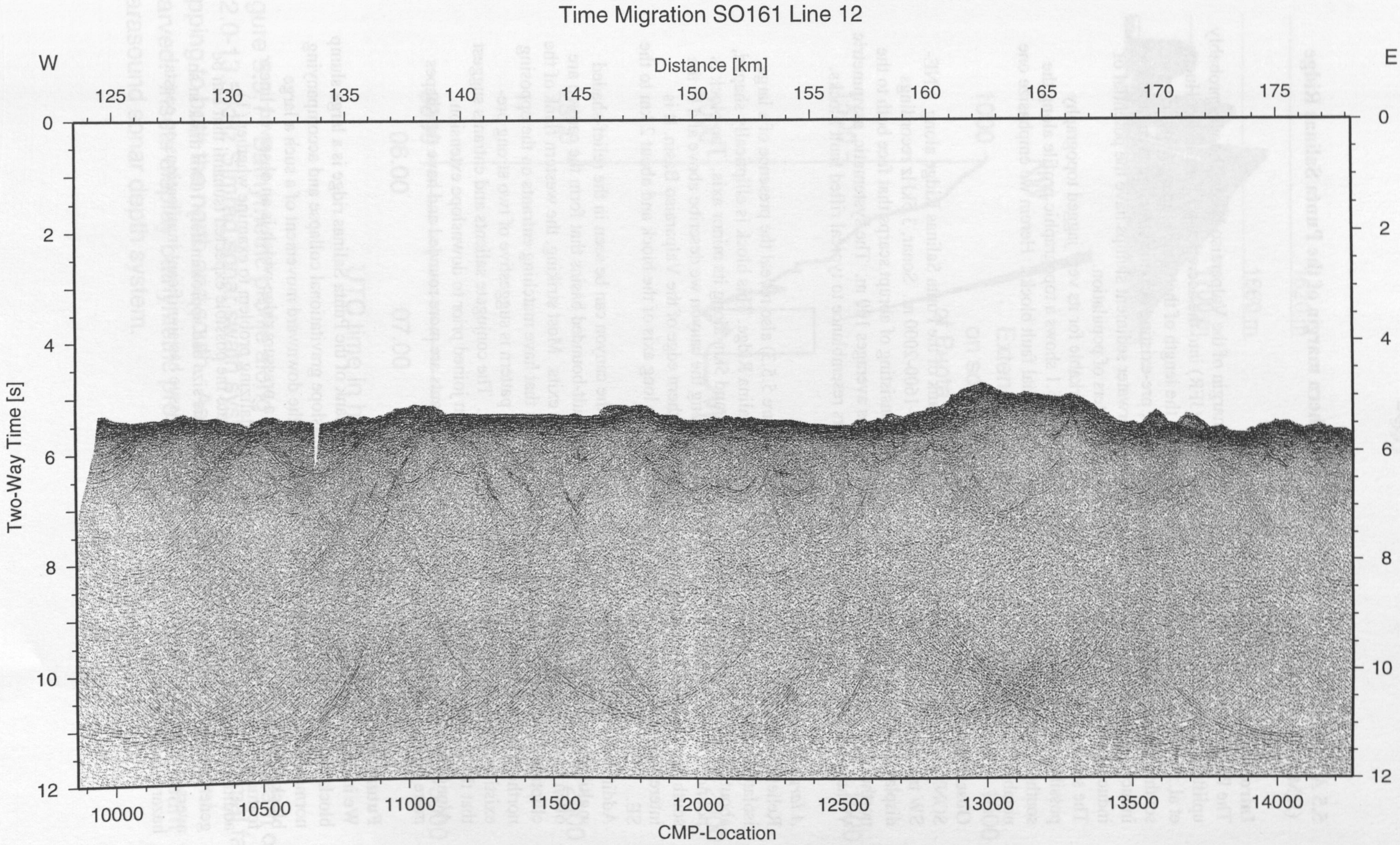

**Figure 5.4.5.42:** Post-stack time migration of Line SO161-12. Superimposed the obh/s locations of Profile 501/502.

## 5.5 A Possible Slump Structure on the southern margin of the Punta Salinas Ridge

(J. M. Lorenzo and E. E. Vera)

### Introduction

The Punta Salinas Ridge buttresses the northern margin of the Valparaiso Basin and was probably uplifted during entry of the Juan Fernandez Ridge (JFR) into the accretionary prism (von Huene et al., 1997). The trend of the JFR lies oblique to the length of the Chilean margin inducing a southward migration of the uplift with time. Thus, pre-existing oceanic structure is capable of inducing slope instability. Sufficiently large underwater sediment slumps have the potential of inducing tsunamis and affecting nearby coastal centers of population.

The southern flank of the Punta Salina Ridge is remarkable for its very jagged topography possibly related to active slope instability. Figure 5.5.1 shows a topographic profile along the southern flank of this ridge with many isolated potential fault blocks. Herein we emphasize one notable feature on the upper portions of the slope.

### Observations

SONNE Cruise 161, Leg 4 traverses the southern flank of the Punta Salinas Ridge along a NE-SW trending mid-slope canyon in water depths of ~1600-2000 m. Sonar, 3.5kHz recordings display a highly serrated canyon floor and walls consisting of abrupt scarps that face both to the northeast and southwest. Relief across these scarps averages 100 m. The systematic, asymmetric V-shaped depressions generated by this relief bears resemblance to typical rifted fault blocks.

*A large slump block*?

Relief-shaded and contoured multibeam data (Figure 5.5.3) also reveal the presence of a large, isolated block on the southern flank of the Punta Salina Ridge. This block is elliptically shaped, about 10 km in length along its major NE-SW axis and 5km along its minor axis. The block is bounded to the north by the normal fault blocks along the canyon we describe above and to the south it is bounded by the gentler slopes of the northern edge of the Valparaiso Basin. It is interesting to note a small ridge lying parallel to the long axis of the block and about 2 km to the SE.

Additional evidence for the normal faulting within the canyon can be seen in the relief-shaded multibeam data (Figure 5.5.2). In plan view, the fault-bounded basins that form the canyon are often square in shape with narrow corridors at their exits. Most striking, the western flank of the elliptical block shows a step-like edge with salients that have matching entrants on the opposing northern side (Figure 5.5.3) The "chocolate tablet" pattern is suggestive of two strong pre-existing directions of weakness controlling faulting. The conjugate salients and entrants suggest that the opposing sides of the canyon may have been joined prior to downslope extension.

Along the northern canyon wall, in general, the entrants are more rounded and have the shapes more typical of slump scars.

### Future Work

We interpret that the large block observed on the flank of the Punta Salinas ridge is a large slump block, separated along its northern side via down-slope gravitational collapse and accompanying normal-faulting. A corollary of this model is that the downward movement of a such a large block could push the sediments in front to produce a pressure ridge which is an observed linear feature near the foot of the block. It remains a tantalizing problem to examine whether (1) additional blocks exist in the area and to (2) calculate the possible expected tsunami that can be generated by the sudden movement of a block of this size and approximately 100m thick in an average of about 2000 m of water depth. This last issue has significant implications on coastal hazard assessment.

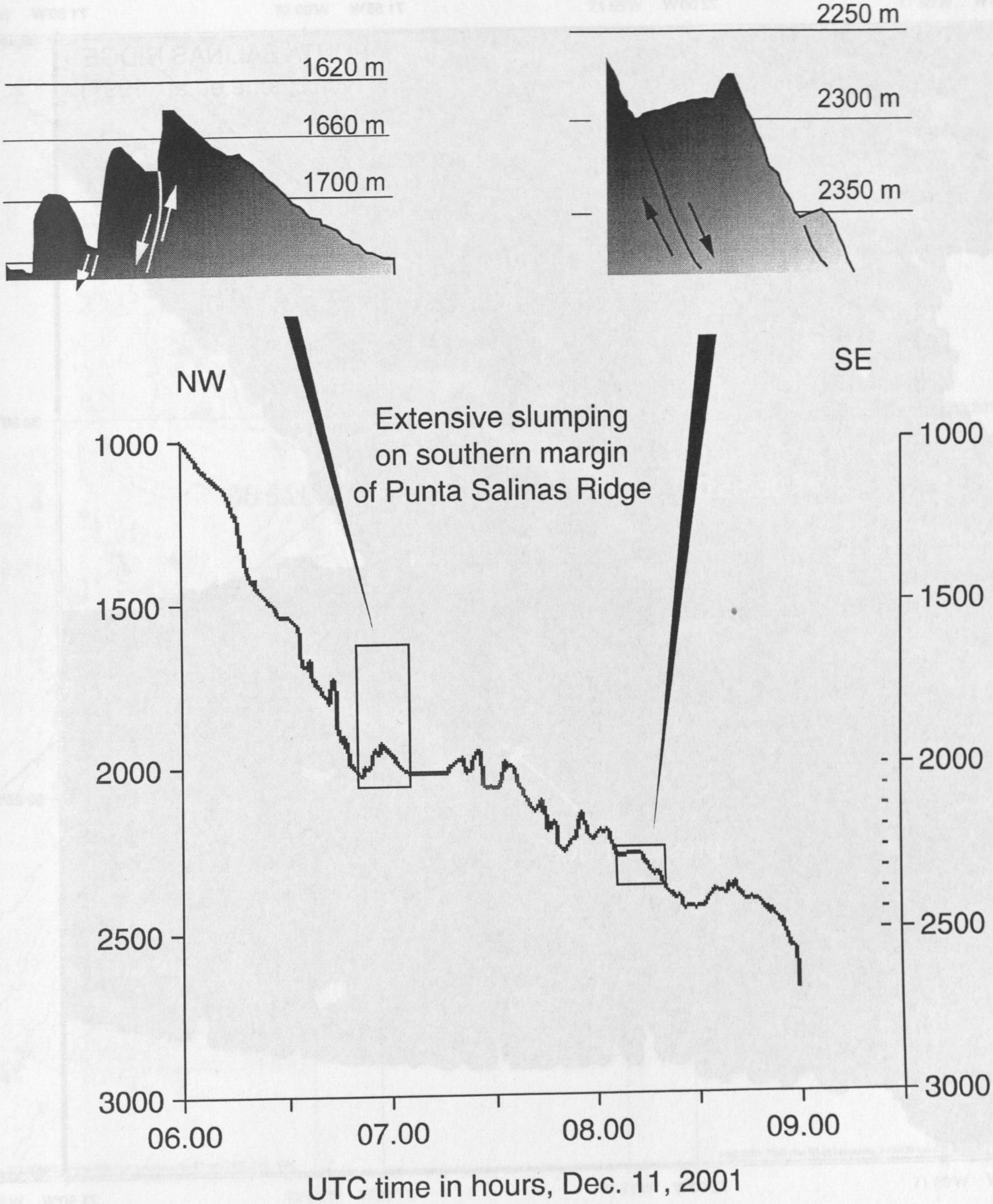

Figure 5.5.1 Bathymetric profile along ship trqack tacken from middle beam of 12.0-13.5 kHz SImrad sonar swath system. Insets show interpreted normal faults dipping to both the north and south. Asymmetic half-grabens are sediment starved. Insets display bathymetric profile derived from 3.5 kHz single-beam Parasound sonar depth system.

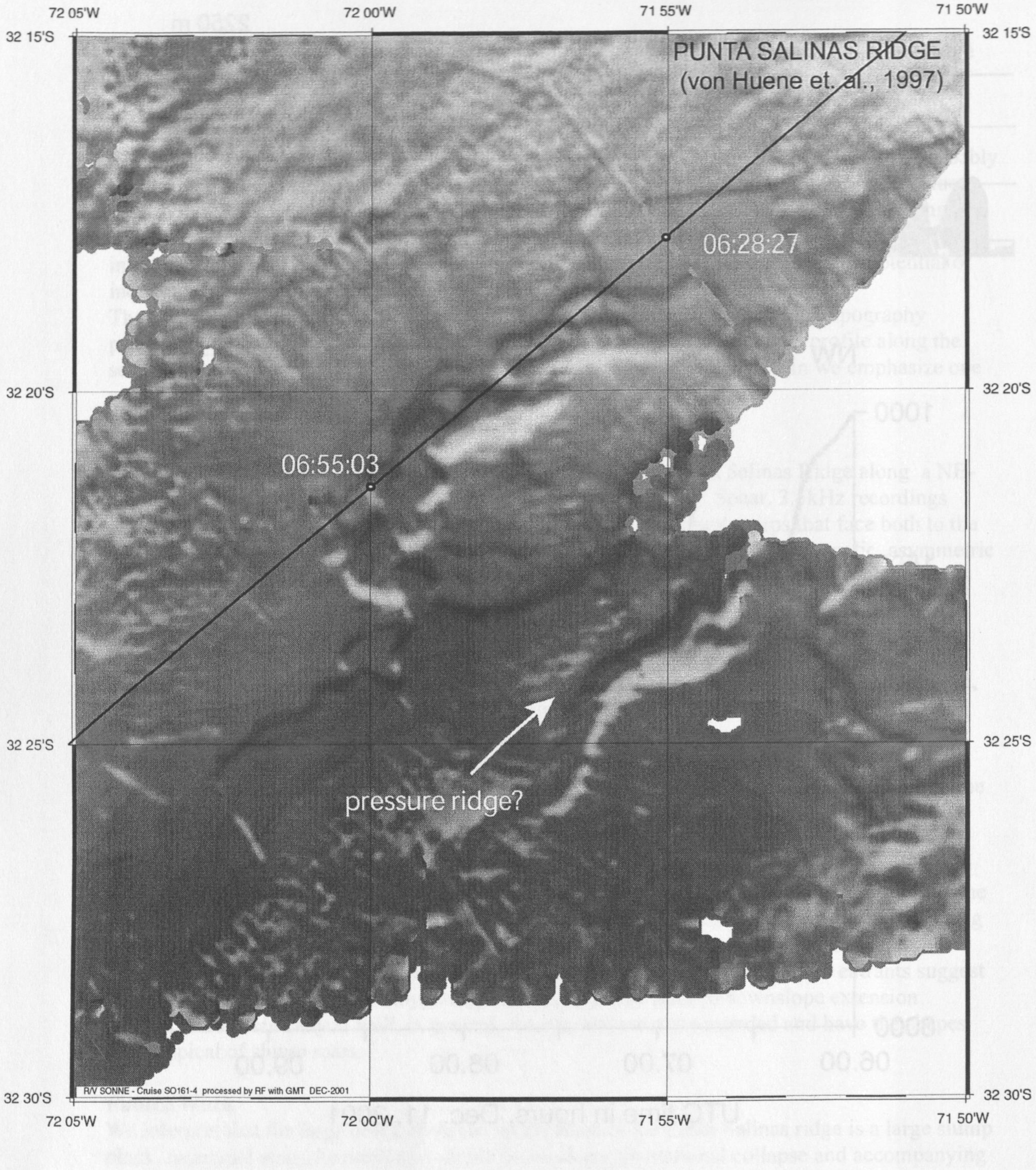

**SPOC**
**GEOMAR Kiel**
R/V SONNE - Cruise 161-4
Area North - Punta Salinas Ridge

Shaded Bathymetrie
Light Azimuth 340 and 150
Mercator Projection (WGS 84)
Scale 1:150.000 at 32S
Grid 90 m

Map processed with GMT on Board R/V Sonne
by RF Reedereigemeinschaft Forschungsschiffahrt GmbH
DEC-2001

Figure 5.5.2

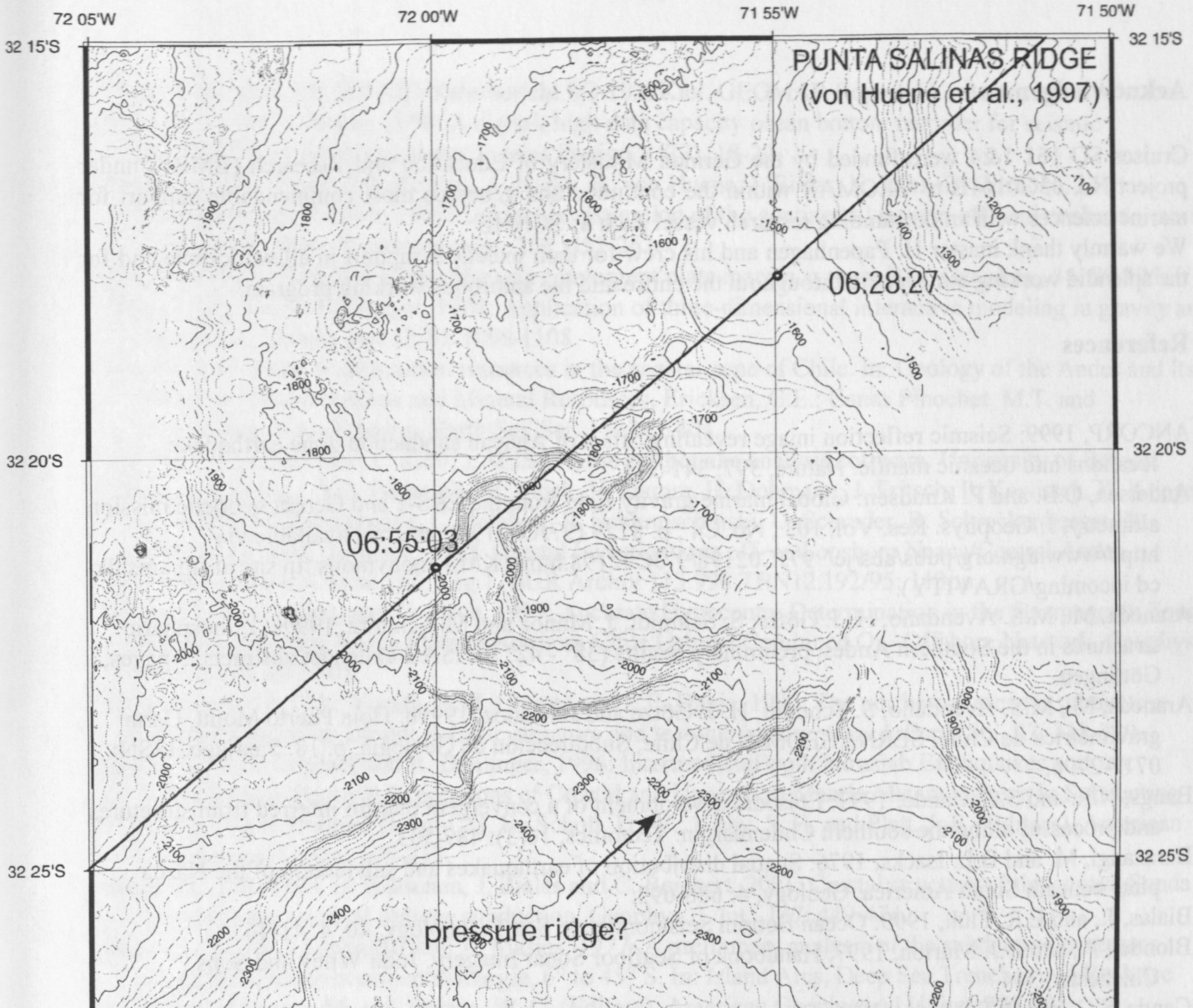

**SPOC**
**GEOMAR Kiel**
R/V SONNE - Cruise 161-4
Area North - Punta Salinas Ridge

Mercator Projection (WGS 84)
Scale 1:150.000 at 32S
Grid 90 m Contour 20 m

Map processed with GMT on Board R/V Sonne
by RF Reedereigemeinschaft Forschungsschiffahrt GmbH
DEC-2001

Figure 5.5.3

## Acknowledgements

Cruises SO 161 1&4 were funded by the German Ministery of Education and Research (BMBF) under project No. 03G0161B to GEOMAR within the continued and generous most commendable support for marine sciences with an outstanding research vessel such as SONNE

We warmly thank master H. Papenhagen and his crew for their excellent support in all work done and for the splendid working atmosphere throughout the entire and the ambitious working program.

## References

ANCORP, 1999: Seismic reflection image revealing offset of Andean subduction-zone earthquake locations into oceanic mantle. Nature, 397: 341-344.

Andersen, O.B. and P. Knudsen: Global marine gravity field from the ERS-1 and Geosat geodetic mission altimetry, J. Geophys. Res. Vol. 103 , No. C4 , p. 8129 (97JC02198); abstract available via http://www.agu.org/pubs/abs/jc/ 97JC02198/97JC02198.html (KMS anonymous ftp site at ftp.kms.dk cd incoming/GRAVITY).

Araneda, M., M.S. Avendaño, H.-J. Götze, S. Schmidt, J. Munoz and M. Schmitz, 1999a: Lithospheric structures in the Southern Andes, preliminary results (38° - 42° S). ISAG exdendet abstracts, 5 pages, Göttingen.

Araneda, M., M.S. Avendaño, S. Schmidt, H.-J. Götze and J. Muñoz, 1999b: Hoja Puerto Montt, Carta gravimétrica de Chile. SERNAGEOMIN de Chile, Subdirección de Geología, p. 18. Santiago. ISSN: 0717-2796.

Bangs, N.L. and S.C. Cande, 1997: Episodic development of a convergent margin inferred from structures and processes along the southern Chile margin. Tectonics, 16(3): 489-503.

Barazangi, M. and B.L. Isacks, 1976: Spatial distribution of earthquakes and subduction of the Nazca plate beneath South America. Geology, 4: 686-692.

Bialas, J., and E.R. Flüh, 1999: Ocean Bottom Seismometers; Sea Technology, 40, 4, 41-46.

Blondel, P., and B.J. Murton, 1997: Handbook of Seafloor Sonar Imagery, John Wiley and Sons, Chichester, 314.

Cande, S.C. and W.F. Haxby, 1991: Eocene propagating rifts in the Southwest Pacific and their conjugate features on the Nazca Plate. J. Geophys. Res., 96(B12): 19,609-19,622.

Cande, S.C., J.L. LaBrecque, R.L Larson, W.C. Pitman III, X. Golovchenko and W.F. Haxby, 1989: Magnetic lineations of the World's Ocean Basins, scale 1:27,400,000, AAPG, Tulsa, Oklahoma.

Cahill, T. and B.L. Isacks, 1992: Seismicity and Shape of the Subducted Nazca Plate. J. of Geophys. Res., 97(B12): 17,50317,529.

Caress, D.W., M.K. McNutt, R.S. Detrick and J.C. Mutter, 1995: Seismic imaging of hotspot-related crustal underplating beneath the Marquesas Islands. Nature, 373: 600-603.

Cande, S. C. and R.B. Leslie, 1986: Late Cenozoic tectonics of the southern Chile trench. J. Geophys. Res, 91: 471-496.

Christensen, D.H. and T. Lay, 1988: Large earthquakes in the Tonga region associated with subduction of the Louisville Ridge. J. Geophys. Res., 93: 13,367-13,389.

DeMets, C., R.G., Gordon, D.F. Argus and S. Stein, 1990: Current plate motions. Geophys. J. Int., 101: 425-478.

Eilers, G., H.A. Röser and P. Kewitsch, 1994: Die Reduktion geomagnetischer Variationen bei seemagnetischen Messungen durch ein Gradientenmagnetometer. BGR-Report, 73 S., Hannover.

Flüh, E.R., et al., 1998: Seismic investigation of the continental margin off- and onshore Valparaiso. Chile, Tectonophysics, 288: 251-263.

Flüh, E. R.; Vidal, N.; Ranero, C. R.; Hojka, A.; von Huene,R.; Bialas, J.; Hinz,K.; Cordoba, D.; Danobeitia, J. J. and Zelt, C. (1998). Seismic investigation of the continental margin off- and onshore Valparaiso, Chile. Tectonophysics, 288: 251-263.

Flüh, E. R. 1995: FS SONNE: Fahrtbericht SO 103. Kiel. GEOMAR Report 41.

Flüh, E. R., and J. Bialas, 1996: A digital, high data capacity ocean bottom recorder for seismic investigations; Int. Underwater Sytems Design, 18(3), 18-20.

Flüh, E. R., N. Vidal, C.R. Ranero, A. Hojka, R. von Huene, J. Bialas, K. Hinz, D. Cordoba, J.J. Danobeitia and C. Zelt, 1998: Seismic investigation of the continental margin off- and onshore Valparaiso, Chile. Tectonophysics, 288: 251-263.

Fryer, P. 1996: Evolution of the Mariana convergent plate margin system. Rev. Geophys., 34: 89-125.

Götze, H.-J. and B. Lahmeyer, 1988: Application of three-dimensional interactive modeling in gravity and magnetics. Geophysics 53(8): 1096-1108.

Gonzáles, E. 1989: Hydrocarbon resources in the coastal zone of Chile. In: Geology of the Andes and Its Relation to Hydrocarbon and Mineral Resources. Ericksen, G.E.; Canas Pinochet, M.T. and Reinemung, J.A. (Editors), Earth Sci. Ser. 11, 383-404.

Havskov, J.; Ottemöller, L. (2001). SEISAN, the earthquake analysis software. University of Bergen.

Hinz, K., J. Adam, H.O. Bargeloh, M. Block, V. Damm, H. Dohmann, J. Fritsch, P. Kewitsch, K. Krieger, S. Neben, K. Puskeppeleit, C. Reichert, B. Schlumschinski, U. Schrader, B. Schreckenberger, B. Sievers and H.N. Jimenez, 1995: Crustal Investigations off- and onshore Nazca/Central Andes, CINCA, Sonne Cruise 104, Leg 1. BGR Archiv 113.998 TBN12.192/95: 113pp.

Husen, S., E. Kissling, and G. Asch, 1999: Accurate Hypocentre Determination in the Seismogenic Zone of the Subducting Nazca Plate in Northern Chile Using a Combined On- Offshore Network. Geophys. J. Int., 138: 687-701.

Hyndman, R. D., C.Y. Yorath, R.M. Clowes and E.E. Davis, 1990: The northern Cascadia subduction zone at Vancouver Island: Seismic structure and tectonic history. Can. J. Earth Sci, 27: 313-329.

Kirby, S., E.R. Engdahl and R. Denlinger, 1996: IntermediateDepth Intraslab Earthquakes and Arc Volcanism as Physical Expressions of Crustal and Uppermost Mantle Metamorphism in Subducting Slabs. Top to Bottom. Bebout, G. E.; Scholl, D. W.; Kirby, S. H. and Platt, J. P. (Editors). American Geophysical Union. 195-213.

Kopp, H., E.R. Flüh, D. Kläschen, J. Bialas and C. Reichert, 2001: Crustal structure of the central Sunda margin at the onset of oblique subduction. Geophys. J. Int., 147: 449-474.

Kulm, L. D., W.J. Schweller and A. Masias, 1977: A prelimnary analysis of the subduction processes along the Andean continental margin, 6° to 45° S. In: Island Arcs, Deep Sea Trenches and BackArc Basins. Talwani, M. and Pitman, W. C. (Editors). American Geophysical Union. 285-301.

Lallemand, S. E. and P. Schnürle, 1994: Coulomb theory applied to accretionary and nonaccretionary wedges: Possible causes for tectonic erosion and/ or frontal accretion. J. of Geophys. Res., 99(B6): 12,033-12,055.

Lienert, B.R.. (1994). Hypocenter 3.2. A computer program for locating earthquakes locally, regionally, and globally. Hawaii Institute of Geophysics and Planetology.

Moore, G. F., T.H. Shipley, P.L. Stoffa and D.E. Karig, 1990: Structure of the Nankai Trough Accretionary Zone from Multichannel Seismic Reflection Data. J. Geophys. Res., 95(B6): 8753-8765.

Morelli, C., 1974: The International Standardization Net 1971. International Association of Geodesy Special Publication 4, p 194.

Nur, A. and Z. Ben-Avraham, 1981: Volcanic gaps and the consumption of aseismic ridges in South America. Mem. Geol. Soc. Am., 154: 729-740.

Patzwahl, R., J. Mechie, A. Schulze and P. Giese, 1999: Two-dimensional velocity models of the Nazca plate subduction zone between 19.5° and 25° S from wide-angle seismic measurements during CINCA 95 project. J. of Geophys. Res., 104(B4): 7293-7317.

Pilger, R. H., Jr. 1981: Plate reconstructiona, aseismic ridges, and low-angle subduction beneath the andes. Bull. Geol. Soc. Am., 92: 448-456.

Rabassa, J. and C.M. Clapperton, 1990: Quaternary glaciations of the southern Andes. Quat. Sci. Rev., 9: 153-174.

Ranero, C. R. and R. von Huene, 2000: Subduction erosion along the Middle America convergent margin. Nature, 404: 748-752.

Reichert, C., B. Schreckenberger and shipboard Science Party, 2002: in preparation: SPOC Legs 2 and 3 SONNE cruise SO-161: Subduction Processes Off Chile - Cruise Report.

Röser, H.A., H.O. Bargeloh and B. Schreckenberger, 1992: Technischer Bericht über ein kleines Navigationssystem für seegeophysikalische Arbeiten. BGR report, 31 pages, Hannover.

Russo, R. M. and P.G. Silver, 1994: Trench-Parallel Flow Beneath the Nazca Plate from Seismic Anisotropy. Science, 263: 1105-1111.

Sandwell, D. T. and W.H.F. Smith, 1997: Marine Gravity Anomaly from Geosat and ERS-1 Altimetry, J. Geophys. Res. 102: 10039-10054.

source: anonymous ftp server baltica.ucsd.edu

Schmidt, S. and H.-J. Götze, 1998: Interactive visualization and modification of 3D-models using GIS-functions. Physics and Chemistry of the Earth, 23(3): 289-295.

Schweller, W. J. and L.D. Kulm, 1978: Extensional Rupture of Oceanic Crust in the Chile Trench. Marine Geology, 28: 271-291.

Seeber, G., 1996: Stand und Einsatzmöglichkeiten von GPS - ein Überblick, Proc. 11th Annual Meeting of the German Hydrographic Society, Glücksburg, 3.-5.6.

Sievers, J. and J. Adam, 1997: Übersicht und Beschreibung über das Digitalstreamersystem der BGR.- BGR report, archive no. 116877, Hannover.

Thornburg, T. M. and L.D. Kulm, 1987: Sedimentation in the Chile Trench: Depositional morphologies, lithofacies, and stratigraphy. Geol. Soc. of America Bull., 98: 33-52.

Vera, E. E., J.C. Mutter, P. Buhl, J.A. Orcutt, A.J. Harding, M.E. Kappus, R.S. Detrick, and T.M. Brocher, 1990: The Structure of 0- to 0.2-m.y.-old Oceanic Crust at 9°N on the East Pacific Rise from Expanded Spread Profiles. J. Geophys. Res., 95: 15,529-15,556.

von Huene, R. and D.W. Scholl, 1991: Observations at convergent margins concerning sediment subduction, subduction erosion, and the growth of continental crust. Rev. of Geophysics, 29(3): 279-316.

von Huene, R., J. Corvalan, E.R. Flüh, K. Hinz, J. Korstgard, C.R. Ranero, W. Weinrebe, and the CONDOR Scientists, 1997: Tectonic control of the subduction Juan Fernandez Ridge along the Andean margin near Valparaiso, Chile. Tectonics, 16(3): 474-488.

von Huene, R., L.D. Kulm and J. Miller, 1985: Structure of the frontal part of the Andean convergent margin. J. Geophys. Res., 90: 5429-5442.

von Huene, R., W. Weinrebe and F. Heeren, 1999: Subduction erosion along the North Chile margin. Geodynamics, 27: 345-358.

Yanez, G. A., C.R. Ranero, R. von Huene and J. Diaz, 2001: Magnetic anomaly interpretation across the southern central Andes (32°N - 34°S): The role of the Juan Fernandez Ridge in the late Tertiary evolution of the margin. J. of Geophys. Res., 106(B4): 6325-6345.

Zapata, R. D., 2001: Estudio batimétrico del magen Chileno. Master thesis, Departamento de Geofísica, Universidad de Chile, Santiago (Chile), unpublished thesis.

# Appendices

I - Captains Report

II - Airgun Protocols

III - OBH/S Deployments

IV - Magnetic Profiles

RF Reedereigemeinschaft
Forschungsschiffahrt GmbH

## F.S. "SONNE" Reise SO 161/1

| **Eingesetzte Geräte** | | **Einsätze** |
|---|---|---|
| CTD/Releaser | CTD/Rel | : 1 |
| SM | SIMRAD Profile | : 401 sm |
| OBS | Ocean Bottom Seismometer ( Ausgesetzt ) | : 27 |
| OBS | Oean Bottom Seismometer ( Aufgen. ) | : 4 |

**Eingesetzte Winden :**

| *Winde* | *D/M* | *Typ* | *RF-Nr* | *SO 161/1 Einsatz* | *Gesamt Einsatz* | *SO 161/1 S`länge* | *Gesamt S`länge* | *Zust.* |
|---|---|---|---|---|---|---|---|---|
| W 1 | 18,2 | LWL | 816233 | 0000 h | 1922 h | 000000 m | 1241262 m | 5 |
| W 2 | 18,2 | LWL | 810001 | 0000 | 0239 | 000000 | 0082684 | 2 |
| W 4 | 11,0 | NSW | 817141 | 0000 | 0241 | 000000 | 0162553 | 3 |
| W 5 | 11,0 | NSW | 817164 | 0000 | 0209 | 000000 | 0184173 | 3 |
| W 6 | 18,2 | DRAKO | 814150 | 0004 | 1963 | 004001 | 16752280 | 3 |

| *Winde* | *SO 161/1 gefierte max.Länge* | *jemals gefierte max.Länge* |
|---|---|---|
| W 1 | 0000 m | 6474 m ( nur noch 5340 m lang ) |
| W 2 | 0000 | 3000 |
| W 4 | 0000 | 6100 |
| W 5 | 0000 | 5200 |
| W 6 | 4700 | 7900 ( SL = 6466 m ) |

**Geräteverluste** :
Keine

**Abkürzungen im Stationsprotokoll:**

| | |
|---|---|
| z.W. | zu Wasser |
| a.D. | an Deck |
| Boko | Bodenkontakt |
| Bosi | Bodensicht |
| SL(max.) | (maximale)Seillänge |
| LT | Lottiefe nach Hydrosweep |
| W x | eingesetzte Winde |
| SM | Simrad- Multibeam-Lot |
| PS | Parasound |
| XPNDR | Transponder |

**Zeit : UTC – 03 Stunden**

**10.10.01**

Releaser Test W6

| | | | |
|---|---|---|---|
| 0858 | Beginn Station | LT = ungef. 5000 m | 26-30.85S 71-23.76W |
| 0900 | CTD/Rel. Z/W | | |
| 1013 | Slmax 4001m | LT = ungef. 5000 m | 26-31.24S 71-24.20W |
| 1224 | CTD/Rel a/D | | |
| 1225 | Ende Station | | |

Profil SM 01

| | | | |
|---|---|---|---|
| 2027 | Beginn Profil | | 28-00.00S 71-45.00W |

**11.10.01**

| | | | |
|---|---|---|---|
| 0303 | Ende Profil | 64 sm | 29-00.00S 72-10.00W |

Profil SM 02

| | | | |
|---|---|---|---|
| 0303 | Beginn Profil | | 29-00.00S 72-10.00W |
| 1624 | Ende Profil | 151 sm | 31-30.00S 72-30.00W |

Profil SM 03

| | | | |
|---|---|---|---|
| 1624 | Beginn Profil | | 31-30.00S 72-30.00W |
| 2030 | Ende Profil | 49 sm | 32-04.96S 71-50.02W |
| 2052 | OBS #1 z/W | LT = 1344m | 32-04.96S 71-50.02W |
| 2146 | OBS #2 z/W | LT = 3186m | 32-04.97S 72-00.03W |
| 2245 | OBS #3 z/W | LT = 3909m | 32-04.99S 72-12.00W |

**12.10.01**

| | | | |
|---|---|---|---|
| 0012 | OBS #4 z/W | LT = 4572m | 32-05.00S 72-25.00W |
| 0112 | OBS #5 z/W | LT = 4574m | 32-15.00S 72-25.00W |
| 0224 | OBS #6 z/W | LT = 3356m | 32-15.00S 72-12.00W |
| 0324 | OBS #7 z/W | LT = 1758m | 32-15.00S 72-00.00W |
| 0436 | OBS #8 z/W | LT = 784m | 32-15.00S 71-45.00W |
| 0558 | OBS #9 z/W | LT = 492m | 32-25.00S 71-40.00W |
| 0733 | OBS #10 z/W | LT = 2430m | 32-24.99S 72-00.00W |
| 0835 | OBS #11 z/W | LT = 2406m | 32-25.02S 72-12.01W |
| 0949 | OBS #12 z/W | LT = 4316m | 32-25.01S 72-24.98W |
| 1226 | OBS #13 z/W | LT = 4620m | 32-25.00S 72-55.02W |
| 1640 | OBS #14 z/W | LT = 5170m | 33-00.00S 72-58.00W |
| 1942 | OBS #15 z/W | LT = 1937m | 33-17.99S 72-25.01W |
| 2048 | OBS #16 z/W | LT = 2112m | 33-17.99S 72-11.97W |
| 2207 | OBS #17 z/W | LT = 1218m | 33-18.00S 72-00.00W |
| 2311 | OBS #18 z/W | LT = 696m | 33-07.98S 71-55.00W |

**13.11.01**

| | | | |
|---|---|---|---|
| 0040 | OBS #19 z/W | LT = 1897m | 33-08.00S 72-12.00W |
| 0205 | OBS #21 z/W | LT = 3049m | 33-08.00S 72-25.00W |
| 0300 | OBS #20 z/W | LT = 2713m | 33-00.00S 72-25.00W |

| | | | |
|---|---|---|---|
| 0402 | OBS #22 z/W | LT = 2177m | 33-00.00S 72-12.20W |
| 0502 | OBS #23 z/W | LT = 2432m | 32-50.00S 72-12.20W |

### Obs #12

| | | |
|---|---|---|
| 0702 | Release Command | |
| 0800 | Div. Release Commands | |
| 0825 | OBS gesichtet | |
| 0838 | OBS a/D | 32-24.94S 72-24.95W |

### OBS #4

| | | | |
|---|---|---|---|
| 1005 | Release Command | | |
| 1102 | OBS gesichtet | | |
| 1123 | OBS a/D | | 32-04.86S 72-25.24W |
| | | | |
| 1203 | OBS #4 z/W | LT = 4572m | 32-04.99S 72-25.02W |

### Profil SM 04

| | | | |
|---|---|---|---|
| 1314 | Beginn Profil | | 31-52.00S 72-30.00W |
| 1603 | Ende Profil | 34 sm | 31-55.00S 71-50.00W |

### OBS #1

| | | | |
|---|---|---|---|
| 1650 | Release Command | | |
| 1713 | OBS gesichtet | | |
| 1726 | OBS a/D | | 32-05.04S 71-49.98W |
| 1730-1735 | Schwimmtest | | |
| | | | |
| 1821 | OBS #1 z/W | LT = 1344m | 32-04.99S 71-49.98W |
| 2058 | OBS #9 z/W | LT = 495m | 32-24.99S 71-39.99W |

### OBS #9

| | | |
|---|---|---|
| 2059 | Release Command | |
| 2104 | OBS gesichtet | |
| 2134 | OBS a/D | 32-24.99S 71-39.99W |

### Profil SM 05

| | | | |
|---|---|---|---|
| 2134 | Beginn Profil | | 32-24.99S 71-39.99W |
| **14.10.01** | | | |
| 0010 | Ende Profil | 24 sm | 31-53.00S 71-45.00W |

### Profil SM 06

| | | | |
|---|---|---|---|
| 0010 | Beginn Profil | | 31-53.00S 71-45.00W |
| 0327 | Ende Profil | 39 sm | 31-45.00S 72-30.00W |

### Profil SM 07

| | | | |
|---|---|---|---|
| 0327 | Beginn Profil | | 31-45.00S 72-30.00W |
| 0714 | Ende Profil | 40 sm | 32-24.99S 72-25.00W |
| | | | |
| 0720 | OBS #12 z/W | LT = 4317m | 32-24.00S 72-25.00W |

RF Reedereigemeinschaft
Forschungsschiffahrt GmbH

## F.S. "SONNE" Reise SO 161/4

| **Eingesetzte Geräte** | | **Einsätze** |
|---|---|---|
| OBH | Ocean Bottom Hydrophone | 90 |
| OBS | Ocean Bottom Seismographe | 35 |
| OBH | nur aufgenommen | 17 |
| OBS | nur aufgenommen | 06 |
| 2 x BGR airgun array | | |
| CTD | CTD-Sonde | |
| MAG | Magnetometer | |
| GRA | Gravimeter | |
| Weitwinkel-Seismik | | 0658 sml |
| Magnetik-Profile | | 1188 sml |
| Simrad-Lot und Parasoundvermessung | | 0170 sml |
| Gravimetrie | | 3489 sml |

**Eingesetzte Winden :**

| *Winde* | *D/M* | *Typ* | *RF-Nr* | *SO 161/4 Einsatz* | *Gesamt Einsatz* | *SO 161/4 S`länge* | *Gesamt S`länge* | *Zust.* |
|---|---|---|---|---|---|---|---|---|
| W 1 | 18,2 | LWL | 816233 | 0000 h | 1922 h | 000000 m | 1241262 m | 5 |
| W 2 | 18,2 | LWL | 810001 | 0000 | 0239 | 000000 | 0082684 | 3 |
| W 4 | 11,0 | NSW | 817141 | 0002 | 0245 | 001067 | 0164685 | 4 |
| W 5 | 11,0 | NSW | 817164 | 0000 | 0209 | 000000 | 0184173 | 4 |
| W 6 | 18,2 | DRAKO | 814150 | 0004 | 1971 | 005000 | 1686228 | 3 |

| *Winde* | *SO 161/4 gefierte max.Länge* | *jemals gefierte max.Länge* |
|---|---|---|
| W 1 | 0000 m | 6474 m ( SL aktuell = 5340 m ) |
| W 2 | 0000 | 3000 |
| W 4 | 1067 | 6100 |
| W 5 | 0000 | 5200 |
| W 6 | 5000 | 7900 ( SL aktuell = 6466 m ) |

**Geräteverluste** :

Keine

**Abkürzungen im Stationsprotokoll:**

| | |
|---|---|
| z.W. | zu Wasser |
| a.D. | an Deck |
| Boko | Bodenkontakt |
| Bosi | Bodensicht |
| SL(max.) | (maximale)Seillänge |
| LT | Lottiefe nach Hydrosweep |
| W x | eingesetzte Winde |
| SM | Simrad- Multibeam-Lot |
| PS | Parasound |
| XPNDR | Transponder |

**Zeit : UTC – 03 Stunden**

**01.12.01**

Aufnahme OBH und OBS

| | | | | | |
|---|---|---|---|---|---|
| 0000 | OBH 09 ausgelöst | 0021 gesichtet | 0030 an Bord | 32 24,88 S | 71 40,21 W |
| 0128 | OBH 08 | 0137 | 0147 | 32 14,91 S | 71 45,08 W |
| 0243 | OBS 01 | 0310 | 0322 | 32 05,08 S | 71 50,01 W |
| 0405 | OBH 02 | 0435 | 0444 | 32 04,96 S | 72 00,24 W |
| 0532 | OBH 07 | 0553 | 0625 | 32 15,06 S | 72 00,30 W |
| 0717 | OBH 10 | 0747 | 0756 | 32 24,83 S | 72 00,17 W |
| 0845 | OBH 11 | 0914 | 0921 | 32 24,95 S | 72 12,14 W |
| 1006 | OBH 06 | 1037 | 1051 | 32 14,96 S | 72 12,37 W |
| 1139 | OBH 03 | 1217 | 1228 | 32 04,80 S | 72 12,04 W |
| 1333 | OBS 04 | 1512 | 1526 | 32 04,62 S | 72 24,95 W |
| 1627 | OBH 05 | 1717 | 1726 | 32 14,79 S | 72 25,17 W |
| 1811 | OBS 12 | 1905 | 1915 | 32 24,91 S | 72 25,19 W |
| 2150 | OBH 23 | 2216 | 2239 | 32 49,88 S | 72 12,30 W |
| 2329 | OBH 22 | 2352 | | | |
| **02.12.01** | | | | | |
| | | | 0005 | 32 59,98 S | 72 12,23 W |
| 0045 | OBH 19 | 0107 | 0118 | 33 08,00 S | 72 11,92 W |
| 0239 | OBH 18 | 0246 | 0254 | 33 07,94 S | 71 05,05 W |
| 0351 | OBS 17 | 0423 | 0430 | 33 18,01 S | 71 59,87 W |
| 0525 | OBH 16 | 0547 | 0600 | 33 18,08 S | 72 11,93 W |
| 0652 | OBH 15 | 0720 | 0727 | 33 17,90 S | 72 24,99 W |
| 0810 | OBS 21 | 0909 | 0923 | 33 07,95 S | 72 24,67 W |
| 1005 | OBH 20 | 1029 | 1045 | 33 59,88 S | 72 24,98 W |
| 1317 | OBS 14 | 1458 | 1508 | 32 59,93 S | 72 57,98 W |

Releaser-Teststation W 6

| | | | | |
|---|---|---|---|---|
| 1632 | Beginn Station | LT = 5410 m | 33 09.94 S | 72 50,07 W |
| 1634 | 5 releaser im Korb z.W. | | | |
| 1650 | SL = 200 m | 1 Glas-Auftriebskörper z.W. | | |
| 1739 | SL = 3000 m | Simrad-Sonde z.W. | | |
| 1815 | Slmax = 5000 m | LT = 5403 m | 33 09,78 S | 72 50,08 W |
| 1903 | Simrad-Sonde a.D. | | | |
| 2006 | Releaser a.D. Ende Station | | | |

Magnetikprofile 101 bis 107 v = 10,0 kn

| | | | | | |
|---|---|---|---|---|---|
| 2006 | Beginn Profil 106 | | 33 09,78 S | 72 50,08 W | |
| 2037 | Magnetometer z.W. | l = 749 m | | | |
| 2400 | | | 33 43,68 S | 72 48,84 W | |
| **03.12.01** | | | | | |
| 0142 | Profilwechsel 101/102 | | 34 00,00 S | 72 48,29 W | 050 sml |
| 1502 | Profilwechsel 102/103 | | 36 00,00 S | 73 35,00 W | 126 sml |
| 1722 | Profilwechsel 103/104 | | 36 15,00 S | 74 00,00 W | 025 sml |
| 2000 | Profilwechsel 104/105 | | 36 42,00 S | 74 09,00 W | 028 sml |
| 2039 | Profilwechsel 105/106 | | 36 44,00 S | 74 00,00 W | 007 sml |
| **04.12.01** | | | | | |
| 0316 | Profilwechsel 106/107 | | 37 55,00 S | 74 17,50 W | 072 sml |
| 0535 – 0600 | hieven Magnetometer ein | | | | |

| | | | |
|---|---|---|---|
| 0600 | Ende Profil 107 | | 38 05,62 S 73 42,00 W |

<u>Auslegung OBH/S 24 bis 47 des Profils 1</u>

| | | | | | |
|---|---|---|---|---|---|
| 0647 | OBH | 24 | z.W. | LT = 0017 m | 38 10,13 S 73 43,16 W |
| 0717 | OBH | 25 | | LT = 0309 m | 38 09,58 S 73 45,49 W |
| 0741 | OBH | 26 | | LT = 0452 m | 38 09,19 S 73 47,67 W |
| 0806 | OBS | 27 | | LT = 0558 m | 38 08,47 S 73 51,09 W |
| 0827 | OBS | 28 | | LT = 0610 m | 38 07,74 S 73 54,52 W |
| 0849 | OBH | 29 | | LT = 0674 m | 38 07,04 S 73 57,94 W |
| 0911 | OBH | 30 | | LT = 0605 m | 38 06,33 S 74 01,34 W |
| 0935 | OBH | 31 | | LT = 0764 m | 38 05,72 S 74 04,29 W |
| 0958 | OBH | 32 | | LT = 0730 m | 38 05,99 S 74 07,25 W |
| 1020 | OBS | 33 | | LT = 0687 m | 38 04,47 S 74 10,19 W |
| 1041 | OBH | 34 | | LT = 1027 m | 38 03,79 S 74 13,62 W |
| 1057 | OBH | 35 | | LT = 1233 m | 38 03,29 S 74 15,93 W |
| 1120 | OBH | 36 | | LT = 1558 m | 38 02,86 S 74 18,28 W |
| 1143 | OBH | 37 | | LT = 2026 m | 38 02,36 S 74 20,46 W |
| 1207 | OBH | 38 | | LT = 3150 m | 38 01,61 S 74 23,90 W |
| 1225 | OBH | 39 | | LT = 3851 m | 38 01,17 S 74 26,36 W |
| 1243 | OBH | 40 | | LT = 3803 m | 38 00,62 S 74 28,90 W |
| 1312 | OBH | 41 | | LT = 4594 m | 37 59,58 S 74 34,08 W |
| 1342 | OBS | 42 | | LT = 4668 m | 37 58,55 S 74 39,19 W |
| 1412 | OBS | 43 | | LT = 4679 m | 37 57,45 S 74 44,33 W |
| 1434 | OBS | 44 | | LT = 4665 m | 37 56,77 S 74 47,76 W |
| 1502 | OBH | 45 | | LT = 4717 m | 37 55,88 S 74 51,89 W |
| 1530 | OBS | 46 | | LT = 4573 m | 37 55,02 S 74 56,09 W |
| 1557 | OBS | 47 | | LT = 4543 m | 37 54,27 S 74 59,70 W |

<u>Magnetikprofil 108v = 11,0 kn</u>

| | | | | |
|---|---|---|---|---|
| 1802 – 1830 | bringen Magnetometer aus, KL = 750 m | | | |
| 1831 | Beginn Profil | LT = 4500 m | 38 09,18 S 75 06,56 W | |
| 2029 | Ende Profil | LT = 4161 m | 37 56,95 S 75 29,67 W | 22 sml |

<u>Seismikprofil 01 v = 5,0 kn</u>

| | | | |
|---|---|---|---|
| 2120 – 2129 | bringen Bb-airgun-array aus | | |
| 2139 – 2139 | bringen Stb-airgun-array aus | | |
| 2151 | Beginn Profil | LT = 4105 m | 37 48,82 S 75 26,02 W |
| 2400 | | | 37 51,49 S 75 13,03 W |

**05.12.01**

| | | | | |
|---|---|---|---|---|
| 0600 | | | 37 59,10 S 74 36,38 w | |
| 1200 | | | 38 06,2 S 73 59,52 W | |
| 1450 – 1500 | kürzen Magnetomer auf, KL = 300 m | | | |
| 1611 – 1618 | kürzen Magnetometer auf, KL = 150 m | | | |
| 1620 | Ende Profil | LT = 64,6 m | 38 12,21 S 73 32,88 W | 93 sml |
| 1622 – 1630 | hieven Bb-airgun-array ein | | | |
| 1632 – 1646 | hieven Magnetometer ein | | | |
| 1648 – 1655 | hieven Stb-airgun-array ein | | | |

**05.12.01**

## Aufnahme OBH/S 24 bis 47 des Profils 1

| | | | | | | | | |
|---|---|---|---|---|---|---|---|---|
| 1735 | OBH 24 | ausgelöst | 1738 | gesichtet | 1754 | an Deck | 38 09,96 S | 73 43,17 W |
| 1806 | OBH 25 | | 1816 | | 1833 | | 38 09,39 S | 73 45,47 W |
| 1844 | OBH 26 | | 1847 | | 1854 | | 38 09,16 S | 73 47,62 W |
| 1905 | OBS 27 | | 1915 | | 1930 | | 38 08,17 S | 73 50,93 W |
| 1950 | OBS 28 | | 2000 | | 2010 | | 38 07,67 S | 73 54,56 W |
| 2028 | OBH 29 | | 2035 | | 2047 | | 38 06,98 S | 73 58,00 W |
| 2059 | OBH 30 | | 2106 | | 2118 | | 38 06,33 S | 74 01,40 W |
| 2128 | OBH 31 | | 2138 | | 2148 | | 38 05,71 S | 74 04,34 W |
| 2158 | OBH 32 | | 2206 | | 2218 | | 38 05,08 S | 74 07,30 W |
| 2228 | OBS 33 | | 2235 | | 2246 | | 38 04,29 S | 74 10,28 W |
| 2258 | OBH 34 | | 2308 | | 2326 | | 38 03,27 S | 74 13,87 W |
| 2330 | OBH 35 | | 2345 | | 2359 | | 38 02,78 S | 74 16,23 W |

**06.12.01**

| | | | | | |
|---|---|---|---|---|---|
| 0005 | OBH 36 | 0022 | 0034 | 38 02,34 S | 74 18,65 W |
| 0025 | OBH 37 | 0050 | 0103 | 38 01,97 S | 74 20,90 W |
| 0050 | OBH 38 | 0122 | 0133 | 38 01,24 S | 74 24,31 W |
| 0122 | OBH 39 | 0212 | 0224 | 38 00,88 S | 74 26,67 W |
| 0150 | OBH 40 | 0239 | 0248 | 38 00,41 S | 74 29,08 W |
| 0239 | OBH 41 | 0333 | 0349 | 37 59,43 S | 74 34,16 W |
| 0320 | OBS 42 | 0452 | 0506 | 37 58,55 S | 74 39,26 W |
| 0430 | OBS 43 | 0621 | 0636 | 37 57,38 S | 74 44,26 W |
| 0536 | OBS 44 | 0653 | 0708 | 37 56,53 S | 74 47,75 W |
| 0716 | OBH 45 | 0742 | 0754 | 37 55,80 S | 74 51,84 W |
| 0734 | OBS 46 | 0830 | 0842 | 37 54,95 S | 74 55,92 W |
| 0810 | OBS 47 | 0939 | 0947 | 37 54,19 S | 74 59,57 W |

## Magnetikprofile 110 bis 116

0954 – 1020 bringen Magnetometer aus, KL = 700 m

| | | | | | |
|---|---|---|---|---|---|
| 1107 | Beginn Profil 110 | LT = 4544 m | 37 44,19 S | 74 58,81 W | |
| 1336 | Profilwechsel 110/111 | LT = 4140 m | 37 40,00 S | 75 35,00 W | 029 sml |
| 1728 | Profilwechsel 111/112 | LT = 4109 m | 36 54,00 S | 75 20,00 W | 047 sml |
| 1930 | Profilwechsel 112/113 | LT = 4253 m | 36 35,00 S | 75 00,00 W | 025 sml |
| 2116 | Profilwechsel 113/114 | LT = 4789 m | 36 37,00 S | 74 35,00 W | 020 sml |

**07.12.01**

| | | | | | |
|---|---|---|---|---|---|
| 0055 | Profilwechsel 114/115 | LT = 4675 m | 36 00,00 S | 74 00,00 W | 047 sml |
| 1121 | Profilwechsel 115/116 | LT = 4921 m | 34 00,00 S | 73 00,00 W | 130 sml |
| 1930 | Ende Profil 111 | LT = 4825 m | 32 23,23 S | 72 54,96 W | 116 sml |
| 1958 | Magnetometer a.D. | | | | |
| 1959 | | | | | |

## Aufnahme OBS 13

1838 ausgelöst 2054 gesichtet 2106 a.D. 32 24,93 S 72 55,26 W

**08.12.01.**

## Auslegung OBH/S 48 bis 72 des Profils 2

| | | | | | |
|---|---|---|---|---|---|
| 0323 | OBH 48 | z.W. | LT = 0202 m | 32 05,00 S | 71 36,9 W |
| 0345 | OBS 49 | | LT = 431 m | 32 05,00 S | 71 40,00 W |
| 0416 | OBH 50 | | LT = 0620 m | 32 05,01 S | 71 43,03 W |
| 0436 | OBS 51 | | LT = 817 m | 32 05,00 S | 71 46,01 W |
| 0500 | OBH 52 | | LT = 1178 m | 32 04,99 S | 71 49,02 W |
| 0528 | OBS 53 | | LT = 1595 m | 32 04,99 S | 71 52,03 W |

| | | | |
|---|---|---|---|
| 0555 | OBH 54 | LT = 2349 m | 32 05,01 S 71 54,99 W |
| 0618 | OBS 55 | LT = 2816 m | 32 05,00 S 71 58,01 W |
| 0641 | OBH 56 | LT = 3249 m | 32 05,00 S 72 01,00 W |
| 0706 | OBS 57 | LT = 3631 m | 32 05,00 S 72 04,00 W |
| 0736 | OBH 58 | LT = 3820 m | 32 05,00 S 72 07,02 W |
| 0821 | OBS 59 | LT = 3908 m | 32 05,00 S 72 09,99 W |
| 0848 | OBS 60 | LT = 3828 m | 32 05,00 S 72 14,00 W |
| 0916 | OBS 61 | LT = 3775 m | 32 05,00 S 72 18,01 W |
| 0942 | OBH 62 | LT 4123 m | 32 05,00 S 72 22,01 W |
| 1009 | OBH 63 | LT = 4752 m | 32 04,99 S 72 26,00 W |
| 1040 | OBH 64 | LT = 5301 m | 32 05,00 S 72 30,00 W |
| 1113 | OBH 65 | LT = 5524 m | 32 05,00 S 72 35,00 W |
| 1200 | OBH 66 | LT = 5705 m | 32 05,00 S 72 43,04 W |
| 1230 | OBH 67 | LT = 5130 m | 32 05,00 S 72 48,00 W |
| 1300 | OBH 68 | LT = 4669 m | 32 05,00 S 72 52,99 W |
| 1328 | OBH 69 | LT = 4179 m | 32 05,01 S 72 58,00 W |
| 1357 | OBH 70 | LT = 4103 m | 32 05,00 S 73 03,00 W |
| 1425 | OBH 71 | LT = 4104 m | 32 04,99 S 73 08,01 W |
| 1455 | OBH 72 | LT = 3973 m | 32 05,01 S 73 13,00 W |

### Seismikprofil 2 A Kurs = 90 Grad v = 5,0 kn

1504 – 1513 bringen Stb-airgun-array aus
1515 – 1540 bringen Magnetometer aus KL = 750 m
1534 – 1542 bringen Bb-airgun-array aus
1545 Beginn Profil LT 4018 m 32 05,01 S 73 09,13 W

**09.12.01**

0715 – 0725 hieven Bb-array und Magnetometer vor ( KL = 150 m )
0728 Ende Profil LT = 185 m 32 05,00 S 71 36,47 W 79 sml
0728 – 0800 Schleife über Bb

### Seismikprofil 2 B Kurs = 270 Grad v = 5,0 kn

0801 Beginn Profil LT = 254 m 32 05,00 S 71 37,74 W
0805 Bb-airgun-array ausgesteckt
0809 Magnetometer ausgesteckt KL = 750 m
1200 32 05,00 S 72 01,33 W
1800 32 05,00 S 72 36,67 W
2400 32 05,00 S 73 12,04 W

**10.12.04**

0448 Ende Profil LT = 4076 m 32 05,00 S 73 40,00 W 104
sml
0450 – 0500 hieven Bb-array ein
0502 – 0509 hieven Stb-array ein
0510 – 0522 hieven Magnetometer ein

### Aufnahme OBH/S 72 bis 48 des Profils 2

| | | | | | |
|---|---|---|---|---|---|
| 0710 | OBH 72 | ausgelöst 0743 | gesichtet 0754 | a.D. | 32 05,11 S 73 12,94 W |
| 0748 | OBH 71 | 0827 | 0832 | | 32 05,01 S 73 07,90 W |
| 0821 | OBH 70 | 0920 | 0927 | | 32 04,94 S 73 02,81 W |
| 0856 | OBH 69 | 1000 | 1023 | | 32 05,01 S 72 57,66 W |
| 0952 | OBH 68 | 1045 | 1111 | | 32 04,89 S 72 52,64 W |
| 1055 | OBH 67 | 1146 | 1204 | | 32 04,79 S 72 47,75 W |

| | | | | |
|---|---|---|---|---|
| 1143 | OBH 66 | 1303 | 1326 | 32 04,64 S 72 43,09 W |
| 1250 | OBH 65 | 1355 | 1426 | 32 04,79 S 72 34,74 W |
| 1408 | OBH 64 | 1520 | 1528 | 32 04,79 S 72 30,00 W |
| 1454 | OBH 63 | 1549 | 1559 | 32 04,73 S 72 25,94 W |
| 1550 | OBH 62 | 1617 | 1626 | 32 04,81 S 72 21,87 W |
| 1620 | OBS 61 | 1700 | 1721 | 32 04,94 S 72 17,91 W |
| 1645 | OBS 60 | 1736 | 1754 | 32 04,86 S 72 13,57 W |
| 1740 | OBS 59 | 1853 | 1907 | 32 05,05 S 72 09,85 W |
| 1815 | OBS 58 | 1908 | 1939 | 32 05,11 S 72 06,91 W |
| 1930 | OBS 57 | 2012 | 2021 | 32 05,07 S 72 04,00 W |
| 1958 | OBH 56 | 2039 | 2055 | 32 05,14 S 72 00,99 W |
| 2045 | OBS 55 | 2140 | 2149 | 32 05,12 S 71 58,06 W |
| 2120 | OBH 54 | 2157 | 2223 | 32 05,00 S 71 55,18 W |
| 2215 | OBS 53 | 2230 | 2255 | 32 05,09 S 71 52,22 W |
| 2244 | OBH 52 | 2258 | 2327 | 32 04,96 S 71 49,14 W |
| 2320 | OBS 51 | 2335 | 2358 | 32 05,00 S 71 46,11 W |
| 2348 | OBH 50 | | | |
| **11.12.01** | | 0015 | 0035 | 32 04,83 S 71 43,15 W |
| 0035 | OBS 49 | 0050 | 0106 | 32 04,89 S 71 40,10 W |
| 0130 | OBH 48 | 0135 | 0146 | 32 04,88 S 71 37,15 W |

### Station 02 SIMRAD/Sonde – Batterypack W 4

0830 Beginn Station LT = 5814 m 32 57,19 S 72 46,76 W
0832 Dummy z.W.
0836 SL = 20 m Simrad-Sonde z.W.
0842 SL = 40 m battery pack z.W.
0900 SL = 998 m Störung Winde
0900 –1013 Versuch Reparatur ; Slmax = 1067 m
1013 brechen Station ab, hieven ein
1058 Dummy a.D. / Ende Station

### Auslegung OBH/S 73 bis 99 auf Profil 03

| | | | | |
|---|---|---|---|---|
| 1314 | OBS 73 | z.W. | LT = 4642 m | 33 13,55 S 73 08,01 W |
| 1333 | OBH 74 | | 4151 m | 33 12,00 S 73 10,00 W |
| 1402 | OBH 75 | | 3864 m | 33 10,35 S 73 12,08 W |
| 1424 | OBS 76 | | 3946 m | 33 08,78 S 73 14,09 W |
| 1444 | OBH 77 | | 3986 m | 33 07,32 S 73 15,94 W |
| 1504 | OBH 78 | | 3992 m | 33 05,82 S 73 17,85 W |
| 1526 | OBS 79 | | 3624 m | 33 04,32 S 73 19,77 W |
| 1544 | OBH 80 | | 3791 m | 33 02,84 S 73 21,68 W |
| 1625 | OBS 81 | | 3788 m | 33 01,32 S 73 23,60 W |
| 1651 | OBS 82 | | 3685 m | 32 59,83 S 73 25,53 W |
| 1708 | OBS 83 | | 3777 m | 32 58,30 S 73 27,43 W |
| 1727 | OBS 84 | | 3750 m | 32 56,81 S 73 29,34 W |
| 1745 | OBH 85 | | 3691 m | 32 55,30 S 73 31,30 W |
| 1817 | OBS 86 | | 3165 m | 32 53,82 S 73 33,23 W |
| 1836 | OBH 87 | | 2361 m | 32 32,35 S 73 35,11 W |
| 1901 | OBS 88 | | 1080 m | 32 50,84 S 73 36,99 W |
| 1921 | OBH 89 | | 1523 m | 32 49,32 S 73 38,94 W |
| 1941 | OBH 90 | | 2595 m | 32 47,83 S 73 40,82 W |
| 2003 | OBH 91 | | 3154 m | 32 46,30 S 73 42,70 W |

| | | | | |
|---|---|---|---|---|
| 2023 | OBH 92 | 3269 m | 32 44,83 S | 73 44,63 W |
| 2042 | OBH 93 | 3516 m | 32 43,30 S | 73 46,52 W |
| 2102 | OBH 94 | 3512 m | 32 41,82 S | 73 48,41 W |
| 2122 | OBH 95 | 3590 m | 32 40,31 S | 73 50,34 W |
| 2141 | OBH 96 | 3701 m | 32 38,83 S | 73 52,22 W |
| 2204 | OBH 97 | 3835 m | 32 36,80 S | 73 54,81 W |
| 2227 | OBH 98 | 4002 m | 32 34,72 S | 73 57,46 W |
| 2250 | OBH 99 | 4073 m | 3 32,69 S | 74 00,00 W |

Magnetikprofil 117

2251 – 2320 bringen Magnetometer aus KL = 750 m
2342 Beginn Profil LT = 4126 m 32 27,22 S 73 59,87 W
Kurs = 314 Grad ; v = ca. 12 kn

**12.12.01**

0240 Ende Profil LT = 4301 m 32 01,67 S 74 30,45 W 037 sml

Seismikprofil 03 Kurs = 132 Grad v = 5,0 kn

0322 – 0330 bringen Stb-airgun-array aus
0333 – 0341 bringen Bb-airgun-array aus
0355 Beginn Profil LT = 3903 m 32 04,36 S 74 35,78 W 107 sml
1200 32 32,02 S 74 00,89 W
2400 33 11,59 S 73 10,55 W

**13.12.01**

0358 Ende Profil 33 24,50 S 72 54,00 W
0402 – 0412 holen Stb-airgun-array ein
0414 – 0435 holen Bb-airgun-array ein
0600 – 0625 holen Magnetometer ein

Aufnahme OBH/S 74 bis 99 des Seismikprofils 03

| | | | | | | | | |
|---|---|---|---|---|---|---|---|---|
| 0600 | OBS 73 | ausgelöst | 0732 | gesichtert | 0744 | a.D. | 33 13,19 S | 73 07,93 W |
| 0703 | OBH 74 | | 0804 | | 0814 | | 33 11,61 S | 73 09,86 W |
| 0805 | OBH 75 | | 0904 | | 0814 | | 33 10,11 S | 73 11,94 W |
| 0828 | OBS 76 | | 0927 | | 0941 | | 33 08,32 S | 73 14,02 W |
| 0925 | OBH 77 | | 1009 | | 1017 | | 33 07,04 S | 73 15,84 W |
| 0951 | OBH 78 | | 1036 | | 1046 | | 33 05,53 S | 73 17,81 W |
| 1027 | OBH 79 | | 1111 | | 1118 | | 33 04,09 S | 73 19,78 W |
| 1051 | OBH 80 | | 1131 | | 1147 | | 33 02,56 S | 73 21,62 W |
| 1128 | OBS 81 | | 1212 | | 1220 | | 33 01,04 S | 73 23,47 W |
| 1200 | OBS 82 | | 1241 | | 1252 | | 32 59,56 S | 73 25,47 W |
| 1241 | OBH 83 | | 1317 | | 1323 | | 32 58,10 S | 73 27,39 W |
| 1317 | OBS 84 | | 1430 | | 1437 | | 32 56,56 S | 73 29,26 W |
| 1335 | OBH 85 | | 1456 | | 1511 | | 32 54,78 S | 73 31,38 W |
| 1503 | OBS 86 | | 1602 | | 1614 | | 32 53,70 S | 73 33,30 W |
| 1540 | OBH 87 | | 1628 | | 1639 | | 32 52,22 S | 73 35,45 W |
| 1630 | OBS 88 | | 1702 | | 1713 | | 32 50,88 S | 73 37,17 W |
| 1704 | OBH 89 | | 1755 | | 1809 | | 32 49,35 S | 73 39,14 W |
| 1812 | OBH 90 | | 1821 | | 1836 | | 32 47,86 S | 73 41,17 W |
| 1812 | OBH 91 | | 1911 | | 1930 | | 32 46,40 S | 73 43,03 W |
| 1836 | OBH 92 | | 1938 | | 1955 | | 32 44,94 S | 73 45,42 W |
| 1930 | OBH 93 | | 2013 | | 2024 | | 32 43,41 S | 73 46,85 W |
| 1955 | OBH 94 | | 2041 | | 2051 | | 32 41,91 S | 73 48,79 W |

| | | | | |
|---|---|---|---|---|
| 2025 | OBH 95 | 2114 | 2125 | 32 40,38 S 73 50,57 W |
| 2054 | OBH 96 | 2136 | 2151 | 32 38,94 S 73 52,66 W |
| 2125 | OBH 97 | 2151 | 2224 | 32 37,09 S 73 55,34 W |
| 2144 | OBH 98 | 2230 | 2255 | 32 34,97 S 73 57,61 W |
| 2246 | OBH 99 | 2318 | 2333 | 32 32,76 S 74 00,14 W |

<u>SM/PS Vermessung v = 11 kn</u>

| | | | |
|---|---|---|---|
| 2333 | Beginn Vermessung | 32 32,76 S 74 00,14 W | |
| 2400 | | 32 29,15 S 74 00,12 W | 04 sml |

**14.12.01**

| | | | |
|---|---|---|---|
| 0020 | | 32 25,00 S 73 59,97 W | 04 sml |
| 0147 | | 32 25,00 S 73 39,54 W | 17 sml |
| 0358 | Ende Vermessung | 32 37,60 S 73 14,62 W | 25 sml |

<u>Auslegung OBH/S 100 bis 122 auf Seismikprofil 04</u>

| | | | |
|---|---|---|---|
| 0358 | OBS 100 z.W. | LT= 3972 m | 32 37,60 S 73 14,62 W |
| 0422 | OBS 101 | 3925 m | 32 39,06 S 73 17,65 W |
| 0446 | OBS 102 | 3954 m | 32 40,66 S 73 20,68 W |
| 0509 | OBS 103 | 3700 m | 32 42,01 S 73 23,64 W |
| 0532 | OBH 104 | 3750 m | 32 43,52 S 73 26,69 W |
| 0555 | OBS 105 | 3726 m | 32 45,00 S 73 29,67 W |
| 0617 | OBH 106 | 3630 m | 32 46,42 S 73 32,63 W |
| 0641 | OBH 107 | 2406 m | 32 47,93 S 73 35,60 W |
| 0704 | OBH 108 | 1572 m | 32 49,42 S 73 38,63 W |
| 0726 | OBH 109 | 2164 m | 32 50,92 S 73 41,62 W |
| 0749 | OBH 110 | 2374 m | 32 52,40 S 73 44,61 W |
| 0810 | OBH 111 | 2128 m | 32 53,84 S 73 47,63 W |
| 0833 | OBH 112 | 1028 m | 32 55,31 S 73 50,65 W |
| 0858 | OBH 113 | 0610 m | 32 56,76 S 73 53,58 W |
| 0919 | OBH 114 | 1977 m | 32 58,23 S 73 56,56 W |
| 0941 | OBH 115 | 2774 m | 32 59,71 S 73 59,57 W |
| 1002 | OBH 116 | 3248 m | 33 01,20 S 74 02,50 W |
| 1021 | OBH 117 | 3490 m | 33 02,64 S 74 05,47 W |
| 1043 | OBH 118 | 3672 m | 33 04,11 S 74 08,95 W |
| 1105 | OBH 119 | 3775 m | 33 05,63 S 74 11,55 W |
| 1125 | OBH 120 | 3755 m | 33 07,12 S 74 14,55 W |
| 1245 | OBH 121 | 4021 m | 33 08,59 S 74 17,63 W |
| 1205 | OBS 122 | 4052 m | 33 09,99 S 74 20,45 W |

<u>Magnetikprofil 118Kurs = 143 Grad v = 11,5 kn</u>

| | | | | |
|---|---|---|---|---|
| 1257 | Beginn Profil | LT = 4070 m | 33 13,94 S 74 16,92 W | |
| 1437 | Ende Profil | LT = 3929 m | 33 24,26 S 74 37,57 W | 20 sml |

<u>Seismikprofil 04 Kurs = 59 Grad v = 5,0 kn</u>

| | | | |
|---|---|---|---|
| 1523 – 1531 | setzen Bb-airgun-array aus | | |
| 1532 – 1539 | setzen Stb-airgun-array aus | | |
| 1540 | Beginn Profil | 33 20,43 S 74 41,79 W | 110 sml |
| 2400 | | 32 59,33 S 73 58,86 W | |

**15.12.01**

| | | |
|---|---|---|
| 1337 | Ende Profil | 32 25,15 S 72 49,47 W |
| 1339 – 1345 | holen Stb-airgun-array ein | |
| 1347 – 1357 | holen Bb-airgun-array ein | |
| 1406 – 1431 | hieven Magnetometer ein | |

Aufnahme OBH/S 100 – 122 von Profil 4

| | | | | | |
|---|---|---|---|---|---|
| 1620 | OBS 100 ausgelöst | 1724 gesichtet | 1736 a.D. | 32 37,07 S | 73 14,86 W |
| 1705 | OBS 101 | 1817 | 1825 | 32 38,70 S | 73 17,77 W |
| 1820 | OBS 102 | 1934 | 1943 | 32 40,21 S | 73 20,94 W |
| 1934 | OBH 103 | 2011 | 2023 | 32 41,48 S | 73 24,05 W |
| 2014 | OBH 104 | 2044 | 2058 | 32 43,18 S | 73 26,91 W |
| 2048 | OBS 105 | 2124 | 2136 | 32 44,68 S | 73 29,92 W |
| 2124 | OBH 106 | 2151 | 2216 | 32 46,16 S | 73 32,96 W |
| 2205 | OBH 107 | 2231 | 2307 | 32 47,65 S | 73 35,81 W |
| 2307 | OBH 108 | 2326 | 2343 | 32 49,36 S | 73 38,71 W |
| 2340 | OBH 109 | **16.12.01** | | | |
| | | 0005 | 0014 | 32 50,93 S | 73 41,64 W |
| 0018 | OBH 110 | 0050 | 0058 | 32 52,38 S | 73 44,61 W |
| 0103 | OBH 111 | 0134 | 0141 | 32 53,74 S | 73 47,68 W |
| 0147 | OBH 112 | 0205 | 0216 | 32 55,08 S | 73 50,47 W |
| 0230 | OBH 113 | 0238 | 0252 | 32 56,54 S | 73 53,66 W |
| 0300 | OBH 114 | 0415 | 0422 | 32 58,03 S | 73 56,51 W |
| 0420 | OBH 115 | 0452 | 0500 | 32 59,60 S | 73 59,66 W |
| 0452 | OBH 116 | 0533 | 0542 | 33 01,07 S | 74 02,76 W |
| 0533 | OBH 116 | 0616 | 0629 | 33 02,60 S | 74 05,63 W |
| 0620 | OBH 118 | 0658 | 0705 | 33 04,10 S | 74 08,60 W |
| 0658 | OBH 119 | 0739 | 0742 | 33 05,67 S | 74 11,71 W |
| 0742 | OBH 120 | 0827 | 0838 | 33 07,21 S | 74 14,73 W |
| 0828 | OBH 121 | 0904 | 0920 | 33 08,67 S | 74 17,93 W |
| 0847 | OBS 122 | 1010 | 1019 | 33 10,16 S | 74 20,62 W |

Magnetikprofil 119 bis 127

| | | | | |
|---|---|---|---|---|
| 1031 – 1052 | bringen Magnetometer aus | | | |
| 1052 | Beginn MAG-Profil 119 | LT = 4000 m | 33 09,01 S 74 21,02 W | |
| 1442 | Profilwechsel 119 / 120 | LT = 4064 m | 32 25,0 S 74 20,0 W | 32 sml |
| 1549 | Profilwechsel 120 / 121 | LT = 4248 m | 32 15,0 S 74 10,0 W | 13 sml |
| 1912 | Profilwechsel 121 / 122 | LT = 3974 m | 32 15,0 S 73 25,0 W | 38 sml |
| 2140 | Profilwechsel 122 / 123 | LT = 4026 m | 31 45,0 S 73 25,0 W | 30 aml |
| **17.12.01** | | | | |
| 0036 | Profilwechsel 123 / 124 | LT = 4115 m | 31 45,0 S 74 00,0 W | 30 sml |
| 0158 | Profilwechsel 124 / 125 | LT = 4685 m | 31 55,0 S 74 00,0 W | 10 sml |
| 0725 | Profilwechsel 125 / 126 | LT = 5050 m | 31 55,0 S 72 30,0 W | 60 sml |
| 1300 | Profilwechsel 126 / 127 | LT = 808 m | 31 22,0 S 71 45,0 W | 65 sml |
| 1442 | Ende Profil 127 | LT = 438 m | 31 02,85 S 71 45,05 W | 22 sml |
| 140 – 1512 | hieven Magnetometer ein | | | |

Auslegung OBS/H 123 bis 148 auf dem WS-Profil 5

| | | | |
|---|---|---|---|
| 1529 | OBH 123 z.W. | LT = 0148 m | 30 59,99 S 71 42,99 W |
| 1553 | OBH 124 | 0507 m | 30 59,99 S 71 46,00 W |
| 1613 | OBS 125 | 1009 m | 31 00,00 S 71 49,00 W |

| | | | | |
|---|---|---|---|---|
| 1634 | OBS 126 | 1343 m | 31 00,00 S | 71 52,01 W |
| 1655 | OBS 127 | 1512 m | 31 00,02 S | 71 55,00 W |
| 1716 | OBS 128 | 1652 m | 31 00,01 S | 71 57,99 W |
| 1748 | OBH 129 | 2416 m | 31 00,02 S | 72 00,89 W |
| 2022 | OBH 130 | 2649 m | 31 00,01 S | 72 04,48 W |
| 2046 | OBH 131 | 2822 m | 31 00,00 S | 72 07,97 W |
| 2111 | OBH 132 | 3420 m | 31 00,00 S | 72 11,49 W |
| 2135 | OBH 133 | 3721 m | 31 00,00 S | 72 13,99 W |
| 2200 | OBH 134 | 4027 m | 31 00,00 S | 72 17,50 W |
| 2223 | OBH 135 | 4583 m | 31 00,00 S | 72 21,00 W |
| 2246 | OBH 136 | 5198 m | 31 00,00 S | 72 28,01 W |
| 2309 | OBH 137 | 5568 m | 31 00,00 S | 7228,01 W |
| 2332 | OBH 138 | 5943 m | 31 00,00 S | 72 31,50 W |
| **18.12.01** | | | | |
| 0004 | OBH 139 | 5720 m | 31 00,00 S | 72 37,27 W |
| 0022 | OBH 140 | 5790 m | 31 00,00 S | 72 40,01 W |
| 0050 | OBH 141 | 5172 m | 31 00,00 S | 72 45,00 W |
| 0113 | OBS 142 | 4819 m | 31 00,00 S | 72 49,03 W |
| 0135 | OBS 143 | 4733 m | 31 00,00 S | 72 53,00 W |
| 0159 | OBH 144 | 4467 m | 31 00,00 S | 72 57,02 W |
| 0223 | OBH 145 | 4347 m | 30 59,99 S | 73 01,01 W |
| 0242 | OBH 146 | 4317 m | 31 00,00 S | 73 04,00 W |
| 0302 | OBH 147 | 4275 m | 31 00,00 S | 73 07,00 W |
| 0321 | OBS 148 | 4181 m | 31 00,00 S | 73 10,00 W |

Seismik-Profil 5.1/2 v = 5,0 kn Kurs = 90 / 270 Grad

| | | | | | |
|---|---|---|---|---|---|
| 0332 – 0350 | bringen Magnetometer aus KL = 750 m | | | | |
| 0400 – 0412 | bringen Stb-airgun-array aus | | | | |
| 0414 – 0425 | bringen Bb-airgun-array aus | | | | |
| 0429 | Beginn Profil 5.1 | LT = 4324 m | 31 00,00 S | 73 05,57 W | |
| 1200 | | | 31 00,00 S | 72 21,13 W | |
| 1812 - 1822 | hieven Magnetometer vor bis KL = 150 m | | | | |
| 1817 – 1822 | hieven Bb-airgun-array ein | | | | |
| 1835 | Ende Profil 5.1 | LT = 152 m | 31 00,00 S | 71 43,10 W | 63 sml |
| 1835 – 1903 | Schleife über Bb | | | | |
| 1903 – 1911 | setzen Bb-airgun-array aus | | | | |
| 1903 – 1915 | bringen Magnetometer auf KL = 750 m | | | | |
| 1915 | Beginn Profil 5.1 | LT = 465 m | 31 00,00 S | 71 45,47 W | 102 sml |
| 2400 | | | 31 00,00 S | 72 13,44 W | |
| **19.12.01** | | | | | |
| 1200 | | | 31 00,00 S | 73 23,82 W | |
| 1526 | Ende Profil 5.2 | LT = 4003 m | 31 00,00 S | 73 44,00 W | |
| 1529 – 1636 | holen Stb-airgun-array ein | | | | |
| 1639 – 1646 | holen Bb-airgun-array ein | | | | |
| 1646 – 1652 | drehen über Bb | | | | |

MAG-Profil 128 Kurs = 90 Grad v = 11,5 kn

| | | | | |
|---|---|---|---|---|
| 1652 | Beginn Profil | 31 00,21 S | 73 46,25 W | 31 sml |
| 1800 | Ende Profil | 31 00,00 S | 73 16,20 W | |
| 1805 – 1834 | hieven Magnetometer ein | | | |

### Aufnahme OBS/H 148 – 123 von WS-Profil 5

| | | | | | |
|---|---|---|---|---|---|
| 1805 | OBS 148 ausgelöst | 1943 gesichtet | 1953 a.D. | 30 59,97 S | 73 09,93 W |
| 1943 | OBH 147 | 2039 | 2048 | 30 59,83 S | 73 07,07 W |
| 2011 | OBH 146 | 2135 | 2148 | 30 59,84 S | 73 04,13 W |
| 2041 | OBH 145 | 2148 | 2243 | 30 59,32 S | 73 01,65 W |
| 2129 | OBH 144 | 2214 | 2314 | 30 59,42 S | 72 57,89 W |
| 2221 | OBH 143 | **20.12.01** | | | |
| | | 0035 | 0045 | 30 59,49 S | 72 54,00 W |
| 2335 | OBH 142 | 0020 | 0123 | 30 59,74 S | 72 49,92 W |
| 2356 | OBH 141 | | 0224 | 30 59,80 S | 72 46,36 W |
| 0156 | OBH 140 | 0307 | 0320 | 31 00,09 S | 72 40,16 W |
| 0255 | OBH 139 | 0400 | 0424 | 31 00,22 S | 72 37,52 W |
| 0355 | OBH 138 | 0500 | 0510 | 31 00,20 S | 72 31,57 W |
| 0456 | OBH 137 | 0603 | 0611 | 31 00,08 S | 72 28,09 W |
| 0530 | OBH 136 | 0651 | 0658 | 31 00,07 S | 72 24,68 W |
| 0639 | OBH 135 | 0719 | 0731 | 31 00,11 S | 72 21,25 W |
| 0714 | OBH 134 | 0747 | 0805 | 30 59,99 S | 72 17,78 W |
| 0751 | OBH 133 | 0820 | 0835 | 30 59,95 S | 72 14,17 W |
| 0828 | OBH 132 | 0907 | 0916 | 31 00,06 S | 72 11,63 W |
| 0851 | OBH 131 | 0938 | 0947 | 31 00,43 S | 72 09,09 W |
| 0940 | OBH 130 | 1013 | 1025 | 31 00,54 S | 72 04,43 W |
| 1006 | OBH 129 | 1030 | 1053 | 31 00,46 S | 72 00,89 W |
| 1045 | OBS 128 | 1104 | 1118 | 31 00,31 S | 71 57,91 W |
| 1111 | OBS 127 | 1140 | 1150 | 31 00,29 S | 71 55,04 W |
| 1136 | OBS 126 | 1210 | 1220 | 31 00,20 S | 71 52,06 W |
| 1210 | OBS 125 | 1245 | 1302 | 31 00,05 S | 71 49,00 W |
| 1322 | OBH 124 | 1332 | 1338 | 30 59,99 S | 71 45,96 W |
| 1355 | OBH 123 | 1400 | 1407 | 30 59,91 S | 71 42,96 W |

### MAG-Profile 129 bis 130 v = 11,5 kn

| | | | | |
|---|---|---|---|---|
| 1419 – 1430 | bringen Magnetometer aus | | | |
| 1516 | Beginn Profil 129 | 30 50,07 S | 71 45,69 W | |
| 2149 | Profilwechsel 129 / 130 | 30 50,00 S | 73 10,00 W | 43 sml |
| 2400 | Ende Profil 130 | 31 07,83 S | 73 24,23 W | 21 sm |

**21.12.01**

### EM/PS- Profil 130 bis 134

| | | | | |
|---|---|---|---|---|
| 0015 | Magnetometer a.D. | | | |
| 0057 | Profilwechsel 130 / 131 | 31 15,00 S | 73 30,00 W | 09 sml |
| 0354 | Profilwechsel 131 / 132 | 31 32,00 S | 73 00,00 W | 31 sml |
| 0750 | Profilwechsel 132 / 133 | 31 35,00 S | 72 10,00 W | 20 sml |
| 0950 | Profilwechsel 133 / 134 | 31 49,99 S | 71 48,03 W | 24 sml |
| 1310 | Ende Profil 133 | 32 30,00 S | 71 41,00 W | 40 sml |

## Appendix 9.2

### Airgun Shots

| PROFILE | PULSE NO. | DATE | TIME UTC | LAT | LON | REMARKS |
|---|---|---|---|---|---|---|
| SO161-01 | 1 | 05.12.01 | 00:51 | -37.81273 | -75.43761 | 60s both arrays |
| | 1109 | 05.12.01 | 19:19 | -38.20311 | -73.54955 | EOL |
| SO161-02A | 1 | 08.12.01 | 18:45 | -32.08330 | -73.15234 | 40s both arrays |
| | 47 | 08.12.01 | 19:18:41 | -32.08365 | -73.09620 | EOL |
| SO161-02B | 1 | 08.12.01 | 19:21 | -32.08355 | -73.09250 | 40s both arrays |
| | 33 | 08.12.01 | 19:44:41 | -32.08407 | -73.05384 | EOL |
| SO161-02C | 1 | 08.12.01 | 19:46 | -32.08407 | -73.05154 | 40s both arrays |
| | 1324 | 09.12.01 | 10:28 | -32.08331 | -71.60869 | EOL |
| SO161-02D | 1 | 09.12.01 | 11:01 | -32.08323 | -71.62923 | 60s port array off |
| | 6 | 09.12.01 | 11:06 | -32.08321 | -71.63723 | port array on |
| | 1248 | 10.12.01 | 07:48 | -32.08316 | -73.66637 | EOL |
| SO161-03 | 1 | 12.12.01 | 06:55 | -32.07203 | -74.59738 | 60s both arrays |
| | 1445 | 13.12.01 | 06:59 | -33.40892 | -72.89902 | EOL |
| SO161-04 | 1 | 14.12.01 | 18:44 | -33.33786 | -74.69122 | 60s both arrays |
| | 1314 | 15.12.01 | 16:37 | -32.41948 | -72.82477 | EOL |
| SO161-05A | 1 | 18.12.01 | 07:29 | -30.99986 | -73.09360 | 30s both arays |
| | 1654 | 18.12.01 | 21:15 | -30.99977 | -71.74937 | port array off |
| | 1694 | 18.12.01 | 21:35 | -31.00011 | -71.71773 | EOL |
| SO161-05B | 1 | 18.12.01 | 22:15 | -30.99998 | -71.75749 | 60s both arrays |
| | 1211 | 19.12.01 | 18:25 | -30.99985 | -73.73226 | EOL |

## SPOC

| INST. | LAT (S) D:M | LON (W) D:M | DIST. TO NEXT (nm) | DEPTH (m) | REL. CODE | ANT. CH. | REC. NO. | SKEW (ms) | TIME SLIPS (s) | SENSORS | REMARKS |
|---|---|---|---|---|---|---|---|---|---|---|---|
| **OBS01** | 32: 04. 984 | 71: 49. 976 | 8.5 | 1340 | 0398+0355 | D | 991248 | no skew | -0.64 | PMD 541 + Hyd 27 | redeployed 13 Oct. |
| **OBH02** | 32: 04. 973 | 72: 00. 038 | 10.2 | 3183 | 6334 | C | 00709 | -66 | -6.86 | DPG 186 | |
| **OBH03** | 32: 04. 991 | 72: 12. 007 | 11.04 | 3907 | 0399+0355 | C | 990701 | 66 | -2.26 | Hyd 29 | |
| **OBS04** | 32: 04. 979 | 72: 25. 025 | 9.98 | 4560 | 3624 | B | 991249 | no skew | | PMD 509+ DPG 91 | redeployed 13 Oct. |
| **OBH05** | 32: 15. 002 | 72: 25. 002 | 11.02 | 4577 | 9314 | C | 991242 | -58 | -15.44 | DPG 93 | |
| **OBH06** | 32: 19. 992 | 72: 12. 022 | 10.18 | 3353 | 5924 | C | 991236 | -51 | -4.42 | Hyd. 38 | |
| **OBH07** | 32: 14. 998 | 71: 59. 988 | 12.72 | 1783 | D629 | C | 000711 | -62 | -7.00 | DPG 78 | |
| **OBH08** | 32: 15. 000 | 71: 45. 009 | 10.84 | 784 | D674 | C | 991256 | -95 | -10.39 | Hyd. 34 | |
| **OBS09** | 32: 24. 990 | 71: 39. 991 | 16.93 | 495 | 0387+0355 | B | 000706 | no skew | -2.48 | PMD 539+ DPG 74 | redeployed 13 Oct. |
| **OBH10** | 32: 24. 997 | 72: 00. 022 | 10.16 | 2434 | 9344 | C | 991259 | -128 | -5.04 | Hyd. 28 | |
| **OBH11** | 32: 25. 035 | 72: 12. 008 | 11.00 | 2403 | B495 | D | 991250 | 125 | -12.84 | Hyd 31 | |
| **OBS12** | 32: 24. 989 | 72: 25. 000 | 25.40 | 4312 | 3609 | D | 991246 | no skew | -1.8 | PMD 543 + DPG 75 | redeployed 13 Oct. |
| **OBS13** | 32: 24. 994 | 72: 55. 042 | 35.02 | 4617 | 0397+0355 | D | 991237 | -111 | -13.44 | Webb 2329 + DPG 87 | |
| **OBS14** | 33: 00. 001 | 72: 58. 000 | 33.02 | 5169 | 039A+0355 | D | 000713 | 61 | -10.54 | Webb 2352 + DPG 95 | |
| **OBH15** | 33: 17. 988 | 72: 25. 014 | 10.90 | 1941 | 3659 | C | 991238 | -90 | -7.61 | Hyd. 46 | |
| **OBH16** | 33: 17. 991 | 72: 11. 967 | 10.06 | 2122 | 6959 | D | 991243 | 82 | -0.82 | Hyd. 90 | |
| **OBS17** | 33: 17. 993 | 71: 59. 996 | 10.83 | 1223 | 3614 | D | 991235 | 77 | 6.82 | Webb 2353 + DPG 92 | |
| **OBH18** | 33: 07. 983 | 71: 54. 987 | 14.28 | 696 | 9329 | D | 991252 | -86 | -6.05 | Hyd. 09 | |
| **OBH19** | 33: 08. 009 | 72: 12. 014 | 10.92 | 1901 | B479 | D | 010403 | 42 | -4.75 | Hyd. 22 | |
| **OBH20** | 32: 59. 993 | 72: 25. 045 | 7.99 | 2712 | 4A44 | B | 000707 | -157 | -6.11 | Hyd. 30 | |
| **OBS21** | 33: 07. 991 | 72: 24. 983 | 10.76 | 3052 | 3674 | A | 991244 | | | PMD + DPG 77 | no data |
| **OBH22** | 32: 59. 981 | 72: 12. 199 | 9.98 | 2185 | 0386+0355 | D | 010405 | -10 | -11.29 | Hyd. 41 | |
| **OBH23** | 32: 49. 986 | 72: 12. 222 | | 2431 | 4949 | A | 991247 | | | AWI Hyd. | no data |

SPOC

| INST. | LAT (S) D:M | LON (W) D:M | DIST. TO NEXT (nm) | DEPTH (m) | REL. CODE | ANT. CH. | REC. NO. | SKEW (ms) | REMARKS | SENSOR | FIGURE 5.4.1. |
|---|---|---|---|---|---|---|---|---|---|---|---|
| **OBH24** | 38 10. 129 | 73 43. 162 | 1.82 | 171 | 0386+0355 | B | 991248 | -2 | | OAS41 | 2 |
| **OBH25** | 38 09. 579 | 73 45. 486 | 1.76 | 312 | 9314 | D | 000711 | -2 | | DPG83?93 | 3 |
| **OBH26** | 38 09. 157 | 73 47. 659 | 2.80 | 453 | 0399+0355 | C | 010401 | -272 | | OAS29 | 4 |
| **OBS27** | 38 08. 445 | 73 51. 009 | 2.79 | 559 | 4A44 | B | 971202 | -3 | | OAS30+Owen2, 4.5 Hz | 5, 6 |
| **OBS28** | 38 07. 741 | 73 54. 524 | 2.79 | 607 | 039A+0355 | A | 980401 | -4 | | OAS14+Owen11, 30 Hz | 7, 8 |
| **OBH29** | 38 07. 040 | 73 57. 943 | 2.79 | 678 | 5924 | D | 709 | -2 | | DPG95 | 9 |
| **OBH30** | 38 06. 334 | 74 01. 336 | 2.40 | 605 | B495 | C | 991259 | -3 | | OAS31 | 10 |
| **OBH31** | 38 05. 716 | 74 04. 286 | 2.41 | 764 | 9344 | D | 713 | +2 | | DPG78 | 11 |
| **OBH32** | 38 05. 100 | 74 07. 248 | 2.40 | 731 | D629 | A | 991247 | +1 | | OAS28 | 12 |
| **OBS33** | 38 04. 469 | 74 10. 190 | 2.79 | 687 | 0387+0355 | B | 00612 | +1 | | OAS02+Arne1, 4.5 Hz | 13, 14 |
| **OBH34** | 38 03. 784 | 74 13. 620 | 1.90 | 1026 | 6334 | D | 991244 | +1 | | DPG86 | card problem |
| **OBH35** | 38 03. 234 | 74 15. 940 | 1.91 | 1223 | D674 | D | 991243 | +2 | | OAS34 | 15 |
| **OBH36** | 38 02. 783 | 74 18. 258 | 1.79 | 1555 | 3659 | C | 991238 | -2 | | OAS46 | 16 |
| **OBH37** | 38 02. 352 | 74 20. 476 | 2.81 | 2027 | 6959 | C | 991252 | -2 | | OAS06 | 17 |
| **OBH38** | 38 01. 608 | 74 23. 912 | 2.04 | 3136 | 9329 | C | 10403 | +1 | | OAS09 | 18 |
| **OBH39** | 38 01. 180 | 74 26. 358 | 2.06 | 3851 | B479 | D | 991235 | +1 | | DPG92 | poor signal |
| **OBH40** | 38 00. 622 | 74 28. 888 | 4.20 | 3800 | 4949 | C | 614 | -4 | | OAS22 | 19 |
| **OBH41** | 38 59. 606 | 74 34. 084 | 4.18 | 4594 | 3664 | C | 10402 | -2 | | OAS38 | 20 |
| **OBS42** | 38 58. 568 | 74 39. 220 | 4.20 | 4689 | 3614 | C | 991249 | +4 | | DPG74+PMD541 | 21 |
| **OBS43** | 37 57. 460 | 74 44. 373 | 2.80 | 4679 | 3674 | A | 708 | | | DPG77+WEBB2353 | 22 |
| **OBS44** | 37 56. 784 | 74 47. 759 | 3.39 | 4665 | 0398+0355 | D | 980901 | +12 | | OAS27+Owen16, 30 Hz | 23 |
| **OBH45** | 37 55. 882 | 74 51. 899 | 3.42 | 4718 | B474 | D | 010405 | 0 | | OAS75 | 24 |
| **OBS46** | 37 55. 023 | 74 56. 059 | 2.99 | 4573 | 3609 | C | 991242 | -1 | | DPG75+PMD543 | 25 |
| **OBS47** | 37 54. 264 | 74 59. 696 | | 4545 | 3624 | D | 991246 | | | DPG91+PMD509 | card problem |
| **Trigger** | | | | | | | 611 | 0 | | | |

| INST. | LAT (S) | LON (W) | DIST. TO | DEPTH | REL. | ANT. | REC. | SKEW | REMARKS | SENSOR | FIGURE |
|---|---|---|---|---|---|---|---|---|---|---|---|
| | D:M | D:M | NEXT (nm) | (m) | CODE | CH. | NO. | (ms) | | | 5.4.2. |
| OBH48 | 32 05. 000 | 71 36. 990 | 2.55 | 202 | D629 | D | 991248 | -4 | | OAS28 | poor signal |
| OBS49 | 32 05. 005 | 71 39. 980 | 2.55 | 432 | 0397+0355 | C | 991237 | | power failure | | |
| OBH50 | 32 05. 017 | 71 43. 053 | 2.55 | 621 | 9344 | C | 0711 | -4 | | DPG78 | 2, 21 |
| OBS51 | 32 05. 006 | 71 46. 011 | 2.55 | 817 | 3624 | D | 706 | +6 | | DPG91+PMD509 | 3, 22 |
| OBH52 | 32 04. 986 | 71 49. 030 | 2.55 | 1178 | B495 | C | 10403 | +1 | | OAS31 | 4, 23 |
| OBS53 | 32 05. 000 | 71 52. 055 | 2.55 | 1603 | 0387+0355 | D | 0612 | +3 | | OAS02+Arne1, 4.5Hz | 5, 6, 24, 25 |
| OBH54 | 32 05. 024 | 71 54. 974 | 2.55 | 2350 | 5924 | D | 709 | -3 | | DPG95 | poor signal |
| OBS55 | 32 05. 030 | 71 58. 050 | 2.55 | 2814 | 3614 | A | 991249 | +7 | | DPG74+PMD540 | 7, 26 |
| OBH56 | 32 05. 000 | 72 00. 990 | 2.55 | 3257 | 0399+0355 | B | 010401 | -6 | | OAS29 | 8, 27 |
| OBS57 | 32 04. 983 | 72 04. 002 | 2.55 | 3629 | 3609 | D | 991241 | +3 | | DPG75+PMD539 | 9, 28 |
| OBH58 | 32 04. 983 | 72 07. 016 | 2.55 | 3810 | 9314 | C | 0713 | +2 | | DPG93 | poor signal |
| OBS59 | 32 05. 002 | 72 09. 991 | 3.40 | 3905 | 3674 | B | 000707 | -7 | | OAS13+WEBB2353 | 10, 11, 29 |
| OBS60 | 32 04. 993 | 72 14. 004 | 3.40 | 3831 | 039A+0355 | C | 971202 | -6 | | OAS14+Owen | 12, 30 |
| OBS61 | 32 05. 004 | 72 18. 007 | 3.40 | 3767 | 4A44 | D | 980401 | -5 | | OAS30+Owen2, 4.5Hz | 13, 31 |
| OBH62 | 32 04. 999 | 72 22. 015 | 3.40 | 4125 | 0398+0355 | D | 0610 | -11 | | OAS27 | 14, 32 |
| OBH63 | 32 04. 988 | 72 26. 005 | 3.40 | 4752 | 0386+0355 | C | 991243 | +2 | | OAS41 | 15, 33 |
| OBH64 | 32 04. 985 | 72 29. 987 | 4.25 | 5299 | 3664 | C | 000614 | -6 | | OAS38 | poor signal |
| OBH65 | 32 05. 000 | 72 34. 991 | 6.80 | 5524 | 4949 | D | 991247 | +2 | | OAS22 | 16, 34 |
| OBH66 | 32 04. 994 | 72 43. 048 | 4.25 | 5693 | B479 | A | 991250 | +5 | | OAS04 | 17, 35 |
| OBH67 | 32 04. 990 | 72 47. 993 | 4.25 | 5130 | 9329 | D | 010402 | -1 | | OAS09 | 18, 36 |
| OBH68 | 32 05. 000 | 72 52. 991 | 4.25 | 4666 | 6959 | C | 991238 | -2 | | OAS06 | 19, 37 |
| OBH69 | 32 05. 011 | 72 57. 998 | 4.25 | 4179 | 3659 | C | 980901 | +14 | | OAS46 | 20, 38 |
| OBH70 | 32 05. 000 | 73 03. 010 | 4.25 | 4030 | D674 | C | 991259 | -4 | | OAS34 | poor signal |
| OBH71 | 32 04. 994 | 73 08. 020 | 4.25 | 4073 | 6334 | B | 991242 | 0 | | DPG86 | 39 |
| OBH72 | 32 05. 015 | 73 13. 001 | | 4037 | B474 | A | 991236 | -1 | | OAS75 | 40 |
| Trigger | | | | | | | 611 | 0 | | | |

Appendix 9.3.4 SPOC SO 161-Leg 4 - Profil 03

| INST. | LAT (S) | LON (W) | DIST. TO | DEPTH | REL. | ANT. | REC. | SKEW | REMARKS | SENSOR | FIGURE |
|---|---|---|---|---|---|---|---|---|---|---|---|
| | D:M | D:M | NEXT (nm) | (m) | CODE | CH. | NO. | (ms) | | | 5.4.3. |
| OBS73 | 33 13. 536 | 73 08. 019 | 2.29 | 4637 | 3624 | C | 000706 | +4 | | DPG91+PMD509 | 2, 3 |
| OBH74 | 33 12. 010 | 73 10. 000 | 2.40 | 4152 | 3669 | C | ?? | -3 | | OAS28 | 4 |
| OBH75 | 33 10. 359 | 73 12. 074 | 2.21 | 3860 | 9344 | C | 000711 | -2 | | DPG78 | poor signal |
| OBS76 | 33 08. 751 | 73 14. 108 | 2.21 | 3950 | 0387+0355 | D | 991259 | -3 | | OAS02+Webb2352 | 5 |
| OBH77 | 33 07. 316 | 73 15. 944 | 2.20 | 3993 | B495 | D | 10401 | -5 | | OAS31 | 6 |
| OBH78 | 33 05. 817 | 73 17. 852 | 2.18 | 3989 | 5924 | D | 991242 | 0 | | DPG95 | poor signal |
| OBS79 | 33 04. 322 | 73 19. 769 | 2.21 | 3623 | 039A+0355 | B | 612 | +1 | | OAS11+Owen14, 30Hz | 7 |
| OBH80 | 33 02. 839 | 73 21. 681 | 2.20 | 3796 | 0399+0355 | D | 991243 | +1 | | OAS19 | 8 |
| OBS81 | 33 01. 317 | 73 23. 601 | 2.22 | 3789 | 3609 | D | 980901 | +12 | | OAS22+Arne1 | 9, 10 |
| OBS82 | 32 59. 834 | 73 25. 524 | 2.20 | 3683 | 4A44 | C | 971202 | -5 | | OAS30+Owen02, 4.5Hz | 11, 12 |
| OBH83 | 32 58. 296 | 73 27. 429 | 2.19 | 3778 | 9314 | C | 000709 | -2 | | DPG93 | 13 |
| OBS84 | 32 56. 809 | 73 29. 337 | 2.21 | 3746 | 0397+0355 | D | 991246 | -1 | | DPG87+Webb2329 | 14 |
| OBH85 | 32 55. 308 | 73 31. 317 | 2.22 | 3704 | 0386+0355 | B | 010402 | -2 | | OAS41 | 15 |
| OBS86 | 32 53. 804 | 73 33. 230 | 2.16 | 3179 | 3614 | D | 991249 | +5 | | DPG74+PMD540 | 16, 17 |
| OBH87 | 32 52. 348 | 73 35. 113 | 2.20 | 2375 | 0398+0355 | D | 000610 | -8 | | OAS04, 27, 34, 38 | 18, 19, 20 |
| OBS88 | 32 50. 843 | 73 36. 994 | 2.20 | 1080 | 3674 | C | 991252 | -3 | | OAS13+PMD539 | 21 |
| OBH89 | 32 49. 324 | 73 38. 938 | 2.19 | 1527 | 3664 | D | 0614 | -7 | | OAS18 | 22 |
| OBH90 | 32 47. 833 | 73 40. 823 | 2.18 | 2596 | 4949 | A | 991244 | 0 | | DPG75 | 23 |
| OBH91 | 32 46. 300 | 73 42. 699 | 2.21 | 3150 | B479 | D | 991247 | +2 | | OAS04 | 24 |
| OBH92 | 32 44. 835 | 73 44. 625 | 2.19 | 3268 | 9329 | B | 010403 | 0 | | OAS09 | 25 |
| OBH93 | 32 43. 297 | 73 46. 519 | 2.18 | 3537 | 6959 | C | 980401 | -5 | | OAS06 | 26 |
| OBH94 | 32 41. 826 | 73 48. 415 | 2.20 | 3524 | 3659 | D | 991250 | +3 | | OAS46 | 27 |
| OBH95 | 32 40. 316 | 73 50. 339 | 2.18 | 3589 | D674 | A | 991241 | +3 | | DPG77 | 28 |
| OBH96 | 32 38. 833 | 73 52. 234 | 2.99 | 3701 | 6334 | A | 0713 | +3 | | DPG86 | 29 |
| OBH97 | 32 36. 806 | 73 54. 819 | 3.06 | 3835 | B474 | C | 991236 | -1 | | OAS75 | 30 |
| OBH98 | 32 34. 741 | 73 57. 468 | 2.93 | 4008 | 5929 | C | 0616 | -6 | | OAS05 | 31 |
| OBH99 | 32 32. 694 | 73 59. 999 | | 4076 | D629 | 156.675 | 991256 | -1 | | OAS01 | 32 |
| Trigger | | | | | | | 611 | -1 | | | |

Appendix 9.3.5 SPOC SO 161-Leg 4 - Profil 04

| INST. | LAT (S) | LON (W) | DIST. TO | DEPTH | REL. | ANT. | REC. | SKEW | REMARKS | SENSOR | FIGURE |
|---|---|---|---|---|---|---|---|---|---|---|---|
|  | D:M | D:M | NEXT (nm) | (m) | CODE | CH. | NO. | (ms) |  |  | 5.4.4. |
| OBS100 | 32 37. 567 | 73 14. 611 | 2.92 | 3972 | 0398+0355 | A | 980901 | +10 |  | OAS27. Arne01 | 2, 3 |
| OBS101 | 32 39. 059 | 73 17. 641 | 2.95 | 3920 | 3614 | A | 991252 | -3 |  | PMD540 | 4 |
| OBS102 | 32 40. 561 | 73 20. 718 | 2.88 | 3954 | 3674 | C | 706 | +4 |  | DPG87, PMD539 | 5 |
| OBH103 | 32 41. 970 | 73 23. 711 | 2.99 | 3707 | 039A+0355 | A | 000614 |  |  | OAS14 | 6 |
| OBH104 | 32 45. 523 | 73 26. 678 | 2.91 | 3747 | 0397+0355 | D | 010403 | +1 |  | OAS13 | 7 |
| OBS105 | 32 45. 003 | 73 29. 651 | 2.87 | 3683 | 4A44 | C | 971202 | -5 |  | OAS30, Owen02, 4.5 Hz | 8, 9 |
| OBH106 | 32 46. 413 | 73 32. 653 | 2.92 | 3627 | 3609 | C | 000610 | -7 |  | OAS04, 22, 34, 38 | 10, 11 |
| OBH107 | 32 47. 928 | 73 35. 606 | 2.96 | 2402 | 0387+0355 | D | 000612 | +1 |  | OAS02 | 12 |
| OBH108 | 32 49. 419 | 73 38. 634 | 2.95 | 1397 | 4949 | D | 991242 | -1 |  | DPG75 | 13 |
| OBH109 | 32 50. 925 | 73 41. 619 | 2.94 | 2165 | 3664 | D | 991243 | +1 |  | OAS18 | poor signal |
| OBH110 | 32 52. 398 | 73 44. 610 | 2.87 | 2374 | 0386+0355 | C | 010401 | -4 |  | OAS41 | 14 |
| OBH111 | 32 53. 836 | 73 47. 632 | 2.96 | 2121 | 9314 | C | 000709 | -2 |  | DPG93 | card problem |
| OBH112 | 32 55. 308 | 73 50. 650 | 2.84 | 1028 | 0399+0355 | A | 010402 | -3 |  | OAS29 | 15 |
| OBH113 | 32 56. 773 | 73 53. 642 | 2.91 | 606 | 5924 | B | 991246 | -1 |  | DPG95 | poor signal |
| OBH114 | 32 58. 233 | 73 56. 585 | 2.92 | 2000 | B495 | D | 991248 | -2 |  | OAS31 | 16 |
| OBH115 | 32 59. 713 | 73 59. 573 | 2.95 | 2791 | 3669 | C | 991238 | 0 |  | OAS28 | 17 |
| OBH116 | 33 01. 203 | 74 02. 598 | 2.86 | 3248 | D674 | B | 000711 | -2 |  | DPG77 | poor signal |
| OBH117 | 33 02. 642 | 74 05. 469 | 2.89 | 3490 | 3659 | D | 991259 | -4 |  | OAS46 | 18 |
| OBH118 | 33 04. 114 | 74 08. 454 | 2.99 | 3673 | 6959 | D | 991250 | +4 |  | OAS06 | 19 |
| OBH119 | 33 05. 636 | 74 11. 545 | 2.92 | 3776 | 9329 | C | 991247 | +2 |  | OAS09 | 20 |
| OBH120 | 33 07. 117 | 74 14. 557 | 2.98 | 3756 | B479 | A | 980401 | -5 |  | OAS04 | 21 |
| OBH121 | 33 08. 588 | 74 17. 630 | 2.73 | 4021 | D629 | C | 000616 | -7 |  | OAS01 | 22 |
| OBS122 | 33 09. 990 | 74 20. 454 |  | 4054 | 3624 | D | 991244 | +1 |  | DPG91, PMD509 | 23 |
| Trigger |  |  |  |  |  |  | 611 | -121 |  |  |  |

| INST. | LAT (S) | LON (W) | DIST. TO | DEPTH | REL. | ANT. | REC. | SKEW | REMARKS | SENSOR | FIGURE |
|---|---|---|---|---|---|---|---|---|---|---|---|
| | D:M | D:M | NEXT (nm) | (m) | CODE | CH. | NO. | (ms) | | | |
| **OBH123** | 30 59. 991 | 71 42. 985 | 2.58 | 148 | B495 | A | 10403 | | | OAS31 | |
| **OBH124** | 30 59. 994 | 71 46. 007 | 2.58 | 507 | 5924 | C | 991246 | | | DPG95 | |
| **OBS125** | 31 00. 001 | 71 48. 999 | 2.58 | 1009 | 039A+0355 | D | 971202 | | mounted directly to frame | OAS14, Owen16, 30 Hz | |
| **OBS126** | 30 59. 999 | 71 52. 009 | 2.58 | 1344 | 3674 | C | 000706 | | | DPG87, PMD539 | |
| **OBS127** | 31 00. 015 | 71 55. 007 | 2.58 | 1510 | 3614 | D | 991252 | | | OAS38, PMD540 | |
| **OBS128** | 31 00. 015 | 71 57. 974 | 2.58 | 1651 | 0398+0355 | B | 980901 | | | OAS27, A01 | |
| **OBH129** | 31 00. 023 | 72 00. 882 | 3.01 | 2417 | 0387+0355 | C | 000614 | | | OAS02 | |
| **OBH130** | 31 00. 100 | 72 14. 470 | 3.01 | 2647 | 3609 | A | 010402 | | | OAS22 | |
| **OBH131** | 30 59. 969 | 72 07. 966 | 3.01 | 2822 | 0399+0355 | C | 000610 | | | OAS29 | |
| **OBH132** | 30 59. 973 | 72 11. 485 | 2.15 | 3417 | 9314 | D | 991241 | | | DPG93 | |
| **OBH133** | 31 00. 013 | 72 13. 979 | 3.01 | 3716 | D629 | C | 000616 | | | OAS01 | |
| **OBH134** | 31 00. 030 | 72 17. 505 | 3.01 | 4028 | 5929 | C | 980401 | | | OAS05 | |
| **OBH135** | 31 59. 998 | 72 21. 011 | 3.01 | 4579 | B474 | A | 000612 | | | OAS75 | |
| **OBH136** | 31 59. 987 | 72 24. 516 | 3.01 | 5159 | 0386+0355 | D | 991259 | | | OAS41 | |
| **OBH137** | 30 59. 994 | 72 28. 017 | 3.01 | 5568 | 3664 | C | 991238 | | | OAS18 | |
| **OBH138** | 30 59. 991 | 72 31. 501 | 4.96 | 5941 | 4949 | B | 000711 | | | DPG75 | |
| **OBH139** | 31 00. 000 | 72 37. 261 | 2.35 | 5723 | 6334 | D | 991244 | | | DPG92 | |
| **OBH140** | 31 00. 004 | 72 40. 013 | 4.30 | 5776 | B479 | D | 991250 | | | OAS04 | |
| **OBH141** | 31 00. 004 | 72 45. 013 | 3.44 | 5167 | 9329 | D | 991248 | | | OAS09 | |
| **OBH142** | 31 00. 010 | 72 49. 049 | 3.44 | 4821 | 4A44 | C | 991243 | | | OAS30 | |
| **OBH143** | 30 59. 998 | 72 52. 996 | 3.44 | 4724 | 0397+0355 | C | 010401 | | | OAS13 | |
| **OBH144** | 30 59. 998 | 72 57. 027 | 3.44 | 4467 | 6959 | B? | 991247 | | | OAS06 | |
| **OBH145** | 30 59. 992 | 73 01. 040 | 2.58 | 4347 | 3659 | D | 991256 | | | OAS46 | |
| **OBH146** | 30 59. 998 | 73 03. 983 | 2.58 | 4312 | D674 | B | 010405 | | | OAS05 | |
| **OBH147** | 31 00. 003 | 73 07. 012 | 2.58 | 4277 | 3669 | D | 010404 | | | OAS28 | |
| **OBS148** | 31 00. 026 | 73 10. 002 | | 4188 | 3624 | D | 709 | | | DPG91, PMD509 | |
| **Trigger** | | | | | | | 611 | | | | |

## Appendix IV

### Magnetic profiles

| Line number | Shot points | Date | Time | Position | | Course | Methods |
|---|---|---|---|---|---|---|---|
| SO161-101 | | 02.12.01 | 23:53 | 33° 12.984 S | 72° 49.884 W | 179° | G M P |
| | | 03.12.01 | 04:43 | 34° 00.024 S | 72° 48.302 W | | 87.11 km |
| SO161-102 | | 03.12.01 | 04:43 | 34° 00.024 S | 72° 48.302 W | 197° | G M P |
| | | 03.12.01 | 18:02 | 36° 00.038 S | 73° 35.040 W | | 233.26 km |
| SO161-103 | | 03.12.01 | 18:02 | 36° 00.038 S | 73° 35.040 W | 233° | G M P |
| | | 03.12.01 | 20:23 | 36° 15.043 S | 74° 00.020 W | | 46.52 km |
| SO161-104 | | 03.12.01 | 20:23 | 36° 15.043 S | 74° 00.020 W | 195° | G M P |
| | | 03.12.01 | 22:59 | 36° 41.756 S | 74° 08.908 W | | 51.17 km |
| SO161-105 | | 03.12.01 | 22:59 | 36° 41.756 S | 74° 08.908 W | 110° | G M P |
| | | 03.12.01 | 23:40 | 36° 44.289 S | 74° 99.117 W | | 13.72 km |
| SO161-106 | | 03.12.01 | 23:40 | 36° 44.289 S | 74° 99.117 W | 191° | G M P |
| | | 04.12.01 | 06:15 | 37° 55.107 S | 74° 17.368 W | | 133.55 km |
| SO161-107 | | 04.12.01 | 06:15 | 37° 55.107 S | 74° 17.487 W | 111° | G M P |
| | | 04.12.01 | 08:36 | 38° 04.766 S | 73° 44.859 W | | 50.79 km |
| SO161-108 | | 04.12.01 | 21:35 | 38° 08.950 S | 75° 06.976 W | 304° | G M P |
| | | 04.12.01 | 23:30 | 37° 56.981 S | 75° 29.542 W | | 39.62 km |
| SO161-109 | | 04.12.01 | 23:30 | 37° 56.981 S | 75° 29.542 W | 356° | G M P |
| | | 05.12.01 | 00:14 | 37° 48.522 S | 75° 29.919 W | | 15.70 km |
| SO161-201 | 1 | 05.12.01 | 00:51 | 37° 48.764 S | 75° 26.258 W | 105° | S G M P |
| | 1109 | 05.12.01 | 19:19 | 38° 12.194 S | 73° 32.941 W | | 170.90 km |
| SO161-110 | | 06.12.01 | 14:05 | 37° 44.353 S | 74° 58.403 W | 280° | G M P |
| | | 06.12.01 | 16:41 | 37° 39.386 S | 75° 34.822 W | | 54.15 km |
| SO161-111 | | 06.12.01 | 16:41 | 37° 39.386 S | 75° 34.822 W | 15° | G M P |
| | | 06.12.01 | 20:28 | 36° 54.081 S | 75° 20.024 W | | 86.70 km |
| SO161-112 | | 06.12.01 | 20:28 | 36° 54.081 S | 75° 20.024 W | 41° | G M P |
| | | 06.12.01 | 22:31 | 36° 36.832 S | 74° 59.740 W | | 46.47 km |
| SO161-113 | | 06.12.01 | 22:31 | 36° 36.832 S | 74° 59.740 W | 95° | G M P |
| | | 07.12.01 | 00:17 | 36° 36.832 S | 74° 34.845 W | | 37.23 km |
| SO161-114 | | 07.12.01 | 00:17 | 36° 36.832 S | 74° 34.845 W | 38° | G M P |
| | | 07.12.01 | 03:55 | 36° 00.008 S | 74° 00.009 W | | 85.72 km |
| SO161-115 | | 07.12.01 | 03:55 | 36° 00.008 S | 74° 00.009 W | 25° | G M P |
| | | 07.12.01 | 14:21 | 34° 00.000 S | 73° 00.000 W | | 240.13 km |

| Line number | Shot points | Date | Time | Position | | Course | Methods |
|---|---|---|---|---|---|---|---|
| SO161-116 | | 07.12.01 | 14:21 | 34° 00.000 S | 73° 00.000 W | 3° | G M P |
| | | 07.12.01 | 22:23 | 32° 24.018 S | 72° 54.906 W | | 177.91 km |
| SO161-202A | 1 | 08.12.01 | 18:44:41 | 32° 05.001 S | 73° 09.096 W | 90° | S G M P |
| | 47 | 08.12.01 | 19:18:41 | 32° 05.019 S | 73° 05.775 W | | 145.31 km |
| SO161-202AB | 1 | 08.12.01 | 19:21:00 | 32° 05.013 S | 73° 05.552 W | | |
| | 33 | 08.12.01 | 19:44:41 | 32° 05.043 S | 73° 03.234 W | | |
| SO161-202AC | 1 | 08.12.01 | 19:46:06 | 32° 05.043 S | 73° 03.104 W | | |
| | 1324 | 09.12.01 | 10:28:06 | 32° 04.996 S | 71° 36.465 W | | |
| SO161-202B | 1 | 09.12.01 | 11:01:00 | 32° 04.994 S | 71° 37.373 W | 269° | S G M P |
| | 1248 | 10.12.01 | 07:48:00 | 32° 05.990 S | 73° 39.981 W | | 192.35 km |
| S161-117 | | 12.12.01 | 02:41 | 32° 27.451 S | 73° 30.462 W | 315° | G M P |
| | | 12.12.01 | 05:40 | 32° 01.672 S | 74° 30.462 W | | 67.74 km |
| SO161-203 | 1 | 12.12.01 | 06:55:00 | 32° 04.320 S | 74° 35.844 W | 134° | S G M P |
| | 1445 | 13.12.01 | 06:59:00 | 33° 24.535 S | 72° 53.943 W | | 217.36 km |
| SO161-118 | | 14.12.01 | 15:56 | 33° 13.857 S | 74° 16.809 W | 239° | G M P |
| | | 14.12.01 | 17:39 | 33° 24.380 S | 74° 37.779 W | | 37.81 km |
| SO161-204 | 1 | 14.12.01 | 18:44:00 | 33° 20.272 S | 74° 41.475 W | 60° | S G M P |
| | 1314 | 15.12.01 | 16:37:00 | 32° 25.269 S | 72° 49.488 W | | 201.84 km |
| SO161-119 | | 16.12.01 | 13:56 | 33° 08.751 S | 74° 21.018 W | 2° | G M P |
| | | 16.12.01 | 17:43 | 32° 25.100 S | 74° 19.995 W | | 80.87 km |
| SO161-120 | | 16.12.01 | 17:43 | 32° 25.100 S | 74° 19.995 W | 40° | G M P |
| | | 16.12.01 | 18:50 | 32° 15.023 S | 74° 09.920 W | | 24.37 km |
| SO161-121 | | 16.12.01 | 18:50 | 32° 15.023 S | 74° 09.920 W | 90° | G M P |
| | | 16.12.01 | 22:11 | 32° 14.991 S | 73° 25.429 W | | 69.67 km |
| SO161-122 | | 16.12.01 | 22:11 | 32° 14.991 S | 73° 25.429 W | 0° | G M P |
| | | 17.12.01 | 00:42 | 31° 45.009 S | 73° 25.415 W | | 55.51 km |
| SO161-123 | | 17.12.01 | 00:42 | 31° 45.009 S | 73° 25.415 W | 270° | G M P |
| | | 17.12.01 | 03:38 | 31° 45.084 S | 73° 59.953 W | | 54.37 km |
| SO161-124 | | 17.12.01 | 03:38 | 31° 45.084 S | 73° 59.953 W | 177° | G M P |
| | | 17.12.01 | 05:01 | 31° 55.002 S | 73° 59.698 W | | 18.37 km |
| SO161-125 | | 17.12.01 | 05:01 | 31° 55.002 S | 73° 59.698 W | 90° | G M P |
| | | 17.12.01 | 10:25 | 31° 54.999 S | 72° 50.209 W | | 109.19 km |
| SO161-126 | | 17.12.01 | 10:25 | 31° 54.999 S | 72° 50.209 W | 60° | G M P |
| | | 17.12.01 | 16:00 | 31° 22.102 S | 71° 45.211 W | | 120.14 km |

| Line number | Shot points | Date | Time | Position | | Course | Methods |
|---|---|---|---|---|---|---|---|
| SO161-127 | | 17.12.01<br>17.12.01 | 16:00<br>16:00 | 31° 22.102 S<br>31° 01.267 S | 71° 45.211 W<br>71° 44.808 W | 357° | G M P<br>38.63 km |
| SO161-205A | 1<br>1695 | 18.12.01<br>18.12.01 | 07:28:31<br>21:35:33 | 30° 59.991 S<br>30° 59.982 S | 73° 05.637 W<br>71° 42.940 W | 90° | S G M P<br>131.25 km |
| SO161-205B | 1<br>1212 | 18.12.01<br>19.12.01 | 22:15:00<br>18:26:00 | 30° 59.999 S<br>30° 59.988 S | 71° 45.448 W<br>73° 44.114 W | 270° | S G M P<br>188.34 km |
| SO161-128 | | 19.12.01<br>19.12.01 | 18:51<br>20:57 | 31° 00.204 S<br>30° 59.987 S | 73° 46.333 W<br>73° 16.688 W | 90° | G M P<br>47.03 km |

Methods used:

| | |
|---|---|
| G | - gravity |
| M | - magnetics |
| P | - Simrad,Parasound |
| S | - seismics |